



# THE UNIVERSITY *of* EDINBURGH

This thesis has been submitted in fulfilment of the requirements for a postgraduate degree (e.g. PhD, MPhil, DClinPsychol) at the University of Edinburgh. Please note the following terms and conditions of use:

This work is protected by copyright and other intellectual property rights, which are retained by the thesis author, unless otherwise stated.

A copy can be downloaded for personal non-commercial research or study, without prior permission or charge.

This thesis cannot be reproduced or quoted extensively from without first obtaining permission in writing from the author.

The content must not be changed in any way or sold commercially in any format or medium without the formal permission of the author.

When referring to this work, full bibliographic details including the author, title, awarding institution and date of the thesis must be given.

---

# Electrospinning for Skin Tissue Engineering and Drug-Eluting Antimicrobial Biomaterials

---

Antonios Keirouz



A thesis presented for the degree of  
Doctor of Philosophy

University of Edinburgh  
School of Engineering  
Year of Submission 2020

**Title**

Electrospinning for skin tissue engineering and drug-eluting antimicrobial biomaterials

© December 2020

**Author**

Antonios (Tony) Keirouz

**Supervisors**

Dr Norbert Radacsi (School of Engineering, The University of Edinburgh, UK)

Dr Giuseppino Fortunato (Empa, St. Gallen, Switzerland)

Dr Anthony Callanan (School of Engineering, The University of Edinburgh, UK)

Prof Vasileios Koutsos (School of Engineering, The University of Edinburgh, UK)

**Location**

Edinburgh, UK

The author would like to express his gratitude to the School of Engineering of the University of Edinburgh and the Swiss Federal Laboratories for Materials Science and Technology (Empa) for co-funding this PhD studentship.

---

# Abstract

---

A critical challenge in the design of biomaterials for tissue engineering relies on the development of tissue-specific biomimetic scaffolds capable of replacing cell-matrix interactions required for the repair of injured tissues. Further, such biomaterials with the additional capacity to prevent bacteria contamination can resolve issues surrounding surgical prosthesis infection. Fibrous micro- and nanostructures are extensively researched in tissue engineering due to their intrinsic similarities to decellularised human tissues. Among the several fibre-forming processes, electrospinning has drawn much attention due to its ability to produce scaffolds that morphologically resemble the native extracellular matrix (ECM) of human tissues.

Electrospinning is a versatile method that uses electrohydrodynamic principles to produce fibres with diameters ranging from microns to tens of nanometres. By varying the chemistry and morphology of the fibres, it is feasible to attain different physiological and mechanical responses. The wide array of raw natural and synthetic materials – including polymers and complex molecules – that can be used to electrospin fibres can resolve well-documented problems associated with the inferiority of synthetic biomaterials and the limitations of biological tissues.

In this thesis, electrospinning is utilised to contribute to the engineering of advanced ECM-mimicking biomaterials. The work will focus on (1) improving the physicochemical and mechanical responses of skin substitutes and (2) preventing mesh-associated surgical site infection.

The initial study of this thesis presents the design and construction of a nozzle-free electrospinning device, which is an economically viable method of scaling-up fibre production output. The equipment is then used to fabricate elastic skin-like composite nanofibres consisting of poly(vinylpyrrolidone) (PVP) and poly(glycerol sebacate) (PGS). The findings indicate that the mechanical properties of the electrospun mats could be tuned by varying the concentration of PGS and the molecular weight of PVP within the blends. Photocrosslinking the fibres prevented the rapid degradation of the composite mats due to the hydrophilic nature of PVP, making it feasible to assess the biological responses of the construct *in vitro*, displaying good viability and proliferation of human dermal fibroblasts. This study provides a different approach towards the development of skin substitutes, based on the fact that

mechanical stimuli influence the ability of dermal cells to adapt and reconstruct the ECM at an injured site; being able to adjust the mechanics to those of different anatomical sites of the body can have a positive effect on the overall outcome of a healing wound.

Synthetic biomaterials tend to present suboptimal cell growth and proliferation, with many studies linking this phenomenon to the hydrophobicity of such surfaces. This thesis continues with the development of a protocol for silk fibroin extraction from *Bombyx mori* cocoons, which achieved significantly increased yields of the protein in a third of the time required by the conventional molecular cut-off extraction approach. The extracted silk fibroin was then used to produce electrospun membranes consisting of poly(caprolactone) (PCL) blended with variant forms of PGS. The main aim of this work was the development of fibre mats with tuneable hydrophobicity/hydrophilicity properties, depending on the esterification degree and concentration of PGS within each composite. By altering the surface properties of the electrospun membranes, the trinary composite biomaterial presented improved fibroblast attachment behaviour and optimal growth in comparison to PCL-only fibrous mats.

The study continued with the development of an ultralight-weight nanostructured bicomponent antimicrobial construct with a similar microstructure to biologic meshes, which preserved the required mechanical integrity of synthetic mesh materials. A core/shell nanofibrous structure was developed, consisting of nylon-6 in the core and chitosan/polyethylene oxide in the shell. The bicomponent fibre structure comprised a binary antimicrobial system incorporating 5-chloro-8-quinolinol in the chitosan-shell, with the sustained release of poly(hexanide) from the nylon-6 core of the fibres. The antimicrobial nanofibres were found to elicit a robust bactericidal response, *in vitro*, against the two most commonly occurring pathogenic bacteria in deep incisional surgical site infections; *Staphylococcus aureus* and *Pseudomonas aeruginosa*. The results of this study advocate that the bicomponent nanofibres developed can be a promising alternative to biologic meshes, employed for hernia repair today, due to similar architecture and mechanics, but at the same time capable of actively protecting the patient from subsequent mesh-associated infections, thus tackling this life-threatening postoperative complication.

Overall, the work in this thesis has expanded upon the fields of skin tissue engineering and drug-eluting antimicrobial biomaterials, potentially guiding new areas of research.

---

# Lay Summary

---

Tissue engineering is a rapidly evolving interdisciplinary field that applies the principles of engineering and life sciences to restore or replace tissue functions. It is among the major domains of biomedical engineering, where the goal is to develop advanced biomaterials with the ability to mimic complex tissues. This involves the integration of scaffold matrices with cells, which can then support their viability and promote growth.

This thesis involves the use of a technique called electrospinning to advance the properties of such biomaterials. Electrospinning is an emerging fabrication technology that has attracted considerable attention in recent years in fields ranging from medicine and tissue engineering to energy and environmental science due to the ease of producing well-defined, fibrous woven or nonwoven materials. The process begins when a polymer solution or melt is exposed to a high electric field that causes it to deform and spin, which manipulates it to very fine meshes of micro-/nanostructured fibres. The constant advancement and unfolding of such material, along with the beneficial features of micro-/nanoscale structures, have made them eligible candidates for the progress and development of an array of therapies.

The two key areas touched upon in this thesis encompass biomaterials for wound healing in the form of biocompatible dermal substitutes and the development of antimicrobial prostheses capable of preventing post-operative hernia mesh infection.

Initially, a high-throughput free-surface electrospinning device was constructed, capable of solving issues associated with the meagre production rate of the traditional electrospinning process. This device permits the scaling-up of electrospinning by allowing for filaments to form from a wider surface rather than the conventionally used needle-tip. After this, a novel approach was employed to extract higher quantities of the silk fibroin protein in reduced processing time from silkworm cocoons. This was then used to produce a range of novel biocompatible skin-like constructs by integrating the properties of variant synthetic and natural polymers. By adjusting the chemistry and proportion of each material used, it was feasible to tune the mechanics and wetting properties of the developed constructs, ultimately attaining good biocompatibility and cellular proliferation required for wound healing and tissue repair.

On a different note, post-surgical infections affect millions of people, and likewise cost billions; thus, making it a prevalent problem. While advances have been made in infection

control practices, surgical site infections remain a substantial cause of morbidity, prolonged hospitalisation, and death. In the case of hernia treatment, battling an infection that has settled on an implantable mesh is an arduous process.

Surgical meshes are used to provide additional support to weakened or damaged tissue. However, when an infection occurs directly on the mesh, the bacteria can colonise the foreign material, where antibiotics cannot adequately defeat the infection due to the blood-mesh barrier. Thus, the only viable option is the removal of the hernia mesh – something that can significantly increase the chances of hernia reoccurrence, along with all the surgery-related implications.

The hernia meshes available on the market today are textile-based products that provide good mechanics but lack any antimicrobial properties. Hence, part of this thesis focused on the development of a prosthetic mesh that can further protect patients from bacterial infections.

A variation of the conventional electrospinning technique described earlier, referred to as co-axial electrospinning, was used, capable of formulating drug-containing fibres that present properties of different materials in a fibre-within-a-fibre format. The developed bicomponent nanofibrous construct was able to attain the sustained release of a dual antimicrobial system, capable of suppressing the growth of the pathogenic bacteria commonly associated with surgical site infections while presenting the suitable mechanical and physicochemical properties required for hernia repair.

The work presented in this thesis advocates the significance of the electrospinning process towards the engineering of state-of-the-art nanofibrous biomaterials, by exploring new avenues of research for the advancement of skin substitutes and antimicrobial hernia meshes.

---

# Declaration of Originality

---

I hereby declare that this thesis has been composed by myself and that the work contained, including sections deriving from published peer-reviewed articles that I have first-authored, is my own, except where stated. In addition, I divulge that this work has not been previously submitted for any other degree or professional qualification.

*Antonios Keirouz*

December 2020



In the memory of Dr Giuseppino Fortunato

(17 Mar. 1966 – 30 Jun. 2020)

---

# Acknowledgements

---

I would like to take this opportunity to thank the following people who made this thesis possible.

Thank you to my principal supervisor Dr Norbert Radacsi for your support and unwavering encouragement towards my research and personal development. I would also like to express my sincere gratitude to my co-first supervisor, late Dr Giuseppino Fortunato. Pino was an inspiring and compassionate mentor and instrumental in defining the path of my thesis. He will always be remembered fondly and missed by so many.

My sincere appreciation goes to my assistant supervisors, Prof Vasileios Koutsos and Prof René Rossi, for your dedicated time, guidance, valuable input, financial support, and for the opportunities given to disseminate my work. For your positive criticism towards my work and valuable advice in the early stages, thank you to Dr Anthony Callanan.

It goes without saying that interdisciplinary work is not feasible without the assistance and input of many experts. I would like to thank Dr Qun Ren and Prof Katharina Maniura-Weber for your feedback, and for allowing me to use your S2-lab facilities to conduct the bacteria work at Empa. Thank you, as well, to Prof Guido Beldi for your insights towards the hernia mesh requirements from a surgeon's perspective.

I want to express a special note of gratitude for the time given to me by Dr Michael Chen, Dr Mike Davidson, Prof Alex Dommann, Dr Colin Roberts, Dr Junxi Wu, Dr Coinneach Dover, Luzia Wiesli, Katalin Kis, Liliane Diener, David Stewart, Straub Herve, Jules Velentin, Maria Kana, Wesley Shao, Fergus Ferguson, and whomever I may have forgotten.

A special thank you goes to my friend and colleague Jean Scholler, that as a chemist was invaluable in assisting me at many stages of my work at Empa. An immense thank you to Mariia Zakharova and David Kwon, the students I supervised, for their support with experiments at the Nanomaterials Laboratory at the University of Edinburgh.

I believe that it is paramount to express my gratitude towards the sixteen peer-reviewers that dedicated their valuable time to transform the published work presented in this thesis. Thank you, whole-heartedly, to Gregory Myles, Kate, Lilian for willing to read through my thesis and provide valuable feedback and suggestions, and to surgeon Dr Dimitrios Damaskos for your valued input while proofreading the hernia-related section of my literature review.

I am deeply grateful for the colleagues and new friends I have gained at King's Buildings and Empa, making these past years irreplaceable and pleasant to remember. A special thanks to all my lovely friends here and back home that helped make this difficult time more bearable. Thank you, Roberta, for encouraging me to pursue this degree and for your early on tutoring over mechanical engineering concepts.

Last and foremost, there are no words to thank my mom and dad, Harriet and Tony, my sister Stella, and my grandma, for their unconditional support throughout my life. I could not have been more fortunate than having such a supportive, loving, and close-knit family. Finally, to my partner Virag, for being patiently and consistently there for me in every way, and for getting to the point that she can now explain to others my research.

This work goes to all those who have directly or indirectly contributed to my personal and professional development, and to the completion of this thesis. Thank you.

---

# Publications & Conference Contributions

---

## Research articles

**Keirouz, A.**; Fortunato, G.; Zhang, M.; Callanan, A.; Radacsi, N. Nozzle-free electrospinning of polyvinylpyrrolidone/poly(glycerol sebacate) fibrous scaffolds for skin tissue engineering applications. *Medical Engineering & Physics*, 2019, 71 (1), 56-67.

DOI: 10.1016/j.medengphy.2019.06.009.

**Keirouz, A.**; Zakharova, M.; Kwon, J.; Robert, C.; Koutsos, V.; Callanan, A.; Chen, X.; Fortunato, G.; Radacsi, N. High-throughput production of silk fibroin-based electrospun nanofibres as a biomaterial for skin tissue engineering applications. *Materials Science & Engineering C*, 2020, 112 (1), 1-11. DOI: 10.1016/j.msec.2020.110939.

**Keirouz, A.**; Radacsi, N.; Ren, Q.; Dommann, A.; Beldi, G.; Maniura-Weber, K.; Rossi, R.M.; Fortunato, G. Nylon-6/chitosan core/shell antimicrobial nanofibres for the prevention of mesh-associated surgical site infection. *Journal of Nanobiotechnology*, 2020, 18 (1), 1-17.

DOI: 10.1186/s12951-020-00602-9

Tan, H.L.; Kana, M.; Putri, S.; Idris, S.S.; Hartikainen, N.; Bakar, N.F.; **Keirouz, A.**; Radacsi, N. High-throughput fabrication of carbonized electrospun polyacrylonitrile/poly(acrylic acid) nanofibres with additives for enhanced electrochemical sensing. *Journal of Polymer Science*, 2020, 137 (43), 1-15. DOI: 10.1002/app.49341.

Waqas, M.; **Keirouz, A.**; Kana, M.; Fazal, F.; Diaz-Sanchez, F.J.; Roy, D.; Koutsos, V.; Radacsi, N. Nozzle-free electrospinning setup for low cost and high yield production of nanofibers. Co-first author. Submitted.

Vong, M.; Diaz-Sanchez, F.J.; **Keirouz, A.**; Nuansing, W.; Radacsi, N. 3D electrospinning: A technology for the facile and precise fabrication of 3d macrostructures with microfibrillar features. Submitted.

## Review papers

**Keirouz, A.**; Chung, M.; Kwon, J.; Fortunato, J.; Radacsi, N. 2D and 3D electrospinning technologies for the fabrication of nanofibrous scaffolds for skin tissue engineering: a review. *Wiley Interdisciplinary Reviews: Nanomedicine and Nanobiotechnology*, 2020, 12 (4), 1-32. DOI: 10.1002/wnan.1626.

Cleeton, C.; **Keirouz, A.**; Chen, X.; Radacsi, N. Electrospun nanofibres for drug delivery and biosensing. *ACS Biomaterial Science & Engineering*, 2019, 5 (9), 4183-4205. DOI: 10.1021/acsbomaterials.9b00853.

Sivanesvaran, S.; **Keirouz, A.**; Loening, U.; Radacsi, N. Effects of strong fields in living organisms: A review. In preparation.

**Keirouz, A.**; Wang, Z.; Nagy, Z.M.; Vass, P.; Williams, G.; Buzgo, M.; Nuansing, W.; Radacsi, N. The history of electrospinning: past, present, and future developments. In preparation.

## Conferences

**Keirouz, A.**; Fortunato, G.; Callanan, A.; Radacsi, N. Needleless electrospinning of PVP/PGS blends for skin tissue scaffold fabrication. Poster presentation (1st place – best presentation award). **Electrospin2018, The 5<sup>th</sup> International Conference on Electrospinning, January 16–18, 2018, Stellenbosch, South Africa.**

**Keirouz, A.**; Radacsi, N.; Ren, Q.; Fortunato, G. Electrospun nylon-6-poly(hexanide)/chitosan-5-chloro-8-quinolinol core/shell antimicrobial nanofibers for the prevention of surgical site infection on hernia meshes. Oral presentation. **Electrospin2019, The 6<sup>th</sup> International Conference on Electrospinning, June 19–21, 2019, Shanghai, China.**

**Keirouz, A.**; Zakharova, M.; Kwon, J.; Callanan, A.; Koutsos, V.; Fortunato, G.; Radacsi, N. Nozzle-free electrospinning of PCL-backbone silk fibroin/poly(glycerol sebacate) fibrous skin substitute membranes. Poster presentation. **Electrospin2019, The 6<sup>th</sup> International Conference on Electrospinning, June 19–21, 2019, Shanghai, China.**

**Keirouz, A.**; Radacsi, N.; Ren, Q.; Dommann, A.; Beldi, G.; Maniura-Weber, K.; Rossi, R.M.; Fortunato, G. Nylon-6/chitosan core/shell nanofibers with spatially controlled release of

antimicrobials for the prevention of surgical site infection on hernia meshes. Poster presentation. **NART-2019, The Institute for Nanomaterials, Advanced Technologies and Innovation, Technical University of Liberec, September 18–20, 2019, Liberec, Czech Republic.**

**Keirouz, A.;** Callanan, A.; Koutsos, V.; Radacsi, N.; Fortunato, G. Co-axially electrospun hernia meshes with spatially-controlled release of antimicrobials. **The University of Edinburgh, School of Engineering Conference, April 15, 2018, Edinburgh, United Kingdom.**

**Keirouz, A.;** Radacsi, N.; Ren, Q.; Rossi, R.M.; Fortunato, G. Nylon-6/chitosan core/shell nanofibers with spatially controlled release of antimicrobials for the prevention of surgical site infection on hernia meshes. Oral presentation. **BioMedEng2019, Imperial College, September 5–6, 2019, London, United Kingdom.**

**Keirouz, A.;** Fortunato, G.; Koutsos, V.; Radacsi, N. Developing advanced nanofibrous moieties via electrospinning for tissue engineering. Oral presentation. **Tissue Engineering and Regenerative Medicine International Society (TERMIS), European Chapter Meeting 2020, May 26–29, 2020, Manchester, United Kingdom.** Abstract published; conference postponed due to COVID-19.

**Keirouz, A.** Drug-eluting antimicrobial textiles fabricated through electrospinning: trends, advantages, and limitations. Virtual seminar on biomedical textiles for tissue engineering. Invited speaker. **North Carolina State University, June 22, 2020, United States (webinar).**

---

# Table of Contents

---

Abstract.....	ii
Lay Summary.....	iv
Declaration of Originality.....	vi
Acknowledgements.....	viii
Publications & Conference Contributions.....	x
Table of Contents.....	xiii
List of Figures.....	xviii
List of Tables.....	xxii
Acronyms.....	xxiv
Nomenclature.....	xxviii
<b>1. Introduction.....</b>	<b>1</b>
1.1 Problem statement and motivation.....	1
1.2 Thesis aims and objectives.....	5
1.3 Thesis outline.....	6
1.4 References.....	8
<b>2. Literature Review.....</b>	<b>11</b>
2.1 Skin physiology and function.....	11
2.1.1 Components of the skin.....	11
2.1.2 Layers and functions of the skin.....	12
2.1.3 The role of the extracellular matrix (ECM).....	14
2.1.4 Anatomical characteristics and mechanics of the skin.....	17
2.2 Skin burns and wounds.....	19
2.2.1 Classifications of wound types.....	19
2.2.2 The wound healing cascade.....	20
2.3 Skin tissue engineering so far; advances and challenges.....	24
2.3.1 Traditional and impregnated dressings.....	24

2.3.2	Current treatment and management options for excessive and chronic wounds ....	26
2.3.3	New trends of electrospun biomaterials for wound healing.....	28
2.4	Hernia.....	32
2.4.1	Hernia mesh architecture: morphological, physiochemical and mechanical properties.....	34
2.4.2	Mesh-specific surgical infections.....	39
2.4.3	Current advancements and future perspectives in hernia mesh development .....	45
2.5	Electrospinning.....	48
2.5.1	Principles of electrospinning .....	48
2.5.1.1	Jetting mechanism, fibre growth and deposition .....	51
2.5.1.2	Parameters affecting the electrospinning process .....	54
2.6	Co-axial electrospinning .....	60
2.7	Nozzle-free electrospinning .....	63
2.8	Selection of polymers and antimicrobial agents .....	66
2.8.1	Natural and synthetic polymers.....	66
2.8.2	Polymers .....	67
2.8.3	Antimicrobial agents .....	72
2.9	Conclusions .....	75
2.10	References.....	76
<b>3.</b>	<b>General Materials &amp; Methods.....</b>	<b>97</b>
3.1	Introduction.....	97
3.2	Scaffold fabrication by electrospinning.....	97
3.3	Materials .....	98
3.3.1	Poly(glycerol sebacate) (PGS).....	98
3.3.2	Stock chemicals, reagents, cells and equipment.....	101
3.4	Characterisation .....	106
3.4.1	Scanning electron microscopy (SEM) .....	107
3.4.1.1	Determining the fibre diameter, pore size and porosity .....	107
3.4.2	Transmission electron microscopy (TEM) .....	108
3.4.3	Fourier transform infrared (FTIR) spectroscopy .....	109



3.4.4 X-ray photoelectron spectroscopy (XPS) .....	109
3.4.5 Mechanical testing .....	110
3.4.6 Thermogravimetric analysis (TGA).....	113
3.4.7 Differential scanning calorimetry (DSC) .....	114
3.4.8 Water contact angle (WCA) measurements .....	115
3.4.9 Degradation studies.....	116
3.4.10 <i>In vitro</i> drug release studies.....	117
3.5 <i>In vitro</i> biocompatibility evaluation .....	119
3.5.1 Scaffold sterilisation.....	119
3.5.2 Cell culture technique .....	120
3.5.3 Cell seeding efficiency (SE) .....	121
3.5.4 Cell proliferation.....	122
3.5.5 Fixing cells for SEM imaging.....	123
3.6 Antimicrobial testing on S2 pathogenic bacterial strains .....	124
3.6.1 Disc diffusion susceptibility testing .....	124
3.6.2 Bacterial growth kinetics using spectrophotometry .....	125
3.6.3 Fluorescence and confocal microscopy (live/dead assay) .....	126
3.6.4 Fixing bacteria for SEM imaging .....	126
3.7 Statistical analysis.....	127
3.8 References.....	128
<b>4. Nozzle-Free Electrospinning of PVP/PGS Blends; Design, Fabrication &amp; Characterisation</b> .....	<b>131</b>
4.1 Introduction.....	131
4.2 Methodology .....	131
4.2.1 Device development.....	132
4.2.2 Preparation of PVP/PGS Blends .....	136
4.2.3 Scaffold fabrication and processing .....	136
4.2.4 UV crosslinking of PVP/PGS mediated by riboflavin .....	137
4.3 Results and discussion.....	142
4.3.1 Production rate of the nozzle-free device.....	142

4.3.2 The effect of varying the molecular weight of PVP on the fibre morphology .....	143
4.3.3 Chemical characterisation.....	146
4.3.4 Tuning the mechanical properties of the composite fibres.....	148
4.3.5 Wettability.....	151
4.3.6 Cellular behaviour of HDFs in response to the PVP/PGS scaffolds <i>in vitro</i> .....	152
4.4 Conclusions .....	157
4.5 References.....	158
<b>5. Nozzle-Free Electrospinning of Silk Fibroin-Based Composite Scaffolds for Skin Regeneration .....</b>	<b>163</b>
5.1 Introduction.....	163
5.2 Methodology .....	165
5.2.1 Extraction and purification of the silk fibroin protein.....	165
5.2.2 Preparation of binary and trinary electrospinning solutions.....	167
5.2.3 High-throughput scaffold fabrication and processing.....	168
5.3 Results and discussion.....	169
5.3.1 Electrospun scaffold morphology .....	169
5.3.2 Chemical analysis and fibre surface composition.....	173
5.3.3 The influence of PGS in the degradation of the electrospun mats .....	176
5.3.4 Wettability.....	179
5.3.5 Cell adhesion, viability, and proliferation .....	182
5.4 Conclusions .....	186
5.5 References.....	187
<b>6. Core/Shell Bicomponent Antimicrobial Nanofibres for the Prevention of Mesh -Associated Bacterial Infections .....</b>	<b>191</b>
6.1 Introduction.....	191
6.2 Methodology .....	193
6.2.1 Solution preparation.....	195
6.2.2 Co-axial electrospinning .....	195
6.3 Results and discussion.....	197
6.3.1 Electrospun fibre morphology and core/shell structure.....	197

6.3.2 Chemical composition of the core/shell electrospun NFs .....	203
6.3.3 Surface chemistry of the core/shell PA6-PHMB/CS-5CL8Q NFs.....	205
6.3.4 Thermal properties and PA6 content within the core/shell NFs .....	206
6.3.5 Mechanical characteristics of the produced core/shell NFs .....	210
6.3.6 Drug release mechanism of the antimicrobial NFs .....	212
6.3.6.1 The release kinetics of the single-drug containing NFs.....	212
6.3.6.2 The effect of the core/shell structure in the release of PHMB .....	213
6.3.7 Antimicrobial activity of the single and core/shell NFs .....	214
6.4 Conclusions .....	221
6.5 References.....	223
<b>7. Conclusions &amp; Recommendations.....</b>	<b>227</b>
7.1 Concluding remarks .....	227
7.1.1 Conclusions regarding the skin-substitute, biomaterials.....	228
7.1.2 Conclusions regarding the nanostructured antimicrobial hernia mesh.....	232
7.1.3 Research and experimental limitations.....	234
7.2 Thesis contributions .....	237
7.3 Recommendations and future directions.....	241
7.4 References.....	245
<b>Appendix A: Supplement.....</b>	<b>249</b>
<b>Appendix B: Copyright Permissions, Publications and Conferences.....</b>	<b>265</b>
<b>Appendix C: Grafting PHMB on O-Carboxymethylated Chitosan.....</b>	<b>287</b>

---

# List of Figures

---

## Chapter 2

<b>Figure 2.1</b> Antimicrobial peptides (AMPs) secreted from the skin offer direct and indirect pathogen protection pathways.....	12
<b>Figure 2.2</b> Schematic representation of the structure of the skin layers and appendages ...	13
<b>Figure 2.3</b> Schematic representation of the cell-ECM interactions on different substrates and ECM remodelling .....	16
<b>Figure 2.4</b> The wound healing cascade.....	23
<b>Figure 2.5</b> Morphological characteristics of synthetic versus biologic mesh reinforcement.	37
<b>Figure 2.6</b> Comparisons between the bacterial colonisation on synthetic mono-/multifilament, absorbable and biologic surgical meshes .....	42
<b>Figure 2.7</b> Fundamentals of electrospinning .....	49
<b>Figure 2.8</b> Structural diversity of individual electrospun fibre morphologies.....	50
<b>Figure 2.9</b> The effect of solution viscosity towards polymer solution electrospinnability.....	57
<b>Figure 2.10</b> Generation of co-axial electrospun fibres .....	62
<b>Figure 2.11</b> Free-surface electrospinning.....	65
<b>Figure 2.12</b> The condensation polymerisation reaction of glycerol and sebacic acid that yields the poly(glycerol sebacate) polyester.....	68
<b>Figure 2.13</b> Chemical structures of the synthetic polymers.....	69
<b>Figure 2.14</b> Chemical structure of the silk fibroin (SF) protein.....	71
<b>Figure 2.15</b> Chemical structure of chitosan.....	72
<b>Figure 2.16</b> Chemical structures of the antimicrobial substances .....	74

## Chapter 3

<b>Figure 3.1</b> Standards for determining tensile properties of thin films and sheets.....	111
<b>Figure 3.2</b> Stress-strain curve of "model" fibre specimen.....	113

## Chapter 4

<b>Figure 4.1</b> Schematic of the nozzle-free electrospinning device .....	134
<b>Figure 4.2</b> Schematic illustration providing an overview of the PGS synthesis, solution preparation and electrospinning that results in stretchable semi-transparent fibrous mats. 137	
<b>Figure 4.3</b> Energy gaps of the different electronic transitions upon light absorption.....	138
<b>Figure 4.4</b> Schematic representation of the PVP/PGS crosslinking mediated by riboflavin under UV light. ....	141
<b>Figure 4.5</b> Comparison of the production rate between the in-house built nozzle-free electrospinning device, and a commercial needle-based electrospinning device.....	142
<b>Figure 4.6</b> Electrospun scaffolds morphology of the PVP/PGS fibres.....	144
<b>Figure 4.7</b> Photographs depicting the transparency of the electrospun membranes apropos to the incremental increase in the proportion of PGS within the PVP/PGS blends.....	145
<b>Figure 4.8</b> ATR-FTIR spectra of (a) sebacic acid, (b) glycerol, (c) PGS gel, (d) PVP powder and (e) PVP/PGS 60:40 fibres.....	147
<b>Figure 4.9</b> Representative tensile stress-strain curves of the various PVP/PGS fibrous membranes. PVP/PGS ratio of (a) 80:20, (b) 70:30, (c) 60:40 and (d) 50:50. ....	150
<b>Figure 4.10</b> Water contact angle measurements of the electrospun PVP/PGS 60:40 fibres irradiated with ultraviolet light for 0, 30 and 60 min.....	151
<b>Figure 4.11</b> The proliferation of HDFs on the PVP/PGS scaffolds of variant proportions ...	153
<b>Figure 4.12</b> Cell spreading area occupied by the HDFs after 3 and 5 days of incubation on the electrospun PVP/PGS scaffolds of variant ratios .....	156

## Chapter 5

<b>Figure 5.1</b> Silk fibroin extraction and processing to obtain the regenerated form .....	166
<b>Figure 5.2</b> Schematic representation of the nozzle-free electrospinning process, showing a macrograph of the produced fibrous scaffold and SEM micrographs of the fibres, with and without fibroblasts. ....	168
<b>Figure 5.3</b> Average fibre diameters of the (a) ternary, SF:PCL:PGS and SF:PCL:pPGS, and (b) binary, SF:PGS and SF:pPGS, blends .....	170
<b>Figure 5.4</b> ATR-FTIR spectra of (a) the individual polymers and the (b) binary and ternary electrospun mats. Scaffolds that contain PGS are shown in blue, whereas scaffolds that contain pPGS are shown in pink. Binary blend ratios were SF:(p)PGS 2:1 (w/w), whereas the ternary SF:PCL:(p)PGS ratio was 1:0.5:0.5 (w/w).....	174
<b>Figure 5.5</b> XPS survey of the ternary SF:PCL:(p)PGS and binary SF:(p)PGS electrospun mats .....	175

<b>Figure 5.6</b> Percentage of mass loss for the PGS-containing fibres, at varying incubation times. Blend (w/w) ratios of (a) SF:PCL:PGS, and (b) SF:PCL:(p)PGS .....	177
<b>Figure 5.7</b> Fibroin crystallinity. Macroscopic observation of the effects of ethanol, (a) before and (b) after the treatment of SF:PCL:(p)PGS electrospun mats.....	178
<b>Figure 5.8</b> Water contact angle over time. PCL, binary SF:PGS and SF:pPGS and trinary PCL-backbone SF:PGS and SF:pPGS electrospun mats .....	180
<b>Figure 5.9</b> Water contact angle measurements of the trinary SF:PCL:(p)PGS, binary SF:(p)PGS and PCL electrospun mats .....	182
<b>Figure 5.10</b> Attachment and proliferation of HDFs on SF:PCL:(p)PGS electrospun membranes .....	183
<b>Figure 5.11</b> Comparisons of fibroblast morphologies, assessed by SEM, after seeding on (a, c) trinary SF:PCL:(p)PGS or (b, d) PCL electrospun mats.....	184
<b>Figure 5.12</b> Cryo-FIB-SEM micrographs obtained from trinary SF:PCL:(p)PGS scaffolds, 5-days after being seeded with fibroblasts.....	185

## Chapter 6

<b>Figure 6.1</b> Schematic diagram depicting the fabrication methodology used to produce the core/shell PA6-PHMB/CS-5CLO8Q nanofibrous mats and the subsequent experimental and investigative scheme followed in this study.....	194
<b>Figure 6.2</b> Schematic representation of the co-axial, electrospinning setup used for the production of core/shell PA6-PHMB/CS-5CLO8Q nanofibrous membranes.....	196
<b>Figure 6.3</b> Nanofibre structures and surface morphologies of the electrospun mats. (a) Macrograph of the electrospun mat. SEM micrographs of (b) CS, (c) PA6, (d) CS-5CLO8Q, (e) PA6-PHMB, and (f) core/shell PA6-PHMB/CS-5CLO8Q electrospun mats. (g-i) TEM micrographs of the core/shell PA6-PHMB/CS-5CLO8Q nanofibrous mats.....	198
<b>Figure 6.4</b> Fibre diameter distributions of the electrospun (a) CS, (b) PA6, (c) CS-5CLO8Q, (d) PA6-PHMB, and (e) core/shell PA6-PHMB/CS-5CLO8Q nanofibrous mats.....	199
<b>Figure 6.5</b> TEM micrographs of the PA6-PHMB/CS-5CLO8Q core/shell NFs formulated using various flow rates, under the same electrospinning and solution parameters..	201
<b>Figure 6.6</b> Water contact angles of the electrospun NFs, both with and without antimicrobial agents, and the drug-containing core/shell nanofibres..	202
<b>Figure 6.7</b> FTIR-ATR spectra of the produced (a) core/shell, PA6-PHMB and CS-5CLO8Q drug-containing NFs, and (b) drug-free 3% (w/v) CS [CS:PEO at 80:20 (w/w)] NFs, 21% (w/v) PA6 NFs, and pristine CS and PEO powders.....	204
<b>Figure 6.8</b> TGA analysis of (a) the pristine CS powder, PA6 pellets, PEO powder, 5CLO8Q powder, PHMB powder, and the drug-free nanofibres mats formed by 3% (w/v) CS [CS:PEO	

at 80:20 (w/w)] (CS NFs) and 21% (w/v) PA6 (PA6 NFs); (b) the drug-containing core/shell, CS-5CLO8Q and PA6-PHMB NFs.....	207
<b>Figure 6.9</b> DSC analysis of (a) the pristine CS powder, PA6 pellets, PEO powder, 5CLO8Q powder, PHMB powder, and the drug-free nanofibre mats composed of 3% (w/v) CS [CS:PEO at 80:20 (w/w)] (CS NFs) and 21% (w/v) PA6 (PA6 NFs); (b) the drug-containing core/shell, CS-5CLO8Q and PA6-PHMB NFs.....	208
<b>Figure 6.10</b> Mechanical properties (a) Representative tensile stress-strain curves of the drug-containing, drug-free, and core/shell electrospun mats. (b) Young's modulus and (c) Ultimate tensile strength of the drug-containing and core/shell NFs.....	211
<b>Figure 6.11</b> Comparative cumulative release of (a) 5CLO8Q and (b) PHMB, from the antimicrobial CS and core/shell NFs, at pH 7.2 and 6.2. ....	213
<b>Figure 6.12</b> Antimicrobial properties of the electrospun mats.....	216
<b>Figure 6.13</b> <i>Escherichia coli</i> growth kinetics assessment. Comparison of the core/shell nanofibres with variant forms of microfibrils, a polyester-based hernia mesh, and a biologic hernia mesh. ....	218
<b>Figure 6.14</b> SEM micrographs of <i>S. aureus</i> and <i>P. aeruginosa</i> morphological properties upon exposure for 6 h to the electrospun core/shell and PA6 (control) nanofibrous mats. ....	219
<b>Figure 6.15</b> Confocal laser scanning microscopy (CLSM) images of variant textiles, hernia meshes and the developed core/shell antimicrobial NFs .....	220

## Chapter 7

<b>Figure 7.1</b> Schematic representation depicting the direct electrospinning of antimicrobial nanofibres to coat the surface of a synthetic macroporous polypropylene hernia mesh. ....	244
--	-----

---

# List of Tables

---

## Chapter 2

<b>Table 2.1</b> Comparison of the tensile mechanical properties of the skin in comparison to different electrospun-based biomaterials .....	18
<b>Table 2.2</b> List of the key properties of interest of electrospun fibres for skin tissue engineering applications .....	31
<b>Table 2.3</b> Prosthetic meshes with different forms of antimicrobial properties available on the market, and in clinical trials or preclinical studies .....	43
<b>Table 2.4</b> List of parameters affecting the fibre formation during electrospinning .....	58

## Chapter 3

<b>Table 3.1</b> The synthesis protocol and some key aspects of the two PGS forms (pPGS and PGS) used for the development of the novel biomaterial systems in this thesis. PGS was synthesised based on the initially published polycondensation method with modifications to obtain the pre-polymerised (pPGS) form.....	100
<b>Table 3.2</b> List of the materials, CAS registry number, and the corresponding suppliers used in the experiments.....	101
<b>Table 3.3</b> Equipment used to characterise the pristine material, synthesised polymers and composite electrospun mats. The specific chapters that each equipment was used are indicated in brackets ( ).....	104
<b>Table 3.4</b> Different drug release mechanisms .....	118

## Chapter 4

<b>Table 4.1</b> Summary of the polymer blend constituents and blending ratios .....	136
<b>Table 4.2</b> Surface chemical composition of the electrospun PVP/PGS mats at different ratios for the two distinct molecular weights of PVP examined, compared to the theoretical elemental ratios.....	148
<b>Table 4.3</b> Overview of the mechanical properties of each composite fibre mat .....	150



<b>Table 4.4</b> Rapid cell adhesion capability evaluated by comparing the number of non-adherent cells 4 h after seeding the HDFs in the surface of the electrospun mats over cells grown directly on tissue culture plates (n=3) .....	154
--	-----

## Chapter 5

<b>Table 5.1</b> Blend compositions. Tertiary blends, consisting of PCL-backbone SF:(p)PGS, binary blends, consisting of SF:(p)PGS, and PCL alone. Total polymer solution concentration of 13.5% (w/v) for the tertiary blend, 21% (w/v) for binary blends, and 15% (w/v) for the PCL. ....	167
---	-----

<b>Table 5.2</b> The morphological properties of tertiary and binary electrospun mats. Nozzle-free electrospinning was performed at a potential difference of 60 kV (+30/-30 kV), in an upward motion, under N <sub>2</sub> airflow. All values are presented as the mean ± SD .....	171
--	-----

<b>Table 5.3</b> Surface chemical compositions of the electrospun tertiary 1:0.5:0.5 (w/w) SF:PCL:(p)PGS and binary 2:1 (w/w) SF:(p)PGS mats, via XPS analysis. The percentages in brackets refer to the theoretical values of each polymer .....	176
---	-----

## Chapter 6

<b>Table 6.1</b> The morphological properties of the single and core/shell electrospun mats. Electrospinning was performed at 22 kV potential (+18/-4 kV), from a needle tip-to-collector distance of 20 cm, using a rotating collector at 500 rpm. ....	200
--	-----

<b>Table 6.2</b> Surface chemical compositions of the electrospun NFs. The percentages in brackets refer to the theoretical values of each polymer. ....	205
--	-----

<b>Table 6.3</b> XPS analysis of the carbon C1s binding energies. ....	206
--	-----

<b>Table 6.4</b> Thermal properties of the electrospun nanofibrous scaffolds. All chitosan solutions were made as 80:20 (w/w) CS:PEO. The values in parenthesis ( ) refer to transitions of the composite fibres, corresponding to the PEO present within the CS blends .....	209
---	-----

<b>Table 6.5</b> Overview of the mechanical properties of the electrospun scaffolds.....	211
--	-----

---

# Acronyms

---

<b>Abbreviation</b>	<b>Definition</b>
2D	Two-dimensional
3D	Three-dimensional
5CLO8Q	5-chloro-8-hydroxyquinoline
$\alpha$ -SMA	$\alpha$ -smooth muscle actin
A.u.	Arbitrary units
AB	Alamar blue (reagent)
AC	Alternating current
AcOH	Acetic acid
Ag	Silver
AG	Aktiengesellschaft (German for 'public company')
Ala	Alanine
AMPs	Antimicrobial peptides
ANOVA	Analysis of variance
AOC3	Surface enzyme amine oxidase, copper containing 3
App.	Approximately
ATR	Attenuated total reflectance
At. Conc.	Atomic concentration
Au	Gold
BHI	Brain–heart infusion (broth)
BSE	Back-scattered electron
BSL-2	Biosafety level-2
CAD	Computer-aided design
CF	Chloroform
CFU	Colony-forming unit
CI	Confidence interval
CLSM	Confocal laser scanning microscopy
Corp.	Cooperation (company)
CS	Chitosan
CT	Computerised tomography
DAPI	4',6-Diamidino-2-phenylindole

DC	Direct current
DE	Degree of esterification
DI water	Deionised water
DMEM	Dulbecco's modified eagle medium
DMF	Dimethylformamide
DMOG	Dimethyloxalylglycine
DMSO	Dimethyl sulfoxide
DSC	Differential scanning calorimetry
ECM	Extracellular matrix
EDTA	Ethylenediaminetetraacetic acid
EFD	Electro-fluid-dynamics
EG	Epidermal grafting
ePTFE	Expanded polytetrafluoroethylene
EtOH	Ethanol
FA	Formic acid
FBS	Fetal bovine serum
FDA	Federal Drug Administration
FIB	Focused ion beam
FTIR	Fourier-transform infrared spectroscopy
GAGs	Glycosaminoglycans
Gly	Glycine
HA	Hyaluronic acid
HBSS	Hanks' balanced salt solution
HDFs	Human dermal fibroblasts
HDMS	Hexamethyldisilazane
hFDM	Human fibroblast-derived ECM
HFIP	1,1,1,3,3,3-Hexafluoro-2-propanol
HIF-1	Hypoxia-inducible factor-1A
HMSCs	Human mesenchymal stem cells
HPLC	High performance liquid chromatography
hTERT	Human telomerase reverse transcriptase
HUVECs	Human umbilical vein endothelial cells
HV	High voltage
IAP	Intraabdominal pressure
IL	Interleukins
IMBs	Immunomodulatory biomaterials

Inc.	Incorporated (company)
ISO	International Organization for Standardization
ISRCTN	International Standard Randomised Controlled Trial Number
KP	Korsmeyer-Peppas formula
LB	Lysogeny broth
Ltd. and GmbH	Limited (company)
MDA	European Medicines Agency
MH	Mueller–Hinton (broth)
MMPs	Metalloproteinases
MRSA	Methicillin-resistant Staphylococcus aureus
MW	Molecular weight
NHS	National Health Service (UK)
NF	Nanofibre
OD	Optical density
PA6	Nylon-6 (polyamide-6)
PBS	Phosphate-buffered saline
PBS-HCl	Phosphate buffered saline - hydrochloric acid
PCL	Polycaprolactone
PE	Polyester
PEEK	Poly(ether ether ketone)
PEG	Poly(ethylene glycol)
PEO	Poly(ethylene oxide)
PET	Poly(ethylene terephthalate)
PGS	Poly(glycerol sebacate)
PHB	Poly(hydroxybutyrate)
PHBV	Poly(3-hydroxybutyrate-co-3-hydroxyvalerate)
PHMB	Poly(hexamethylene biguanide); polyhexanide
PI	Propidium iodide
PLCL	Poly(L-lactide-co-caprolactone)
PLGA	Poly(lactic-co-glycolic acid)
PP	Polypropylene
pPGS	Prepolymerised form of PGS
PTFE; Teflon®	Polytetrafluoroethylene
PU	Polyurethane
PVA	Poly(vinyl alcohol)
PVP	Polyvinylpyrrolidone

ROP	Ring-opening polymerisation
SCCS	Scientific Committee on Consumer Safety
SD	Standard deviation
SE	Secondary electrons
SEM	Scanning Electron Microscopy
Ser	Sericin
SF	Silk fibroin
SPSS	Statistical Package for Social Sciences
SSG	Split-thickness skin grafting
SSI	Surgical site infection
TAPP	Transabdominal preperitoneal repair
TBSA	Total body surface area
TE	Tissue engineering
TEM	Transmission electron microscopy
TEP	Total extraperitoneal repair
TGA	Thermogravimetric analysis
TGF	Tumour growth factor
TIME	Tissue infection moisture epithelialisation (mnemonic)
UK	United Kingdom
USA	United States of America
UTS	Ultimate tensile strength
UV	Ultraviolet
VAC	Vacuum-assisted closure
WCA	Water contact angle
WHO	World Health Organization
XPS	X-ray photoelectron spectroscopy

---

# Nomenclature

---

<b>Symbol</b>	<b>Description (relevant to)</b>
$a$	Intercept (standard calibration curve)
$b$	Slope (standard calibration curve)
$CDR$	Cumulative drug release (drug release)
$C_i$	Drug concentration (drug release)
$C_o$	Overlap concentration (drug release)
$C_p$	Heat capacity (DSC)
$D$	Total diameter (disc diffusion test)
$d$	The diameter of the antimicrobial disc (disc diffusion test)
$E$	Applied voltage (electrospinning theory)
$E_o$	The electric field at time point 0 (electrospinning theory)
$E_{bin}$	The binding energy of the electron (XPS)
$E_{kin}$	Maximum kinetic energy (XPS)
$F$	Force (mechanical testing)
$g$	Gravitational acceleration
$H$	Distance between the needle-tip and the collector
$h$	Length of needle's capillary (electrospinning theory)
$H$	Enthalpy (DSC)
$h\nu$	Incoming energy of an X-ray photon (XPS)
$I$	Current
$IZ$	Inhibition zone (disc diffusion test)
$k$	Dimensionless conductivity of a fluid
$K_{kp}$	Korsmeyer release constant (drug release)
$L$	Litre and length
$m$	Mass
$m$	Metre
$m_o$	The total amount of the drug-loaded (drug release)
$M_\infty$	Amount of drug released after time ( $\infty$ ) (drug release)
$Mt$	Amount of drug released in time (t) (drug release)
$n$	Drug release exponent for KP formula (drug release)
$n$	Number of specimens

$N_A$	Avogadro's constant
$p$	p-value
$pH$	Potential of hydrogen
$pK_a$	-log of the acid dissociation constant
$Q$	Flow rate (electrospinning theory)
$R$	The radius of the needle (electrospinning theory)
$r$	The radius of the jet (electrospinning theory)
$rpm$	Revolutions per minute
$T$	Temperature
$t$	Time
$T_c$	The onset of crystallisation temperature (DSC)
$T_g$	Glass transition temperature (DSC)
$T_m$	Melting temperature (DSC)
$T_{onset}$	Onset decomposition temperature (TGA)
$V_0$	The total volume of the release medium (drug release)
$V_c$	Critical tension (electrospinning theory)
$V_e$	The volume of release medium withdrawn (drug release)
$W_i$	Dry mass post-submersion (degradation study)
$W_0$	Initial mass (degradation study)
$Y$	Absorbance (standard calibration curve)
$\gamma$	The surface tension of the solution
$\Delta H_m$	The heat of fusion (DSC)
$\epsilon$ and $\epsilon'$	Dielectric constants (electrospinning theory)
$\epsilon_0$	Absolute permittivity (electrospinning theory)
$\mu$	Weight loss (degradation study)
$\rho$	The density of the polymer or liquid mass
$\sigma$	Surface charge (electrospinning theory)
$\phi$	Analyser work function (XPS)
$\phi_0$	Polymer entanglement concentration

---

# Chapter 1

## Introduction

---

### 1.1 Problem statement and motivation

The development of nanotechnology-enabled biomaterials is an accelerating field that has attracted considerable attention, with its hallmark relying on multidisciplinary [1]. Nanotechnological approaches have had a substantial impact on the way we visualise biomaterials and their limitations today. Skin tissue engineering (TE) has been evolving since the idea of "tissue engineering" was first established in the 1960s, and the term "biocompatible" has come to distinguish "biomaterials" from other "materials" [2]. However, to progress further, the gap between the physicians' practical experience and the clinical translation of this knowledge needs to be addressed first.

The perception of biomaterials surrounds the idea of mimicking nature's tissue template, the extracellular matrix (ECM). In tissue engineering and regenerative medicine, a biomaterial acts as a scaffold to provide the mechanical support and physiology in a similar manner to that of the intrinsic ECM [3]. Such an environment encourages biochemical signalling for modulating cell recruitment, attachment, and tissue regeneration, paving the way for reinstating homeostasis [3].

Methods for procuring ECM-based biomaterials from decellularised donor sources through physical (high hydrostatic pressure, dissection, agitation etc.), chemical (surfactants, ionic solutions etc.), and enzymatic approaches have to an extent expanded since the early 2000s [4]. Where measuring the amount of the double-stranded DNA remains the gold standard of evaluating the degree of decellularisation [4, 5]. Nevertheless, the question "how good is good enough?" raises issues regarding the limitations of decellularised ECM products. These limitations pertain to the materials (mechanics, adjusting the degradation etc.), the biology (induced immunological responses due to DNA fragments), donor limitations, and the complexity of obtaining these materials, as well as raising ethical issues [5, 6]. Products, such as Alloderm® (acellular human cadaveric-derived matrix), can be used for various applications ranging from dermal grafts and plastic surgery to transabdominal hernia repair, but in general, are not engineered to meet specific tissue requirements [7, 8]. To improve the medical



precision of biomaterials and to avoid a "one-size-fits-all" approach, ECM-mimicking technologies need to further advance and provide application-specific solutions.

The skin is an interface that establishes a barrier between the body and the environment [9]. When the structural integrity of the skin is compromised, a wound occurs. This can be due to rupture of the tissue by trauma, burn, congenital anomalies, diseases imposing physical distress or chronic defects [10]. Upon injury, it is imperative to reinstate the skin's structural integrity.

The World Health Organization (WHO) estimates that burns cause 180,000 deaths every year [11]. Although the majority of non-fatal wounds and burns heal through the self-regenerative capacity of the skin, extensive injured lesions and chronic (non-healing) wounds are considered a leading cause of morbidity [11]. The rising proportion of the population living with diabetes is causing an alarming increase in the frequency of chronic wound diagnosis [12]. The current gold standard for handling wounds, depending on the severity, relies on varied types of wound dressings, gauzes, hydrogels, semipermeable films, and foams and in severe cases, skin substitute models [13–15]. Rather than initiating healing, the purpose of wound dressings is to protect the wound environment while retaining appropriate hydration of the wound bed [14]. By contrast, skin substitute products are based on autographing or acellularized tissues; they are expensive and difficult to obtain, can be of limited use if the affected area is extensive, and the body may have an adverse immune reaction to the transplant [16]. Consequently, the treatment and management of wound-related skin impairments pose significant challenges to the medical community.

Skin TE requires the development of biomimetic scaffolds that play an active role in the wound healing process, prompting efficient tissue regeneration [16]. Many biodegradable polymers such as poly(caprolactone) (PCL), polyvinylpyrrolidone (PVP), poly(lactic-co-glycolic acid) (PLGA), polylactide-based and natural polymers such as collagen, cellulose, silk and hyaluronic acid among others have been extensively studied to develop bioinspired materials to advance wound care and wound healing [17–19]. Nonetheless, many requirements must be fulfilled to develop easily obtainable biomaterials that elicit the required properties and can be scaled up to a clinically relevant extent.

Similarly, the use of biomaterials for prostheses to prevent hernia reoccurrence has progressed alongside dermal substitute products [20]. Hernia repair surgery is one of the most commonly performed elective operations. Every year, approximately 100,000 hernia repair surgeries are carried out in the UK, over 700,000 are performed in the US, and 1,100,000 inguinal and abdominal wall hernia surgeries take place in China every year [21, 22]. Studies of large groups of patients undergoing hernioplasty (use of a polymer-based prosthetic mesh)

or herniorrhaphy (repositioning the hernia and suturing without the use of a mesh) have shown that the use of a mesh presents at least a 50% reduction in hernia recurrence risk [23].

However, there is uncertainty regarding the use of synthetic materials, such as polypropylene- and polyester-based meshes that are cost-effective and present good mechanics, compared to biologic (primarily collagen-based) meshes that are derived from decellularized tissues, resemble the native fascia, and can be partially bioabsorbed over time [19, 24]. As synthetic meshes are permanent, they are associated with numerous postoperative complications, such as discomfort, inflammation and tissue ingrowth; whereas biologic meshes are expensive to obtain, present poor mechanics, can be difficult to regulate in terms of degradation, are more prominent to infections and may induce adverse immune responses [25, 26].

A number of challenges need to be taken into consideration when developing a mesh biomaterial, including minimising the sensation of a foreign body, preventing rapid cell ingrowth (deep tissue adhesion), shrinkage, chronic scarring, and reduce immunogenic responses [23, 27]. The mesh also must remain adequately flexible, mechanically durable, chemically inert and be resistant to bacterial contamination and subsequent biofilm formation [23, 27]. Currently, there is no mesh available on the market that preserves an ECM-like architecture while preventing bacterial colonisation, either for synthetic or biologically-derived mesh materials. Bacterial contamination of a mesh during insertion, due to the primary incision, occurs in 1/3 to 2/3 of all hernia operations, from which 1%–8% will develop a deep incisional mesh surgical site infection, with the rates varying between open and laparoscopic surgery [27–29]. When considering that the implementation of medical devices increases the susceptibility of infection by a factor of 10,000 to 100,000, someone can recognise the magnitude of the need to advance the antimicrobial properties of implants [29].

Other forms of mesh implants such as transvaginal meshes; used to treat stress urinary incontinence and pelvic organ prolapse, have been recently suspended by the Independent Medicines and Medical Devices Safety Review in the UK due to an increased number of reported complications subsequent to mesh surgery, including debilitating pain, infection, inflammation, mobility problems and depression [30, 31]. In the UK alone in the past six years, the National Health Service (NHS) trust estimated that somewhere between 68,000 and 170,000 patients had been adversely affected due to hernia mesh-related complications, leading to many surgeons estimating that the complication rate can be anywhere between 12% and 30% [32]. The need to develop better engineered, more reliable mesh prosthesis that can address these pressing issues, the medical community is facing, and resolve such significant complications remains of utmost importance.

The potential of using biomaterials in wound treatment requires further advancement, while the prevention of mesh-specific surgical infection needs to be addressed. Synthetic polymers have intrinsic limitations in their biocompatibility, whereas natural polymers suffer from variations in their chemistry and show relatively poor mechanical performance [2].

In this thesis, the concept of integrating naturally-derived polymers with synthetic polymers is explored to assess whether improved biocompatibility, good mechanics and appropriate antimicrobial properties can be obtained to provide suitable biomaterials for wound healing and hernia repair.

To address these issues, the work in this thesis focuses on scaffold development by electrospinning. Electrospinning is a technique that uses electrohydrodynamic principles to fabricate micro-/nanofibres from a polymer solution or melt [33]. The physicochemical and morphological properties of the fibres can be manipulated by modifying the process, solution and ambient parameters; in this way, the induction and regulation of cell-specific responses can be achieved [34]. The spatiotemporal configuration of electrospun membranes makes it feasible for them to sequester active agents, such as antimicrobial substances, in various compartments of the fibres [35]. This means that it is possible to modulate the release kinetics by manipulating the morphological properties, localisation, and drug-polymer interactions of the fibres [36].

Electrospun fibres present remarkable advantages as dermal substitutes compared to conventional dressings such as woven and nonwoven gauzes and non-fibrous structures (e.g., hydrogels) [15]. This is because electrospun fibres permit the development of structures that closely resemble the native ECM of the skin and abdominal wall fascia where cells can adhere, proliferate, infiltrate the scaffold, and induce neodermis regeneration [35, 37].

## 1.2 Thesis aims and objectives

This thesis aims to investigate the potential use of fibre-based biomaterials in the form of advanced skin substitutes and antimicrobial hernia meshes to address some of the challenges associated with aiding chronic wound healing and preventing mesh-specific surgical site infections. This will be accomplished by utilising different electrospinning approaches using a combination of natural and synthetic polymers.

The cutting-edge technologies used in the biomedical sector for managing and treating wounds present many limitations, and they are often either insufficient or overly complicated to obtain. Further, surgical meshes used by surgeons for hernia repair lack an antimicrobial profile, making the establishment of an infection on a mesh an ongoing imminent problem. With regard to these concerns, this thesis will expand on the progress made in the fields of skin tissue engineering and advanced antimicrobial surfaces by investigating material-oriented engineering solutions. This proof-of-concept study will facilitate a discussion within the field of biomedical engineering and provide alternative routes to tackle these issues from a material science perspective.

The research objectives, as presented in this thesis, are as follows:

1. Manufacture electrospun fibre-based biomaterials with tuneable properties.
  - i. Produce biocompatible, fibrous skin-like substitutes with adjustable mechanical properties, tuneable hydrophilicity, and an ECM-like morphology.
  - ii. Produce core/shell (bicomponent) antimicrobial nanofibres that facilitate a spatiotemporal configuration that allows the controlled release of antimicrobial agents while fulfilling the mechanical requirements of a prosthetic mesh.
2. Assess the impact of the electrospun scaffolds architecture regarding the following:
  - i. Physicochemical and mechanical stability.
  - ii. Biocompatibility in the case of skin-like substitutes.
  - iii. Drug release profile and antimicrobial efficiency in the case of hernia meshes.
3. Assess the effect of different forms of poly(glycerol sebacate) towards the mechanics and wetting properties of the skin-like fibrous mats.
4. Describe the photocrosslinking process of the PVP/PGS fibres.
5. Design and build a nozzle-free electrospinning device intended to augment the meagre fibre production associated with lab-based electrospinning equipment.
6. Develop a straightforward, efficient and rapid protocol of extracting silk fibroin from *Bombyx mori* silkworm cocoons.
7. Compare the antimicrobial efficacy of the developed bicomponent electrospun nanofibres to those of the currently available synthetic and biologic meshes.

### 1.3 Thesis outline

This thesis spans two distinctive and well-explored domains of biomedical engineering; tissue engineering and biomaterials science. As a multidisciplinary work, the research conducted touches the fields of chemical, mechanical, and bioengineering, nanotechnology, material science, and microbiology.

**Chapter 2:** This chapter presents a literature review that introduces the anatomy and physiology of the skin, the concept of wound healing and discusses the current challenges and advancements in the development of advanced wound healing dressings and skin-like platforms. An introduction to hernia repair is then provided from a surgical perspective, and the material science behind surgical meshes is described. The major implications and an overview of the current advancements in research are discussed. Finally, the theory and significant parameters of the electrospinning technique are provided, followed by descriptions of free-surface and co-axial electrospinning.

**Chapter 3:** This chapter describes in detail the materials, methods and methodology followed in this thesis. Where appropriate, the background justifying the choice of specific materials and substances and the logic behind the characterisation techniques employed are discussed. The methodology is divided according to characterisation techniques. Included are morphological, physicochemical and mechanical assessment, drug release profiling, and an *in vitro* evaluation of the biocompatibility using fibroblasts and antimicrobial assessment based on class S2 pathogenic bacteria.

**Chapter 4:** This chapter presents the design and construction of the nozzle-free electrospinning apparatus. This device is used to fabricate poly(glycerol sebacate) (PGS)/polyvinylpyrrolidone (PVP) microfibrinous mats. The chemistry behind the riboflavin-induced ultraviolet (UV) crosslinking of the fibrous dressings is discussed. Additionally, the effect of the proportion and the molecular weight of PVP on the physicochemical properties and the tensile properties of the biomaterial are assessed, and an *in vitro* evaluation of its biocompatibility is provided.

**Chapter 5:** The nozzle-free electrospinning device described in the previous chapter is used for high-throughput fabrication of ternary electrospun scaffolds consisting of silk fibroin, PGS and PCL, capable of adjusting the wetting properties of the biomaterial. A novel protocol for the extraction of larger quantities of silk fibroin protein from *Bombyx mori* cocoons in a reduced timeframe is also described. Finally, the developed biomaterial is assessed for its ability to act as a skin substitute *in vitro*.

**Chapter 6:** Here, the issues described in Chapter 2 relating to the development of a mechanically stable, lightweight, antimicrobial nanostructured hernia mesh are considered. A dual antimicrobial system consisting of poly(hexamethylene biguanide) (PHMB) and 5-chloro-8-hydroxyquinoline (5CLO8Q) in a core/shell structure comprised of nylon-6 in the core and chitosan in the shell is developed. The nanofibrous mesh core/shell structure, chemistry, mechanical properties, drug release profile and antimicrobial properties are evaluated against pathogenic bacteria and further compared to those of the counterpart nanofibres, synthetic and natural microfibrils, as well as, biologically derived and synthetic meshes that are currently available on the market and used by surgeons for hernia repair.

**Chapter 7:** This chapter provides conclusions, the limitations of the research conducted, the thesis contributions, and considers future research areas to further advance the work conducted herein.

## 1.4 References

1. Li, C., Guo, C., Fitzpatrick, V., Ibrahim, A., Zwierstra, M. J., Hanna, P., Lechtig, A., Nazarian, A., Lin, S. J., & Kaplan, D. L. (2020). Design of biodegradable, implantable devices towards clinical translation. *Nature Reviews Materials*, 5(1), 61–81. <https://doi.org/10.1038/s41578-019-0150-z>
2. Ratner, B. D. (2019). Biomaterials: Been there, done that, and evolving into the future. *Annual Review of Biomedical Engineering*, 21(1), 171–191. <https://doi.org/10.1146/annurev-bioeng-062117-120940>
3. Hussey, G. S., Dziki, J. L., & Badylak, S. F. (2018). Extracellular matrix-based materials for regenerative medicine. *Nature Reviews Materials*, 3(7), 159–173. <https://doi.org/10.1038/s41578-018-0023-x>
4. Gilpin, A., & Yang, Y. (2017). Decellularization Strategies for Regenerative Medicine: From Processing Techniques to Applications. *BioMed Research International*, 17(1), 1–13. <https://doi.org/10.1155/2017/9831534>
5. Chakraborty, J., Roy, S., & Ghosh, S. (2020). Regulation of decellularized matrix mediated immune response. *Biomaterials Science*, 8(5), 1194–1215. <https://doi.org/10.1039/c9bm01780a>
6. Williams, D. F. (2019). Challenges with the development of biomaterials for sustainable tissue engineering. *Frontiers in Bioengineering and Biotechnology*, 7(1), 1–10. <https://doi.org/10.3389/fbioe.2019.00127>
7. Amirlak, B., Gerdes, J., Puri, V., & Fitzgibbons, R. J. (2014). Allograft AlloDerm® tissue for laparoscopic transabdominal preperitoneal groin hernia repair: A case report. *International Journal of Surgery Case Reports*, 5(1), 294–297. <https://doi.org/10.1016/j.ijscr.2014.02.015>
8. Fosnot, J., Kovach Iii, S. J., & Serletti, J. M. (2017). Acellular dermal matrix: General principles for the plastic surgeon. *Introduction Aesthetic Surgery Journal*, 31(7), 5–12. <https://doi.org/10.1177/1090820X11417576>
9. Lu, Y., Huang, J., Yu, G., Cardenas, R., Wei, S., Wujcik, E. K., & Guo, Z. (2016). Coaxial electrospun fibers: applications in drug delivery and tissue engineering. *Wiley Interdisciplinary Reviews: Nanomedicine and Nanobiotechnology*, 8(5), 654–677. <https://doi.org/10.1002/wnan.1391>
10. Schultz, G. S., Sibbald, R. G., Falanga, V., Ayello, E. A., Dowsett, C., Harding, K., Marco, M., Stacey, M.C., Teot, L.C., & Vanscheidt, W. (2013). Wound bed preparation: a systematic approach to wound management. *Wound Repair and Regeneration*, 11(11), (Supplement 1) 1-28. <https://doi.org/10.1046/j.1524-475X.11.s2.1.x>
11. Mock, C., Peck, M., Peden, M., Krug, E., Ahuja, R., Albertyn, H., & Potokar, T. (2020). *A WHO plan for burn prevention and care*. WHO Press, Geneva, Switzerland. <https://who.int/news-room/fact-sheets/detail/burns>
12. Dreifke, M. B., Jayasuriya, A. A., & Jayasuriya, A. C. (2017). Current wound healing procedures and potential care. *Materials Science and Engineering C*, 48(15), 651–662. <https://doi.org/10.1016/j.msec.2014.12.068>
13. Green, J. J., & Elisseff, J. H. (2016). Mimicking biological functionality with polymers for biomedical applications. *Nature*, 540(7633), 386–394. <https://doi.org/10.1038/nature21005>
14. Kathawala, M. H., Ng, W. L., Liu, D., Naing, M. W., Yeong, W. Y., Spiller, K. L., & Ng, K. W. (2019). Healing of chronic wounds: An update of recent developments and future possibilities. *Tissue Engineering Part B: Reviews*, 25(5), 429–444. <https://doi.org/10.1089/ten.TEB.2019.0019>

15. Vig, K., Chaudhari, A., Tripathi, S., Dixit, S., Sahu, R., Pillai, S., Dennis, V. A., & Singh, S. R. (2017). Advances in skin regeneration using tissue engineering. *International Journal of Molecular Sciences*, 18(4), 789–798. <https://doi.org/10.3390/ijms18040789>
16. Yu, J. R., Navarro, J., Coburn, J. C., Mahadik, B., Molnar, J., Holmes, J. H., Nam, A. J., & Fisher, J. P. (2019). Current and future perspectives on skin tissue engineering: Key features of biomedical research, translational assessment, and clinical application. *Advanced Healthcare Materials*, 8(5), 1–19. <https://doi.org/10.1002/adhm.201801471>
17. Rahmati, M., Blaker, J. J., Lyngstadaas, S. P., Mano, J. F., & Haugen, H. J. (2020). Designing multigradient biomaterials for skin regeneration. *Materials Today Advances*, 5(1), 1–14. <https://doi.org/10.1016/j.mtadv.2019.100051>
18. Chouhan, D., Dey, N., Bhardwaj, N., & Mandal, B. B. (2019). Emerging and innovative approaches for wound healing and skin regeneration: Current status and advances. *Biomaterials*, 216(1), 1–19. <https://doi.org/10.1016/j.biomaterials.2019.119267>
19. Gritsch, L., Conoscenti, G., La Carrubba, V., Noeaid, P., & Boccaccini, A. R. (2019). Polylactide-based materials science strategies to improve tissue-material interface without the use of growth factors or other biological molecules. *Materials Science and Engineering C*, 94, 1083–1101. <https://doi.org/10.1016/j.msec.2018.09.038>
20. Costa, A., Adamo, S., Gossetti, F., D'Amore, L., Ceci, F., Negro, P., & Bruzzone, P. (2019). Biological scaffolds for abdominal wall repair: Future in clinical application? *Materials*, 12(15), 1–15. <https://doi.org/10.3390/ma12152375>
21. Adrales, G., Morales-conde, S., Heniford, B. T., Sharma, A., Rosen, M., Muysoms, F., & Adrales, G. (2018). International Hernia Congress. *Hernia*, 22(1), 1–204. <https://doi.org/10.1007/s10029-018-1733-0>
22. Knowlton, L. M., Minei, J., Tennakoon, L., Davis, K. A., Doucet, J., Bernard, A., Haider, A., Scherer, A., Tres, L.R., Spain D.A., & Staudenmayer, K. L. (2019). The economic footprint of acute care surgery in the United States: Implications for systems development. *Journal of Trauma and Acute Care Surgery*, 86(4), 609–614. <https://doi.org/10.1097/TA.0000000000002181>
23. Simons, M. P., Smietanski, M., Bonjer, H. J., Bittner, R., Miserez, M., Aufenacker, T. J., & Wijsmuller, A. R. (2019). International guidelines for groin hernia management. *European Hernia Society*, 22(1), 1–165. <https://doi.org/10.1007/s10029-017-1668-x>
24. Cornwell, K. G., Jessee, C. B., & Adelman, D. M. (2020). Clinically available reinforcing materials for soft tissue reconstruction. *British Journal of Hospital Medicine*, 81(3), 1–10. <https://doi.org/10.12968/hmed.2018.0428b>
25. Köckerling, F., Alam, N. N., Antoniou, S. A., Daniels, I. R., Famiglietti, F., Fortelny, R. H., Heiss, M. M., Kallinowski, F., Kyle-Leinhase, I., Mayer, F., Miserez, M., Montgomery, A., Morales-Conde, S., Muysoms, F., Narang, S. K., Petter-Puchner, A., Reinhold, W., Scheuerlein, H., Smietanski, M., Stechemesser, B., Strey, Woeste, C. G., & Smart, N. J. (2018). What is the evidence for the use of biologic or biosynthetic meshes in abdominal wall reconstruction? *Hernia*, 22(2), 249–269. <https://doi.org/10.1007/s10029-018-1735-y>
26. Fitzgerald, J. F., & Kumar, A. S. (2014). Biologic versus synthetic mesh reinforcement: What are the pros and cons? *Clinics in Colon and Rectal Surgery*, 27(4), 140–148. <https://doi.org/10.1055/s-0034-1394155>
27. Orelio, C. C., van Hessen, C., Sanchez-Manuel, F. J., Aufenacker, T. J., & Scholten, R. J. (2020). Antibiotic prophylaxis for prevention of postoperative wound infection in adults undergoing open elective inguinal or femoral hernia repair. *The Cochrane database of systematic reviews*, 4(4), 1–12. <https://doi.org/10.1002/14651858.CD003769>
28. Birolini, C., de Miranda, J. S., Tanaka, E. Y., Utiyama, E. M., Rasslan, S., & Birolini, D. (2020). The use of synthetic mesh in contaminated and infected abdominal wall repairs: challenging the dogma—A long-term prospective clinical trial. *Hernia*, 24(2), 307–323. <https://doi.org/10.1007/s10029-019-02035-2>



29. Guillaume, O., Pérez-Tanoira, R., Fortelny, R., Redl, H., Moriarty, T. F., Richards, R. G., Eglin, D., & Petter-Puchner, A. (2018). Infections associated with mesh repairs of abdominal wall hernias: Are antimicrobial biomaterials the longed-for solution? *Biomaterials*, *167*(1), 15–31. <https://doi.org/10.1016/j.biomaterials.2018.03.017>
30. Wise, J. (2018). Surgical mesh for stress urinary incontinence to be halted immediately in England. *BMJ (Clinical Research)*, *362*, 3035. <https://doi.org/10.1136/bmj.k3035>
31. Kmietowicz, Z. (2018). Use mesh implants for stress urinary incontinence only as last resort, says NICE. *BMJ (Clinical Research)*, *363*, 4242. <https://doi.org/10.1136/bmj.k4242>
32. Wise, J. (2018). Hernia mesh complications may have affected up to 170 000 patients, investigation finds. *BMJ (Clinical Research)*, *362*, 4104. <https://doi.org/10.1136/bmj.k4104>
33. Wang, C., Wang, J., Zeng, L., Qiao, Z., Liu, X., Liu, H., Zhang, J., & Ding, J. (2019). Fabrication of electrospun polymer nanofibers with diverse morphologies. *Molecules*, *24*(5), 1–33. <https://doi.org/10.3390/molecules24050834>
34. Xue, J., Wu, T., Dai, Y., & Xia, Y. (2019). Electrospinning and electrospun nanofibers: Methods, materials, and applications. *Chemical Reviews*, *119*(8), 5298–5415. <https://doi.org/10.1021/acs.chemrev.8b00593>
35. Goldberg, M., Langer, R., & Jia, X. (2007). Nanostructured materials for applications in drug delivery and tissue engineering. *Journal of Biomaterials Science, Polymer Edition*, *18*(3), 241–268. <https://doi.org/10.1163/156856207779996931>
36. Lee, C., Wood, D., Edmondson, D., Yao, D., Erickson, A. E., Tsao, C. T., Revia, R. A., Kim, H., & Zhang, M. (2016). Electrospun uniaxially-aligned composite nanofibers as highly-efficient piezoelectric material. *Ceramics International*, *42*(2), 2734–2740. <https://doi.org/10.1016/j.ceramint.2015.10.170>
37. Bacakova, M., Musilkova, J., Riedel, T., Stranska, D., Brynda, E., Bacakova, L., & Zaloudkova, M. (2016). The potential applications of fibrin-coated electrospun polylactide nanofibers in skin tissue engineering. *International Journal of Nanomedicine*, *11*(1), 771–189. <https://doi.org/10.2147/IJN.S99317>

---

# Chapter 2

## Literature Review

---

### 2.1 Skin physiology and function

The skin is the largest organ of the human body, with a surface area of approximately 16,000 to 18,000 cm<sup>2</sup>, and it accounts for approximately 16% (5 kg) of a person's total body mass [1]. Most importantly, as a mucous ectodermal tissue, the skin works as a first line of defence and is responsible for the majority of the muscle, bone, tendon, fasciae, and ligament tissue compartmentalisation [2]. It is necessary to understand the function and mechanisms of the skin, as it can provide valuable insights into the requirements that have to be considered when engineering a synthetic skin-tissue-like platform. The subsections below describe the major components of the skin, its structure, functions, anatomical characteristics, and the role of the ECM.

Part of the literature presented in this chapter draws from the author's previously published review entitled "*2D and 3D electrospinning technologies for the fabrication of nanofibrous scaffolds for skin tissue engineering: A review*" (Keirouz et al., 2020a) and is used with the permission of the publisher (Appendix B).

#### 2.1.1 Components of the skin

The skin carries out numerous tasks to maintain the physiological and biochemical conditions of the human body at an optimum level [3]. The integrated appendages into the skin's structure allow it to serve as a cushion for deeper structures [3, 4]. Amongst other functions, the skin also can regulate the body's temperature via eccrine and apocrine sweat glands, act as an external barrier against toxins and pathogens, and secrete and excrete substances with antimicrobial and bactericidal properties [2, 5]. Moreover, through the cutaneous production of small cationic antimicrobial peptides (AMPs) such as defensins, cathelicidins, and histatins, the skin can provide the first line of defence against pathogens through direct antimicrobial activity or by modulating host immunity responses, as Figure 2.1 indicates [6]. Furthermore, the skin provides mechanical support to the human body, it is an important sensory organ, carrying out primary immunological mediations, and it is responsible for the synthesis of

vitamin D upon exposure to sunlight [7]. In addition, as an excretory organ – the skin helps remove waste urea, salts, and water from the body [7].

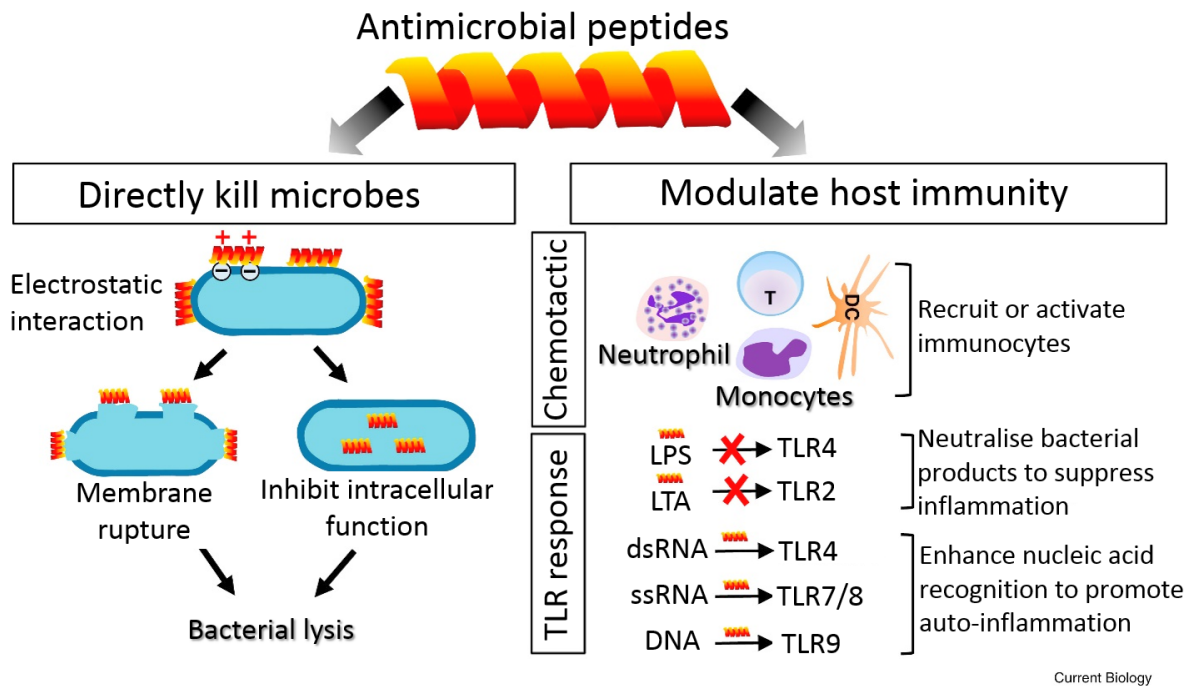


**Figure 2.1 Antimicrobial peptides (AMPs) secreted from the skin offer direct and indirect pathogen protection pathways.** Firstly, it induces membrane disruption due to electrostatic interactions between the bacterial membrane and AMPs. Secondly, through modulated host immunity, as it recruits/activates immunocytes or promotes the downstream regulation of Toll-like receptors (TLR) which in turn promote the recognition of microbial metabolites, membrane constituents, or nucleic acids released by the damaged tissue. DC, dendritic cells; LPS, lipopolysaccharide; LTA, lipoteichoic acid; MAVS, mitochondrial antiviral signalling protein. Modified from Zhang et al. [6].

### 2.1.2 Layers and functions of the skin

The general structure of the skin consists of a stratified tissue that has three layers; the epidermis, dermis and hypodermis (subcutaneous fat), from outermost to innermost, as illustrated in Figure 2.2. Each layer carries different physiological functions, and thus evolves and ages differently [3]. Regardless of its continuity, the morphological and mechanical properties of the skin differ significantly among diverse anatomical positions, where its thickness varies from 0.5 mm to 4.0 mm [8]. Healthy epidermis regenerates entirely from the basement membrane approximately every 28 days [9].

The epidermis is the outer layer of the skin, with a thickness ranging between  $50\ \mu\text{m}$  (eyelids) up to  $1,550\ \mu\text{m}$  (palms and soles of feet), where sex discrepancies exist, with male skin being about 25% thicker [10]. The epidermis accounts for approximately 5% of the skin's weight and is composed of five strata or layers: *basale*, *spinosum*, *granulosum*, *lucidum*, and *corneum* [3]. The stratum corneum is the outer layer of the epidermis and is composed of dead corneocytes containing keratin that conceal the ECM, thus acting as a physical protective barrier [10]. The epidermis has no blood supply of its own (avascular), and it receives nutritional support (oxygen and glucose) via a primary papillary layer of loose connecting tissue that is present in the dermis [11]. The epidermis is mostly composed of multiple layers of keratinocytes, along with Langerhans (dendritic) cells, melanocytes and produces basement collagens and keratin [12].

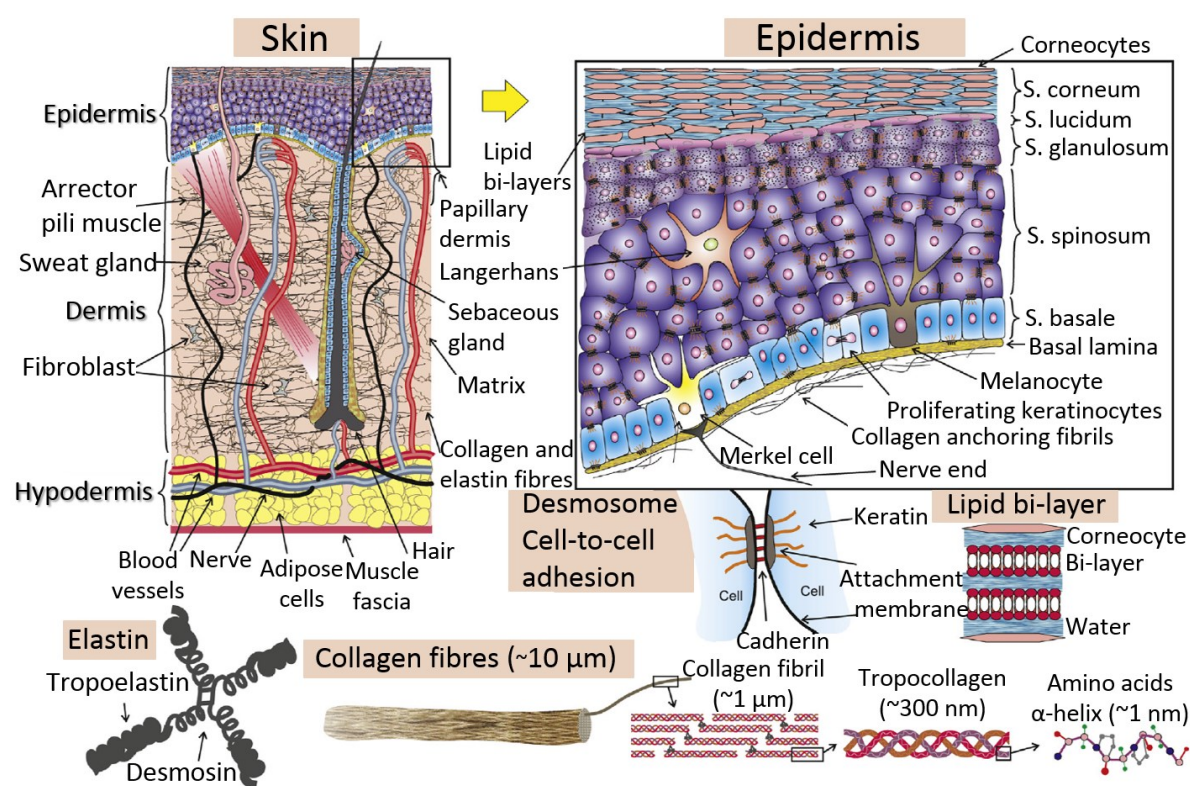


**Figure 2.2 Schematic representation of the structure of the skin layers and appendages.**

The architecture of the skin and epidermis, as well as the morphological properties of key reconstruction proteins. The letter “S.” stands for stratum. Modified from Benitez and Montans[10].

The dermis (1 to 2 mm thick) is a rich in blood vessels (vascular) layer of connective tissue interconnected (via junctions) beneath the epidermis layer [9]. The dermis provides structural and mechanical support, regulates the water content, and conveys neural sensory receptors such as Merkel cells (nerve endings) that act upon external stimuli [13]. Furthermore, it

facilitates adrenal (eccrine, apocrine, and sebaceous) glands, hair follicles, and permits blood and lymphatic circulation based on the confined metabolic requirements of the specific skin area [9, 12]. It predominately presents fibroblasts that synthesise type I, and IV/VII collagens [12, 13].

Lastly, beneath the dermis, the hypodermis facilitates the conjunction of skin with bones, muscles, and tendons [14]. The dermis further presents blood vessels, hair follicles, nerves, type I collagen fibres and elastin [12, 14]. The main cell types present are adipocytes and endothelial cells [13]. Moreover, the hypodermis acts as a storage site for adipose tissue (producing and storing triglycerides), and it is responsible for the photolysis of pre-vitamin D3 and the excretion of vitamin D3 [9, 13].

### **2.1.3 The role of the extracellular matrix (ECM)**

The ECM is nature's template, responsible for maintaining the structural integrity of tissues and organs. Stem cells place ECM components in their surroundings from the starting point of embryogenesis [15]. The ECM regulates a range of intrinsic biochemical and mechanical signals that facilitate cell survival, phenotyping, cell-to-cell contact, and is responsible for the multicellular compartmentalisation of tissues and organs [13]. Dynamic reciprocity, defined as the constant bidirectional communication between the ECM and cells that allows for tissues to communicate with the external environment, is of great importance in identifying the required microenvironment responses of a wound [16].

The skin's ECM is of fundamental importance when investigating the wound healing cascade for the development of efficient synthetic skin substitutes that can aid in wound healing as it directly – and indirectly – influences the architecture and composition of the newly forming tissue. During wound healing, the surviving cells in the wound bed will modify their secreted ECM products in response to fluctuations in oxygen level and nutrient depletion, the mechanical instability of the injured matrix, and numerous other factors from the surrounding niche [16]. These signals, then, travel through the ECM and are detected by cell-surface receptors that, in turn, activate the downstream regulation of genes that facilitate the skin's response to the injured area [17, 18].

Cells modify their secreted ECM products in response to various stimuli, including mechanical cues, oxygen, nutrient concentration, and many other factors taken up from the tissue's microenvironmental niche [19]. The ECM is composed of an array of approximately 300 multidomain macromolecules [15]. The processes of the multifaceted wound healing cascade are mediated by ECM components such as collagen, fibronectin, vitronectin, elastin,

proteoglycans, a range of biochemical mediators, cytokines, and growth factors, among others [20]. That dynamic process also involves the coordination of blood cells, several growth factors (epidermal, platelet-derived, transforming, basic, and tumour necrosis), and ECM elements. Those factors regulate the haemostasis, inflammation, proliferation and differentiation of cells, ECM biosynthesis, epithelialisation and tissue remodelling, ultimately reinstating the continuity and physiochemical functionalities of the newly formed tissue [17, 18]. The ECM's microenvironment is critical for cell growth, survival, and differentiation; cells cannot survive without the ECM as it provides the basic template required for growth and maintenance [21].

Among the skin's proteins, collagens are of pivotal and comprise more than 70% of the total dry weight of the dermis [22]. Type I collagen is a triple helix of repeated sequences of glycine with proline and hydroxyproline (MW 290,000 Da) that constitute approximately 80% of the entire dermis, whereas type II, III and IV (fetal) constitute for the remaining 20% of its total mass [23]. Type I fibres tend to be thick and elongated, whereas type III fibres are reticular and work as a framework for the synthesis of type I collagen. Collagen is almost solely responsible for the tensile strength and most of the mechanical properties of the skin [22].

Another protein present in the dermis, elastin, is a water-insoluble protein that makes skin pliable, via the secretion of the precursor tropoelastin [24]. Tropoelastin gives the epidermis its elasticity; it is approximately one thousand times as flexible as collagen and is the reason skin can distort [24].

On the other hand, vitronectin (MW 75,000 Da) is a proteolytic glycoprotein of the hemopexin family, present in the blood plasma that interacts with the ECM to assist clot formation during wounding [22]. Lamins (Type-A 400,000 Da and Type-B 210,000 Da) are present between the dermal and epidermal layers of the skin, where they crosslink cell surface receptors that ultimately assist cellular organisation and tissue generation [25]. Lamins are one of the first structural proteins that are produced during embryogenesis (from the 16-cells stage), followed by collagen IV [15].

Hyaluronic acid (HA) is a hydrophilic, anionic, non-sulphated glycosaminoglycan [26]. HA is capable of retaining moisture due to its molecular structure, thus keeping the skin layers hydrated [27]. Furthermore, HA acts as a short-term membranous frame during the wound healing process, transporting biomolecules, nutrients, and laminates keratinocytes to the damaged site [27, 28].

Figure 2.3 shows the interaction of cells within an ECM-like scaffold, as well as how the ECM provides conditions that facilitate survival, growth, and expansion of the cells. Moreover, engineered ECM biomimetic analogues deriving from decellularised ECM components,

synthetic or natural polymers, or a combination of these materials, can act as a template in replacing injured ECM substrate. ECM-like scaffolds promote healing and growth of the tissue and are especially helpful in cases where the extent of an injury makes the response of the body insufficient to heal the wound properly [15].

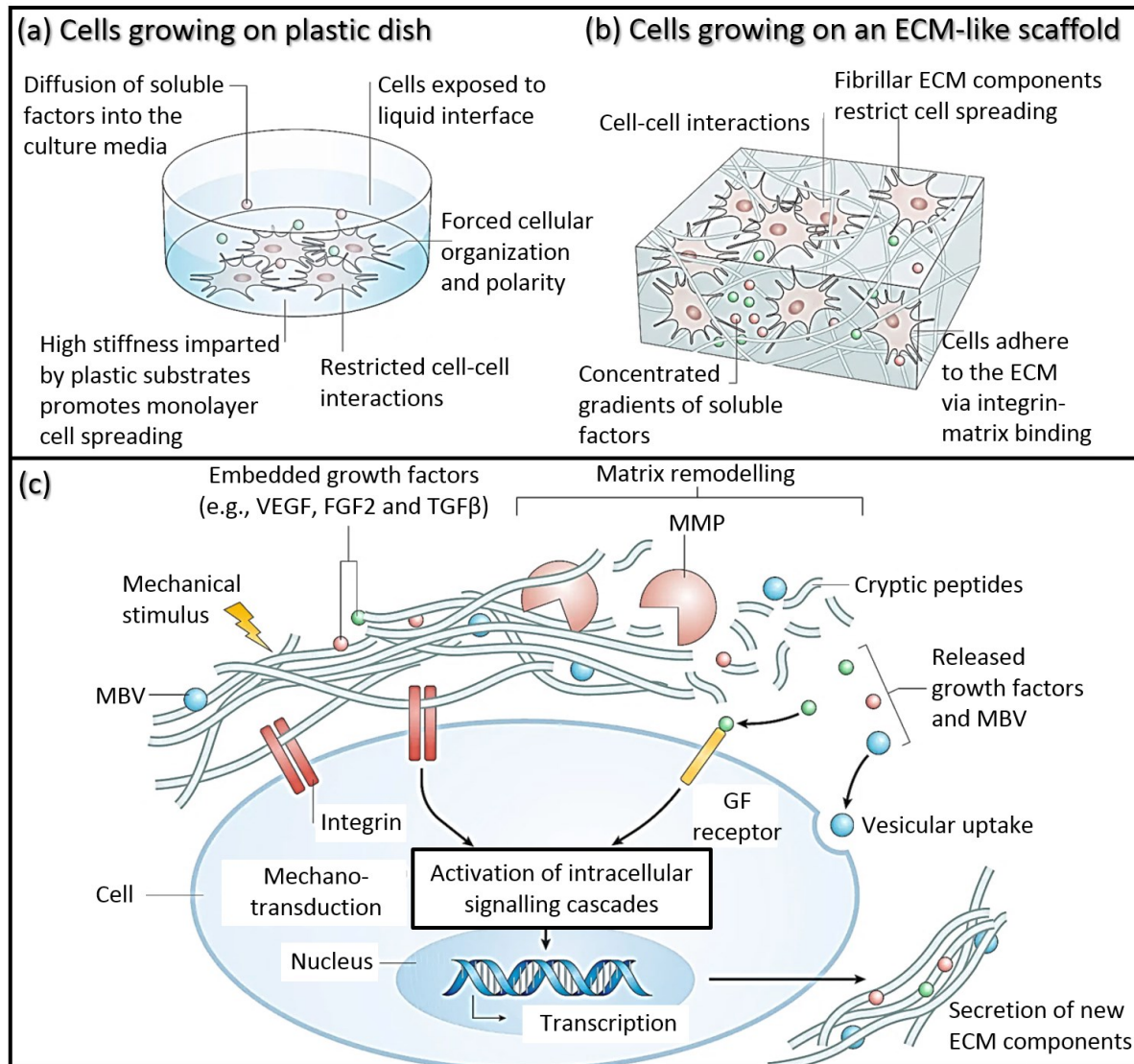


**Figure 2.3 Schematic representation of the cell-ECM interactions on different substrates and ECM remodelling.** **(a)** Cells growing on a culture substrate dish. In this scenario, cells are grown in a planar direction, following an apical-basal polarity within a culture medium. **(b)** Cells growing on an ECM-like biomimetic scaffold. The biocompatible scaffold allows for planar and perpendicular growth without limiting the polarity of the cells. The matrix provides a biomimetic environment where cells can secrete growth factors and ECM-related components along the scaffold's fibrils. **(c)** A summary of the physiochemical and mechanical stimuli that, in turn, activate downstream intracellular signalling cascades and, ultimately, the transcription of ECM-related factors. Afterwards, the secreted factors interact with cells that promote functions such

as proliferation, migration, differentiation, and tissue remodelling. MBV, matrix-bound nanovesicles; MMP, matrix metalloproteinase; FGF2, fibroblast growth factor 2; TGF- $\beta$ , Transforming growth factor- $\beta$ ; VEGF, vascular endothelial growth factor. Modified from Springer-Nature, Hussey et al. [15].

### 2.1.4 Anatomical characteristics and mechanics of the skin

The skin will differ in structure and function based on different regions of the body [29]. Soft tissues are made of complex material and, structurally, can greatly differ among different anatomical sites [30]. The skin is a mechanically complicated tissue due to the heterogenic, anisotropic, highly nonlinear, and viscoelastic multidimensional behaviour [10].

Dermal cells are regularly subjected to mechanical stimuli deriving from the ECM's surroundings and other neighbouring cells [31]. The way dermal cells adapt and reconstruct the ECM at an injured site depends on the dermis mechanics, where the viscoelasticity of the skin can influence the activity and phenotype of the resident fibroblasts [32]. Accordingly, the fibroblasts in the area will adapt the cytoskeletal actin remodelling according to the rigidity of the ECM, which in turn will directly impact the cell's phenotype, lineage and state [31].

Research has focused on determining the correlation between the axial and transverse mechanics of the skin and its microstructural characteristics, based on location and collagen fibre orientation [33]. In a rat model, this was found to be influenced by variations in the quantity of collagen and the micro-organisation of collagen fibres present in different anatomical areas of the skin [33]. When determining the tensile properties of different regions of the skin, the Langer lines of skin tension are taken into account that define the natural orientation of collagen fibres within the dermis [34]. The fibrils present in the ECM of the skin range between 10–500 nm depending on the collagen ageing and maturation, where mechanically different anatomical sites can differ significantly in tensile strength, based on quasistatic and dynamic measurements, as indicated in Table 2.1 [19, 35, 36].

From a mechanical perspective, electrospun fibres are broadly researched as graft implants or dressings in order to improve both wound healing time and outcome [37]. Electrospun fibres can present tuneable tensile mechanical anisotropy that can facilitate cellular contact guidance similar to that of the native ECM [37]. The biomechanical behaviour of the different skin sites can be used as a standard for the development of skin-like electrospun mats. By adjusting the mechanical properties of the electrospun fibrous biomaterial to match those of the specific skin area that endured the injury, the physiochemical responses deriving by the mechanical stimuli can be positively influenced, reducing the inflammation rate and subsequent fibrotic scarring.



**Table 2.1** Comparison of the tensile mechanical properties of the skin in comparison to different electrospun-based biomaterials.

<b>Skin/Biomaterial (anatomical site)</b>	<b>Young's modulus (MPa)</b>	<b>Tensile strength (MPa)</b>	<b>Elongation at break (%)</b>	<b>Ref.</b>
Human skin	15 - 135	2 - 30	20 - 150	[35]
(Arm)	87 - 101	13 - 15	59 - 102	[38]
(Abdomen)	19 - 25	2 - 15	60 - 80	[8]
(Back)	48 - 118	13 - 30	37 - 71	[34]
(Forehead)	20 - 24	5 - 6	27 - 34	[38]
<b>Electrospun fibres</b>				
Collagen	25 ± 5.2	1.5 ± 0.2	33 ± 9	[39]
Collagen/Chitosan	380 ± 150	8.0 ± 2.2	30 ± 12	[40]
Collagen/PCL	82.1 ± 17.9	8.6 ± 1.4	24 ± 7.2	[41]
PCL	21.4 ± 0.1	6.9 ± 0.3	116 ± 6.5	[41]
PCL/Gelatin	12.5 ± 2.8	4.9 ± 0.6	75.7 ± 9.1	[42]
PLCL	47.7 ± 2.2	7.2 ± 0.2	158 ± 6.7	[43]
PLGA	355 ± 58	5.6 ± 1.1	107 ± 20	[44]
PLGA/Chitosan	75 ± 11	4.3 ± 0.7	32 ± 11	[44]
PLGA/Chitosan/PVA	296 ± 32	5.4 ± 0.6	14.7 ± 6.6	[44]

## 2.2 Skin burns and wounds

The skin is an interface that establishes a barrier between the body and the environment [45]. When the structural integrity of the skin is compromised, a wound occurs. A wound is formed due to loss of continuity of the skin tissue layers, inclusive or exclusive of loss of function [46]. This can be due to the rupture of the tissue by trauma, burn, congenital anomalies, disease imposing physical distress, or other chronic defects [47]. Upon a skin injury, it is imperative to reinstate the skin's structural integrity to assure haemostasis, inflammation, cell migration, proliferation, and tissue maturation.

### 2.2.1 Classifications of wound types

Wounds can be classified as acute or chronic, based on anatomical properties and characteristics of the wound bed [46]. An acute wound arises when the continuity of the skin is fractured superficially [48]. The majority of acute wounds are due to minor trauma, avulsion fractures, surgical incisions or burns [49]. For a healthy individual that is not suffering from an excessive wound or does not have any underlying health conditions, an acute wound will generally self-regenerate and repair within 14 days to a month, following the stages of the cutaneous wound healing cascade described in the next section [46].

If the impaired skin area is incapable of reinstating the tissue's functions, restoring a functional ECM and promoting re-epithelialisation, the wound is defined as chronic or non-healing [47]. Non-healing wounds can also be present in excessive wounds [47]. Chronic wounds do not follow the typical wound healing cascade, usually because of endogenous mechanisms related to predisposing pathological conditions or other risk factors that compromise the skin's structure [47, 50]. Upon haemostasis, a chronic wound is followed by constant inflammation on-site and a lack of healing; this ultimately causes ECM destruction, hypoxia, reactive oxygen species production, and an increased likelihood of bacterial colonisation and subsequent infection [51]. Factors such as autoimmune diseases, chemotherapy, obesity, malnutrition and ageing may worsen the chances of complete recovery and facilitate the development of chronic wounds [52]. Leg or foot ulcers and pressure sores are the most common chronic wounds, primarily present due to poor vasculature [52].

By contrast, burns are formed due to trauma of the skin tissue through exposure to extreme heat or cold, radiation, chemical agents, or high current electricity [53]. In trauma medicine, the 'rule of nines' is used to assess the total body surface area (TBSA) covered by the burn

[53]. For adults, each upper limb corresponds to 9% of TBSA, and each lower limb to 18%, the trunk (abdomen and chest) accounts for 18%, while the head and neck together make up 9% [29]. The thermal injury of the skin will depend upon the temperature, thermal propagation and the duration of contact or exposure [54]. For instance, exposure of hot water at 65 °C will produce a full-thickness burn in 45 s, will create a deep partial-thickness burn in 15 s, and a superficial partial-thickness burn in 7 s [29].

Burns are commonly classified visually into first, second or third-degree burns based on the severity of the injury [55]. Typically, superficial first-degree and second-degree burns confine the epidermis and are visually red due to hyperaemia in the area and heal within two weeks without residual scarring [55]. However, deep (partial thickness) second-degree burns extend from the dermis, pass through the dermal papillae, and reach the reticular layer of the dermis [56]. The exposed dermis, along with the hyperaemia, forms vesications (blisters) and oedema. Medical intervention in second-degree burns will depend upon the extent of the burn, as they may lead to secondary infections and hypertrophic scarring [56]. Third-degree (full thickness) burns extend through the dermis to the hypodermis, which is composed of adipose and connective tissue [55]. Third-degree burns fully destroy the dermis, and consequently, the blood supply in the area. Moreover, due to the lack of blood and thrombosed vessels underneath the dermis, the area is visually ischemic with loss of sensation due to nerve damage [54]. Such burns require critical medical intervention and almost always requires some type of grafting to prevent systemic shock, due to body-fluid loss, and infection [57].

### **2.2.2 The wound healing cascade**

Healing is a normal response of a tissue to an injury. Wound healing is a multifaceted pathway of well-controlled and defined cellular responses, which facilitate the restoration of the skin's continuity along with its physiochemical functionalities [58]. This dynamic process involves the coordination of blood cells, biomolecules, growth factors, and ECM elements. The wound healing cascade can be separated into three distinct stages: (a) haemostasis and inflammation, (b) proliferation, and (c) remodelling and maturation [58]. The key aspects of the biochemical responses that take place during wound healing are outlined in Figure 2.4.

### **a. Haemostasis and inflammation**

Once a penetrating trauma occurs, damaged epithelial cells initiate the antifibrinolytic-coagulation pathway due to the release of inflammatory mediators [59]. Thrombin and clotting factors generate a platelet-rich plasma which coagulates the wound, within minutes [59]. In response to anti-inflammatory stimuli, prostaglandin is secreted from inflammatory cells, causing vasoconstriction, to limit blood loss in the wounded area [58]. The epithelial and endothelial cells on-site then secrete growth factors and chemokines that stimulate the recruitment of neutrophils and macrophages that, in turn, stimulate the production of interleukins (IL-13) and growth factors (e.g., TGF- $\beta$ ) [60].

The neutrophils infiltrate the area within the first 24-48 h, clearing necrotic tissue and bacteria [60]. The circulating monocytes in the area will then differentiate to macrophages and further polarise to types M1 (pro-inflammatory) and M2 (anti-inflammatory) [59, 60]. Type M1 is necessary as part of early defence responses, where M2 stimulate tissue regeneration. The ratio between M1/M2 plays a crucial role in chronic wounds, where M1 is the predominate form present, inducing chronic inflammation, via the constant secretion of IL-1 $\beta$  and TNF- $\alpha$ , and thus, preventing M2-mediated healing [59 – 61]. The myofibroblasts work towards contracting the wound, reducing the margins [59]. Stimulated myofibroblasts and epithelial cells also secrete matrix metalloproteinases (MMPs), which break down the basement membrane to allow for the recruitment of cells on the site [61]. The neutrophils and macrophages mature and cause complement-mediated opsonisation and phagocytosis, respectively, which remove tissue debris and dead cells [61]. Connective tissue matrix deposition allows for the development of a new ECM [62].

### **b. Proliferation**

During the proliferative phase, granulation and epithelialisation occur, epithelial and endothelial cells move from the basement membrane of the tissue towards the epithelial layer [62]. Afterwards, fibroblasts and keratinocytes derived from local mesenchymal cells or bone marrow are recruited and activated in the area [62].

The low oxygen tension and low pH due to an increase in the concentration of lactic acid stimulate the revascularisation of the area, to fulfil the energy requirements of the newly formed build-up [60]. Additionally, myofibroblasts cause wound contraction, which facilitates the closure of the wound from the edges towards its centre [63]. As the wound area starts to

recover, lymphocytes stimulate the prolonged release of TGF- $\beta$  which in turn downregulates the gene expression of proteases that are responsible for the breakdown of the ECM and upregulate fibroblast release growth factors, interleukins and tumour necrosis factors [64]. As fibroblasts are deposited to the newly formed ECM, secreted collagen chains undergo processing, ultimately causing matrix reorganisation that can start to reinstate the proper state and responsiveness of the newly formed tissue [62].

### **c. Remodelling and maturation**

In the final phase, the epithelial cells in the area divide and migrate through the basal layer of the skin to reinstate the normal structure of the tissue, completing the wound healing process [63]. Repeated injury or chronic inflammation can cause the newly formed granulated tissue to experience increased tensile strength due to extensive deposition of ECM components, eventually forming a fibrotic scar [65]. After, pro-fibrotic mediators (e.g., IL-13 and TGF- $\beta$ ) augment collagen deposition from the myofibroblasts in the area [65]. If the actin-myosin complex does not induce apoptosis to remove the myofibroblasts in the area (through the upregulation of TGF- $\beta$ ), the constant expansion of the ECM, through collagen deposition, can form excessive scars, such as keloids [63, 65]. MMPs and tissue inhibitors will control and provide a balance between the upregulation and downregulation of collagen-related factors, based on the net amount of collagen present in the newly formed tissue [62]. Several growth factors and ECM proteins slowly guide tissue maturation, which will ultimately restore 70%–80% of the previously unwounded skin's mechanical strength within a year [63].

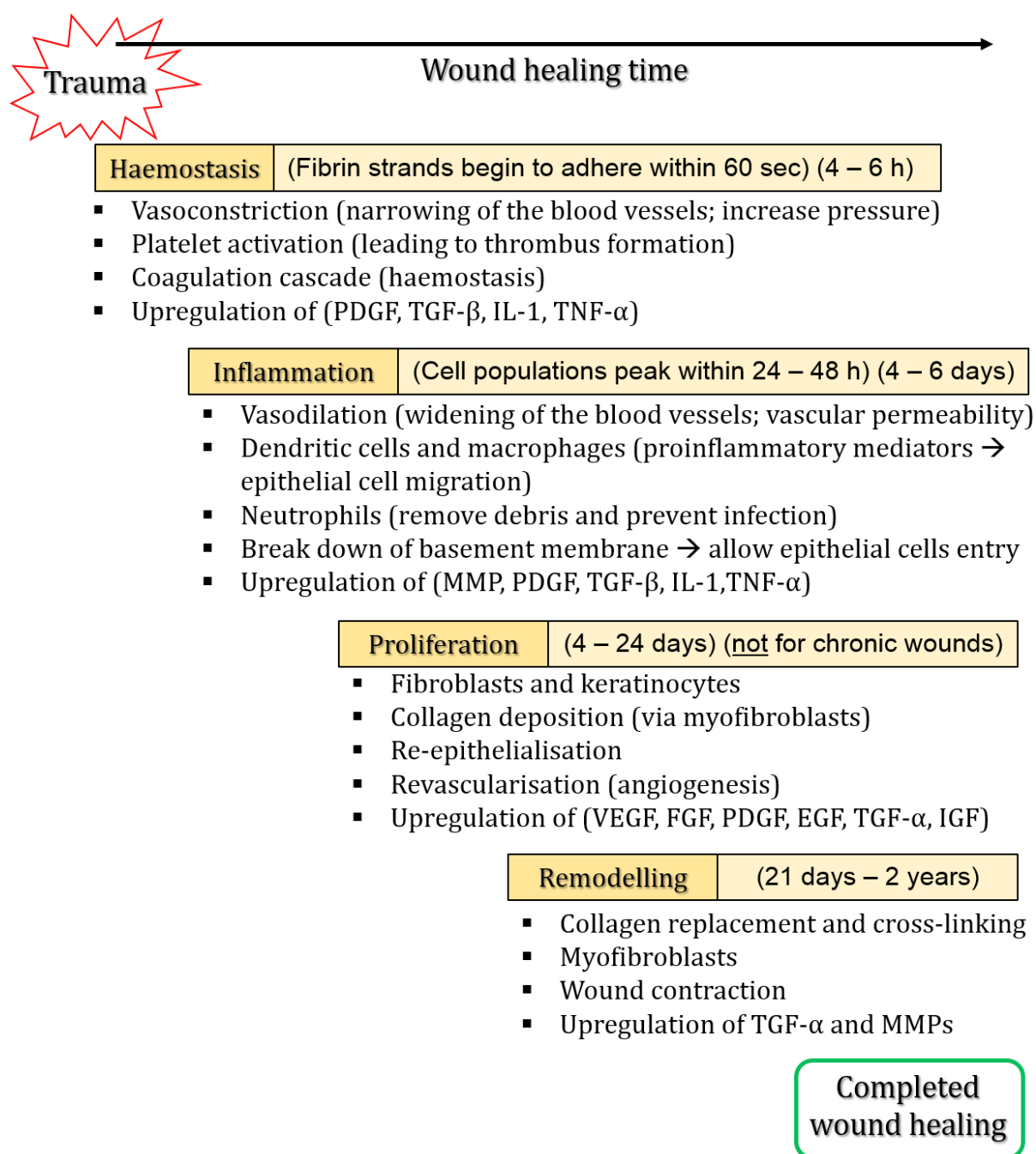


**Figure 2.4 The wound healing cascade.** The major phases of the wound healing process: Haemostasis, inflammatory response, proliferation, and remodelling. Whereas various cell lineages, cellular and ECM components contribute to coherent wound closure. EGF, epidermal GF; FGF, fibroblast GF; IGF, insulin-like GF; IL-1, interleukin-1; MMP, matrix metalloproteinase; PDGF, platelet-derived GF; TGF, transforming GF; TNF- $\alpha$ , tumour necrosis factor- $\alpha$ ; VEGF, vascular endothelial GF. Light yellow colour boxes indicate an estimate timeframe for each phase.

## 2.3 Skin tissue engineering so far; advances and challenges

Aiding wound healing and managing chronic wounds has been a critical issue since the onset of tissue engineering. Skin equivalents Integra® (Integra LifeSciences, Inc., USA) and Apligraf® (Organogenesis, Inc., USA) for treating burns and venous leg ulcers, respectively, were the first tissue-engineered products to obtain Federal Drug Administration (FDA) approval in the mid-late 90s [66]. The prospects for tissue engineering flourished in the next two decades, with many technical and regulatory challenges met. Nanotechnology and the benefits of nanoscale materials in all disciplines, including medicine, surfaced with the global nanomedicine market cap predicted to exceed 350 billion USD, from which over 26 billion USD will account from the global wound care market by 2023 [67]. Nonetheless, the current treatment options for handling chronic wounds, expounded in the section below, remain limited and – in many scenarios – ineffective. With approximately 1 in 5 diabetic patients developing a chronic non-healing wound, this is becoming an increasingly important issue worldwide [68]. Recent trends in developing such therapeutic approaches focus on achieving synergy between the biology that facilitates wound healing and the physicochemical aspects that a biomaterial system can provide.

### 2.3.1 Traditional and impregnated dressings

The Wound Healing Society has introduced the use of the acronym TIME to evaluate a wound and the corresponding healing steps required. "T" stands for tissue, referring to the assessment of the wound bed for dead or devitalised tissue. The "I" refers to the incidence of infection or inflammation. The "M" refers to the required moisture balance of the wound bed, and the "E" stands for the wound edges and extent of re-epithelialisation required [68]. Conventionally, this requires debridement of the wound followed by vacuum-assisted closure (VAC), which applies localised negative pressure to the surface and margins of the wound thus reducing the fluid around the wound while supporting granulation tissue formation [69]. This is followed by the use of the appropriate wound dressing, of which there are various choices available on the market, with the selection depending upon the stage of the wound and its pathophysiology.

Traditional dressings and gauzes in the form of cotton, wool, and natural or synthetic polymers play a passive role in wound care, by preventing bleeding and initial contamination deriving from contact with the external environment [70]. The main advantage of such dressings is that they are affordable. However, they present poor bacterial protection, are

prone to dehydration, and damage of the newly formed epithelium, and can be painful to remove [70]. The use of topical antimicrobials such as iodine-releasing agents, chlorine-releasing solutions, honey or – most popularly – silver nanoparticles are some of the approaches taken to improve the comfort of the patient and the antimicrobial effect of such dressings [71]. There are no findings that suggest that the use of a traditional dressing improves the outcome or timeframe of the wound closure [70].

A hydrogel is a three-dimensional (3D) network of crosslinked hydrophilic polymers capable of carrying large amounts of water due to the hydrophilic nature of its polymer chains [72]. Crosslinking of hydrogels can be based on covalent bonds or non-covalent interactions while adjusting the crosslink density will affect the porosity and swelling properties of the hydrogel [73]. Although hydrogels have been thoroughly studied, with several hydrogel-based dressings available on the market today, the excessive swelling due to the high-water content (>80%) limits the absorption of exudates [74]. Further, the prolonged exposure of the wound bed to moisture makes the injured site more prone to skin maceration and biofilm development [74]. The physical properties of hydrogels allow for tailored drug-delivery of antibiotics and other antimicrobial substances, which can be entrapped in the hydrogel's network during gelling [75]. Nonetheless, high-water retention formulates mechanically unstable structures [73]. Considerable work has been focused on reinforcing the structure of hydrogels, with the integration of materials such as graphene oxide and boron nitride. Nevertheless, this forms more brittle hydrogels that lack elasticity, a prerequisite for a wound dressing in order to be capable of adjusting to different anatomical sites of the body [32, 75].

Semipermeable film dressings made of polyurethane (PU), such as Tegaderm® (3M Company, Inc., USA) and Opsite® (Smith & Nephew, Plc., UK) can adhere to the surroundings of the wound, while the transparency of the dressing allows monitoring the progression of wound healing [67]. Although such dressings provide a protective environment that does not permit the entry of moisture and limits contamination, they have poor breathability, thus entrapping CO<sub>2</sub> and not allowing the entry of oxygen on the site [70]. Further, PU has a high water contact angle, which limits the film's ability to uptake exudates from the wound bed and is, therefore, only recommended for superficial wounds [70, 76]. Bilayer structures of semipermeable films integrating a hydrogel to increase the uptake of exudates have been developed, and films have been produced in literature by a range of materials, including chitosan, collagen, hyaluronic acid among others. However, it has been challenging to improve the degradability, breathability and mechanical stability of such dressings *in vitro* and *in vivo* [77].



Foam dressings are absorbent porous structures, typically of PU or poly(vinyl alcohol) (PVA), capable of retaining the moisture required by the wound bed while absorbing wound exudate [78]. Foam dressings provide a "cushioning", an initial barrier to bacterial contamination, are not adhesive and are effective for the treatment of hypergranulation [78]. Such dressings are commonly used with secondary dressings to attain the required mechanical stability. However, they can easily desiccate the wound bed if there is no exudate present, which in turn can drop the wound bed temperature that has a direct negative effect on the wound healing process by delaying cell and enzymatic functions [67]. Further, decreased local temperature can increase the chances of infection due to vasoconstriction [70].

In general, such dressings are contraindicated from being used in the case of full-thickness wounds and third-degree burns, as aside from providing a barrier to contamination they do not actively facilitate any part of the wound healing process. Lowering the temperature of the wound bed, not permitting gas transport, completely draining or overfilling the site with exudate, and thus increasing the chances of infection are some of the drawbacks of the conventional wound dressings described above. In any instance, acute and chronic wounds may demand the use of dermal substitute and skin-like constructs if the damage is severe.

### **2.3.2 Current treatment and management options for excessive and chronic wounds**

The types of traditional wound care approaches described above aim to underpin the prevention of infection, limit ischemia and oedema by maintaining various states of hydration, thus allowing for the body to heal the injury naturally. Epidermal wounds can regenerate, but consequent breach to the dermis relegates granulation and subsequent scar formation [68]. The use of tissue engineering approaches through the advancements of biologic scaffolds can transform the scar tissue response to constructive remodelling of the wound bed [68]. Biologic-derived scaffold materials consist of decellularised tissues, ECM components or hybrids composed of biologic and synthetic materials that can mimic the ECM's architecture. In contrast to the wound dressings described earlier, biologic scaffolds ultimately act as an inductive microenvironment that through altering biochemical cues can facilitate the prompt restoration of the healthy skin's architecture, actively.

The current standard for the treatment of non-healing wounds, wounds larger than 4 cm<sup>2</sup>, and excessive third-degree burns involve the use of different types of dermal substitutes or

skin grafts [79]. During the tissue flap procedure, skin is harvested from a non-affected part of the body – usually the thigh area – and transplanted to the wound. The current standard for skin harvesting is split-thickness skin grafting (SSG), which comprises the excision of the epidermis and a small portion of the dermis, leaving behind the bottom layer (reticular) dermis, which eventually heals by secondary intention [79]. In a different emerging approach of autologous grafting, epidermal grafting (EG), harvesting of only the epidermal layer, is achieved by applying heat to the area to form and raise blisters by negative pressure [80]. Nonetheless, autologous skin grafts can be associated with infection, pain, discolouration, and hypertrophic scarring; moreover, the total amount of skin that can be harvested from a patient is limited [81].

Epidermal and dermal substitutes are bio-derived scaffolds 1–2mm thick composed of synthetic polymers or ECM components that incorporate autologous-derived cells that act as a dermal layer that assists wound healing [82]. Dermal substitutes can be used as less invasive alternatives to skin grafts. Dermal substitutes are not a new concept, with numerous products being well-established on the market today. Those can be (1) human-derived: Alloderm® (derived from acellularized cadaver skin); Glyaderm® (ETB-Bislife, Inc., Netherlands) (Glycerol-preserved acellular dermis), (2) porcine-derived such as Apligraf®, Permacol® (Metronic, Inc., USA) and Xenoderm® (MBP, GmbH, Germany) (3) bio-derived polymer material such as lyophilised collagen-based Integra®, Matriderm® (MedSkin Solutions, AG, Germany), OrCel® (Ortec International, Inc., USA) and hyaluronic acid-based Hyalomatrix® (Haemo-Pharma, GmbH, Austria) as well as (4) synthetic-based Dermagraft® (Organogenesis, Inc., USA) (polyglactin) and Transcyte® (Advanced Tissue Sciences, Inc., USA) (nylon coated with porcine collagen) [83, 84].

Due to the complexity of the immune system, a successful dermal implant will involve complicated interactions between the wounded tissue and the biomaterial. Patients can receive immunosuppressive treatment to overcome those immunological challenges that are associated with artificial skin grafts derived from autologous cells, allogeneic cells, or xenographic tissues [85]. Moreover, immunomodulatory biomaterials (IBMs) can enable localised and targeted immunomodulation to the wound site, promoting specific immune responses that prevent the need for immunosuppressive medications, while prolonging the implant's lifetime [86]. Although considerable success has been associated with the use of dermal substitutes, complete bio-integration of the scaffolds requires an infection-free wound bed that is well-vascularised to promote tissue adhesion. However, such constructs are prone to infection and haematomas due to the poor integration with the injured host-tissue and immune rejection and are associated with prolonged periods of immobility [84, 87].

### 2.3.3 New trends of electrospun biomaterials for wound healing

Although significant advances in dermal skin substitutes have improved the outcome for many patients, there are many issues relating to the repair process of a wound yet to be solved [88]. Skin grafts, acellularized and synthetic bio-derived scaffolds are still associated with immunorejection, contraction, fibrosis, insufficient blood supply, inadequate bacterial protection, sensory loss, defective pigmentation and a high cost of production [4, 21]. These issues make the development of effective bioengineered skin models that can completely restore skin functions a current need.

Electrospinning (Described in detail in *Section 2.6*) has always played a pivotal role in the fabrication of skin substitute products that encompass all the desired properties for successful wound closure and skin regeneration. Natural polymers have, from an early point, been considered suitable candidates for the development of electrospun materials due to their intrinsic architecture and elicited biological properties [89]. Furthermore, natural polymers also carry various tissue niche requirements, are biocompatible, and may present antimicrobial properties. Due to their high resemblance with ECM components, these materials are less prone to induce chronic inflammatory responses and immunotoxicity, which is more often encountered in the case of synthetic polymers [90].

Many *in vitro* and *in vivo* studies suggest that naturally derived polymers, such as collagen and silk fibroin-based fibrous membranes, present better cell adhesion and proliferation properties than synthetic polymer-based fibres [91, 92]. Collagen nanofibrous scaffolds with sustainable release of silver (Ag) nanoparticles showed increased antimicrobial activity against *Staphylococcus aureus* and *Pseudomonas aeruginosa*, with no signs of oedema and complete re-epithelialisation of a full-thickness wound in a rat model within 14 days [93]. A Silk fibroin-PEO composite where sodium chloride crystals were incorporated to increase the porosity of the electrospun nanofibrous membrane upregulated the expression of burn-induced cytokines and growth factors and induced re-epithelialisation of rat models of tissue burns in 21 days [94].

Nonetheless, naturally derived scaffolds present poor mechanical stability; moreover, their rapid degradation may affect the subsequent phases of the healing cascade [95]. Furthermore, the overlap concentration ( $C_0$ ), the degree of polymer branching, and the chosen solvent system may be hard to adjust and thus affect the electrospinnability, reproducibility, and homogeneity of natural-derived fibres, as insufficient solubility, stiff molecular conformations, and low conductivity can halt a solution from being electrospun [96]. For this reason, many studies have focused on the development of scaffolds that integrate the cytocompatibility of

natural polymers with the mechanical and physiochemical integrity of synthetic polymers. The incorporation of natural-derived polymers such as silk fibroin, chitin, and cellulose with synthetic polymers can increase their mechanical complexity while alleviating their processability. Combining such materials and forming polymer blends can increase the chemical bonding, for instance by forming higher ratios of polyester and polyether linkages, thus vastly improving the mechanics, surface wettability, and cell-scaffold interplay [97].

Synthetic non-toxic polymers such as poly(vinyl pyrrolidone) (PVP), poly(vinyl alcohol) (PVA), poly(ethylene oxide) (PEO), poly(caprolactone) (PCL), poly(lactic-co-caprolactone) (PLCL) are some of the most used polymers for skin TE applications. Variations of such polymers within the electrospinning polymer mixture can directly impact the characteristics of the fibres formed, such as the fibre diameter, pore size, and mechanical properties of the fibrous mats.

The first requisite of a skin substitute is that it maintains a microenvironment that favours wound contraction and re-epithelisation, while minimising excessive collagen deposition and subsequent scarring. Factors such as fluid uptake and water vapour retention can support the required moisture in the wound site and remove any excess drainage appropriately. Due to the micro/-nanostructure and increased porosity, electrospun materials are better at taking up fluids than conventional dressings and dermal substitute products [94]. A dressing with high water vapour transmission rate dehydrates the wound, making it more prone to scarring, whereas the low water vapour transmission rate increases the risk of infection and may impair the healing process due to the build-up of exudates in the wound bed, consequently finding the balance between the two remains challenging. An electrospun wound dressing developed out of cellulose acetate/gelatin with variant amounts of hydroxyapatite showed that increasing the concentration of hydroxyapatite increased the water vapour transmission rate (WVTR) because of the wider pores ( $15.6 \pm 7.1 \mu\text{m}$ ) of the dressing [98].

Altering the biomechanics of the electrospun mats with an aim to increase the flexibility and mechanical stability of the wound dressing is also crucial for wounds in “difficult” anatomical sites, such as places where the skin naturally curves or is more rigid. Being able to produce a skin-like product tailored to the mechanics of a specific anatomical site can directly impact the ECM depositions and subsequently, the cellular response, reducing the chances of fibrotic tissue formation [31]. Contrary to the observations relating to guided cell infiltration and improved unidirectional mechanical properties, randomly oriented fibres grant better outcomes for wound healing due to the higher complexity and better stability. The matrices composed of random fibres present polymer chains entangled to formulate distinct voids and porosities, which can further promote wound healing of difficult anatomical sites due

to bidirectional mechanical stability [99]. A recent study found that PCL cast films are inferior to randomly oriented or aligned nanofibres (NFs) due to their semi-crystalline brittle and inflexible nature, in contrast with the enhanced plasticity linked to the amorphousness of the electrospun mats [99]. It has been shown that scaffolds with aligned NFs promote better cell migration, where the orientation of the fibres may play a crucial role in promoting actin growth [100]. Nonetheless, aligned fibres present poor bidirectional mechanical properties, do not present the advanced interconnectivity provided by the increased porosity in randomly oriented matrices, and cannot prevent bacteria entry.

Common strategies have been developed to implement the immunomodulatory activity in electrospun fibres via M1/M2 macrophage polarisation [101], glycosaminoglycans (GAGs) [102], and decellularised ECM material [103]. Castellano et al. [100] developed a poly(hydroxybutyrate) (PHB) electrospun bilayer dermo-epidermal skin equivalent implant consisting of human keratinocyte and fibroblast isolates, which was compared with Matrigel® and PCL NFs. The PHB dermo-epidermal graft was implanted as a xenograft onto mice and was found to be superior in terms of cell adhesion and proliferation; capable of inducing M2 macrophage polarisation (based on CD206<sup>+</sup> CD68<sup>+</sup> quantifications of the biopsied tissue), with a significant reduction in the M1/M2 ratio, increased angiogenesis, and absence of hyperplasia during the re-epithelialisation of the wound site (the dorsal region of NOD/SCID mice) compared to the other groups examined. Recently, sustained release of a synthetic GAG-mimicking polymer structurally-tailored glycopolymers, in the form of core-shell NFs consisting of PCL, modulated endothelialisation due to VEGF and bFGF bound endothelial receptors triggering downstream events [101]. Moreover, a fibrillar structured Human umbilical vein endothelial cells (HUVECs) cultivated biodegradable poly(L-lactide-co-caprolactone) (PLCL) human fibroblast-derived ECM (hFDM) electrospun membrane, formulated a mechanically stable construct that promoted re-epithelialisation, collagen deposition, neovascularisation, and effective wound closure within 28 days [102].

Several *in vivo* studies using a variety of cell types have indicated that seeded scaffolds with the corresponding dermal lines, or cells deriving from a recipient donor, are associated with better healing properties than acellular scaffolds [104]. Electrospun scaffolds cultivated with dermal cells can improve the skin regeneration properties as they can engage in the injured site and accelerate the repair and restoration processes. The versatility of biocompatible synthetic and natural materials for electrospinning allows the development of lightweight constructs with tuneable mechanics and elasticities, reducing the morbidity associated with dermal substitutes [105]. The small pores and increased porosity of the electrospun mats, which is in general over 80% for TE constructs [105], along with the range

of different tactics that can facilitate the integration of antimicrobial substances, can deter an infection from occurring through physical or active barriers.

Various functionalities, such as the wetting behaviour of the matrices, antimicrobial properties, drug release, and stimulant-responsiveness can be adjusted to attain the best available requirements for wound protection and healing [106]. Table 2.2 summarises the key properties of interest of electrospun fibres for skin tissue engineering applications.

**Table 2.2** List of the key properties of interest of electrospun fibres for skin tissue engineering applications.

Property	Purpose	Ref.
Vast choice of natural and synthetic polymers	Capable of attaining biocompatible constructs with variant morphologies and properties. Possible to adjust the degradability of the biomaterial.	[90]
Fibre diameter ranging from nano to micrometres	Mimics the physical geometry of the natural ECM.	[90]
High surface area-to-mass (or volume)-ratio	Haemostasis promotion. Surface functionalisation. Increased space available for cells to expand and transport substances.	[90]
High porosity (60%–90%)	Cell respiration; cellular ingrowth; gas permeability; prevention of wound dehydration.	[94]
Interconnected porosity	Prevention from microbial infiltration and cell ingrowth.	[94]
Mechanical properties	Can be adjusted to those of the human skin.	[99]
Lightweight	Ease pain and reduce foreign body sensation.	[105]
Thermal insulation	Preserve the wound bed temperature.	[94]
Design the drug release profile of interest	Release biomolecules, growth factors and nanoparticles of interest.	[106]

## 2.4 Hernia

A hernia is the abnormal protrusion or prolapse of a tissue or organ through the wall of the cavity that usually contains it [107]. Weakening of the abdominal muscle, deserted connective tissue and increased abdominal pressure incite the organ to bulge out [108]. The protrusion through the peritoneum (the lining of the abdominal cavity) forms the hernial sac that consists of fatty tissue, bowel, other organs or fluid [107]. Typically, the hernia bulging can be seen and felt externally.

A substantial body of evidence supports a genetic predisposition to hernia formation and reherniation, with a genetic profile displaying a decreased expression of collagen I and increased expression of collagen III [109]. In general, hernia formation occurs in anatomical sites where there is an absence of fascia and muscle [108, 109]. Such areas include the inguinal canal (groin), umbilicus, pelvis, and the femoral canal [108]. Early or late postoperative wound-related issues, such as wound infections, seromas or wound dehiscence, can also predispose to the creation of incisional hernias [110]. Other contributing factors linked with hernia occurrence include ageing, obesity, smoking and pregnancy, among others [110].

Inguinal and paraumbilical/umbilical hernias are the most common, accounting for over 75%, followed by epigastric and incisional 15% and other forms 10% [111]. The majority of inguinal hernias occur in men (98%), with 30% of the patients developing a second hernia at the opposite side of the groin [112]. Approximately 5% of the population aged over 45 years will develop a hernia; where it is 10–fold more likely to occur in men than in women [113].

Hernias are classified according to location, size and their ability to reduce [114]. Reducible hernias can be dealt with by applying manual pressure using a supportive undergarment, such as a hernia truss or belt [115]. Irreducible hernias, on the other hand, can constitute a medical emergency and over time, require surgical intervention [115]. Hernia repair is one of the most commonly performed elective operations [116]. Surgically, hernia repair involves reduction of the hernia, closure of the hernia defect, and reinforcement of the abdominal wall by either sutures or a net-like prosthesis [107]. The two common approaches of surgical intervention involve hernioplasty (open or laparoscopically) or herniorrhaphy (open hernia repair) [114].

- During herniorrhaphy, also known as the Bassini technique, an incision is made in the abdominal wall followed by excision of the contents of the hernial sac, sewing the weakened tissue, and suturing the opening [117]. As the sewing and the placement of the sutures induce tension in the region, herniorrhaphy presents higher risks of hernia reoccurrence, post-operative chronic pain and prolonged recovery and is thus

generally not the avenue of choice today [118]. However, herniorrhaphy remains the most prevalent form of hernia repair in most of the developing world due to its low cost [114].

- During hernioplasty, the hernia is reduced into the abdomen and reinforced with a mesh that is fixed on the site with fibrin glue, staples or sutures [107, 119]. There are different mesh placement techniques (onlay, inlay, sublay, and underlay) that take into account the area of the hernial sac and the corresponding fascia [117]. The post-operative probability of surgical complications will be influenced by the type of mesh and the surgical technique chosen, as well as the surgeon's "learning curve" [120].
  - Among the hernioplasties, the two most common laparoscopic techniques for hernia mesh placement are transabdominal preperitoneal (TAPP) repair and total extraperitoneal (TEP) repair [119]. These two laparoscopic techniques are less invasive procedures. The TAPP technique involves entering the peritoneal cavity and placing the mesh over the probable hernia site, whereas the TEP technique, does not enter the peritoneal cavity, but rather, places the mesh at the transversalis fascia region, the area between the parietal peritoneum (the peritoneum of the abdominal wall) and the visceral peritoneum (the peritoneum of the internal organs) [117, 119].

Suture closure for hernia repair is acknowledged for having high recurrence rates, while the use of synthetic and biologic meshes can reduce the chances of hernia reoccurrence by over 50% [121–123]. Nonetheless, surgical prosthesis has been associated with foreign body sensation, rapid cell ingrowth (deep tissue adhesion), shrinkage, chronic scarring, immunogenic responses, and mesh-specific surgical site infections (SSI) [107].

Although the chances of mesh-related SSI are typically low, ranging from 0.7%–2.0% for laparoscopic and as high as 9%–18% for open hernia repair, due to the high number of hernia operations performed annually, this corresponds to tens of thousands of cases [124]. In the United States, the Clinical Congress of the American College of Surgeons has determined that the total excess of mesh infection treatment surpasses \$100,000 USD, taking into account hospitalisation expenses and follow-up costs for the span of a year [125]. Unfortunately, once an infection settles on a surgical mesh, a limited number of options are available, where re-operating to surgically remove the implant will be required for more than 40% of the incidents, which significantly increases the chances of hernia reoccurrence and predisposes the patient to surgery-related complications [126]. There have been significant efforts in the literature to functionalise meshes to provide some form of antimicrobial protection, with some being



clinically available today. Nevertheless, further understanding the risk factors, pathogenicity, and limiting aspects of the prosthetic meshes available today, can further advance the properties of such implants and their post-implantation responses over time.

### **2.4.1 Hernia mesh architecture: morphological, physiochemical and mechanical properties**

Since the first reported hernia mesh developed in the mid-1950s by Dr Francis Usher consisting of a woven type of polyolefin plastic, research, and development of surgical meshes has focused on textile-based constructs that provide good mechanics and porosity for efficient transport of intracellular metabolites, nutrients, and gases [107]. At this point, the aim of a prosthetic mesh was to replace and reinforce the defected area, stabilising the abdominal wall, providing long-term relief of symptoms and preventing hernia recurrence [127]. Subsequently, the development of mesh implants has shifted towards nonwoven, knitted and warp-knitted structures due to their macroporous morphology and high anisotropic elastic strength, rather than woven meshes that offer tightly packed structures of low filament density that have been linked to poor cell ingrowth [128].

After that, as more synthetic polymers obtained FDA-approvals based on their biodegradability, biocompatibility and non-toxic properties, mesh implants started being classified based on the material's biological response as absorbable, non-absorbable, or partially-absorbable [128]. Absorbable meshes degrade within the body over time, gradually reducing the mechanical strength of the implant, while non-absorbable meshes do not fully degrade and can provide long-term reinforcement of the repaired hernia [128, 129]. Partially absorbable mesh implants are based on bicomponent fibres, consisting of a biodegradable and a non-biodegradable polymer drawn together to a single filament in the format of side-by-side, core-sheath, segmented or matrix-fibril [129].

The majority of synthetic polymers used for prosthesis are characterised as nonpolar, highly hydrophobic, electrostatically neutral, and resistant to enzymatic degradation [130]. Polypropylene (PP), polyester (PE) and expanded polytetrafluoroethylene (ePTFE) are the most commonly used polymers employed for the development of mesh materials [131]. Numerous factors need to be considered when examining a material towards its ability to be used as an implant for hernia repair, including the material's mechanics, morphological properties, and biological responses. From a design perspective, the biomechanical and compositional properties of a mesh are distinguished based on filament construction (mono-/multifilament), pore size (macro/micro) and weight [132].

The porosity and pore size of the mesh refers to the ratio of nonsolid (voids) to solid space of a defined area and the diameter of the pores, respectively [131]. The porosity is a significant indicator of an implant, as it incites the proportion of host tissue incorporation that may, to an extent, also reduce the chances of bacterial colonisation [133]. Currently, the pore size of prosthetics is defined as; very large ( $> 2000 \mu\text{m}$ ), large ( $1000\text{--}2000 \mu\text{m}$ ), medium ( $600\text{--}1000 \mu\text{m}$ ), small ( $100\text{--}600 \mu\text{m}$ ), and microporous, also referred to as solid ( $< 100 \mu\text{m}$ ) [134]. Studies suggest that meshes with wide pores ( $> 1.5 \text{ mm}$ ), referred to as macroporous, can promote collagen deposition and vascularisation while minimising granuloma bridging, a process where individual granulomas become confluent encapsulating the entire mesh [135]. This event is commonly associated with microporous structures where the pores are in close proximity [135].

Nevertheless, macroporous meshes may induce enterocutaneous fistulas; the connection of the bowel lumen to the skin wound formed due to the surgical incision when the mesh is placed intraabdominally in direct contact with the viscera, a severe condition with a high mortality rate ( $\leq 15\%$ ) [136, 137]. To minimise bowel adhesion, second-generation (composite) meshes, capable of being placed in the intraperitoneal space preventing adhesion between viscera and parietal regions have been developed [138]. Parietex® (Medtronic, Plc., Ireland) and Proceed® (Ethicon, Inc., USA) offering a resorbable collagen coating on one side, 4DryField® PH (PlantTec Medical, GmbH, Germany) offering a barrier gel basing deriving from potato starch, as well as DualMesh® (W.L. Gore & Associates, Inc., USA), Dulex® and Composix® (Bard Davol, Inc., USA), which offer micro and macroporous sides, are commercially available products that have been used to limit visceral attachment [107, 138].

Over the years, “heavyweight” meshes ( $\geq 80 \text{ g}\cdot\text{m}^{-2}$ ), have been associated with chronic pain, foreign body response, fibrosis, as well as enterocutaneous fistula [127]. Ever since prostheses design has focused on reducing the density of the material while attaining the appropriate mechanics [127]. Today, a prosthetic mesh can be defined as medium-weight ( $50\text{--}80 \text{ g}\cdot\text{m}^{-2}$ ); lightweight ( $35\text{--}50 \text{ g}\cdot\text{m}^{-2}$ ); and ultralight-weight ( $\leq 35 \text{ g}\cdot\text{m}^{-2}$ ) [139]. Reducing the thickness of the filaments during extrusion is the main approach used to decrease the overall weight of the material and the corresponding weight to foreign material density ratio [140]. Several studies have indicated that the use of lightweight meshes is substantially more advantageous in reducing long-term complications, such as scar formation and are less prone to severe inflammatory reactions and foreign body responses, compared to heavyweight meshes [141].

The filaments of synthetic meshes are produced via extrusion in the form of multi-/or monofilaments [107]. Monofilament yarns are larger in diameter, whereas multifilament yarns

consist of a series of braided, smaller diameter fibres [142]. The monofilament diameter ranges from 0.065 to 0.165 mm [107], where the multifilament diameter is at a similar range but consists of fine monofilaments ranging between 10–50  $\mu\text{m}$  each [143]. Nevertheless, the risk of infection is a prominent issue of multifilament meshes, as small approximately 10  $\mu\text{m}$  interstices created in-between braided fibres, can allow for the infiltration and sufficient colonisation of bacteria, thus causing infection [132]. In general, monofilament meshes are less prompt to bacteria adherence, due to low pore interconnectivity, and have been found to present an enhanced bacterial clearance compared to multifilament meshes, by readily allowing access of the immune cells onto the mesh [142, 143]. In such instance, mesh explantation due to an infection is also more commonly associated with multifilament compared to monofilament meshes, mostly due to the better bacterial adherence and the poor infiltration of macrophages and neutrophils at the area [139]; a macrophage is about 20–30  $\mu\text{m}$  in diameter, although it can deform to fit through gaps as small as 5  $\mu\text{m}$  [144], as oppose to *Staphylococci* species that range between 0.5–1.0  $\mu\text{m}$  [145]. Electrospinning can resolve this issue while attaining a multifilament morphology through the loading of antimicrobial or antibiotic substances within the fibres; by fibre surface modification (e.g., polycationic surface) that can induce contact killing; or by creating wider pores (e.g., cryogenic electrospinning, salt leaching), which can produce pores ranging from 10–500  $\mu\text{m}$  [146].

The abdominal wall has a laminar organisation that underlies several broad, sheet-like muscles attached on the deep fascia that form tendon fibres and fibre bundles oriented in various directions [147]. Due to the anatomy of the abdominal muscles, the transverse and oblique muscle groups produce lateral forces significantly greater than the stress produced by the longitudinal rectus abdominis muscles, making the abdomen naturally more rigid horizontally and elastic vertically [148]. A prosthesis should be able to mimic the abdominal wall biomechanically and withstand the intraabdominal pressure, which will depend upon the material chosen and the architecture of the drawn filaments [132]. Cobb et al. [149] measured the intraabdominal pressure (IAP) of a group of individuals under different scenarios; such as, sitting and standing, coughing, jumping while lifting weights, and found the highest IAP to be 171 mmHg, which did not differ based on sex. Klinge and co-workers [150] used the Laplace equation and the thin-walled cylinder theory; that states that the overall tensile strength required will not dependent upon the thickness of the mesh, to define the maximum physiological tensile strength per unit of width at 32  $\text{N}\cdot\text{cm}^{-1}$  in the lateral direction. Pott et al. [148], examined the longitudinal and transverse mechanical properties of six commercially available hernia meshes using a uniaxial tensile tester and discovered that the maximum force ( $11.1 \pm 6.4$  to  $100.9 \pm 9.4 \text{ N}\cdot\text{cm}^{-1}$ ) and stiffness ( $0.3 \pm 0.4$  to  $4.6 \pm 0.5 \text{ N}\cdot\text{mm}^{-1}$ ) differ significantly considering the direction of tension.

At a force of 16 N, Junge and co-workers [151] have defined the elasticity of the abdomen to be 15%–69% vertically and 7%–25% horizontally. In general, knitted structures present higher elasticity in comparison to woven structures, due to unidirectional stretching of the fibres [132]. Depending on the weight of the mesh, the elasticity of most commercially available meshes ranges between 4%–16% for heavyweight meshes and 20%–35% for a lightweight prosthesis [152]. Further, the rate of degradation of the mesh has a direct impact on its tensile strength over time and if the required mechanical stability is lost early on (five months post-implementation), it may contribute to hernia reoccurrence [153].

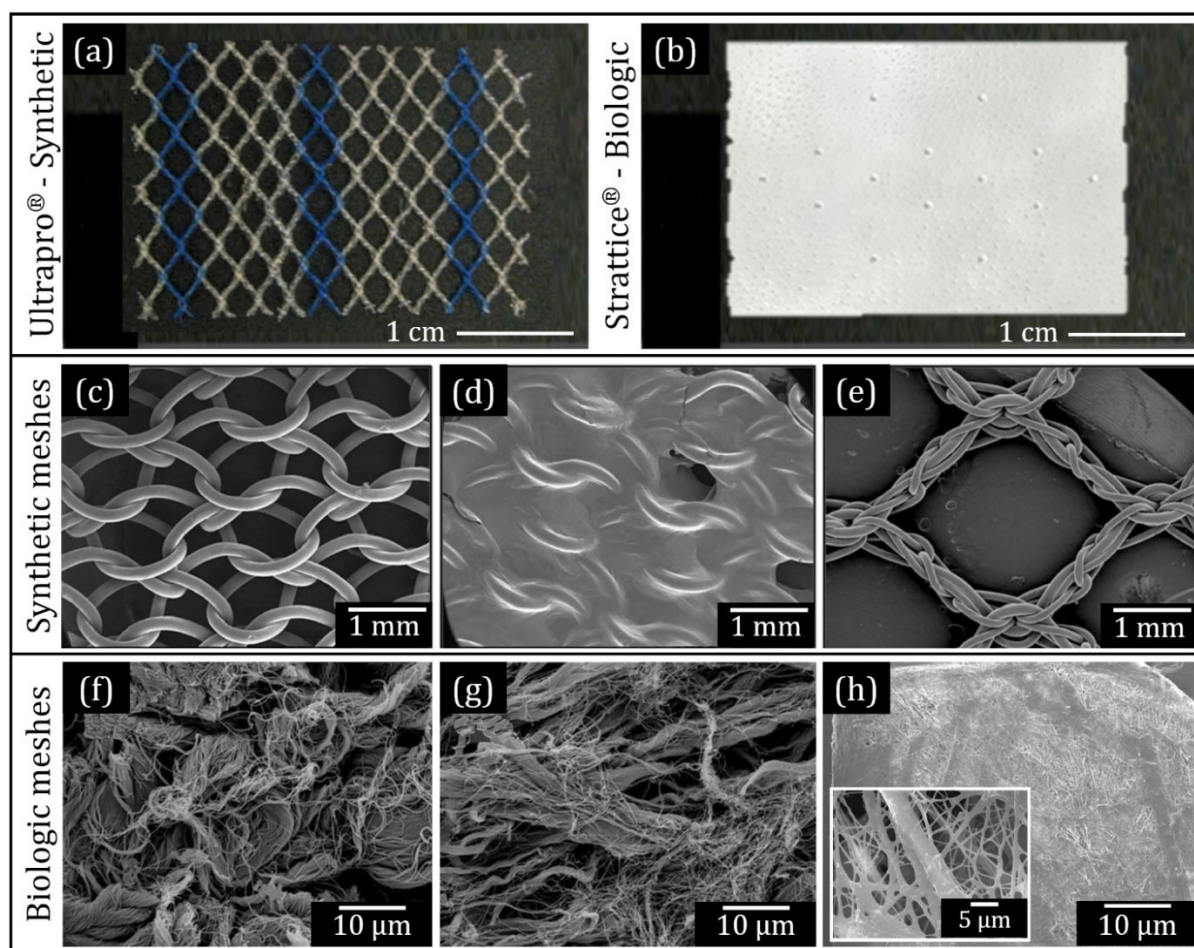


**Figure 2.5 Morphological characteristics of synthetic versus biologic mesh reinforcement.** Macroscopic images of **(a)** synthetic polypropylene mesh; Ultrapro® (Ethicon, Inc., USA) and **(b)** Biologic collagen-derived mesh; Strattice™ Reconstructive Tissue Matrix (Allergan, Plc., Ireland). SEM micrographs of synthetic polypropylene meshes **(c)** BARD™ (C. R. Bard, Inc., USA), **(d)** ECM-coated BARD™ and **(e)** Ultrapro®. SEM micrographs of biologic meshes **(f)** Strattice™, **(g)** Veritas™ collagen matrix (Veritas Technologies, LLC., USA) and **(h)** Alloderm® acellular human tissue matrix (Biohorizons Implant Systems, Inc., USA). The images were obtained as follow, (a, c-e) derived from [160], (b, f and g) from [161], and (h) from [162].

To achieve permanent repair of the fascia defect and prevent reherniation, the implemented mesh needs to finely regulate the integration of material within the host tissue, in a process that involves inflammation, proceeded by cellular and vascular infiltration and ECM remodelling [133]. As with skin grafts and dermal substitute products discussed in the previous section, biologic prostheses are referred to as third-generation meshes; deriving from decellularised animal (xenografic) or human (allograft) sources [154]. In general, biologic meshes are in the form of collagen matrices and have been introduced as a promising alternative to first-generation (non-absorbable) and second-generation (absorbable) synthetic prostheses [154]. Due to the morphological and intrinsic similarities with the native ECM fascia, biologic meshes can better promote tissue reconstruction at a cellular level [155].

Synthetic meshes are commonly associated with chronic pain, bowel adhesion (enterocutaneous fistula), shrinkage, discomfort and infection [128, 156]. Unlike synthetic meshes, biologic meshes can grow into a highly vascularised mesh-tissue complex, that over time and through the constant deposition of collagen can provide the appropriate strength and integrity to the affected region [132]. This occurs similarly with the closure of a wound. The long-term success of a biologic graft will depend upon the fine-tuning of its properties to avoid strong inflammatory responses that may lead to excessive scarring and allow for the efficient collagen deposition and tissue remodelling to replace the fibrotic tissue, followed by the latent resorption of the implant [133]. Figure 2.5 compares the macro- and micromorphology of various commercially available synthetic and biologic, surgical meshes.

Adjusting the degradation properties of biologic-derived materials can be hard to obtain and mostly inconsistent, predominately done by adjusting the number of collagenase binding sites, ultimately retarding the degradation of the donor collagen [133, 155]. Crosslinking the biologic tissue can also be used to adjust the degradation rate but at the expense of not preserving the ECM structure of the mesh that may increase the chances of chronic foreign body type reactions [157]. Even so, when comparing absorbable with biologic prostheses, absorbable meshes are associated with an 8%–10% rate of enterocutaneous fistula and higher chances of reherniation ( $\geq 50\%$ ), as they do not offer an appropriate substrate for effective wall reconstruction, but rather just the resorbability of the mesh material over a poorly defined period [128, 158, 159]. Nevertheless, the cost of producing and preserving biologic meshes is high due to tissue donor limitations, manufacturing, decellularisation methods and the requirement of biologic tissue-derived materials being kept under constant rehydration [158].

The probability of hernia reoccurrence after implantation of a biologic mesh over a permanent synthetic prosthesis, is higher, as demonstrated in large groups (660 participants)

of patients undergoing hernia repair using collagen-based Surgisis Gold® (Cook Biotech, Inc., USA) or conventional polypropylene prosthesis (19% over 5% recurrence, 95% CI,  $p \leq 0.05$ ) based on the LAPSIS trial (ISRCTN: 34532248). Nevertheless, it is hard to equate the reoccurrence rate in a “one-fits-all” approach, with many groups arguing that the type of biologic prosthesis and the period that the construct maintains its tensile strength for, will affect the rate of collagen deposition and the “quality” of the reconstructed tissue [130, 133, 163].

Overall, biologic meshes are expensive to obtain, carry ethical concerns (animal treatment, religious concerns, etc.), can be limited to the size of the graft, can be challenging to determine the degradation rate of the material, may present high recurrence rate, and can present poor mechanical stability [139]. Nevertheless, the high resemblance with the native fascia and the high vascularisation and scar remodelling, makes them a useful candidate in the market.

## 2.4.2 Mesh-specific surgical infections

Along with mesh erosion, mesh migration and enterocutaneous fistula, hernia mesh-related infection is a prevalent and potentially serious condition for which the patient will require further interventions, incurring significant health costs. Approximately 60,000 mesh-related surgical site infections occur in the US alone every year, with similar numbers being reported in Europe [139]. In contrast with superficial surgical site infections (SSI), where the infection only interferes with the skin and subcutaneous tissue and can be dealt with by draining the wound bed, deep incisional SSI occur on the surface of the mesh and are extremely complicated to manage [164]. Further, monitoring and treatment of a deep incisional SSI will account for a year, rather than two months in the case of superficial SSI [164].

In general, the most frequent route of mesh contamination is during the initial incision, where endospores and other bacteria forms on the skin flora or the intestine due to missed bowel injuries may relocate to the surface of the mesh upon contact with the skin during emplacement [165]. Gram-positive *Staphylococci* species, primarily *S. aureus*, are the most common pathogen, accounting for 90% of mesh-related infections [166]. Other Gram-negative bacteria that have been isolated from infected meshes, such as *Pseudomonas aeruginosa* and *Enterobacteriaceae* species are also commonly found [166]. Polymicrobial mesh infections may also occur [167].

It has been shown that the implantation of a medical device increases the chances of infection by a factor of 10,000 – 100,000; in the case of surgical meshes, even though about a third up to a half of the implanted meshes will be contaminated with bacteria, only a small

number of them will develop an infection under clean surgical practices [139]. The chances of mesh-specific infection will depend upon the type of hernia and the surgical method; the chances of incurring deep tissue mesh infection during open surgery is between 2%–4% for most hernia operations, but as high as 6%–10% for incisional hernia repair [168]. Nevertheless, laparoscopy decreases the chances of infection to below 2% [164]. Other factors negatively affecting the chances of infection include the “learning curve” of the surgeon, the size of the hernia, the type, density and form of the mesh filaments, the patient’s long-term health conditions, such as diabetes, obesity, or autoimmune disorders among others [126].

Pre-administering antibiotics is a common practice, although there are no studies that have indicated that doing so reduces the chances of establishing a mesh infection [169]. Mesh infection diagnosis is based on clinical, microbiological and radiological findings, and can be categorised as early or late. Diagnosing a deep mesh infection is conducted by imaging via ultrasound or computerised tomography (CT) and serologically by fluid aspiration [170]. In many instances, the low number of bacteria obtained during collection may result in false-negative cultures [165].

Late diagnosis of a mesh infection constitutes to a mortality rate of 1% [139]. Treatment consists of wound irrigation, prolonged antibiotics, partial or complete mesh removal or a combination of these [171]. Despite all the efforts, the blood-mesh barrier and poor incorporation of the surrounding tissue limit the innate cells from reaching the formed biofilm, ultimately necessitating for the surgical removal of the mesh in over 40% of the cases [164]. Re-operation to surgically remove the mesh, predominately in the form of open surgery, may require as many as five surgical interventions, thus significantly increasing the risk of subsequent reherniation by over 20% [172].

As previously noted, with over 200 hernia meshes being commercially available today, there is a direct correlation between the variant types of surgical prostheses available and the chances of infection [173]. Adherence of bacteria is highly variable, where the microscopic structure of the filaments directly influence the adherence and subsequent colonisation, where multifilament meshes have been found to be twice as likely to lead to infection than monofilament meshes [173]. Biologic meshes are generally less prone to infections due to better revascularisation and cellular infiltration through their inherent ECM morphology [174]. Figure 2.6 indicates the ineffectiveness of the different types of surgical prostheses to circumvent bacteria colonization and subsequent infection. Darehzereshki et al. (2014) and Kanitra et al. (2019), in two independent studies, through the meta-analysis of clinical outcomes have demonstrated that the incidence of infection using biologic mesh is only 10%–11% compared to 33%–40% with the use of synthetic prosthesis in a contaminated

setting [174, 175]. Nevertheless, the extremely high costs of biologic prostheses that in most instances exceed 30,000 USD compared to a monofilament polypropylene meshes that cost between 80-150 USD [158] makes the use of biologic-derived prostheses improbable for the majority health care providers and most economies around the world.

Over the years, several approaches have been proposed in an attempt to reduce the incidence of mesh contamination. Initially, several groups have attempted presoaking the mesh within an antibiotic solution, such as gentamicin or vancomycin, a method that was found to reduce the occurrence of methicillin-resistant *S. aureus* (MRSA) but did not prevent biofilm formation in the long-run as it only provided protection over a 6 h period [169, 176]. Some spore-forming bacteria can stay dormant in the form of endospores for extended periods before they enter germination [177]. Furthermore, many antibiotics, such as aminoglycosides and amoxicillin, have shown increased resistance ( $\geq 25\%$ ) against *Staphylococci* species, with predominately only vancomycin left to handle MRSA infections [139]. Due to this, the European Medicines Agency (EMA) and FDA have positioned themselves strongly against the direct use of antibiotics as a prophylactic measure for surgical implants, due to the prolonged antibiotic resistance implications that may carry.

Delivering antiseptics is a great approach to circumvent antibiotic resistance as they are effective over a broad spectrum of bacteria and are rarely associated with resistance [178]. Bioabsorbable sutures that elicit triclosan are commercially available by Ethicon under the brand name Vicryl®Plus and are recommended for all types of surgeries, but are not routinely used due to high costs [179]. Today, the manufacturing methods used to develop prostheses that provide certain antimicrobial properties are based on (1) dipping or soaking the material [176], (2) physical coating of the mesh [180] or (3) chemically functionalizing the surface, such as grafting [178]. Submerging a surgical mesh with an antimicrobial agent or antibiotics has only been found to offer protection for a 6-h window post-operation [181], where no superiority over systematic administration of antibiotics has been observed [164].



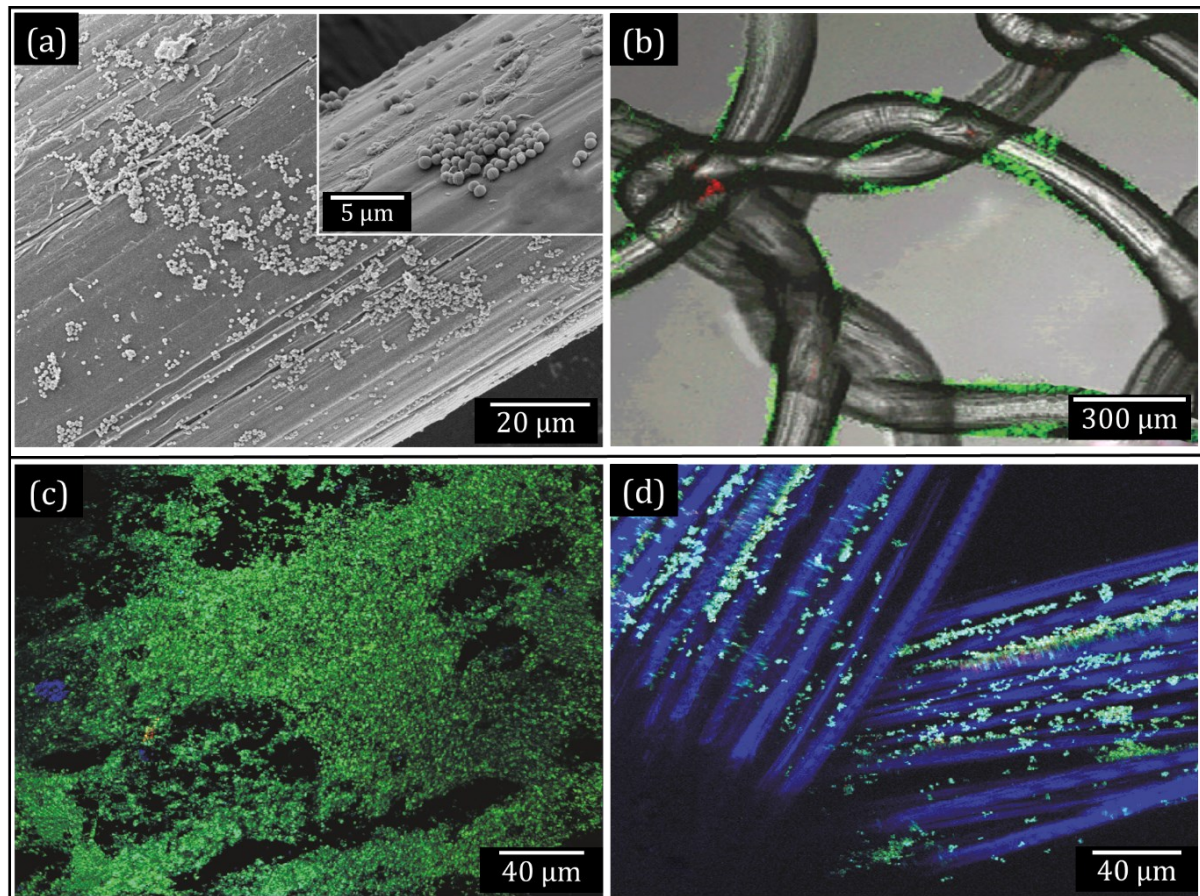


**Figure 2.6 Comparisons between the bacterial colonisation on synthetic mono-/multifilament, absorbable and biologic surgical meshes.** Contaminated biofilm-forming *S. aureus* on **(a)** multifilament (braided) polypropylene mesh, SEM image (Credit: The Institute of Photonic Sciences, ICFO, Spain); **(b)** Bard® monofilament knitted polypropylene mesh [167]; **(c)** biologic mesh from human dermal collagen (Bard® Davol Inc., USA) [182], and; **(d)** Vicryl® (Johnson & Johnson Innovation, LLC., USA) polyglactin 910 absorbable mesh [182]. For b, c, and d the specimens were stained with live/dead Baclight® bacterial viability stain and image using a confocal scanning microscope. Note: This figure presents different types of bacteria-contaminated hernia meshes *in vitro*, in an attempt to demonstrate the inability of commercially available mesh implants to provide active protection against bacterial infection. The responses would have differed significantly *in vivo*, post-implementation, where the body's immune system would have mitigated bacterial growth and prompt clearance.

The FDA approved antimicrobial prostheses and ongoing clinical and preclinical trials presented in Table 2.3, refer to mesh material being impregnated via physical coating or chemical surface modifications with antimicrobial substances. Such approaches are

predominately based on solvent casting by drop-by-drop or immersion and grafting and generally allow for 7 days up to one month of some form of antimicrobial activity [183, 184]. Nevertheless, it is difficult to control the deposition and thickness of the coatings, as well as the overall efficiency of most grafted meshes. As the architecture of the meshes listed on the table below does not offer any advantages over the commercially available conventional meshes, with the majority of them incorporating antibiotic substances, at present, those products have not been widely popular among the surgical community.

**Table 2.3** Prosthetic meshes with different forms of antimicrobial properties available on the market, and in clinical trials or preclinical studies.

Mesh	Mesh architecture and highlights	Ref.
<b>Mycromesh® Plus</b> (W. L. Gore and Associates, Inc., USA)	Expanded-polytetrafluoroethylene (ePTFE) patches impregnated with chlorhexidine diacetate and silver carbonate. <b>Note:</b> Poor fibroblast penetration and tissue adhesion [184]. Succeeded by Dualmesh® Plus. (FDA approved; K946106).	[185]
<b>Dualmesh® Plus</b> (W. L. Gore and Associates, Inc., USA)	Similar to Dualmesh® Plus but with an improved architecture; consisting of a “smooth” side and a Corduroy® (ribbed pattern) surface side, in an attempt to induce bacteria contact-killing. <b>Note:</b> Not allowed for intraperitoneal use due to increase toxicity levels correlating with the presence of silver [184]. A recent study has indicated several a log decrease of bacteria present per implant compared to Mycromesh® Plus; $2.85 \times 10^2$ colony forming units (cfu)/implant, but was concluded not sufficient to render an infection from occurring [186]. The use of Corduroy® surface to encourage and enhance cell ingrowth did not appear to significantly differ compared with conventional ePTFE prostheses [187]. (FDA approved; K946106b).	[188]
<b>Xenmatrix™ antimicrobial surgical graft</b> (C. R. Bard, Inc., USA)	A non-crosslinked porcine dermal graft coated with rifampin and minocycline. <b>Note:</b> First bio-prostheses to provide a form of bacterial protection. Nonetheless, the use of antibiotics is a widely unpopular approach due to risks associated with antibiotic resistance. (FDA approved; K151177).	[183]
<b>Ventrio™ hernia patch with TRM antimicrobial coating.</b>	A double-side mesh consisting of macroporous polypropylene from one side and an anti-adhesive submicron ePTFE coating from the other, integrating $115 \text{ mg}\cdot\text{cm}^{-2}$ rifampin/minocycline within a biodegradable matrix of tyrosine-based polyacrylate (TRM).	[139]

---

(C. R. Bard, Inc., USA)	<b>Note:</b> The adhesion area, tenacity, and tissue ingrowth were found to be similar to other commercially available meshes. Complete absorption of the coating by hydrolysis was noted within 24-32 weeks [189]. Nonetheless, the use of antibiotics is a widely unpopular approach due to risks associated with antibiotic resistance. (FDA approved; K081777).	
<b>Cook® antimicrobial hernia repair device</b> (Cook Biotech, Inc., USA)	A porcine-derived submucosa biologic graft incorporating gentamicin sulfate. <b>Note:</b> A unique architecture where the antibiotic is kept within raised wall craters. Gentamicin is one of the last remaining effective antibiotics against MRSA, where studies have shown that long-term exposure in low concentration increases the chances of antibiotic-resistance [190]. Further, ethical concerns may be an issue due to the use of porcine for some groups. A study concluded earlier this year that no adverse toxicity is directly attributable to the presence of gentamicin within the mesh. Nevertheless, the clinical study recorded graft infection at 8% of the patients undergoing single-stage ventral hernia in contaminated settings [190]. (Clinical trial; NCT02401334).	[190]
<b>Ariste Medical drug-eluting mesh</b> (Ariste Medical, Inc., USA)	A macroporous mesh consisting of polypropylene knitted filaments incorporating rifampin and minocycline. <b>Note:</b> No information available or published, only the granted patent. Since then, the company has filed for Chapter 11 bankruptcy. (Preclinical study; US10314912B2).	[191]

---

### 2.4.3 Current advancements and future perspectives in hernia mesh development

The progression of material science can divert the trajectory of the current "passive" approach; where the key focuses are the structural integrity and mechanical stability of the hernia mesh, and move it towards a more "active" approach that can further influence mesh-tissue integration and attain antimicrobial protection. The key research areas in the development of advanced hernia meshes involve limiting acute and chronic forms of inflammation, obtaining physiologically relevant tensile properties, formulating a microscopic niche that can induce cell ingrowth and vascularisation, and preventing mesh-related SSI.

Despite the research focus and progression to date, and since the early 2000s, there have been minimal, predominately inconsequential, advancements in the engineering of hernia meshes. Non-absorbable synthetic meshes, predominately made of polypropylene, remain the most widely used prosthesis, possibly due to its low cost and the surgeon's familiarity with the material. As aforementioned, absorbable mesh materials were initially linked with higher chances of hernia reoccurrence, mostly due to the lack of controlling the degradation of such implants. On the other hand, biologic meshes are too expensive to be used in every-day practice and are usually reserved for specific circumstances, such as contaminated fields. The future requires an economically viable surgical mesh that can further advance the implant's properties to fulfil today's critical clinical challenges.

Different methodologies can be used to compose an environment that can prevent or limit infection. Research on antimicrobial surgical prostheses has focused on antimicrobial coatings, drug-eluting implants, antifouling surfaces, or electrospun NFs [132, 139, 192].

The development of antimicrobial surfaces by covalently grafting polycationic polymers and macromolecules, such as poly(quaternary) ammoniums, chitosan, and antimicrobial peptides, at the surface of the implant, ultimately inducing contact killing by lysing the bacteria's negatively charged membranes, has been considered as an interesting approach [193]. Nevertheless, although such a tactic can reduce the need for antibiotic use and limit the chances of multidrug resistance, upon the integration of the mesh by the host tissue, the surface of the implant gets rapidly coated by tissue-related proteins, thus substantially limiting its bactericidal activity [194].

Coating the mesh filaments with a drug-impregnated hydrophilic hydrogel by embedding or immersing; such as dip-coating, the implant to form an antimicrobial layer has also been found to be ineffective, mostly due to the ease of enzymatically breaking down hydrogel

coatings *in vivo* [192]. This is ultimately associated with high cytotoxicity and antiproliferative activity due to the rapid release of the entrapped drug in the surroundings, which can further encourage bacterial resistance [192]. For instance, a nitric oxide (NO)-releasing poly(ethylene-vinyl acetate) coating on a polypropylene mesh initially presented effective anti-biofilm activity against a range of Gram-positive and Gram-negative pathogenic bacterial strains but was found to be ineffective in a subsequent murine model, *in vivo* study [195]. Further, antifouling layers on mesh material based on superhydrophobic and superhydrophilic surfaces have been found to be effective in preventing bacterial colonisation, but at the same time, vastly reported in the literature to inhibit the proliferation of adherent cells, preventing subsequent tissue ingrowth [139, 196].

Another approach widely studied has been the use of metal ions, which are effective against a wide range of bacteria, and not generally associated with microbial resistance [197]. Among the metal ions, silver and gold have been readily coated on the surface of surgical materials by sputter coating, physical vapour deposition, and plasma polymerisation to form nanoparticle agglomerates [197]. Recently a nano-crystalline silver-coated polypropylene mesh produced via the electrospaying technique, with an average particle size of 200 nm, was found to induce a significant ( $p < 0.05$ ) bactericidal effect in comparison to an uncoated commercially available polypropylene mesh, in a rat model [198]. Nevertheless, the particle distribution was inhomogenous, making the toxicity findings of the *in vivo* study inconclusive [198]. However, the induced mechanical alterations on a mesh due to the addition of a metal layer, along with ion leaching-induced cytotoxicity due to erosion have limited the willingness of the FDA to approve such constructs as implantable devices [192].

The favourable morphological and surface properties of electrospun fibres toward mimicking the tissue's native fascia that can, thus, promote mesh-tissue integration in a similar manner with biologic meshes, has led to different tactics of employing NFs as prosthesis [199]. Such approaches involve either direct deposition of electrospun fibres, as functional coatings, at the surface of commercially available meshes, or through the fabrication of nanofibrous mesh constructs. The most commonly employed polymers for the construction of such mesh material have been PCL, PP, and PLLA [200–202].

The majority of the studies have focused on the compliance of electrospun mesh material towards improving mesh-tissue ingrowth and subsequent abdominal wall reconstruction, with no published work to date focusing on drug-loaded antimicrobial systems for the prevention of mesh-associated SSI while circumventing the incorporation of antibiotics [203, 204]. Although electrospun NFs have illustrated their ability to act as hernia meshes for hernia reconstruction

due to their good biocompatibility, several studies have demonstrated insufficient mechanical stability [200, 203].

A recent study developed a large pore PP mesh integrating a coating consisting of PCL nanofibres integrating antimicrobial peptides (PEP-1) [205]. The findings suggested no toxicity on dermal fibroblasts and similar mechanics with commercially available surgical meshes. However, antimicrobial efficiency was only apparent over a span of 48 h against *E. coli*, but not for the most commonly associated SSI pathogen, *S. aureus* [205]. In recent work Liu and colleagues [204], assessed the effectiveness of PCL-only, PCL-irgasan, and PCL-levofloxacin loaded nanofibres produced via conventional blend electrospinning to act as hernia mesh material. The loaded fibres presented a first-order release of half of the loaded drug within a week, where the antimicrobial properties were only assessed in the form of inhibition zones by disc diffusion (approximately 2.6 cm clearance zone in *E.coli* and *S. aureus*) and did not evaluate the constructs mechanics [204]. Further, as aforementioned, it should be noted that the incorporation of antibiotics within implants is widely disregarded as an effective long-term approach.

A nanofibrous mesh is yet to reach a clinical study with a substantial amount of work still required in assessing the *in vitro* antimicrobial efficiency, mechanical stability, and, in later stages, the *in vivo* evaluation of mesh integration and tissue in-growth capabilities, allowing for an infection-free hernia repair process.

## 2.5 Electrospinning

Among the several processing techniques, including thermal-induced phase separation, drawing, template synthesis, and self-assembly, electrospinning is of considerable significance as a rapidly evolving fibre preparation method [206]. It is a highly versatile method used to process solutions, suspensions or melts into continuous fibres of nano/microscale diameters [207], and is the only method for mass-producing continuous fibres at this range [208]. A detailed description of this process is provided in the following section.

### 2.5.1 Principles of electrospinning

Electrospinning is one of the most conventional methods used in TE, and it is based on the principle that electrostatic forces can be used to form and expand fibres out of a polymer solution [209]. The principle of this process was first described in a patent entitled "*Process and Apparatus for Preparing Artificial Threads*" in the 1930s by Anton Formhals, who was considered by many to be the father of electrospinning [210]. However, considerable emphasis was not given to the process until the 1990s, with works led by Reneker and Rutledge, who described the process [211].

The electrospinning process uses high voltage to charge a liquid solution or a melt by placing it between two conductors that endure the electromagnetic charge of opposite polarities to form fibres [212]. A standard laboratory-scale setup consists of four main components: a high-voltage DC (or AC) power supply, a syringe pump, a nozzle (usually metallic capillary), and a collector that can simply be a metallic foil/plate/disc [213]. The electrostatic force produced by the high-voltage supply is applied to a polymer solution or melt, which is dispensed through the fine needle orifice at a controlled rate. When electrospinning, the precursor solution extruded from the spinneret orifice forms a small droplet that is subject to an accumulated charge in the presence of an electric field [97]. The electrified discharged polymer induces a conically-shaped geometry referred to as the 'Taylor cone' [213, 214]. Increasing the strength of the electric field causes an increased accumulation of charges at the surface of the polymer bud. After this, the repulsive electric forces overcome the surface tension of the polymer solution/melt, and that leads to vigorous whipping and splitting motions due to the bending instabilities generated, which causes the fibre to elongate through the application of mechanical force [215]. At this point, the geometry of the formed asymmetrically electrospun (as-spun) fibres is directed by the electrostatic repulsion, colloid stability, the incoming surface ratio, and gravity [209, 212]. Solidification of the liquid solution occurs by

establishing a zone that thrusts the charged molecules, allowing for solvent evaporation to occur continuously, stretching the drawn polymer threads as they advance towards the grounded or oppositely charged collector [209]. This transition between the liquid and solid phase is due to the Ohmic current that presents a low acceleration being transitioned primarily to convective flow, thus increasing its acceleration [216]. Figure 2.7 (a-b) illustrates the basic concept behind the electrospinning process.

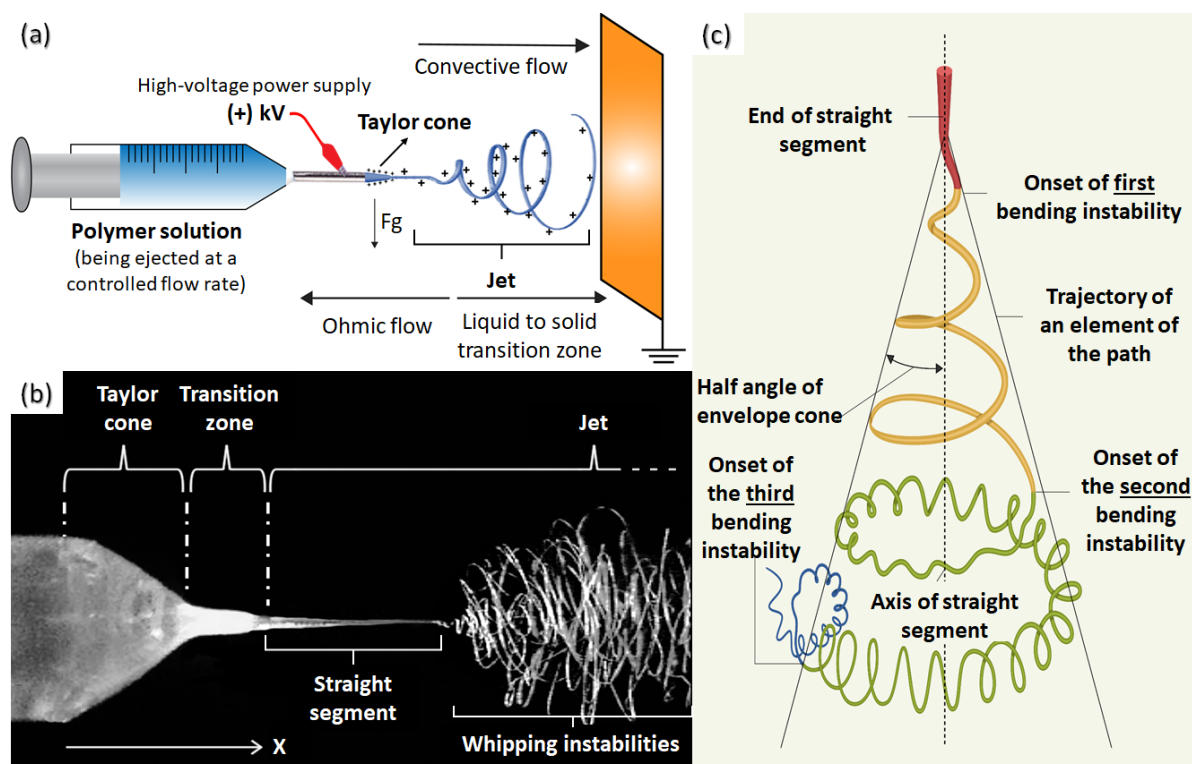


**Figure 2.7 Fundamentals of electrospinning.** (a) Conventional electrospinning concept; (b) high-speed photograph outlining the Taylor cone formation where it shows the linear segment of the polymer jet, followed by the whipping jet region, modified from [217] and [218]; (c) the prototypical instantaneous position of the jet path succeeding through the three sequential bending instabilities, modified from Xue et al. [97].



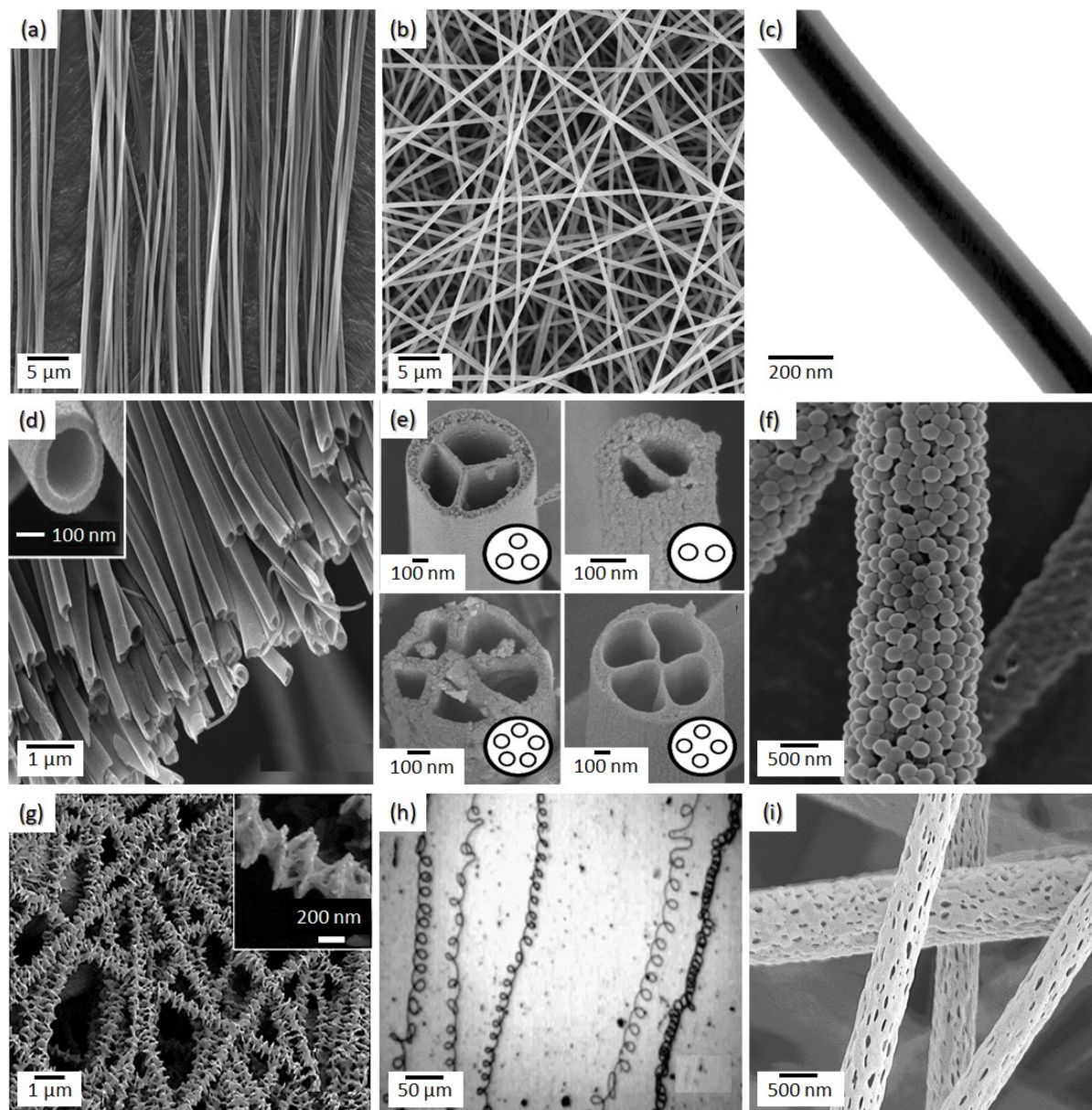


**Figure 2.8 Structural diversity of individual electrospun fibre morphologies. (a)** Aligned; **(b)** randomly-oriented; **(c)** core/shell [221]; **(d)** hollow [222]; **(e)** multichannel microtubes [223]; **(f)** colloidal nanoparticle-decorated [224]; **(g)** shish-kebab [225]; **(h)** helical [226]; **(i)** porous, electrospun fibres.

The unique properties carried out by engineered nanofibres include a high specific surface area, a large surface-to-volume ratio, and a large fibre length-to-diameter aspect ratio [97]. Moreover, those properties allow the construction of highly-porous ECM-like constructs that mimic membranes with adjustable pore size and wide surfaces that allow chemical functionalization [219].

The formed electrospun mats exhibit a web-like fibrous structure, due to the considerable extent of plastic deformation caused by the high charge density of the jet and the unstable whipping motion [220]. This phenomenon is known as bending instability, and it leads to a randomly-oriented and non-aligned fibrous mats [220]. Nonetheless, through the continuous research and evolution of these basic principles, as well as the manipulation of the conventional electrospinning apparatus, unique morphologies and structures have been successfully produced over the past two decades, as indicated in Figure 2.8.

Recently, several nano/microfibre structures were generated using a variety of electrospinnable organic and inorganic materials, and the size-dependent structural behaviour of the generated nanofibres has made them of interest in many fields, including tissue engineering, drug delivery [227], sensing [228], energy [229], fibre reinforcement [230], and more.

### **2.5.1.1 Jetting mechanism, fibre growth and deposition**

The electrospinning process represents an electro-fluid-dynamics (EFD) problem, which stimulates electrified liquid jets to whip and elongate to form fine fibres [231]. In the interest of controlling the morphology, structure, and output of the fibres, the underlying processes that cause a polymer droplet to undergo this transition can be described into three principal stages: (a) the formation of the Taylor cone, which is also known as the post-liquid droplet charging; (b) jet stretching (whipping instabilities), accompanied by jet elongation and branching; and (c) the expansion, solidification, and deposition of the formed fibres. The three stages are described in detail below.

#### **a. Formation of the Taylor cone (post-liquid droplet charging)**

As the name suggests, electrical forces are the driving force of the electrospinning process. As the droplet gets electrified, it gradually reduces in size at the orifice of the needle in an attempt to keep an equilibrium force. As the voltage amply increases, the spherical droplet electrifies and deforms to a hemisphere-shaped cone denoted “Taylor cone”, with the electric force being directed towards the tip of the Taylor cone [232]. When the surface tension of the solution overcomes the applied electric field, jets get ejected from the Taylor cone’s surface [232]. Taylor [233] calculated the critical tension ( $V_c$  in kV) at which the eruption occurs based on the following equation:

$$V_c = \frac{4H^2}{h^2} \left( \ln \left( \frac{2h}{R} \right) - 1.5 \right) (1.3\pi R\gamma)(0.09) \quad (2.1)$$

where,  $H$  is the distance between the needle-tip and the collector (in cm),  $h$  is the length of the needle's capillary (in cm),  $R$  is the radius of the needle (in cm),  $\gamma$  is the surface tension of the polymer solution (in  $\text{dyn}\cdot\text{cm}^{-1}$ ), and 0.09 is the conversion factor to express the voltage (in kV). Several groups have calculated the velocity of the electrospinning jet at the point of collection using high-speed cameras [234, 235]. As expected, increasing the voltage increases the repulsive forces between the needle-tip and the collector and thus the jet's velocity, which has been calculated to be between 0.6 and 15  $\text{m}\cdot\text{s}^{-1}$  [234, 235]. Cauchy–Schwarz inequality has been applied to predict the critical length of a jet before it enters the instability regions and branching (Figure 2.7(c)), which has been evaluated and verified experimentally on cellulose and poly(3-hydroxybutyrate-co-3-hydroxyvalerate) (PHBV) polymer solutions [236], based on the following equation:

$$L = \frac{4\kappa Q^3}{\pi\rho^2 I^2} (R_0^{-2} - r_0^{-2}) \text{ for } R_0 = (2\sigma Q/\pi\kappa Q E)^{1/3} \quad (2.2)$$

where,  $L$  is the critical length (in cm),  $\sigma$  is the surface charge (in  $\text{C}\cdot\text{m}^{-2}$ ),  $Q$  is the flow rate (in  $\text{mL}\cdot\text{h}^{-1}$ ),  $r$  is the radius of the jet (in cm),  $k$  is the dimensionless conductivity of the fluid,  $\rho$  is the density of the polymer solution (in  $\text{g}\cdot\text{cm}^{-3}$ ),  $E$  is the applied voltage (in kV), and  $I$  is the current passing through the jet (in nA).

### b. Jet stretching and elongation

As the straight segment of the jet begins to decrease monotonically (in relation to the travelling distance of the jet to the collector), the time required for the excess charges to be redistributed along the jet prolongates [237]. Those excess charges redistribute within the surface and the centre of the jet, causing electrically-driven bending instabilities that deform the straight segment to produce coils through the remainder of the jet path [237]. These system instabilities can be explained based on the Earnshaw theorem [220] that states:

*“Collection of point charges cannot be maintained in a static equilibrium solely by the electrostatic interactions of the point charges.”*

Research conducted at the University of Akron and the Israeli Institute of Technology, led by Reneker and Yarin [238], first described the complex series of sequential events causing

bending, coil formation, and stretching onto thin fibres. Afterwards, studies carried out by different groups [232, 238, 239] mathematically described the three types of instabilities that occur during the elongation of each travelling segment of a jet, as can be seen in Figure 2.7(c).

**i. Rayleigh (capillary driven) instabilities due to high ion currents**

The Rayleigh instability is symmetrical to the straight segment axis [240], where surface tension is suppressed due to the applied electric field  $E_0$ , and the surface charge density overcomes the threshold given by:

$$(\varepsilon - \varepsilon')E_0^2 + \frac{4\pi^2\sigma^2}{\varepsilon'} = \frac{2\pi\gamma}{H} \quad (2.3)$$

where,  $\varepsilon$  and  $\varepsilon'$  are the dielectric constants within the jet and at the surface of the jet respectively, (with  $\varepsilon/\varepsilon' \gg 1$ ,  $\sigma$  being the surface charge),  $\gamma$  is the surface tension (in  $\text{mN}\cdot\text{m}^{-1}$ ), and  $h$  is the distance from the pendant drop to the grounded or oppositely charged collector (in cm).

**ii. Axisymmetric instabilities**

Axisymmetric instabilities are presented at higher electric fields when the Rayleigh instability of the jet is suppressed by the accumulation of viscoelastic stresses caused by the excessive stretching of the polymer [241].

**iii. Non-axisymmetric (whipping or bending) instabilities**

The non-axisymmetric instabilities are rapid bending instabilities that the jet experiences at the final stages and when the travel path of the jet has expanded significantly [242]. They are presented as a fluid column with long disordered waves that are directed by the lateral direction of the electric force (due to the dipolar nature of the distributed energy) and unsteady aerodynamic interactions [242].

The three instabilities evolve as the electric field increases, with Rayleigh instability presenting the lowest and the non-axisymmetric instability presenting the highest electric field strength. As the path through the bending instabilities is electrically driven, it is not influenced by the surface tension of the polymer solution.

These instabilities ultimately cause the cylindrically-shaped jet to collapse and grow to unstable segments [238]. Bending and branching may co-occur or progress in independent

segments [238]. Moreover, it is common that the established coils form beads and branches during the segmentation of the jet. Also, when the charge per unit area is too low (characteristic of less viscous solutions), beads form due to droplet division, whereas branches build up as the electric field exceeds the requirements for generating a single jet in highly viscous solutions [243].

### **c. Expansion, solidification, and deposition**

During the elongation process, the solvent evaporates, allowing for charged polymer fibres to get deposited at the collector's surface. As the fibre forms, expands and dries from the spinneret to the collector, a portion of the initial polymer fluid will be collected in the final stage. The solid fibre has been calculated, by Yarin and co-workers, to be on average, 0.0013 times that of the fluid jet, although it will differ among variant polymers and by altering the concentration of the polymer solution [244]. Through the prolongation of the solidification process, the jets can further expand and generate thinner fibres. Furthermore, manipulating the diameter and morphology of the fibres can be achieved by different approaches that are explained in detail in the following section (*2.5.1.2 Parameters Affecting the Electrospinning Process*).

Finally, the morphological properties of the fibres will be predominately determined by the configuration of the collector where the fibres are deposited. After deposition, the electrical charges are still captured at the surface of the dry fibres but will be quickly dissipated, with no further apparent instabilities [245]. Nonetheless, the low conductivity of most dried polymeric fibres leads to the accumulation of residual charges that will repel jets that carry a similar charge from being deposited due to a pendulum-like motion. This ultimately limits the thickness of nonwoven mats to less than 1 mm [97].

#### **2.5.1.2 Parameters affecting the electrospinning process**

Whilst electrospinning can be overall considered a straightforward fabrication method; many parameters affect the formation of fine fibres from a polymer solution. In the interest of producing electrospun fibres for tissue engineering, their structural properties need to be tweaked to generate the appropriate fibre morphology, diameter and porosity, fibre orientation (aligned or randomly oriented), and cell-scaffold interactions that provide a biocompatible environment that can facilitate improved cellular expansion and proliferation [213, 214].

A list of the most critical parameters that affect the production of electrospun fibres is presented in Table 2.4. These can be classified based on solution, electrospinning, and ambient parameters. Solution parameters refer to polymer concentration and polymer molecular weight, solvent volatility, solution viscosity, surface tension and solution conductivity, among others. With regard to the electrospinning parameters, the electric field strength, electrostatic potential, flow rate, and distance between the spinneret and the collector need to be adjusted. Finally, ambient parameters refer to the chamber and solution temperature, humidity and type of atmosphere, among others.

In general, by prolonging the fibre elongation or flight time during the electrospinning process, finer fibres can be produced, which can be achieved by increasing the distance between the collector and the spinneret. Moreover, using low volatility solvents and raising the temperature to increase the evaporation rate of the solvent is also possible. However, it must be noted that increasing the working distance beyond the critical threshold (the point at which the stability of the Taylor cone is impaired) results in a significantly longer flight time, which can lead to inhomogeneous fibre formation [29]. Insufficient solvent volatility and low temperatures may lead to wet fibre fusion during deposition [29]. Therefore, it is crucial to observe and monitor the different parameters that affect the electrospinning process to determine the ideal operating conditions that yield optimised fibre characteristics tailored to the specific requirements of each study.

One of the most important parameters for obtaining an electrospinnable solution is determining the chain entanglement of the polymer solution from the molecular weight and its concentration. Within a solution, the root-mean-square distance of the segment of a molecular chain towards the centre of its mass provides the average radius of gyration ( $R_g$ ) [246]. If the concentration is too low (diluted solutions), the polymer chains do not overlap, with the viscoelasticity of the solution being governed by shorter polymer chains. By increasing the concentration of the polymer, entanglement occurs as the polymeric chain begins to overlap.

The critical concentration ( $C_c^*$ ) is generally accepted to be proportional between the polymer's molecular weight ( $M_w$ ) and the effective solvent volume:

$$C_c^* = \frac{3M_w}{4\pi R_g^3 N_A} \quad (2.4)$$

where,  $N_A$  is the Avogadro's constant [247]. When the polymer concentration is below the critical point ( $C < C_c^*$ ), inadequate chain entanglement renders the formation of a stable jet due to Rayleigh instabilities (Figure 2.9(a-b)). For stable electrospinning, the polymer

concentration needs to be higher than the critical point ( $C < C_c^*$ ) (Figure 2.9(c)) [248]. The rheological behaviour of the polymer solution from which the  $C_c^*$  of the polymer solution can be evaluated is presented in Figure 2.9(d). Evidently, there is a clear correlation between the  $M_w$  of a polymer solution and the corresponding  $R_g$  value, and thus, in many cases, attempting to electrospin variant molecular weights of the same polymer can ultimately contribute to the procurement of the required concentration (beyond  $C_c^*$ ) for effective and stable electrospinning.

The ideal operating range of electrospinning conditions differ significantly due to the vast selection of polymers and the corresponding solvent systems. Moreover, most of the parameters listed, in Table 2.4, are interdependent, leading to non-linear causalities that are one of the many great challenges in the electrospinning field.

At the moment, the majority of the research conducted for skin TE surrounds the use of the conventional needle-based setup described earlier (with either a drum or a flat collector). Understanding the parameters that influence the electrospinnability of a polymer solution and the subsequent properties of the formulated fibres, have made it possible to advance the polymer chemistry further and evolve the capabilities of the produced electrospun scaffolds. However, a significant amount of research has focused on further manipulating the design of electrospinning devices, based on these fundamental principles that were described in this section, to further advance on the producibility and morphological architecture of the fibres.

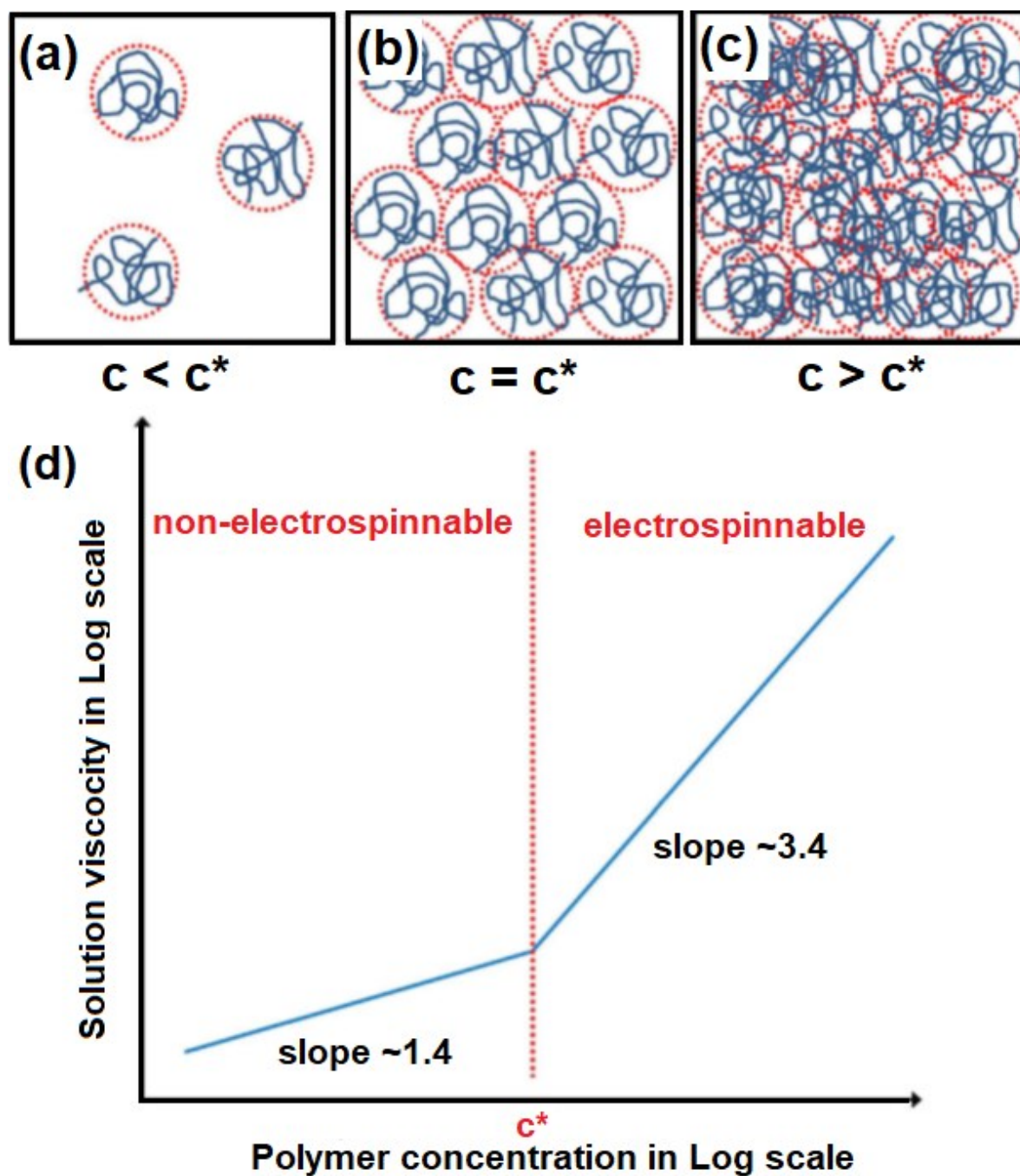


**Figure 2.9** The effect of solution viscosity towards the electrospinnability of a polymer solution. **(a)** The concentration is too low; **(b)** chain entanglement on critical concentration; **(c)** chain entanglement above critical concentration; **(d)** log phase of solution viscosity over polymer concentration. Modified by Han and Steckl [248].



**Table 2.4** List of parameters affecting the fibre formation during electrospinning [29, 227].

Parameters		Influence on fibre formation
<b>Solution Parameters</b>	Viscosity	<ul style="list-style-type: none"> <li>- Low viscosity → electrospaying, bead defects, may require higher voltage or higher solution viscosity for electrospinning.</li> <li>- High viscosity → fibre diameter generally increases while the chances of bead forming decreases.</li> </ul>
	Molecular mass	<ul style="list-style-type: none"> <li>- High molecular chain entanglement → viscosity increases, which in turn decreases the electrospinnability of the solution → increases fibre thickness.</li> <li>- Influences viscosity (<i>vide supra</i>) → a higher molecular mass results in a more uniform fibre scaffold morphology.</li> </ul>
	Concentration	<ul style="list-style-type: none"> <li>- A sufficient polymer concentration allows for the required molecular chain entanglement → overcoming surface tension without fragmentation of the jet → resulting in uniform continuous fibres.</li> </ul>
	Conductivity	<ul style="list-style-type: none"> <li>- A correct conductivity will promote charge accumulation → requiring less voltage for the jet eruption.</li> <li>- High conductivity has been reported to cause unstable multi-jetting because of electrical discharges to the surrounding air.</li> <li>- The fibre diameter decreases with increasing conductivity; where ionic materials can reduce atomisation of polymer jet.</li> </ul>
	Dielectric constant	<ul style="list-style-type: none"> <li>- A solvent's higher capability to retain an electric charge within a solution helps to distribute the surface charge of the jet uniformly and leads to improved electrospinnability and thinner fibres.</li> </ul>
<b>Solvent Properties</b>	Solvent volatility	<ul style="list-style-type: none"> <li>- Sufficiently volatile solutions → prevent the collection of wet fused fibres.</li> <li>- Highly volatile solutions → induce premature solidification without sufficient elongation of the fibres and subsequent morphological defects, hinder thin fibre production, while increasing the risk of spinneret blockage (clogged needle).</li> </ul>
	Surface tension	<ul style="list-style-type: none"> <li>- Beads may form if surface tension is considerably higher than the critical Wenzel level; this can be appropriately adjusted by adding a compatible surfactant within the polymer solution.</li> </ul>
	Vapour pressure (vapour diffusivity)	<ul style="list-style-type: none"> <li>- Influences the solvent evaporation rate during electrospinning.</li> <li>- Rapid solvent evaporation may influence the formation of non-cylindrical secondary morphologies, e.g., net-like spider webs.</li> </ul>
<b>Operating Conditions</b>	Applied voltage	<ul style="list-style-type: none"> <li>- Must exceed critical voltage, <math>V_K</math>, to overcome the surface tension of the polymer solution and maintain a jet.</li> <li>- By increasing voltage → the jet's flight time can be significantly reduced, that can increase the diameter of the fibres. Commonly this is dealt with by adjusting the working distance, or by lowering the voltage potential difference between the spinneret and the collector.</li> <li>- Above <math>V_K</math>, it may induce an erratic jet and form secondary morphologies, and <i>vice versa</i>.</li> </ul>
	Solution flow rate	<ul style="list-style-type: none"> <li>- An increased flow rate → generally constitutes in a shorter jet stretching path, larger pore size, and thicker fibres, and <i>vice versa</i>. Secondary morphologies, as well as completely rending the electrospinnability of a solution, will occur beyond a critical distance, which will be specific to the polymer and solvent system.</li> </ul>
	Working distance	<ul style="list-style-type: none"> <li>- By decreasing the distance beyond a critical point → thicker fibres and morphological defects may arise.</li> <li>- By increasing the distance → thinner fibres can be obtained, but an increase in the corona discharge and Rayleigh instabilities, can result in beaded or fused fibre defects beyond a critical distance.</li> </ul>

Collector geometry	<ul style="list-style-type: none"> <li>- Different fibre arrangements are possible with different collector configurations. Aligned and randomly oriented, crossed array, braided, nanoweb, or coil fibres can be obtained through collector geometries, such as drum, plate, disc, honeycomb, parallel wires, rings, centrifuge walls, and others.</li> </ul>
Spinneret orifice	<ul style="list-style-type: none"> <li>- A smaller spinneret orifice diameter (smaller gauge size, for instance, a 24G needle instead of 21G) → may produce narrower fibres and reduce morphological defects, but at the same time can increase the probability of nozzle clogging.</li> <li>- Hollow, core/shell and multicomponent fibre configurations can be obtained through special co-axial and multi-axial needles.</li> </ul>
<b>Ambient Conditions</b>	<p>Temperature affects most of the parameters listed above; it is solution specific and can influence the fibre production yield. When:</p> <ul style="list-style-type: none"> <li>- Temperature increases → it decreases the solution's viscosity, increases the electrical conductivity → producing thinner uniform fibres with a greater polymer chain alignment.</li> <li>- Temperature decreases → it decreases the evaporation and elongation time of the jet before solidification → that counteracts the formation of finer fibres.</li> </ul> <p>Relative humidity</p> <ul style="list-style-type: none"> <li>- Increased humidity → can delay the solidification of the fibres prior to deposition → increasing the elongation time → producing thinner fibres.</li> <li>- High humidity (generally &gt; 60%) has been known to produce non-uniform fused fibres or circular pore formations, such as beads, especially in the case of hygroscopic polymers such as nylon, cellulose and polyvinylpyrrolidone. Furthermore, high humidity can affect the total charge distribution on the Taylor cone, reducing the surface charge density, and thus affecting the polymer solution's electrospinnability.</li> <li>- Low humidity may produce thicker fibres due to rapid solvent evaporation.</li> </ul>

## 2.6 Co-axial electrospinning

Co-axial electrospinning is a modification of the conventional electrospinning technique that enables independent reservoirs of two or more different solutions fed onto a co-axial needle, to formulate single composite fibres that present a core/shell morphology [45]. The co-axial spinneret consists of a double capillary compartment arranged concentrically, with the inner needle fitted within the outer needle. Independent solutions travel to the orifice of the co-axial needle from separate pumps, where the flow rates are adjusted accordingly. The inner capillary contains the core solution, while the outer capillary produces the shell polymer [249]. At the orifice, a compound Taylor cone forms as the shell polymer solution entraps the core fluid and is then subjected to an applied electric field, conceptually similar to conventional electrospinning [213]. After the solvents evaporate, a heterogeneous but continuous fibre composed of the core and shell constituents will be collected [250]. The basic concept of co-axial electrospinning is illustrated in Figure 2.10.

The interactions that govern the resultant core/shell fibre properties derive from the degree of rheological, physical, and chemical dissimilarities of the two solutions [251]. However, a uniformly assembled core/shell fibre forms if a stable Taylor cone is maintained [252]. Processing parameters relating to co-axial electrospinning have been reviewed in the literature [253, 254], all of which agree that the complexity of co-axial electrospinning originates from the difficulty in maintaining a stable Taylor cone.

To induce a stable Taylor cone, process parameters should be such that: (1) an electrospinnable shell solution is utilised; (2) the shell solution viscosity is higher than the core solution viscosity, so the stress relating to the viscosity between the core and shell solutions overcome the interfacial tension between them [255]; (3) a low vapour pressure solvent should be used (as fast evaporation may destabilise the Taylor cone); and (4) the conductivity of the shell solution has to be greater than that of the core solution to inhibit core/shell structural discontinuities induced by the rapid elongation of the core polymer [251].

Co-axial electrospinning can produce fibres from highly diverse polymer pairs; core-sheath, hollow, nanoparticle decorated, while each one can maintain its separate material identity [253]. Through this process, it is feasible to electrospin materials that are not electrospinnable per se due to their chemistry (such as oligomers), by accommodating them within the core of the fibre [253]. By exploiting this feature, sophisticated pairs of materials can combine desired properties into a single fibre. Highly unstable materials, such as enzymes, growth factors, and rapidly degradable compounds that would otherwise be rapidly broken down within an intricate niche, can be preserved by the sheath material [256]. For this reason,

the properties of the material can be manipulated while employing the co-axial electrospinning technique, which is of interest in the biomedical sector because it can be used to develop biocompatible and mechanically stable materials [256].

Co-axially electrospun fibres are also widely employed for the development of drug delivery systems that can attain a tailored substance release [257]. For example, co-axially electrospun fibres consisting of a silk fibroin/hyaluronic acid in the shell and PEO/polyphenols from olive leaf extracts (OLE) in the core, presented the sustained release of OLE for 30 days with no apparent cytotoxicity [258].

In another study, *Gao et al., 2018* [260], co-axially electrospun dimethyloxallylglycine (DMOG)/PCL-collagente type I core-shell fibres. DMOG is a competitive inhibitor of procollagen-proline dioxygenase, an enzyme that plays key roles in prolonging ischemia and upregulating inflammatory responses. Moreover, they found that in both the *in vitro* and *in vivo* assessments, the DMOG sustained release from the fibres stabilized the hypoxia-inducible factor-1A (HIF-1) that, in turn, accelerated the expression of genes that induce re-epithelialization and angiogenesis prompting to successful wound closure within 14 days in diabetic mice. On the other hand, there is a need to research and develop bicomponent antimicrobial surfaces that can present the appropriate physicochemical properties and mechanical stability for advancing the properties of hernia meshes, and the co-axial electrospinning technique was chosen to develop such a nanofibrous construct in this thesis (*Chapter 6*).

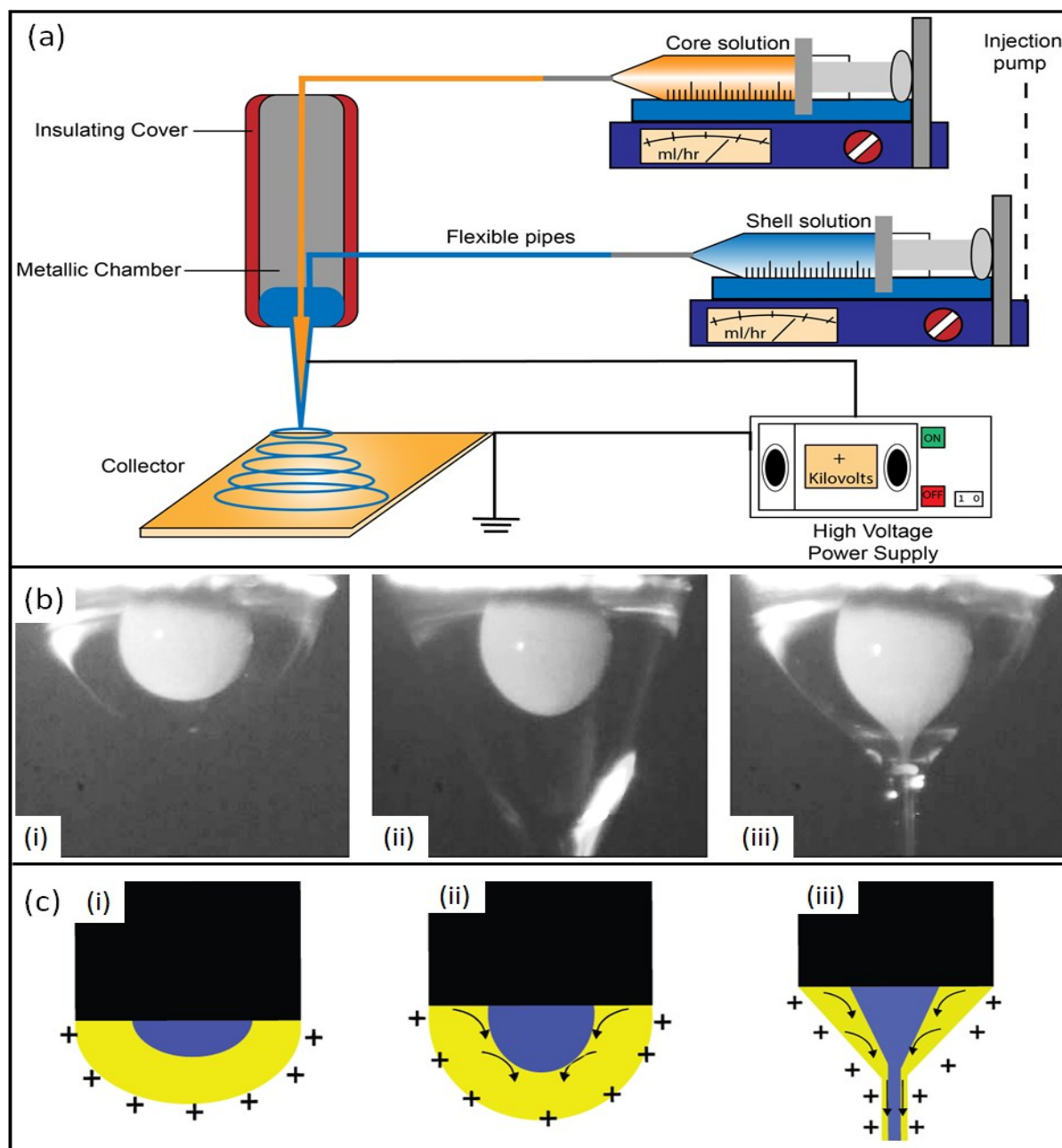


**Figure 2.10** Generation of co-axial electrospun fibres. **(a)** Schematic of a standard co-axial electrospinning setup; **(b)** configuration of the co-axial Taylor cone, following the evolution of the electrified jet as the voltage amplitude increases, where polyvinylpyrrolidone (PVP) is the shell and mineral oil is the core solution [259]; **(c)** schematic representation of the charges forming the co-axial Taylor cone, **(i)** surface charges develop around the surface of the shell solution, **(ii)** a viscous electrified strain exerts the droplet causing it to be deformed, **(iii)** a stable core-sheath jet develops.

## 2.7 Nozzle-free electrospinning

Considering that the production output of needle-based electrospinning devices is commonly meagre; ranging at 0.01–0.3 g·h<sup>-1</sup> [261], scaling up the process has been progressively studied as a suitable approach of industrialising this fabrication process. This can be generally achieved by scaling up the spinneret's structure while retaining an energetically stable and well-distributed configuration [262]. As opposed to multi-needle electrospinning, where the electric field around a given needle is affected by the nearby jets, which can produce inhomogeneous fibres, free-surface electrospinning is an alternative method capable of producing fibres at high-throughput with no constraints of clogged needles.

In 2004, Yarin and Zussman initially described the production of free-surface nanofibres by placing a layer of polymer solution underneath a magnetic liquid (that was overlapping a permanent magnet) against a vertically placed oppositely charged magnet by applying high DC voltage [263]. A year later, Jiri and co-workers patented a process where a rotating charged electrode, immersed within a polymer solution, placed at a close distance to a counter electrode, at a bottom-up manner, could be used to fabricate nanofibres at an increased production rate with the assistance of an airstream to increase the auxiliary drying efficiency of the system [264].

Lukas et al. developed an electrohydrodynamic theory that describes the self-organization of electrified liquid jets from an open flat surface, founded on the fact that fibres can arise during electrospinning from linear clefts even without the support of a magnetic fluid underneath [265]. The critical electric field intensity ( $E_c$ ) to produce fibres deriving from free-surface electrospinning was described as:

$$E_c = \sqrt[4]{4\gamma\rho g/\varepsilon_0^2} \quad (2.5)$$

Where,  $\gamma$  is the surface tension of the solution (N·cm<sup>-1</sup>),  $\rho$  is the density of the liquid mass (g·cm<sup>-3</sup>),  $g$  is the gravitational acceleration (cm·s<sup>-2</sup>), and  $\varepsilon_0$  is the absolute permittivity (F·cm<sup>-1</sup>). During the onset of free-surface electrospinning, the electric force is essential for Taylor cone formation and subsequent jet initiation. Prior to jet growth and the corresponding bending instabilities, the initial straight segment of the jets is amplified as the Coulomb forces concentrate towards the leading segments that are trying to reach the collector [237]. The ultra-slow-motion images presented in Figure 2.11(b) indicate the stages from Taylor cone formation to jet depletion, which occur within a tenth of a second.

During nozzle-free electrospinning, the polymer solution is submerged in a bath containing a rotating cylinder electrode against a biased rotating collector electrode under constant airflow. By controlling the motor, the rotating speed of the roller can be fixed. High-voltage power with a potential greater than 50 kV needs to be applied between the two rotating electrodes, which induces the formation of multiple Taylor cones emerging from the rotating electrode surface that is immersed in the solution bath. When voltage is applied on the roller, the liquid changes to a conical shape and forms a great number of Taylor cones (Figure 2.11(c)) on the surface of the rotating spinneret. When the voltage reaches a critical value, multiple jets stretch from numerous locations to form fibres in an upward motion at a large scale. Under a strong electrical field, the jets will move and get deposited on the collector's surface, which is placed at a fixed distance over the roller. Because of this, the roller electrospinning method is a continuous and efficient process to fabricate nanofibres [266]. Besides fluctuations in the conductivity of the polymer solution [267], variations in the shape of the spinneret play a vital role in the morphology and diameter of the formed fibres [268–271].

Although free-surface electrospinning presents a high-volume output and is easy to operate once the appropriate solution and electrospinning parameters have been met, it can be challenging to maintain a consistent solution concentration and viscosity. Furthermore, due to the high electric force, incomplete solidification of the fibres may allow residual solvents to get incorporated into the scaffolds, affecting the biocompatibility of the developed constructs; nevertheless, post-fabrication treatments may resolve this issue in most cases. Additionally, and of major concern is that as the polymer solution is being openly exposed to the ambient conditions, highly volatile solvents may rapidly evaporate, where fluctuations in the conductivity and viscosity of the solution can negatively affect the uniformity of the fibres, as well as the consistency of process between experiments. This can be partially regulated by restraining the exposure of the polymer solution in the open, the solvent system selection, regulating the ambient conditions, and the configuration of the spinneret. Thus, all solution, electrospinning and ambient parameters need to be accurately tuned to obtain a consistent fibres production output.

In a recent study by Agrawal and Pramanik [272], chitosan-PVA blended nanofibrous scaffolds (with an average fibre diameter of 269 nm), formed using a needleless setup, were successfully fabricated and found to present good attachment, growth, and expansion in human mesenchymal stem cells (HMSCs). Free-surface electrospinning is at an early stage, and it is yet to be explored extensively for tissue engineering applications. To date, Nanospider™ (Elmarco, Ltd., Czech Republic) has developed a commercially available

industrial-scale electrospinner based upon this concept, where a high-voltage potential (up to 80 kV) facilitates the formation of fibres out of a polymer-layered thread at a defined rate [273].

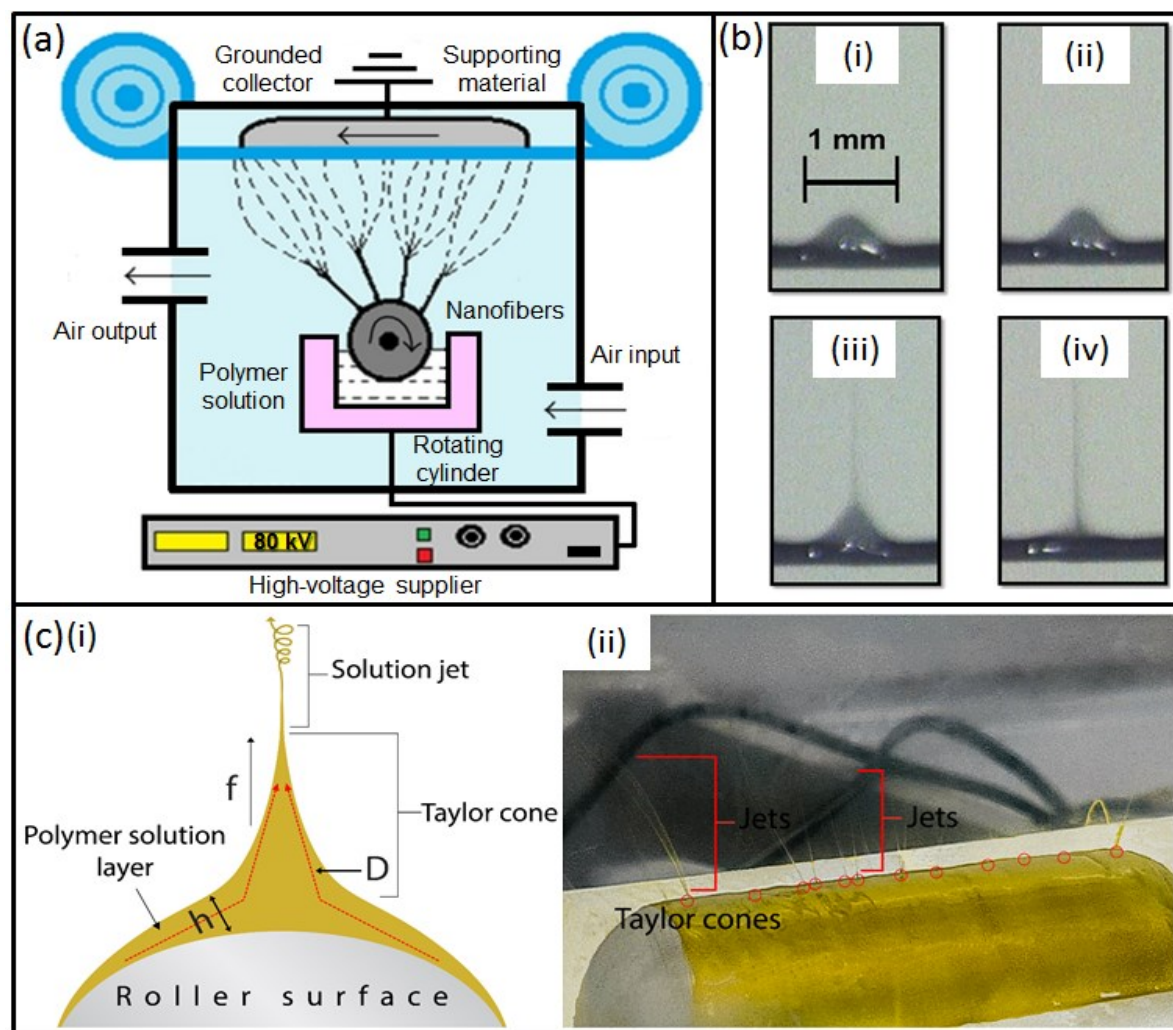


**Figure 2.11 Free-surface electrospinning.** (a) Diagram of a roller electrospinning setup. Modified from [266]. (b) Jet formation. (i) Conical droplet on an open surface in the presence of an electric field (time = 0 s), (ii) extended conical droplet (time = 33 ms), (iii) Taylor cone and jetting of the droplet (time = 66 ms), (iv) depletion of the droplet (time = 99 ms) [274]. (c) Schematic diagram of the roller electrospinning method [275]. (c) Taylor cone formation, (i) schematic diagram where  $h$  is the thickness of the layer,  $D$  is the diameter covered by the Taylor cone, and  $f$  is the electrostatic force, (ii) a photograph depicting the initiation of the process, taken by the device developed as part of the work conducted in this thesis.



## 2.8 Selection of polymers and antimicrobial agents

For each research work presented in the following chapters, polymers and solvents were chosen based on extended parametric studies, which examined the effect of a specific polymer/solvent system to the reproducibility, Taylor cone stability (optically inspected using a magnifying monocular), and fibre properties. Factors such as the polymer's concentration, its solubility and compatibility to a specific solvent system, viscosity, and conductivity measurements, had to be predetermined.

### 2.8.1 Natural and synthetic polymers

Natural polymers have been considered as suitable candidates for TE applications due to their superior intrinsic architecture and biological properties in comparison to synthetic derivatives [276]. Due to their high resemblance with ECM components, these materials are less prone to induce chronic inflammatory responses that are more often encountered in the case of synthetic polymers [277]. Furthermore, natural polymers also carry various tissue niche requirements, are biocompatible, and may present antimicrobial properties [278].

Naturally occurring polymers are produced by an organism, where the desired polymer material can then be extracted [279]. Natural polymers can be components of the ECM, polysaccharides (chitosan, cellulose, aloe vera, hyaluronic acid, etc.), proteins (collagen, elastin, fibroin, sericin, gelatin, etc.) or polynucleotides (DNA, RNA, etc.) [278]. Such polymers can increase the efficacy of cellular communication and enhance the biological interactions between the developed construct and the host tissue due to sharing similar intramolecular domains [278].

Nonetheless, the rapid degradation of scaffolds produced using naturally derived polymers may affect the subsequent phases of the wound healing cascade, as well as present inadequate mechanical stability; a prerequisite of hernia meshes [279]. Furthermore, the overlap concentration ( $C_o$ ), the degree of polymer branching, and the chosen solvent system may be hard to adjust and thus affect the spinnability, reproducibility, and homogeneity of natural-derived fibres, as insufficient solubility, stiff molecular conformations, and low conductivity can halt a solution from being electrospun [280]. For this reason, synthetic polymers were further incorporated within the electrospinning solutions. Blend electrospinning can develop scaffolds that integrate the improved cytocompatibility of natural polymers with the mechanical stability and physicochemical integrity of synthetic polymers. The incorporation of naturally derived polymers such as silk fibroin with synthetic polymers can increase their

mechanical complexity while alleviating their difficult processability. Combining such materials and forming polymer blends can increase the chemical bonding, such as higher ratios of polyester and polyether linkages, thus vastly improving the mechanics, surface wettability, and the subsequent ability of such matrices to support cell growth.

## 2.8.2 Polymers

Throughout this thesis, several polymers were examined, chosen based on their application-specific properties of interest and their corresponding electrospinnabilities. This section summarises the polymers that were ultimately selected to develop the biomaterial systems presented in the upcoming research chapters.

- **Poly(glycerol sebacate) (PGS)**

Poly(glycerol sebacate) (PGS) is an FDA approved semicrystalline thermoset, mostly studied for soft tissue engineering applications [276, 278]. As shown in Figure 2.12, PGS is synthesised via the polycondensation of glycerol and sebacic acid to form a pre-polymer, which can then be further covalently esterified [281]. Poly(polyol sebacate)-derived polymers, such as PGS, refer to a family of ester-bonded elastomers formed via the polycondensation of polyol alcohols, containing multiple hydroxyl groups (e.g., glycerol, isomalt, xylitol), and the dicarboxylic acid present in sebacic acid [282]. One of the main advantages of PGS is that it can gradually degrade (hydrolytically and enzymatically) to non-toxic by-products (e.g., glycol acid that can further promote antibacterial activity at neutral pH levels) [283]. Most importantly, PGS is an attractive polymer as it exhibits tailored mechanical properties and bioresorbability pertinent to varying the polycondensation parameters and stoichiometry, which correlate to the surface degradability of its ester linkages [284].

- **Poly(caprolactone) (PCL)**

Polycaprolactone (PCL) is a non-aromatic polymer synthesised mainly through ring-opening polymerisation (ROP) of  $\epsilon$ -caprolactone (Figure 2.13c) [285]. It is semi-crystalline, biocompatible, slow-degrading, and relatively inexpensive to synthesise. Its prevalent use lies on its superior mechanical strength over most other biopolymers and its ability to act as a mechanically stable backbone for the development of tissue scaffolds. However, PCL is known to be hydrophobic, and pure PCL constructs have been found to lead to suboptimal cell adhesion and proliferation, as indicated by several studies [286, 287]. Hence, in the work

described in this thesis, PCL was incorporated as a copolymer with the bioactive natural polymer, silk fibroin in an attempt to promote enhanced cell attachment and proliferation.

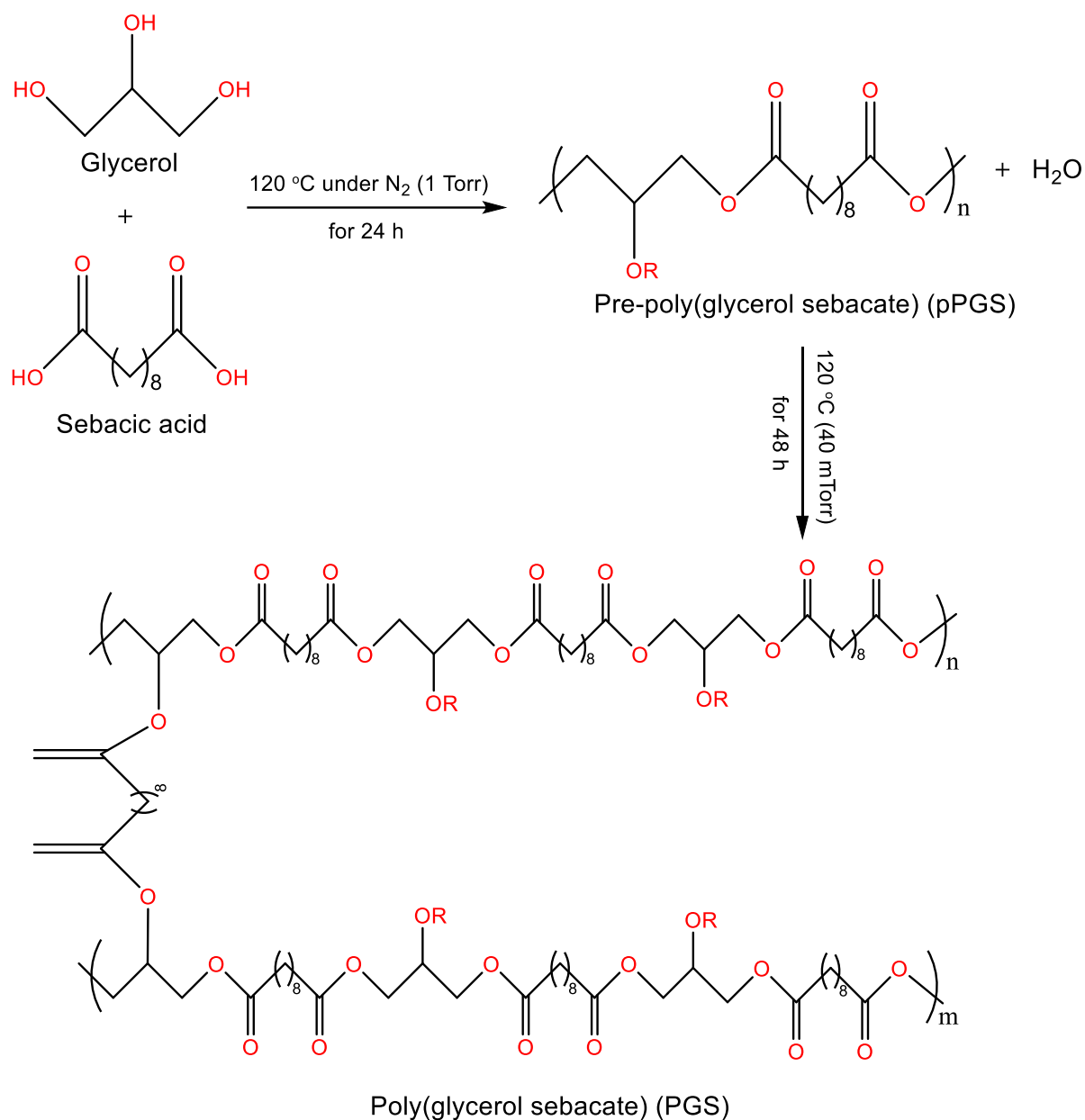


**Figure 2.12** The condensation polymerisation reaction of glycerol and sebacic acid that yields the poly(glycerol sebacate) polyester. The hydroxyl groups of the glycerol act as the initiator of the reaction by forming a monoester with the carboxylic acid of the sebacic acid. In the first stage, the pre-polymer (pPGS) is synthesised. In the second stage, the pre-polymer is cured under heat and vacuum to form a 3D network between the polyester chains, giving rise to the PGS thermoset.

- **Polyvinylpyrrolidone (PVP)**

Polyvinylpyrrolidone (PVP) is a well-established hydrophilic polymer that is soluble in a range of solvents, making it an attractive material for several applications (Figure 2.13(b)). PVP can be easily processed in various forms such as films, hydrogels, and porous sheets. Moreover, it has been proven to be biocompatible and chemically inert as a biomaterial; therefore, it is widely used in biomedical applications [288]. The utilisation of PVP as a carrier polymer during free-surface electrospinning can efficiently increase the fibre production output of the process. As part of this thesis, PVP 360,000 and 1,300,000 g·mol<sup>-1</sup> were blended with highly esterified PGS, electrospun and crosslinked in an attempt to tune the mechanical properties of the electrospun membranes to mimic the skin while creating an environment that presents adequate swelling to absorb exudate [288]. The developed protocol and chemistry behind the photocrosslinking of the PVP/PGS electrospun fibrous mats submerged in a riboflavin solution is described in detail in *Chapter 4*.

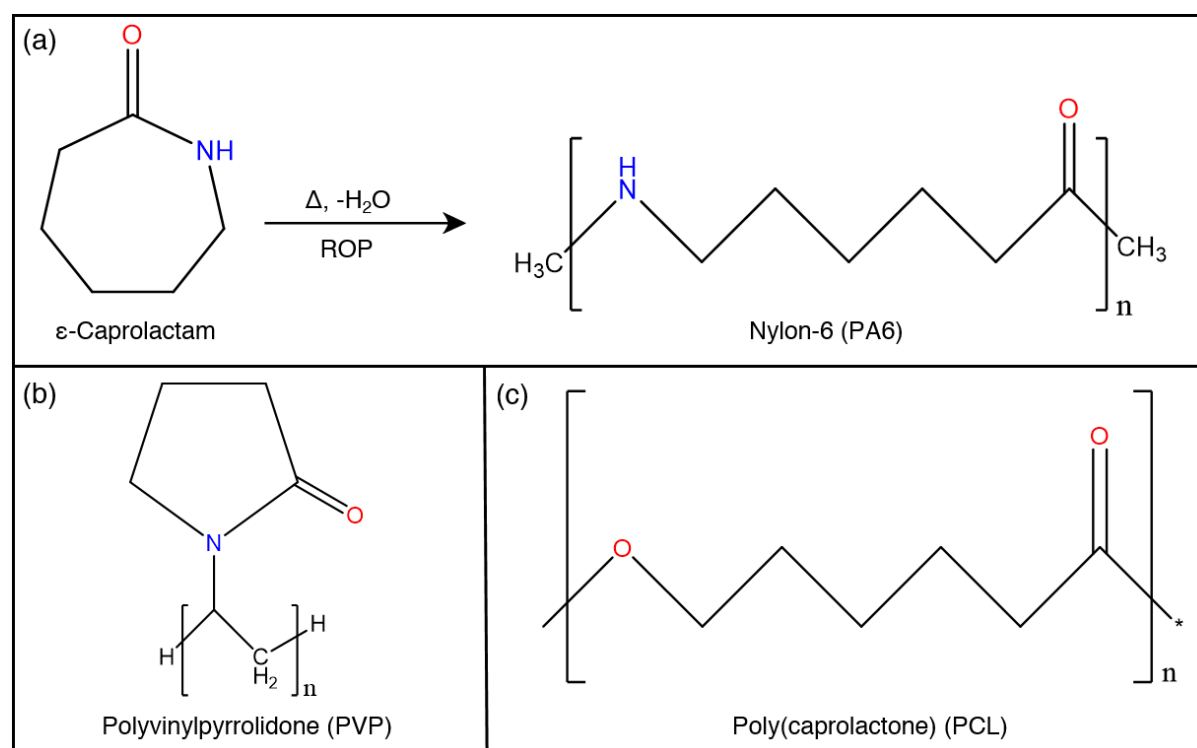


**Figure 2.13** Chemical structures of the synthetic polymers. **(a)** Nylon-6 (PA6); **(b)** polyvinylpyrrolidone (PVP); **(c)** poly(caprolactone) (PCL).

- **Nylon-6 (PA6)**

Polyamides are condensation polymers produced via amide bonding between amines and acids, in a similar manner with protein synthesis in the body (Figure 2.13(a)). Nylon-6 (polyamide-6, PA6) is synthesised by the formation of free-radicals via thermal decomposition of the  $\epsilon$ -caprolactam ring, followed by chain growth through ring-opening polymerisation [289]. PA6 is a commonly used polymer as surgical material for non-absorbable synthetic sutures, while PA6 and polyurethane are conjointly used as balloon material in angioplasty, due to the superior tensile strength of PA6 [290]. PA6 has several advantageous characteristics, such as flexible functionalisation possibilities and superior mechanical performance compared to many other polymer materials [291]. PA6 has been shown to carry good responses and increased stability in bodily fluids [291]. As part of *Chapter 6*, PA6 was chosen as the core material of the bicomponent core/shell NFs, due to its mechanical stability.

- **Silk fibroin (SF)**

The silk fibroin protein extracted from *Bombyx mori* cocoons is composed of fibroin (70%–80%) and sericin (20%–30%) [292]. *B. mori* silkworms have been domestically bred and part of the textile industry for centuries [293]. Silk fibres are protein-based fibrous biopolymers, formed of repetitive hydrophobic motifs of hexapeptides that consist of [Gly-Ser-Gly-Ala-Gly-Ala]<sub>x</sub>, which form a stable anti-parallel beta-sheet structure with [Gly-Ala/Ser] dipeptides (Figure 2.14) [294, 295]. The strong hydrogen bonding between the beta-sheets contributes to the semi-crystalline structure of the macromolecule; making SF mechanically superior to most of the other bio-derived polymers [294, 296]. It has been shown that SF is a valuable material for the development of wound management products because of its excellent biocompatibility, good oxygen and vapour permeability while inducing minimum inflammatory responses [297]. The conventional extraction protocol of silk fibroin from *B. mori* cocoons, via molecular cassette cut-off methods, is a time consuming and expensive process that delivers low yields of the protein. *Chapter 5* describes a variation of the conventional protocol, based on ethanol precipitation, which was developed and employed in this thesis to reduce the time required and obtain substantially increased quantities of silk fibroin.

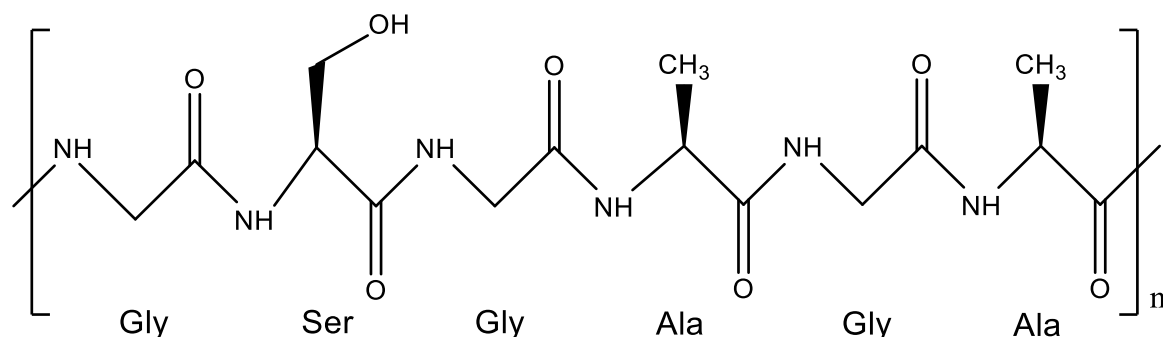


**Figure 2.14** Chemical structure of the silk fibroin (SF) protein.

- **Chitosan (CS)**

Chitosan (CS, a partially deacetylated chitin) is an abundant in nature, polycationic polymer, composed through an extended number of  $\beta(1-4)$  linked glucosamine and *N*-acetyl glucosamine units, and it is considered as a valuable biopolymer with strong bactericidal properties (Figure 2.15(a)) [298, 299]. It carries three reactive functional sites, an amine and a secondary hydroxyl group at C-6, and a primary hydroxyl group at C-3 [298]. Solid chitosan fibres can act through a wide range of mechanisms against both Gram (+) and (-) bacteria, where chitosan is considered as both a bactericidal and a bacteriostatic agent [300]. Due to its polycationic structure, CS can permeabilise the cell wall of prokaryotes by forming ionic complexes with the negative charges found: (1) on the phospholipids and lipopolysaccharides present in the outer and inner membrane on Gram (-) bacteria, and (2) the teichoic acids linked to the peptidoglycan present in the cell wall of Gram (+) bacteria [301]. Such interactions provoke internal osmotic imbalances, leakage of intracellular electrolytes, and other low molecular weight proteinaceous constituents, consequently inhibiting growth. Hydrolysed products of microbial DNA and RNA, also negatively charged, can ultimately inhibit downstream transcription and translation [302]. Further, the chelating capacity of the chitosan matrix can uptake nutrients and essential metals needed for microbial growth (Figure 2.15(b)) [303].

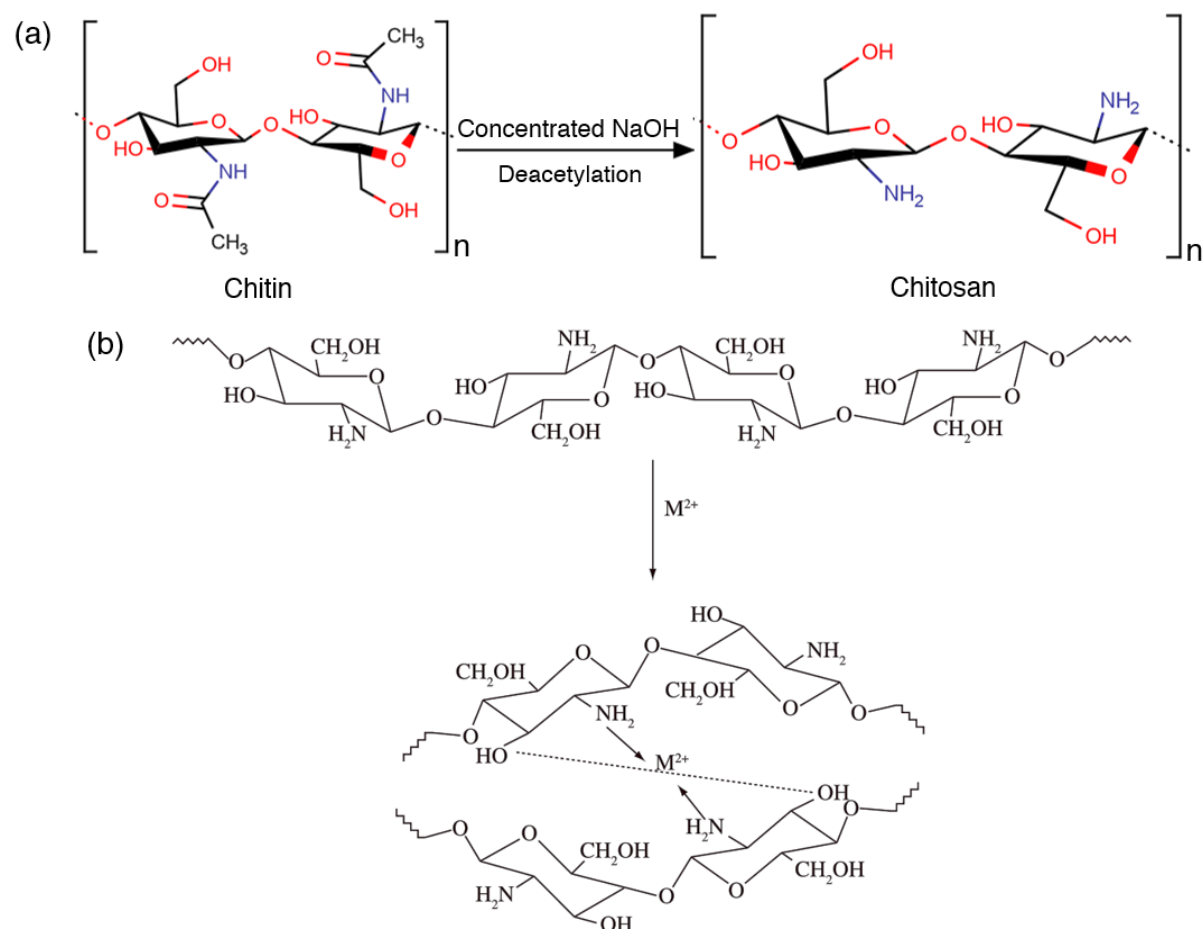


**Figure 2.15** Chitosan (a) chemical structure of chitosan deriving from the deacetylation of chitin; (b) model of the metal-chitosan chelation complex, based on Wang et al. [304].

### 2.8.3 Antimicrobial agents

As part of the co-axially electrospun nanofibrous hernia mesh construct developed for the prevention of mesh-associated surgical site infections in *Chapter 6*, the antimicrobial agents used were selected by carefully evaluating their chemistry, encapsulation properties, and drug release profile limitations. The selection of antibiotics was excluded due to numerous studies indicating a correlation between long-term exposure and the establishment of resistant bacterial strains [305, 306]. The incorporation of nanoparticles and active particles to improve the efficiency of the antimicrobial agents were excluded due to the low reproducibility of formulating nanoparticle-containing fibres via co-axial electrospinning [307, 308]. Essential oils and other natural compounds were found to be less susceptible to the pathogenic bacteria of interest [309]. Then, taking into consideration that the selected antimicrobial agents presented the appropriate chemical profile to be incorporated within a nanofibre-platform, and while possessing the required bactericidal mechanisms against the most commonly

associated surgical site infection pathogenic bacteria, it was narrowed down to the binary antimicrobial system, consisting of 5-chloro-8-hydroxyquinoline (5CLO8Q) and polyhexanide (PHMB).

- **Polyhexanide (PHMB) mechanism of action**

Poly(hexamethylene biguanide) (polyhexanide, PHMB) is a well-known antiseptic of mucous membranes and wounds, increasingly appearing in a variety of products, such as a skin disinfectant in wound dressings (Figure 2.16(a)) [310]. PHMB is a small molecule, with a characteristic carbon tail adjacent to a biguanide complex. PHMB's chemical structure closely resembles that of chlorhexidine, the most commonly used disinfectant/antiseptic employed by surgeons to disinfect surgical instruments and the skin prior to surgical incisions [311]. From a chemical perspective, chlorhexidine's solubility in water is  $0.8 \text{ mg}\cdot\text{mL}^{-1}$  as opposed to  $426 \text{ mg}\cdot\text{mL}^{-1}$  for PHMB [312], thus limiting its ability to be homogeneously distributed within the NFs. From a medical perspective, as opposed to PHMB, which is FDA-approved for internal use at concentrations below 0.4% (w/v), chlorhexidine has been proven by the FDA to be highly toxic in both *in vitro* and *in vivo* studies (FDA hazardous substance 7196). For this reason, PHMB was chosen over chlorhexidine.

At physiological pH, PHMB is polycationic due to the monoprotonation of each biguanide residue [313]. PHMB can widely permeabilise bacterial membranes, due to its small size (180-500 Da), and is able to infiltrate the bacterial wall and intercept cell division by condensing the negatively charged chromosomes – a property that previously has not been considered and has been since shown to be selective to prokaryotes with no adverse responses to mammalian cells [312]. This has been observed in the Gram (+) *Bacillus megaterium*, where growth inhibitory concentrations of PHMB (0.25%–0.4% (w/v)), were able to arrest cellular division, as observed by DAPI-stained bacterial foci [312]. PHMB is an effective antimicrobial agent against Gram (+) and Gram (-) bacterial species with 100% bactericidal activity, at concentrations as low as  $4 \text{ mg}\cdot\text{L}^{-1}$  [312]. In this thesis, a PHMB concentration of 0.3% (w/v) was loaded within the core of the core/shell nanofibrous membranes – selected based on the regulations of the *Scientific Committee on Consumer Safety* (SCCS) of the European Union [314] and the FDA [315].



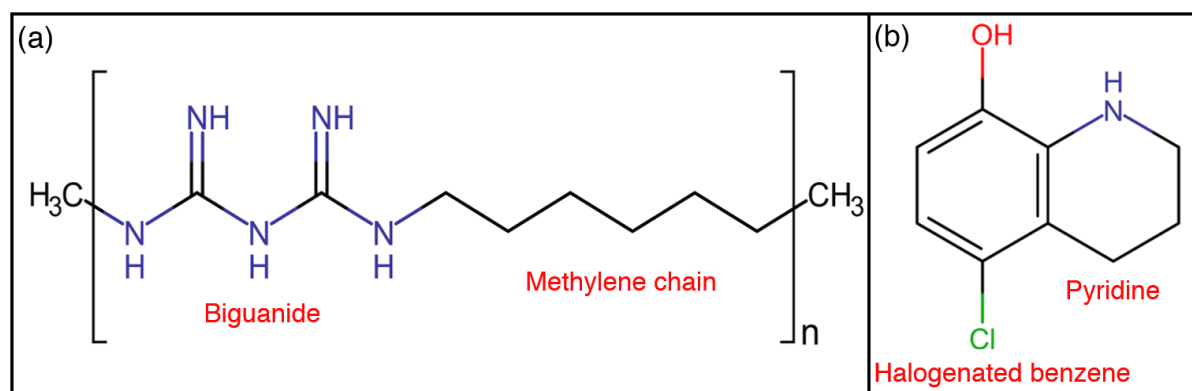


**Figure 2.16** Chemical structures of the antimicrobial substances. **(a)** Poly(hexamethylene biguanide) (PHMB) and **(b)** 5-chloro-8-hydroxyquinoline (5CLO8Q).

- **5-Chloro-8-hydroxyquinoline (5CLO8Q) mechanism of action**

5-Chloro-8-hydroxyquinoline (Cloxyquin, 5CLO8Q) is a derivative of quinoline and belongs to the bihalogenated 8-hydroxyquinolines family. 5CLO8Q is slightly soluble in water and has been previously shown to be active against various bacteria, as well as fungal and amoebic organisms [316, 317]. Quinolines are aromatic nitrogen compounds that present a bicyclic structure consisting of a saturated benzene ring being joint at two carbons with a pyridine ring (Figure 2.16(b)). Hongmanee et al. tested the bactericidal activity of 5CLO8Q against 150 strains of *Mycobacterium tuberculosis* – a species of pathogenic bacteria whose cell wall has features of both Gram (+) and Gram (-) bacteria – and demonstrated good bactericidal responses [318, 319]. The mechanisms through which 5CLO8Q acts against bacteria are poorly understood, but they are thought to relate to its chelating abilities. Iron chelation deprives microorganisms of essential nutrients [47]. It has been proposed, in a recent study, that 5CLO8Q can inhibit the RNA-dependent DNA polymerase of respiratory syncytial viruses by chelation of copper [320] and inhibit the synthesis of RNA by chelation of  $Mg^{2+}$ ,  $Zn^{2+}$ , and  $Mn^{2+}$ , with a conviction that a similar mechanism could be valid for bacterial species [321].

## 2.9 Conclusions

This chapter provided an overall description of the skin and hernia physiology and went through the current issues faced by clinicians in the management of wounds and the prevention of deep surgical infections, respectively. The advancement of these constructs over the years up to the current state-of-the-art skin substitute products and hernia mesh materials are elaborated while underlying the challenges that are yet to be met. The reasons why electrospinning was chosen for the work conducted in this thesis is substantiated, and the theory and advancements in the field of electrospinning are discussed.

In this thesis, the electrospinning device designed, based on the free-surface electrospinning theory described above, was employed for the research conducted in *Chapters 4* and *5* aiming to facilitate the high-throughput production of electrospun biocompatible materials that through the chemistry and morphology of the fibres can facilitate an “active” and protective environment for improved wound healing responses. Co-axial electrospinning, as aforementioned, was chosen to facilitate the development of bicomponent fibres that integrate antimicrobial substances in a spatiotemporal configuration, while attaining mechanical stability from the core and shell material, respectively.

The work presented in this thesis will aim to:

1. Manufacture electrospun fibre-based biomaterials with tuneable properties.
2. Assess the impact of the electrospun scaffolds architecture regarding physicochemical and mechanical stability, biocompatibility (in the case of skin-like substitutes), and drug release profile and antimicrobial efficiency (in the case of hernia meshes).
3. Design and build a nozzle-free electrospinning device intended to augment the meagre fibre production associated with lab-based electrospinning equipment.
4. Assess the effect of different forms of poly(glycerol sebacate) towards the mechanics and wetting properties of the skin-like substitutes.
5. Describe the photocrosslinking process of the PVP/PGS fibres.
6. Develop a straightforward, efficient and rapid protocol for the extraction of silk fibroin from *Bombyx mori* silkworm cocoons.
7. Compare the antimicrobial efficacy of the developed bicomponent electrospun nanofibres to those of the currently available synthetic and biologic meshes.

The following chapter describes the general methodology, synthesis, materials, *in vitro* cell and bacteria evaluation, drug release study and characterisation techniques employed in this thesis. It further provides some in-depth rationale behind the materials and techniques that were chosen to facilitate the development and assessment of the constructs.

## 2.10 References

1. Goossens, R. H. M. (2009). Fundamentals of pressure, shear and friction and their effects on the human body at supported postures. In A. Gefen (Ed.), *Studies in Mechanobiology, Tissue Engineering and Biomaterials* (2nd ed., vol. 1, pp. 1–30). Berlin, Germany: Springer-Verlag. [https://doi.org/10.1007/978-3-642-00534-3\\_1](https://doi.org/10.1007/978-3-642-00534-3_1)
2. Kanitakis, J. (2002). Anatomy, histology and immunohistochemistry of normal human skin. *European Journal of Dermatology*, 12(4), 390–399. <https://doi.org/10.1122/12095893>
3. Humbert, P., Maibach, H. I., Fanian, F., & Agache, P. (2017). Non-invasive investigations, physiology, normal constants. In P. Agache (Ed.), *Agache's Measuring the Skin* (2nd ed., vol. 3, pp. 363–367). Springer International Publishing. <https://doi.org/10.1007/978-3-319-32383-1>
4. Urciuolo, F., Casale, C., Imparato, G., & Netti, P. A. (2019). Bioengineered skin substitutes: The role of extracellular matrix and vascularization in the healing of deep wounds. *Journal of Clinical Medicine*, 8(12), 2083–2092. <https://doi.org/10.3390/jcm8122083>
5. Ramanathan, G., Singaravelu, S., Raja, M. D., Nagiah, N., Padmapriya, P., Ruban, K., Kaveri, R., Natarajan, T. S., Sivagnanam, U. T., & Kong, X. (2016). Fabrication and characterization of a collagen coated electrospun poly(3-hydroxybutyric acid)-gelatin nanofibrous scaffold as a soft bio-mimetic material for skin tissue engineering applications. *RSC Advances*, 6(10), 7914–7922. <https://doi.org/10.1039/C5RA19529B>
6. Zhang, L. J., & Gallo, R. L. (2016). Antimicrobial peptides. *Current Biology*, 26(1), 14–19. <https://doi.org/10.1016/j.cub.2015.11.017>
7. Nair, R., & Maseeh, A. (2012). Vitamin D: The "sunshine" vitamin. *Journal of Pharmacology & Pharmacotherapeutics*, 3(2), 118–126. <https://doi.org/10.4103/0976-500X.95506>
8. Silver, F. H., Freeman, J. W., & DeVore, D. (2001). Viscoelastic properties of human skin and processed dermis. *Skin Research and Technology*, 7(1), 18–23. <https://doi.org/10.1034/j.1600-0846.2001.007001018.x>
9. Venus, M., Waterman, J., & McNab, I. (2011). Basic physiology of the skin. *Surgery*, 29(10), 471–474. <https://doi.org/10.1016/j.mpsur.2011.06.010>
10. Benítez, J. M., & Montáns, F. J. (2017). The mechanical behavior of skin: Structures and models for the finite element analysis. *Computers and Structures*, 190(1), 75–107. <https://doi.org/10.1016/j.compstruc.2017.05.003>
11. Sundaramurthi, D., Vasanthan, K. S., Kuppan, P., Krishnan, U. M., & Sethuraman, S. (2012). Electrospun nanostructured chitosan-poly(vinyl alcohol) scaffolds: a biomimetic extracellular matrix as dermal substitute. *Biomedical Materials*, 7(4), 1–12. <https://doi.org/10.1088/1748-6041/7/4/045005>
12. Hagsawa, S., & Shimada, T. (2005). Skin morphology and its mechanical properties associated with loading. In S. Hagsawa (Ed.), *Pressure Ulcer Research* (1st ed., pp. 161–185). Berlin, Germany: Springer-Verlag. [https://doi.org/10.1007/3-540-28804-X\\_11](https://doi.org/10.1007/3-540-28804-X_11)
13. Olczyk, P., Mencner, Ł., Komosinska-Vassev, K., & Komosinska-Vassev, K. (2014). The role of the extracellular matrix components in cutaneous wound healing. *BioMed Research International*, 89(3), 1–8. <https://doi.org/10.1155/2014/747584>
14. Gantwerker, E. A., & Hom, D. B. (2012). Skin: histology and physiology of wound healing. *Clinics in Plastic Surgery*, 39(1), 85–97. <https://doi.org/10.1016/j.cps.2011.09.005>
15. Hussey, G. S., Dziki, J. L., & Badylak, S. F. (2018). Extracellular matrix-based materials for regenerative medicine. *Nature Reviews Materials*, 3(7), 159–173. <https://doi.org/10.1038/s41578-018-0023-x>
16. Schultz, G. S., Davidson, J. M., Kirsner, R. S., Bornstein, P., & Herman, I. M. (2011). Dynamic reciprocity in the wound microenvironment. *Wound Repair and Regeneration*, 19(2), 134–148. <https://doi.org/10.1111/j.1524-475X.2011.00673.x>

17. Adair-Kirk, T. L., & Senior, R. M. (2008). Fragments of extracellular matrix as mediators of inflammation. *The International Journal of Biochemistry & Cell Biology*, 40(6–7), 1101–10. <https://doi.org/10.1016/j.biocel.2007.12.005>
18. Slater, D. (2005). Histologic diagnosis of inflammatory skin diseases: an algorithmic method based on pattern analysis. *Histopathology*, 47(6), 641–642. <https://doi.org/10.1111/j.1365-2559.2005.02260.x>
19. Mouw, J. K., Ou, G., & Weaver, V. M. (2014). Extracellular matrix assembly: A multiscale deconstruction. *Nature Reviews Molecular Cell Biology*, 15(5), 771–785. <https://doi.org/10.1038/nrm3902>
20. Tracy, L. E., Minasian, R. A., & Caterson, E. J. (2016). Extracellular matrix and dermal fibroblast function in the healing wound. *Advances in Wound Care*, 5(3), 119–136. <https://doi.org/10.1089/wound.2014.0561>
21. Nasalapure, A. V., Chalannavar, R. K., Gani, R. S., Malabadi, R. B., & Kasai, D. R. (2017). Tissue engineering of skin: A review. *Trends in Biomaterials and Artificial Organs*, 31(2), 69–80. <https://doi.org/10.4172/2157-7552.1000150>
22. Xu, J., Mosher, D., Xu, J., & Mosher, D. (2010). Fibronectin and other adhesive glycoproteins. In R. P. Mecham (Ed.), *The Extracellular Matrix: an Overview* (1st ed., pp. 41–75). Berlin, USA: Springer-Verlag. <https://doi.org/10.1007/978-3-642-16555-9>
23. Liu, Q. Y., Wu, S. Z., Tan, T. W., Weng, J. Y., Zhang, L. Q., Liu, L., Tian, W., & Chen, D. F. (2009). Preparation and properties of a novel biodegradable polyester elastomer with functional groups. *Journal of Biomaterials Science, Polymer Edition*, 20(11), 1567–1578. <https://doi.org/10.1163/092050609X12464345064325>
24. Wise, S. G., Yeo, G. C., Hiob, M. A., Rnjak-Kovacina, J., Kaplan, D. L., Ng, M. K. C., & Weiss, A. (2014). Tropoelastin -a versatile, bioactive assembly module. *Acta Biomater*, 10(4), 1532–1541. <https://doi.org/10.1016/j.actbio.2013.08.003>
25. Osmanagic-Myers, S., Dechat, T., & Foisner, R. (2015). Lamins at the crossroads of mechanosignaling. *Genes & development*, 29(3), 225–37. <https://doi.org/10.1101/gad.255968.114>
26. Hussain, S. N., Goodman, G. J., & Rahman, E. (2017). Treatment of a traumatic atrophic depressed scar with hyaluronic acid fillers: a case report. *Clinical, Cosmetic and Investigational Dermatology*, 10, 285–287. <https://doi.org/10.2147/CCID.S132626>
27. Papakonstantinou, E., Roth, M., & Karakiulakis, G. (2012). Hyaluronic acid: A key molecule in skin aging. *Dermato-endocrinology*, 4(3), 253–8. <https://doi.org/10.4161/derm.21923>
28. Dickinson, L. E., & Gerecht, S. (2010). Micropatterned surfaces to study hyaluronic acid interactions with cancer cells. *Journal of Visualized Experiments*, 2(46), 78–85. <https://doi.org/10.3791/2413>
29. Williams, N. S., O'Connell, P. R., & McCaskie, A. W. (2017). Early assessment and management of trauma. In *Short Practice of Surgery* (26th ed., pp. 380–400). Bailey & Love's, CRC Press. <https://doi.org/10.1201/b13454-34>
30. Guimarães, C. F., Gasperini, L., Marques, A. P., & Reis, R. L. (2020). The stiffness of living tissues and its implications for tissue engineering. *Nature Reviews Materials*, 5(1), 351–370. <https://doi.org/10.1038/s41578-019-0169-1>
31. Martino, F., Perestrelo, A. R., Vinarský, V., Pagliari, S., & Forte, G. (2018). Cellular mechanotransduction: From tension to function. *Frontiers in Physiology*, 9(1), 1–21. <https://doi.org/10.3389/fphys.2018.00824>
32. Achterberg, V. F., Buscemi, L., Diekmann, H., Smith-Clerc, J., Schwengler, H., Meister, J. J., Wenck, H., Gallinant, S., & Hinz, B. (2019). The nano-scale mechanical properties of the extracellular matrix regulate dermal fibroblast function. *Journal of Investigative Dermatology*, 134(7), 1862–1872. <https://doi.org/10.1038/jid.2014.90>

33. Chen, S., Ní Annaidh, A., & Roccabianca, S. (2020). A microstructurally inspired constitutive model for skin mechanics. *Biomechanics and Modeling in Mechanobiology*, 19(1), 275–289. <https://doi.org/10.1007/s10237-019-01210-9>
34. Ní Annaidh, A., Bruyère, K., Destrade, M., Gilchrist, M. D., & Otténio, M. (2012). Characterization of the anisotropic mechanical properties of excised human skin. *Journal of the Mechanical Behavior of Biomedical Materials*, 5(1), 139–148. <https://doi.org/10.1016/j.jmbbm.2011.08.016>
35. Keshel, S. H., Biazar, E., Rezaei Tavirani, M., Rahmati Roodsari, M., Ronaghi, A., Ebrahimi, M., & Afsordeh, K. (2014). The healing effect of unrestricted somatic stem cells loaded in collagen-modified nanofibrous PHBV scaffold on full-thickness skin defects. *Artificial Cells, Nanomedicine, and Biotechnology*, 42(3), 210–216. <https://doi.org/10.3109/21691401.2013.800080>
36. Goh, K. L., & Holmes, D. F. (2017). Collagenous extracellular matrix biomaterials for tissue engineering: Lessons from the common sea urchin tissue. *International Journal of Molecular Sciences*, 18(5), 1–15. <https://doi.org/10.3390/ijms18050901>
37. Sandri, G., Rossi, S., Bonferoni, M. C., Caramella, C., & Ferrari, F. (2020). Electrospinning technologies in wound dressing applications. In J. Boateng (Ed.), *Therapeutic Dressings and Wound Healing Applications* (1st ed., vol. 14, pp. 315–336). Greenwich, UK: John Wiley & Sons. <https://doi.org/10.1002/9781119433316.ch14>
38. Jacquemoud, C., Bruyere-Garnier, K., & Coret, M. (2007). Methodology to determine failure characteristics of planar soft tissues using a dynamic tensile test. *Journal of Biomechanics*, 40(2), 468–475. <https://doi.org/10.1016/j.jbiomech.2005.12.010>
39. Carlisle, C. R., Coulais, C., & Guthold, M. (2010). The mechanical stress-strain properties of single electrospun collagen type I nanofibers. *Acta Biomaterialia*, 6(8), 2997–3003. <https://doi.org/10.1016/j.actbio.2010.02.050>
40. Chen, Z. G., Wang, P. W., Wei, B., Mo, X. M., & Cui, F. Z. (2010). Electrospun collagen-chitosan nanofiber: A biomimetic extracellular matrix for endothelial cell and smooth muscle cell. *Acta Biomaterialia*, 6(2), 372–382. <https://doi.org/10.1016/j.actbio.2009.07.024>
41. Dias, J. R., Granja, P. L., & Bártolo, P. J. (2016). Advances in electrospun skin substitutes. *Progress in Materials Science*, 84(1), 314–334. <https://doi.org/10.1016/j.pmatsci.2016.09.006>
42. Ramalingam, R., Dhand, C., Leung, C. M., Ezhilarasu, H., Prasannan, P., Ong, S. T., Subramanian, S., Kamruddin, M., Lakshminarayanan, R., Ramakrishna, S., Verma, N. M., Arunachalam, K. D. (2019). Poly-ε-caprolactone/gelatin hybrid electrospun composite nanofibrous mats containing ultrasound assisted herbal extract: Antimicrobial and cell proliferation study. *Nanomaterials*, 9(3), 1–21. <https://doi.org/10.3390/nano9030462>
43. Chandrasekaran, A. R., Venugopal, J., Sundarajan, S., & Ramakrishna, S. (2011). Fabrication of a nanofibrous scaffold with improved bioactivity for culture of human dermal fibroblasts for skin regeneration. *Biomedical Materials*, 6(1), 105–118. <https://doi.org/10.1088/1748-6041/6/1/015001>
44. Arpanaei, A., Ajallouei, F., Fransson, M., Tavanai, H., Massumi, M., Hilborn, J., Leblanc, K., Arpanaei, A., & Magnusson, P. U. (2015). Investigation of human mesenchymal stromal cells cultured on PLGA or PLGA/chitosan electrospun nanofibers. *Journal of Bioprocess Biotech*, 5(6), 1–9. <https://doi.org/10.4172/2155-9821.1000230>
45. Lu, Y., Huang, J., Yu, G., Cardenas, R., Wei, S., Wujcik, E. K., & Guo, Z. (2016). Coaxial electrospun fibers: applications in drug delivery and tissue engineering. *Wiley Interdisciplinary Reviews: Nanomedicine and Nanobiotechnology*, 8(5), 654–677. <https://doi.org/10.1002/wnan.1391>
46. Lin, H.-Y., Chen, H.-H., Chang, S.-H., & Ni, T.-S. (2013). Pectin-chitosan-PVA nanofibrous scaffold made by electrospinning and its potential use as a skin tissue scaffold. *Journal of Biomaterials Science, Polymer Edition*, 24(4), 470–484. <https://doi.org/10.1080/09205063.2012.693047>

47. Schultz, G. S., Sibbald, R. G., Falanga, V., Ayello, E. A., Dowsett, C., Harding, K., & Vanscheidt, W. (2013). Wound bed preparation: a systematic approach to wound management. *Wound Repair and Regeneration*, 11(11), (Supplement 1) 1-28. <https://doi.org/10.1046/j.1524-475X.11.s2.1.x>
48. Kaye, B. B., & Ennis, W. M. (2002). Classification of wounds and their treatment. *The American Journal of Surgery*, 59(1), 94–98. [https://doi.org/10.1016/S0002-9610\(43\)90510-0](https://doi.org/10.1016/S0002-9610(43)90510-0)
49. Tiwari, V. K. (2012). Burn wound: How it differs from other wounds? *Indian journal of plastic surgery : official publication of the Association of Plastic Surgeons of India*, 45(2), 364–73. <https://doi.org/10.4103/0970-0358.101319>
50. Latiff, A. A., Teoh, S. L., & Das, S. (2010). Wound healing in diabetes mellitus: Traditional treatment modalities. *Clinical Therapeutics*, 161(4), 359–364. <https://doi.org/10.4554.2093-1161.10>
51. Azzimonti, B., Sabbatini, M., Rimondini, L., & Cannas, M. (2016). Manipulating the healing response. In *Wound Healing Biomaterials* (1st ed., pp. 101–116). New York: USA, Elsevier. <https://doi.org/10.1016/B978-1-78242-455-0.00004-5>
52. Zhao, R., Liang, H., Clarke, E., Jackson, C., & Xue, M. (2016). Inflammation in Chronic Wounds. *International Journal of Molecular Sciences*, 17(12), 1–14. <https://doi.org/10.3390/ijms17122085>
53. Moore, R. A., Abdul, W., & Burns, B. (2019). *Rule of Nines*. In R. A. Moore (Ed.), *Wound Management* (3rd ed., vol. 2, pp. 55–62). Tennessee, USA: StatPearls Publishing. <https://doi.org/10.5122/10.30020/B659>
54. Ye, H., & De, S. (2017). Thermal injury of skin and subcutaneous tissues: A review of experimental approaches and numerical models. *Burns*, 43(5), 909–932. <https://doi.org/10.1016/j.burns.2016.11.014>
55. Abraham, J. P., Plourde, B. D., Vallez, L. J., Brittany Nelson-Cheeseman, Stark, J. R., Sparrow, E. M., & Gorman, J. M. (2018). Skin burns. In J. P. Abraham (Ed.), *Theory and Applications of Heat Transfer in Humans* (2nd ed., pp. 723–739). Wiley-Blackwell. <https://doi.org/10.1002/9781119127420>
56. Gerd Plewig, Lars French, Thomas Ruzicka, Roland Kaufmann, & Michael Hertl. (2020). Braun-Falco's Dermatology. In M. Hertl (Ed.), *Dermatology* (1st ed., vol. 6, pp. 102–115). Berlin, Germany: Springer. <https://doi.org/10.1007/978-3-662-58713-3>
57. Norbury, W., Herndon, D. N., Tanksley, J., Jeschke, M. G., & Finnerty, C. C. (2016). Infection in burns. *Surgical Infections*, 17(2), 250–255. <https://doi.org/10.1089/sur.2013.134>
58. Ho, J., Walsh, C., Yue, D., Dardik, A., & Cheema, U. (2017). Current advancements and strategies in tissue engineering for wound healing: A comprehensive review. *Advances in Wound Care*, 6(6), 191–209. <https://doi.org/10.1089/wound.2016.0723>
59. Reece, T. B., Maxey, T. S., & Kron, I. L. (2011). A prospectus on tissue adhesives. *The American Journal of Surgery*, 182(2), (Supplement 1) 40-44. [https://doi.org/10.1016/S0002-9610\(01\)00742-5](https://doi.org/10.1016/S0002-9610(01)00742-5)
60. Velasco, J. M. (2011). Soft tissue, hernia and breast. In B. Velasco, M. Deziel, & P. McCarthy (Eds.), *Rush University Medical Center Review of Surgery* (5th ed., pp. 181–224). Chicago, USA: Elsevier Health Sciences. <https://doi.org/10.1177/10600/280209/3251-3>
61. Eming, S. A., Krieg, T., & Davidson, J. M. (2007). Inflammation in wound repair: Molecular and cellular mechanisms. *Journal of Investigative Dermatology*, 127(3), 514–525. <https://doi.org/10.1038/sj.jid.5700701>
62. Diegelmann, R. F., & Evans, M. C. (2004). Wound healing: an overview of acute, fibrotic and delayed healing. *Frontiers in Bioscience*, 9(3), 283–289. <https://doi.org/10.2741/1184>
63. Wynn, T. A. (2004). Fibrotic disease and the TH1/TH2 paradigm. *Nature Reviews Immunology*, 4(8), 583–594. <https://doi.org/10.1038/nri1412>

64. Sprague, A. H., & Khalil, R. A. (2009). Inflammatory cytokines in vascular dysfunction and vascular disease. *Biochemical Pharmacology*, 78(6), 539–552. <https://doi.org/10.1016/j.bcp.2009.04.029>
65. Busse, B. (2016). Improving outcomes in wound healing. In B. Busse (Ed.), *Wound Management in Urgent Care* (2nd ed., vol. 1, pp. 7–11). California, USA: Springer International Publishing. <https://doi.org/10.1007/978-3-319-27428-7>
66. Persidis, A. (2000). Tissue engineering. *Nature Biotechnology*, 17(5), 508–510. <https://doi.org/10.1038/8700>
67. Weller, C. D., Team, V., & Sussman, G. (2020). First-line interactive wound dressing update: A comprehensive review of the evidence. *Frontiers in Pharmacology*, 11(2), 1–13. <https://doi.org/10.3389/fphar.2020.00155>
68. Turner, N. J., & Badylak, S. F. (2015). The use of biologic scaffolds in the treatment of chronic nonhealing wounds. *Advances in Wound Care*, 4(8), 490–500. <https://doi.org/10.1089/wound.2014.0604>
69. Das, S., & Baker, A. B. (2016, October). Biomaterials and nanotherapeutics for enhancing skin wound healing. *Frontiers in Bioengineering and Biotechnology*. Frontiers Media S.A. <https://doi.org/10.3389/fbioe.2016.00082>
70. Bianchera, A., Catanzano, O., Boateng, J., & Elviri, L. (2020). The place of biomaterials in wound healing. In A. Bianchera (Ed.), *Therapeutic Dressings and Wound Healing Applications* (1st ed., pp. 337–366). Wiley. <https://doi.org/10.1002/9781119433316.ch15>
71. Dhivya, S., Padma, V. V., & Santhini, E. (2015). Wound dressings - A review. *BioMedicine*, 5(4), 24–28. <https://doi.org/10.7603/s40681-015-0022-9>
72. Chai, Q., Jiao, Y., & Yu, X. (2017). Hydrogels for biomedical applications: Their characteristics and the mechanisms behind them. *Gels*, 3(1), 1–8. <https://doi.org/10.3390/gels3010006>
73. Catoira, M. C., Fusaro, L., Di Francesco, D., Ramella, M., & Boccafoschi, F. (2019). Overview of natural hydrogels for regenerative medicine applications. *Journal of Materials Science: Materials in Medicine*, 30(10), 1–8. <https://doi.org/10.1007/s10856-019-6318-7>
74. Murray, R. Z., West, Z. E., Cowin, A. J., & Farrugia, B. L. (2019). Development and use of biomaterials as wound healing therapies. *Burns & Trauma*, 7(2), 1–6. <https://doi.org/10.1186/s41038-018-0139-7>
75. Radvar, E., & Azevedo, H. S. (2019). Supramolecular peptide/polymer hybrid hydrogels for biomedical applications. *Macromolecular Bioscience*, 19(1), 1–16. <https://doi.org/10.1002/mabi.201800221>
76. Kuang, P., & Constant, K. (2015). Increased wettability and surface free energy of polyurethane by ultraviolet ozone treatment. In M. Aliofkhaezai (Ed.), *Wetting and Wettability* (1st ed., vol. 4, pp. 50–78). New York, USA: InTech. <https://doi.org/10.5772/60798>
77. Boateng, J., & Catanzano, O. (2017). Advanced therapeutic dressings for effective wound healing: A review. *Journal of Pharmaceutical Sciences*, 104(11), 3653–3680. <https://doi.org/10.1002/jps.24610>
78. Liu, X., Niu, Y., Chen, K. C., & Chen, S. (2017). Rapid hemostatic and mild polyurethane-urea foam wound dressing for promoting wound healing. *Materials Science and Engineering C*, 71(1), 289–297. <https://doi.org/10.1016/j.msec.2016.10.019>
79. Kanapathy, M., Hachach-Haram, N., Bystrzonowski, N., Harding, K., Mosahebi, A., & Richards, T. (2016). Epidermal grafting versus split-thickness skin grafting for wound healing (EPIGRAFT): Study protocol for a randomised controlled trial. *Trials*, 17(1), 245–252. <https://doi.org/10.1186/s13063-016-1352-y>
80. Herskovitz, I., Hughes, O. B., Macquhae, F., Rakosi, A., & Kirsner, R. (2016). Epidermal skin grafting. *International Wound Journal*, 13(3), 52–56. <https://doi.org/10.1111/iwj.12631>

81. Hulseley, A., Linneman, P., & Litt, J. (2016). Clinical usage and economic effectiveness of a recently developed epidermal autograft harvesting system in 13 chronic wound patients in a university-based wound center. *Cureus*, *8*(11), 23–30. <https://doi.org/10.7759/cureus.878>
82. Nicholas, M. N., Jeschke, M. G., & Amini-Nik, S. (2016). Methodologies in creating skin substitutes. *Cellular and Molecular Life Sciences*, *73*(18), 3453–3472. <https://doi.org/10.1007/s00018-016-2252-8>
83. Wang, Y., Beekman, J., Hew, J., Jackson, S., Issler-Fisher, A. C., Parungao, R., Lajevardi, S. S., Li, Z., & Maitz, P. K. M. (2018). Burn injury: Challenges and advances in burn wound healing, infection, pain and scarring. *Advanced Drug Delivery Reviews*, *123*(1), 3–17. <https://doi.org/10.1016/j.addr.2017.09.018>
84. Vig, K., Chaudhari, A., Tripathi, S., Dixit, S., Sahu, R., Pillai, S., Dennis, V. A., & Singh, S. R. (2017). Advances in skin regeneration using tissue engineering. *International Journal of Molecular Sciences*, *18*(4), 789–798. <https://doi.org/10.3390/ijms18040789>
85. Dixit, S., Baganizi, D. R., Sahu, R., Dosunmu, E., Chaudhari, A., Vig, K., Pillai, S. R., Singh, S. R., & Dennis, V. A. (2017). Immunological challenges associated with artificial skin grafts: Available solutions and stem cells in future design of synthetic skin. *Journal of Biological Engineering*, *11*(49), 1–19. <https://doi.org/10.1186/s13036-017-0089-9>
86. Stabler, C. L., Li, Y., Stewart, J. M., & Keselowsky, B. G. (2019). Engineering immunomodulatory biomaterials for type 1 diabetes. *Nature Reviews Materials*, *4*(6), 429–450. <https://doi.org/10.1038/s41578-019-0112-5>
87. Arno, A. I., & Jeschke, M. G. (2014). The use of dermal substitutes in burn surgery: Acute phase. *Dermal Replacements in General, Burn, and Plastic Surgery: Tissue Engineering in Clinical Practice*, *22*(1), 193–210. [https://doi.org/10.1007/978-3-7091-1586-2\\_16](https://doi.org/10.1007/978-3-7091-1586-2_16)
88. Boyce, S. T., & Lalley, A. L. (2018). Tissue engineering of skin and regenerative medicine for wound care. *Burns & Trauma*, *6*(1) 1–8. <https://doi.org/10.1186/s41038-017-0103-y>
89. Ige, O. O., Umoru, L. E., & Aribo, S. (2012). Natural products: A minefield of biomaterials. *ISRN Materials Science*, *12*(1), 1–20. <https://doi.org/10.5402/2012/983062>
90. Mano, J. F., Silva, G. A., Azevedo, H. S., Malafaya, P. B., Sousa, R. A., Silva, S. S., Boesel, S. F., Oliveira, J. M., Santos, T. C., Marques, A. P., Neves, N. M., & Reis, R. L. (2007). Natural origin biodegradable systems in tissue engineering and regenerative medicine: Present status and some moving trends. *Journal of the Royal Society Interface*, *4*(17), 999–1030. <https://doi.org/10.1098/rsif.2007.0220>
91. Spicer, C. D. (2019). Hydrogel scaffolds for tissue engineering: the importance of polymer choice. *Polymer Chemistry*, *11*(2), 184–219. <https://doi.org/10.1039/c9py01021a>
92. Dhandayuthapani, B., Yoshida, Y., Maekawa, T., & Kumar, D. S. (2011). Polymeric scaffolds in tissue engineering application: A review. *International Journal of Polymer Science*, *11*(1), 1–20. <https://doi.org/10.1155/2011/290602>
93. Rath, G., Hussain, T., Chauhan, G., Garg, T., & Goyal, A. K. (2016). Collagen nanofiber containing silver nanoparticles for improved wound-healing applications. *J Drug Target*, *24*(6), 1061–1066. <https://doi.org/10.3109/1061186X.2015.1095922>
94. Ju, H. W., Lee, O. J., Lee, J. M., Moon, B. M., Park, H. J., Park, Y. R., Lee, M. C., Kim, S. H., Chao, J. R., K., C. S., & Park, C. H. (2016). Wound healing effect of electrospun silk fibroin nanomatrix in burn-model. *International Journal of Biological Macromolecules*, *85*(4), 29–39. <https://doi.org/10.1016/j.ijbiomac.2015.12.055>
95. Yildirim, L., Thanh, N. T. K., & Seifalian, A. M. (2012). Skin regeneration scaffolds: A multimodal bottom-up approach. *Trends in Biotechnology*, *30*(12), 638–648. <https://doi.org/10.1016/j.tibtech.2012.08.004>
96. Tiwari, S. K., & Venkatraman, S. S. (2012). Importance of viscosity parameters in electrospinning: Of monolithic and core-shell fibers. *Materials Science and Engineering C*, *32*(5), 1037–1042. <https://doi.org/10.1016/j.msec.2012.02.019>



97. Xue, J., Wu, T., Dai, Y., & Xia, Y. (2019). Electrospinning and electrospun nanofibers: Methods, materials, and applications. *Chemical Reviews*, 119(8), 5298–5415. <https://doi.org/10.1021/acs.chemrev.8b00593>
98. Samadian, H., Salehi, M., Farzamfar, S., Vaez, A., Ehterami, A., Sahrapeyma, H., Goodarzi, A., & Ghorbani, S. (2018). In vitro and in vivo evaluation of electrospun cellulose acetate/gelatin/hydroxyapatite nanocomposite mats for wound dressing applications. *Artificial Cells, Nanomedicine and Biotechnology*, 46(1), 964–974. <https://doi.org/10.1080/21691401.2018.1439842>
99. Ghosal, K., Chandra, A., Praveen, G., Snigdha, S., Roy, S., Agatemor, C., Thomas, S., & Provaznik, I. (2018). Electrospinning over Solvent Casting: Tuning of Mechanical Properties of Membranes. *Scientific Reports*, 8(1), 1–9. <https://doi.org/10.1038/s41598-018-23378-3>
100. Kim, Y. J., Ebara, M., & Aoyagi, T. (2013). A smart hyperthermia nanofiber with switchable drug release for inducing cancer apoptosis. *Advanced Functional Materials*, 23(46), 5753–5761. <https://doi.org/10.1002/adfm.201300746>
101. Castellano, D., Sanchis, A., Blanes, M., Pérez del Caz, M. D., Ruiz-Saurí, A., Piquer-Gil, M., & Sepúlveda, P. (2018). Electrospun poly(hydroxybutyrate) scaffolds promote engraftment of human skin equivalents via macrophage M2 polarization and angiogenesis. *Journal of Tissue Engineering and Regenerative Medicine*, 12(2), e983–e994. <https://doi.org/10.1002/term.2420>
102. Jiang, S., Wu, J., Hang, Y., Liu, Q., Li, D., Chen, H., & Brash, J. L. (2019). Sustained release of a synthetic structurally-tailored glycopolymer modulates endothelial cells for enhanced endothelialization of materials. *Journal of Materials Chemistry B*, 7(1), 4017–4029. <https://doi.org/10.1039/c9tb00714h>
103. Gholipourmalekabadi, M., Khosravimelal, S., Nokhbedehghan, Z., Sameni, M., Jajarmi, V., Urbanska, A. M., & Kundu, S. C. (2019). Modulation of hypertrophic scar formation using amniotic membrane/electrospun silk fibroin bilayer membrane in a rabbit ear model. *ACS Biomaterials Science and Engineering*, 5(3), 1487–1496. <https://doi.org/10.1021/acsbiomaterials.8b01521>
104. Pina, S., Ribeiro, V. P., Marques, C. F., Maia, F. R., Silva, T. H., Reis, R. L., & Oliveira, J. M. (2019). Scaffolding strategies for tissue engineering and regenerative medicine applications. *Materials*, 12(11), 1–16. <https://doi.org/10.3390/ma12111824>
105. Gizaw, M., Faglie, A., Pieper, M., Poudel, S., & Chou, S.-F. (2020). The role of electrospun fiber scaffolds in stem cell therapy for skin tissue regeneration. *Med One*, 4(1), 1–12. <https://doi.org/10.20900/mo.20190002>
106. Saghazadeh, S., Rinoldi, C., Schot, M., Kashaf, S. S., Sharifi, F., Jalilian, E., Nuutila, K., Giatsidis, G., Mostafalu, P., Derakhshandeh, H., Yue, K., Swieszkowski, W., Memic, A., Tamayol, A., & Khademhosseini, A. (2018). Drug delivery systems and materials for wound healing applications. *Advanced Drug Delivery Reviews*, 127(1), 138–166. <https://doi.org/10.1016/j.addr.2018.04.008>
107. Baylón, K., Rodríguez-Camarillo, P., Elías-Zúñiga, A., Díaz-Elizondo, J. A., Gilkerson, R., & Lozano, K. (2017). Past, present and future of surgical meshes: A review. *Membranes*, 7(3), 1–23. <https://doi.org/10.3390/membranes7030047>
108. Aljubairy, A. M., Alqahtani, A. M., Hakeem, H. F., Mohammed, A., Almalki, D., Alrefaai, A. W., & Alhazmy, S. A. (2017). Prevalence of inguinal hernia in relation to various risk factors. *EC Microbiology*, 9(2), 182–192. <https://doi.org/ECMI-09-00293>
109. Harrison, B., Sanniec, K., & Janis, J. E. (2019). Collagenopathies—implications for abdominal wall reconstruction. *Plastic and Reconstructive Surgery - Global Open*, 4(10), 10–36. <https://doi.org/10.1097/GOX.0000000000001036>
110. Desarda, M. (2017). Concepts that Prevent Inguinal Hernia Formation—Revisited New Concepts of Inguinal Hernia Prevention. *Ann Emerg Surg*, 2(1), 1007–1012. <https://doi.org/10.1186/1471-2482-3-2>

111. Lassandro, F. (2011). Abdominal hernias: Radiological features. *World Journal of Gastrointestinal Endoscopy*, 3(6), 1–8. <https://doi.org/10.4253/wjge.v3.i6.110>
112. Shouldice, E. B. (2003). The shouldice repair for groin hernias. *Surgical Clinics of North America*, 83(5), 1163–1187. [https://doi.org/10.1016/S0039-6109\(03\)00121-X](https://doi.org/10.1016/S0039-6109(03)00121-X)
113. Khairy, M., Madbouly, A. E.-W., & Sharaf, M. (2020). Evaluation of Desarda technique in inguinal herniorrhaphy. *International Medical Journal*, 1(7), 193–197. <https://doi.org/10.21608/aimj.2020.23116.1116>
114. Chowbey, P. (2020). Complications inguinal hernias: Strangulated incarcerated and obstructed hernias. In P. Chowbey (Ed.), *Techniques of Abdominal Wall Hernia Repair* (2nd ed., pp.163–168). Springer India. [https://doi.org/10.1007/978-81-322-3944-4\\_14](https://doi.org/10.1007/978-81-322-3944-4_14)
115. McCormack, K., Wake, B., Perez, J., Fraser, C., Cook, J., McIntosh, E., & Grant, A. (2005). Laparoscopic surgery for inguinal hernia repair: Systematic review of effectiveness and economic evaluation. *Health Technology Assessment*, 9(14), 198–203. <https://doi.org/10.3310/hta9140>
116. Adrales, G., Morales-conde, S., Heniford, B. T., Sharma, A., Rosen, M., Muysoms, F., & Adrales, G. (2018). International Hernia Congress. *Hernia*, 22(1), 1–204. <https://doi.org/10.1007/s10029-018-1733-0>
117. Walgenbach, M., Mathes, T., Siegel, R., & Eikermann, M. (2015). Mesh fixation techniques in primary ventral or incisional hernia repair. *Cochrane Database of Systematic Reviews*, 15(3), 1–15. <https://doi.org/10.1002/14651858.CD011563>
118. Gopal, S. V., & Warriar, A. (2017). Recurrence after groin hernia repair-revisited. *International Journal of Surgery*, 11(5), 374–377. <https://doi.org/10.1016/j.ijssu.2013.03.012>
119. Argiroff, A., & Camacho, D. (2019). TAPP vs. TEP vs. rTAPP: What does the evidence show? In A. Argiroff (Ed.), *The SAGES Manual of Hernia Surgery* (1st ed., vol. 4, pp. 439–447). Springer International Publishing. [https://doi.org/10.1007/978-3-319-78411-3\\_32](https://doi.org/10.1007/978-3-319-78411-3_32)
120. Vikraman, J., Donath, S., & Hutson, J. M. (2019). Frequency of inguinal herniotomy in Australia (1998–2017). *Pediatric Surgery International*, 35(7), 759–763. <https://doi.org/10.1007/s00383-019-04483-4>
121. Simons, M. P., Smietanski, M., Bonjer, H. J., Bittner, R., Miserez, M., Aufenacker, T. J., & Wijsmuller, A. R. (2019). International guidelines for groin hernia management. *European Hernia Society*, 22(1), 1–165. <https://doi.org/10.1007/s10029-017-1668-x>
122. Al Chalabi, H., Larkin, J., Mehigan, B., & McCormick, P. (2015). A systematic review of laparoscopic versus open abdominal incisional hernia repair, with meta-analysis of randomized controlled trials. *International Journal of Surgery*, 20(1), 65–74. <https://doi.org/10.1016/j.ijssu.2015.05.050>
123. Cobb, W. S., Kercher, K. W., & Heniford, B. T. (2005). Laparoscopic repair of incisional hernias. *Surgical Clinics of North America*, 85(1), 97–103. <https://doi.org/10.1016/j.suc.2004.09.006>
124. Taylor, D. (2018). The failure of polypropylene surgical mesh in vivo. *Journal of the Mechanical Behavior of Biomedical Materials*, 88(12), 370–376. <https://doi.org/10.1016/j.jmbbm.2018.08.041>
125. C. Frangou. (2014). Study reveals staggering costs of ventral hernia repair complication mesh infection general surgery news. *General Surgery News*. Retrieved (Jun 2020) from: <https://www.generalsurgerynews.com/Article/PrintArticle?articleID=24813>
126. Erdas, E., Medas, F., Pisano, G., Nicolosi, A., & Calò, P. G. (2016). Antibiotic prophylaxis for open mesh repair of groin hernia: systematic review and meta-analysis. *Hernia*, 20(6), 765–776. <https://doi.org/10.1007/s10029-016-1536-0>
127. Bringman, S., Conze, J., Cuccurullo, D., Deprest, J., Junge, K., Klosterhalfen, B., Parra-Davila, E., Ramshaw, B., & Schumpelick, V. (2010). Hernia repair: The search for ideal meshes.

- Hernia*, 14(1), 81–87. <https://doi.org/10.1007/s10029-009-0587-x>
128. Elango, S., Perumalsamy, S., Ramachandran, K., & Vadodaria, K. (2017). Mesh materials and hernia repair. *BioMedicine*, 7(3), 1–7. <https://doi.org/10.1051/BMDCN/2017070316>
  129. Kuo, C. J., & Lan, W. L. (2016). Bi-component and bi-constituent spinning of synthetic polymer fibres. In C. Kuo (Ed.), *Advances in Filament Yarn Spinning of Textiles and Polymers* (1st ed., vol. 6, pp. 120–145). New York, USA: Elsevier. <https://doi.org/10.1533/9780857099174.2.100>
  130. Melman, L., Jenkins, E. D., Hamilton, N. A., Bender, L. C., Brodt, M. D., Deeken, C. R., Greco, S. C., Frisella, M. M., & Matthews, B. D. (2011). Early biocompatibility of crosslinked and non-crosslinked biologic meshes in a porcine model of ventral hernia repair. *Hernia*, 15(2), 157–164. <https://doi.org/10.1007/s10029-010-0770-0>
  131. Mao, N. (2016). Methods for characterisation of nonwoven structure, property, and performance. In G. Kellie (Ed.), *Advances in Technical Nonwovens* (1st ed., vol. 6, pp. 155–211). Michigan, USA: Woodhead Publishing. <https://doi.org/10.1016/B978-0-08-100575-0.00006-1>
  132. Kalaba, S., Gerhard, E., Winder, J. S., Pauli, E. M., Haluck, R. S., & Yang, J. (2016). Design strategies and applications of biomaterials and devices for Hernia repair. *Bioactive Materials*, 1(2), 2–17. <https://doi.org/10.1016/j.bioactmat.2016.05.002>
  133. Fitzgerald, J. F., & Kumar, A. S. (2014). Biologic versus synthetic mesh reinforcement: What are the pros and cons? *Clinics in Colon and Rectal Surgery*, 27(4), 140–148. <https://doi.org/10.1055/s-0034-1394155>
  134. Köckerling, F., & Schug-Pass, C. (2014). What do we know about titanized polypropylene meshes? An evidence-based review of the literature. *Hernia*, 18(4), 445–457. <https://doi.org/10.1007/s10029-013-1187-3>
  135. Brown, C. N., & Finch, J. G. (2010). Which mesh for hernia repair? *Annals of the Royal College of Surgeons of England*, 92(4), 272–278. <https://doi.org/10.1308/003588410X12664192076296>
  136. Gribovskaja-Rupp, I., & Melton, G. B. (2016). Enterocutaneous fistula: Proven strategies and updates. *Clinics in Colon and Rectal Surgery*, 29(2), 130–137. <https://doi.org/10.1055/s-0036-1580732>
  137. Phuong, M. P., & Oscar, J. H. (2010). Management of bowel complications. *Complications of Urologic Surgery*, 22(4), 251–261. <https://doi.org/10.1016/B978-1-4160-4572-4.X0001-5>
  138. Winny, M., Maegel, L., Grethe, L., Lippmann, T., Jonigk, D., Schrem, H., Kaltenborn, A., Klemptner, J., & Poehnert, D. (2016). Adhesion prevention efficacy of composite meshes parietex®, proceed® and 4dryfield® PH covered polypropylene meshes in an IPOM rat model. *International Journal of Medical Sciences*, 13(12), 936–941. <https://doi.org/10.7150/ijms.16215>
  139. Guillaume, O., Pérez-Tanoira, R., Fortelny, R., Redl, H., Moriarty, T. F., Richards, R. G., Eglin, D., & Petter-Puchner, A. (2018). Infections associated with mesh repairs of abdominal wall hernias: Are antimicrobial biomaterials the longed-for solution? *Biomaterials*, 167(1), 15–31. <https://doi.org/10.1016/j.biomaterials.2018.03.017>
  140. Bilsel, Y., & Abci, I. (2012). The search for ideal hernia repair; mesh materials and types. *International Journal of Surgery*, 10(6), 317–321. <https://doi.org/10.1016/j.ijsu.2012.05.002>
  141. Doctor, H. G. (2006). Evaluation of various prosthetic materials and newer meshes for hernia repairs. In *Journal of Minimal Access Surgery* (2nd ed., pp. 110–116). Medknow Publications. <https://doi.org/10.4103/0972-9941.27721>
  142. McGarrigle, C., Rodgers, I., McIlhagger, A., Harkin-Jones, E., Major, I., Devine, D., & Archer, E. (2017). Extruded monofilament and multifilament thermoplastic stitching yarns. *Fibers*, 5(4), 45–52. <https://doi.org/10.3390/fib5040045>
  143. Tausif, M., Cassidy, T., & Butcher, I. (2018). Yarn and thread manufacturing methods for high-performance apparel. In J. McLoughlin & T. Sabir (Eds.), *High-Performance Apparel*:

- Materials, Development, and Applications* (1st ed., Vol. 3, pp. 33–73). Manchester, UK: Woodhead Publishing. <https://doi.org/10.1016/B978-0-08-100904-8.00003-1>
144. Guertin, D. A., & Sabatini, D. M. (2005). Cell size control. *Encyclopedia of Life Sciences*, 10(3), 1–10. <https://doi.org/10.1038/npg.els.0003359>
145. Gillaspay, A. F., Iandolo, J. J., Tang, Y. W., & Stratton, C. W. (2019). Staphylococcus. In A. F. Gillaspay (Ed.), *Encyclopedia of Microbiology* (4th ed., vol. 12, pp. 309–320). New York, USA: Elsevier. <https://doi.org/10.1016/B978-0-12-801238-3.02304-7>
146. Millan, C., Zenobi-wong, M., Akashi, M., Akagi, T., & Editors, M. M. (2017). Engineering and manipulating cells. In M. Akashi, T. Akagi, & M. M. (Eds.), *Engineered Cell Manipulation for Biomedical Application* (2nd ed., vol. 3, pp. 78–85). Tokyo, Japan: Springer. <https://doi.org/10.1007/978-4-431-55139-3>
147. Brown, S. H. M., & McGill, S. M. (2008). An ultrasound investigation into the morphology of the human abdominal wall uncovers complex deformation patterns during contraction. *European Journal of Applied Physiology*, 104(6), 1021–1030. <https://doi.org/10.1007/s00421-008-0858-8>
148. Pott, P. P., Schwarz, M. L. R., Gundling, R., Nowak, K., Hohenberger, P., & Roessner, E. D. (2012). Mechanical properties of mesh materials used for hernia repair and soft tissue augmentation. *PLoS ONE*, 7(10), 1–10. <https://doi.org/10.1371/journal.pone.0046978>
149. Cobb, W. S., Burns, J. M., Kercher, K. W., Matthews, B. D., James Norton, H., & Todd Heniford, B. (2005). Normal intraabdominal pressure in healthy adults. *Journal of Surgical Research*, 129(2), 231–235. <https://doi.org/10.1016/j.jss.2005.06.015>
150. Klinge, U., Zheng, H., Si, Z., Schumpelick, V., Bhardwaj, R. S., Muys, L., & Surg, E. (1999). Expression of the extracellular matrix proteins collagen I, collagen III and fibronectin and matrix metalloproteinase-1 and -13 in the skin of patients with inguinal. *Eur Surg Res*, 31(1), 480–490. <https://doi.org/10.1159/000008728>
151. Junge, K., Klinge, U., Prescher, A., Giboni, P., Niewiera, M., & Schumpelick, V. (2001). Elasticity of the anterior abdominal wall and impact for reparation of incisional hernias using mesh implants. *Hernia*, 5(3), 113–118. <https://doi.org/10.1007/s100290100019>
152. Klosterhalfen, B., Junge, K., & Klinge, U. (2005). The lightweight and large porous mesh concept for hernia repair. *Expert Review of Medical Devices*, 2(1), 103–117. <https://doi.org/10.1586/17434440.2.1.103>
153. Anurov, M. V., Titkova, S. M., & Oettinger, A. P. (2012). Biomechanical compatibility of surgical mesh and fascia being reinforced: Dependence of experimental hernia defect repair results on anisotropic surgical mesh positioning. *Hernia*, 16(2), 199–210. <https://doi.org/10.1007/s10029-011-0877-y>
154. Delgado, L. M., Bayon, Y., Pandit, A., & Zeugolis, D. I. (2015). To cross-link or not to cross-link? Cross-linking associated foreign body response of collagen-based devices. *Tissue Engineering - Part B: Reviews*, 21(3), 298–313. <https://doi.org/10.1089/ten.teb.2014.0290>
155. Köckerling, F., Alam, N. N., Antoniou, S. A., Daniels, I. R., Familietti, F., Fortelny, R. H., Heiss, M. M., Kallinowski, F., Kyle-Leinhase, I., Mayer, F., Miserez, M., Montgomery, A., Morales-Conde, S., Muysoms, F., Narang, S. K., Petter-Puchner, A., Reinhold, W., Scheuerlein, H., Smietanski, M., Stechemesser, B., Strey, Woeste, C. G., & Smart, N. J. (2018). What is the evidence for the use of biologic or biosynthetic meshes in abdominal wall reconstruction? *Hernia*, 22(2), 249–269. <https://doi.org/10.1007/s10029-018-1735-y>
156. Langbach, O., Holmedal, S. H., Grandal, O. J., & Røkke, O. (2016). Adhesions to mesh after ventral hernia mesh repair are detected by mri but are not a cause of long term chronic abdominal pain. *Gastroenterology Research and Practice*, 2(6), 1–8. <https://doi.org/10.1155/2016/2631598>
157. Fadaee, N., Mazer, L., Sharma, R., Capati, I., Balzer, B., & Towfigh, S. (2019). Clinical value of hernia mesh pathology evaluation. *American College of Surgeons*, 228(5), 776–781. <https://doi.org/10.1016/j.jamcollsurg.2019.02.038>

158. Majumder, A., Winder, J. S., Wen, Y., Pauli, E. M., Belyansky, I., & Novitsky, Y. W. (2016). Comparative analysis of biologic versus synthetic mesh outcomes in contaminated hernia repairs. *Surgery (United States)*, *160*(4), 828–838. <https://doi.org/10.1016/j.surg.2016.04.041>
159. Liu, Y., Zheng, Y., & Hayes, B. (2017). Degradable, absorbable or resorbable—what is the best grammatical modifier for an implant that is eventually absorbed by the body? *Science China Materials*, *60*(5), 377–391. <https://doi.org/10.1007/s40843-017-9023-9>
160. Wolf, M. T., Carruthers, C. A., Dearth, C. L., Crapo, P. M., Huber, A., Burnsed, O. A., Londono, R., Johnson, S. A., Daly, K. A., Stahl, E. C., Freund, J. M., Medberry, C. J., Carey, L. E., Nieponice, A., Amoroso, N. J., & Badylak, S. F. (2014). Polypropylene surgical mesh coated with extracellular matrix mitigates the host foreign body response. *Journal of Biomedical Materials Research Part A*, *102*(1), 234–246. <https://doi.org/10.1002/jbm.a.34671>
161. Sun, W. Q., Xu, H., Sandor, M., & Lombardi, J. (2013). Process-induced extracellular matrix alterations affect the mechanisms of soft tissue repair and regeneration. *Journal of Tissue Engineering*, *4*(1), 1–13. <https://doi.org/10.1177/2041731413505305>
162. Bottino, M. C., Thomas, V., Schmidt, G., Vohra, Y. K., Chu, T. M. G., Kowolik, M. J., & Janowski, G. M. (2012). Recent advances in the development of GTR/GBR membranes for periodontal regeneration - A materials perspective. *Dental Materials*, *28*(7), 703–721. <https://doi.org/10.1016/j.dental.2012.04.022>
163. Ibrahim, A. M. S., Vargas, C. R., Colakoglu, S., Nguyen, J. T., Lin, S. J., & Lee, B. T. (2015). Properties of meshes used in hernia repair: A comprehensive review of synthetic and biologic meshes. *Journal of Reconstructive Microsurgery*, *31*(2), 83–94. <https://doi.org/10.1055/s-0034-1376886>
164. Orelia, C. C., van Hessen, C., Sanchez-Manuel, F. J., Aufenacker, T. J., & Scholten, R. J. (2020). Antibiotic prophylaxis for prevention of postoperative wound infection in adults undergoing open elective inguinal or femoral hernia repair. *The Cochrane database of systematic reviews*, *4*(4), 1–12. <https://doi.org/10.1002/14651858.CD003769.pub5>
165. Langbach, O., Kristoffersen, A. K., Abesha-Belay, E., Enersen, M., Røkke, O., & Olsen, I. (2016). Oral, intestinal, and skin bacteria in ventral hernia mesh implants. *Journal of Oral Microbiology*, *8*(1), 1–15. <https://doi.org/10.3402/jom.v8.31854>
166. Meagher, H., Clarke Moloney, M., & Grace, P. A. (2015). Conservative management of mesh-site infection in hernia repair surgery: a case series. *Hernia*, *19*(2), 231–237. <https://doi.org/10.1007/s10029-013-1069-8>
167. Stoodley, P., Sidhu, S., Nistico, L., Mather, M., Boucek, A., Hall-Stoodley, L., & Kathju, S. (2012). Kinetics and morphology of polymicrobial biofilm formation on polypropylene mesh. *FEMS Immunology & Medical Microbiology*, *65*(2), 283–290. <https://doi.org/10.1111/j.1574-695X.2012.00948.x>
168. Birolini, C., de Miranda, J. S., Tanaka, E. Y., Utiyama, E. M., Rasslan, S., & Birolini, D. (2020). The use of synthetic mesh in contaminated and infected abdominal wall repairs: challenging the dogma—A long-term prospective clinical trial. *Hernia*, *24*(2), 307–323. <https://doi.org/10.1007/s10029-019-02035-2>
169. Narkhede, R., Shah, N. M., Dalal, P. R., Mangukia, C., & Dholaria, S. (2018). Postoperative mesh infection—still a concern in laparoscopic era. *Indian Journal of Surgery*, *77*(4), 322–326. <https://doi.org/10.1007/s12262-015-1304-x>
170. Chen, T., Zhang, Y. H., Wang, H. L., Chen, W., & Wang, J. (2016). Late-onset deep mesh infection: A study of eight cases detected from 2666 consecutive patients with abdominal wall hernia repairs. *Chinese Medical Journal*, *129*(15), 1870–1872. <https://doi.org/10.4103/0366-6999.186651>
171. Alston, D., Parnell, S., Hoonjan, B., Sebastian, A., & Howard, A. (2013). Conservative management of an infected laparoscopic hernia mesh: A case study. *International Journal of Surgery Case Reports*, *4*(11), 1035–1037. <https://doi.org/10.1016/j.ijscr.2013.08.008>

172. Akyol, C., Kocaay, F., Orozakunov, E., Genc, V., Bayram, I. K., Cakmak, A., Baskan, S., & Kuterdem, E. (2013). Outcome of the patients with chronic mesh infection following open inguinal hernia repair. *Journal of the Korean Surgical Society*, *84*(5), 287–291. <https://doi.org/10.4174/jkss.2013.84.5.287>
173. Le, D., Deveney, C. W., Reaven, N. L., Funk, S. E., McGaughey, K. J., & Martindale, R. G. (2013). Mesh choice in ventral hernia repair: So many choices, so little time. *American Journal of Surgery*, *205*(5), 602–607. <https://doi.org/10.1016/j.amjsurg.2013.01.026>
174. Kanitra, J. J., Hess, A. L., Haan, P. S., Anderson, C. I., & Kavuturu, S. (2019). Hernia recurrence and infection rate in elective complex abdominal wall repair using biologic mesh. *BMC surgery*, *19*(1), 1–8. <https://doi.org/10.1186/s12893-019-0640-3>
175. Darehzereshki, A., Goldfarb, M., Zehetner, J., Moazzez, A., Lipham, J. C., Mason, R. J., & Katkhouda, N. (2014). Biologic versus nonbiologic mesh in ventral hernia repair: A systematic review and meta-analysis. *World Journal of Surgery*, *38*(1), 40–50. <https://doi.org/10.1007/s00268-013-2232-1>
176. Sadava, E. E., Krpata, D. M., Gao, Y., Novitsky, Y. W., & Rosen, M. J. (2013). Does presoaking synthetic mesh in antibiotic solution reduce mesh infections? An experimental study. *Journal of Gastrointestinal Surgery*, *17*(3), 562–568. <https://doi.org/10.1007/s11605-012-2099-8>
177. Swick, M. C., Koehler, T. M., & Driks, A. (2016). Surviving between hosts: Sporulation and transmission. *Microbiology Spectrum*, *4*(4), 1–29. <https://doi.org/10.1128/microbiolspec.vmbf-0029-2015>
178. McDonnell, G., & Russell, A. D. (2004). Antiseptics and disinfectants: Activity, action, and resistance. *Clinical Microbiology Reviews*, *12*(1), 147–179. <https://doi.org/10.1128/CMR.12.1.147>
179. Zhang, Q., Zhang, C., Fang, X., Luo, X., & Guo, J. (2018). Biomaterial suture Vicryl Plus reduces wound-related complications. *Therapeutics and Clinical Risk Management*, *14*(1), 1417–1421. <https://doi.org/10.2147/TCRM.S164658>
180. Arnab, M., Ruel, N., & Yuri W, N. (2015). Antibiotic Coating of Hernia Meshes: The Next Step Toward Preventing Mesh Infection. *Surg. Technol. Int.*, *5*(27), 147–153. <https://doi.org/10.26680390>
181. Poelstra, K. A., Barekzi, N. A., Rediske, A. M., Felts, A. G., Slunt, J. B., & Grainger, D. W. (2002). Prophylactic treatment of Gram-positive and Gram-negative abdominal implant infections using locally delivered polyclonal antibodies. *Journal of Biomedical Materials Research*, *60*(1), 206–215. <https://doi.org/10.1002/jbm.10069>
182. Kallick, E., Nistico, L., Longwell, M., Byers, B., Cartieri, F., Kreft, R., & Edington, H. (2019). Resistance of synthetic and biologic surgical meshes to methicillin-resistant *Staphylococcus aureus* biofilm: An in vitro investigation. *International Journal of Biomaterials*, *83*(5), 1–8. <https://doi.org/10.1155/2019/1063643>
183. Chapin, K., Khalifa, A., Mbimba, T., McClellan, P., Anderson, J., Novitsky, Y., Hijaz, A., & Akkus, O. (2019). In vivo biocompatibility and time-dependent changes in mechanical properties of woven collagen meshes: A comparison to xenograft and synthetic mid-urethral sling materials. *Journal of Biomedical Materials Research Part B: Applied Biomaterials*, *107*(3), 479–489. <https://doi.org/10.1002/jbm.b.34138>
184. Kingsnorth, A. N., & Le Blanc, K. A. (2014). Management of abdominal hernias. In A.N., Kingsnorth (Ed.), *Management of Abdominal Hernias* (4th ed., vol. 2). London, UK: Springer-Verlag. <https://doi.org/10.1007/978-1-84882-877-3>
185. Baar, S., Schörner, C., Röllinghoff, M., Radespiel-Tröger, M., Hümmer, H. P., & Carbon, R. T. (2001). Collagen patches impregnated with antimicrobial agents have high local antimicrobial efficacy and achieve effective tissue gluing. *Infection*, *29*(1), 27–31. <https://doi.org/10.1007/s15010-001-0073-6>

186. Bhende, S., Barbolt, T., Rothenburger, S., & Piccoli, L. (2007). Infection potentiation study of synthetic and naturally derived surgical mesh in mice. *Surgical Infections*, 8(3), 405–414. <https://doi.org/10.1089/sur.2005.061>
187. Sanders, D. L., & Kingsnorth, A. N. (2012). Prosthetic mesh materials used in hernia surgery. *Expert Review of Medical Devices*, 9(2), 159–179. <https://doi.org/10.1586/erd.11.65>
188. Hindman, N. M., Kang, S., & Parikh, M. S. (2014). Common postoperative findings unique to laparoscopic surgery. *Radiographics*, 34(1), 119–138. <https://doi.org/10.1148/rg.341125181>
189. Lasses Martínez, B., Peña Soria, M. J., Cabeza Gómez, J. J., Jiménez Valladolid, D., Flores Gamarra, M., Fernández Pérez, C., Torres-Garcia, A., & Delgado Lillo, I. (2017). Surgical treatment of large incisional hernias with intraperitoneal composite mesh: a cohort study. *Hernia*, 21(2), 253–260. <https://doi.org/10.1007/s10029-016-1557-8>
190. Minor, S., Brown, C. J., Rooney, P. S., Hodde, J. P., Julien, L., Scott, T. M., Karimuddin, A. A., Raval, M. J., & Phang, P. T. (2020). Single-stage repair of contaminated hernias using a novel antibiotic-impregnated biologic porcine submucosa tissue matrix. *BMC Surgery*, 20(1), 1–7. <https://doi.org/10.1186/s12893-020-00715-w>
191. Grafmiller, K. T., Zuckerman, S. T., Petro, C., Liu, L., von Recum, H. A., Rosen, M. J., & Korley, J. N. (2017). Antibiotic-releasing microspheres prevent mesh infection in vivo. *Journal of Surgical Research*, 206(1), 41–47. <https://doi.org/10.1016/j.jss.2016.06.099>
192. Guillaume, O., Teuschl, A. H., Gruber-Blum, S., Fortelny, R. H., Redl, H., & Petter-Puchner, A. (2015). Emerging trends in abdominal wall reinforcement: Bringing bio-functionality to meshes. *Advanced Healthcare Materials*, 4(12), 1763–1789. <https://doi.org/10.1002/adhm.201500201>
193. Shtreimer Kandiyote, N., Avidris, T., Arnusch, C. J., & Kasher, R. (2019). Grafted polymer coatings enhance fouling inhibition by an antimicrobial peptide on reverse osmosis membranes. *Langmuir*, 35(5), 1935–1943. <https://doi.org/10.1021/acs.langmuir.8b03851>
194. Ahmed, W., Zhai, Z., & Gao, C. (2019). Adaptive antibacterial biomaterial surfaces and their applications. *Materials Today Bio*, 2(3), 1–17. <https://doi.org/10.1016/j.mtbio.2019.100017>
195. Engelsman, A. F., Krom, B. P., Busscher, H. J., van Dam, G. M., Ploeg, R. J., & van der Mei, H. C. (2009). Antimicrobial effects of an NO-releasing poly(ethylene vinylacetate) coating on soft-tissue implants in vitro and in a murine model. *Acta Biomaterialia*, 5(6), 1905–1910. <https://doi.org/10.1016/j.actbio.2009.01.041>
196. Lourenço, B. N., Marchioli, G., Song, W., Reis, R. L., van Blitterswijk, C. A., Karperien, M., Apeldoorn, A. V., & Mano, J. F. (2012). Wettability influences cell behavior on superhydrophobic surfaces with different topographies. *Biointerphases*, 7(1–4), 1–11. <https://doi.org/10.1007/s13758-012-0046-6>
197. Cyphert, E. L., & von Recum, H. A. (2017). Emerging technologies for long-term antimicrobial device coatings: advantages and limitations. *Experimental Biology and Medicine*, 242(8), 788–798. <https://doi.org/10.1177/1535370216688572>
198. Nergiz Adiguzel, E., Esen, E., Aylaz, G., Keskinilic Yagiz, B., Kiyani, M., Dogan, A., & Unal, A. E. (2018). Do nano-crystalline silver-coated hernia grafts reduce infection? *World Journal of Surgery*, 42(11), 3537–3542. <https://doi.org/10.1007/s00268-018-4661-3>
199. Liu, P., Chen, N., Jiang, J., & Wen, X. (2019). New surgical meshes with patterned nanofiber mats. *RSC Advances*, 9(31), 17679–17690. <https://doi.org/10.1039/c9ra01917k>
200. Hympanova, L., Mori da Cunha, M. G. M. C., Rynkevic, R., Wach, R. A., Olejnik, A. K., Dankers, P. Y. W., Arts, B., Mes, T., Bosman, A. W., Albersen, M., & Deprest, J. (2018). Experimental reconstruction of an abdominal wall defect with electrospun polycaprolactone-ureidopyrimidinone mesh conserves compliance yet may have insufficient strength. *Journal of the Mechanical Behavior of Biomedical Materials*, 88(1), 431–441. <https://doi.org/10.1016/j.jmbbm.2018.08.026>
201. Böhm, G., Groll, J., Heffels, K.-H., Heussen, N., Ink, P., Alizai, H. P., Neumann, U. P., Schnabel, R., & Mirastschijski, U. (2018). Influence of MMP inhibitor GM6001 loading of fibre

- coated polypropylene meshes on wound healing: Implications for hernia repair. *Journal of Biomaterials Applications*, 32(10), 1343–1359. <https://doi.org/10.1177/0885328218759043>
202. Li, S., Xiao, H., Yang, L., Hua, L., Qiu, Z., Hu, X., Ping, D., Zheng, K., He, H., & Tang, J. (2019). Electrospun P(LLA-CL) nanoscale fibrinogen patch vs porcine small intestine submucosa graft repair of inguinal hernia in adults: A randomized, single-blind, controlled, multicenter, noninferiority trial. *Journal of the American College of Surgeons*, 229, 541–551. <https://doi.org/10.1016/j.jamcollsurg.2019.08.1446>
203. Mori da Cunha, M. G. M. C., Arts, B., Hympanova, L., Rynkevic, R., Mackova, K., Bosman, A. W., Dankers, P. Y. W., & Deprest, J. (2020). Functional supramolecular bioactivated electrospun mesh improves tissue ingrowth in experimental abdominal wall reconstruction in rats. *Acta Biomaterialia*, 106(4), 82–91. <https://doi.org/10.1016/j.actbio.2020.01.041>
204. Hall Barrientos, I. J., Paladino, E., Brozio, S., Passarelli, M. K., Moug, S., Black, R. A., Wilson, C. G., & Lamprou, D. A. (2017). Fabrication and characterisation of drug-loaded electrospun polymeric nanofibers for controlled release in hernia repair. *International Journal of Pharmaceutics*, 517(2), 329–337. <https://doi.org/10.1016/j.ijpharm.2016.12.022>
205. Liu, P., Chen, N., Jiang, J., & Wen, X. (2019). Preparation and in vitro evaluation of new composite mesh functionalized with cationic antimicrobial peptide. *Materials*, 12(10), 1–12. <https://doi.org/10.3390/MA12101676>
206. Gundloori, R. V., Singam, A., & Killi, N. (2019). Nanobased intravenous and transdermal drug delivery systems. In S. S. Mohapatra, S. Ranjan, N. Dasgupta, R. K. Mishra, & S. Thomas (Eds.), *Applications of Targeted Nano Drugs and Delivery Systems* (1st ed., pp. 551–594). Florida, USA: Elsevier. <https://doi.org/10.1016/b978-0-12-814029-1.00019-3>
207. Greiner, A., & Wendorff, J. H. (2017). Electrospinning: A fascinating method for the preparation of ultrathin fibers. *Angewandte Chemie - International Edition*, 46(30), 5670–5703. <https://doi.org/10.1002/anie.200604646>
208. Long, Y. Z., Li, M. M., Gu, C., Wan, M., Duvail, J. L., Liu, Z., & Fan, Z. (2011). Recent advances in synthesis, physical properties and applications of conducting polymer nanotubes and nanofibers. *Progress in Polymer Science (Oxford)*, 36(10), 1415–1442. <https://doi.org/10.1016/j.progpolymsci.2011.04.001>
209. Garg, K., & Bowlin, G. L. (2011). Electrospinning jets and nanofibrous structures. *Biomicrofluidics*, 5(1), 1–11. <https://doi.org/10.1063/1.3567097>
210. Formhals Anton. (1930, December 5). Process and apparatus for preparing artificial threads (US patent no. US1975504A).
211. Doshi, J., & Reneker, D. H. (1995). Electrospinning process and applications of electrospun fibers. *Journal of Electrostatics*, 35(2–3), 151–160. [https://doi.org/10.1016/0304-3886\(95\)00041-8](https://doi.org/10.1016/0304-3886(95)00041-8)
212. Guarino, V., & Ambrosio, L. (2018). Electrofluidodynamic technologies (EFDTs) for biomaterials and medical devices: principles and advances. In V. Guarino & A. Luigi (Eds.), *Medical devices and Biomaterials* (1st ed., pp. 230–255). Naples, Italy: Woodhead Publishing. <https://doi.org/978-0-08-101745-6>
213. Mitchell, G. R., Mohan, S. D., Davis, F. J., Ahn, K., Al-Azab, M., El Hadi, A., Elliott, D., Kariduraganavar, M. Y., Nagarajan, A., & Nazhipkyzy, M. (2015). Structure development in electrospun fibres. In Geoffrey R Mitchell (Ed.), *Electrospinning: Principles, Practice and Possibilities* (1st ed., pp. 136–171). Warsaw, Poland: RSC Publishing. <https://doi.org/10.1039/9781849735575-00136>
214. Sapountzi, E., Braiek, M., Chateaux, J. F., Jaffrezic-Renault, N., & Lagarde, F. (2017). Recent advances in electrospun nanofiber interfaces for biosensing devices. *Sensors*, 17(8), 1–13. <https://doi.org/10.3390/s17081887>
215. Huang, C., Soenen, S. J., Rejman, J., Lucas, B., Braeckmans, K., Demeester, J., & Smedt, S. C. De. (2011). Stimuli-responsive electrospun fibers and their applications. *Chemical Society*



- Reviews*, 40(5), 2417–2434. <https://doi.org/10.1039/c0cs00181c>
216. Yarin, A. L., Pourdeyhimi, B., & Ramakrishna, S. (2014). Electrospinning micro- and nanofibers. In A. L. Yarin (Ed.), *Fundamentals and applications of micro and nanofibers* (1st ed., pp. 179–261). Chicago, USA: Cambridge University Press.
217. Han, T., Reneker, D. H., & Yarin, A. L. (2007). Buckling of jets in electrospinning. *Polymer*, 48(20), 6064–6076. <https://doi.org/10.1016/j.polymer.2007.08.002>
218. Khalil, A., Singh Lalia, B., Hashaikh, R., & Khraisheh, M. (2013, November 7). Electrospun metallic nanowires: Synthesis, characterization, and applications. *Journal of Applied Physics*. American Institute of Physics. <https://doi.org/10.1063/1.4822482>
219. Aldossari, A. A., Shannahan, J. H., Podila, R., & Brown, J. M. (2015). Influence of physicochemical properties of silver nanoparticles on mast cell activation and degranulation. *Toxicology in Vitro*, 29(1), 195–203. <https://doi.org/10.1016/j.tiv.2014.10.008>
220. Asmatulu, R., & Khan, W. S. (2019). Historical background of the electrospinning process. In R. Asmatulu (Ed.), *Synthesis and Applications of Electrospun Nanofibers* (2nd ed., pp. 17–39). Elsevier. <https://doi.org/10.1016/b978-0-12-813914-1.00002-x>
221. Naeimirad, M., Zadhoush, A., Kotek, R., Esmaeely Neisiany, R., Nouri Khorasani, S., & Ramakrishna, S. (2018). Recent advances in core/shell bicomponent fibers and nanofibers: A review. *Journal of Applied Polymer Science*, 135(21), 1–12. <https://doi.org/10.1002/app.46265>
222. Li, D., & Xia, Y. (2014). Direct fabrication of composite and ceramic hollow nanofibers by electrospinning. *Nano Letters*, 4(5), 933–938. <https://doi.org/10.1021/nl049590f>
223. Zhao, Y., Cao, X., & Jiang, L. (2007). Bio-mimic multichannel microtubes by a facile method. *Journal of the American Chemical Society*, 129(4), 764–765. <https://doi.org/10.1021/ja068165g>
224. Yuan, W., & Zhang, K. Q. (2012). Structural evolution of electrospun composite fibers from the blend of polyvinyl alcohol and polymer nanoparticles. *Langmuir*, 28(43), 15418–15424. <https://doi.org/10.1021/la303312q>
225. Chen, X., Wang, W., Cheng, S., Dong, B., & Li, C. Y. (2013). Mimicking bone nanostructure by combining block copolymer self-assembly and 1D crystal nucleation. *ACS Nano*, 7(9), 8251–8257. <https://doi.org/10.1021/nn403742f>
226. Yu, J., Qiu, Y., Zha, X., Yu, M., Yu, J., Rafique, J., & Yin, J. (2008). Production of aligned helical polymer nanofibers by electrospinning. *European Polymer Journal*, 44(9), 2838–2844. <https://doi.org/10.1016/j.eurpolymj.2008.05.020>
227. Cleeton, C., Keirouz, A., Chen, X., & Radacsi, N. (2019). Electrospun nanofibers for drug delivery and biosensing. *ACS Biomaterials Science & Engineering*, 5(9), 4183–4205. <https://doi.org/10.1021/acsbiomaterials.9b00853>
228. Chung, M., Fortunato, G., & Radacsi, N. (2019). Wearable flexible sweat sensors for healthcare monitoring: a review. *Journal of The Royal Society Interface*, 16(159), 1–15. <https://doi.org/10.1098/rsif.2019.0217>
229. Radacsi, N., Campos, F. D., Chisholm, C. R. I., & Giapis, K. P. (2018). Spontaneous formation of nanoparticles on electrospun nanofibers. *Nature Communications*, 9(1), 1–8. <https://doi.org/10.1038/s41467-018-07243-5>
230. Vijay Kumar, V., Ramakrishna, S., Kong Yoong, J. L., Esmaeely Neisiany, R., Surendran, S., & Balaganesan, G. (2019). Electrospun nanofiber interleaving in fiber reinforced composites — Recent trends. *Material Design & Processing Communications*, 1(1), 8–24. <https://doi.org/10.1002/mdp2.24>
231. Kong, T., Stone, H. A., Wang, L., & Shum, H. C. (2018). Dynamic regimes of electrified liquid filaments. *Proceedings of the National Academy of Sciences of the United States of America*, 115(24), 6159–6164. <https://doi.org/10.1073/pnas.1801053115>
232. Yarin, A. L., Koombhongse, S., & Reneker, D. H. (2001). Taylor cone and jetting from liquid

- droplets in electrospinning of nanofibers. *Journal of Applied Physics*, 90(9), 4836–4846. <https://doi.org/10.1063/1.1408260>
233. Taylor, G. I. (1969). Electrically driven jets. *Proceedings of the Royal Society of London. A. Mathematical and Physical Sciences*, 313(1515), 453–475. <https://doi.org/10.1098/rspa.1969.0205>
234. Yuan, H., Zhou, Q., & Zhang, Y. (2017). Improving fiber alignment during electrospinning. In M. Afshari (Ed.), *Electrospun Nanofibers* (1st ed., pp. 125–147). North Carolina, USA: Woodhead Publishing. <https://doi.org/10.1016/B978-0-08-100907-9.00006-4>
235. Montinaro, M., Fasano, V., Moffa, M., Camposeo, A., Persano, L., Lauricella, M., Succi, S., & Pisignano, D. (2015). Sub-ms dynamics of the instability onset of electrospinning. *Soft Matter*, 17(11), 3424–3431. <https://doi.org/10.1039/C4SM02708F>
236. He, J. H., Wu, Y., & Zuo, W. W. (2005). Critical length of straight jet in electrospinning. *Polymer*, 46(26), 12637–12640. <https://doi.org/10.1016/j.polymer.2005.10.130>
237. Reneker, D. H., & Yarin, A. L. (2008). Electrospinning jets and polymer nanofibers. *Polymer*, 49(10), 2387–2425. <https://doi.org/10.1016/j.polymer.2008.02.002>
238. Reneker, D. H., Yarin, A. L., Fong, H., & Koombhongse, S. (2000). Bending instability of electrically charged liquid jets of polymer solutions in electrospinning. *Journal of Applied Physics*, 87(9), 4531–4547. <https://doi.org/10.1063/1.373532>
239. Shin, Y. M., Hohman, M. M., Brenner, M. P., & Rutledge, G. C. (2001). Electrospinning: A whipping fluid jet generates submicron polymer fibers. *Applied Physics Letters*, 78(8), 1149–1151. <https://doi.org/10.1063/1.1345798>
240. Hohman, M. M., Shin, M., Rutledge, G., & Brenner, M. P. (2001). electrospinning and electrically forced jets: Stability theory. *Physics of Fluids*, 13(8), 2201–2220. <https://doi.org/10.1063/1.1383791>
241. Carroll, C. P., & Joo, Y. L. (2009). Axisymmetric instabilities in electrospinning of highly conducting, viscoelastic polymer solutions. *Physics of Fluids*, 21(10), 103101. <https://doi.org/10.1063/1.3246024>
242. Luo, C. J., Stoyanov, S. D., Stride, E., Pelan, E., & Edirisinghe, M. (2012). Electrospinning versus fibre production methods: From specifics to technological convergence. *Chemical Society Reviews*, 41(13), 4708–4735. <https://doi.org/10.1039/c2cs35083a>
243. Yarin, A. L., Kataphinan, W., & Reneker, D. H. (2005). Branching in electrospinning of nanofibers. *Journal of Applied Physics*, 98(6), 1–12. <https://doi.org/10.1063/1.2060928>
244. Yarin, A. L., Koombhongse, S., & Reneker, D. H. (2001). Bending instability in electrospinning of nanofibers. *Journal of Applied Physics*, 89(5), 3018–3026. <https://doi.org/10.1063/1.1333035>
245. Sun, B., Long, Y. Z., Zhang, H. D., Li, M. M., Duvail, J. L., Jiang, X. Y., & Yin, H. L. (2014). Advances in three-dimensional nanofibrous macrostructures via electrospinning. *Progress in Polymer Science*, 39(5), 862–890. <https://doi.org/10.1016/j.progpolymsci.2013.06.002>
246. Rudin, A., & Choi, P. (2013). Practical aspects of molecular weight measurements. In A. Rudin & U. of Alberta (Eds.), *The Elements of Polymer Science & Engineering* (3rd ed., pp. 89–148). Alberta, Canada: Elsevier. <https://doi.org/10.1016/b978-0-12-382178-2.00003-1>
247. Salas, C. (2017). Solution electrospinning of nanofibers. In Mehdi Afshari (Ed.), *Electrospun Nanofibers* (1st ed., pp. 73–108). North Carolina, USA: Woodhead Publishing. <https://doi.org/10.1016/B978-0-08-100907-9.00004-0>
248. Han, D., & Steckl, A. J. (2019). Coaxial electrospinning formation of complex polymer fibers and their applications. *ChemPlusChem*, 84(1), 1453–1497. <https://doi.org/10.1002/cplu.201900281>
249. Elahi, F., & Lu, W. (2013). Core-shell fibers for biomedical applications: A review. *Journal of*

- Bioengineering & Biomedical Science*, 3(1), 1–14. <https://doi.org/10.4172/2155-9538.1000121>
250. Liu, W., Ni, C., Chase, D. B., & Rabolt, J. F. (2013). Preparation of multilayer biodegradable nanofibers by triaxial electrospinning. *ACS Macro Letters*, 2(6), 466–468. <https://doi.org/10.1021/mz4000688>
251. Khalf, A., & Madihally, S. V. (2017). Recent advances in multiaxial electrospinning for drug delivery. *European Journal of Pharmaceutics and Biopharmaceutics*, 112(1), 1–17. <https://doi.org/10.1016/j.ejpb.2016.11.010>
252. Sun, Z., Zussman, E., Yarin, A. L., Wendorff, J. H., & Greiner, A. (2003). Compound core-shell polymer nanofibers by co-electrospinning. *Advanced Materials*, 15(22), 1929–1932. <https://doi.org/10.1002/adma.200305136>
253. Wang, C., Yan, K. W., Lin, Y. D., & Hsieh, P. C. H. (2010). Biodegradable core/shell fibers by coaxial electrospinning: Processing, fiber characterization, and its application in sustained drug release. *Macromolecules*, 43(15), 6389–6397. <https://doi.org/10.1021/ma100423x>
254. Rahmani, S., Arefazar, A., & Latifi, M. (2017). PMMA / PS coaxial electrospinning: core – shell fiber morphology as a function of material parameters. *Materials Research Express*, 4(3), 35–43. <https://doi.org/10.1088/2053-1591/aa600c>
255. Díaz, J. E., Barrero, A., Márquez, M., & Loscertales, I. G. (2006). Controlled encapsulation of hydrophobic liquids in hydrophilic polymer nanofibers by co-electrospinning. *Advanced Functional Materials*, 16(16), 2110–2116. <https://doi.org/10.1002/adfm.200600204>
256. Han, D., Boyce, S. T., & Steckl, A. J. (2008). Versatile core-sheath biofibers using coaxial electrospinning. *Materials Research Society Symposium Proceedings*, 1094, 33–38. <https://doi.org/10.1557/proc-1094-dd06-02>
257. Yu, D. G., Li, X. Y., Wang, X., Yang, J. H., Bligh, S. W. A., & Williams, G. R. (2015). Nanofibers fabricated using triaxial electrospinning as zero order drug delivery systems. *ACS Applied Materials and Interfaces*, 7(33), 18891–18897. <https://doi.org/10.1021/acsami.5b06007>
258. Basal, G., Tetik, G. D., Kurkcu, G., Bayraktar, O., Gurhan, I. D., & Atabey, A. (2016). Olive leaf extract loaded silk fibroin/hyaluronic acid nanofiber webs for wound dressing applications. *Digest Journal of Nanomaterials and Biostructures*, 11(4), 1113–1123. <https://doi.org/10.18423582>
259. Qin, X. (2017). Coaxial electrospinning of nanofibers. In M. Afshari (Ed.), *Electrospun Nanofibers* (1st ed., pp. 41–71). North Carolina, USA: Woodhead Publishing. <https://doi.org/10.1016/B978-0-08-100907-9.00003-9>
260. Gao, W., Sun, L., Fu, X., Lin, Z., Xie, W., Zhang, W., & Chen, X. (2018). Enhanced diabetic wound healing by electrospun core–sheath fibers loaded with dimethylxylalylglycine. *Journal of Materials Chemistry B*, 6(2), 277–288. <https://doi.org/10.1039/C7TB02342A>
261. Jiang, G., Zhang, S., Wang, Y., & Qin, X. (2015). An improved free surface electrospinning with micro-bubble solution system for massive production of nanofibers. *Materials Letters*, 144, 22–25. <https://doi.org/10.1016/j.matlet.2014.12.139>
262. Williams, G. R., Raimi-Abraham, B. T., & Luo, C. J. (2018). *Moving from the bench to the clinic*. (G. R. Williams, Ed.) *Nanofibres in Drug Delivery*. London, UK: UCL Press. <https://doi.org/10.2307/j.ctv550dd1>
263. Yarin, A. L., & Zussman, E. (2004). Upward needleless electrospinning of multiple nanofibers. *Polymer*, 45(9), 2977–2980. <https://doi.org/10.1016/j.polymer.2004.02.066>
264. Oldrich, J., Filip, S., David, L., Kotek, L., & MartinovaJiri, C. (2005, September 8). Method of nanofibres production from a polymer solution using electrostatic spinning and a device for carrying out the method (US patent no. US7585437B2).
265. Lin, D., & Wang, X. (2014). Needleless electrospinning of nanofibers: technology and applications. In X. Wang & T. Lin (Eds.), *Needleless Electrospinning* (1st ed., pp. 30–48).

- Shanghai, China: Jenny Stanford Publishing. <https://doi.org/10.3390/pr8060673>
266. Yener, F., & Jirsak, O. (2012). Comparison between the needle and roller electrospinning of polyvinylbutyral. *Journal of Nanomaterials*, *12*(4), 1–6. <https://doi.org/10.1155/2012/839317>
267. Itoh, H., Li, Y., Chan, K. H. K., & Kotaki, M. (2016). Morphology and mechanical properties of PVA nanofibers spun by free surface electrospinning. *Polymer Bulletin*, *73*(10), 2761–2777. <https://doi.org/10.1007/s00289-016-1620-8>
268. Jiang, G., Zhang, S., & Qin, X. (2016). Effect of processing parameters on free surface electrospinning from a stepped pyramid stage. *Journal of Industrial Textiles*, *45*(4), 483–494. <https://doi.org/10.1177/1528083714537101>
269. Bhattacharyya, I., Molaro, M. C., Braatz, R. D., & Rutledge, G. C. (2016). Free-surface electrospinning of aqueous polymer solutions from a wire electrode. *Chemical Engineering Journal*, *289*, 203–211. <https://doi.org/10.1016/j.cej.2015.12.067>
270. Nurwaha, D., & Wang, X. (2015). Free surface electrospinning: investigation of the combined effects of process parameters on the morphology of electrospun fibers. *Fibers and Polymers*, *16*(4), 850–866. <https://doi.org/10.1007/s12221-015-0850-y>
271. Shao, Z., Yu, L., Xu, L., & Wang, M. (2017). High-throughput fabrication of quality nanofibers using a modified free surface electrospinning. *Nanoscale Research Letters*, *12*(1), 1–9. <https://doi.org/10.1186/s11671-017-2240-4>
272. Agrawal, P., & Pramanik, K. (2016). Chitosan-poly(vinyl alcohol) nanofibers by free surface electrospinning for tissue engineering applications. *Tissue Engineering and Regenerative Medicine*, *13*(5), 485–497. <https://doi.org/10.1007/s13770-016-9092-3>
273. El-Newehy, M. H., Al-Deyab, S. S., Kenawy, E. R., & Abdel-Megeed, A. (2012). Fabrication of electrospun antimicrobial nanofibers containing metronidazole using nanospider technology. *Fibers and Polymers*, *13*(6), 709–717. <https://doi.org/10.1007/s12221-012-0709-4>
274. Brettmann, B. K., Tsang, S., Forward, K. M., Rutledge, G. C., Myerson, A. S., & Trout, B. L. (2012). Free-surface electrospinning of fibers containing microparticles. *Langmuir*, *28*(25), 9714–9721. <https://doi.org/10.1021/la301422x>
275. Molnár, K., Nagy, K., Marosi, G., & Mészáros, L. (2012). Electrospinning spinneret and modified electrospinning method for producing nanofibers in productive ways (Hungarian patent no. P1200677).
276. Ige, O. O., Umoru, L. E., & Aribo, S. (2012). Natural products: A minefield of biomaterials. *ISRN Materials Science*, *12*(1), 1–20. <https://doi.org/10.5402/2012/983062>
277. Mano, J. F., Silva, G. A., Azevedo, H. S., Malafaya, P. B., Sousa, R. A., Silva, S. S., Boesel, L. F., Oliveira, J. M., Santos, T. C., Maques, A. P., Neves, N. M., & Reis, R. L. (2007). Natural origin biodegradable systems in tissue engineering and regenerative medicine: Present status and some moving trends. *Journal of the Royal Society Interface*, *4*(17), 999–1030. <https://doi.org/10.1098/rsif.2007.0220>
278. Asti, A., & Gioglio, L. (2014). Natural and synthetic biodegradable polymers: Different scaffolds for cell expansion and tissue formation. *International Journal of Artificial Organs*, *37*(3), 187–205. <https://doi.org/10.530/ijao.5000307>
279. Bhattarai, D. P., Aguilar, L. E., Park, C. H., & Kim, C. S. (2018). A review on properties of natural and synthetic based electrospun fibrous materials for bone tissue engineering. *Membranes*, *8*(3), 1–12. <https://doi.org/10.3390/membranes8030062>
280. Yildirim, L., Thanh, N. T. K., & Seifalian, A. M. (2012). Skin regeneration scaffolds: A multimodal bottom-up approach. *Trends in Biotechnology*, *30*(12), 638–648. <https://doi.org/10.1016/j.tibtech.2012.08.004>
281. Tiwari, S. K., & Venkatraman, S. S. (2012). Importance of viscosity parameters in electrospinning: Of monolithic and core-shell fibers. *Materials Science and Engineering C*, *32*(5), 1037–1042. <https://doi.org/10.1016/j.msec.2012.02.019>

282. Wang, Y., Ameer, G. A., Sheppard, B. J., & Langer, R. (2002). A tough biodegradable elastomer. *Nature Biotechnology*, 20(6), 602–606. <https://doi.org/10.1038/nbt0602-602>
283. Tham, W. H., Wahit, M. U., Abdul Kadir, M. R., Wong, T. W., & Hassan, O. (2016). Polyol-based biodegradable polyesters: A short review. *Reviews in Chemical Engineering*, 32(2), 201–221. <https://doi.org/10.1515/revce-2015-0035>
284. Wang, Y., Kim, Y. M., & Langer, R. (2003). In vivo degradation characteristics of poly(glycerol sebacate). *Journal of Biomedical Materials Research*, 66(1), 192–197. <https://doi.org/10.1002/jbm.a.10534>
285. Jaafar, I. H., Ammar, M. M., Jedlicka, S. S., Pearson, R. A., & Coulter, J. P. (2010). Spectroscopic evaluation, thermal, and thermomechanical characterization of poly(glycerol-sebacate) with variations in curing temperatures and durations. *Journal of Materials Science*, 45(9), 2525–2529. <https://doi.org/10.1007/s10853-010-4259-0>
286. Mondal, D., Griffith, M., & Venkatraman, S. S. (2016). Polycaprolactone-based biomaterials for tissue engineering and drug delivery: Current scenario and challenges. *International Journal of Polymeric Materials and Polymeric Biomaterials*, 65(5), 255–265. <https://doi.org/10.1080/00914037.2015.1103241>
287. Sharif, S., Ai, J., Azami, M., Verdi, J., Atlasi, M. A., Shirian, S., & Samadikuchaksaraei, A. (2018). Collagen-coated nano-electrospun PCL seeded with human endometrial stem cells for skin tissue engineering applications. *Journal of Biomedical Materials Research Part B: Applied Biomaterials*, 106(4), 1578–1586. <https://doi.org/10.1002/jbm.b.33966>
288. Fogaça, R., & Catalani, L. H. (2013). PVP hydrogel membranes produced by electrospinning for protein release devices. *Soft Materials*, 11(1), 61–68. <https://doi.org/10.1080/1539445X.2011.580411>
289. Ageyeva, T., Sibikin, I., & Karger-Kocsis, J. (2018). Polymers and related composites via anionic ring-opening polymerization of lactams: recent developments and future trends. *Polymers*, 10(4), 1–29. <https://doi.org/10.3390/polym10040357>
290. Stephens, J. S., Chase, D. B., & Rabolt, J. F. (2004). Effect of the electrospinning process on polymer crystallization chain conformation in nylon-6 and nylon-12. *Macromolecules*, 37(3), 877–881. <https://doi.org/10.1021/ma0351569>
291. Abdal-Hay, A., Oh, Y. S., Yousef, A., Pant, H. R., Vanegas, P., & Lim, J. K. (2014). In vitro deposition of Ca-P nanoparticles on air jet spinning Nylon 6 nanofibers scaffold for bone tissue engineering. *Applied Surface Science*, 307(1), 69–76. <https://doi.org/10.1016/j.apsusc.2014.03.161>
292. Li, Z. H., Ji, S. C., Wang, Y. Z., Shen, X. C., & Liang, H. (2013). Silk fibroin-based scaffolds for tissue engineering. *Frontiers of Materials Science*, 7(3), 237–247. <https://doi.org/10.1007/s11706-013-0214-8>
293. Chen, F., Porter, D., & Vollrath, F. (2012). Structure and physical properties of silkworm cocoons. *Journal of the Royal Society Interface*, 9(74), 2299–2308. <https://doi.org/10.1098/rsif.2011.0887>
294. Qi, Y., Wang, H., Wei, K., Yang, Y., Zheng, R. Y., Kim, I. S., & Zhang, K. Q. (2017). A review of structure construction of silk fibroin biomaterials from single structures to multi-level structures. *International Journal of Molecular Sciences*, 18(3), 1–21. <https://doi.org/10.3390/ijms18030237>
295. Zhou, C. Z., Confalonieri, F., Jacquet, M., Perasso, R., Li, Z. G., & Janin, J. (2001). Silk fibroin: Structural implications of a remarkable amino acid sequence. *Proteins: Structure, Function and Genetics*, 44(2), 119–122. <https://doi.org/10.1002/prot.1078>
296. Tian, D., Li, T., Zhang, R., Wu, Q., Chen, T., Sun, P., & Ramamoorthy, A. (2017). Conformations and intermolecular interactions in cellulose/silk fibroin blend films: A solid-state NMR perspective. *Journal of Physical Chemistry B*, 121(25), 6108–6116. <https://doi.org/10.1021/acs.jpcc.7b02838>

297. Zhang, W., Chen, L., Chen, J., Wang, L., Gui, X., Ran, J., Xu, G., Zhao, H., Zeng, M., Ji, J., Qian, L., Zhou, J., Ouyang, H., & Zou, X. (2017). Silk fibroin biomaterial shows safe and effective wound healing in animal models and a randomized controlled clinical trial. *Advanced Healthcare Materials*, 6(10), 1–16. <https://doi.org/10.1002/adhm.201700121>
298. Goy, R. C., Morais, S. T. B., & Assis, O. B. G. (2016). Evaluation of the antimicrobial activity of chitosan and its quaternized derivative on *E. Coli* and *S. aureus* growth. *Brazilian Journal of Pharmacognosy*, 26(1), 122–127. <https://doi.org/10.1016/j.bjp.2015.09.010>
299. Cheung, R. C. F., Ng, T. B., Wong, J. H., & Chan, W. Y. (2015). Chitosan: An update on potential biomedical and pharmaceutical applications. *Marine Drugs*, 13(8), 5156–5186. <https://doi.org/10.3390/md13085156>
300. Arkoun, M., Daigle, F., Heuzey, M. C., & Aji, A. (2017). Mechanism of action of electrospun chitosan-based nanofibers against meat spoilage and pathogenic bacteria. *Molecules*, 22(4), 1–17. <https://doi.org/10.3390/molecules22040585>
301. Croisier, F., & Jérôme, C. (2013). Chitosan-based biomaterials for tissue engineering. *European Polymer Journal*, 49(4), 780–792. <https://doi.org/10.1016/j.eurpolymj.2012.12.009>
302. Dutta, P. K. (2016). Prospects of bioactive chitosan-based scaffolds in tissue engineering and regenerative medicine. In P. K. Dutta (Ed.), *Chitin and Chitosan for Regenerative Medicine* (1st ed., pp. 16–48). New Delhi, India: Springer. <https://doi.org/10.1007/978-81-322-2511-9>
303. Aranaz, I., Mengibar, M., Harris, R., Panos, I., Miralles, B., Acosta, N., Galed, G., & Heras, A. (2009). Functional characterization of chitin and chitosan. *Current Chemical Biology*, 3(2), 203–230. <https://doi.org/10.2174/2212796810903020203>
304. Wang, X., Du, Y., Fan, L., Liu, H., & Hu, Y. (2005). Chitosan- metal complexes as antimicrobial agent: Synthesis, characterization and Structure-activity study. *Polymer Bulletin*, 55(1–2), 105–113. <https://doi.org/10.1007/s00289-005-0414-1>
305. Luo, G., Li, B., Li, L. G., Zhang, T., & Angelidaki, I. (2017). Antibiotic resistance genes and correlations with microbial community and metal resistance genes in full-scale biogas reactors as revealed by metagenomic analysis. *Environmental Science and Technology*, 51(7), 4069–4080. <https://doi.org/10.1021/acs.est.6b05100>
306. Peterson, E., & Kaur, P. (2018). Antibiotic resistance mechanisms in bacteria: Relationships between resistance determinants of antibiotic producers, environmental bacteria, and clinical pathogens. *Frontiers in Microbiology*, 9(11), 1–8. <https://doi.org/10.3389/fmicb.2018.02928>
307. Haider, A., Haider, S., & Kang, I. K. (2018). A comprehensive review summarizing the effect of electrospinning parameters and potential applications of nanofibers in biomedical and biotechnology. *Arabian Journal of Chemistry*, 11(8), 1165–1188. <https://doi.org/10.1016/j.arabjc.2015.11.015>
308. Zhang, S., Jia, Z., Liu, T., Wei, G., & Su, Z. (2019). Electrospinning nanoparticles-based materials interfaces for sensor applications. *Sensors*, 19(29), 1–13. <https://doi.org/10.3390/s19183977>
309. Swamy, M. K., Akhtar, M. S., & Sinniah, U. R. (2016). Antimicrobial properties of plant essential oils against human pathogens and their mode of action: An updated review. *Evidence-based Complementary and Alternative Medicine : eCAM*, 5(1), 105–126. <https://doi.org/10.1155/2016/3012462>
310. Asiedu-Gyekye, I. J., Mahmood, A. S., Awortwe, C., & Nyarko, A. K. (2015). Toxicological assessment of polyhexamethylene biguanide for water treatment. *Interdisciplinary Toxicology*, 8(4), 193–202. <https://doi.org/10.1515/intox-2015-0029>
311. Fjeld, H., & Lingaas, E. (2016). Polyhexanide - Safety and efficacy as an antiseptic. *Journal of the Norwegian Medical Association*, 136(8), 707–711. <https://doi.org/10.4045/tidsskr.14.1041>
312. Chindera, K., Mahato, M., Kumar Sharma, A., Horsley, H., Kloc-Muniak, K., Kamaruzzaman, N. F., Kumar, S., McFarlane, A., Stach, J., Bentin, T. & Good, L. (2016). The antimicrobial polymer PHMB enters cells and selectively condenses bacterial chromosomes. *Scientific*

- Reports*, 6(1), 1–13. <https://doi.org/10.1038/srep23121>
313. Kaehn, K. (2010). Polyhexanide: A safe and highly effective biocide. *Skin Pharmacology and Physiology*, 23(1), 7–16. <https://doi.org/10.1159/000318237>
314. Committee on Consumer Safety, E. C. (2017). Final opinion on polyaminopropyl biguanide (PHMB) - Submission III. *European Scientific Committee on Consumer Safety (SCCS)*, 1581(16), 1–90. <https://doi.org/10.2875/144004>
315. Lachapelle, J. M. (2014). A comparison of the irritant and allergenic properties of antiseptics. *European Journal of Dermatology*, 24(1), 3–9. <https://doi.org/10.1684/ejd.2013.2198>
316. Finch, R. G., Greenwood, D., Whitley, R. J., & Norrby, S. R. (2010). Antibiotic and chemotherapy: anti-infective agents and their use in therapy. *Journal of Antimicrobial Chemotherapy*, 52(4), 740–751. <https://doi.org/10.1016/j.jmcm.2011.12.011>
317. Fabio, P. F., Fields, T. L., Lin, Y. i., Burden, E. J., Carvajal, S., Murdock, K. C., & Lang, S. A. (1978). Bisamidines of 2,6-diaminoanthraquinone as antiamebic agents. *Journal of Medicinal Chemistry*, 21(3), 273–276. <https://doi.org/10.1021/jm00201a007>
318. Hongmanee, P., Rukseree, K., Buabut, B., Somsri, B., Palittapongarnpim, P., Ibrahim, M., & Veziris, N. (2007). In vitro activities of cloxyquin (5-chloroquinolin-8-ol) against Mycobacterium tuberculosis. *Antimicrobial agents and chemotherapy*, 7(5), 1105–1106. <https://doi.org/10.1128/AAC.01310-06>
319. Darby, C. M., & Nathan, C. F. (2010). Killing of non-replicating Mycobacterium tuberculosis by 8-hydroxyquinoline. *Journal of Antimicrobial Chemotherapy*, 65(7), 1424–1427. <https://doi.org/10.1093/jac/dkq145>
320. Rohde, W., Cordell, B., Webster, R., & Levinson, W. (1977). Inhibition of amino acyl tRNA synthetase activity by copper complexes of two metal binding ligands N-methyl isatin beta-thiosemicarbazone and 8-hydroxyquinoline. *Biochimica et Biophysica Acta (BBA) - Nucleic Acids and Protein Synthesis*, 2(477), 102–111. [https://doi.org/10.1016/0005-2787\(77\)90226-X](https://doi.org/10.1016/0005-2787(77)90226-X)
321. Fraser, R. S., & Creanor, J. (1975). The mechanism of inhibition of ribonucleic acid synthesis by 8-hydroxyquinoline and the antibiotic lomofungin. *The Biochemical journal*, 147(3), 401–410. <https://doi.org/10.1042/bj1470401>

---

# Chapter 3

## General Materials & Methods

---

### 3.1 Introduction

This chapter provides a general description of the materials, chemicals, reagents, experimental protocols, and characterisation techniques implemented in this thesis. Thereafter, project-specific methodologies will be provided in detail in the subsequent research chapters.

### 3.2 Scaffold fabrication by electrospinning

Electrospinning is the principal fabrication method used, in this thesis, for the development of the skin substitute constructs and antimicrobial hernia meshes, in the form of nonwoven fibrous biomaterials. For the high-throughput production of the skin-like substitute electrospun mats, a nozzle-free electrospinning device, consisting of two rotating mandrels positioned parallel and at a defined distance from each other – where the fibres were collected in an upward motion – was designed and built as described in *Section 4.2.1*. For the development of the drug-eluting antimicrobial nanofibrous membranes; considered for the prevention of mesh-associated surgical site infections, the co-axial electrospinning technique was employed as described in *Section 6.2.2*. Randomly oriented fibres were collected on a mandrel rotating at 500 rpm. A collector drum can be used at a low rotation speed to improve the efficiency at which fibres are collected. It has been shown that for a particular electrospinning solution, potential difference, and flying path, low rpm can be used to collect randomly oriented rather than aligned fibres [1].

Although the National Science Foundation deems fibrils of less than 100 nm as nanofibres (NFs), polymeric fibres in the submicron scale are considered as NFs in the literature [2], and thus throughout this thesis fibres are described based on their diameter as nano-scale ( $\leq 1 \mu\text{m}$ ) or micro-scale ( $> 1 \mu\text{m}$ ). Details on specific electrospinning, solution preparation, and post-processing procedures are provided at the corresponding methodology sections of the research *Chapters 4, 5, and 6*.



### 3.3 Materials

For each research work presented in the following chapters, polymers and solvents were chosen based on extended parametric studies, which examined the effect of a specific polymer/solvent system to the reproducibility, Taylor cone stability (optically inspected using a magnifying monocular), and fibre properties. Factors such as the polymer's concentration, its solubility and compatibility to a specific solvent system, viscosity, and conductivity measurements, had to be predetermined.

#### 3.3.1 Poly(glycerol sebacate) (PGS)

Poly(polyol sebacate) is a family of ester-bonded crosslinked elastomers. A polyol is an alcohol containing multiple hydroxyl groups; in the case of PGS, glycerol. Sebacic acid is a ten carbon-long dicarboxylic acid [3].

Pre-polymerisation and esterification are the two steps involved in the synthesis process. The pre-polymer is a result of the pre-polymerisation stage when the linear chain of the polymer is formed through an esterification reaction between glycerol and sebacic acid. The initiator of the reaction is the hydroxyl groups of the polyol [3]. The primary hydroxyl group of the glycerol grasps a carboxyl group to form a monoester with a free carboxyl group and water as a by-product. Subsequently, the monoester reacts with another primary group of glycerol to form another monoester, and it continues until all the available functional groups have been used. In the next stage, curing is required to evaporate glycerol and water residues, enabling the synthesised PGS to form a stiffer, crosslinked network. The fully cured form of the thermoset presents a three-dimensional (3D) network of the polyester chains via intra-hydrogen bonding [4].

The product of the first stage of this reaction – due to the esterification between the two monomers, results in the formation of linear chains of pre-polymer which are referred to as pre-PGS (pPGS) throughout this thesis. The hydroxyl groups ( $-OH$ ) of glycerol act as the initiator of the reaction by binding to the carboxyl group ( $R-COOH$ ) of the sebacic acid to form a monoester that presents a free carboxyl domain and water as a by-product. At the second step, the formed monoester reacts further with the remainder of the  $-OH$  groups of glycerol until all its functional groups have been replaced. At the end, water evaporation produces a stiff network of PGS chains.

Distinct physicochemical properties of the synthesised PGS polymer can be obtained by fluctuating the temperature, reaction time, and atmospheric pressure at the second stage of the synthesis scheme. Pre-polymerisation of PGS can produce pPGS of varying degree of esterification (DE) ranging from 0% to 100%. The DE can be used as a measure of the polymerisation degree and, more importantly, for predicting the unreacted alcohol groups after the pre-polymerisation process, which will depend upon the temperature and curing time [4].

$$\text{DE}(\%) = \frac{\text{Amount of water collected (mL)}}{\text{Theoretical amount of water (mL)}} \times 100 \quad (3.1)$$

The synthesis protocol followed to obtain the two different esterification degrees of the polymer referred to as PGS and pPGS are described in Table 3.1. Electrospinning neat PGS into homogenous fibres is an arduous process because its low molecular weight does not allow sufficient chain entanglement of the pre-polymer and the high viscosity of the cured polymer makes it insoluble in most organic solvents [3]. For this reason, in this work PGS and pPGS were electrospun in the presence of carrier polymers as explained in detail in *Chapter 5* (where PGS was incorporated with different molecular weights of PVP) and *Chapter 6* (where PGS and pPGS were incorporated with silk fibroin and PCL).

**Table 3.1** The synthesis protocol and some key aspects of the two PGS forms (pPGS and PGS) used for the development of the novel biomaterial systems in this thesis. PGS was synthesised based on the initially published polycondensation method [5] with modifications to obtain the pre-polymerised (pPGS) form.

pPGS	PGS
Low esterification degree.	High esterification degree.
No exogenous catalysts or solvents are required for the synthesis.	No exogenous catalysts or solvents are required for the synthesis.
The pre-polymer PGS (pPGS) was produced by thoroughly mixing equimolar (1:1 M) glycerol and sebacic acid at 120 °C under N <sub>2</sub> gas purged at a flow rate of approximately 120 cm <sup>3</sup> ·min <sup>-1</sup> , using a round bottom three-necked reactor at reduced pressure (1 Torr) for 24 h.	The cured form of the polyester, PGS, was then obtained by steadily reducing the pressure to 40 mTorr, at 120 °C for an additional 48 h, under a reduced atmosphere.
pPGS is a white elastomer with a wax-like texture.	Pure PGS is a viscous, yellowish, “sticky” elastomer.
PGS and pPGS 15% (w/v) were prepared by separately dissolving them in HFIP, while still in the viscous liquid phase of the polymer, by pouring each polymer directly from the three-neck flask before cooling off.	
The (p)PGS polymer solutions were then thoroughly stirred at 500 rpm overnight prior to incorporating predetermined amounts of the polymer to each blend developed and electrospun as described in <i>Chapters 4 and 5</i> .	

### 3.3.2 Stock chemicals, reagents, cells and equipment

To ensure the reproducibility of the performed experiments, the tables below list the specific polymers, solvents, reagents, chemicals, and cell-lines (Table 3.2) and the equipment used (Table 3.3) to conduct the research presented in this thesis.

**Table 3.2** List of the materials, CAS registry number, and the corresponding suppliers used in the experiments.

Materials	CAS Number	Supplier
<b>Polymers</b>		
<i>Bombyx mori</i> silkworm cocoons	-	Local sericulture
Chitosan powder (CS, degree of de-acetylation 85/100, MW 100,000 – 300,000 g·mol <sup>-1</sup> )	9012-76-4	Heppe Medical Chitosan GmbH
Nylon-6 pellets (polyamide-6; PA6)	25038-54-4	Sigma-Aldrich
O-carboxymethyl chitosan (O-CMC, degree of de-acetylation 90/100, MW 100,000 – 300,000 g·mol <sup>-1</sup> )	83512-85-0	Santa Cruz Biotechnology
Poly(caprolactone) (PCL, MW 80,000 g·mol <sup>-1</sup> )	24980-41-4	Sigma-Aldrich
Poly(ethylene oxide) (PEO, MW 900,000 g·mol <sup>-1</sup> )	25322-68-3	Sigma-Aldrich
Polyvinylpyrrolidone (PVP) (MW 360,000 and 1,300,000 g·mol <sup>-1</sup> )	9003-39-8	Sigma-Aldrich
<b>Poly(glycerol sebacate) synthesis</b>		
Glycerol (≥ 99.5%, MW 92.09 g·mol <sup>-1</sup> )	56-81-5	Alfa-Aesar
Sebacic acid (≥ 98%, MW 202.20 g·mol <sup>-1</sup> )	111-20-6	Alfa-Aesar
<b>Antimicrobial agents</b>		
5-Chloro-8-hydroxyquinoline (5CLO8Q, ≥ 95%, C <sub>9</sub> H <sub>6</sub> ClNO, MW 179.60 g·mol <sup>-1</sup> )	130-16-5	Sigma-Aldrich
Poly(hexamethylene biguanide) hydrochloride (PHMB, ≥98%, MW 213.33 g·mol <sup>-1</sup> )	32289-58-0	Sigma-Aldrich
<b>Solvents</b>		
1,1,1,3,3,3-Hexafluoro-2-propanol (HFIP, ≥ 99%)	920-66-1	Fluorochem
Acetic acid (AcOH, ≥ 99.8%)	64-19-7	Sigma-Aldrich
Chloroform (CF, ≥ 99.8%)	67-66-3	Acros Organics
Dimethylformamide (DMF, ≥ 99%)	68-12-2	Acros Organics
Ethanol (EtOH, anhydrous, ≥ 99.8%)	64-17-5	Acros Organics
Formic acid (FA, ≥ 99%) (Chapter 5)	64-18-6	Acros Organics (Chapter 5)
(FA, ≥ 95%) (Chapter 6)	-/-	Sigma-Aldrich (Chapter 6)
Ultrapure water	-	Distilled in-house
<b>Chemicals</b>		
Calcium chloride (CaCl <sub>2</sub> , ≥ 96%, MW 110.98 g·mol <sup>-1</sup> )	10043-52-4	Thermo-Fisher Scientific
Hydrochloric acid (HCl, 34%–37% in H <sub>2</sub> O, pH < 1)	7647-01-0	Sigma-Aldrich
Lithium bromide (LiBr, ≥ 99%, MW 86.84 g·mol <sup>-1</sup> )	7550-35-8	Thermo-Fisher Scientific

Sodium carbonate (Na <sub>2</sub> CO <sub>3</sub> , anhydrous, ≥ 99.5%, MW 105.99 g·mol <sup>-1</sup> )	497-19-8	Thermo-Fisher Scientific
<b>PVP:PGS UV photoinitiator</b>		
Riboflavin (≥ 98%, MW 376.36 g·mol <sup>-1</sup> )	83-88-5	Alfa-Aesar
<b>O-carboxymethyl chitosan grafting</b>		
N-(3-dimethylaminopropyl)-N'-ethylcarbodiimide hydrochloride (EDC, ≥ 98%, MW 115.09 g·mol <sup>-1</sup> )	25952-53-8	Sigma-Aldrich
N-hydroxysulfosuccinimide (Sulfo-NHS, ≥ 99%, MW 217.13 g·mol <sup>-1</sup> )	106627-54-7	Thermo-Fisher Scientific
<b>TEM ruthenium tetroxide staining</b>		
Ruthenium(III) chloride hydrate (RuCl <sub>3</sub> , 45%–55% in H <sub>2</sub> O, MW 207.43 g·mol <sup>-1</sup> )	14898-67-0	Sigma-Aldrich
Sodium hypochlorite (NaClO, 14% in H <sub>2</sub> O, MW 74.44 g·mol <sup>-1</sup> )	7681-52-9	Sigma-Aldrich
<b>Mounting media for microscopy</b>		
1,4-Diazabicyclo[2.2.2]octane (DABCO, ≥ 97%)	280-57-9	Acros Organics
Glycerol (≥ 99%, MW 92.09 g·mol <sup>-1</sup> )	56-81-5	Sigma-Aldrich
M Tris-Cl buffer (pH 8.0)	Invitrogen 15568-025	Thermo-Fisher Scientific
Mowiol® 4-88 (PVP, MW 31,000 g·mol <sup>-1</sup> )	9002-89-5	Sigma-Aldrich
<b>Cell-lines</b>		
Fibroblasts immortalised with hTERT (Isolated from human foreskin) (pGRN145 hTERT-expressing plasmid) (Biosafety level 1)	ATCC CRL-4001 (BJ-5ta)	American Type Culture Collection
<i>Escherichia coli</i> (Migula); Castellani and Chalmers (Isolated from urine) (Biosafety level 1/2)	ATCC 11775 (DSM 30083)	American Type Culture Collection
<i>Pseudomonas aeruginosa</i> (Isolated from human skin burn) (Biosafety level 2)	ATCC 43390 (CMCC(B) 10117)	American Type Culture Collection
<i>Staphylococcus aureus</i> (subsp. <i>aureus</i> Rosenbach) (Isolated from human lesion) (Biosafety level 2)	ATCC 6538 (FDA 209)	American Type Culture Collection
<b>Mammalian cell culture</b>		
Dulbecco's Modified Eagle Medium (DMEM), high glucose, sodium pyruvate, L-glutamine, phenol red	Gibco 11995-065	Thermo-Fisher Scientific
Fetal bovine serum (FBS)	Gibco A3160802	Thermo-Fisher Scientific
L-glutamine	HyClone SH30034.01	Thermo-Fisher Scientific
Non-essential amino acids	Gibco 11140-035	Thermo-Fisher Scientific
Penicillin-Streptomycin (10,000 U·mL <sup>-1</sup> )	Gibco 15140148	Thermo-Fisher Scientific
Phosphate-buffered saline (PBS) (10X, pH 7.4)	Gibco 11504526	Thermo-Fisher Scientific
Trypsin-EDTA (0.05%), phenol red	Gibco 25300-054	Thermo-Fisher Scientific
Triton X-100 (10% (v/v) detergent in ultrapure water)	9002-93-1	Thermo-Fisher Scientific
Tween-20 (PEG sorbitan monolaurate)	9005-64-5	Sigma-Aldrich
Trypan blue solution (0.4%), sterile filtered	72-57-1	Sigma-Aldrich
AlamarBlue® cell viability reagent	Invitrogen DAL1025	Thermo-Fisher Scientific

<b>SEM cell-seeded scaffolds fixation</b>		
Ethanol (anhydrous, ≥ 99.5%)	64-17-5	Sigma-Aldrich
Glutaraldehyde (C <sub>5</sub> H <sub>8</sub> O <sub>2</sub> , Grade II, 25% (v/v) in H <sub>2</sub> O)	111-30-8	Sigma-Aldrich
Hanks' Balanced Salt Solution (HBSS) HBSS, calcium, magnesium	Gibco 24020-117	Thermo-Fisher Scientific
Hexamethyldisilane (HDMS, ≥ 98%)	999-97-3	Alfa-Aesar
Sucrose (D-Saccharose, ≥98%, MW 342.30 g·mol <sup>-1</sup> )	57-50-1	Alfa-Aesar
<b>Bacteriological culture</b>		
Agar powder ((C <sub>12</sub> H <sub>18</sub> O <sub>9</sub> ) <sub>n</sub> )	Merck 05040	Sigma-Aldrich
Brain–heart infusion broth (BHI, 5 g/L calf brains infusion from 200g, 12.5 g/L disodium hydrogen phosphate, 2.5 g/L D(+)-glucose, 2 g/L, peptone, 10 g/L sodium chloride)	Merck 70192	Thermo-Fischer Scientific
Lysogeny broth (LB, 10 g/L tryptone, 5 g/L yeast extract, 5 g/L NaCl)	Miller L2542	Sigma-Aldrich
Mueller–Hinton broth (MH, 2.0 g/L beef infusion, 17.5 g/L casein hydrolysate, 1.5 g/L starch)	Merck 53286	Thermo-Fischer Scientific
Phosphate-buffered saline (PBS, pH 7.4)	Merck P3813	Sigma-Aldrich
<b>SEM bacteria seeded scaffolds fixation</b>		
Ethanol (anhydrous, ≥ 99.8%)	64-17-5	Sigma-Aldrich
Formaldehyde solution 4% (v/v) in PBS (pH 6.7–7.1)	50-00-0	Sigma-Aldrich
Hexamethyldisilane (HDMS, ≥ 99%)	999-97-3	Sigma-Aldrich
<b>Bacteria fluorescence imaging</b>		
BaClight™ live/dead bacterial viability kit (consisting of SYTO™ 9 and propidium iodide)	Invitrogen L7007	Thermo-Fisher Scientific

**Table 3.3** Equipment used to characterise the pristine material, synthesised polymers and composite electrospun mats. The specific chapters that each equipment was used are indicated in brackets ( ).

Equipment	Model	Manufacturer
<b>Fibre morphology</b>		
Scanning electron microscopy (SEM)	JSM 6010 PLUS (Chapter 4)	JEOL, Ltd, Japan
	JSM IT100 (Chapter 5)	JEOL, Ltd, Japan
	Zeiss Crossbeam 550 focused ion beam (FIB), (cryo-SEM) (Chapter 5)	Carl Zeiss Microscopy, GmbH, Germany
	Hitachi S-4800 (Chapter 6)	Hitachi-High Technologies, Corp., Japan
Scanning transmission electron microscopy (STEM)	Hitachi S-4800 (Chapter 6)	Hitachi-High Technologies, Corp., Japan
Transmission electron microscopy (TEM)	Zeiss EM 900 (Chapter 6)	Carl Zeiss Microscopy, GmbH, Germany
Sputter coater	Balzers BAS450 (target Au) (Chapter 4)	Oerlikon Balzers Coating, Ltd, UK
	Agar AGB7341 (target Au) (Chapter 5)	Agar Scientific, Ltd, UK
	Leica ACE 600 – ICN2 (Pt/Au) (Chapter 6)	Leica, AG, Germany
<b>Polymer solution evaluation</b>		
Conductivity meter	HI99301 (Res. 0.01 mS·cm <sup>-1</sup> ) (Chapters 4 and 5)	Hanna Instruments, SRL, USA
pH meter	HI98129 (Chapters 4 and 5)	Hanna Instruments, SRL, USA
	SevenCompact S210-Bio (Chapter 6)	Mettler-Toledo, Inc., USA
Rheometer	MCR 301 Viscometer (Chapter 6)	Anton Paar, GmbH, Austria
<b>Physicochemical characterisation</b>		
Fourier-transform infrared spectroscopy, attenuated total reflection (FTIR-ATR)	Spectrum-ONE (Chapter 4)	Perkin-Elmer, Inc., USA
	Varian 640-IR (Chapter 5 and 6)	Varian Medical Systems, Corp., USA
Surface chemistry	PHI 5000 Versaprobe-II (Al K $\alpha$ X-ray source) (All chapters)	Ulvac-Phi, Inc., Japan
Water contact angle (WCA)	Drop Shape Analyser, DSA100 (Chapters 4 and 5)	Krüss, GmbH, Germany
	Drop Shape Analyser, DSA25 (Chapter 6)	Krüss, GmbH, Germany
<b>Thermal and mechanical analysis</b>		
Thermogravimetric Analysis (TGA)	TG-209 F1 Iris (Chapters 6)	Erich Netzsch, GmbH, Germany
Differential scanning calorimetry (DSC)	DSC214 (Chapter 6)	Erich Netzsch, GmbH, Germany

Mechanical testing	Instron UTM 3367 (Chapters 4 and 5)	Illinois Tool Works, Corp., USA
	Z100-Retroline (Chapter 6)	Zwick-Roell Group, GmbH, Germany
Profilometer	XP-1 Stylus Profiler (Chapter 6)	Ambios Technology, Inc., USA
Digital micrometre	Mitutoyo 293-340-30 (Chapter 4)	Mitutoyo, Ltd., Japan
<b><i>In vitro</i> and drug release studies</b>		
Fluorescence microscopy	DM6000B Fluorescence (Chapter 6)	Leica, AG, Germany
Confocal laser scanning microscopy (CLSM)	LSM 710 (Chapter 6)	Carl Zeiss Microscopy, GmbH, Germany
Spectrophotometer	Modulus II Microplate Reader (Chapters 4 and 5)	BioTek Instruments, Inc., USA
	SynergyMX Microplate Reader (Chapter 6)	BioTek Instruments, Inc., USA
Ultraviolet-visible (UV) spectroscopy	SynergyMX Microplate Reader (Chapter 6)	BioTek Instruments, Inc., USA
Petri dish analyser	Scan 500 (Chapter 6)	Interscience, Ltd., France



### 3.4 Characterisation

Engineering a biomaterial is designing it to tackle a particular medical problem. It is essential to comprehensively characterise the biomaterial's physicochemical properties and biological responses, to better understand whether the requirements to tackle that specific medical problem have been met. Multidisciplinary characterisation allows the development of biomaterial that carry the required features while being adequately reproducible.

The physicochemical properties of a biomaterial play key roles toward its ability to provide a biomimetic niche that integrates the appropriate architecture and material-tissue interface capacities to facilitate better cellular interactions. The physical properties of electrospun biomaterials are heavily dependent on the intrinsic properties of the incorporated materials, as well as the micro/-nanoarchitecture of the fibres; such as fibre structure (e.g., core/shell) and diameter, surface area, density, fibre orientation, pore size, and porosity. The electrospun biomaterials were characterised towards their micro/-nanostructural features by scanning electron microscopy (SEM) and transmission electron microscopy (TEM). The chemical characterisation of the fibres was based on qualitatively identifying the polymers' composition and chemical interactions, as well as quantitatively by determining the surface chemistry of the fibres. Fourier transform infrared spectroscopy (FTIR), and X-ray photoelectron spectroscopy (XPS) were employed to determine the chemical structures of the synthesised polymers, the composition of the developed composite electrospun fibres, and the surface chemistry of the fibres.

The wettability and degradation of a biomedical implant are also of great importance, as variations in the hydrophilicity/hydrophobicity and the rate at which the material breaks down can directly or indirectly affect the biocompatibility, cell attachment behaviour, elicited immune responses and antimicrobial activity of the biomaterial. For this reason, the water contact angles, and degradation behaviour of the fibre-based biomaterials were also investigated, with drop shape analysing equipment and prolonged degradation studies.

In addition, the mechanical properties of the electrospun membranes were evaluated under standardised conditions based on the stress-strain relationships, using universal tensile testing equipment. This was conducted as part of *Chapter 4*; while attempting to mimic the mechanics of variant anatomical sites of the skin, and as part of *Chapter 6*; while attempting to meet the mechanical requirements of hernia mesh materials.

In connection with the core/shell antimicrobial nanofibrous meshes, developed in *Chapter 6*, understanding and evaluating the drug release profile of each substance and the conditions

under which it is released can provide further insights towards the capabilities of the biomaterial to act as a drug-loading matrix and provide the required bactericidal activity. Carefully designed drug release experiments examined the drug release of the antimicrobial agents at defined pH conditions and temperature, over an extended period of time using UV spectroscopy. The various characterisation techniques employed in this thesis are described in detail in the subsequent sections.

### **3.4.1 Scanning electron microscopy (SEM)**

During scanning electron microscopy (SEM), electrons are emitted from a filament through thermionic emission, which accelerates to the surface of the sample by means of a bias voltage between the electron source and the target. The scanning beam irradiates the specimen causing it to interact with the electrons at the surface to produce the detecting signals: secondary electrons (SE) and backscattered electrons (BSE), which are subsequently taken up by an X-ray detector. The detector accelerates the secondary electrons into a scintillator that converts the electron-based signal into a light signal, followed by a photomultiplier, which converts the photons into an electronic pulse that is then amplified to modulate the intensity of the image projected on a computer screen.

SEM imaging is vastly used in this thesis to determine the quality, reproducibility, and morphological properties of the electrospun fibres. All specimens were mounted on aluminium stubs using double-sided carbon adhesive tape and sputter-coated with a thin layer of Au (ranging from 8 to 10 nm thickness) to form an electrically conductive surface. As several SEM devices were used, the voltage of the electron beam (ranging from 2 to 20 kV) and current (ranging from 5 to 20 mA) were adjusted accordingly every time. Images were obtained at consistent magnifications of 200x, 500x, 1000x, 2000x, 5000x, 10000x and 20000x, depending on the thickness of the fibres for each specimen examined.

#### **3.4.1.1 Determining the fibre diameter, pore size and porosity**

The mean fibre diameter and pore size were measured using the Fiji-ImageJ software (v.1.52, National Institutes of Health, USA); where at least three different SEM micrographs were chosen, and randomly a total of 90–120 fibre width values were measured manually per sample. This was done by determining the known distance of the SEM micrograph's scale bar (in pixels) and converting them to units of length. Fibre diameter distribution graphs and normal

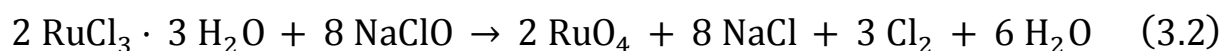
distribution histograms were also produced in SPSS (v.24, Statistical Package for Social Sciences, IBM, USA).

The surface porosity and density of the nanofibrous scaffolds were then evaluated using the ImageJ add-on 'DiameterJ' from  $n \geq 1000$  fibre-points. The margin of error between the manually calculated and automatically measured computations was, for all specimens  $\leq 5\%$ . Porosities were determined via threshold image analysis of the SEM micrographs using ImageJ. The density of the fibrous scaffolds was determined as "intersections per  $\mu\text{m}^2$ ", using DiameterJ, where; the average length of the fibres was divided by its radius determined based on four points for each fibre per image that was analysed. Then, the total number of intersections were calculated as the specific area (in pixels)  $\times 10^4$ , which corresponds to  $1/1000^{\text{th}}$  points per pixel of the image.

### 3.4.2 Transmission electron microscopy (TEM)

Transmission electron microscopy (TEM) differs from SEM, as the electron beam is transmitted rather than scattered, and thus it can be used to obtain details on a thin specimen over its internal composition.

The TEM was one of the methods employed to confirm the core/shell structure of the antimicrobial hernia mesh nanofibrous mats. The double contrast method was utilised to distinguish between the shell consisting of chitosan, and the core of the fibre made of nylon-6. Ethanol was used to mount the TEM copper grids to the surface of the collector, on which fibres were directly electrospun and deposited for a few seconds. After drying, the fibre-containing grids were stained by placing them on a desiccator containing a ruthenium tetroxide ( $\text{RuO}_4$ ) solution at the gaseous phase, prepared by dissolving  $\text{RuCl}_3$  in 10 wt.%  $\text{NaClO}$  solution, for 2 h, in order to attain an increased contrast between the two polymers when exposed to the transmission electron beam. Ruthenium tetroxide closely relates to osmium tetroxide but is less toxic and volatile. As a strong oxidising agent, it can react with many organic compounds, including primary and secondary alcohols like the ones present in the chitosan's structure. Further,  $\text{RuO}_4$  staining can carry a stabilising effect against fibre damage that can be caused by exposure to the electron beam [6].



The stained grids were then analysed at an acceleration voltage of 80 kV, and the obtained images were evaluated using ImageJ.

### 3.4.3 Fourier transform infrared (FTIR) spectroscopy

The Fourier transform infrared (FTIR) spectroscopy technique was used to determine the chemical structure and interactions between the polymers and drugs in their pristine, fibrous and crosslinked forms. The FTIR technique identifies the presence of the chemical bonds in a molecular structure (in the form of bending, symmetric and asymmetric stretching) by interacting the specimens with infrared light and producing an infrared absorption spectrum. IR radiation is absorbed by chemical bonds; as the stretching and bending of every bond result in a change in the molecule's dipole moment. As electromagnetic radiation interacts with the bond's altered dipole moment, radiation from the IR-emitter is absorbed and can be computed by measuring the change in the intensity of the beam, prior and post, passing through the specimen. When all measurements have been taken, a Fourier transform decomposes the raw absorbance data as the amount of energy absorbed per wavelength over time, through a mathematical transform.

In this thesis, the measurements of each specimen were directly analysed using the attenuated total reflectance (ATR) crystal mode of the FTIR equipment. All samples were dried to obtain sharper spectra and avoid broadening of the polar group absorptions. The mid-infrared scanning range was 650 and 4000  $\text{cm}^{-1}$  with a spectral resolution of 2  $\text{cm}^{-1}$  (32 scans) for *Chapter 4*, 600–4200  $\text{cm}^{-1}$  with a spectral resolution of 2  $\text{cm}^{-1}$  (72 scans) for *Chapter 5*, and 600–4500  $\text{cm}^{-1}$  with a spectral resolution of 2  $\text{cm}^{-1}$  (126 scans) for *Chapter 6*. Silk fibroin and chitosan region-specific scans ranging from 800–2000  $\text{cm}^{-1}$  and 1200–2000  $\text{cm}^{-1}$ , respectively, were also obtained. The spectra were examined in Origin (v.10, OriginLab, Corp., USA), and the graphs were produced in Matlab (v.R2019a, MathWorks, Inc., USA).

### 3.4.4 X-ray photoelectron spectroscopy (XPS)

X-ray photoelectron spectroscopy (XPS) is a surface-sensitive analytical technique that quantifies the photoelectron energy (50–2000 eV) released when the surface of a material is bombarded with X-rays under high vacuum ( $\geq 10^{-7}$  Pa) at a depth that extends from the surface of the specimen to approximately 50–70 Å [7]. If the incoming energy of an X-ray photon is  $h\nu$ , the maximum kinetic energy ( $E_{\text{kin}}$ ) of the electron leaving the surface of the material is defined as:

$$E_{\text{kin}} = h\nu - E_{\text{bin}} - \varphi \quad (3.3)$$

where,  $E_{bin}$  is the binding energy of the electron and  $\phi$  the analyser work function (specific to the device, typically between 2–5 eV for the equipment used). XPS is an excellent technique for determining a surface's elemental composition and the binding states of the elements present.

An XPS with an Al K $\alpha$  X-ray source was used in this thesis to determine the surface chemistry of the electrospun skin substitute fibres and further validate the core/shell structure of the antimicrobial hernia meshes, by quantifying the elements present at the surface and the corresponding binding energies. The energy resolution of the spectrometer was set to 0.8 eV/step at a pass-energy of 187.85 eV for the survey scans. Carbon at 284.5 eV binding energy was used as a reference to correct for charge effects. The elemental compositions were determined using instrument-dependent atom sensitivity factors based on the C1s peak area. The photoelectron-transitions of C1s, O1s, N1s, Ca2p, Cl2p, and Si2p were chosen to determine the surface elemental concentration of the fibres. Spectra analysis and peak fitting were carried out using CasaXPS (v2.1, Casa Software Ltd, UK) to determine the atomic ratios (at. %), as well as carbon and nitrogen bonding contents. The theoretical atomic ratios of the composite electrospun mats, based on the molecular structures of each polymer and drug, were also calculated to determine and further validate the core/shell structure, as the C, N and O content is distinctively different between chitosan (shell) and nylon-6 (core).

### 3.4.5 Mechanical testing

Determining the tensile properties of the developed fibrous biomaterials is essential to obtain an initial appraisal of their ability to withstand mechanical forces upon incorporation onto the defected site. The mechanics were of special relevance to *Chapter 4*, where variant blends of crosslinked PVP/PGS fibres were examined towards their ability to mimic the mechanics of different anatomical regions of the skin, as well as for the antimicrobial NFs produced in *Chapter 6*, where nylon-6 was incorporated within the core of the core/shell chitosan-5CLO8Q/nylon-6-PHMB NFs to improve the composite's mechanics and bring it closer to the mechanical requirements of a hernia mesh.

The scaffolds were cut using a customised mould into dog bone-shaped specimens with an outer area (115 mm (length)  $\times$  25 mm (width)) and an inner area (84 mm (length)  $\times$  6 mm (width)), based on ISO 527–3 Type 5 for determining tensile properties of thin films and sheets (*Chapter 4*) or into rectangular 10  $\times$  40 mm strips based on ISO 527–3 Type 2 (*Chapter 6*) (Figure 3.1) [8]. The thickness of each electrospun mat was measured with a high-precision digital micrometre (*Chapter 4*) or a profilometer (*Chapter 6*). The weight of each specimen was

also determined. The thickness was between 0.1–0.8 mm (*Chapter 4*) and 0.05–0.15 mm (*Chapter 6*). The specimens were then placed into an acclimatised room under standard atmospheric conditions ( $22 \pm 2$  °C and  $65\% \pm 5\%$  RH) for two days prior to the measurements.

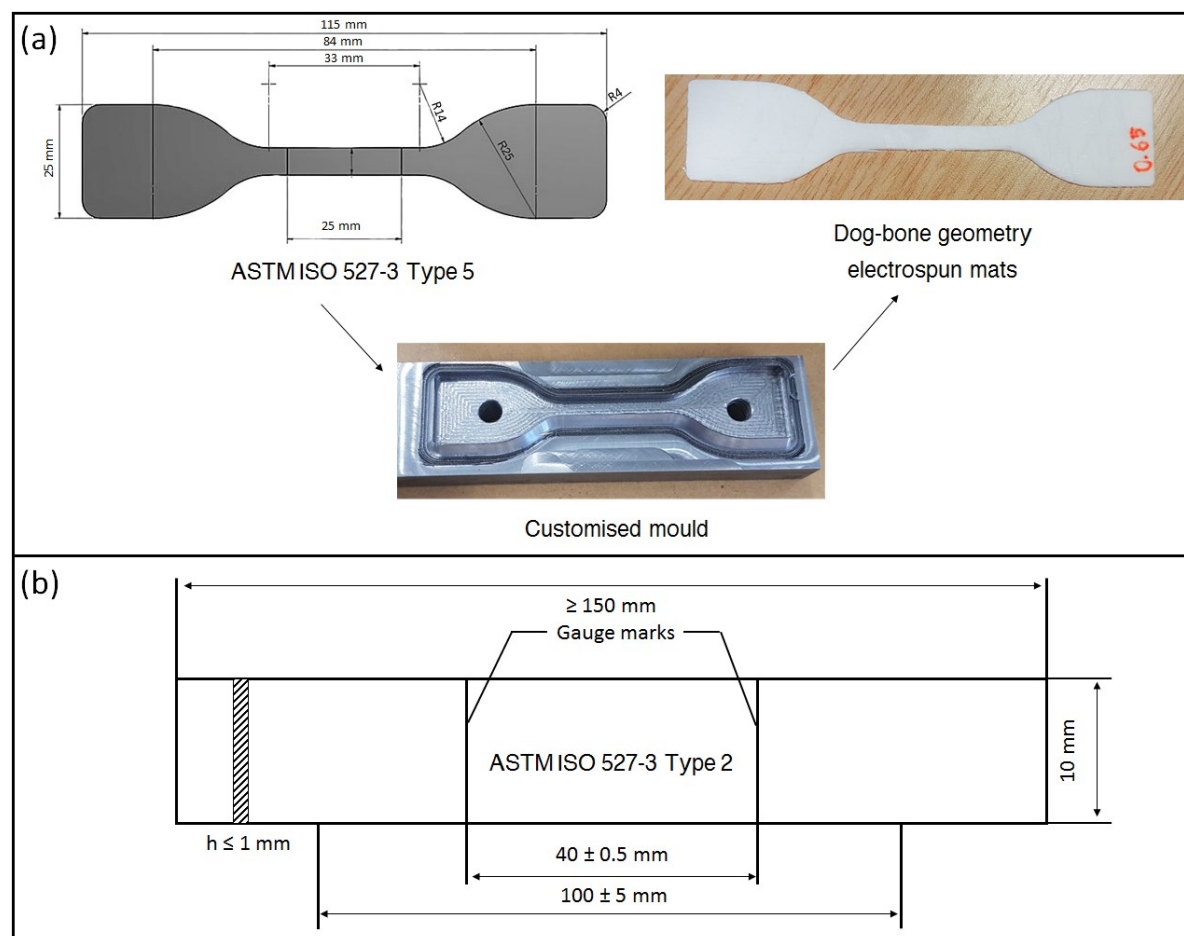


**Figure 3.1 Standards for determining tensile properties of thin films and sheets. (a)** Schematic representation and a photograph of the mould designed based on ISO 527–3 Type 5 to determine the mechanical properties in *Chapter 4*; **(b)** schematic representation of ISO 527–3 Type 2 used to determine the mechanical properties in *Chapter 6*.

The specimens were tested in axial tensile load 100 N, at a constant crosshead speed of  $50 \text{ mm} \cdot \text{min}^{-1}$  (5% of non-load value) (*Chapter 4*) or using a 10 N load cell at a crosshead speed of  $10 \text{ mm} \cdot \text{min}^{-1}$  (*Chapter 6*). Each specimen was stretched apart gradually from the gripping units moving in opposite directions until failure.

In this thesis, the tensile properties of each biomaterial assessed were obtained to determine the Young's modulus and ultimate tensile strength (UTS). The Young's modulus

describes how easily a material can stretch or deform as a ratio between the force applied to a material and the subsequent strain. Stress is defined as the force ( $F$ ) per unit of area, while the strain is calculated from the absolute deflection divided by the original deflection. The Young's modulus, UTS and elongation-at-break were calculated based on:

$$\text{UTS (MPa)} = \frac{\text{Force (N)}}{\text{Area (mm}^2\text{)}} \quad (3.4)$$

where,

$$\text{Area (mm}^2\text{)} = \text{Specimen thickness (mm)} \times \text{Specimen width (mm)}$$

and,

$$\text{Elongation at break (\%)} = \frac{\text{Specimen elongation (mm)}}{\text{Original length (mm)}} \times 100 \quad (3.5)$$

and,

$$\text{Young's modulus (MPa)} = \frac{\text{Stress (MPa)}}{\text{Strain}} \quad (3.6)$$

The UTS determines the maximum stress that the specimen can endure before failure. The Young's modulus was based on the tangential modulus determined from the tangent line placed to the envelope, prior to the elastic limit (before permanent deformation occurs), of the tensile stress-strain curve plotted for each specimen (Figure 3.2). At least six specimens were prepared for every type of electrospun mat, and the average values are represented as the mean  $\pm$  SD. The stress-strain graphs were produced in Matlab, and statistical significance between the different groups for the Young's modulus and UTS measurements were determined by one-way analysis of variance (ANOVA) using SPSS.

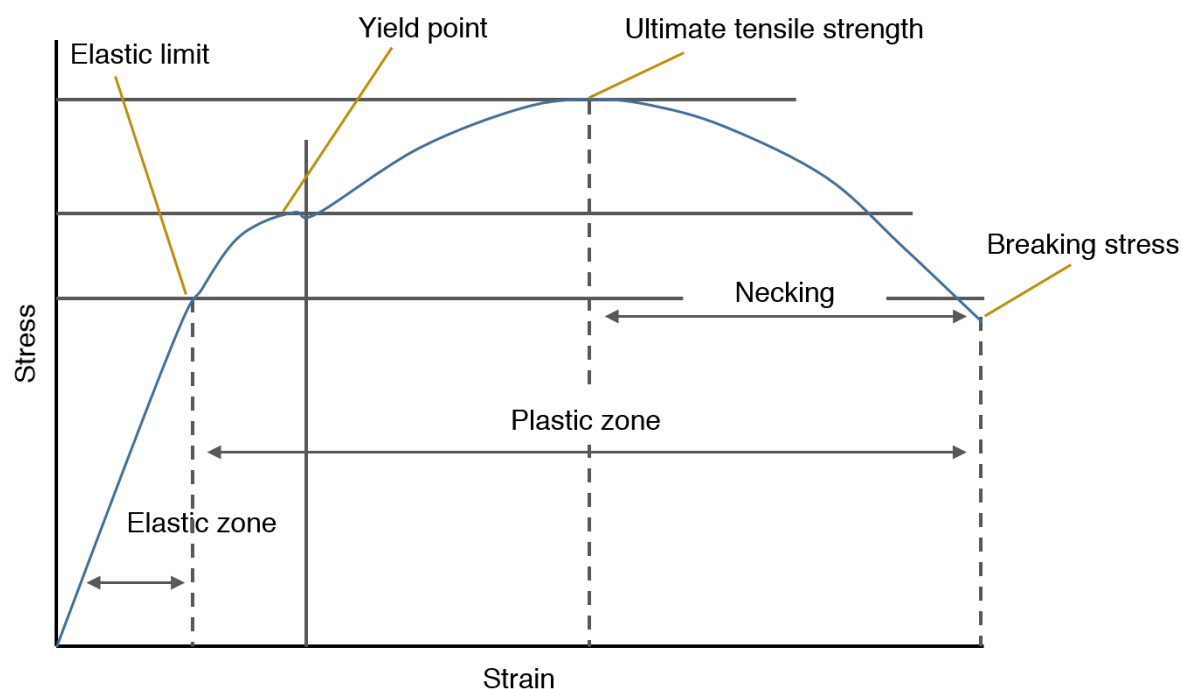


**Figure 3.2** Stress-strain curve of "model" fibre specimen. Redrawn, based on [8].

### 3.4.6 Thermogravimetric analysis (TGA)

Thermogravimetric analysis (TGA) was conducted to provide indications, where appropriate, towards the composition of the composite electrospun mats in comparison to the pristine material and neat (non-composite or non-drug containing) fibres. TGA is a quantitative method that records mass change in solid material, due to phase transitions and thermal degradation, as the temperature amply increases over time. Heat is used to trigger chemical reactions and physical alterations in materials [9]. As the sample heats up, weight is lost due to dehydration and decomposition or weight is gained due to oxidation. The device is placed on an anti-vibration table, where a thermocouple is used to monitor the temperature, and a high precision microbalance is used to determine the weight of the specimen over time.

Thermograms were obtained to determine the thermal stability and the onset of decomposition temperature ( $T_{\text{onset}}$ ) of the composite fibres using thermogravimetry. Each dried specimen weighing between 2.5–3.0 mg was placed on an open ceramic crucible and heated from room temperature up to 800 °C at a rate of 10 °C·min<sup>-1</sup> under nitrogen atmosphere at an outlet pressure of 10 mL·min<sup>-1</sup>.



### 3.4.7 Differential scanning calorimetry (DSC)

Differential scanning calorimetry (DSC) was used to observe thermodynamic properties, such as fusion and crystallisation events, as well as the glass transition temperatures ( $T_g$ ) of the composite electrospun mats in comparison to the pristine material and neat fibres. DSC is a destructive thermoanalytical technique that measures the difference in the amount of heat required to raise the temperature of a specimen set side by side to a well-defined reference sample (empty aluminium crucible), as a function of temperature [10].

The specific heat capacity ( $C_p$ ) in a given system is the total amount of heat required to raise the temperature of 1 kg of a substance by 1 K, while the heat flow refers to the amount of heat supplied per unit of time (in  $J \cdot s^{-1}$ ). The following formulas were applied to determine the heat capacity:

$$\text{Heat Capacity } (C_p) = \frac{\text{Heat flow}}{\text{Heat rate}} = \frac{60 \times \text{Heat flow (mW/mg)}}{10 \text{ K/min}} \quad (3.7)$$

The enthalpy was determined as:

$$\text{Enthalpy (H)} = \text{Heatflow} \times \text{Time (min)} \times 60 \quad (3.8)$$

and the temperature was given by:

$$\text{Temperature (T)} = \frac{H}{m \cdot C_p \cdot dT} \quad (3.9)$$

The  $T_g$  refers to the temperature at which a phase change is observed that transforms a polymer from a ductile material into a hard and brittle material. Different materials will differ significantly and will present unique glass transition temperatures, which makes a given polymer better suited or worse for a particular application. For the composite polymer fibres described in the following chapters, the glass transition temperature is dependent on the proportion of the individual components of polymers present in the blend, as well as the individual  $T_g$  of these components. Crystallisation ( $T_c$ ) is an exothermic process apparent just above  $T_g$ , where most polymers will experience molecular chain mobility. This results in a decrease in the recorded heat flow since less heat is required to keep the heating rate of the specimen than that of the reference crucible in the DSC.  $T_c$  is observed as a sharp decreasing peak by plotting the heat flow against temperature. At the melting temperature ( $T_m$ ), the molecular chains of the polymers are mobile and do not follow an ordered arrangement.

Melting is considered an endothermic process that is accompanied by absorption of heat, with the temperature remaining constant during melting beside the continuous heating of the specimen.

Since nylon-6 (PA6) is a thermoplastic, it presents a very distinct  $T_m$  value, in comparison to chitosan that is an amorphous polymer. Based on this observation, the amount of PA6 present within the core of the core/shell NFs could be estimated. The amount was determined based on the enthalpy change ( $\Delta H_m$ ) values of the PA6-only and the core/shell PA6-PHMB/CS-5CLO8Q NFs corresponding to the polyamide melting enthalpies, based on:

$$\text{Amount of PA6 within the core (\%)} = \frac{\Delta H_m (\text{core/shell})}{\Delta H_m (\text{PA6})} \times 100 \quad (3.10)$$

where,  $\Delta H_{m(\text{core/shell})}$  and  $\Delta H_{m(\text{PA6})}$  are the heat of fusion values of the core/shell and PA6-only electrospun mats, respectively.

DSC measurements of the specimens were taken at a heat rate of  $10 \text{ }^\circ\text{C}\cdot\text{min}^{-1}$  under nitrogen flow. Dried samples (weighing between 5–20 mg) were sealed into aluminium crucibles and placed into controlled heating and cooling cycles at a temperature range of  $-20 \text{ }^\circ\text{C}$  ( $-70^\circ\text{C}$  for the PEO powder) to  $320 \text{ }^\circ\text{C}$  (*Chapter 6*).

### 3.4.8 Water contact angle (WCA) measurements

Wettability refers to the preference of a liquid to form contact with a solid and is determined by cohesive and adhesive forces between the liquid and the solid. In the case of cohesive forces, molecules of the same kind (similar polarities, reactive groups, among others) are pulled towards each other, while adhesive forces refer to interactions between unlike molecules. The ability of a material to balance these two forces determines its wettability. A contact angle is used to measure wettability. The contact angle of  $90^\circ$  is considered as the threshold number. When the angle exceeds  $90^\circ$ , the material is deemed hydrophobic, while a contact angle below  $90^\circ$  is defined as a hydrophilic surface.

In tissue engineering, scaffolds are required to implement various requirements, among which are surface properties. These properties include wettability, morphology, and surface energy, which affect cell adhesion and migration at the interface of tissue-scaffolds. Polymer surface engineering is a tool used to improve the behaviour of scaffolds by tuning surface

characteristics. Altering the wetting capabilities of a scaffold can determine how a mammalian cell adapts to it, since cells tend to be more responsive to energy free surfaces. The composite's interfacial energy will determine the tissue's regeneration capabilities, as well as its antimicrobial behaviour. Biomaterial with lower interfacial energy can offer a higher cell-surface affinity [11]. These surfaces usually have hydrophilic energy that is slightly larger than the energy of the water surface tension, therefore leading to better cell attachment by ligand-receptor interactions, and may, further, prevent bacterial colonization [12].

The water contact angle (WCA) measurements of the electrospun membranes were determined by the sessile drop method. For each scaffold, at least 8 measurements were obtained by dispensing a 5  $\mu$ L droplet of deionised water (*Chapters 4 and 5*) or ultrapure HPLC-grade water (*Chapter 6*) and letting it settle at the surface of orderly unswerving fibre mats at room temperature. The values were computed from recorded videos on Advance (v1.9, Krüss GmbH, Germany) (*Chapters 4 and 5*) or with the contact angle add-on of the ImageJ. The means  $\pm$  SD were determined, and statistical analysis using repeated-measures ANOVA with confidence interval adjustment Bonferroni was conducted in SPSS.

### 3.4.9 Degradation studies

The degradation rate of a biomaterial over time can provide key information of its ability to co-exist within a tissue, long-term biocompatibility, tissue adhesion properties and ultimately act as an indicator of whether the construct can be considered bioabsorbable, prior to an *in vivo* study [13]. For each electrospun mat (*Chapters 4 and 5*), five specimens were punched into 5  $\times$  5 mm<sup>2</sup> pieces obtained from three independently electrospun mats, adapted from a previously published protocol [14]. Subsequently, the specimens were weighed (initial mass,  $W_o$ ) and placed in Petri dishes containing PBS (1x, pH 7.2) at room temperature under ambient conditions, where the solution was refreshed daily. After being immersed for predetermined time points, ranging from 15 min to 30 days, the specimens were dried at 50 °C and weighed (dry mass post submersion,  $W_i$ ). The residual mass (weight loss,  $\mu$ ) of each specimen was calculated as:

$$\text{Weight loss } (\mu)(\%) = \frac{(W_o - W_i)}{W_o} \times 100 \quad (3.11)$$

### 3.4.10 *In vitro* drug release studies

For the core/shell antimicrobial nanofibrous mats, consisting of nylon-6-PHMB in the core and chitosan-5CLO8Q in the shell, the drug release profiles were determined at pH 7.2 and 6.2, at 37 °C. The pH values were based on the fact that infections surrounding the peritoneal fluid of the abdomen range between pH 7.0 and 7.8 (for healthy tissue) and between pH 6.0 and 7.2 for diseased tissue; where pH 6.0 is found only in anorectal abscesses caused by non-encapsulated bacterial species. The applicable temperature was chosen at 37 °C to approximate the human body temperature.

By utilising the high surface area of co-axially electrospun NFs, a high drug loading efficiency can be obtained by pairing the hydrophilic PHMB with the hydrophobic nylon-6 in the core and the hydrophobic 5CLO8Q with the hydrophilic chitosan present at the surface of the electrospun mats.

The dried electrospun mats were cut into pieces weighing ~ 6 mg and placed in 20 mL centrifuge tubes containing 10 mL of PBS pH 7.2 or PBS-HCl pH 6.2. All the vials were incubated at 37 °C at 30 rpm. At specified time intervals, 1 mL of release medium was pipetted and replaced with an equal volume of fresh solution. The drug release profiles of the single CS-5CLO8Q and PA6-PHMB, as well as the core/shell PA6-PHMB/CS-5CLO8Q NFs, were determined using UV spectroscopy, based on the specific absorption spectra of each drug. For 5CLO8Q a designated absorption peak was ascertained as the average of 247/257 nm, where PHMB was measured at wavelength maximum of 236 nm (Appendix A: Figure A-1). Fortunately, no secondary absorbance peaks, at the corresponding wavenumbers of each drug, were present between the two antimicrobial substances, making it feasible to assess the drug release of both substances in the core/shell structure.

The cumulative release of the antimicrobial compounds from the electrospun NFs was expressed based on the standard calibration curve of each substance for each medium (Appendix A: Figure A-2). The standard curves were produced based on serial dilutions 2, 5, 10, 15, 20, 25, 50  $\mu\text{g}\cdot\text{mL}^{-1}$  of each drug, where readings were obtained at the corresponding wavelengths using UV transmittable acrylic 96-well plates. The drug concentration ( $C_i$ ) at each time point was determined as:

$$C_i (\mu\text{g}/\text{mL}) = (a \times Y) \pm b \quad (3.12)$$

where  $a$  is the intercept,  $b$  the slope and  $Y$  the absorbance obtained from each reading at time ( $t$ ). Then, the cumulative drug release (CDR) was calculated as:

$$\text{CDR (\%)} = \frac{V_e \sum_1^{n-1} C_i + V_0 C_n}{m_0} \times 100 \quad (3.13)$$

where,  $V_e$  the volume of release medium removed at each time point (1 mL),  $V_0$  the total volume of the release medium (10 mL), and  $m_0$  the total amount of the drug-loaded on the electrospun mats. All measurements were taken in quadruplicates, and the results are expressed as the cumulative drug release (in %) over time (in h) as average values  $\pm$ SD as computed in Matlab, based on two independent drug release experiments obtained using electrospun mats from different batches.

Characterising the drug pharmacokinetics of nanofibrous materials is difficult due to the complex morphologies of these polymer matrices and the structural variations they may undergo due to swelling. Various mathematical models have been proposed to describe drug release kinetics, including first-order models, the Higuchi model, the Hixson-Crowell model, and the Korsmeyer-Peppas (KP) model [15]. To further investigate the drug release mechanisms, the well-established KP model was used. Korsmeyer-Peppas classifies the drug profile based on the release exponent ( $n$ ) value obtained from the fitting equation:

$$\frac{M_t}{M_\infty} = K_{kp} t^n \leftrightarrow \log\left(\frac{M_t}{M_\infty}\right) = \log(K_{kp}) + n \log(t) \quad (3.14)$$

where  $M_t$  is the amount of drug released in time ( $t$ ),  $M_\infty$  is the amount of drug released after time ( $\infty$ ),  $n$  is the drug release exponent, and  $K_{kp}$  is the Korsmeyer release constant of the apparent release. To determine whether the mechanism occurs by diffusion, leaching, or a combination of the two, the exponent variable  $n$  is used to describe drug release of cylindrical shaped matrices. Table 3.4 provides boundaries of the mechanism.

**Table 3.4** Different drug release mechanisms.

Release exponent ( $n$ )	Drug transport mechanism	Rate as a function of time
$\leq 0.45$	Fickian diffusion	$t^{-0.5}$
$0.45 < n < 0.89$	Non-Fickian (kinetic) transport	$t^{(n-1)}$
0.89	Case II transport*	Zero order release
$> 0.89$	Super Case II transport**	$t^{(n-1)}$

\*drug release is constant and controlled by polymer relaxation. \*\*drug release is polymer erosion-controlled

### 3.5 *In vitro* biocompatibility evaluation

Evaluating the *in vitro* cellular responses and the way the material interacts using a relevant cell-line can provide an initial appraisal over the ability of the electrospun membranes to act as a biomaterial. In this thesis, the biocompatibility of the electrospun fibres was assessed on fibroblasts-seeded scaffolds using a proliferation assay, where the fibroblasts' morphology, expansion and adhesion properties were evaluated on fixed scaffolds using SEM. The following sections describe the methods used to culture and seed fibroblasts on the electrospun mats and subsequently assess their biocompatibility.

#### 3.5.1 Scaffold sterilisation

There are several sterilisation methods that can be used to produce aseptic scaffolds that are considered effective for non-clinical proof of concept studies [16]. When selecting from the available techniques including UV radiation, ethanol treatment, argon plasma, autoclaving, gamma radiation and ethylene oxide, the scaffold's chemistry needs to be taken under account, as it can influence several of its physiochemical and mechanical aspects [17]. Considering that the sterilisation method can directly influence the surface topography and subsequent *in vitro* cell behaviour, distinct protocols were selected for the sterilisation of the different biomaterial system developed, based on the material's profile [18, 19]. In *Chapter 4*, 70% (v/v) ethanol was used to disinfect the crosslinked PVP/PGS scaffolds. In *Chapter 5*, the binary (SF:(p)PGS) and ternary (SF:PCL:(p)PGS) fibre mats were initially immersed for 2 h in 100% (v/v) ethanol to induce crystallisation of  $\beta$ -sheets in the fibroin structure, resulting in water-insoluble membranes, followed by 70% (v/v) ethanol treatment for disinfection. For the bacteria work carried out in *Chapter 6*, the core/shell nanofibrous mats containing chitosan, were disinfected by shining UV light, as ethanol or ethylene oxide, dry heat, saturated steam during autoclaving and  $\gamma$ -irradiation treatment have been shown to alter the chemical structure, mechanical properties and solubility of chitosan [20].

In *Chapters 4* and *5*, dry scaffolds were punched in 4- or 8-mm round discs, placed in sterile 48-well plates and treated overnight in 70% (v/v) ethanol, washed thoroughly with PBS, and pre-soaked in DMEM medium for 48 h. The extended period of washing also allowed for the removal of any residual solvents that may have been entrapped during electrospinning

and were not able to evaporate during drying. In *Chapter 6*, the electrospun core/shell nanofibrous mats were punched into 8 mm circular discs weighing approximately 1 mg and placed in sterile Petri dishes that were subjected to UV radiation for 1 h under the fume hood.

### 3.5.2 Cell culture technique

As the application of interest in *Chapters 4* and *5*, is the development of ECM-like skin substitutes, fibroblasts were used to assess the biocompatibility, spreading, and morphological properties of the electrospun membranes. Immortalised human dermal fibroblasts (HDF) were donated from the *MRC Centre for Cardiovascular Science*, Edinburgh, UK, and used for the cell culture experiments.

The HDFs cryogenic vials (1 mL,  $1 \times 10^6$  cells) were gently thawed from liquid nitrogen using warm media to prevent osmosis, centrifuged at 180 g for 10 min, and carefully aspirated the media to remove the cryoprotectant (DMSO). The cell palette was then resuspended in a warm fresh culture medium, thoroughly mixed by gentle pipetting and transferred to 75 cm<sup>2</sup> culture (T75) flasks, and the total volume was raised to 15–20 mL. The complete-DMEM medium consisted of a basal medium of high glucose-pyruvate DMEM supplemented with 10% (v/v) FBS, 1% (v/v) Penicillin-Streptomycin, and 1% (v/v) L-Glutamine. The cultures were maintained in a humidified atmosphere (37 °C and 5% CO<sub>2</sub>), with the media being replaced every two days. The cell growth on the surface of the flask was continuously monitored using an inverted microscope and examined for confluence and morphological changes, up until subculturing.

Cells stop growing when they reach confluence. The HDFs were passage prior to becoming fully confluent (70%–80% confluence) so that the proliferation phenotype is maintained. Based on the number of cells obtained, cells were either subcultured in a 1:4 passage ratio or seeded on electrospun mats. The cells were subcultured by discarding the old medium and washing the flasks with PBS. Then, 2000  $\mu$ L of trypsin-EDTA were applied to the cell-containing side of the flask's surface and incubated for 5 min, in order to dissociate the cells. A 1:2 (v/v) ratio of DMEM was added to stop the trypsinisation of the cells. The DMEM-trypsin solution containing the cells was thoroughly mixed, centrifuged and resuspended. Then, 10  $\mu$ L of cell solution was added to an Eppendorf tube containing 190  $\mu$ L trypan blue and mixed. From this suspension, 10  $\mu$ L were transferred on a haemocytometer, where the cells present in the four corner chambers were counted. The number of cells per ml of suspension was then determined as:

$$\text{Cells per 1 mL of suspension} = n/4 \times 20 \times 10,000 \quad (3.15)$$

where  $n$  the number of cells counted. Trypan blue is a 960 Da diazo dye, which can only bind positively charged intracellular domains of compromised cell membranes, and does not bind intact cells as their membrane are also negatively charged [65]. This method is used to enumerate and distinguish live (white) from dead cells that have taken up the dye (blue). The cells were then, based on the number of cells calculated, if low, subcultured to new T75 flasks or, if adequate, used to seed the electrospun mats.

When the required experiments were concluded, aliquots of 1 mL cryogenic vials containing  $1 \times 10^6$  cells were refrozen. The freezing medium consisted of complete-DMEM with 20% (v/v) FBS and 7% (v/v) DMSO, which acts as a cryoprotectant that prevents cell damage caused due to ice crystal formation. The cells were frozen slowly, to allow for the sufficient efflux of water and prevent intracellular ice formation due to the high osmotic strength present. The vials were placed in a freezing container (Mr. Frosty®, Nalgene, Thermo-Fischer, UK) filled with 100% isopropyl alcohol and placed overnight at  $-80 \text{ }^\circ\text{C}$ , allowing for the temperature to decline at a rate of  $-1 \text{ }^\circ\text{C}\cdot\text{min}^{-1}$ . The next day the cryogenic vials were submerged back to the liquid nitrogen tank.

When the needed number of fibroblasts was reached, the cells were resuspended to the appropriate volume in DMEM, based on specific experiment requirements. Then, a 20  $\mu\text{L}$  cells-DMEM suspension was adjusted to a concentration of  $1 \times 10^5$  (*Chapter 4*) or  $2.5 \times 10^5$  (*Chapter 5*) HDFs per electrospun mat. The suspension was carefully placed in the centre of each sterilised scaffold, following the same pipetting motion to achieve the best possible cell distribution. Scaffolds consisting of PCL-only fibres and cells cultured directly on the bottom of tissue cultured 48-well plates were also seeded. The 20  $\mu\text{L}$  cells-DMEM seeded scaffolds were left still for 2 h under the hood and then for 4 h within the incubator ( $37 \text{ }^\circ\text{C}$  and 5%  $\text{CO}_2$ ) to allow for the cells to adhere prior to warm fresh DMEM perfusion. DMEM was discarded and replaced every second day in a manner of 50/50 fresh/old to replenish nutrients provided by the media and at the same time, maintain positive growth factors secreted by the cells.

### 3.5.3 Cell seeding efficiency (SE)

The efficiency at which HDFs attach on the electrospun scaffolds was assessed as a prerequisite of cell proliferation and expansion. This was attained by calculating the number of living cells that did not attach on the scaffolds to the proportion of the cells that were initially



seeded. At 4 h post-seeding, the cell-containing scaffolds were carefully removed and placed on new culture plates, while the well's culture medium was transferred to a centrifuge tube. Trypsinization of the wells was also conducted to obtain any adherent cells and added to the corresponding centrifuge tube. The pellet obtained after centrifugation was resuspended, and the cells enumerated as described previously. Then, the cell seeding efficiency was calculated for each group based on the formula below, where the data are presented as average values  $\pm$  SD. The seeding efficiency of cells grown directly on tissue culture plates was also evaluated as a control group.

$$SE (\%) = \frac{(\text{No. of cells seeded}) - (\text{No. of unattached cells})}{\text{No. of cells seeded}} \times 100 \quad (3.16)$$

### 3.5.4 Cell proliferation

The metabolic activity and proliferation of the cells after being attached to the electrospun membranes was determined by the colourimetric Alamar blue™ (AB) assay. The active agent of the AB assay is Resazurin (blue), a cell-permeable, weakly fluorescent, redox-sensitive compound. Metabolically active (viable) cells continuously chemically reduce Resazurin, intracellularly via mitochondrial dehydrogenase activity, to resorufin (purple, fluorescent compound). Subsequently, resorufin diffuses from the cells back into the surrounding medium [21]. This conversion of the compound occurs continuously from the viable cells, rapidly increasing the fluorescent signal, but is unable to occur from metabolically dysfunctional (dead) cells.

The metabolic activity was determined 1, 3, 5, and 7 days after incubation. At each time interval, triplicates of each cell-containing electrospun mat group were carefully removed using sterile tweezers, transferred to new 24-well plates and rinsed three times with warm PBS for 15 min. Unseeded scaffolds (blanks) were also produced as a negative control for the readings. As Resazurin is light-sensitive, the AB reagent was diluted 1 in 10 with DMEM, in the dark, to produce 10% (v/v) AB solution. Subsequently, 350  $\mu$ L of 10% AB-DMEM was poured in each scaffold-containing well, wrapped in aluminium foil to avoid light exposure, and placed for 4 h at 37 °C / 5% CO<sub>2</sub>. Measurements were obtained by transferring 100  $\mu$ L aliquots of each specimen in triplicates (including the negative control) to black-walled, clear-bottom 96-well plates. The accumulation of reduced AB (resorufin) was determined using a microplate reader set at 560 nm excitation and 590 nm emission. The “real” fluorescence intensities were determined by subtracting the specimen readings from the negative control, to exclude any

fluorescence input due to the scaffold's composition. In some instances, the seeded scaffolds were then fixed for SEM imaging, as explained in *Section 3.5.5*.

### **3.5.5 Fixing cells for SEM imaging**

The cellular attachment and spreading of the fibroblasts on the various electrospun mats were assessed by SEM. The seeded scaffolds at day 1, 3, and 5 were carefully transferred using sterile tweezers to fresh 24-well plates and thoroughly rinsed in warm Hank's balanced salt solution. Then, the cell-containing scaffolds were fixed overnight at 4 °C with 3% (v/v) glutaraldehyde prepared by diluting 25% glutaraldehyde in an SEM buffer consisting of sodium phosphate and 0.1 M sucrose at pH 7.4. The next day the scaffolds were thoroughly washed in the SEM buffer and gradually dehydrated in ethanol (20%, 35%, 50%, 70%, 95%, and 100%, v/v) for 15-min increments, and left to chemically dry in hexamethyldisilane. The dried specimens were cut using a scalpel, mounted on a metal stub using carbon tape, and sputtered with 10 nm Au. Images were taken at high magnifications to examine the morphological characteristics of the fibroblasts on the electrospun fibrous mats, and at low magnifications to assess the spreading efficiency (confluence). The ImageJ software was used to determine the confluence of the scaffolds (in %) via threshold analysis by determining the proportion covered by fibroblasts over the total area of the scaffold.

### 3.6 Antimicrobial testing on S2 pathogenic bacterial strains

The antimicrobial efficacy of the electrospun hernia meshes was thoroughly assessed using four methods: (1) disc diffusion testing, (3) real-time spectrophotometry (bacterial growth kinetics), (3) live/dead staining using fluorescence and confocal microscopy and (4) morphological evaluation of fixed bacteria-contaminated scaffolds. Experiments were carried out on *Staphylococcus aureus* and *Pseudomonas aeruginosa*, the pathogenic bacterial species most commonly associated with surgical site infection, and by comparing the bicomponent antimicrobial NFs with commercially available hernia meshes and other forms of textile-based fibres using *Escherichia coli*. The techniques used to determine the antimicrobial efficiency of the variant electrospun mats are described in detail in the following sections. As the antimicrobial assessment was conducted on pathogenic bacteria strains, all the processes described below were carried on a biosafety level-2 (BSL-2) laboratory. *E. coli* was only used for a limited number of experiments, due to ongoing refurbishments significantly limiting the access to the BSL-2 facilities, and it was chosen as a similar Gram-negative organism to *P. aeruginosa*.

#### 3.6.1 Disc diffusion susceptibility testing

An initial appraisal of the antimicrobial effect of the core/shell dual antimicrobial system, as well as the single drug-loaded fibre mats, were evaluated via the disc diffusion method based on EN ISO 20645 "...for determining the effect of antibacterial treatments applied to woven, knitted and other flat textiles". The Kirby-Bauer disc diffusion susceptibility test assesses the effect of an antimicrobial compound on agar plates that have been inoculated with a specific pathogen, by the absence or presence of an inhibitory zone.

All media and material were prepared as explained in the Methods Section 3.3.4 and sterilised using a pressure cooker (121 °C, 15 psi for 20 min). Initially, for each experiment, pure strains were isolated for each pathogen using standard Luria broth agar plates, prepared via the streak plate method. Then, the bacterial strains picked from isolated single colonies were cultivated in 10 mL of Lysogeny broth (LB) overnight at 37 °C on a rotary shaker (160 rpm). The following day, 100 µL of the bacterial solution was spread using a sterilised plate spreader on Petri dishes containing Mueller-Hinton agar. Directly after, two 8 mm discs of each antimicrobial electrospun mat, weighing 1–2 mg, were placed firmly on the surface of each plate and incubated for 24 h at 37 °C. CS and PA6-only fibre discs were also prepared as control groups. Images were taken using a petri dish analyser on the following day, and the

radius of inhibition of each plate was measured using ImageJ. The zones of inhibition were measured as:

$$\text{Inhibition zone (IZ)} = \frac{(D - d)}{2} \quad (3.17)$$

where,  $IZ$  the inhibition zone (in mm),  $D$  the total diameter of the antimicrobial disc including the inhibition zone and  $d$  the diameter of the antimicrobial disc. The results are presented as average values  $\pm$  SD, based on two independent experiments, from different electrospun batches, carried in triplicate plates (two discs per plate) for *S. aureus* and *P. aeruginosa*.

### 3.6.2 Bacterial growth kinetics using spectrophotometry

The optical density (OD) that correlates to the number of living bacteria present within the culture after being exposed to the antimicrobial NFs was evaluated using a spectrophotometer at  $OD_{600\text{nm}}$  absorbance.

Pre-cultures of 100  $\mu\text{L}$  *S. aureus*, *P. aeruginosa* and *E. coli* deriving from single colonies, were prepared in 5 mL Brain heart infusion broth (BHI) and incubated for 37 °C at 160 rpm. The following day, the pre-cultures were suspended to  $OD_{600}$  value 0.1 in BHI and incubated for 1 h to obtain exponentially growing cells. After, the culture was resuspended to  $OD_{600}$  value 0.05 in 0.2% (v/v) BHI broth, corresponding to  $2.2 \times 10^7$ ,  $1.8 \times 10^6$ ,  $2.0 \times 10^7$  colony forming units (CFU) per mL of *P. aeruginosa*, *S. aureus* and *E. coli*, respectively. Punched electrospun NF discs of each group examined were then placed on the bottom of a 96-well plate in triplicates and disinfected with UV radiation for 1 h. Subsequently, a bacterial solution of 200  $\mu\text{L}$  was carefully pipetted on each well following the same pipetting motion to ensure similar distribution, and the plate was incubated for a further 4 h at 37 °C/30 rpm.

The ability of the pathogens to recover after being exposed on the antimicrobial scaffolds for 4 h was then determined by carefully pipetting from each scaffold-containing well, 20  $\mu\text{L}$  of the bacterial supernatant, and transferring it to a new 96-well plate. A further 180  $\mu\text{L}$  of “fresh” BHI was pipetted to each well for a final volume of 200  $\mu\text{L}$ . The 96-well plate was then placed on the microplate spectrophotometer, where readings were obtained every 30 min for 24 h at 37 °C at  $OD_{600\text{nm}}$ . The control was prepared out of 180  $\mu\text{L}$  BHI and 20  $\mu\text{L}$  0.2% (v/v) BHI broth. The collected real-time data from triplicates based on two independent experiments, from different electrospun batches, were then plotted on Matlab as average values  $\pm$  SD based on the absorbance over time for each group examined.

### 3.6.3 Fluorescence and confocal microscopy (live/dead assay)

Following the same procedure explained in *Section 3.6.2*, the antimicrobial electrospun discs were incubated for 6 h with bacterial inoculum at OD value of 0.1. After, the pathogen-containing scaffolds were carefully transferred on a fresh 24-well plate and washed thoroughly with PBS. Then, a drop of equal volume mixture of SYTO9® (3.34 mM, Excitation 483 nm, emission 503 nm) and propidium iodide (PI; 20 mM, Excitation 535 nm, emission 617 nm) was placed in the centre of each scaffold and incubated at room temperature for 15-min. The fluorescence-labelled scaffolds were then washed three times with PBS and placed on microscope slides with no. 1 coverslips. Images were taken with a fluorescence microscope, using the 40× objective, and by a confocal microscope using the 63× objective at the aforementioned wavelengths. The relative fluorescent from the metadata was quantified by measuring the intensity of the mean relative brightness value, after subtracting the background signal using ImageJ. From this, the relative percentage (%) of live (Syto9, green)/dead (PI, red) cells was determined as the average values  $\pm$  SD in Matlab.

### 3.6.4 Fixing bacteria for SEM imaging

The morphology of the bacteria at the surface of the electrospun mats was assessed by SEM imaging. The bacteria-containing scaffolds used for the growth kinetic experiments (*Section 3.6.2*) were carefully transferred to a fresh 24-well plate, washed thoroughly with PBS, and fixed in 4% (v/v) formaldehyde solution for 2-h at 4 °C. Subsequently, the fixed bacteria-containing scaffolds were gradually dehydrated in ethanol in 1-h intervals (50%, 60%, 70%, 80%, 90%, 95%, 100% v/v) and left to dry in hexamethyldisilazane (HMDS) overnight. The following day, the dried fixed electrospun mats were considered safe to handle outside the BSL-2 facilities, and thus were sputter-coated with 8 nm gold and imaged by SEM.

### 3.7 Statistical analysis

The results are expressed as mean (or average values)  $\pm$  standard deviation (SD) in all the experiments. Statistical analysis was performed in SPSS (v.24, Statistical Package for Social Sciences, IBM, USA). Diameter distribution graphs were also produced using SPSS. Levene's test of equal variance and an interactive statistical test flowchart; to assess whether the data were normally distributed, were used for the selection of the appropriate statistical tests.

The statistical tests used to assess the statistical significance of the difference between the mean values assuming a confidence level of 95% were: one-way analysis of variance (ANOVA) with post-hoc Tukey test and multiple *Student's t-test with Bonferroni* correction. Significance over post-hoc analysis of multiple groups was only accounted if the statistical tests were  $p \leq 0.05$ . Then statistical significance between the groups was determined by the post-hoc as  $p \leq 0.05$  and  $p \leq 0.001$ , where statistically similar and dissimilar groups are distinguished with the use of letters (a, b, c) and symbols ( $\dagger$ , \$, #).

Graphs and tables were produced using Matlab (v.R2019a, MathWorks Inc., USA). The Korsmeyer-Peppas model fitting of the drug release data was determined using the solver parameters add-on in Excel (v. 2016, Microsoft, USA) to define the KP constant and calculate the exponent variable  $n$ . Fibre diameter, porosity, density, contact angle measurements, the radius of bacterial inhibition, and quantification of relative fluorescence intensity were analysed using ImageJ (v.1.52, National Institutes of Health, USA). Where additional software were used, these are mentioned in the corresponding sections above.

### 3.8 References

1. Yu, J., Lee, A. R., Lin, W. H., Lin, C. W., Wu, Y. K., & Tsai, W. B. (2014). Electrospun PLGA fibers incorporated with functionalized biomolecules for cardiac tissue engineering. *Tissue Engineering - Part A*, 20(14), 1896–1907. <https://doi.org/10.1089/ten.tea.2013.0008>
2. S Bhat, G. (2016). Advances in polymeric nanofiber manufacturing technologies. *Journal of Nanomaterials & Molecular Nanotechnology*, 5(1), 1–5. <https://doi.org/10.4172/2324-8777.1000e108>
3. St Thomas, C., Muñoz López, C. N., Jiménez Regalado, E. J., de Jesús Tellez, M. A., Festag, G., Schubert, U. S., & Guerrero-Sánchez, C. (2020). Preparation of hydrophobically modified associating multiblock copolymers via a one-pot aqueous RAFT polymerization. *Polymer Chemistry*, 11(6), 1249–1249. <https://doi.org/10.1039/d0py90011g>
4. Ifkovits, J. L., Devlin, J. J., Eng, G., Martens, T. P., Vunjak-Novakovic, G., & Burdick, J. A. (2009). Biodegradable fibrous scaffolds with tunable properties formed from photo-cross-linkable poly(glycerol sebacate). *ACS Applied Materials and Interfaces*, 1(9), 1878–1886. <https://doi.org/10.1021/am900403k>
5. Wang, Y., Ameer, G. A., Sheppard, B. J., & Langer, R. (2002). A tough biodegradable elastomer. *Nature Biotechnology*, 20(6), 602–606. <https://doi.org/10.1038/nbt0602-602>
6. Trent, J. S., Couchman, P. R., & Scheinbeim, J. I. (2015). Transmission electron microscope studies of polymers stained with ruthenium and osmium tetroxide. In A. Hiltl (Ed.), *Structure-Property Relationships of Polymeric Solids* (1st ed., vol. 22, pp. 205–213). Cleveland, USA: Plenum Press. [https://doi.org/10.1007/978-1-4684-4613-5\\_12](https://doi.org/10.1007/978-1-4684-4613-5_12)
7. Konno, H. (2016). X-ray photoelectron spectroscopy. In M. Inagaki (Ed.), *Materials Science and Engineering of Carbon* (1st ed., pp. 153–171). Shenzhen, China: Butterworth-Heinemann. <https://doi.org/10.1016/B978-0-12-805256-3.00008-8>
8. British Standards Institution (BSI) (2018). *Plastics — Determination of tensile properties — Part 3: Test conditions for films and sheets (ISO 527-3; BS 2782)*. <https://doi.org/iso.org/standard/70307>
9. Singh, J. P., & Verma, S. (2017). Raw materials for terry fabrics. In J. P. Singh & S. Verma (Eds.), *Woven Terry Fabrics* (1st ed., pp. 19–28). New Delhi, India: Woodhead Publishing. <https://doi.org/10.1016/b978-0-08-100686-3.00003-7>
10. Tessier, D. (2018). Testing thermal properties of textiles. In P. Dolez, O. Vermeersch, & V. Izquierdo (Eds.), *Advanced Characterization and Testing of Textiles* (1st ed., pp. 71–92). Alberta, Canada: Woodhead Publishing. <https://doi.org/10.1016/B978-0-08-100453-1.00005-2>
11. Nasrollahzadeh, M., Atarod, M., Sajjadi, M., Sajadi, S. M., & Issaabadi, Z. (2019). Plant-mediated green synthesis of nanostructures: Mechanisms, characterization, and applications. In S.J. Park & M.K. Seo (Eds.), *Interface Science and Technology* (1st ed., vol. 28, pp. 199–322). Shanghai, China: Elsevier. <https://doi.org/10.1016/B978-0-12-813586-0.00006-7>
12. Ferrari, M., Cirisano, F., & Morán, M. C. (2019). Mammalian cell behavior on hydrophobic substrates: Influence of surface properties. *Colloids and Interfaces*, 3(2), 1–18. <https://doi.org/10.3390/colloids3020048>
13. Cheng, Y., Feng, G., & Moraru, C. I. (2019). Micro-and nanotopography sensitive bacterial attachment mechanisms: A review. *Frontiers in Microbiology*, 10(2), 1–13. <https://doi.org/10.3389/fmicb.2019.00191>
14. Anderson, J. M., & Schoen, F. J. (2013). *In vivo* assessment of tissue compatibility. In W. R. Wagner, S. E. Sakiyama-Elbert, G. Zhang, & M. J. Yaszemski (Eds.), *Biomaterials Science: An Introduction to Materials* (3rd ed., pp. 609–617). Pittsburgh, USA: Elsevier. <https://doi.org/10.1016/B978-0-08-087780-8.00054-1>
15. Lau, C. C., Bayazit, M. K., Knowles, J. C., & Tang, J. (2017). Tailoring degree of esterification

- and branching of poly(glycerol sebacate) by energy efficient microwave irradiation. *Polymer Chemistry*, 8(26), 3937–3947. <https://doi.org/10.1039/c7py00862g>
16. Baishya, H. (2017). Application of mathematical models in drug release kinetics of Carbidopa and Levodopa ER tablets. *Journal of Developing Drugs*, 6(2), 1–8. <https://doi.org/10.4172/2329-6631.1000171>
  17. Ghobeira, R., Philips, C., Declercq, H., Cools, P., Geyter, N. De, Cornelissen, R., & Morent, R. (2017). Effects of different sterilization methods on the physicochemical and bioresponsive properties of plasma-treated polycaprolactone films. *Biomedical Materials*, 12(1), 1–13. <https://doi.org/10.1088/1748-605X/AA51D5>
  18. Andrews, K. D., Hunt, J. A., & Black, R. A. (2007). Effects of sterilisation method on surface topography and in-vitro cell behaviour of electrostatically spun scaffolds. *Biomaterials*, 28(6), 1014–1026. <https://doi.org/10.1016/j.biomaterials.2006.10.014>
  19. Griffin, M., Naderi, N., Kalaskar, D. M., Malins, E., Becer, R., Thornton, C. A., Whitaker, I. S., Mosahebi, A., Butler, P. E. M., & Seifalian, A. M. (2018). Evaluation of sterilisation techniques for regenerative medicine scaffolds fabricated with polyurethane nonbiodegradable and bioabsorbable nanocomposite materials. *International Journal of Nanomaterials*, 8(1), 1–15. <https://doi.org/10.1155/2018/6565783>
  20. Khor, E., & Lim, L. Y. (2003). Implantable applications of chitin and chitosan. *Biomaterials*, 24(13), 2339–2349. [https://doi.org/10.1016/S0142-9612\(03\)00026-7](https://doi.org/10.1016/S0142-9612(03)00026-7)
  21. Chan, L. L. Y., Rice, W. L., & Qiu, J. (2020). Observation and quantification of the morphological effect of trypan blue rupturing dead or dying cells. *PLOS ONE*, 15(1), 1–17. <https://doi.org/10.1371/journal.pone.0227950>





---

# Chapter 4

## Nozzle-Free Electrospinning of PVP/PGS Blends; Design, Fabrication & Characterisation

---

### 4.1 Introduction

This chapter describes the design and development of a nozzle-free roller electrospinning device and explores its potential to produce synthetic polymer-based nonwoven fibrous scaffolds as dermal substitutes consisting of variant proportions of PVP and PGS blends. Due to the non-linear, anisotropic and viscoelastic properties of the skin, which, as previously discussed, differ among different anatomical sites, in this work the mechanical properties of the electrospun mats were examined for variant compositions of PVP/PGS fibres by adjusting the blend ratio and the PVP's molecular weight. Subsequently, the electrospun mats were submerged in a riboflavin solution and crosslinked using UV radiation to prevent the rapid degradation of the composite fibres, and, thus, be able to assess the wettability and biocompatibility of the biomaterial using human dermal fibroblasts (HDFs).

The work presented in this chapter has been published in *Medical Engineering and Physics* (Keirouz et al., 2019), with a conference abstract presented at the Electrospin 2018 conference in Stellenbosch, South Africa, where it was awarded first place for the best poster presentation (Appendix B).

### 4.2 Methodology

For full descriptions of the materials and methods used, please see the following sections in *Chapter 3*:

- Materials (Section 3.3)
  - Synthesis of PGS (Section 3.3.1)
  - List of materials, cells, suppliers and equipment (Section 3.3.2)

- Scaffold characterisation (Section 3.4)
  - Scanning electron microscopy (SEM) (Section 3.4.1)
  - Fourier transform infrared spectroscopy (FTIR) (Section 3.4.3)
  - X-ray photoelectron spectroscopy (XPS) (Section 3.4.4)
  - Mechanical testing (Section 3.4.5)
  - Water contact angle measurements (WCA) (Section 3.4.8)
- *In vitro* evaluation (Section 3.5)
  - Scaffold sterilisation (Section 3.5.1)
  - Cell culture technique (Section 3.5.2)
  - Cell seeding efficiency (Section 3.5.3)
  - Cell proliferation (Section 3.5.4)
  - Fixing cells for SEM imaging (Section 3.5.5)

The chapter-specific experimental methods are described, in detail, below.

### 4.2.1 Device development

A schematic of the nozzle-free electrospinning device developed for the work conducted in *Chapters 4* and *5* is shown in Figure 4.1. The setup consists of a rectangular glass tank (aquarium), a three-layer lid assembly, a collector assembly, a spinneret assembly and electronics. Computer-aided designs (CADs) and photographs of the different assemblies can be found in Appendix A: Figure A-3, A-4, A-5 and A-6.

As electrospinning uses high voltage to electrify the polymer solution and draw fibres, the non-conductive compartments of the setup were based on reinforced glass, polytetrafluoroethylene (PTFE; Teflon®) and poly(ether ketone) (PEEK) due to the materials' good thermal, mechanical, and insulating properties.

In total, 16 holes were carefully drilled in various compartments of the glass aquarium using a circular diamond-tipped drill bit hole saw and drill positioning tools. On the upper section, three holes were drilled to position the collector's DC motor, at the same height and on the opposite side, four holes were made to position the metal bearing, one hole at the same height facing the rear of the device for the entry of the high-voltage electrode, and one hole for the exit of the safety interlock cables. On the lower part of the setup, an additional three holes were made to install the spinneret's DC motor parallel to the collector's DC motor, and one hole at the same height facing the rear of the aquarium for the entry of the high-voltage

electrode. A wider hole was also made on the lower rear for the placement of the exhaust tubing. Finally, two holes were made below and antiparallel to the collector's direction to place the safety rod.

At the top of the glass tank, two rectangular acrylic pieces were glued on, using epoxy, facing inwards and parallel to each other, to support the placement of the lid. A safety interlock was mounted on one of the rectangular acrylic pieces, at the midsection between the top of the aquarium and the lid support, where the interlock cables were then soldered to prevent the onset of high voltage at the absence of the lid.

The collector assembly consisted of a Teflon mandrel with a mid-section stainless-steel bearing cylinder being fitted through it, a motor and a stripped HV cable made into a loop. The collector was positioned on the upper section of the device through a metal bearing with a 3D-printed support from one side and a DC motor on the other side using flexible 3D-printed couplers. The collector was fitted with a brushed DC motor rated at 500 revolutions per minute (rpm) when unloaded, with the ability to adjust the rpm appropriately by utilising two controlling mechanisms, one being the speed controller and the other being the DC source feeding the circuit. The device was able to operate with an output voltage 12 V in 0.1 V increments and an output current between 0 and 5 A with 0.1 A increments. Finally, the HV electrode was positioned on the side of the stainless-steel cylinder allowing for good contact with the stripped HV wire.

The spinneret assembly consisted of a Teflon bath, a solid stainless-steel cylinder, a Teflon rod, a PEEK coupler, a HV wire loop and a 12 V DC gear motor. As in free surface electrospinning, the fibres are generated in an upward motion; the Teflon pool was placed on the bottom of the aquarium, parallel to the centre of the collector's surface. Wei et al. [1] found that the electric field intensity reaches the highest values at the ends of the cylinder spinneret and decreases towards the centre, which may hamper jet formation. Electric field profile and intensity simulations using COMSOL have demonstrated that, although the highest electric field profile is generated towards the centre of an annular spinneret, the electric field intensity is at least a 5-fold higher at the edges [1]. For this reason, the stainless-steel spindle presented smooth rounded edges to create a homogenous electric field distribution. A HV wire loop was made by soldering the HV electrode at a radius that provided good contact with the cylinder's surface while allowing it to rotate.

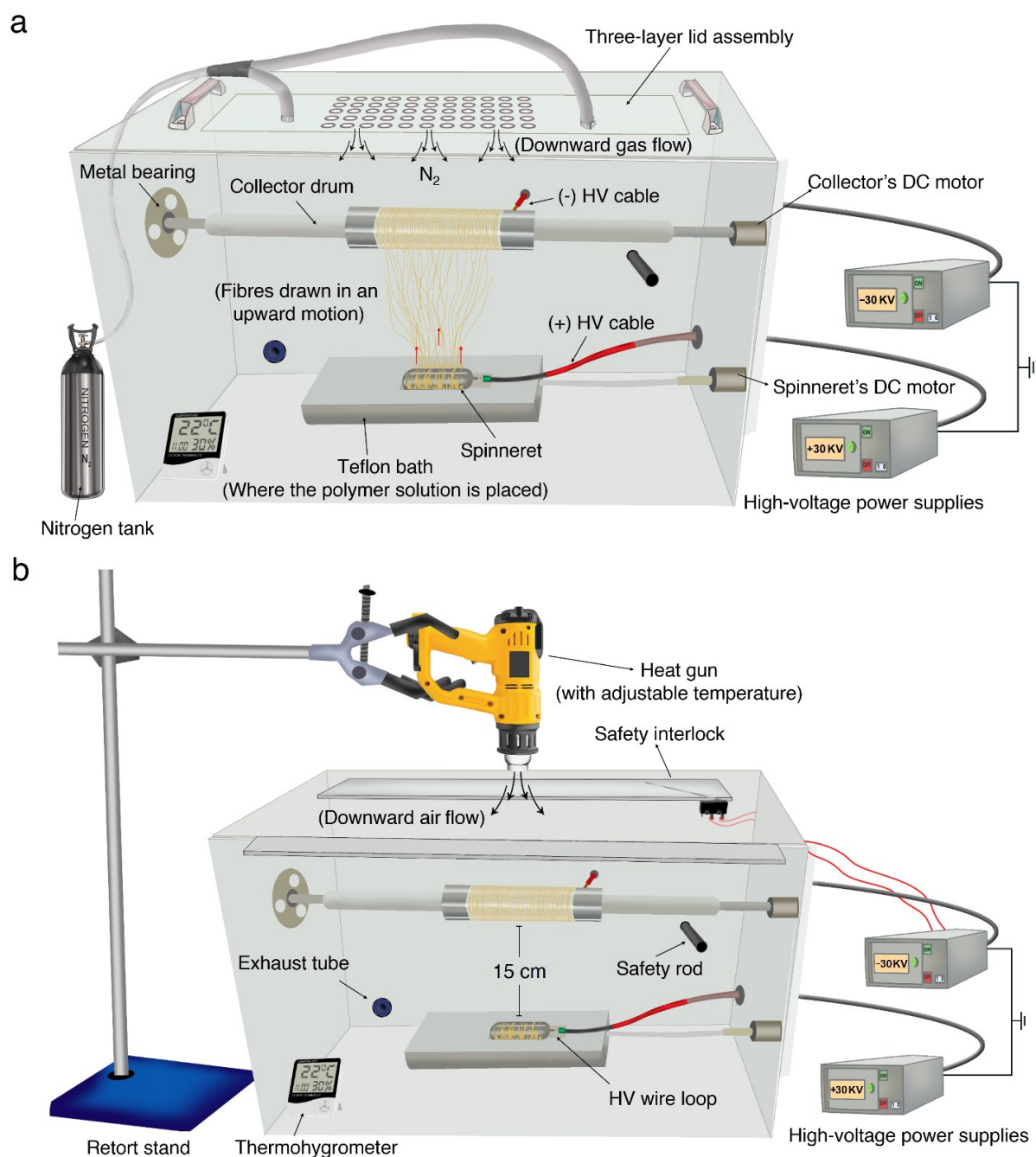


**Figure 4.1** Schematic of the nozzle-free electrospinning device. **(a)** Gas flow provided via the lid assembly within an enclosed setup, **(b)** hot air flow provided via a heat gun, on an open setup. Values on the thermohydrometer and high-voltage power supplies are indicative. HV; high voltage.

The solution bath was machined from a Teflon rod stock to form a rectangular pot that can facilitate the electrospinning of a 40 mL polymer solution (solution bath dimensions: 90 mm (length)  $\times$  30 mm (width)  $\times$  20 mm (depth)) while accommodating the HV electrode. A hole

was drilled on the upper level of the rectangular pot to position the spinneret. Then, an opening was drilled through the other side, where a Teflon rod and a PEEK coupler were used to connect the spinneret with the DC motor. The solution bath, within which the spinneret was submerged, provided a 5% margin on each side of the spinneret to allow for its rotation and polymer coating, and a 10% margin on the coupler-rod side for the positioning of the HV loop. Allowing minimal exposure of the polymer solution is an important aspect of the device, which provides shelter to volatile solvents and allows consistency throughout the electrospinning process. The distance between the spinneret and the collector was 15 cm.

The lid assembly was made up of three rectangular glass plates. The layered glass assembly ensured uniform distribution of air/nitrogen across the glass aquarium. The outermost glass layer had 55 holes of 3 mm diameter arranged at five rows and 11 columns, similar to a perforated glass. A rectangular glass piece was cut out from the middle glass plane at the same position where the 55 holes were presented on the bottom glass plane to allow for the gas distribution. The top glass plane presented two openings for Swagelok tube fittings from where the tubing linked to the gas supply was connected to the lid. An open setup, where a heat gun could be positioned on adjustable heights using a retort stand, was also included for solutions that require hot air rather than air/gas for electrospinning.

Two high voltage DC power supplies, of adjustable output voltage, one of negative and one of positive voltage output were utilised to electrify the polymer solution and draw the fibres towards the collector. Both were able to be adjusted from 0 kV up to 35 kV, thus allowing the user to set a potential difference of up to 70 kV between the rotating collector and the spinneret. A thermohygrometer was also placed within the aquarium to monitor the temperature and humidity of each experiment.

## 4.2.2 Preparation of PVP/PGS Blends

The PGS polymer was synthesised as described in *Section 3.3.2*. Then, PGS was dissolved in HFIP to form 15% (w/v) polymer solution. PVP with molecular weights of 360,000 g·mol<sup>-1</sup> and 1,300,000 g·mol<sup>-1</sup> were dissolved separately in a solvent system encompassing 1:1:0.25 (v/v) ratio of DMF: ethanol: distilled water to form 11.75% (w/v) polymer solution.

**Table 4.1** Summary of the polymer blend constituents and blending ratios.

Polymer blend	Ratio (PVP/PGS) (w/w)
i. 11.75% PVP (w/v) (MW = 1,300,000)	100:0
+	95:5
15% (w/v) PGS	90:10
<b>&amp;</b>	<b>80:20</b>
ii. 11.75% (w/v) PVP (MW = 360,000)	<b>70:30</b>
+	<b>60:40</b>
15% (w/v) PGS	50:50

All solutions were stirred overnight at room temperature before blending. Subsequently, blends of 100:0, 95:5, 90:10, 80:20, 70:30, 60:40 and 50:50 w/w ratio of PVP/PGS (Table 4.1) were prepared and mixed for an additional 12 h at room temperature before electrospinning.

## 4.2.3 Scaffold fabrication and processing

The nozzle-free electrospinning device described in *Section 4.2.1* comprised of a rotating stainless steel cylinder electrode submerged within the Teflon pool containing the polymer solution blends, was used to produce fibres over a biased rotating collector electrode under constant hot air flow (working distance 15 cm, airflow 450 L·min<sup>-1</sup>, and applied temperature 150 °C). A potential difference of 60 kV DC was applied between the two rotating electrodes (+30 kV on the spinneret's electrode and -30 kV on the collector's electrode), resulting in the formation of multiple Taylor cones along the polymer solution-coated rotating electrode surface, from which jets stretched to form fibres in an upward motion. A cellulose-based commercial baking paper was used to collect the fibres. All experiments were carried out under ambient conditions at a relative humidity ranging from 30%–40% and room temperature of 18–22 °C. Figure 4.2 summarises the PGS synthesis, blending and fabrication procedure.

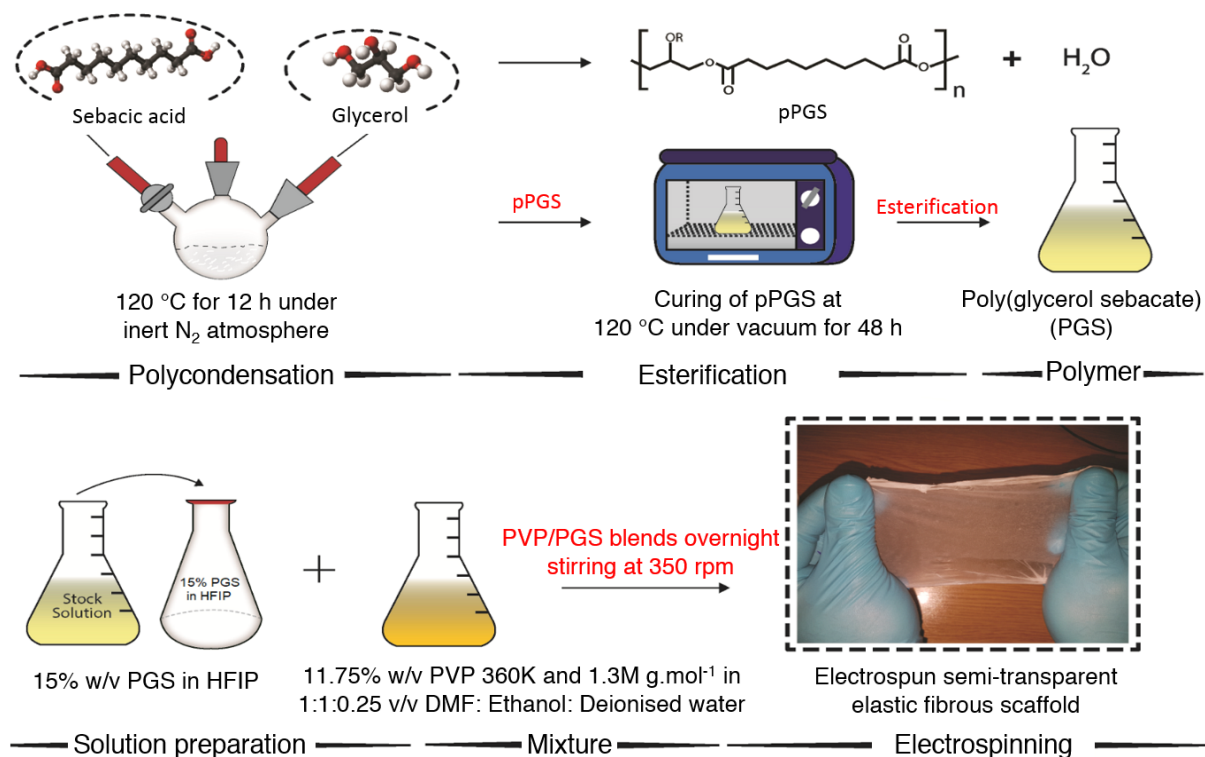


**Figure 4.2** Schematic illustration providing an overview of the PGS synthesis, solution preparation and electrospinning that results in stretchable semi-transparent fibrous mats.

#### 4.2.4 UV crosslinking of PVP/PGS mediated by riboflavin

The dried PVP/PGS electrospun membranes were UV irradiated to induce crosslinking of the two polymers in the presence of a photoinitiator. Riboflavin solution (0.2 mM) was dissolved in a potassium phosphate buffer at pH 8.0 under constant agitation for 2 h and was used as the photosensitizer for crosslinking [2, 3]. Then, the electrospun membranes were submerged within the riboflavin solution and irradiated in the dose of 5 kGy for 30 and 60 min distributed from a 15 cm distance between the exposed surface and the halogen lamp. The light source produced an intensity of  $\sim 45 \text{ mW}\cdot\text{cm}^{-2}$  using a UV lamp (Novascan, USA). The crosslinked membranes were then removed and washed in PBS at pH 7.4.

Photochemical reactions are the result of the interaction between molecules and light. Molecules are able to absorb radiation, leading to different electronic transitions that depend on the particular structural characteristics of the molecule being radiated. In this regard, electrons can “jump” between different molecular orbitals depending on the energy gap; if the energy of the light is equivalent to the energy difference between two molecular orbitals for a specific molecule, then an electronic transition will occur (See Figure 4.3) [4].



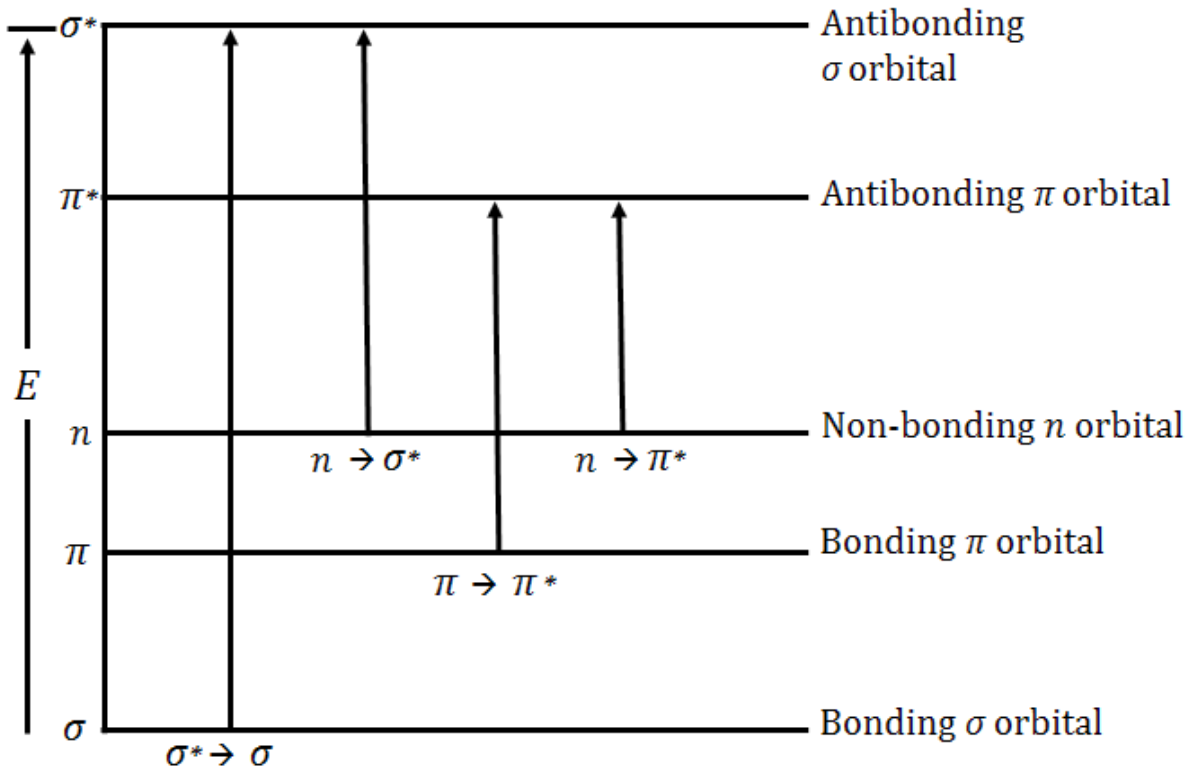


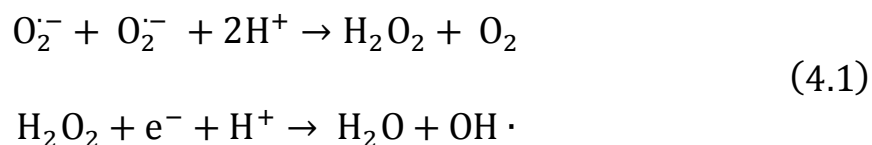
**Figure 4.3** Energy gaps of the different electronic transitions upon light absorption. Redrawn from [4].

Due to conjugation, which decreases the energy gap between non-bonding  $\pi$  electrons and the  $\pi^*$  anti-bonding orbital, riboflavin is a molecule that is capable of absorbing radiation in the visible region of the spectrum, thus acquiring a yellow colour [5, 6]. Once blue or UVA light is absorbed, riboflavin is excited to a singlet state of higher energy (mainly by  $\pi \rightarrow \pi^*$  transitions) that transforms, then, into a triplet state by non-radiating phenomena [5, 6]. The singlet state is characterised by the existence of two unpaired electrons with paired spin, while, in the triplet state, the electron's spin is unpaired. The triplet state has a larger lifespan in comparison to the singlet state. From the triplet excited state, the riboflavin molecule can induce several changes to its environment, mainly based on two routes:

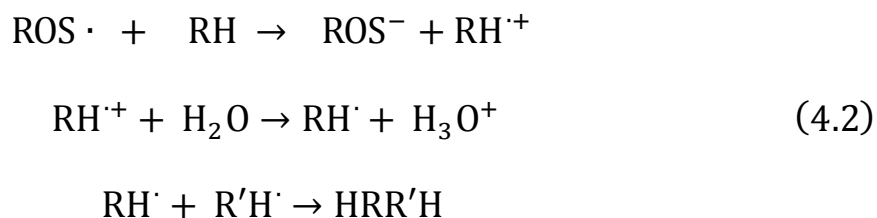
- i. Type I reactions. In this type of reaction (Appendix A: Figure A-7), riboflavin interacts with a substrate and transfers an electron or hydrogen atom that leads to the formation of a radical substrate and radical riboflavin. The radical riboflavin then interacts with the dissolved oxygen in the medium, leading to the formation of reactive oxygen species that can further interact with the polymer to induce radical reactions, which can subsequently increase the crosslinking degree [5, 6]. In general, this route is more common when the dissolved oxygen concentration is low.

- ii. Type II reactions. Riboflavin in the triplet excited state reacts directly with molecular oxygen in the triplet ( $^3\text{O}_2$ ) state (the most common and stable allotrope of oxygen) to produce singlet oxygen, which is much more reactive than the triplet oxygen allotrope (Appendix A: Figure A-8). This molecule can thereupon produce other reactive oxygen species (hydroxyl, peroxide), which can react with the polymer, inducing a greater degree of crosslinking [5, 6].

In both scenarios, the reaction pathway leads to the production of radicals and reactive oxygen species that ultimately allow the crosslinking of the polymer. In this regard, it is important to notice that the superoxide anion can produce new radicals, based on [7]:



Which ultimately induces this series of reactions:



Where *ROS* is reactive oxygen species, *R* and *R'* (as illustrated in Appendix A: Figure A-9) can be any of the pendant groups of the crosslinked PGS. Thus, the addition of riboflavin enhances the crosslinking degree and can have a direct impact on the properties of the final polymer. The same crosslinking reaction also applies for the PVP chains, where the pendant groups may react with the sebacic acid residues of the PGS (Appendix A: Figure A-10). In accordance, below is a summary of the proposed reaction scheme that can describe the crosslinking between PGS and PVP facilitated by riboflavin under UV irradiation (See Figure 4.4).

In Figure 4.4, the third step of the reaction occurs after the PGS and PVP radical cations have transferred a proton to water (as described in the second reaction of equation 4.2). The scheme indicates one possibility among several others, depending on which bond or atom bears the unpaired electron. The riboflavin radical anion leads to the production of superoxide anions (as described in equation 4.1) that may also induce crosslinking reactions. Furthermore, the excited riboflavin decomposes, leading to the production of several other molecules that may also act as photosensitisers. Thus, as can be noted, many schemes in the presence of riboflavin can directly or indirectly induce the photocrosslinking of the PVP/PGS fibres.

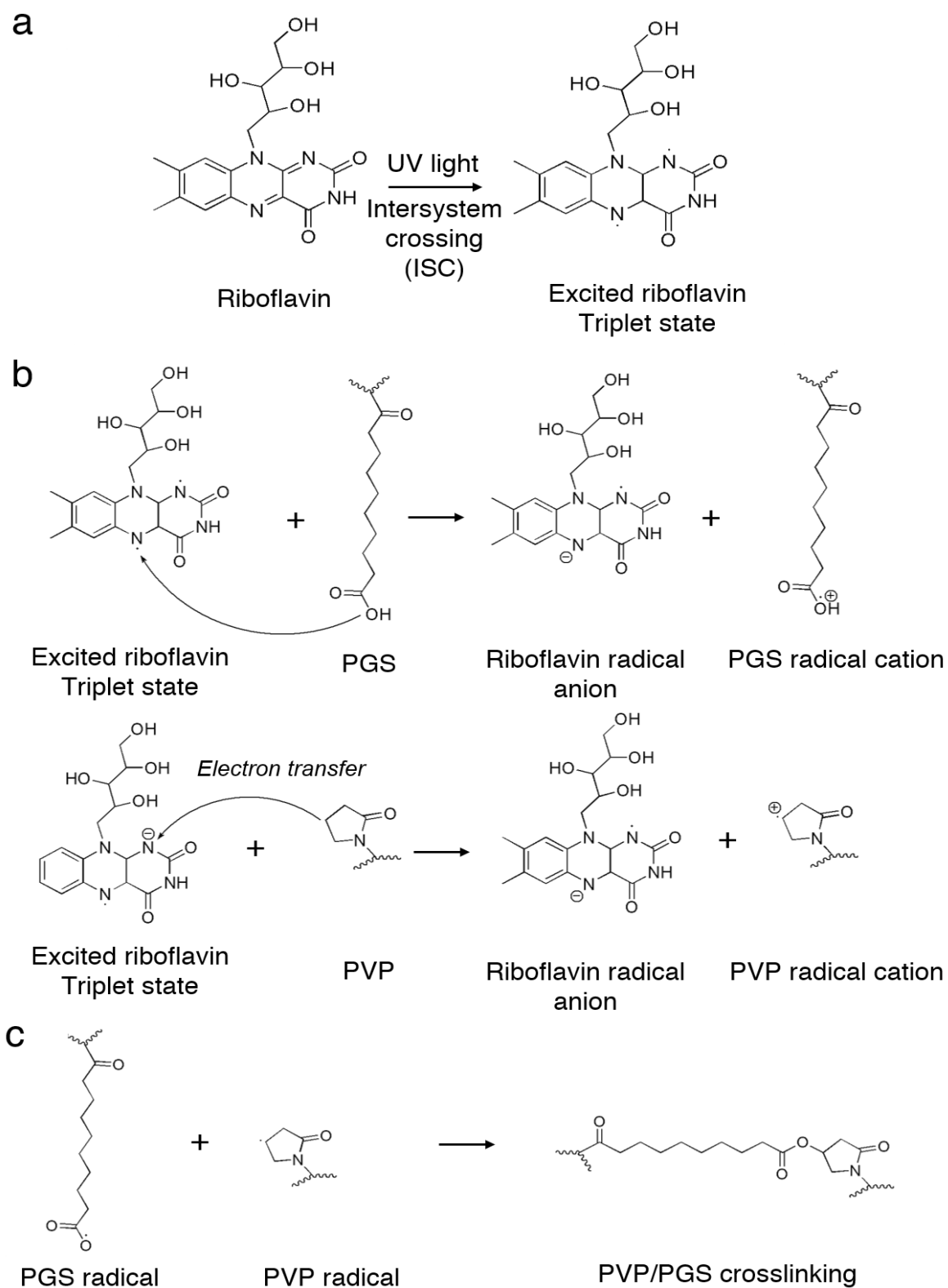


**Figure 4.4** Schematic representation of the PVP/PGS crosslinking mediated by riboflavin under UV light.

## 4.3 Results and discussion

### 4.3.1 Production rate of the nozzle-free device

Nozzle-free electrospinning allows jets to form and stretch from multiple locations at once, thus significantly increasing the production rate in comparison to the conventional needle-based electrospinning setups. While electrospun fibres are vastly suitable for the fabrication of tissue engineering constructs, the low yield of the needle-based electrospinning devices limits the ability to scale up the production, even if this may not constitute a problem in a laboratory setting. The development of multi-needle apparatuses was proven ineffective due to overlapping electrostatic forces between the needles, affecting the travel path of the independent Taylor cone jets [8]. The production rate of the in-house built nozzle-free apparatus developed for this study was compared with a commercial single-nozzle electrospinning device under optimal conditions for an hour using 7.5% (w/v) PCL. As shown in Figure 4.5, the nozzle-free electrospinning device was able to produce and collect dry fibres at an 11-fold increased rate than the conventional electrospinning setup within the span of an hour. These findings are in agreement with a previously published work [9].

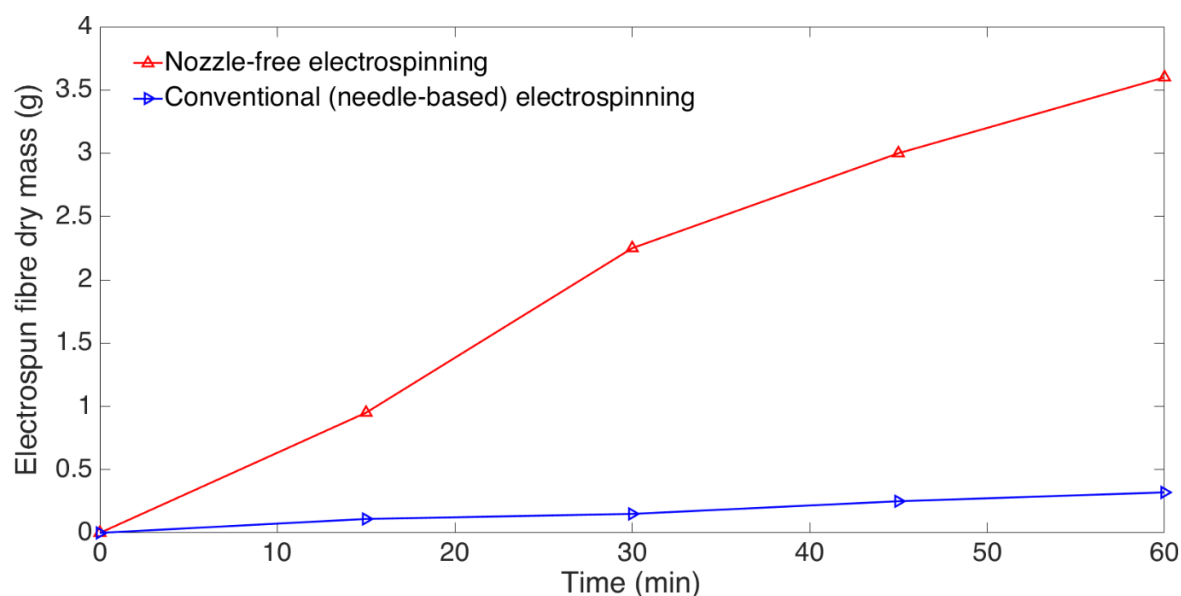


**Figure 4.5** Comparison of the production rate between the in-house built nozzle-free electrospinning device, and a commercial needle-based electrospinning device. PCL 7.5% (w/v) dissolved in HFIP. Nozzle-free electrospinning: 60 kV, conventional electrospinning: 16 kV (+12/-4, 10  $\mu\text{L}\cdot\text{min}^{-1}$ ), needle-tip-to-collector distance 15 cm.

### 4.3.2 The effect of varying the molecular weight of PVP on the fibre morphology

Electrospinning thermosets, such as PGS, can be challenging since uncured pre-polymer forms tend to be very viscous and sticky, whereas their cured counterparts are insoluble in most organic solvents, owing to a low glass transition temperature ( $T_g$ ), eventually forming non-fibrous plasticised scaffolds [10, 11]. By increasing the thermal condensation period during the polymerisation process, the esterification degree of the PGS polymer also increases, where the polar solvents HFIP and tetrahydrofuran (THF) are able to dissolve the chains of the PGS polymer, providing it is dissolved before setting into room temperature and while still in a less-viscous liquid form [12].

Nevertheless, PGS cannot be electrospun without conjugating with polymers that can promptly form fibres [10, 13]. Several polymers, including PCL [14–16], gelatine [17, 18], PVA [10, 19], poly(L-lactide) (PLLA) [20] and PEO [21], have been used as carrier polymers to facilitate the formation of PGS fibres. In this work, PVP was incorporated within the polymer blends to improve the electrospinnability of the synthesised PGS. As PVP is a hydrophilic polymer – dissolvable in water, alcohols and polar solvents – the produced PVP/PGS electrospun mats were photocrosslinked to prevent the rapid degradation of the PVP and, thus, be able to assess cell growth and proliferation on HDFs [22].

Figure 4.6 shows the average fibre diameters and SEM micrographs of the various groups of PVP/PGS electrospun mats produced for 1.3M and 360K  $\text{g}\cdot\text{mol}^{-1}$  PVP. For all the blends, the concentration of PGS is 15% (w/v), whereas the PVP is 11.75% (w/v). Morphologically, the fibre network displays a random ECM-like architecture. The cotton candy-like macroscopic morphology of the PVP mats transformed into paraffin-like scaffolds as the concentration of PGS gradually increased within the blends. This parafilm-like semi-transparent morphology, a trait that is difficult to obtain while attaining a fibrous micro-/nanostructure, can be of use during the wound healing process by allowing the visual monitoring of the wound bed. Figure 4.7 presents photographs that depict the effect of the incremental increase of PGS within the polymer blends toward the transparency of the electrospun composite membranes.

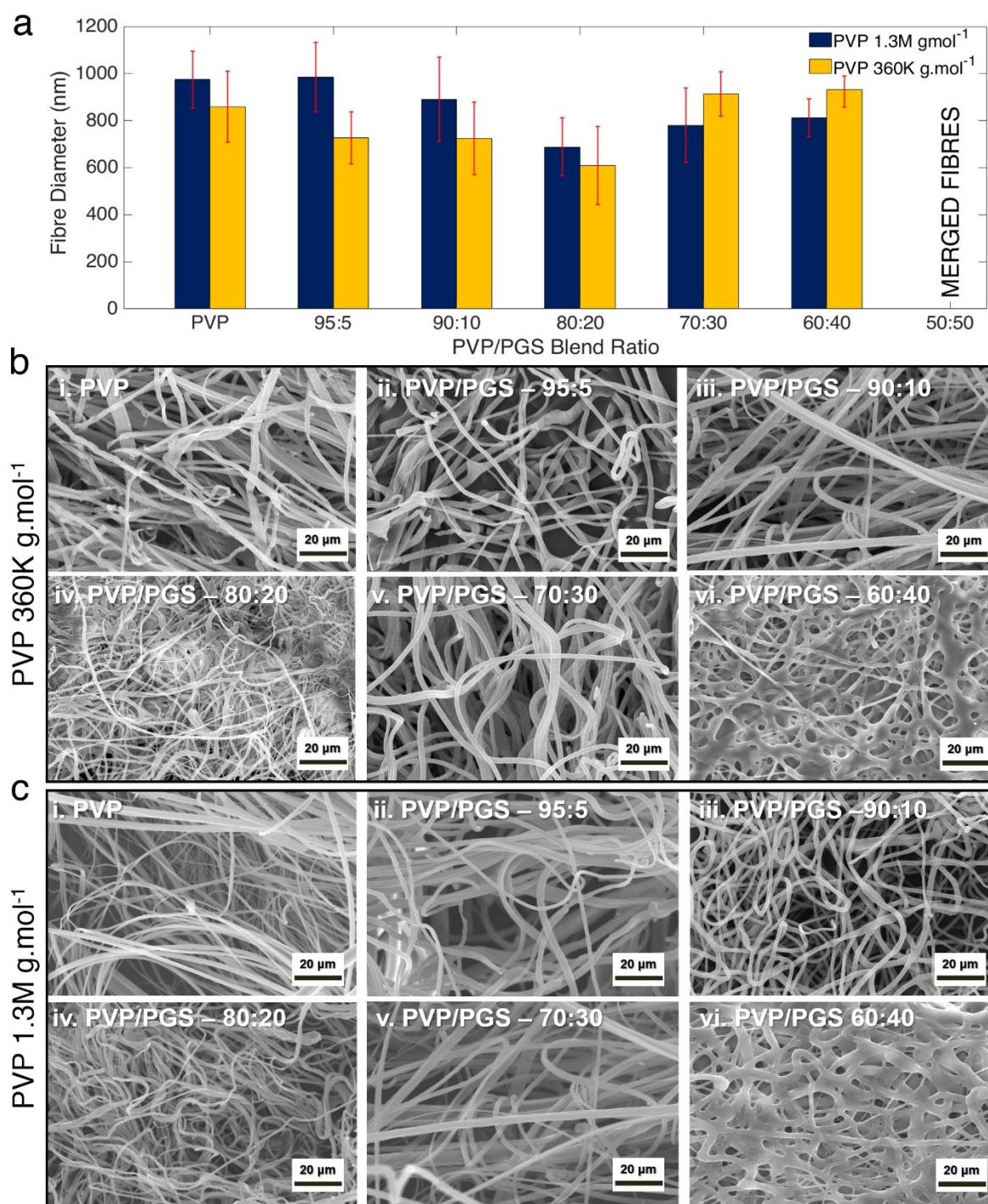


**Figure 4.6** Electrospun scaffolds morphology. **(a)** Average fibre diameters for the variant groups of PVP/PGS examined. Representative SEM micrographs of fibres produced with PVP **(b)** 360K g.mol<sup>-1</sup> and **(c)** 1.3M g.mol<sup>-1</sup>. PVP/PGS ratios are as follows; **(i)** 100:0, **(ii)** 95:5, **(iii)** 90:10, **(iv)** 80:20, **(v)** 70:30 and **(vi)** 60:40. Scaffolds photographs in Appendix A: Figure A-10.

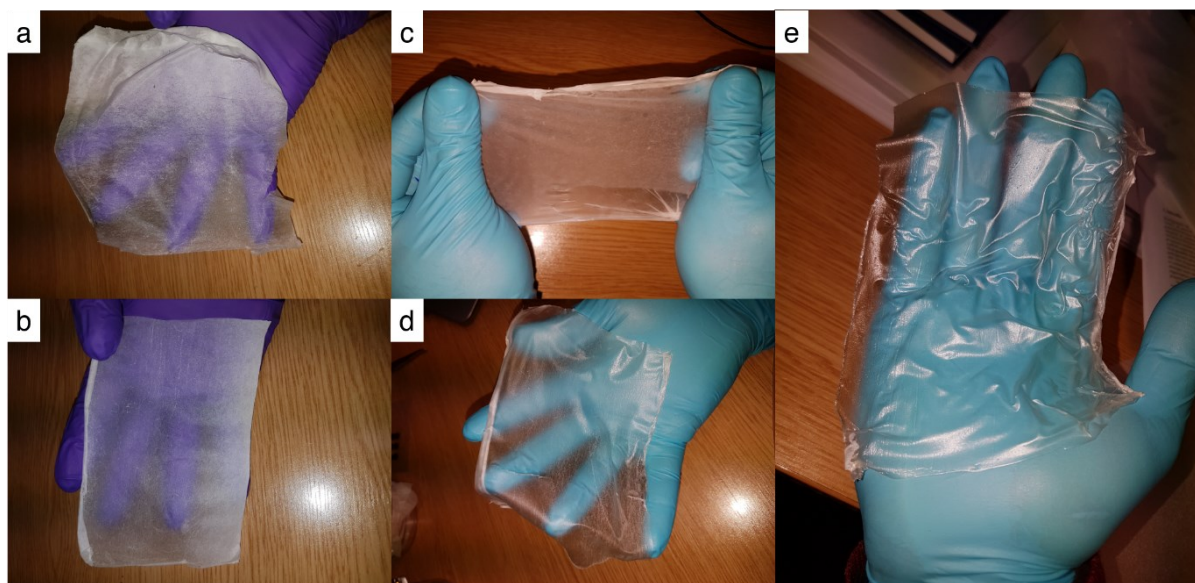


**Figure 4.7** Photographs depicting the transparency of the electrospun membranes apropos to the incremental increase in the proportion of PGS within the PVP/PGS blends; **(a)** 90/10, **(b)** 80/20, **(c)** 70/30, **(d)** 40/60, and **(e)** 50/50 PVP/PGS. The electrospun membranes were produced using PVP 1.3M g·mol<sup>-1</sup>.

A more gelatinised morphology with less homogenous fibre appearance is present for the blends with increased PGS concentration, where the scaffolds appear to form porous gel-like mats, due to PGS being sprayed on the PVP fibres during the electrospinning process. The average fibre diameter of the PVP-only fibres was  $0.97 \pm 0.65 \mu\text{m}$  and  $0.85 \pm 0.58 \mu\text{m}$  for 1.3M and 360K g·mol<sup>-1</sup>, respectively. The average fibre diameter between the blends did not appear to be significantly affected by increasing the PGS concentration; with the 50:50 (w/w) PVP/PGS blend ratio, the fibres appeared to have completely merged, forming a porous gel structure. Nonetheless, the mean pore area appeared to gradually decrease from  $8.52 \pm 0.65 \mu\text{m}^2$  for the pure PVP scaffolds to  $0.70 \pm 0.18 \mu\text{m}^2$  for the 50:50 PVP/PGS blends. The high density of the electrospun membranes in conjunction with the small-diameter pores could further form a barrier to bacterial colonising the wound bed, by (1) minimising exogenous microbial contamination and by (2) decreasing the bacterial load that can trespass to the wound bed by the surrounding tissue.



### 4.3.3 Chemical characterisation

The FTIR was conducted to verify the synthesis of PGS and the presence of the two polymers within the composite fibre composition. The single signal immense loop at the  $1740\text{ cm}^{-1}$  region suggests a very saturated (double-bonded) molecule of strong ester linkages (C=O). At approximately  $3050\text{ cm}^{-1}$ , a stretch is apparent between the hydrogen (X-H) region and the broad loop forming out of a single peak at  $3460\text{ cm}^{-1}$ , which indicates the presence of -OH groups. Two peaks are also present at approximately  $2930\text{ cm}^{-1}$  and  $2860\text{ cm}^{-1}$ , characteristic of C-H  $sp^2$  and  $sp^3$  hybridisations, respectively. The results confirm the successful synthesis of PGS and are in agreement with previously published works [23, 24].

For the PVP/PGS electrospun mats, the stretches at  $2850\text{ cm}^{-1}$  and  $1420\text{ cm}^{-1}$  can be assigned to C-H and -CH<sub>3</sub>  $sp^3$  hybridisations, respectively, while the vibration at  $1280\text{ cm}^{-1}$  to cyanide (CN) stretching of the PVP's lactam ring [25–27]. The PVP/PGS fibres present the distinct peaks of both polymers, at similar intensities to the pristine materials, with no significant shifts present, indicative of successful blending of the two components in the composite fibres. The intense band present at  $1650\text{ cm}^{-1}$  can be attributed to dipole (C=O) stretching of the primary amide and the strong signal at  $1752\text{ cm}^{-1}$  to conjugated ester stretching (C=O), both indicative of the PVP/PGS fibres crosslinking. The spectra of the composite fibres, polymers, glycerol and sebacic acid are presented in Figure 4.8.

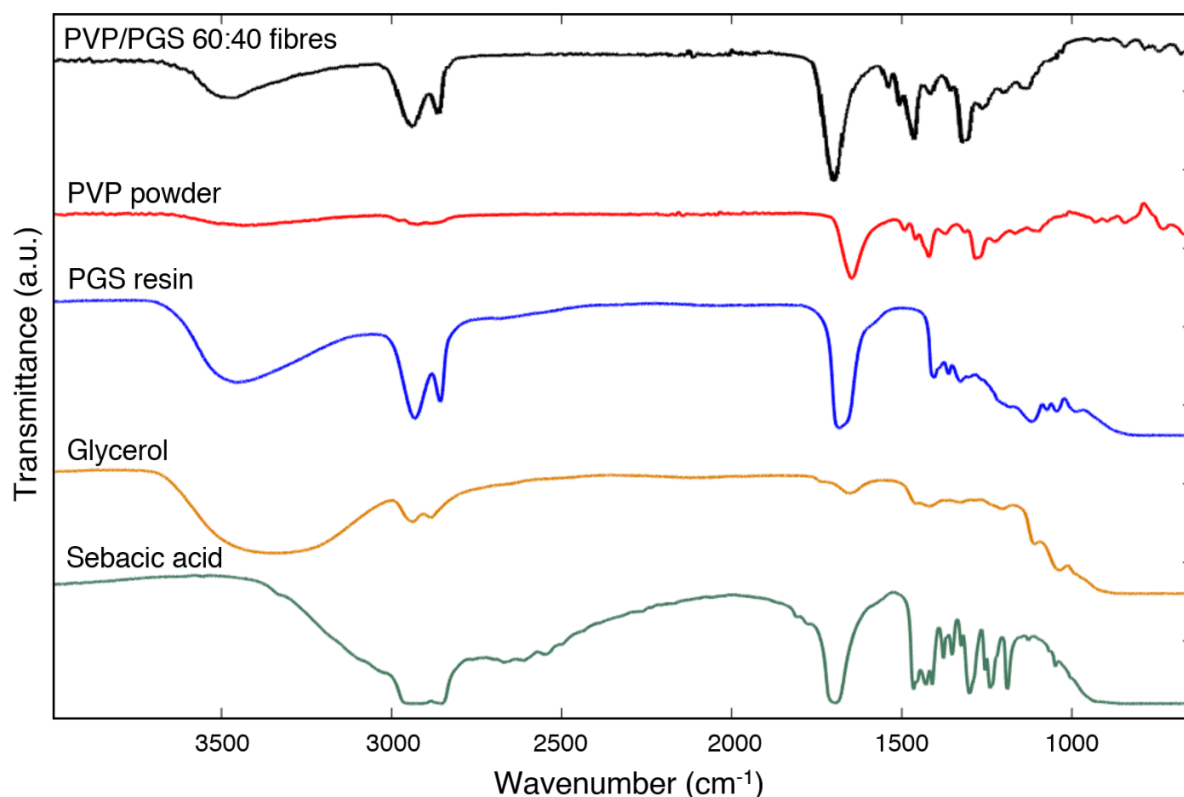


**Figure 4.8** ATR-FTIR spectra of sebacic acid (green); glycerol (yellow); PGS resin (blue); PVP powder (red); and PVP/PGS60:40 fibres (black).

The surface composition of the electrospun mats was examined by XPS incorporating an information depth of about 10 nm. Table 4.2 displays the elemental ratios of each composite fibre group after UV irradiation for 30 min. The surface elemental composition does not appear to be highly affected between the various composite fibres where the chemical distribution correlates to the theoretical composition values within a 5% margin of error. No differences in the ratio profile of each blend are apparent when comparing the two distinct molecular weights of the PVP. As PGS ((C<sub>13</sub>H<sub>22</sub>O<sub>5</sub>)<sub>n</sub>) does not contain nitrogen atoms, as in the case of PVP with a chemical structure of (C<sub>6</sub>H<sub>9</sub>NO)<sub>n</sub>, it is feasible to distinguish the latter one. The presence of the N1s peak between 398–399 eV in all the PVP/PGS samples confirms the presence of PVP within the composite fibres after submersion in riboflavin during photocrosslinking. In the case of blends with an increased concentration of PVP, the nitrogen content appears to be lower than the predicted values for a homogenous mixture. This depletion of nitrogen on the fibres' surface can be construed by the way the fibres are formulated during the electrospinning process, where rapid solvent evaporation and polymer chain migration of the longer PVP chains, in comparison to the PGS, shelter the nitrogen by moving it towards the core of the conjugated structure.

**Table 4.2** Surface chemical composition of the electrospun PVP/PGSmats at different ratios for the two distinct molecular weights of PVP examined, compared to the theoretical elemental ratios.

PVP/PGS Ratio (w/w)	Outcome	Elemental composition (Atomic ratio, %)		
		C1s	O1s	N1s
<b>PVP 1.3M (g·mol<sup>-1</sup>)</b>		<b>C1s</b>	<b>O1s</b>	<b>N1s</b>
80:20	Experimental	78.7	15.0	6.3
	Theoretical	74.4	15.6	10
70:30	Experimental	70.5	21.7	7.8
	Theoretical	74.2	17.3	8.5
60:40	Experimental	75.3	17.1	7.6
	Theoretical	73.8	18.7	7.5
<b>PVP 360K (g·mol<sup>-1</sup>)</b>		<b>C1s</b>	<b>O1s</b>	<b>N1s</b>
80:20	Experimental	64.7	26.7	8.6
	Theoretical	74.4	15.6	10
70:30	Experimental	75.2	20.1	4.7
	Theoretical	74.2	17.3	8.5
60:40	Experimental	73.0	21.8	5.2
	Theoretical	73.8	18.7	7.5

#### 4.3.4 Tuning the mechanical properties of the composite fibres

PGS is a favourable biomaterial in TE due to its soft, robust and flexible nature, capable of coming in close proximity to the mechanical requirements of many soft tissues [28]. Nevertheless, most of the work that has been conducted surrounding PGS has focused on casted gel forms, as it is hard to be processed into fibres, due to the viscous, sticky nature of the material [29]. Here, the effects that the incremental increase in the concentration of PGS has on the tensile properties of the electrospun scaffolds are illustrated in Figure 4.9. By producing PVP/PGS fibres of similar diameter and porosity, it was feasible to attain variations in the tensile properties of the material based solely on the proportion of the two polymers within the electrospun blends and the MW of the PVP. The Young's modulus, ultimate tensile strength (UTS) and elongation-at-break were assessed after conditioning the fibres for 48 h at standard atmospheric conditions ( $22 \pm 2$  °C and  $65\% \pm 5\%$  relative humidity). Stress-strain curves were obtained for the 80:20, 70:30, 60:40 and 50:50 PVP/PGS electrospun mats for the two distinct MW of PVP examined.

For the hybrid fibres with high concentration of PVP (80:20, PVP/PGS), the tensile behaviour of the electrospun fibres, as expected, resembles that of neat PVP fibres with a UTS of  $3.45 \pm 0.3$  MPa and  $3.2 \pm 0.3$  MPa for 1.3M and 360K g·mol<sup>-1</sup> PVP, respectively [30]. The fibres on this group appeared stiffer due to the low proportion of PGS with an elongation-at-break being  $14.5\% \pm 2.8\%$  and  $3.1\% \pm 0.7\%$  for 1.3M and 360K g·mol<sup>-1</sup> PVP, respectively.

Although the capacity of the material to persevere a high UTS gradually decreased as the concentration of PGS within the hybrid fibres increased, the elongation-at-break gradually increased from  $29\% \pm 0.7\%$  and  $106\% \pm 5\%$  for PVP/PGS 70:30 to  $220\% \pm 19\%$  and  $328\% \pm 38\%$  for PVP/PGS 50:50, where PVP is 360K and 1.3M  $\text{g}\cdot\text{mol}^{-1}$ , respectively (Table 4.3). This pattern relates not only to the PGS but also to the MW of the PVP. Nonetheless, the ability of the electrospun fibres to withstand linear deformation decreased by increasing the PGS concentration. The incorporation of PGS within composite fibres has been found to decrease the Young's modulus and UTS sharply; as shown in a recent study where the Young's modulus of collagen fibres decreased from 30.11 MPa to 4.24 MPa after the addition of the elastomer [31].

Targeting the mechanical properties of biomaterials for wound care has been shown to have a direct influence on the fate of cells and, subsequently, to the success of the wound healing process. Clinical evidence has shown that the time required, and quality of wound healing are strongly influenced by the tensile stress and stiffness of the material used [32]. For instance, mesenchymal stem cells have been found to present distinct patterns of differentiation in the presence of matrices of variant elasticities due to stiffness-related mechanisms [33]. Recently, it has been found that epithelial cells carry a mechanical memory mechanism, which actively influences the ability of the cells to migrate and adhere on a material [34]. This has been demonstrated by placing epithelial cells briefly on a hard substrate, subsequently transferring them on soft substrate, and assessing the effect on the epithelial phenotype in comparison with cells that were directly seeded on soft matrices [34].

Biomaterials of aberrant mechano-transduction have been regarded as a driving force of fibrosis [35]. Furthermore, in chronic wounds, the influence of mechanical signals can affect the stiffness-sensing profile of the fibroblasts, ultimately affecting ECM remodelling [36], as well as the transport of growth factors during the trans-differentiation of fibroblasts to myofibroblasts, which coincides with the formation of hypertrophic scars [37]. Additionally, the tuning of the mechanical properties of the PVP/PGS electrospun mats could also indirectly provide a form of antimicrobial activity, as it has been shown that elastic substrates can upregulate the expression and patrolling behaviour of monocyte-derived macrophages [38].

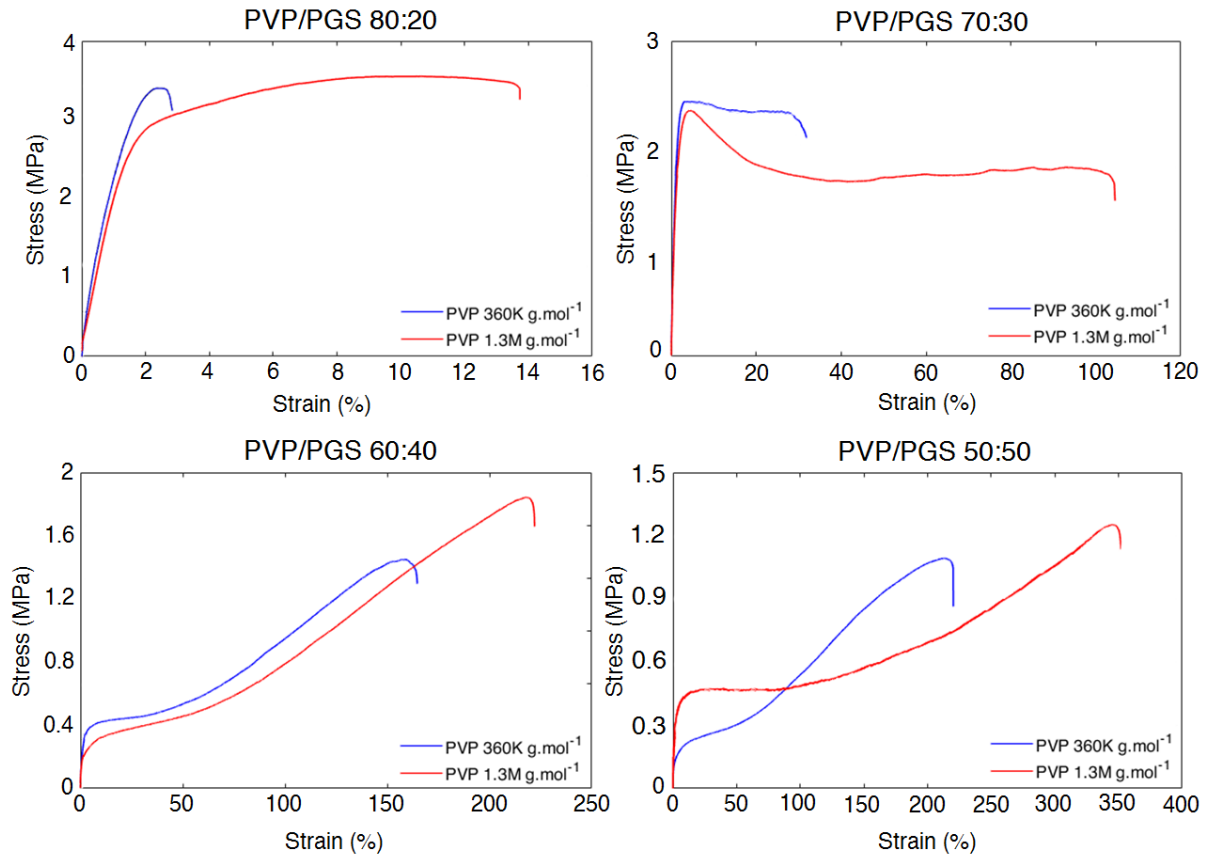


**Figure 4.9** Representative tensile stress–strain curves of the various PVP/PGS fibrous membranes. PVP/PGS ratio of **(a)** 80:20, **(b)** 70:30, **(c)** 60:40 and **(d)** 50:50. Blue: PVP 360K g.mol<sup>-1</sup>, Red: PVP 1.3M g.mol<sup>-1</sup>.

**Table 4.3** Overview of the mechanical properties of each composite fibre mat.

Blend ratio (w/w)	Ultimate Tensile Strength (MPa)		Elongation at Break (%)		Young's Modulus (MPa)	
	1.3M	360K	1.3M	360K	1.3M	360K
PVP (g.mol <sup>-1</sup> )	1.3M	360K	1.3M	360K	1.3M	360K
80:20	3.5 ± 0.3	3.2 ± 0.3	14.5 ± 2.8	3.1 ± 0.7	169 ± 30	170 ± 38
70:30	1.6 ± 0.1	2.1 ± 0.2	106 ± 5.0	29 ± 7.9	40 ± 8.4	38 ± 10
60:40	1.9 ± 0.3	1.7 ± 0.3	225 ± 15	176 ± 23	1.3 ± 0.2	2.2 ± 0.5
50:50	1.1 ± 0.1	1.7 ± 0.6	328 ± 38	220 ± 19	1.4 ± 0.6	1.4 ± 0.7

### 4.3.5 Wettability

Water contact angle (WCA) measurements were carried out to determine the hydrophobic-hydrophilic characteristics and water absorption properties of the PVP/PGS electrospun mats prior and after being irradiated with UV light for 30 and 60 min. As shown in Figure 4.10, an increase in the static WCA is apparent for the electrospun mats that were irradiated, which correlates to the exposure time. The WCA of the PVP fibres was  $20.2^\circ \pm 1.25^\circ$ , while the PVP/PGS was  $30.4^\circ \pm 1.73^\circ$  for the untreated fibres,  $35.4^\circ \pm 1.06^\circ$  after 30 min of UV treatment and  $51.9^\circ \pm 1.98^\circ$  after 60 min. PVP electrospun fibres in the literature appear to have similar values [39].

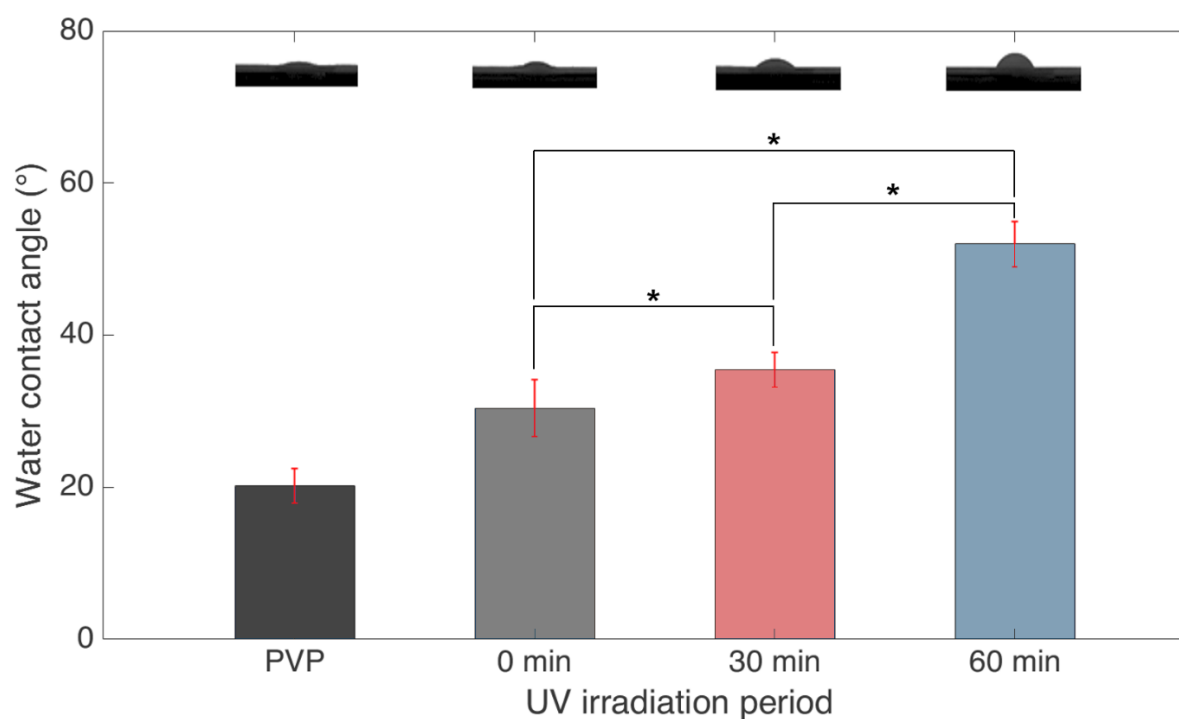


**Figure 4.10** Water contact angle measurements of the electrospun PVP/PGS 60:40 fibres irradiated with ultraviolet light for 0, 30 and 60 min ( $n=8$ ). The data are shown as the mean  $\pm$  SD, where statistical significance is \*  $p < 0.05$ .

In contrast, the WCA of PGS has been found to be between  $53^\circ$  and  $70^\circ$ ; thus, PVP considerably influences the wettability of the electrospun mats, making the hybrid fibres increasingly hydrophilic [39–41]. In the majority of studies, UV treatment of electrospun fibres has been shown to reduce the hydrophobicity of materials such as PCL [42] and PLA [43]. However, the contrary is observed in this study. Poly(vinyl alcohol) (PVA) UV irradiation has

been previously shown to both increase and decrease the hydrophobicity of hydrogels due to an observed increase at the surface temperature of the material [44]. In this study, heat was not applied at the surface of the electrospun mats during this process, as initial observations showed apparent burning of the scaffolds, something that could be explained as PGS is a thermosetting polymer. Thermosets can retain strength and shape upon being heated, due to an increased degree of intramolecular interconnectivity, and will only burn at temperatures higher than the curing temperature, which is 120 °C for PGS. Based on these observations, in conjecture, possible, stable covalent carbon bond formation between the PVP and PGS side chains correlating to the time of exposure to UV light may have resulted in a surface with low surface energy. This indicates that the wettability of the PVP/PGS fibres can be manipulated to an extent via UV irradiation. UV photocrosslinking of PVP via the conjugation of the molecule's monomers in an aqueous solution has been previously proven feasible for hydrogels [2]. A parametric study of the UV intensity and exposure time on the composite fibres could divulge the mechanism behind this phenomenon. This significant increase ( $p < 0.05$ ) of the WCA upon UV irradiation towards a less hydrophilic surface was required to produce a stable electrospun membrane in order to assess the material's biocompatibility *in vitro*.

#### 4.3.6 Cellular behaviour of HDFs in response to the PVP/PGS scaffolds *in vitro*

To appraise whether the UV-treated PVP/PGS fibre mats could be employed as a dermal substitute, HDFs were seeded and assessed in regard to their morphology, cytocompatibility, proliferation rate and attachment properties. As no significant difference was observed in the expansion of HDFs on the PVP/PGS mats produced with PVP 360K and 1.3M g·mol<sup>-1</sup>, the results are presented as one group. Figure 4.11a depicts the fluorescence intensity of HDFs cultured on the PVP/PGS membranes using the cell viability Alamar blue® assay over a span of seven days. A steady increase in the fluorescence corresponding to the number of viable cells present was apparent, with a viability rate of  $\geq 93\%$  for all the time points examined. Based on these preliminary results, the scaffolds do not appear to induce any apparent cytotoxic effect on HDF and display excellent biocompatibility.

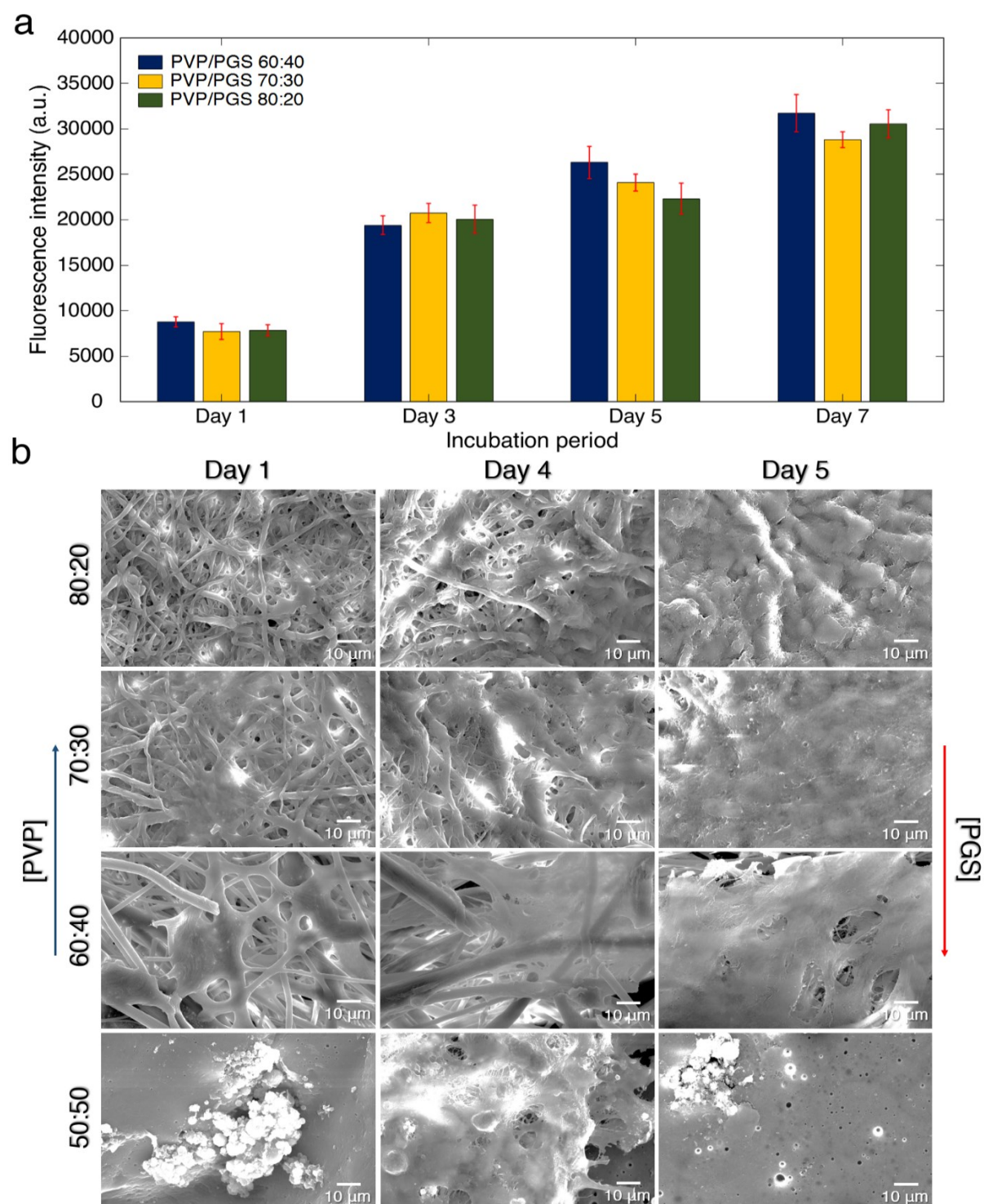


**Figure 4.11** The proliferation of HDFs on the PVP/PGS scaffolds of variant proportions. **(a)** Quantitative analysis using Alamar blue cell viability assay 1, 3, 5 and 7 days after incubation ( $n=6$ ); **(b)** Representative SEM micrographs displaying the influence of the scaffold design on the morphology and proliferation of the HDFs, 1, 4 and 5 days after incubation. PVP/PGS 80:20; 70:30; 60:40 and 50:50 (w/w) for PVP 360K  $\text{g}\cdot\text{mol}^{-1}$ .



The morphology of the cells on the scaffold's surface was obtained by SEM at day 1, 4 and 5. The micrographs (see Figure 4.11b) indicate that the seeded fibroblasts carry a good polygonal, spindle morphology for PVP/PGS ratios of 80:20, 70:30, and 60:40 — characteristic of healthy fibroblasts — compared to the round morphology apparent for PVP/PGS 50:50. Cell attachment to the fibre surface was visibly apparent on the first day of incubation, with good surface interactions present between the HDF and the electrospun fibres, forming numerous attachment sites with the underlying fibrous scaffolds. The cells appear to have spread promptly over the electrospun mats, expanding and covering the scaffolds within five days. No cellular expansion was present for the 50:50 PVP/PGS merged fibre-gel, demonstrating the benefits of an ECM-like architecture towards the expansion of cells.

The cell adherence was evaluated by enumerating the number of non-adherent cells 4-h after seeding, compared to cells grown directly on tissue culture plates. The specimens assessed were pre-soaked in DMEM media (FBS-free) for 48 h, to allow for the removal of any entrapped residual solvents within the membranes. As indicated in Table 4.4, the PVP/PGS 80:20, 70:30, and 60:40 groups were able to adhere  $2.10 \pm 0.18$ ,  $2.75 \pm 0.22$ , and  $1.92 \pm 0.12$ -fold higher than the tissue culture plates. Interestingly, the merged fibres in the form of a gel (PVP/PGS 50:50 group) presented a  $0.52 \pm 0.08$ -fold decrease in cell attachment behaviour, coming into agreement with the SEM observations. The significantly higher ( $p < 0.01$ ) attachment properties of the 70:30 group compared to the other fibrous mats examined could possibly be attributed to the fact that moderately hydrophobic composite membranes have been shown to support greater attachment properties compared to hydrophilic polymers, as protein absorption is favoured by hydrophobic surfaces [12]. Furthermore, the adhesion ability of the cells on moderately hydrophobic surfaces arbitrates via strong interactions between ECM proteins, such as collagen and fibrin, secreted by the cells, as well as the chemical composition of the biomaterial's matrix [45].

**Table 4.4** Rapid cell adhesion capability evaluated by comparing the number of non-adherent cells 4 h after seeding the HDFs in the surface of the electrospun mats over cells grown directly on tissue culture plates (n=3).

Cell adhesion capability	PVP/PGS 80:20	PVP/PGS 70:30	PVP/PGS 60:40	PVP/PGS 50:50
Fold change (s/c)	$2.10 \pm 0.18$	$2.75 \pm 0.22$	$1.92 \pm 0.12$	$0.52 \pm 0.08$

\* s; electrospun scaffolds, c; 24-well culture plate (control)

Figure 4.12 quantifies the cell spreading area occupied by HDFs on the electrospun mats at day 3 and 5. These measurements were conducted by measuring the area covered by cells from SEM micrographs on ImageJ through threshold values and evaluated from pixels per unit of area. There was a quantifiable increase observed for all groups examined between the two time points. The PVP/PGS 70:30 group presented the highest area of  $2850 \pm 320 \mu\text{m}^2$ , followed by  $2672 \pm 245 \mu\text{m}^2$  for 80:20 and  $2450 \pm 450 \mu\text{m}^2$  for 60:40 at day 5. This pattern concurs with the cell adherence behaviour of the cells for the PVP/PGS 70:30 group. Overall, the PVP/PGS fibres are worth considering as a possible biomaterial for skin regeneration, although further work using an animal model could give insights to the wound closure efficiency on different anatomical sites, by evaluating wound contraction, inflammation and histological markers.

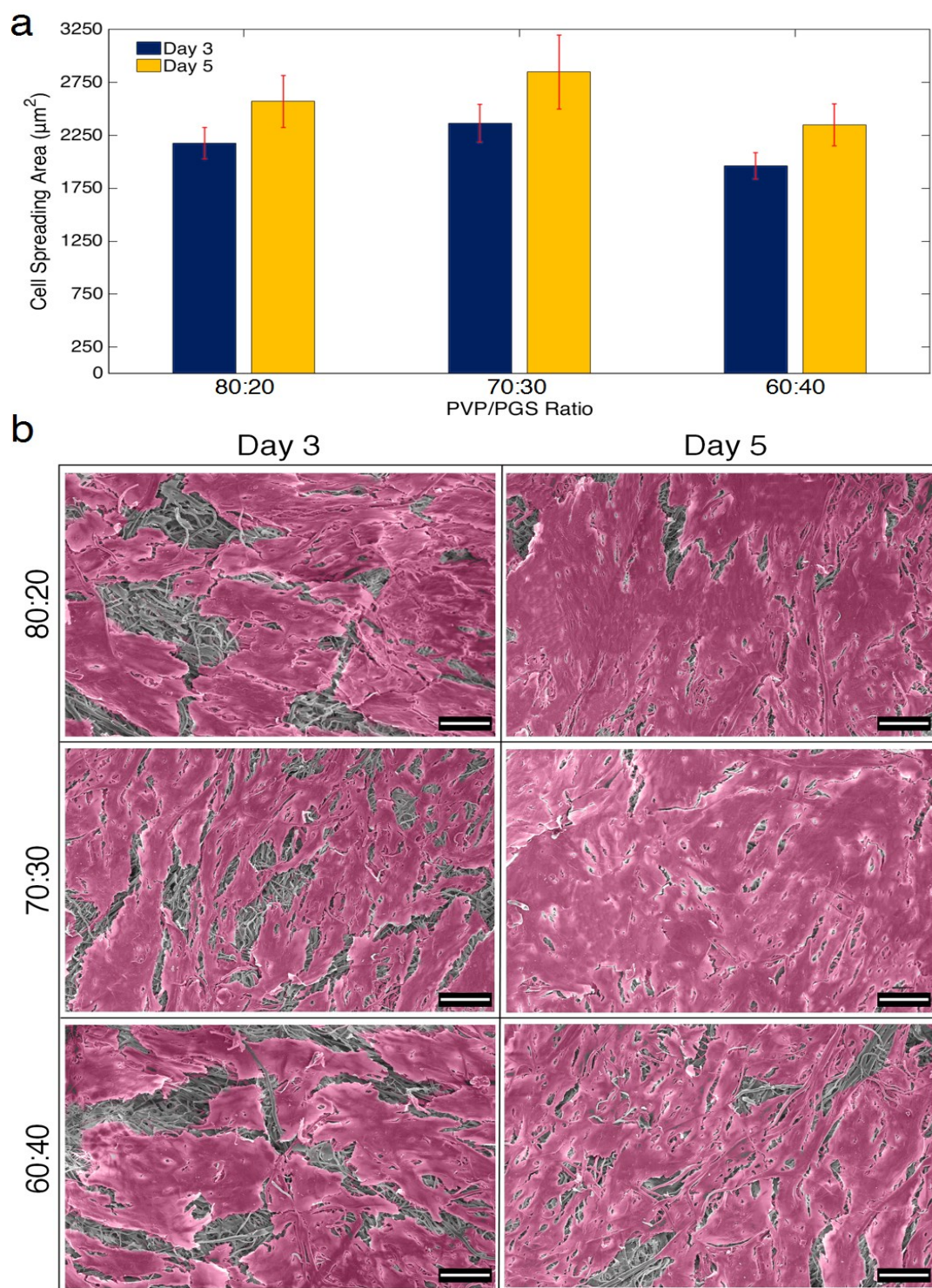


**Figure 4.12** Cell spreading area occupied by the HDFs after 3 and 5 days of incubation on the electrospun PVP/PGS scaffolds of variant ratios. **(a)** Quantification of the cell spreading area (n=5), **(b)** Representative SEM images where cells are depicted with false pink colour. Scale bar; 50  $\mu\text{m}$ .

## 4.4 Conclusions

This chapter describes, for the first time, the fabrication PVP/PGS electrospun fibres as an alternative route for the development of mechanically tuneable ECM-like skin substitute constructs. The composite's morphological, physicochemical, mechanical and water contact angle properties, as well as HDF adhesion, proliferation and spreading, were assessed.

A technical note provides a step-by-step guide, on how to build a nozzle-free electrospinning device capable of generating fibres at eleven times higher yield than conventional (needle-based) electrospinning setups. Subsequently, the device was employed to electrospin PVP/PGS blends of variant ratios. The mechanism responsible for the UV crosslinking of the membranes in the presence of riboflavin was divulged and verified via FTIR spectroscopy. The crosslinked fibrous membranes presented an increased hydrophobicity apropos to the time exposed under UV irradiation.

It was determined that as the [PVP:PGS] ratio increased, so did the elongation-at-break of the corresponding composite scaffolds, while the Young's modulus and ultimate tensile strength gradually decreased. The electrospun membranes produced using PVP 1.3M presented significantly improved elasticity, in comparison to the composites containing PVP 360K. The elastic properties of the fibre mats were substantially improved with the addition of PGS; however, fibre uniformity was not preserved at proportions beyond 60:40 PVP/PGS.

This study has identified knowledge gaps for further study. Firstly, additional work towards the cellular mechanisms in response to the surface chemistry of the developed electrospun constructs could give insights to the fibroblast differentiation pathways (fibroblasts/myofibroblasts) and any resulting upregulation in the expression of wound-related genes. Secondly, it would be worth assessing the effect of the polymer system's degradability at 37 °C, as possible erosion of the composite structure, could have further elevated the pH, making the culture media more acidic. Thirdly, further investigations on the exact mechanism behind the relationship between UV exposure and time can provide better understanding towards its effect on the wettability and degradability of the PVP/PGS scaffolds, which could be beneficial in increasing the lifetime of the construct.

The present study provides valuable input in the ability of PGS to tune the morphological properties and physicochemical behaviour of PVP fibres. This novel composite fibrous structure shows good potential for further investigations focused on improving wound contraction by facilitating elastic ECM-like synthetic dermal matrices analogous to the elasticities of different anatomical sites.

## 4.5 References

1. Wei, L., Sun, R., Liu, C., Xiong, J., & Qin, X. (2019). Mass production of nanofibers from needleless electrospinning by a novel annular spinneret. *Materials and Design*, 179(10), 1–9. <https://doi.org/10.1016/j.matdes.2019.107885>
2. Lopérgolo, L. C., Lugão, A. B., & Catalani, L. H. (2003). Direct UV photocrosslinking of poly (N-vinyl-2-pyrrolidone) (PVP) to produce hydrogels. *Polymer*, 44(20), 6217–6222. [https://doi.org/10.1016/S0032-3861\(03\)00686-4](https://doi.org/10.1016/S0032-3861(03)00686-4)
3. Heo, J., Koh, R. H., Shim, W., Kim, H. D., Yim, H. G., & Hwang, N. S. (2016). Riboflavin-induced photo-crosslinking of collagen hydrogel and its application in meniscus tissue engineering. *Drug Delivery and Translational Research*, 6(2), 148–158. <https://doi.org/10.1007/s13346-015-0224-4>
4. Yadav, L. D. S. (2005). Ultraviolet (UV) and visible spectroscopy. In L. D. S. Yadav (Ed.), *Organic Spectroscopy* (1st ed., vol. 2, pp. 7–51). Dordrecht, Netherlands: Springer. [https://doi.org/10.1007/978-1-4020-2575-4\\_2](https://doi.org/10.1007/978-1-4020-2575-4_2)
5. Cardoso, D. R., Libardi, S. H., & Skibsted, L. H. (2012). Riboflavin as a photosensitizer. Effects on human health and food quality. *Food and Function*, 3(5), 487–502. <https://doi.org/10.1039/c2fo10246c>
6. Ionita, G., & Matei, I. (2020). Application of riboflavin photochemical properties in hydrogel synthesis. In G. Ionita & I. Matei (Eds.), *Biophysical Chemistry - Advance Applications* (1st ed., vol. 3, pp. 1–15). Highly Elastic and Sutureable Electrospun Poly(glycerol sebacate) Fibrous Scaffolds. Bucharest, Romania: Elsevier. <https://doi.org/10.5772/intechopen.88855>
7. Choe, E., & Min, D. B. (2006). Chemistry and reactions of reactive oxygen species in foods. *Critical Reviews in Food Science and Nutrition*, 46(1), 1–22. <https://doi.org/10.1080/10408390500455474>
8. Moon, S., Gil, M., & Lee, K. J. (2017). Syringeless electrospinning toward versatile fabrication of nanofiber web. *Scientific Reports*, 7(1), 1–11. <https://doi.org/10.1038/srep41424>
9. Radacsi, N., Campos, F. D., Chisholm, C. R. I., & Giapis, K. P. (2018). Spontaneous formation of nanoparticles on electrospun nanofibres. *Nature Communications*, 9(1), 1–8. <https://doi.org/10.1038/s41467-018-07243-5>
10. Jeffries, E. M., Allen, R. A., Gao, J., Pesce, M., & Wang, Y. (2015). Highly elastic and sutureable electrospun poly(glycerol sebacate) fibrous scaffolds. *Acta Biomaterialia*, 18(1), 30–39. <https://doi.org/10.1016/j.actbio.2015.02.005>
11. Coativy, G., Misra, M., & Mohanty, A. K. (2017). Synthesis of shape memory poly(glycerol sebacate)-stearate polymer. *Macromolecular Materials and Engineering*, 302(2), 1–6. <https://doi.org/10.1002/mame.201600294>
12. Ifkovits, J. L., Devlin, J. J., Eng, G., Martens, T. P., Vunjak-Novakovic, G., & Burdick, J. A. (2010). Biodegradable fibrous scaffolds with tunable properties formed from photo-cross-linkable poly(glycerol sebacate). *ACS Applied Materials and Interfaces*, 1(9), 1878–1886. <https://doi.org/10.1021/am900403k>
13. Hu, J., Kai, D., Ye, H., Tian, L., Ding, X., Ramakrishna, S., & Loh, X. J. (2017). Electrospinning of poly (glycerol sebacate)-based nanofibers for nerve tissue engineering. *Materials Science and Engineering: C*, 70(2), 1089–1094. <https://doi.org/10.1016/j.msec.2016.03.035>
14. Nadim, A., Khorasani, S. N., Kharaziha, M., & Davoodi, S. M. (2017). Design and characterization of dexamethasone-loaded poly (glycerol sebacate)-poly caprolactone/gelatin scaffold by coaxial electro spinning for soft tissue engineering. *Materials Science and Engineering C*, 78(1), 47–58. <https://doi.org/10.1016/j.msec.2017.04.047>

15. Sant, S., & Khademhosseini, A. (2010). Fabrication and characterization of tough elastomeric fibrous scaffolds for tissue engineering applications. *Annual International Conference of the IEEE Engineering in Medicine and Biology Society*, 10(2), 3546–3548. <https://doi.org/10.1109/IEMBS.2010.5627486>
16. Kemppainen, J. M., & Hollister, S. J. (2010). Tailoring the mechanical properties of 3D-designed poly(glycerol sebacate) scaffolds for cartilage applications. *Journal of Biomedical Materials Research - Part A*, 94(1), 9–18. <https://doi.org/10.1002/jbm.a.32653>
17. Ravichandran, R., Venugopal, J. R., Sundarajan, S., Mukherjee, S., & Ramakrishna, S. (2011). Poly(glycerol sebacate)/gelatin core/shell fibrous structure for regeneration of myocardial infarction. *Tissue Engineering Part A*, 17(9–10), 1363–1373. <https://doi.org/10.1089/ten.tea.2010.0441>
18. Kharaziha, M., Nikkhah, M., Shin, S. R., Annabi, N., Masoumi, N., Gaharwar, A. K., Camci-Unal, G., & Khademhosseini, A. (2013). PGS:Gelatin nanofibrous scaffolds with tunable mechanical and structural properties for engineering cardiac tissues. *Biomaterials*, 34(27), 6355–6366. <https://doi.org/10.1016/j.biomaterials.2013.04.045>
19. Xu, B., Li, Y., Zhu, C., Cook, W. D., Forsythe, J., & Chen, Q. (2015). Fabrication, mechanical properties and cytocompatibility of elastomeric nanofibrous mats of poly(glycerol sebacate). *European Polymer Journal*, 64(2), 79–92. <https://doi.org/10.1016/j.eurpolymj.2014.12.008>
20. Yi, F., & La Van, D. A. (2008). Poly(glycerol sebacate) nanofiber scaffolds by core/shell electrospinning. *Macromolecular Bioscience*, 8(9), 803–806. <https://doi.org/10.1002/mabi.200800041>
21. You, Z. R., Hu, M. H., Tuan-Mu, H. Y., & Hu, J. J. (2016). Fabrication of poly(glycerol sebacate) fibrous membranes by coaxial electrospinning: Influence of shell and core solutions. *Journal of the Mechanical Behavior of Biomedical Materials*, 63, 220–231. <https://doi.org/10.1016/j.jmbbm.2016.06.022>
22. Kao, C. Y., Lo, T. C., & Lee, W. C. (2003). Influence of polyvinylpyrrolidone on the hydrophobic properties of partially porous poly(styrene-divinylbenzene) particles for biological applications. *Journal of Applied Polymer Science*, 87(11), 1818–1824. <https://doi.org/10.1002/app.11653>
23. Yang, B., Lv, W., & Deng, Y. (2017). Drug loaded poly(glycerol sebacate) as a local drug delivery system for the treatment of periodontal disease. *RSC Advances*, 7(59), 37426–37435. <https://doi.org/10.1039/C7RA02796F>
24. Rai, R., Tallawi, M., Grigore, A., & Boccaccini, A. R. (2012). Synthesis, properties and biomedical applications of poly(glycerol sebacate) (PGS): A review. *Progress in Polymer Science*, 37(8), 1051–1078. <https://doi.org/10.1016/j.progpolymsci.2012.02.001>
25. Song, Y. J., Wang, M., Zhang, X. Y., Wu, J. Y., & Zhang, T. (2014). Investigation on the role of the molecular weight of polyvinyl pyrrolidone in the shape control of highyield silver nanospheres and nanowires. *Nanoscale Research Letters*, 9(1), 1–8. <https://doi.org/10.1186/1556-276X-9-17>
26. Abdelghany, A. M., Mekhail, M. S., Abdelrazek, E. M., & Aboud, M. M. (2015). Combined DFT/FTIR structural studies of monodispersed PVP/Gold and silver nano particles. *Journal of Alloys and Compounds*, 646, 326–332. <https://doi.org/10.1016/j.jallcom.2015.05.262>
27. Li, J., Inukai, K., Takahashi, Y., Tsuruta, A., & Shin, W. (2018). Thin film coating with highly dispersible barium titanate-polyvinylpyrrolidone nanoparticles. *Materials*, 11(5), 712. <https://doi.org/10.3390/ma11050712>
28. Singh, D., Harding, A. J., Albadawi, E., Boissonade, F. M., Haycock, J. W., & Claeysens, F. (2018). Additive manufactured biodegradable poly(glycerol sebacate methacrylate) nerve guidance conduits. *Acta Biomaterialia*, 78(2), 48–63. <https://doi.org/10.1016/j.actbio.2018.07.055>
29. Li, X., Hong, A. T. L., Naskar, N., & Chung, H. J. (2015). Criteria for quick and consistent synthesis of poly(glycerol sebacate) for tailored mechanical properties. *Biomacromolecules*, 16(5), 1525–1533. <https://doi.org/10.1021/acs.biomac.5b00018>

30. Huang, S., Zhou, L., Li, M.-C., Wu, Q., Kojima, Y., & Zhou, D. (2016). Preparation and properties of electrospun poly (vinyl pyrrolidone)/cellulose nanocrystal/silver nanoparticle composite fibers. *Materials*, 9(7), 1–14 <https://doi.org/10.3390/ma9070523>
31. Ravichandran, R. (2013). Cardiogenic differentiation of mesenchymal stem cells on elastomeric poly (glycerol sebacate)/collagen core/shell fibers. *World Journal of Cardiology*, 5(3), 1–14. <https://doi.org/10.4330/wjc.v5.i3.28>
32. Wang, Y., Armato, U., & Wu, J. (2020). Targeting tunable physical properties of materials for chronic wound care. *Frontiers in Bioengineering and Biotechnology*, 8(1), 1–14. <https://doi.org/10.3389/fbioe.2020.00584>
33. Engler, A. J., Sen, S., Sweeney, H. L., & Discher, D. E. (2006). Matrix elasticity directs stem cell lineage specification. *Cell*, 126(4), 677–689. <https://doi.org/10.1016/j.cell.2006.06.044>
34. Nasrollahi, S., Walter, C., Loza, A. J., Schimizzi, G. V., Longmore, G. D., & Pathak, A. (2017). Past matrix stiffness primes epithelial cells and regulates their future collective migration through a mechanical memory. *Biomaterials*, 146(1), 146–155. <https://doi.org/10.1016/j.biomaterials.2017.09.012>
35. Brusatin, G., Panciera, T., Gandin, A., Citron, A., & Piccolo, S. (2018). Biomaterials and engineered microenvironments to control YAP/TAZ-dependent cell behaviour. *Nature Materials*, 17(12), 1063–1075. <https://doi.org/10.1038/s41563-018-0180-8>
36. Zhou, C., Jin, S., & Willing, R. (2016). Simulation of extracellular matrix remodeling by fibroblast cells in soft three-dimensional bioresorbable scaffolds. *Biomechanics and Modeling in Mechanobiology*, 15(6), 1685–1698. <https://doi.org/10.1007/s10237-016-0791-4>
37. Jiang, S., Li, S. C., Huang, C., Chan, B. P., & Du, Y. (2018). Physical properties of implanted porous bioscaffolds regulate skin repair: Focusing on Mechanical and structural features. *Advanced Healthcare Materials*, 7(6), 1–17. <https://doi.org/10.1002/adhm.201700894>
38. Adlerz, K. M., Aranda-Espinoza, H., & Hayenga, H. N. (2016). Substrate elasticity regulates the behavior of human monocyte-derived macrophages. *European Biophysics Journal*, 45(4), 301–309. <https://doi.org/10.1007/s00249-015-1096-8>
39. Wang, L., Zhang, C., Wang, H. M. D., Ahmad, Z., Li, J. S., & Chang, M. W. (2018). High throughput engineering and use of multi-fiber composite matrices for controlled active release. *Materials Today Communications*, 17(7), 53–59. <https://doi.org/10.1016/j.mtcomm.2018.08.011>
40. Gaharwar, A. K., Patel, A., Dolatshahi-Pirouz, A., Zhang, H., Rangarajan, K., Iviglia, G., Shin, S. R., Hussain, M. A., & Khademhosseini, A. (2015). Elastomeric nanocomposite scaffolds made from poly(glycerol sebacate) chemically crosslinked with carbon nanotubes. *Biomaterials Science*, 3(1), 46–58. <https://doi.org/10.1039/C4BM00222A>
41. Shi, H., Gan, Q., Liu, X., Ma, Y., Hu, J., Yuan, Y., & Liu, C. (2015). Poly(glycerol sebacate)-modified polylactic acid scaffolds with improved hydrophilicity, mechanical strength and bioactivity for bone tissue regeneration. *RSC Advances*, 5(97), 79703–79714. <https://doi.org/10.1039/c5ra13334c>
42. Augustine, R., Saha, A., Jayachandran, V. P., Thomas, S., & Kalarikkal, N. (2015). Dose-dependent effects of gamma irradiation on the materials properties and cell proliferation of electrospun polycaprolactone tissue engineering scaffolds. *International Journal of Polymeric Materials and Polymeric Biomaterials*, 64(10), 526–533. <https://doi.org/10.1080/00914037.2014.977900>
43. Valente, T. A. M., Silva, D. M., Gomes, P. S., Fernandes, M. H., Santos, J. D., & Sencadas, V. (2016). Effect of sterilization methods on electrospun poly(lactic acid) (PLA) fiber alignment for biomedical applications. *ACS Applied Materials and Interfaces*, 8(5), 3241–3249. <https://doi.org/10.1021/acsami.5b10869>
44. Musskaya, O. N., Kulak, A. I., Krut, V. K., Ulasevich, S. A., Lesnikovich, L. A., & Suchodub, L. F. (2015). Composite films based on hydroxyapatite and polyvinyl alcohol. *Journal of Nano &*

*Electronic Physics*, 7(1), 1–4. <https://doi.org/10.13140/RG.2.1.3430.1042>

45. Place, E. S., Evans, N. D., & Stevens, M. M. (2009). Complexity in biomaterials for tissue engineering. *Nature Materials*, 8(6), 457–470. <https://doi.org/10.1038/nmat2441>





---

## Chapter 5

# Nozzle-Free Electrospinning of Silk Fibroin-Based Composite Scaffolds for Skin Regeneration

---

### 5.1 Introduction

The development of tissue-engineered skin substitutes and advanced wound dressing biomaterials requires that several criteria are met. First, these new materials must be biocompatible, to avoid the potential for immune rejection and inflammatory responses [1]. In addition, an appropriately hydrophilic interface between the tissue and the biomaterial is necessary to effectively facilitate cell adhesion and proliferation. Furthermore, the biomaterial must be lightweight, to minimise foreign body sensations. The material must also be biodegradable; to alleviate pain related to material-tissue adhesion, and present an architecture that allows for appropriate water retention, nutrient transport, breathability, and structural stability, to support an optimal regenerative niche [2, 3].

To fulfil these requirements, a range of biocompatible materials have been extensively studied, with a particular focus on wound management and skin tissue repair [4]. Electrospun biomaterials are favourable for the reconstruction of fibrous skin-tissue-like scaffolds, promoting the development of structures that closely resemble the native ECM, facilitating cellular adherence, proliferation, and migration, and allowing for the induction of neovascularisation [5, 6]. Electrospinning represents an excellent and well-established technique, described in detail in *Chapter 2*, that can be used to fabricate constructs in the form of nonwoven fibre networks [7]. The net-like morphology of electrospun fibres, due to characteristics at both the micro- and nano-levels, can facilitate the absorption of exudates and support efficient gas exchange within the wound bed, while simultaneously modulating the adaptation and proliferation of dermal cells [8, 9]. These features can ultimately improve the care, recovery time, and healing processes of injured skin tissues.

The use of different materials in a polymer system can allow for the integration of unique properties and distinct features into the final composite structure. Therefore, a unique composite structure was developed, based on electrospun fibres and consisting of both synthetic and naturally derived materials. However, obtaining a stable Taylor cone during the electrospinning of natural polymers can be challenging due to low solution viscosities, MWs below the critical chain entanglement concentration, a much lower throughput during the fabrication process, as well as the diversity and greater distribution of the polymer chains giving room to fibre inconsistencies and secondary morphologies (e.g., beads, ejected polymer droplets, spider nets etc.). Therefore, an appropriate solvent system, the critical entanglement concentration of each polymer, and the necessary viscosity above the overlap concentration of the polymer-system were initially determined.

In this study, non-acrylate pre-PGS (pPGS) and PGS were blended with a *Bombyx mori*-derived fibroin-acidic system, in which PCL was incorporated as a backbone-polymer carrier, to stabilise and improve the electrospinnability of the polymer solution. To utilise the advantages of each material, this study systematically studied and employed the nozzle-free electrospinning technique, described in detail in *Chapter 4*, to formulate composite fibres, tune and characterise their properties, to demonstrate the effectiveness of composite electrospun structures towards skin tissue engineering.

For the extraction of silk fibroin from *B. mori* cocoons, a variation of the traditional approach was developed that was found to yield much larger quantities than the conventional molecular cassette cut-off method at a third of the time needed [10]. The morphological and chemical properties of the developed electrospun membranes were assessed. A degradation study was conducted, and contact angle measurements were examined to determine the effects of PGS and SF on the hydrophilicity of the fibrous composite scaffolds incorporating PCL. Human dermal fibroblasts (HDFs) were used to examine the seeding efficiency, adhesion properties, and proliferation on the trinary electrospun membranes.

This is the first study, in literature, to ever describe the development of composite fibres deriving from a three-polymer system using a high-throughput, free surface, electrospinning device.

The work presented in this chapter has been published in *Materials Science and Engineering C* (Keirouz et al., 2020a), and a conference abstract was presented on this topic at Electrospin 2019, the 6<sup>th</sup> International Conference on Electrospinning, in Shanghai, China (Appendix B).

## 5.2 Methodology

For full descriptions of the materials and methods used, please see the following sections in *Chapter 3*:

- Materials (Section 3.3)
  - Synthesis of PGS and pPGS (Section 3.3.1)
  - List of materials, reagents, cells, suppliers, and equipment (Section 3.3.2)
- Scaffold characterisation (Section 3.4)
  - Scanning electron microscopy (SEM) (Section 3.4.1)
  - Fourier-transform infrared spectroscopy (FTIR) (Section 3.4.3)
  - X-ray photoelectron spectroscopy (XPS) (Section 3.4.4)
  - Water contact angle measurements (WCA) (Section 3.4.8)
  - Degradation studies (Section 3.4.9)
- *In vitro* evaluation (Section 3.5)
  - Scaffold sterilisation (Section 3.5.1)
  - Cell culture technique (Section 3.5.2)
  - Cell seeding efficiency (Section 3.5.3)
  - Cell proliferation (Section 3.5.4)
  - Fixing cells for SEM imaging (Section 3.5.5)

The chapter-specific experimental methods are described, in detail, below.

### 5.2.1 Extraction and purification of the silk fibroin protein

SF was extracted from *Bombyx mori* silkworm cocoons, using a newly developed alcohol precipitation method. Sericin was removed by degumming 10 g of cocoons in 0.02 M Na<sub>2</sub>CO<sub>3</sub> solution, at 100 °C for 30 min. The degummed silk cloth was then rinsed thoroughly with deionised water and left to dry under the fume hood overnight. The woven silk filaments were then dissolved in a 9.3 M LiBr aqueous solution, for 4 h at 50 °C, in a narrow beaker (to sustain the temperature produced by the exothermic reaction), to regenerate the SF.

Instead of continuing with the conventional method, which involves the removal of the chaotropic LiBr salt by dialysis, using specific molecular-weight cut-off cassettes [11], ethanol was used to precipitate the SF and remove the LiBr. To achieve an efficient degree of fibroin precipitation, the volume of ethanol used was 30-fold the volume of the aqueous SF-LiBr solution. The dispersed SF solution was added dropwise to ethanol and stirred for 1 h, after

which, the SF residues were attained by filtration (Whatman grade 1573) and washed with ultrapure water. The filtered SF was washed continuously with water until the electrical conductivity of the filtered water was equal to the electrical conductivity of the ultrapure water, prior to washing ( $\leq 0.1 \mu\text{S}\cdot\text{cm}^{-1}$ ), at which point SF was considered to be LiBr-free. The purity of the fibroin protein was also confirmed by X-ray photoelectron spectroscopy (XPS) measurements, which confirmed that traces of LiBr were not present on the material's surface. The paste-like, wet, SF was dried in an oven at  $50^\circ\text{C}$  and milled using a mortar to form a powder (Figure 5.1). Step-by-step photographs of the procedure can be found in Appendix A: Figure A-11.

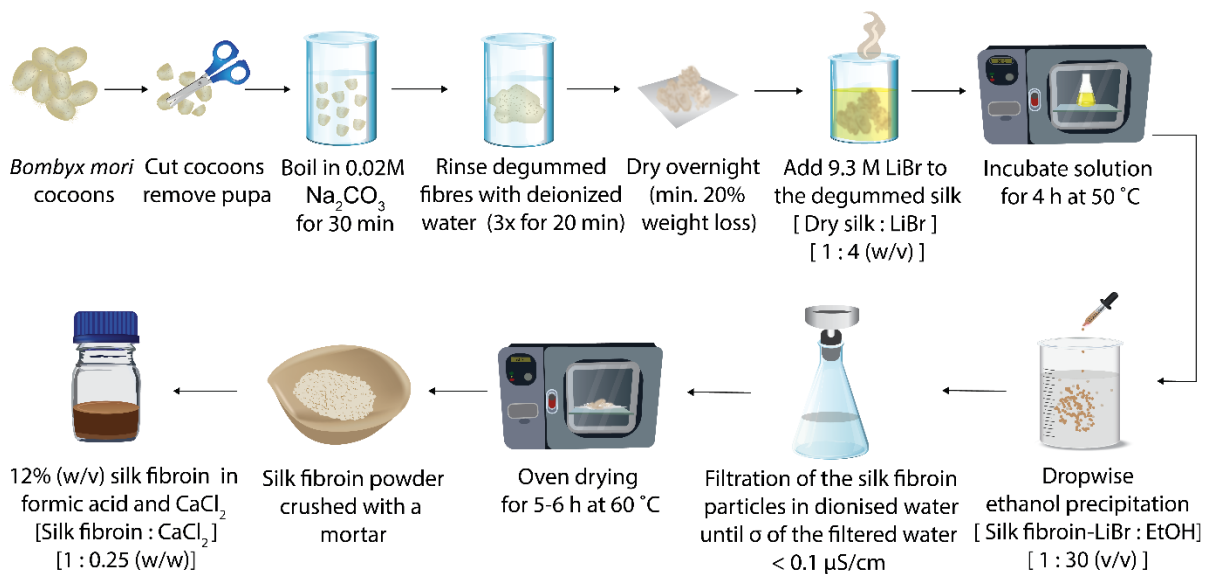


**Figure 5.1 Silk fibroin extraction and processing to obtain the regenerated form.** Initially, *B. mori* cocoons are cut into small pieces and degummed in 0.01 M  $\text{Na}_2\text{CO}_3$ , at  $100^\circ\text{C}$  for 30 min. The degummed silk is rinsed in deionised water, 3 times for 20 min each, and left to dry at room temperature, overnight. Then, 9.3 M LiBr solution is added to the dried silk fibre mesh, at a ratio of 1:4 SF:LiBr solution (w/v), to dissolve the fibroin. The LiBr-SF solution is placed in an oven, for 4 h at  $50^\circ\text{C}$ . Afterwards, SF is precipitated by gradually adding the SF-LiBr solution, dropwise, to pure ethanol, until it reaches a ratio of 1:30 SF-LiBr:EtOH (v/v), under agitation conditions for 1 h. Subsequently, LiBr residues are removed by filtration and washed with ultrapure water. The purified SF is oven-dried, at  $50^\circ\text{C}$ . The dried SF is then milled into a powder, using a mortar, and dissolved in formic acid/ $\text{CaCl}_2$ , to obtain a final SF concentration of 12% (w/v).

## 5.2.2 Preparation of binary and ternary electrospinning solutions

PGS was synthesised based on the previously published polycondensation method [22], as described, in detail, in *Section 3.3.2*.

PCL, at 15% (w/v), was dissolved in a solvent system consisting of 80:20 (w/w) 1,1,1,3,3,3- hexafluoro-2-propanol (HFIP):formic acid. To prepare the SF solution, 12% (w/v), SF powder was dissolved in a solution of CaCl<sub>2</sub> and formic acid. The ratio of SF:CaCl<sub>2</sub> was 1:0.25 (w/w) [12]. All solutions were magnetically stirred (350 rpm), overnight at room temperature. After homogenously mixed solutions were obtained, a ternary blend, consisting of PCL-backbone SF:PGS, and SF:pPGS solutions were prepared. The mass ratio of SF was maintained constant for all blends. Binary blends of SF:PGS and SF:pPGS were also prepared. The blends, which were dissolved in a solvent system consisting of HFIP: formic acid:CaCl<sub>2</sub>, were then magnetically stirred, overnight at room temperature, before electrospinning. The electrical conductivity and pH values of the polymer solutions were measured before every experiment. Table 5.1 indicates the mass ratios for each ternary and binary blend.

**Table 5.1** Blend compositions. Ternary blends, consisting of PCL-backbone SF:(p)PGS, binary blends, consisting of SF:(p)PGS, and PCL alone. Total polymer solution concentration of 13.5% (w/v) for the ternary blend, 19.5% (w/v) for binary blends, and 15% (w/v) for the PCL.

Polymer blend	Ratio [w/w]		
	Silk fibroin 12% (w/v)	PCL 15% (w/v)	PGS 15% (w/v)
<b>SF:PCL:PGS</b>	1	0.75	0.25
<b>&amp;</b>	1	0.50	0.50
<b>SF:PCL:pPGS</b>	1	0.25	0.75
<b>SF:PGS</b>	2	-	1
<b>SF:pPGS</b>	2	-	1
<b>PCL</b>	-	1	-

In the polymer blend column “&” is meant to indicate that all top three rows represent the SF:PCL:(p)PGS ratio blends. The ratio among the blends refers to the proportion of column 1 (SF) towards column 2 (PCL) and column 3 (PGS) so that 1 part of [SF] is equal to 1 part of [PCL+PGS]. e.g.,  $SF:PCL:PGS \rightarrow 1:0.75:0.25 = (12\% + [(0.75 \times 15\%) + (0.25 \times 15\%)]/2 = 13.5\%$ , and  $SF:PGS \rightarrow 2:1 = ((2 \times 12\%) + (1 \times 15\%))/2 = 19.5\%$  of total polymer solution concentration.

### 5.2.3 High-throughput scaffold fabrication and processing

Fibres were produced using the enclosed configuration of the nozzle-free electrospinning device, which was described in *Section 4.2.1*. The ternary and binary polymer blends were submerged within the Teflon pool – where the rotating electrode spinneret was coated with the polymer blend, counter to a biased rotating collector electrode, under constant N<sub>2</sub> flow. A high-voltage power supply, with a potential difference of 60 kV (+30/-30 kV), was applied between the two rotating electrodes, which resulted in the formation of multiple Taylor cones stretching along the surface of the rotating electrode, forming fibres in an upward motion. The process is illustrated in Figure 5.2.

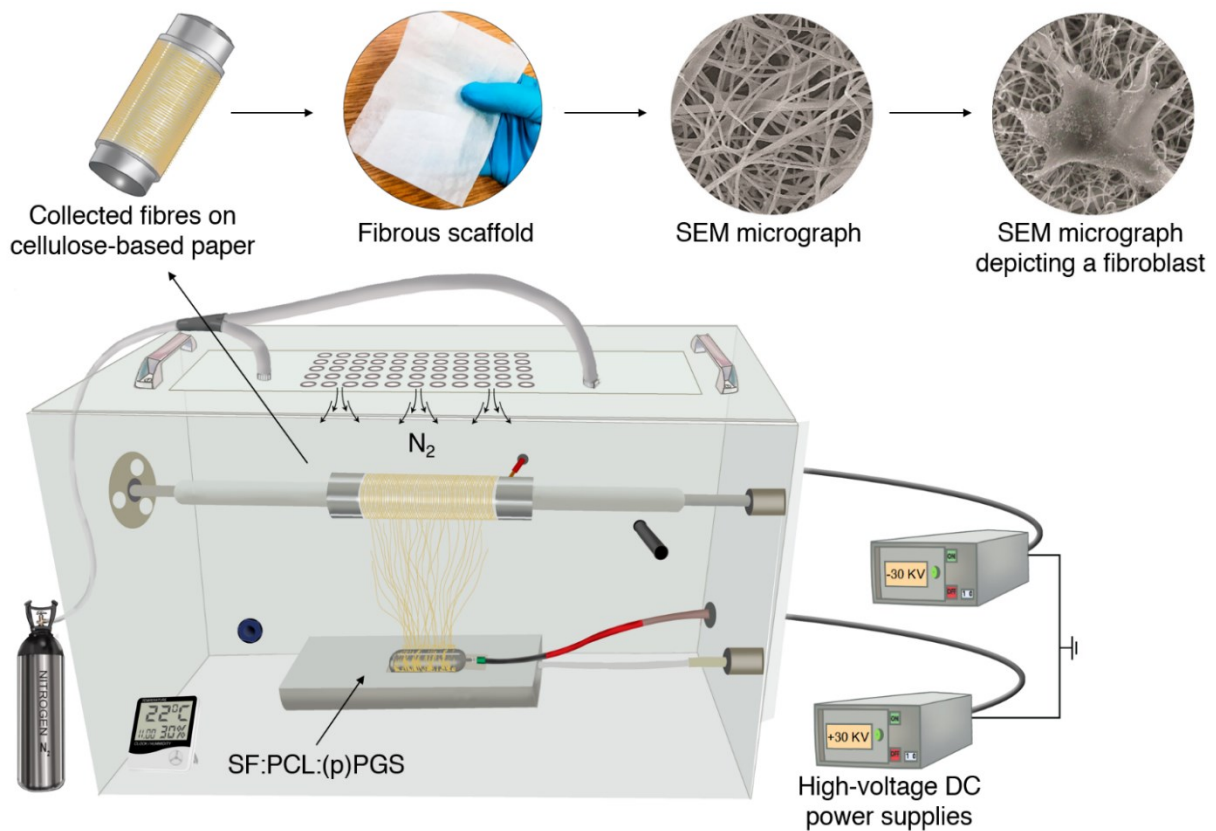


**Figure 5.2** Schematic representation of the nozzle-free electrospinning process, showing a macrograph of the produced fibrous scaffold and SEM micrographs of the fibres, with and without fibroblasts.

## 5.3 Results and discussion

### 5.3.1 Electrospun scaffold morphology

The fibrous constructs were electrospun using the nozzle-free electrospinning apparatus, as described above, and the fibres were collected on cellulose-based (baking) paper. Appendix A: Table A-1 summarises the electrospinning and solution parameters used. When incorporating SF with other synthetic polymers, the inter/-intramolecular interactions that result in the formation of fibroin  $\beta$ -sheets should be considered [13]. The electrospun mats were treated for 2 h, in an ethanol solution, to favour the development of  $\beta$ -sheets. The temperature, pH, fibroin and salt concentrations, shear viscosity, and solvent system used were optimised, to prevent the gelation of the binary and ternary spinning solutions upon blending [14, 15].

The morphological properties of the ternary SF:PCL:(p)PGS and binary SF:(p)PGS blends, at different ratios, were evaluated by SEM imaging (Figure 5.3; Appendix A: Figure A-12). The fibre diameters and pore sizes are listed in Table 5.2. The PGS concentration within the blends played important roles in the morphology of the produced fibres. The images depicted clear differences in the fibre diameters among scaffolds prepared with the two variant forms of synthesised PGS. The ternary SF:PCL scaffolds containing PGS tended to have higher average fibre diameters, ranging from  $2.11 \pm 1.34 \mu\text{m}$  to  $4.1 \pm 3.0 \mu\text{m}$  (Figure 5.3c–e), whereas the pPGS scaffolds presented values in the range of  $1.42 \pm 0.66 \mu\text{m}$  to  $1.62 \pm 0.80 \mu\text{m}$  (Figure 5.3f–h). Moreover, the average fibre diameters noticeably increased in blends with higher ratios of PGS (e.g., the ratio 1:0.25:0.75 resulted in the thickest fibres, at  $4.1 \pm 3.0 \mu\text{m}$ , Figure 5.3c).

PGS was initially difficult to electrospin due to its high viscosity. Moreover, the pPGS glass transition occurs below room temperature; therefore, independent fibres can easily become fused during the electrospinning process, thickening the fibre composition, as well as form secondary morphologies (e.g., beads). In this work, these issues were circumvented by the addition of PCL in the polymer mixture, which stabilised the electrospinnability of the elastomer. The pPGS form of the elastomer was found to produce smaller fibres, with a mean fibre diameter that decreased by 23%–65%, depending on the corresponding blend ratio. These results indicated that the elastomeric PGS characteristics affected fibre morphology.



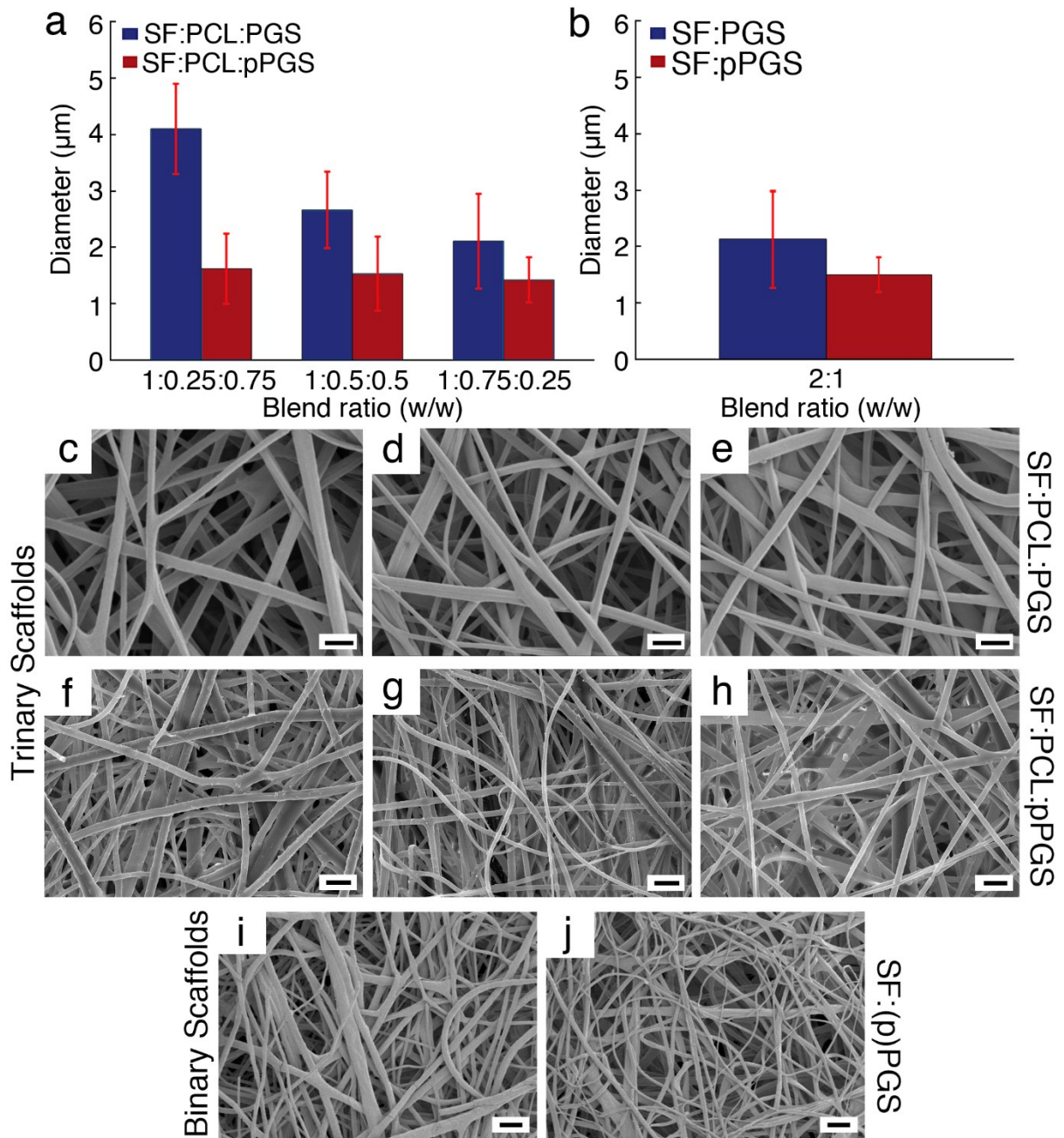


**Figure 5.3** Average fibre diameters of the **(a)** trinary, SF:PCL:PGS and SF:PCL:pPGS, and **(b)** binary, SF:PGS and SF:pPGS, blends. Representative SEM micrographs of the trinary, **(c-e)** SF:PCL:PGS and **(f-h)** SF:PCL:(p)PGS **(d-h)** and binary, **(i)** SF:PGS 2:1 (w/w) and **(j)** SF:(p)PGS 2:1 (w/w), scaffolds. The images were obtained after drying ethanol-treated electrospun mats at 32 °C. Scale bar, 10 µm.

**Table 5.2** The morphological properties of ternary and binary electrospun mats. Nozzle-free electrospinning was performed at a potential difference of 60 kV (+30/-30 kV), in an upward motion, under N2 airflow. All values are presented as the mean  $\pm$  SD.

<b>SF:PCL:PGS [w/w]</b>	<b>Fibre diameter (<math>\mu\text{m}</math>)</b>	<b>Porosity (%)</b>	<b>Pore size (<math>\mu\text{m}</math>)</b>
1:0.25:0.75	4.1 $\pm$ 3.0	70 $\pm$ 7.3	14.7 $\pm$ 7.7
1:0.5:0.5	2.7 $\pm$ 1.7	73 $\pm$ 3.6	15.4 $\pm$ 6.2
1:0.75:0.25	2.1 $\pm$ 1.3	80 $\pm$ 5.5	16.9 $\pm$ 7.4
<b>SF:PCL:pPGS [w/w]</b>	<b>Fibre diameter (<math>\mu\text{m}</math>)</b>	<b>Porosity (%)</b>	<b>Pore size (<math>\mu\text{m}</math>)</b>
1:0.25:0.75	1.4 $\pm$ 0.7	58 $\pm$ 8.5	8.8 $\pm$ 4.3
1:0.5:0.5	1.5 $\pm$ 0.8	61 $\pm$ 5.3	9.2 $\pm$ 5.4
1:0.75:0.25	1.6 $\pm$ 0.8	63 $\pm$ 8.5	9.3 $\pm$ 7.0
<b>SF:PGS</b>			
2:1	2.1 $\pm$ 1.8	58.8 $\pm$ 8.9	7.9 $\pm$ 3.9
<b>SF:pPGS</b>			
2:1	1.0 $\pm$ 1.1	62 $\pm$ 7.1	6.3 $\pm$ 2.6

The mean pore size (Table 5.2) of the ternary blends containing PGS was, on average, twice that of the pPGS-containing electrospun mats, with no significant differences observed among the various concentration of PGS within the blends. The SF:PCL:PGS blend presented a mean pore size of  $15.6 \pm 7.1 \mu\text{m}$  (porosity  $74\% \pm 5.4\%$ ), whereas the SF:PCL:pPGS blend had a mean pore size of  $9.1 \pm 5.7 \mu\text{m}$  (porosity  $61\% \pm 7.4\%$ ). Along with the choice of biomaterial, the pore size must be considered during the development of a scaffold, to promote cell migration, adhesion, and cell-to-cell contacts [16, 17]. The optimal pore size for fibroblast ingrowth is 5–15  $\mu\text{m}$ , with wider, interconnected pores able to better facilitate the diffusion and ingrowth of nutrients [18]. Thus, these ternary blends fall within the optimal range for pore size to promote cellular infiltration. Although the porosity of the produced mats was determined to fall within the required gradient necessary to promote tissue reorganisation and govern effective tissue regeneration, porosity can also negatively affect the mechanical stability of the construct [19]. Consequently, the addition of PCL within ternary blends has been widely considered to represent a good approach for the stabilisation of fibre-based biomaterials [19, 20].

To further analyse the effects of PGS on SF, binary blends of SF:(p)PGS and SF:PGS, at a ratio of 2:1 (w/w), were also electrospun, using the same apparatus under the same conditions. In contrast with the PCL-containing fibres, the distributions of fibres produced using these binary blends were more dispersed, losing their uniformity. The mean fibre diameter of the SF:PGS blend was  $2.13 \pm 1.50 \mu\text{m}$  (Figure 5.3i), whereas the mean fibre diameter of the SF:(p)PGS blend was  $1.04 \pm 0.30 \mu\text{m}$  (Figure 5.3j). The SF:(p)PGS fibres appear to consist

of a smoother fibre morphology compared with their PGS fibre counterparts; however, some fusion of the fibres remained apparent. According to several studies, the subsequent curing of the PGS increases the molecular weight of the polymer, which results in chain mobility restrictions, increased entanglement, and higher internal fluid friction, making jet extension more difficult [21]. These characteristics lead binary and ternary blends containing PGS to form thicker fibres. Furthermore, a correlation between viscosity and fibre diameter was confirmed by the studies reported by Drew et al. [22], and Fong et al. [23], in which increasing the solution viscosity tended to increase the fibre diameter during electrospinning.

When blends with or without PCL were compared, both PCL-containing ternary groups of fibres appeared smoother and with increased diameters than the fibres from the SF:PGS and SF:(p)PGS blends, in most cases, which may be due to changes in the dielectric constant, which is  $0.2 \text{ mS}\cdot\text{cm}^{-1}$  higher in PCL-containing blends. Generally, the solution conductivity of a solvent also plays a significant role in the electrospinning process, with higher dielectric values corresponding to smaller diameters among the resulting electrospun fibres [24]. PCL was dissolved in a binary solvent system, containing HFIP: formic acid at 80:20 (w/w). Because formic acid has a higher dielectric constant than HFIP, the mixture of these two solvents may increase the electrical conductivity of the PCL-containing blends, contributing to the fabrication of smoother fibres during electrospinning [25].

The nozzle-free electrospinning setup, using a cylinder spinneret, results in substantially increased fibre productivity and requires lower operational costs than conventional single or multi-needle spinnerets [26, 27]. However, nozzle-free systems are also comparatively more complex, requiring a range of new electrospinning parameters to be considered, including, but not limited to, the spinneret rotating speed, the electric field distribution, and spinneret geometry. Nonetheless, in this chapter, the development of composite fibres deriving from a three-polymer system was deemed successful, where the presence and physicochemical effects of each polymer to the final composite structure are examined in detail below.

### 5.3.2 Chemical analysis and fibre surface composition

The spectra of SF, PCL, pPGS, and PGS polymers were analysed, along with those of the binary and ternary scaffolds, to determine the compositions of the developed scaffolds, using ATR-FTIR. The infrared spectra are presented in Figure 5.4. The defining peaks of the individual polymers can also be observed in the corresponding composite fibres, at lower intensities. PGS and pPGS share the same spectrum, with slightly lower peak intensities for pPGS. The peaks at 2934–2857  $\text{cm}^{-1}$  can be attributed to  $-\text{CH}$   $\text{sp}^2$  and  $\text{sp}^3$  hybridisation stretching motions. At approximately 3050  $\text{cm}^{-1}$ , a weak stretch is apparent between the hydrogen (X–H) region and the broad loop, which forms out of a single peak at 3455  $\text{cm}^{-1}$ , corresponding to  $-\text{OH}$  stretch. The sharp peak at 1753  $\text{cm}^{-1}$ , which corresponds to carbonyl stretching, indicates the presence of strong ester linkages (C=O).

The spectrum of PCL exhibits all of the polymer's characteristic peaks, with two peaks between 2939 and 2857  $\text{cm}^{-1}$ , attributed to asymmetric and symmetric  $-\text{CH}$  stretches, respectively. A sharp peak at 1724  $\text{cm}^{-1}$  is likely due to carbonyl stretching, and the stretches centred between 1247  $\text{cm}^{-1}$  and 1170  $\text{cm}^{-1}$  are due to asymmetric and symmetric C–O–C ether stretches, respectively. The peak at 1293  $\text{cm}^{-1}$  can be attributed to C–O and C–C stretches, whereas the medium intensity peak at 1364  $\text{cm}^{-1}$  is likely associated with  $\text{CH}_3$  bending.

The spectrum of the specific SF region can be found in Appendix A: Figure A-13. The SF powder spectrum, derived from *B. mori* exhibits a strong amide I peak, at 1641  $\text{cm}^{-1}$ , indicating a random coil structure of C=O stretching, which is typical of regenerated SF dissolved in strong chaotropic salts, such as LiBr. The amide II shows an absorption peak at 1535  $\text{cm}^{-1}$ , which corresponds to NH bending ( $\alpha$ -helix, random coil), and the band that appears at approximately 1120  $\text{cm}^{-1}$  corresponds to amide III CN stretching. The ester functions of PGS and PCL can also be seen in Figure 5.4b, at approximately 1230  $\text{cm}^{-1}$  and 1700  $\text{cm}^{-1}$ , corresponding to out-of-phase C–O–C and C=O stretching, respectively.

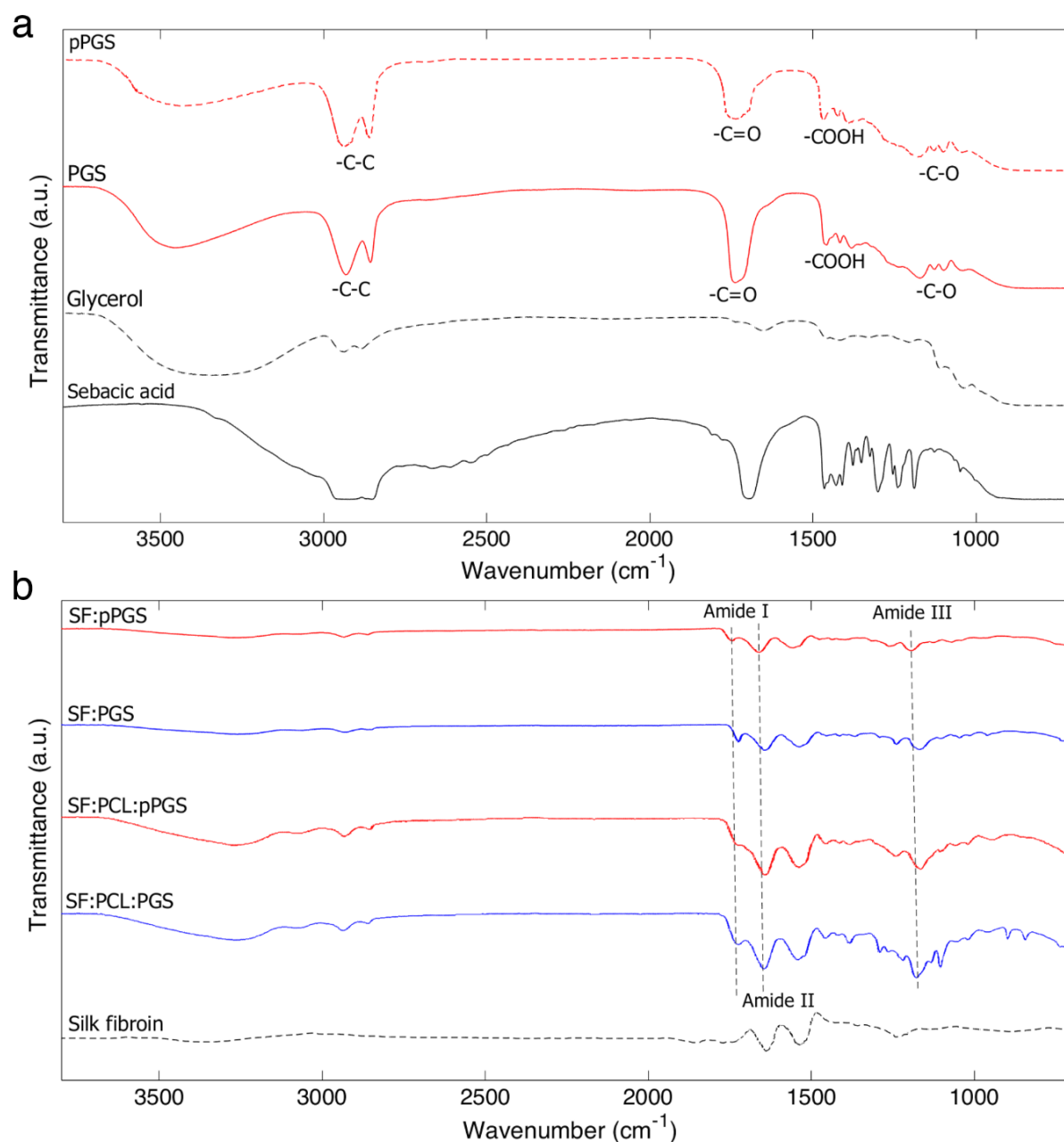


**Figure 5.4** ATR-FTIR spectra of **(a)** the individual polymers and the **(b)** binary and trinary electrospun mats. Scaffolds that contain PGS are shown in blue, whereas scaffolds that contain pPGS are shown in pink. Binary blend ratios were SF:(p)PGS 2:1 (w/w), whereas the trinary SF:PCL:(p)PGS ratio was 1:0.5:0.5 (w/w).

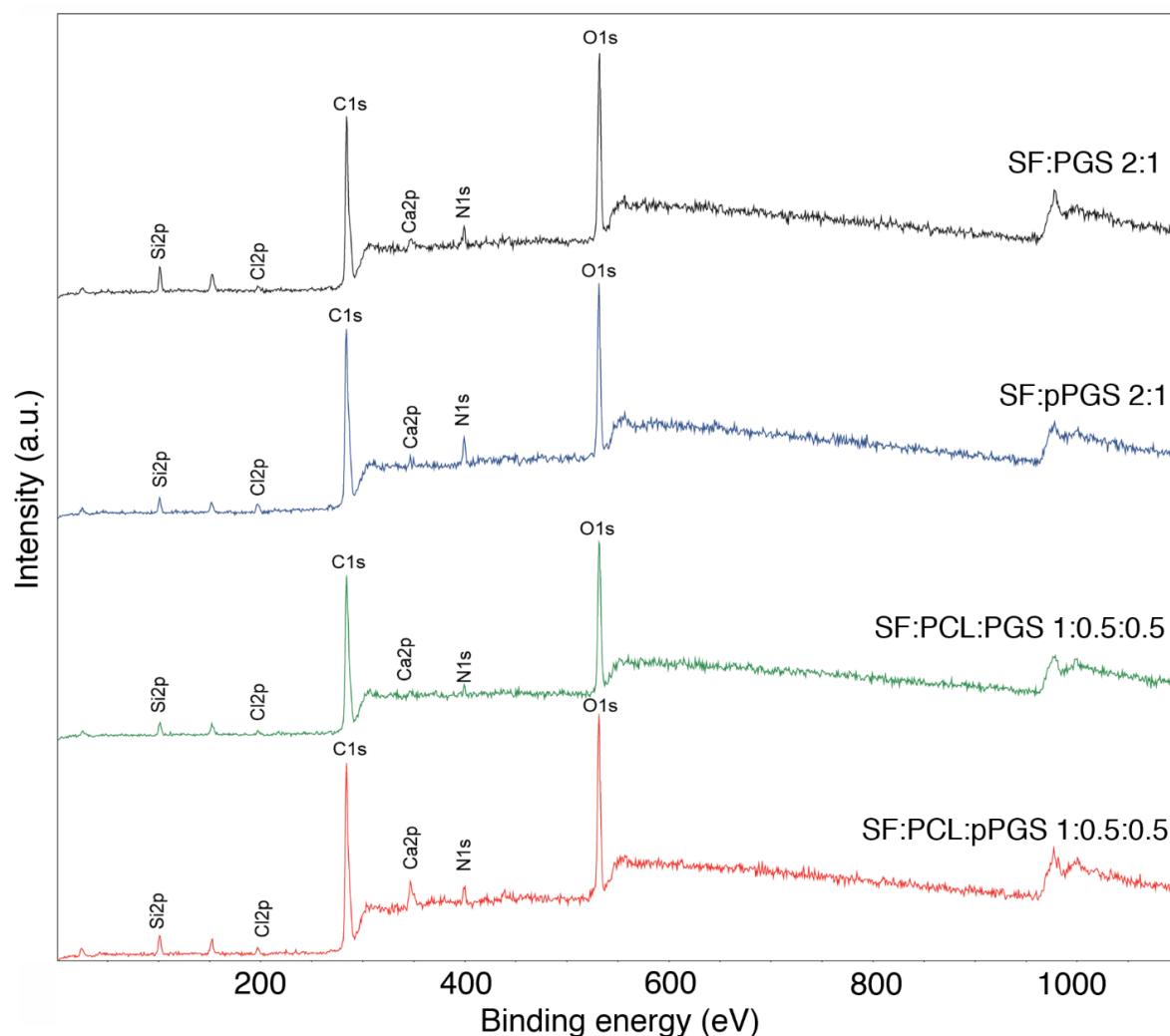


**Figure 5.5** XPS survey of the trinary SF:PCL:(p)PGS and binary SF:(p)PGS electrospun mats.

The surface chemistries of the composite electrospun binary and trinary blends were evaluated by XPS analysis, at an information depth of approximately 10 nm. Figure 5.5 displays the XPS spectra for the 1:0.5:0.5 SF:PCL:(p)PGS and 2:1 SF:(p)PGS fibrous mats. No peaks were apparent at the Li and Br regions of the surveys, verifying the successful removal of LiBr from the regenerated powdered SF, via ethanol precipitation followed by filtration with deionised water. Peak intensities for C1s, at 284 eV; O1s, at 531 eV; N1s, at 399 eV; Ca2p, at 346 eV; Cl2p, at 196 eV; and Si2p, at 101 eV were present in all examined blends. As indicated in Table 5.3, although the calculated theoretical values for each blend fell within a margin of error (5%) for the predicted values, the nitrogen contents were considerably lower for all the blends examined. This suggests that the high in nitrogen content regions of SF polymer chains, at the surface of the fibres, are facing inwards and towards the core of the fibres. Further evaluation by atomic force microscopy in contact mode can shed light on this

observation. The presence of silica traces could be attributed to the use of baking paper to collect the fibres.

**Table 5.3** Surface chemical compositions of the electrospun ternary 1:0.5:0.5 (w/w) SF:PCL:(p)PGS and binary 2:1 (w/w) SF:(p)PGS mats, via XPS analysis. The percentages in brackets () refer to the theoretical values of each polymer.

Ratio (w/w)	Outcome (%)	Elemental Ratio Atom (%)				
		C1s	O1s	N1s	Ca2p	Cl2p
SF:PCL:PGS	Experimental	70.8	27.2	1.35	0.28	0.37
	Theoretical	(56.8)	(25.7)	(15.6)	(0.70)	(1.30)
SF:PCL:pPGS	Experimental	68.7	26.8	2.66	1.36	0.48
	Theoretical	(56.8)	(25.7)	(15.6)	(0.65)	(1.25)
SF:PGS	Experimental	70.1	24.2	4.50	0.31	0.89
	Theoretical	(56.7)	(26.0)	(15.4)	(0.62)	(1.28)
SF:pPGS	Experimental	67.4	28.3	3.20	0.63	0.47
	Theoretical	(56.7)	(26.0)	(15.4)	(0.64)	(1.26)

### 5.3.3 The influence of PGS in the degradation of the electrospun mats

The effect of PGS in the degradation profile of the ternary electrospun mats was assessed in a PBS (pH 7.2) solution at room temperature ( $22 \pm 4$  °C) as described in detail in *Section 3.4.9*. At specific time points, pre-weighed scaffolds were removed from the PBS solution and vacuum dried, followed by determining the net weight loss (%) from time point zero to time point X.

The PGS specimens (Figure 5.6a, Appendix A: Table A-2) retained most of their original mass during 3 days of incubation, with a minimum weight loss of 3%, observed after 30 min of incubation, and a maximum weight loss of 42.6%, after one month of incubation. Within this group, a clear trend towards mass loss was observed with decreasing amounts of PCL within the scaffolds.

A similar pattern was observed for the pPGS group (Figure 5.6b, Appendix A: Table A-2), in which samples with lower PCL ratios demonstrated higher degrees of degradation. A similar finding was reported by Liu et al., in which PCL-containing fibres presented slower degradation rates than PGS-containing fibres [28]. Therefore, by using the two variant forms of PGS and adjusting its ratio within the polymer blends, the degradation of the composite electrospun mats can be modulated. This process can eventually be used to calibrate the breakdown of

the ECM-like fibre structure, to occur at an appropriate rate that complements the natural ECM reorganisation during the wound healing process.

The initial lack of degradation observed for PCL-backbone SF:PGS blends was expected, as many studies have shown that PCL can withstand hydrolytic degradation due to its hydrophobic nature [29–31]. Polyesters, such as PCL, degrade significantly faster via enzyme-mediated hydrolysis [29] and have been shown to have poor degradation behaviour in PBS [30]. Nadim et al. reported only 26% mass loss over 30 days for a fibrous PCL:PGS mat containing an equal mass ratio [32], which is similar to the degradation behaviour observed for the 1:0.5:0.5 SF:PCL:(p)PGS mat in this study (Figure 5.6). The weight loss observed for the SF:PCL:PGS group is lower than that reported by Nadim et al., as the incorporation of SF into the blend, made the resulting fibres even more resistant to water degradation – illustrating one of the ways that the integration of a natural polymer can influence the degradation properties of composite structures [33].

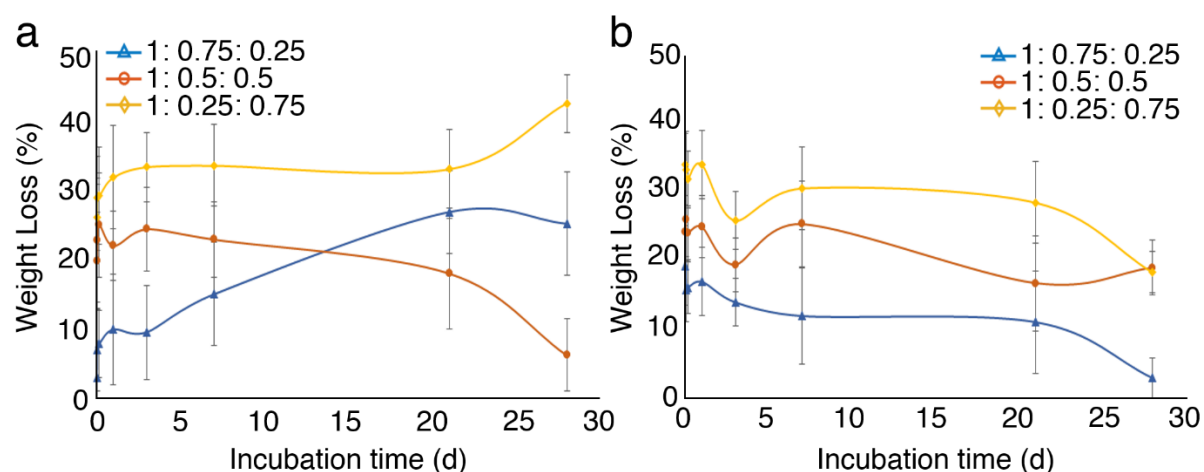


**Figure 5.6** Percentage of mass loss for the PGS-containing fibres, at varying incubation times. Blend (w/w) ratios of **(a)** SF:PCL:PGS, and **(b)** SF:PCL:(p)PGS. The fibres were submerged in PBS solution, pH 7.2, at room temperature ( $22 \pm 4$  °C). A photograph of the specimens used for the weight loss analysis can be found in Appendix A: Figure A-14.

One advantage of SF is its stability in water, which may prevent the premature dissolution of composite electrospun mats. Furthermore, the ethanol treatment of acid-based SF blends can promote the formation of hydrogen-bonded  $\beta$ -sheet structures (silk II), which can be used to manipulate hydrophilicity and improve the scaffold's degradation in aqueous environments [33, 34]. The macroscopic assessment of ternary electrospun mats after ethanol treatment is



displayed in Figure 5.7. Silk II structures have been shown to exhibit higher hydrophobicity, based on the contact angle measurements conducted by Jin et al. [34], which indicated improved stability in PBS solution and would explain the lower degradability of the ternary SF:PCL:PGS composite fibres compared with that of the binary PCL:PGS fibrous mats, not containing SF.

Initially, extended incubation periods were expected to result in additional hydrolysis time, resulting in the increased mass loss of the scaffolds. Although this behaviour was observed for the PGS groups, the opposite event appears to occur for the pPGS groups, for which an inverse correlation between the incubation time and degradation can be observed. The data displayed in Figure 5.6 refer to the average values of the measured degradation of each specimen, rather than the sum of all previously measured degradation.

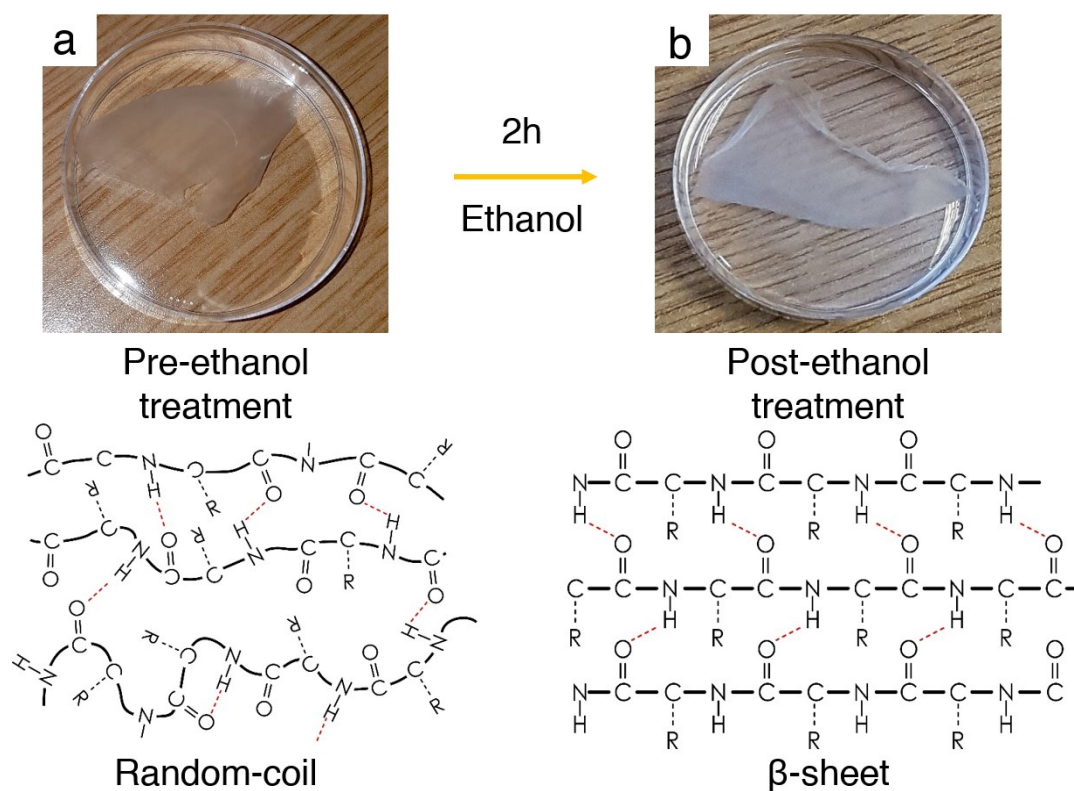


**Figure 5.7** Fibroin crystallinity. Macroscopic observation of the effects of ethanol, **(a)** before and **(b)** after the treatment of SF:PCL:(p)PGS electrospun mats. Upon immersion in ethanol for 2 h, the induced crystallinity of the silk fibroin protein affects the random coil configuration of the molecules, forming  $\beta$ -sheet blocks of amino acids via hydrogen bonding.

A higher degree of esterification density within the PGS structure was expected to hamper degradation relative to structures containing pPGS, but no significant differences were

observed for mass loss between the PGS and pPGS blends, as assessed by the minimum and maximum weight loss values, which agrees with the findings reported by Pomerantseva et al. [35]. However, they further reported that water uptake decreased as the curing time of PGS increased; therefore, pPGS likely displays reduced degradability compared with PGS. Furthermore, the water uptake of PGS was reported to decrease as the curing time of the elastomer increased [35]. Because the pPGS group appears to have a greater capacity to retain water, it may retain water mass, even after the dehydration process, explaining the lower mass loss of pPGS compared with PGS. The scaffold's ability to retain water can be associated with its wettability, which is recognised as a primary factor that governs protein adsorption and cell adhesion [36, 37].

A dressing that readily retains water may dehydrate the wound bed, increasing the likelihood of scarring, whereas a low degree of water retention may increase the risk of infection and halt the healing process due to the build-up of exudates in the wound bed; thus, finding the optimal balance between the two states can be challenging [38]. These results demonstrated that the tuning of all three polymers within the composite fibre structure could influence the upper and lower bounds – that is necessary to identify the appropriate conditions required to control the rate of degradation. Further evaluation of the degradation rate in the presence of the culture media (DMEM-complete), could provide valuable insights towards the degradability of the scaffolds during the *in vitro* cell culture experiments.

#### 5.3.4 Wettability

Surface wettability is a crucial characteristic of polymeric biomaterials, playing critical roles in cellular adhesion, proliferation, migration, and survival [39]. Interactions between the biomaterial and cells can be especially important when determining whether a construct or a device can regulate inflammatory responses and can determine the degree of tissue adhesiveness [40]. Cell attachment is mostly governed by alterations in surface energy, with higher-energy hydrophilic surfaces encouraging adhesion, whereas low-surface-energy substrates typically inhibit cellular adhesion [37]. Moderately hydrophilic/hydrophobic surfaces favour the adsorption of surface proteins, mediating cellular adhesion and activating downstream signalling responses following the activation of specific cell adhesion receptors, which, in turn, induce the deposition of the ECM structural components required for tissue regeneration [37, 41]. Moderately hydrophilising a hydrophobic surface, such as PCL, can alter the surface energy of the biomaterial, improving the adsorption of surface-related proteins and the diffusion of nutrients, which can lead to optimal adhesion, increased cellular infiltration, and tissue in-growth in a wounded area [42].

The contact angles were determined for each binary, trinary, and PCL scaffold examined in this study, to investigate the effects of PGS and SF on the hydrophobicity of PCL. Figure 5.8 presents the contact angle values determined for each group, which were examined following the settlement of a 5- $\mu\text{L}$  water droplet on the surface of the electrospun mats, and the differences among groups were examined. The hydrophobicity of the PCL-only fibres was confirmed, with a high contact angle of  $125.9^\circ \pm 6.5^\circ$ .

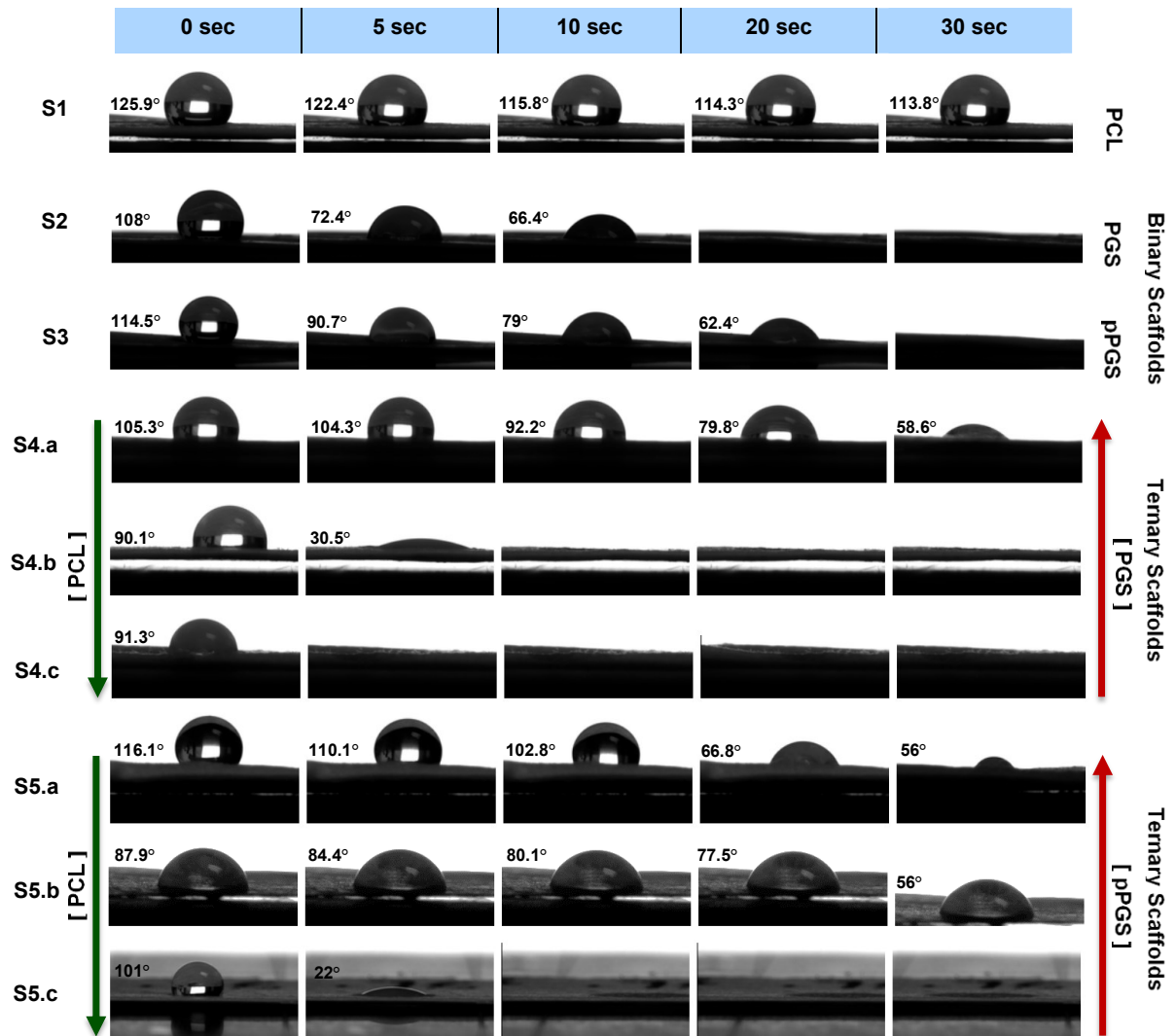


**Figure 5.8** Water contact angle over time. PCL, binary SF:PGS and SF:pPGS and trinary PCL-backbone SF:PGS and SF:pPGS electrospun mats. Time intervals 0, 5, 10, 20, and 30 s. **S1**: PCL; **S2**: SF:PGS; **S3**: SF:pPGS; **S4**: PCL-backbone SF:PGS; and **S5**: PCL-backbone SF:pPGS. The letters indicate the ratios of the trinary blends, where the SF:PCL: (p)PGS ratio is **(a)** 1:0.75:0.25, **(b)** 1:0.50:0.50, and **(c)** 1:0.25:0.75. Red arrows indicate changes in (p)PGS concentrations and green arrows indicate changes in PCL concentrations.

The hydrophilicity/hydrophobicity ratio of a fibrous scaffold affects the adhesion and proliferation behaviours of the cells [43]. By integrating a natural polymer with synthetic, hydrophobic polymers, such as PCL, the contact angle of the fibres can be reduced, improving the hydrophilicity of the final construct. SF fibres can be increasingly hydrophilic due to the high number of amino acid and carboxylic domains that they contain [44]. Based on the XPS analysis, the nitrogen content at the surface of the fibres was significantly lower than the calculated theoretical values, suggesting that the N-rich regions of the SF chains were facing inwards. This concurrently insinuates that the majority of the carboxylic domains of the SF polymer chains will be facing outwards, and thus can directly affect the hydrophilicity of the composite constructs.

The random coil conformation of the fibres can be stabilised through the formation of  $\beta$ -sheets with the  $\text{Ca}^{2+}$  present between the fibroin domains, which occurs during both the electrospinning process and post-treatment with ethanol [45, 46]. PGS is also well-known for its hydrophilicity due to the presence of hydroxyl groups on the polyester backbone. The titration of the total acid numbers can be adjusted by functionalising the elastomer, making it possible to increase the hydrophilicity [47, 48]. As the number of ester linkages increases during esterification, the hydrophilicity of PGS in the composite scaffold is also expected to increase, relative to its pre-polymerised counterpart.

As Figure 5.8 indicates, the addition of higher concentrations of PGS to the composite electrospun membranes increased the wettability of the corresponding scaffolds over a period of 30 s. Additionally, higher concentrations of PGS increased the water absorbability of the trinary scaffolds, in comparison to the mats containing pPGS. For the binary SF:PGS and SF:pPGS scaffolds, which presented contact angles of  $83^\circ \pm 10.6^\circ$  and  $124.5^\circ \pm 8.02^\circ$ , respectively, the PGS-containing membranes concurred with the trinary electrospun mats observations, demonstrating increased wettability and reduced contact angles in comparison to the pPGS-containing mats. Figure 5.9 shows the WCA measurements 0, 5, 10, 20 and 30 s after the application of a deionised water droplet at the surface of each electrospun membrane examined.

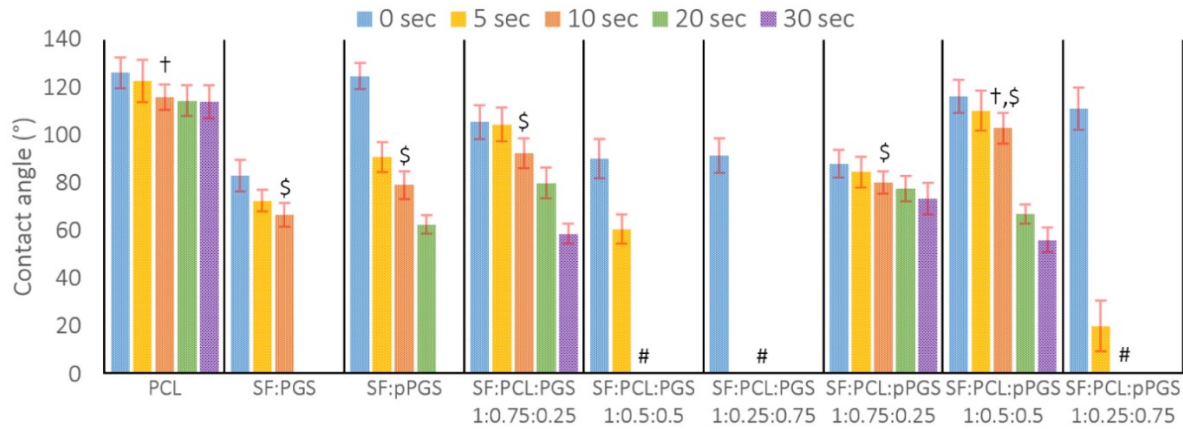


**Figure 5.9** Water contact angle measurements of the ternary SF:PCL:(p)PGS, binary SF:(p)PGS and PCL electrospun mats. Blue, yellow, red, green, and purple bars represent the contact angles measured for a 5- $\mu$ L deionised water droplet settling on the surface of electrospun mats after 0, 5, 10, 20, and 30 s, respectively. The symbols ( $\dagger$ ,  $\$$ ,  $\#$ ) - indicate significant differences and similar values (one-way ANOVA with Tukey multiple comparison test) for time point 10 s between the various groups examined ( $n = 6$ ,  $p \leq 0.05$ ). For instance, SF:PGS presented similar ( $\$$ ,  $p \geq 0.05$ ) contact angle values with SF:pPGS, SF:PCL:PGS 1:0.75:0.25, SF:PCL:pPGS 1:0.75:0.25 and 1:0.5:0.5, significantly lower contact angle values ( $\dagger$ ,  $p \leq 0.05$ ) than PCL, and significantly higher ( $\#$ ,  $p \leq 0.05$ ) contact angle values than SF:PCL:PGS 1:0.55:0.5 and 1:0.25:0.75, and SF:PCL:pPGS 1:0.25:0.75 for time point 10 s.

### 5.3.5 Cell adhesion, viability, and proliferation

Human dermal fibroblasts were passaged in supplemented DMEM and seeded on the electrospun mats. Figure 5.10a depicts the cell growth and expansion of each electrospun SF:PCL:(p)PGS mat composition, 1, 3, 5, and 7 days after initial seeding. The Alamar blue cell viability assay was used to assess cell proliferation on each electrospun membrane. Viable cells reduce the non-fluorescent Resazurin (blue) to a fluorescent, red-coloured complex, called resorufin. The metabolic activity is proportional to cell viability, where resorufin act as an electron acceptor for enzymes (NADP and FADH) during oxygen consumption [49]. Because growth followed the same patterns, with no significant differences in the extent to which seeded cells reduced the reagent between the pPGS and PGS, the results were merged for clarity.

The proliferative properties of the SF:PCL:(p)PGS electrospun membranes were analysed by establishing a relationship between cell growth and the incubation period. The cell viability

on electrospun mats formed from the three tested SF:PCL:(p)PGS ratios were examined and compared with the cell viability on PCL-only electrospun mats. The fibroblasts appeared to gradually expand on the ternary scaffolds, with a consistent and significant ( $p < 0.05$ ) increase in the number of cells present as the number of days in culture increased, compared with the growth of cells in the PCL-only group. This linear increase in cell viability was apparent for all examined blends. Thus, the composite fibres appeared to provide a matrix on which fibroblasts were able to proliferate rapidly.

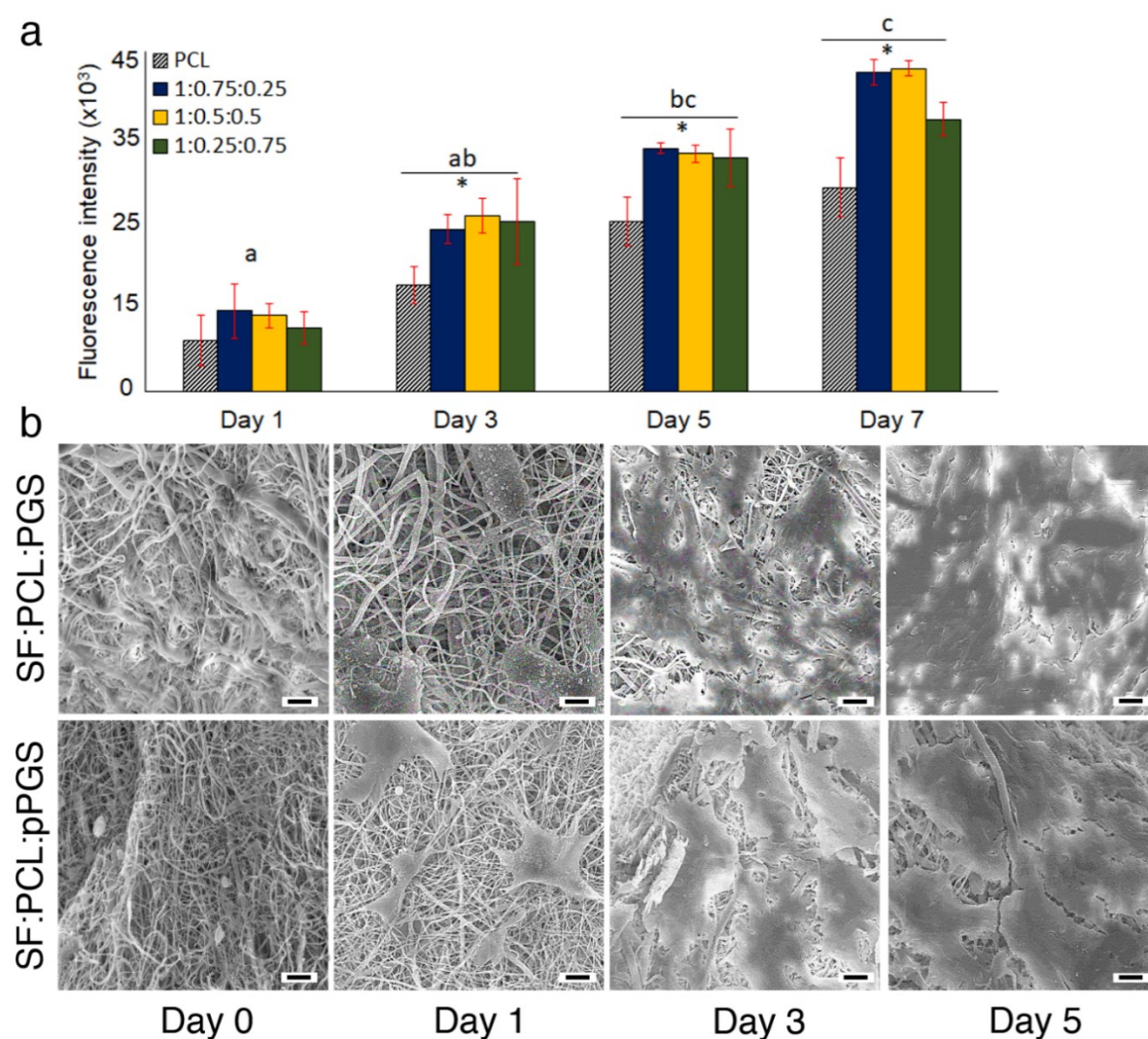


**Figure 5.10** Attachment and proliferation of HDFs on ternary electrospun membranes. **(a)** Alamar blue™ cell viability assay of the SF:PCL:(p)PGS scaffolds. Values represent the mean  $\pm$  SD ( $n = 9$ ,  $p < 0.05$ ). a, b, c indicates significant differences and similar values (ANOVA). (\*) - indicates significant differences between the PCL-only and ternary electrospun mat groups **(b)** SEM images of HDFs seeded morphology on ternary SF:PCL:(p)PGS 1:0.5:0.5 electrospun scaffolds. Scale bar, 10  $\mu$ m.

The proliferative and adhesive properties of the electrospun SF:PCL:PGS and SF:PCL:pPGS mats, at the tested ratio of 1:0.5:0.5, were further assessed by fixing the fibroblast seeded scaffolds and examining cell morphology, using SEM imaging (Figure 5.10b). The SEM micrographs presented fibroblasts with polygonal morphology and elongated spindles, which are characteristic of healthy fibroblasts, unlike the spheroid cells that are predominately found among fibroblasts grown on synthetic materials, such as the pure PCL electrospun membranes, as illustrated in Figure 5.11. Cell attachment to the fibre surface was visibly apparent on the day of inoculation. A good surface interaction occurs between the adherent cells and the electrospun fibres, as shown in the SEM images. This morphological characteristic can be attributed to the addition of the biocompatible PGS and SF protein. The cells appeared to spread quickly over the electrospun mats and were capable of expanding and covering the scaffolds within 5 days, as observed on the SEM micrographs.

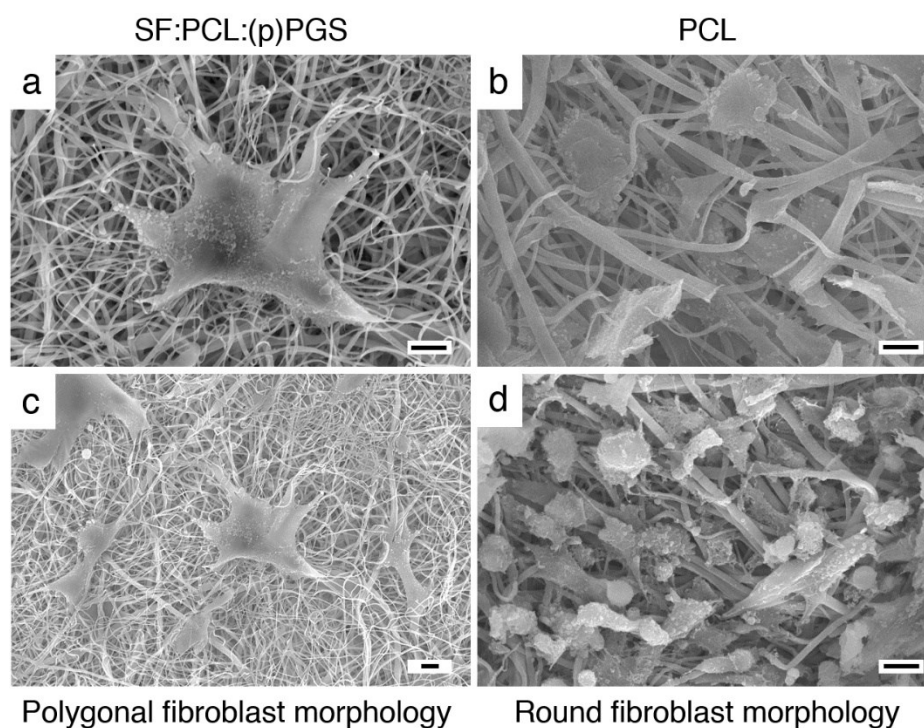


**Figure 5.11** Comparisons of fibroblast morphologies, assessed by SEM, after seeding on **(a, c)** trinary SF:PCL:(p)PGS or **(b, d)** PCL electrospun mats. The characteristic polygonal and elongated fibroblast morphologies, corresponding to a healthy, spindle-shaped fibroblast, is apparent upon interaction with the biocompatible SF protein, in contrast to the round fibroblast morphology observed for cells seeded on the synthetic PCL polymer fibres. Scale bar, 10  $\mu\text{m}$ .

The cryo-SEM micrographs of seeded cells on the electrospun scaffolds were further obtained, imaged by FIB-SEM using an acceleration voltage of 10 kV. To examine cellular

infiltration, a region covered by 5-day cultured fibroblasts was chosen, and the surface was subsequently milled via the ion beam, and the specimen was tilted through a “slice and view” process. Although the presence of crystals was apparent on the surface of the cells, due to the crystallisation of the intracellular fluid, the surface morphology and corresponding infiltration of the cells within the scaffolds can be observed.

Figure 5.12 displays the cryo-SEM micrographs of FIB incisions, obtained for the HDF-seeded trinary, composite fibre mats. Fibroblast ingrowth along the fibrous network of the scaffold indicates the complete ingrowth of the electrospun mats on day 5. These results indicated that the composite fibrous scaffolds allow for strong fibroblast attachment and proliferation.

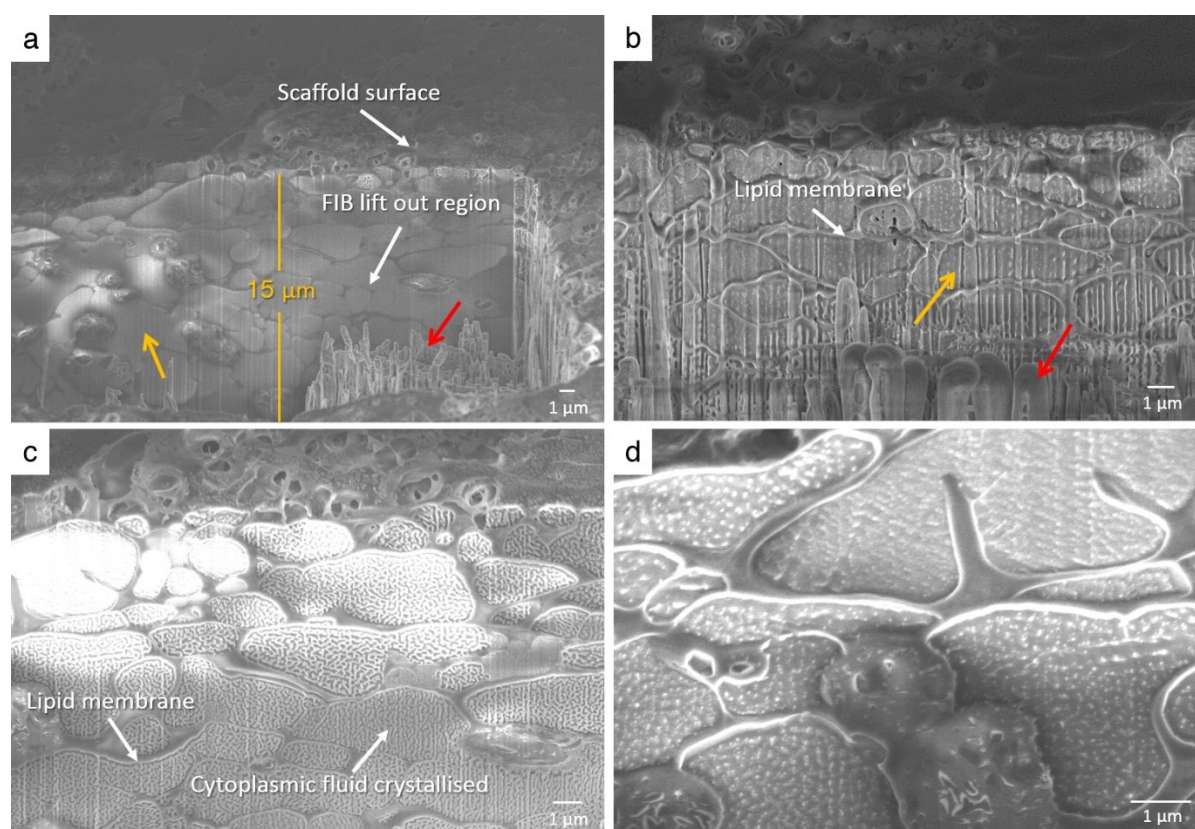


**Figure 5.12** Cryo-FIB-SEM micrographs obtained from trinary SF: PCL: (p)PGS scaffolds, 5-days after being seeded with fibroblasts. The specimens were initially submerged in liquid nitrogen. The figure depicts nanoscale tomography cross-sections of cell-containing scaffolds after being milled with a cryo-focused ion beam milling scanning electron microscope (Zeiss Crossbeam 550 FIB/SEM, Carl Zeiss AG, Germany). (a) Top view of the FIB lift-out region of the specimen at milling depth of approximately 15 µm. (b-c) Tilted views of the cross-section area that depicts the bidirectional growth of the cells within the scaffold. (d) A magnified region from micrograph (c).



The red arrows indicate the polymeric fibres; the yellow arrows indicate fibroblasts. The cells present a well-defined lipid membrane due to variations between the phases of lipid and cytoplasmic fluid crystallization, allowing for the cells to be distinguished. The micrographs were obtained with the assistance of the instrument scientist, Dr Thomas Glen, in the School of Physics at the University of Edinburgh.

## 5.4 Conclusions

Although PCL has been extensively used for tissue engineering applications because of its good mechanical properties and ability to mimic many aspects of the natural ECM architecture, its hydrophobicity makes it an unfavourable candidate, as a biomaterial. To address this problem, PCL-backbone SF:PGS electrospun mats were fabricated, which collectively improved the physicochemical properties of the biomaterial system.

The composite fibres displayed smooth morphologies, with controllable fibre diameters, appropriate pore sizes for fibroblast expansion, and tuneable hydrophobicity/hydrophilicity adjunct to the form and proportion of PGS within the blends. The ternary scaffolds appeared to be biocompatible, allowing for fibroblasts to effectively adhere and proliferate at high viability numbers. The developed nozzle-free electrospinning technology also addresses key challenges encountered during the fabrication of electrospun biomaterials, such as the meagre production rate associated with conventional needle-based setups. In addition, the straightforward SF extraction method developed, minimises the time required to obtain and purify the protein.

This is the first time in literature that electrospun composite fibres deriving from a three-polymer system have been successfully generated through free surface high-throughput electrospinning. The collective properties presented by the PCL-backbone SF:(p)PGS fibres can be recognised as a skin substitute, where, as a next step, further assessment on an animal model can provide essential insights on the wound healing competencies of the biomaterial system.

## 5.5 References

1. Zhu, M., Li, W., Dong, X., Yuan, X., Midgley, A. C., Chang, H., Wang, Y., Wang, H., Wang, K., Ma, P. X., Wang, H., & Kong, D. (2019). In vivo engineered extracellular matrix scaffolds with instructive niches for oriented tissue regeneration. *Nature Communications*, *10*(1), 1–14. <https://doi.org/10.1038/s41467-019-12545-3>
2. Dias, J. R., Granja, P. L., & Bártolo, P. J. (2016). Advances in electrospun skin substitutes. *Progress in Materials Science*, *84*(1), 314–334. <https://doi.org/10.1016/j.pmatsci.2016.09.006>
3. Wu, C., Chen, T., Xin, Y., Zhang, Z., Ren, Z., Lei, J., Chu, B., Wang, Y., & Tang, S. (2016). Nanofibrous asymmetric membranes self-organized from chemically heterogeneous electrospun mats for skin tissue engineering. *Biomedical Materials*, *11*(3), 1–12. <https://doi.org/10.1088/1748-6041/11/3/035019>
4. Bacakova, M., Musilkova, J., Riedel, T., Stranska, D., Brynda, E., Bacakova, L., & Zaloudkova, M. (2016). The potential applications of fibrin-coated electrospun polylactide nanofibers in skin tissue engineering. *International Journal of Nanomedicine*, *11*(1), 771–789. <https://doi.org/10.2147/IJN.S99317>
5. Vig, K., Chaudhari, A., Tripathi, S., Dixit, S., Sahu, R., Pillai, S., Dennis, V. A., & Singh, S. R. (2017). Advances in skin regeneration using tissue engineering. *International Journal of Molecular Sciences*, *18*(4), 789–798. <https://doi.org/10.3390/ijms18040789>
6. Xue, J., Wu, T., Dai, Y., & Xia, Y. (2019). Electrospinning and electrospun nanofibers: Methods, materials, and applications. *Chemical Reviews*, *119*(8), 5298–5415. <https://doi.org/10.1021/acs.chemrev.8b00593>
7. Agarwal, S., Wendorff, J. H., & Greiner, A. (2008). Use of electrospinning technique for biomedical applications. *Polymer*, *49*(26), 5603–5621. <https://doi.org/10.1016/j.polymer.2008.09.014>
8. Huang, C. Y., Hu, K. H., & Wei, Z. H. (2016). Comparison of cell behavior on PVA/PVA-gelatin electrospun nanofibers with random and aligned configuration. *Scientific Reports*, *6*(1), 1–8. <https://doi.org/10.1038/srep37960>
9. Chen, F., Porter, D., & Vollrath, F. (2012). Structure and physical properties of silkworm cocoons. *Journal of the Royal Society Interface*, *9*(74), 2299–2308. <https://doi.org/10.1098/rsif.2011.0887>
10. Wang, Y., Ameer, G. A., Sheppard, B. J., & Langer, R. (2002). A tough biodegradable elastomer. *Nature Biotechnology*, *20*(6), 602–606. <https://doi.org/10.1038/nbt0602-602>
11. Rockwood, D. N., Preda, R. C., Yücel, T., Wang, X., Lovett, M. L., & Kaplan, D. L. (2011). Materials fabrication from *Bombyx mori* silk fibroin. *Nature Protocols*, *6*(10), 1612–1631. <https://doi.org/10.1038/nprot.2011.379>
12. Sasithorn, N., & Martinová, L. (2014). Fabrication of silk nanofibres with needle and roller electrospinning methods. *Journal of Nanomaterials*, *113*(1), 226–234. <https://doi.org/10.1155/2014/947315>
13. Amiraliyan, N., Nouri, M., & Haghghat Kish, M. (2010). Structural characterization and mechanical properties of electrospun silk fibroin nanofiber mats. *Polymer Science Series A*, *52*(4), 407–412. <https://doi.org/10.1134/S0965545X10040097>
14. Zhang, Q., Yan, S., & Li, M. (2009). Silk fibroin based porous materials. *Materials*, *2*(4), 2276–2295. <https://doi.org/10.3390/ma2042276>
15. Zhu, J., Luo, J., Zhao, X., Gao, J., & Xiong, J. (2016). Electrospun homogeneous silk fibroin/poly ( $\epsilon$ -caprolactone) nanofibrous scaffolds by addition of acetic acid for tissue engineering. *Journal of Biomaterials Applications*, *31*(3), 421–437. <https://doi.org/10.1177/0885328216659775>
16. Murphy, C. M., Haugh, M. G., & O'Brien, F. J. (2010). The effect of mean pore size on cell

- attachment, proliferation and migration in collagen-glycosaminoglycan scaffolds for bone tissue engineering. *Biomaterials*, 31(3), 461–466. <https://doi.org/10.1016/j.biomaterials.2009.09.063>
17. Murphy, C. M., & O'Brien, F. J. (2010). Understanding the effect of mean pore size on cell activity in collagen-glycosaminoglycan scaffolds. *Cell Adhesion and Migration*, 4(3), 377–381. <https://doi.org/10.4161/cam.4.3.11747>
  18. Gorth, D., & J Webster, T. (2011). Matrices for tissue engineering and regenerative medicine. In T. J. Webster (Ed.), *Biomaterials for Artificial Organs* (1st ed., pp. 270–286). Rhode Island, USA: Woodhead Publishing. <https://doi.org/10.1533/9780857090843.2.270>
  19. Karageorgiou, V., & Kaplan, D. (2005). Porosity of 3D biomaterial scaffolds and osteogenesis. *Biomaterials*, 26(27), 5474–5491. <https://doi.org/10.1016/j.biomaterials.2005.02.002>
  20. Mallick, K. K., & Cox, S. C. (2013). Biomaterial scaffolds for tissue engineering. *Frontiers in Bioscience - Elite*, 5(1), 341–360. <https://doi.org/10.2741/E620>
  21. Giebel, E., Getze, J., Röcker, T., & Greiner, A. (2013). The importance of crosslinking and glass transition temperature for the mechanical strength of nanofibers obtained by green electrospinning. *Macromolecular Materials and Engineering*, 298(4), 439–446. <https://doi.org/10.1002/mame.201200080>
  22. Drew, C., Wang, X., Samuelson, L. A., & Kumar, J. (2003). The effect of viscosity and filler on electrospun fiber morphology. *Journal of Macromolecular Science - Pure and Applied Chemistry*, 40(12), 1415–1422. <https://doi.org/10.1081/MA-120025320>
  23. Fong, H., Chun, I., & Reneker, D. H. (1999). Beaded nanofibers formed during electrospinning. *Polymer*, 40(19), 4582–4592. [https://doi.org/10.1016/S0032-3861\(99\)00068-3](https://doi.org/10.1016/S0032-3861(99)00068-3)
  24. Luo, C. J., Stride, E., & Edirisinghe, M. (2012). Mapping the influence of solubility and dielectric constant on electrospinning polycaprolactone solutions. *Macromolecules*, 41(11), 4669–4680. <https://doi.org/10.1021/ma300656u>
  25. Gu, X., Song, X., Shao, C., Zeng, P., Lu, X., Shen, X., & Yang, Q. (2014). Electrospinning of poly(butylene-carbonate): Effect of solvents on the properties of the nanofibers film. *International Journal of Electrochemical Science*, 9(1), 8045–8056. <https://doi.org/10.1288/vo91208045u>
  26. Nurwaha, D., Han, W., & Wang, X. (2018). Investigation of a new needleless electrospinning method for the production of nanofibers. *Journal of Engineered Fibers and Fabrics*, 8(4), 42–49. <https://doi.org/10.1177/155892501300800413>
  27. Niu, H., Lin, T., & Wang, X. (2009). Needleless electrospinning. A comparison of cylinder and disk nozzles. *Journal of Applied Polymer Science*, 114(6), 3524–3530. <https://doi.org/10.1002/app.30891>
  28. Liu, Y., Tian, K., Hao, J., Yang, T., Geng, X., & Zhang, W. (2019). Biomimetic poly(glycerol sebacate)/polycaprolactone blend scaffolds for cartilage tissue engineering. *Journal of Materials Science: Materials in Medicine*, 30(5), 1–11. <https://doi.org/10.1007/s10856-019-6257-3>
  29. Liang, S. L., Yang, X. Y., Fang, X. Y., Cook, W. D., Thouas, G. A., & Chen, Q. Z. (2011). In Vitro enzymatic degradation of poly (glycerol sebacate)-based materials. *Biomaterials*, 32(33), 8486–8496. <https://doi.org/10.1016/j.biomaterials.2011.07.080>
  30. Ye, W. P., Du, F. S., Jin, W. H., Yang, J. Y., & Xu, Y. (1997). In vitro degradation of poly(caprolactone), poly(lactide) and their block copolymers: Influence of composition, temperature and morphology. *Reactive and Functional Polymers*, 32(2), 161–168. [https://doi.org/10.1016/S1381-5148\(96\)00081-8](https://doi.org/10.1016/S1381-5148(96)00081-8)
  31. Shalumon, K. T., Anulekha, K. H., Chennazhi, K. P., Tamura, H., Nair, S. V., & Jayakumar, R. (2011). Fabrication of chitosan/poly(caprolactone) nanofibrous scaffold for bone and skin tissue engineering. *International Journal of Biological Macromolecules*, 48(4), 571–576. <https://doi.org/10.1016/j.ijbiomac.2011.01.020>

32. Nadim, A., Khorasani, S. N., Kharaziha, M., & Davoodi, S. M. (2017). Design and characterization of dexamethasone-loaded poly (glycerol sebacate)-poly caprolactone/gelatin scaffold by coaxial electro spinning for soft tissue engineering. *Materials Science and Engineering C*, 78(1), 47–58. <https://doi.org/10.1016/j.msec.2017.04.047>
33. Lu, Q., Zhang, B., Li, M., Zuo, B., Kaplan, D. L., Huang, Y., & Zhu, H. (2011). Degradation mechanism and control of silk fibroin. *Biomacromolecules*, 12(4), 1080–1086. <https://doi.org/10.1021/bm101422j>
34. Jin, H. J., Park, J., Karageorgiou, V., Kim, U. J., Valluzzi, R., Cebe, P., & Kaplan, D. L. (2005). Water-stable silk films with reduced  $\beta$ -sheet content. *Advanced Functional Materials*, 15(8), 1241–1247. <https://doi.org/10.1002/adfm.200400405>
35. Pomerantseva, I., Krebs, N., Hart, A., Neville, C. M., Huang, A. Y., & Sundback, C. A. (2009). Degradation behavior of poly(glycerol sebacate). *Journal of Biomedical Materials Research - Part A*, 91A(4), 1038–1047. <https://doi.org/10.1002/jbm.a.32327>
36. Lin, W. C., & Razali, N. A. M. (2019). Temporary wettability tuning of PCL/PDMS micro pattern using the plasma treatments. *Materials*, 12(4), 1–16. <https://doi.org/10.3390/ma12040644>
37. Ferrari, M., Cirisano, F., & Morán, M. C. (2019). Mammalian Cell Behavior on Hydrophobic Substrates: Influence of Surface Properties. *Colloids and Interfaces*, 3(2), 1–16. <https://doi.org/10.3390/colloids3020048>
38. Kurusu, R. S., & Demarquette, N. R. (2019). Surface modification to control the water wettability of electrospun mats. *International Materials Reviews*, 64(5), 249–287. <https://doi.org/10.1080/09506608.2018.1484577>
39. Wang, G., Hu, X., Lin, W., Dong, C., & Wu, H. (2011). Electrospun PLGA-silk fibroin-collagen nanofibrous scaffolds for nerve tissue engineering. *In Vitro Cellular and Developmental Biology - Animal*, 47(3), 234–240. <https://doi.org/10.1007/s11626-010-9381-4>
40. Mariani, E., Lisignoli, G., Borzi, R. M., & Pulsatelli, L. (2019). Biomaterials: Foreign bodies or tuners for the immune response? *International Journal of Molecular Sciences*, 20(3), 1–42. <https://doi.org/10.3390/ijms20030636>
41. Zheng, J., Li, L., Tsao, H. K., Sheng, Y. J., Chen, S., & Jiang, S. (2005). Strong repulsive forces between protein and oligo (ethylene glycol) self-assembled monolayers: A molecular simulation study. *Biophysical Journal*, 89(1), 158–166. <https://doi.org/10.1529/biophysj.105.059428>
42. Azari, P., Azari, P., Hosseini, S., Murphy, B. P., & Martinez-Chapa, S. O. (2018). Electrospun biopolyesters: Hydrophobic scaffolds with favorable biological response. *Journal of Public Health International*, 1(1), 1–6. <https://doi.org/10.14302/issn.2641-4538.jphi-18-1975>
43. Dhandayuthapani, B., Yoshida, Y., Maekawa, T., & Kumar, D. S. (2011). Polymeric scaffolds in tissue engineering application: A review. *International Journal of Polymer Science*, 11(1), 1–20. <https://doi.org/10.1155/2011/290602>
44. Roy, T., Maity, P., Rameshbabu, A., Das, B., John, A., Dutta, A., Ghorai, S. K., Chattopadhyay, S., & Dhara, S. (2018). Core-shell nanofibrous scaffold based on polycaprolactone-silk fibroin emulsion electrospinning for tissue engineering applications. *Bioengineering*, 5(3), 1–17. <https://doi.org/10.3390/bioengineering5030068>
45. Zhou, W., Feng, Y., Yang, J., Fan, J., Lv, J., Zhang, L., Guo, J., Ren, X., & Zhang, W. (2015). Electrospun scaffolds of silk fibroin and poly(lactide-co-glycolide) for endothelial cell growth. *Journal of Materials Science: Materials in Medicine*, 26(1), 1–14. <https://doi.org/10.1007/s10856-015-5386-6>
46. Ghaeli, I., De Moraes, M. A., Beppu, M. M., Lewandowska, K., Sionkowska, A., Ferreira da Silva, F., Ferraz, M. P., & Monteiro, F. J. (2017). Phase behaviour and miscibility studies of collagen/silk fibroin macromolecular system in dilute solutions and solid state. *Molecules*, 22(8), 1–17. <https://doi.org/10.3390/molecules22081368>
47. De Sanctis, V., Soliman, A., Bernasconi, S., Bianchin, L., Bona, G., Bozzola, M., Buzi, F., De

- Sanctis, C., Tonini, G., Rigon, F., & Perissinotto, E. (2015). Primary dysmenorrhea in adolescents: Prevalence, impact and recent knowledge. *Pediatric Endocrinology Reviews*, 13(2), 512–520. <https://doi.org/10.1002/term>
48. Xu, B., Li, Y., Zhu, C., Cook, W. D., Forsythe, J., & Chen, Q. (2015). Fabrication, mechanical properties and cytocompatibility of elastomeric nanofibrous mats of poly(glycerol sebacate). *European Polymer Journal*, 64(2), 79–92. <https://doi.org/10.1016/j.eurpolymj.2014.12.008>
49. Kandhasamy, S., Perumal, S., Madhan, B., Umamaheswari, N., Banday, J. A., Perumal, P. T., & Santhanakrishnan, V. P. (2017). Synthesis and fabrication of collagen-coated ostholamide electrospun nanofiber scaffold for wound healing. *ACS Applied Materials and Interfaces*, 9(10), 8556–8568. <https://doi.org/10.1021/acsami.6b16488>

---

## Chapter 6

# Core/Shell Bicomponent Antimicrobial Nanofibres for the Prevention of Mesh-Associated Bacterial Infections

---

### 6.1 Introduction

As described in *Chapter 2*, hernia repair is one of the most commonly performed elective operations, for which hernia reduction using suture closures is associated with high reherniation rates; whilst, synthetic and bioprosthetic mesh closures are linked to several serious complications [1]. Among which, foreign body sensation due to being heavyweight, the development of fibrosis due to excessive strength leading to increased inflammation and loss of elasticity, tissue adhesion resulting to enterocutaneous fistula formation, as well as post-surgical deep mesh infections [1, 3].

The use of hernia meshes has been reported to reduce recurrence by 30%–50% compared with suture closure [2, 3]. In general, the intravenous and oral administration of prophylactic antibiotics, cannot ensure sufficient protection against surgical site infections (SSIs), especially those associated with deep incisional infected meshes [4]. In reviewing the different material design approaches that can be employed to produce a hernia mesh capable of addressing the aforementioned challenges, faced by the biomaterials utilised for hernia repair today, electrospun nanofibrous constructs are worth investigating.

Nanofibrous scaffolds, developed via the electrospinning process can represent a valuable step towards the development of an antimicrobial hernia mesh because the NFs formed through this process are lightweight, can attain a large surface area per unit mass, and present controllable fibre configurations [5]. Further, through the co-axial electrospinning technique, the incorporation of antimicrobial agents, in a spatially controlled, bilayer format, is also feasible. The utilisation of the co-axial electrospinning technique can provide further advantages over single-nozzle electrospinning, as selected properties can be combined within a bicomponent fibre, including the following: (1) the fabrication of electrospun membranes that incorporate a hydrophilic surface within a hydrophobic core in a single-core/sheath fibre; (2)

the encapsulation and protection of sensitive substances from the outer environment, by placing the active agent within the fibre core; (3) the design of programmable release kinetics from the fibre core, tailored for sustained release kinetics; and (4) obtain the controlled release of defined concentrations of pharmaceutical compounds [6–8]. Furthermore, by integrating a mechanically adapted polymer into the fibre core, the subsequent mechanical behaviour of the bicomponent fibre can be improved, while concurrently preventing it from influencing the fibre surface properties.

In this study, chitosan (CS) and nylon-6 (PA6) were selected to formulate the shell and core regions of the core/shell NFs, respectively, where polyethylene oxide (PEO) was added to the CS solution, as a carrier polymer, to stabilise and improve its electrospinnability and produce more homogenous fibres. Then, the antimicrobial substances 5-chloro-8-hydroxyquinoline (5CLO8Q) and polyhexanide (PHMB) were loaded within the polymer solutions of CS and PA6, respectively. The co-axial electrospinning process was subsequently employed to develop a bicomponent, nanostructured, hernia mesh biomaterial. Single-drug CS-5CLO8Q and PA6-PHMB electrospun NFs were also produced, and their physicochemical, mechanical and antimicrobial responses were compared against the composite core/shell PA6-PHMB/CS-5CLO8Q structure. The reasons underlying the choices of CS and PA6, as well as the antimicrobial agents 5CLO8Q and PHMB were delineated in Sections 3.3.2 and 3.3.3.

The main goal of this study was the design of a nanostructured mesh construct that incorporates a dual drug delivery system of antimicrobial substances, combined with the mechanical stability of PA6 and the cytocompatibility of CS. The mechanical performance of the biomaterial was evaluated through tensile testing. To obtain further insights regarding the parameters that affect the release of the two substances, the electrospun membranes were evaluated physiochemically, and through drug release kinetic experiments *in vitro*.

The two bacteria species most commonly associated with deep-incisional SSI of hernia meshes; Gram-positive *Staphylococcus aureus* (*S. aureus*) and Gram-negative *Pseudomonas aeruginosa* (*P. aeruginosa*), were chosen to assess the antimicrobial properties of the electrospun NFs. The antimicrobial efficiency of electrospun membranes was evaluated quantitatively and qualitatively via zones of inhibition, growth kinetics, live/dead fluorescence and confocal microscopy, and SEM imaging of bacteria-contaminated specimens. Furthermore, the antimicrobial properties of the core/shell PA6-PHMB/CS-5CLO8Q composite NFs were compared with commercially available synthetic and biologic meshes and other forms of micro polymer-based fibres, using the Gram-negative *Escherichia coli* (*E. coli*) as a model organism that responds in a similar manner to *P. aeruginosa*.

The work presented in this chapter has been previously published in the *Journal of Nanobiotechnology* (Keirouz et al., 2020b), presented with two oral abstracts, at the Electrospin 2019, 6<sup>th</sup> International Conference on Electrospinning, in Shanghai, China and the BioMedEng19 Conference, in Imperial College, London, United Kingdom, and as a poster presentation at the Engineering School's Postgraduate Research Conference 2019, Edinburgh, United Kingdom (Appendix B).

## 6.2 Methodology

For a full description of the materials and methods used, please see the following sections in *Chapter 3*:

- Literature Review
  - Information about the polymers used for the development of the hernia mesh construct (Section 2.8.2)
  - Antimicrobial agents (Section 2.8.3)
- Materials (Section 3.3)
  - Lists of materials, cells, suppliers, and equipment (Section 3.3.2)
- Scaffold characterisation (Section 3.4)
  - Scanning electron microscopy (SEM) (Section 3.4.1)
  - Transmission electron microscopy (TEM) (Section 3.4.2)
  - Fourier-transform infrared spectroscopy (FTIR) (Section 3.4.3)
  - X-ray photoelectron spectroscopy (XPS) (Section 3.4.4)
  - Mechanical testing (Section 3.4.5)
  - Thermogravimetric analysis (TGA) (Section 3.4.6)
  - Differential scanning calorimetry (DSC) (Section 3.4.7)
  - Water contact angle measurements (WCA) (Section 3.4.8)
  - *In vitro* drug release studies (Section 3.4.10)
- Antimicrobial testing on S2 pathogenic bacterial strains (Section 3.6)
  - Disc diffusion susceptibility testing (Section 3.6.1)
  - Bacterial growth kinetics using spectrophotometry (Section 3.6.2)
  - Fluorescence and confocal microscopy (live/dead assay) (Section 3.6.3)
  - Fixing bacteria for SEM imaging (Section 3.6.4)



Details of the chapter-specific experimental methods are described, in detail, below. A summary of the methodology followed in this study is provided in the schematic shown in Figure 6.1.

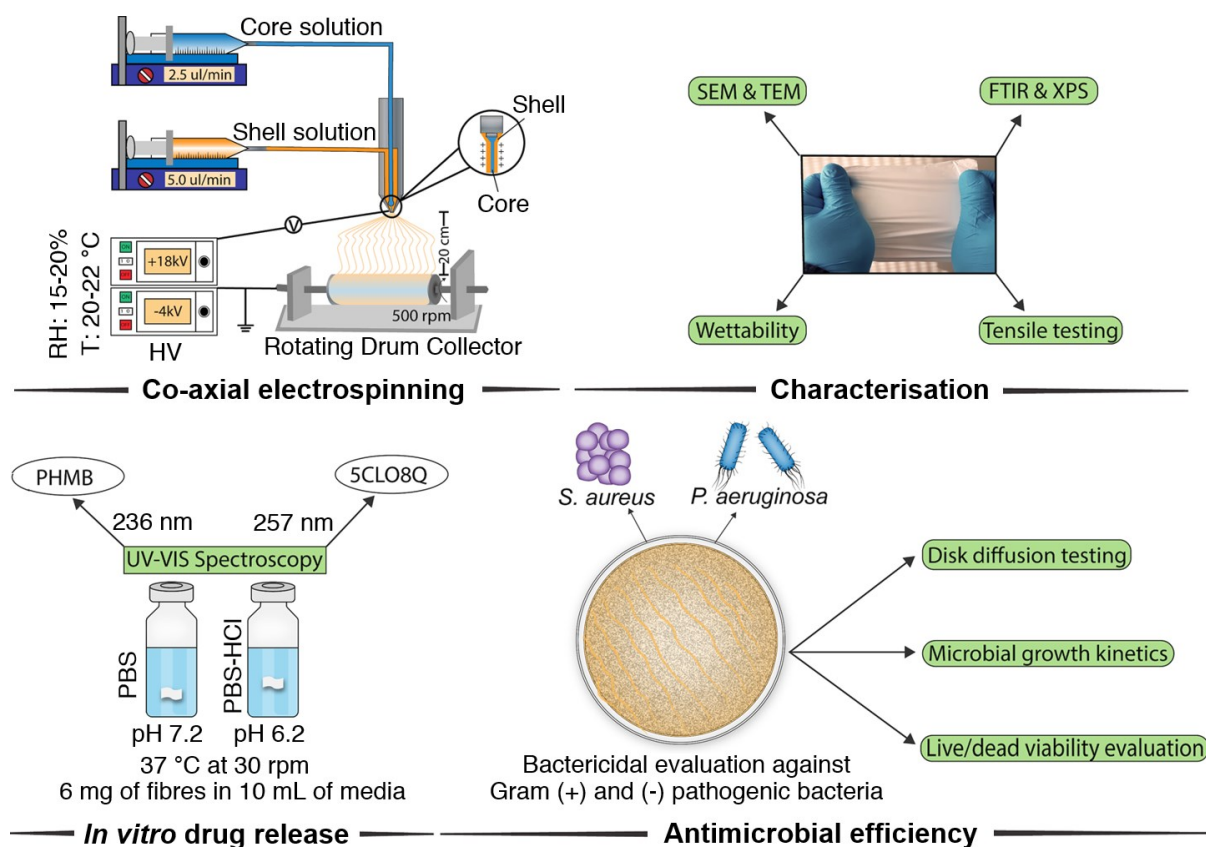


**Figure 6.1.** Schematic diagram depicting the fabrication methodology used to produce the core/shell PA6-PHMB/CS-5CLO8Q nanofibrous mats and the subsequent experimental and investigative scheme followed in this study. HV, high voltage; RH, relative humidity; T, temperature.

### 6.2.1 Solution preparation

Master solutions were prepared by dissolving 3% (w/v) total concentration of CS/PEO, at an 80/20 CS:PEO (w/w) ratio, in 50% (v/v) aqueous acetic acid and 21% (w/v) PA6 in formic acid. For simplification and clarity, throughout this research chapter, CS:PEO is referred to as CS. All the CS solutions electrospun to formulate fibres (including core/shell, drug-free and drug-containing NFs) consist of CS:PEO 80/20 (w/w). Then, 15% (w/w) 5CLO8Q and 0.3% (w/v) PHMB of the total polymer weight of the CS and PA6 solutions, respectively, were added and thoroughly mixed using a vortex mixer. The solutions were placed on a shaker, at 200 rpm, and left overnight at room temperature to obtain homogeneous solutions.

### 6.2.2 Co-axial electrospinning

A parametric study was conducted, until the appropriate polymer solution concentration, CS:PEO proportion within the blend, solvent system and electrospinning parameters were determined to obtain homogeneous nanofibrous mats, of consistent fibre diameters, with a standard deviation of less than 10%, as assessed by SEM. Several short-listed polymers and solvent systems were initially explored as suitable candidates for the core material, based on their compatibility with shell material (CS) during the formation of the core/shell Taylor cone and the jet's stability during electrospinning. The other polymers that were assessed before selecting PA6 were PLLA, PCL, and TPU. The PA6/CS (CS, 85/100 deacetylation degree) system, was ultimately chosen to develop the bicomponent NFs, due to the good solvent system compatibility, stable Taylor cone formation, and excessively assessed in literature, biocompatibility of the two polymers. The process is illustrated in Figure 6.2, and a photograph of the setup can be found in Appendix A: Figure A-15.

The CS and PA6 solutions were electrospun using a horizontal electrospinning setup, with a 0.9-mm diameter co-axial feeding nozzle for the shell and 0.57-mm diameter nozzle for the core, inserted concentrically to the shell solution's needle. The fibres were deposited onto cellulose-based baking paper, which was mounted on a collector, rotating at 500 rpm. The solutions were fed into the core-shell needle, via two separate automatic pumps. The flow rate was set to  $2.5 \mu\text{L}\cdot\text{min}^{-1}$ , for the core, and  $5 \mu\text{L}\cdot\text{min}^{-1}$ , for the shell solution. Single CS-5CLO8Q and PA6-PHMB, in addition to CS and PA6 solutions alone, were also electrospun, using a 0.58-mm needle ( $8 \mu\text{L}\cdot\text{min}^{-1}$  flow rate). For all of the experiments conducted, the distance between the tip of the nozzle and the surface of the collector was set to 20 cm, and electrospinning was conducted under a potential difference of 22 kV (+18 kV nozzle, -4 kV

collector), using a DC power supply, at a 0.1 mA current. The relative humidity was maintained between 15%–20%, and the temperature was kept between 20–22 °C, using a climatic chamber. In order to produce uniform, nonwoven, electrospun mats, each experiment ran for 4–6 h.

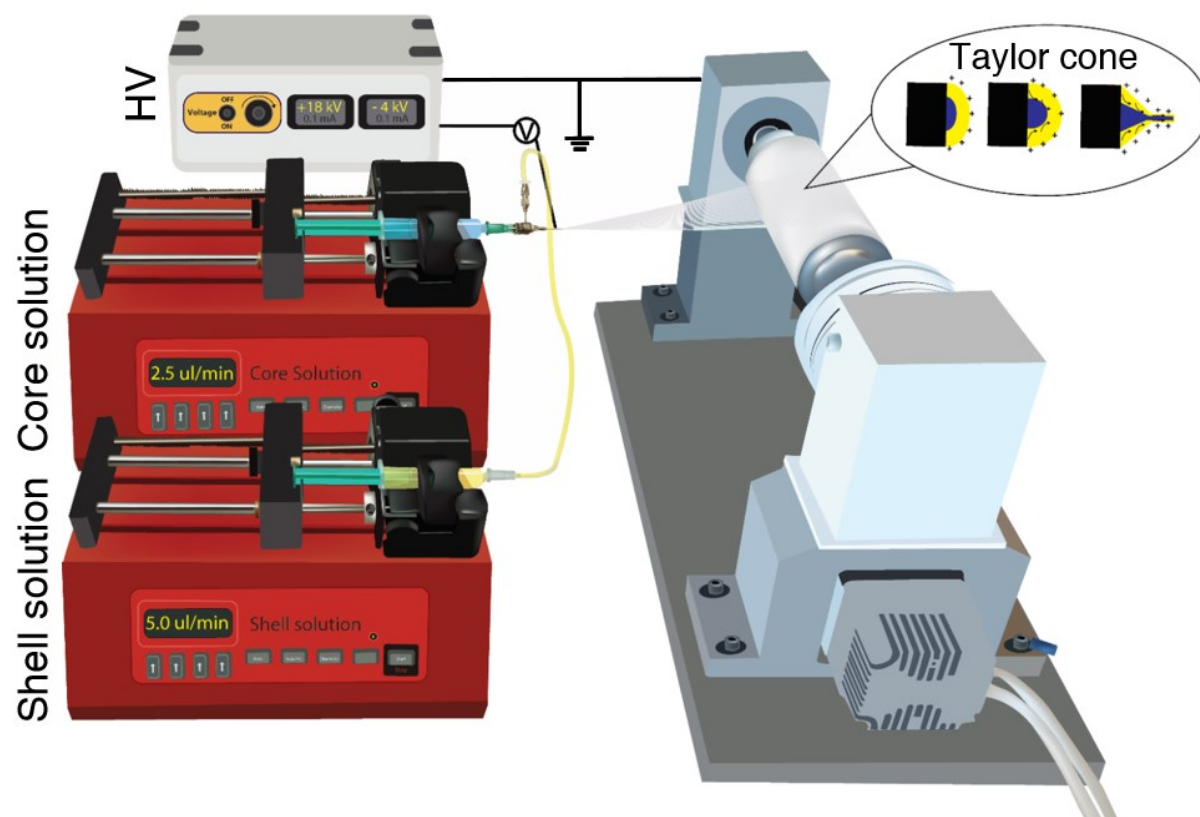


**Figure 6.2.** Schematic representation of the co-axial, electrospinning setup used for the production of core/shell PA6-PHMB/CS-5CLO8Q nanofibrous membranes. The core to shell feed rate was 2.5 to 5.0  $\mu\text{L}\cdot\text{min}^{-1}$ , with potential difference set to 22 kV (+18/-4 kV), and working distance at 20 cm.

## 6.3 Results and discussion

### 6.3.1 Electrospun fibre morphology and core/shell structure

All electrospinning experiments were optimised in terms of the electrospinning parameters (humidity, temperature, flow rate, the distance between the tip of the needle and the collector, potential difference, and needle diameter), as well as by tailoring the solution parameters (blend ratio, molecular weight, polymer concentration, viscosity, solvent system selection, and compatibility) through the performance of parametric studies. The electrospinning system produced jets of single and core/shell fibres from a stable Taylor cone, in a continuous and homogenous manner.

The morphologies and corresponding fibre-diameter distribution plots of the electrospun NFs are shown in the micrographs in Figures 6.3 and 6.4, respectively. To improve the homogeneity and fabrication throughput of the CS NFs during the electrospinning process, an 80:20 (w/w) ratio of CS:PEO was added directly to the dissolved CS polymer solution, in all the experiments [9]. As CS is a polycationic polymer, in an aqueous solution, the electrospinnability of the polymer solution quickly becomes unstable due to polyelectric effects [10]. Numerous studies have shown that the repulsive forces between the ionic groups found on the chitosan backbone become stronger during the electrospinning process, affecting the homogeneous production of fibres [11]. The addition of PEO as a backbone carrier polymer, reduces the repulsion of the CS chains, due to the formation of H-bonds between the –OH of PEO, which acts as a proton acceptor for the water molecules within an aqueous solvent system [10]. This reaction ultimately reduces the polyelectric effect and increases the degree of backbone chain entanglement, allowing for continuous and stable fibre production.

The SEM analysis (Figure 6.3) demonstrated that all of the produced fibres showed smooth morphologies, with no beads or major secondary artefacts and a randomised fibre-matrix architecture. For all groups, the fibres appeared to be uniformly distributed. All scaffolds revealed randomly oriented fibres that were collected on a rotating collector, at a low speed (500 rpm). A collector drum can be used at low rotation speed to improve the deposition of fibres on the collector surface, thus increasing the efficiency of fibre collection during the electrospinning process [12].

A randomised ECM-like matrix morphology was retained by appropriately adjusting the polymer concentration, potential difference, flying pathway (the distance between the needle and the collector) and the rpm of the rotating collector.

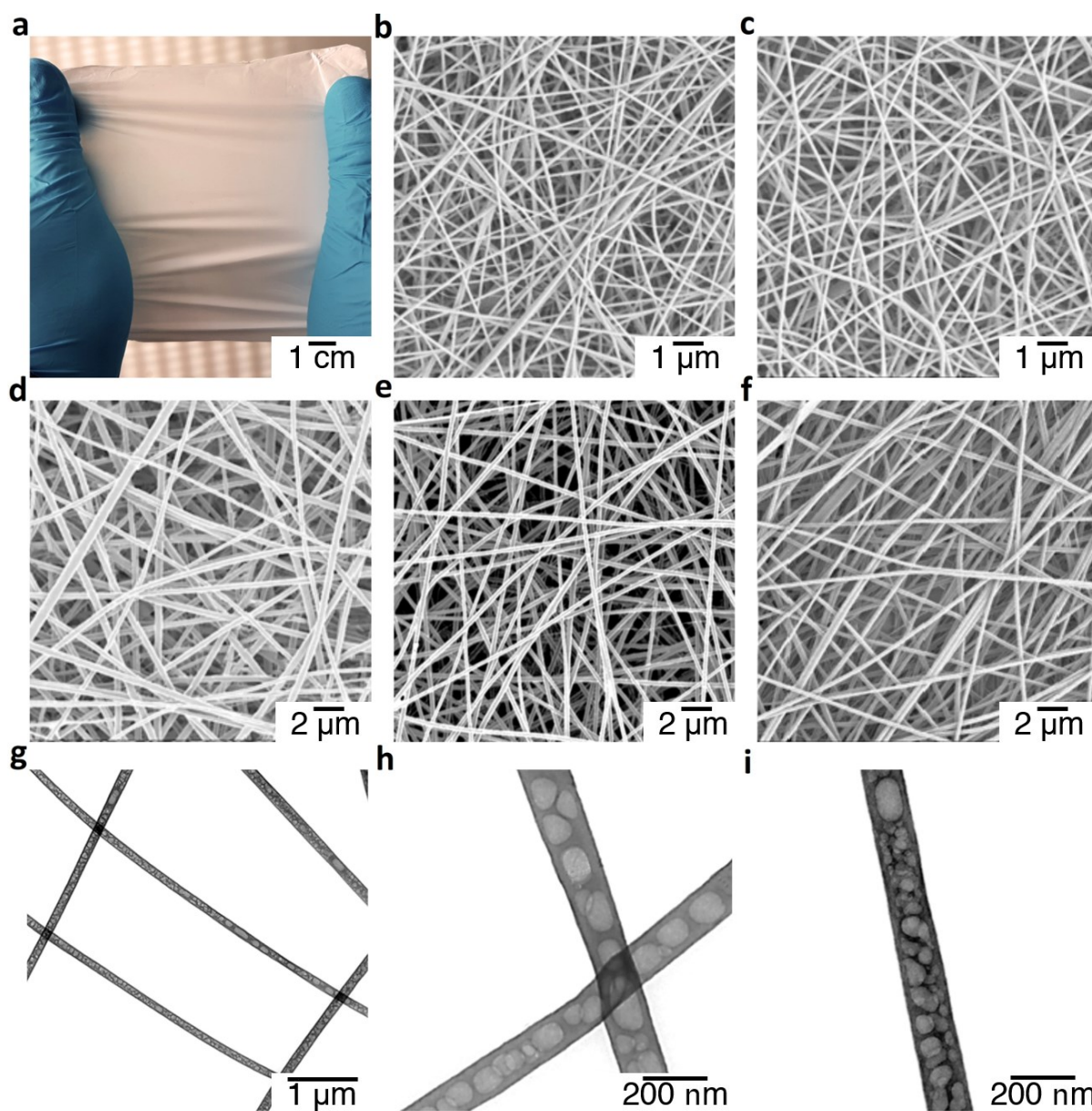


**Figure 6.3.** Nanofibre structures and surface morphologies of the electrospun mats. **(a)** Macrograph of the electrospun mat. SEM micrographs of **(b)** CS, **(c)** PA6, **(d)** CS-5CLO8Q, **(e)** PA6-PHMB, and **(f)** core/shell PA6-PHMB/CS-5CLO8Q electrospun mats. **(g-i)** TEM micrographs of the core/shell PA6-PHMB/CS-5CLO8Q nanofibrous mats. (Core to shell feed rate: 2.5 to 5.0  $\mu\text{L}\cdot\text{min}^{-1}$ ).

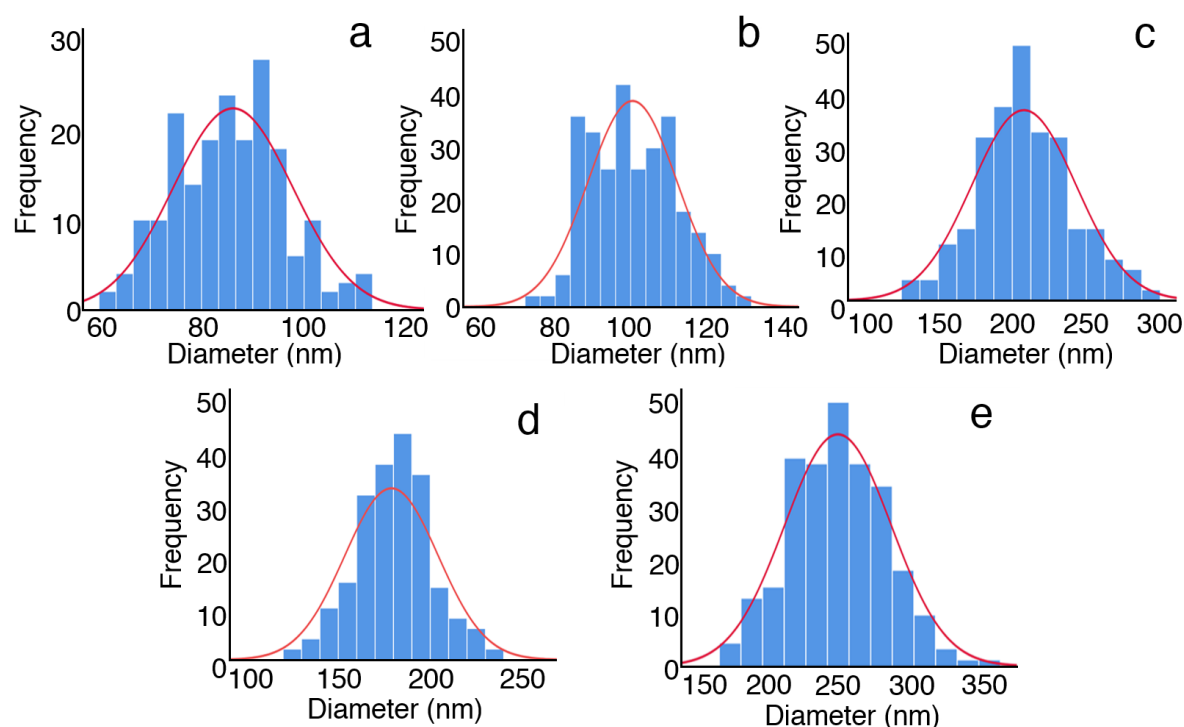


**Figure 6.4.** Fibre diameter distributions of the electrospun **(a)** CS, **(b)** PA6, **(c)** CS-5CLO8Q, **(d)** PA6-PHMB, and **(e)** core/shell PA6-PHMB/CS-5CLO8Q nanofibrous mats.

As illustrated in Figure 6.3b, homogenous, bead-free CS NFs, with an average fibre diameter of  $101 \pm 12$  nm, were successfully developed. PA6-only NFs (Figure 6.3c) presented the smallest fibres, with an average fibre diameter of  $88 \pm 11$  nm. Interestingly, CS NFs that contained 15% (w/w) 5CLO8Q (Figure 6.3d), with a mean fibre thickness of  $210 \pm 31$  nm, were twice the diameter of the drug-free CS NFs, under the same electrospinning parameters. The addition of 5CLO8Q to the solution further upsurges the polycationic charges of the backbone chitosan chain, which can additionally influence both Ohmic flow and convective flow, affecting the electrospinning behaviour. Similarly, PA6 NFs that contained 0.3% (w/v) PHMB (Figure 6.3e) had an average diameter of  $181 \pm 22$  nm, which was twice as thick as the drug-free PA6 NFs ( $88 \pm 11$  nm). Fibre thickness is generally influenced by the electrical conductivity of the polymer solution. Here, the addition of antimicrobial substances increased the electrical conductivity, resulting in the production of thicker fibres [13].

The drug-containing core/shell PA6-PHMB/CS-5CLO8Q NFs (Figure 6.3f) had a slightly larger average fibre diameter than their single-drug containing counter-polymers, at  $270 \pm 68$  nm. Compared with fibres made from single polymer solutions, co-axial electrospinning has been demonstrated to increase the overall solution concentration (of the two separate polymer solutions) on the Taylor cone, which increases the overall fibre diameter [11]. The porosity

was consistent at approximately 80%–90% for all of the produced nanofibrous scaffolds. The morphological properties of the electrospun mats are summarised in Table 6.1.

The electrospun membranes weighed between 5–10 g.m<sup>-2</sup> falling within the extra-light region of the ultralight-weight ( $\leq 35$  g.m<sup>-2</sup>) classification of hernia meshes, which are associated with reduced post-operative pain and long-term foreign body sensation [1, 3].

**Table 6.1.** The morphological properties of the single and core/shell electrospun mats. Electrospinning was performed at 22 kV potential (+18/-4 kV), from a needle tip-to-collector distance of 20 cm, using a rotating collector at 500 rpm.

Nanofibrous Scaffold	Feed rate ( $\mu\text{L}\cdot\text{min}^{-1}$ )	Mean diameter (nm)	Density (Ints. $\cdot\mu\text{m}^{-2}$ )	Porosity (%)
PA6-PHMB	8.0	181 $\pm$ 22	4.05 $\pm$ 1.5	90 $\pm$ 3.2
CS-5CLO8Q	8.0	210 $\pm$ 31	1.83 $\pm$ 0.6	80 $\pm$ 4.5
PA6-PHMB/CS-5CLO8Q*	2.5 / 5.0	270 $\pm$ 68	1.56 $\pm$ 0.5	80 $\pm$ 4.4
Nylon-6 (PA6)	8.0	88 $\pm$ 11	1.54 $\pm$ 0.6	90 $\pm$ 1.8
Chitosan (CS)	8.0	101 $\pm$ 12	1.08 $\pm$ 0.3	91 $\pm$ 2.3

\*Core/shell nanofibres.

The TEM analysis of the core/shell NFs was conducted by depositing electrospun fibres directly on to TEM grids, in a thin layer. The obtained micrographs can be observed in Figure 6.3 (g–i). A distinct morphology was observed, in which a continuous CS phase was apparent in the shell of the fibres, surrounding a discontinuous PA6-PHMB phase, presenting unique, consistent, and well-distributed PA6 particles along the core of the fibres, possibly due to differences in the electric field-induced phase separation and surface tension between the two materials. In this work, this unique fibre structure, which is described for the first time in literature as a single-step formulation process, is referred to as “beads-in-fibres” architecture. Kinetic factors associated with rapid solvent evaporation, caused by differences between the solvent-systems used for the core and shell polymer solutions, may also have played key roles in the formation of this structure [14, 15]. Polymer solutions with concentration below the corresponding polymer entanglement concentration ( $\phi_0$ ) have also been previously shown to yield electrospun NFs with beads-on-a-string configurations, caused by the jet's increased volatility and related to Rayleigh instabilities [16]. This morphology may also indicate that the core-material was encapsulated independently and phase-separated from the matrix wall of the shell material. To further evaluate this unique structure, core/shell NFs were also produced using different flow rates, under the same electrospinning parameters; however, no changes

in the morphological configurations of the core were observed, unaffected of the flow rates used, as shown in Figure 6.5.

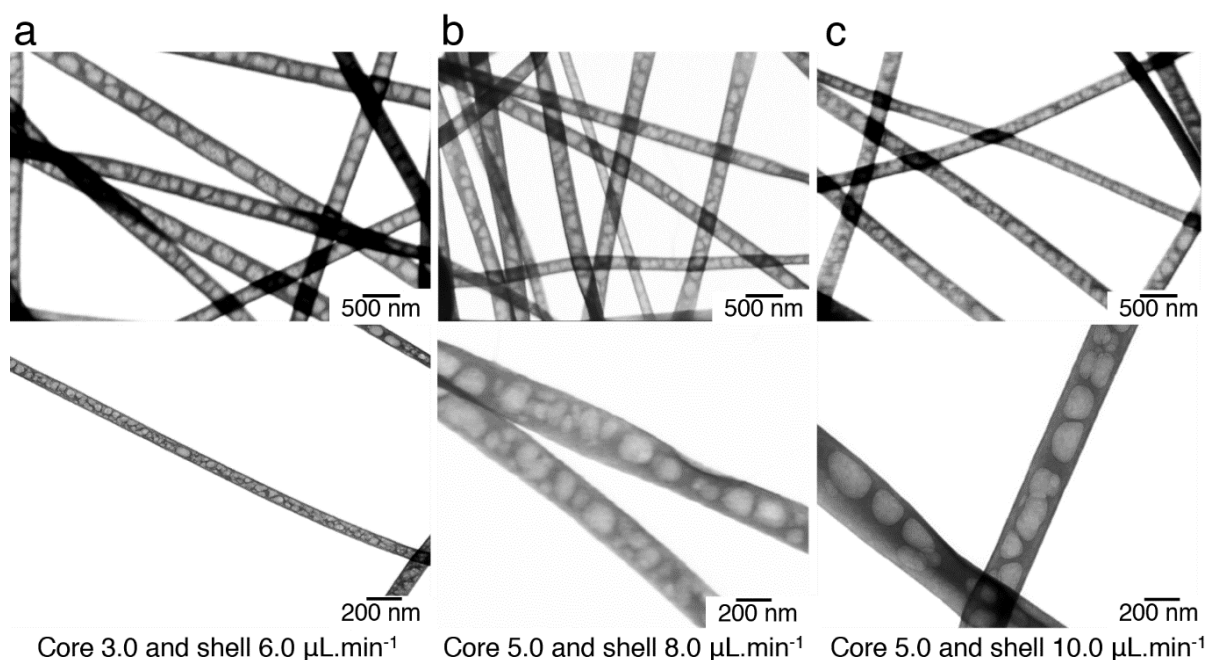


**Figure 6.5.** TEM micrographs of the PA6-PHMB/CS-5CLO8Q core/shell NFs formulated using various flow rates, under the aforementioned electrospinning and solution parameters. Core to shell feed rate of **(a)** 3.0 to 6.0, **(b)** 5.0 to 8.0, and **(c)** 5.0 to 10.0  $\mu\text{L}\cdot\text{min}^{-1}$ .

Water contact angle (WCA) measurements were determined to evaluate the wettability properties of the core/shell NFs, which represents an important parameter for determining the drug-release kinetics and antimicrobial behaviours of NFs. The results presented in Figure 6.6 indicated that the CS NFs that contained 5CLO8Q presented a WCA of  $66^\circ \pm 9^\circ$ , compared with  $75^\circ \pm 5^\circ$  for the drug-free CS NFs. As expected, the addition of PHMB to the PA6 NFs increased the hydrophobicity of the produced scaffolds, likely due to the inherent hydrophobicity of the pure PHMB compound. The core/shell NFs presented the lowest contact angle,  $50^\circ \pm 8^\circ$ , which indicated that the composite structure presents improved wettability properties compared to the other examined fibres. Similarities between the core/shell and the CS-5CLO8Q NFs, in terms of pore area, and the improved pore distribution of the core/shell NFs may play key roles in improving the wettability of the composite structure. Several studies have demonstrated that hydrophilic NF surfaces may encourage better eukaryotic cellular attachment behaviours and improved proliferation than hydrophobic surfaces [17]. Hydrophilic



surfaces have been demonstrated to provide better binding sites that incite cellular adhesion, leading to more efficient scaffold expansion, thus making them suitable substrates for cell growth [18]. Interestingly, the adhesion of bacterial cells on hydrophilic materials has been shown to be influenced by the surface energy of the media (peritoneal fluid, blood, etc.) in which the bacteria are suspended; however, the surface energy of most media is substantially inferior to the native bacterial surface energy [19]. In general, bacteria attach widely to moderately hydrophobic surfaces with lower surface energies [19]. Furthermore, increasingly hydrophilic substrates present low zeta potential values, which limit bacterial binding by introducing repulsive interactions [20].

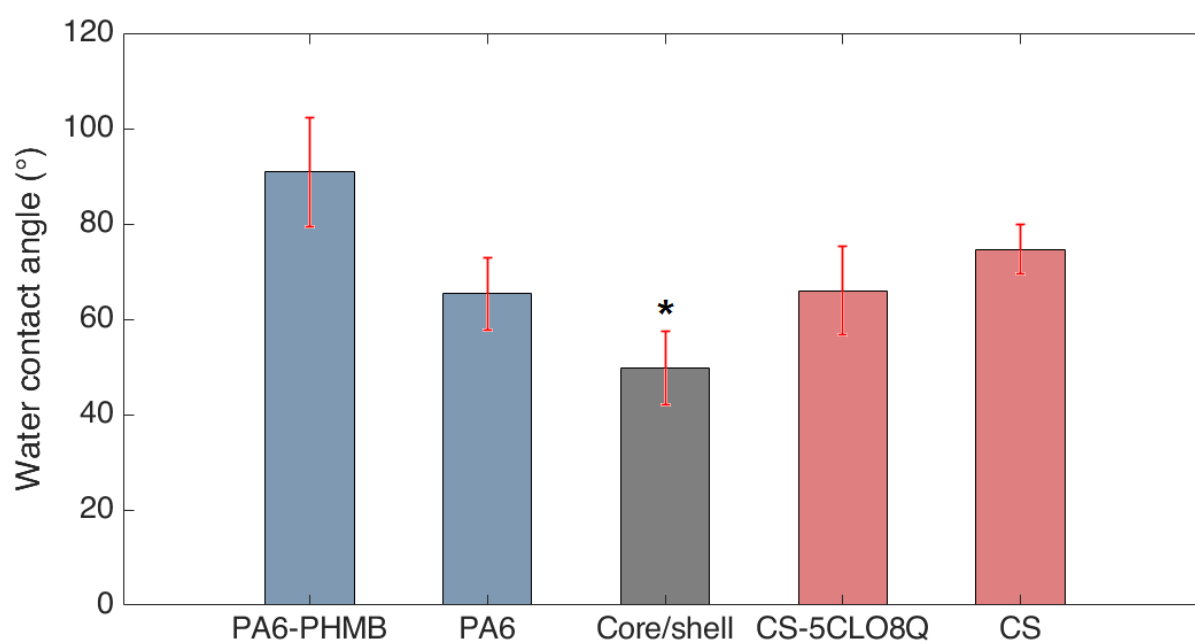


**Figure 6.6.** Water contact angles of the electrospun NFs, both with and without antimicrobial agents, and the drug-containing core/shell nanofibres. Error bars = standard deviations, where star symbol indicates a significant difference between the core/shell NFs and the other groups,  $*p \leq 0.05$ .

### 6.3.2 Chemical composition of the core/shell electrospun NFs

FTIR spectroscopy was performed to characterise the functional groups present on the CS-5CLO8Q, PA6-PHMB, and core/shell nanofibrous mats (Figure 6.7). The IR spectrum of the CS-5CLO8Q fibres indicated the presence of a broad band between 3150–3500  $\text{cm}^{-1}$ , which is characteristic of  $-\text{OH}$  stretching and the  $-\text{NH}$  stretches associated with primary amino groups (Amine I). Intermolecular  $-\text{OH}$  and  $-\text{CH}_2\text{OH}$  hydrogen bond interactions between 5CLO8Q and CS can explain the broadness of the band in the region corresponding to 3380–3420  $\text{cm}^{-1}$  [21]. The peak observed at 2867  $\text{cm}^{-1}$  can be attributed to  $-\text{CH}$  stretching, whereas the peak at 1557  $\text{cm}^{-1}$  may correspond to amide II C–N stretching, coupled with  $-\text{NH}$  in-plane deformation [22]. The sharp bands present near 1033  $\text{cm}^{-1}$  may refer to  $-\text{C}-\text{O}-\text{C}$  stretching of the polysaccharide [23]. Based on the region-specific spectral scans (2000–1200  $\text{cm}^{-1}$ ), the amide I characteristic C=O stretching of the N-acetyl group of the CS backbone is apparent at 1651  $\text{cm}^{-1}$  (Appendix A: Figure A-16a). The peaks at 1414  $\text{cm}^{-1}$  and 1367  $\text{cm}^{-1}$  may correspond to the bending of  $-\text{CH}_2$  and  $-\text{OH}$ , respectively. For comparison, the FTIR spectra of the pristine antimicrobial substances; 5CLO8Q and PHMB can be found in Appendix A: Figure A-16b.

The PA6-PHMB spectrum presented a strong band at 1639  $\text{cm}^{-1}$ , which corresponds to C=O stretching, whereas the peak at 1542  $\text{cm}^{-1}$  clearly corresponds to the characteristic in-plane N–H bending of amide groups. The weak trans amide conformations between 1310–1350  $\text{cm}^{-1}$  and 1440–1490  $\text{cm}^{-1}$  indicated that the amide region is in a gauche-conformation [23, 24]. The two medium peaks at 2930 and 2855  $\text{cm}^{-1}$  represent C–H stretches of the polyamide backbone. In addition, the peak at 1263  $\text{cm}^{-1}$  can be attributed to the amide's C–N stretching.

The spectrum of the core/shell PA6-PHMB/CS-5CLO8Q NFs confirmed the presence of both polymers in the final composite structure. All the characteristic peaks of the two polymers were present at the spectrum of the core/shell structure. The  $-\text{NH}$  stretching appears to have been slightly broadened and less intense, at 3292  $\text{cm}^{-1}$ , which could be due to hydrogen bond interactions between the two polymers. The C=O and  $-\text{CH}$  stretches of the polyamide appeared to remain stable, at 1638 and 1542  $\text{cm}^{-1}$ , respectively, but at lower intensities. All of the CS-specific absorption bands appear to be present in the core/shell nanofibrous mats but at lower intensities. No new peaks were observed for the composite core/shell structure.

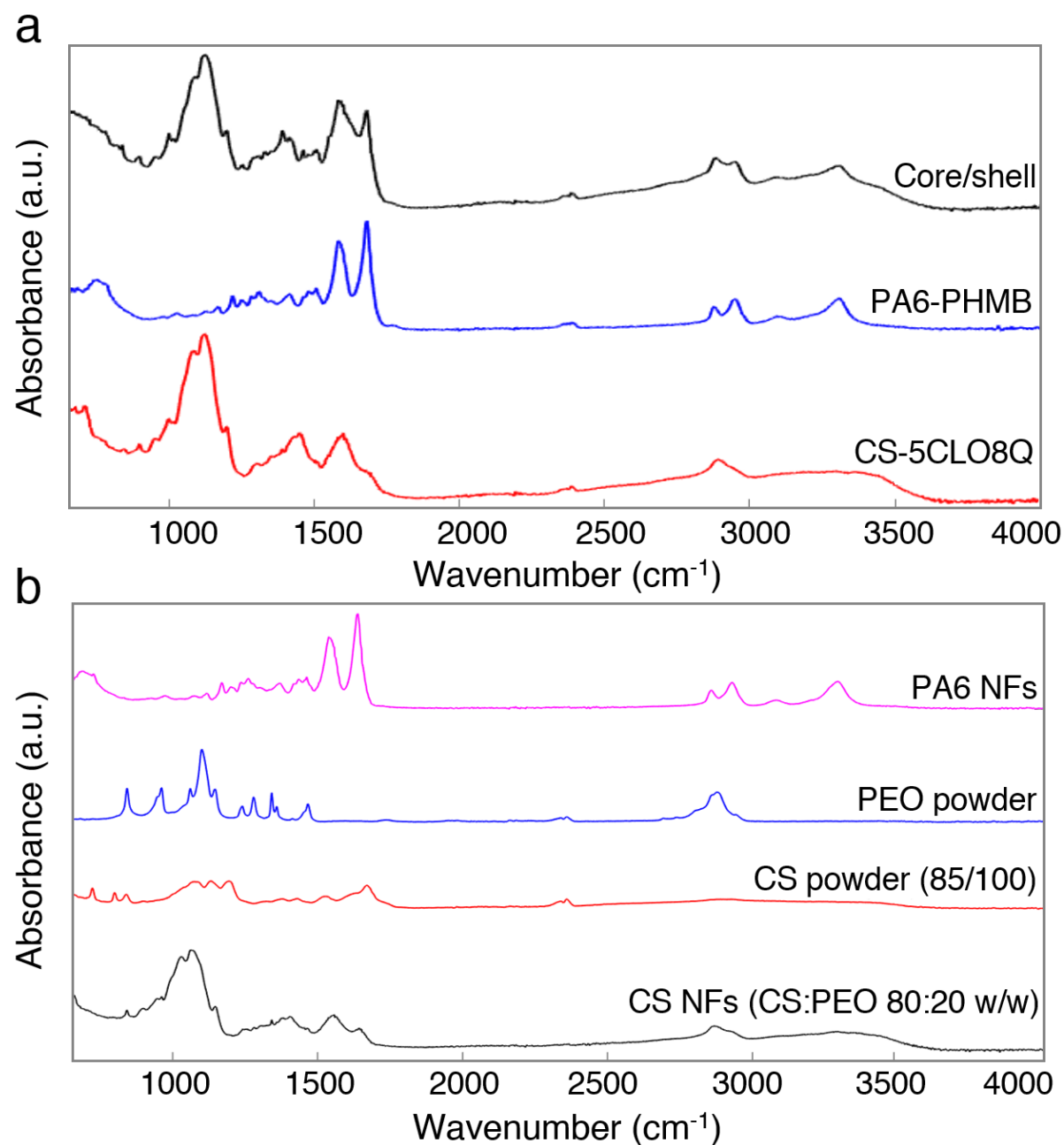


**Figure 6.7.** FTIR-ATR spectra of the produced (a) core/shell, PA6-PHMB and CS-5CLO8Q drug-containing NFs, and (b) drug-free 3% (w/v) CS [CS:PEO at 80:20 (w/w)] NFs, 21% (w/v) PA6 NFs, and pristine CS and PEO powders.

### 6.3.3 Surface chemistry of the core/shell PA6-PHMB/CS-5CL8Q NFs

An XPS analysis, incorporating an information depth of approximately 10 nm, was conducted to determine and compare the elemental composition of the electrospun NFs surface and to further support the measurements obtained by TEM in regard to the core/shell structure. The survey scans for CS-5CLO8Q, PA6-PHMB, and the core/shell NFs are presented in Table 6.2 (Appendix A: Figure A-17, A-18). The PA6-PHMB and CS-5CLO8Q NFs were evaluated based on theoretical values. Effectively, the core/shell fibres appeared to feature similar values to those determined for CS, with high atomic content of O1s and lower N1s contents, as opposed to the PA6-PHMB fibres. Further, chlorine (Cl 2p), a selective element found in 5CLO8Q, was not apparent in the CS-5CLO8Q or core/shell fibres, indicating the successful entrapment of the antimicrobial substance towards the CS core (XPS delivers information of the top 10 nm layer). The 1.3% increase in the amount of nitrogen present in the core/shell composite, compared with the nitrogen contents of CS-5CLO8Q, could denote small irregularities at the fibre surface, due to the stabilisation period of the Taylor cone during the co-axial electrospinning process. Finally, high-resolution scans of the C1s binding energies of the core/shell NFs (Table 6.3) revealed the same carbon bonding structures with the CS-only NFs (margin of error 10%) further confirming the successful interruption of PA6 within the core of the fibres.

**Table 6.2.** Surface chemical compositions of the electrospun NFs. The percentages in brackets refer to the theoretical values of each polymer.

Fibres (group)	C1s		N1s		O1s	
	eV	Atom %	eV	Atom %	eV	Atom %
CS-5CLO8Q	284.4	<b>65.4</b> (61)	399.2	<b>3.0</b> (5)	530.4	<b>31.6</b> (34)
PA6-PHMB	284.2	<b>75.5</b> (75)	397.8	<b>12.2</b> (13)	531.3	<b>12.3</b> (12)
Core/shell*	284.5	<b>65.8</b>	398.1	<b>4.2</b>	530.8	<b>30.0</b>
CS-only	284.5	<b>72.3</b>	399.1	<b>2.1</b>	530.8	<b>25.6</b>
PA6-only	284.4	<b>77.0</b>	399.0	<b>11.3</b>	532.3	<b>11.9</b>

\*Core/shell is PA6-PHMB/CS-5CLO8Q

**Table 6.3.** XPS analysis of the carbon C1s binding energies.

Bending Energy (eV)	Group Peaks (Bond)	Chitosan-5CLO8Q At. Conc. (%)
284.5	C-C, C-H	23.1
285.5	C=O	22.3
286.5	C-N, C-O	54.6
eV	Group	Nylon-6-PHMB At. Conc. (%)
284.4	C-C, C-H	68.5
287.3	C=O	16.4
285.4	C-N	15.1
eV	Group	Core/Shell* At. Conc. (%)
285.7	C-N, C-O	47.2
286.3	C=O	25.0
284.2	C-C, C-H	27.8

\*Core/shell is PA6-PHMB/CS-5CLO8Q. At. Conc. (%) = atomic concentration (%).

### 6.3.4 Thermal properties and PA6 content within the core/shell NFs

Owing to the distinct thermochemical behaviours of CS and PA6, comprehensive thermal analyses were performed, employing TGA (Figure 6.8) and DSC (Figure 6.9). In addition, quantitative analysis was conducted to evaluate the amount of PA6 present within the core of the core/shell NFs. Table 6.4, at the end of the section, outlines the thermal properties of the produced electrospun membranes containing the antimicrobial substances, in addition to the drug-free NFs and raw materials.

The Flory-Huggins theory explains that the compatibility and miscibility of polymer blends depend on the potential of the mixed polymers to form coherent hydrogen bond interactions [25]. Steric impacts and the hydrogen bonding intensity play vital roles in defining the compatibility and thermal properties of the core/shell NFs [25].

The CS powder (deacetylation rate 85/100) used in this study consisted of polymer chains, varying in length from 200,000 to 300,000 g·mol<sup>-1</sup> (according to the manufacturer's specifications). According to the TGA results, raw chitosan (85/100) exhibited degradation in two phases, with a first broad peak at approximately 100 °C, which can be attributed to the loss of bound water moisture vapour, desorbed by the CS backbone. In general, CS is known for its high tendency to form hydrogen bonds, often becoming even more hygroscopic when blended with other polymers [26]. The second degradation phase began at 208 °C and can

be ascribed to the mass loss associated with polymer dehydration and the formation of hydrogen bonds in the saccharide rings [27].

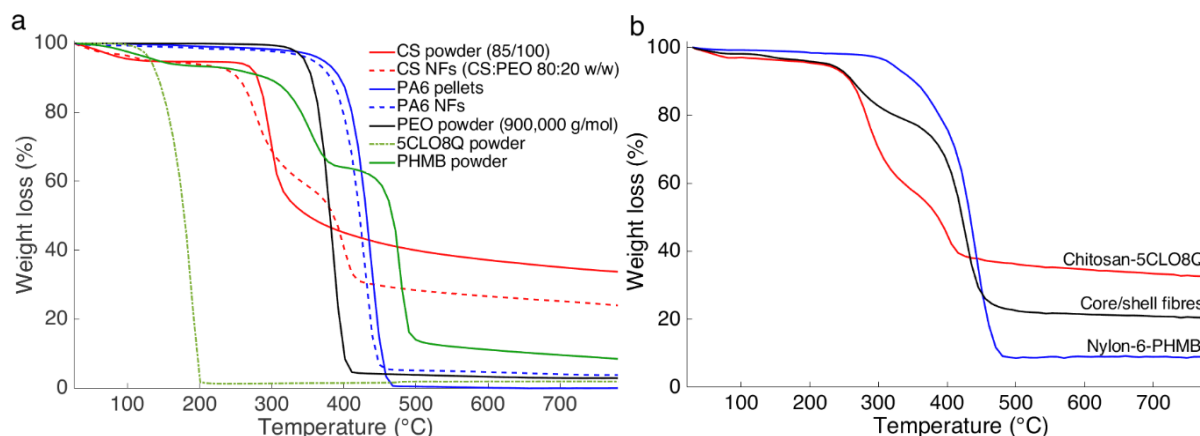


**Figure 6.8.** TGA analysis of **(a)** the pristine CS powder, PA6 pellets, PEO powder, 5CLO8Q powder, PHMB powder, and the drug-free nanofibrous mats consisting of 3% (w/v) CS [CS:PEO at 80:20 (w/w)] (CS NFs) and 21% (w/v) PA6 (PA6 NFs); **(b)** the drug-containing core/shell, CS-5CLO8Q and PA6-PHMB NFs.

The electrospun blends containing CS-only [CS:PEO at 80:20 (w/w)] presented a decomposition peak, at 260 °C, whereas PEO powder exhibited an onset degradation, in one step, at 340 °C. The pristine PA6 pellets used to prepare NFs had a melting temperature ( $T_m$ ) at 224 °C, whereas PA6-only NFs showed less mobile polymer chains, with an increased  $T_m$  at 231 °C. The PA6-PHMB NFs appeared to have been influenced by the presence of PHMB, which has been reported in the literature to have a  $T_m$  at 205-210 °C, [28] leading to a more mobile PA6 chain configuration, with a  $T_m$  at 218 °C.

The onset of PA6 degradation was observed at 365 °C, whereas the onset of PA6-PHMB NF degradation was observed at 340 °C. The core/shell NFs presented two degradation phases, observed at 58.8 and 214 °C, which are similar to the PEO and PA6 temperature configurations, respectively. Furthermore, the core/shell NFs exhibited melting onsets at 240 °C and 365 °C, which are similar to the initial decomposition temperatures observed for CS-5CLO8Q and PA6-PHMB, respectively.

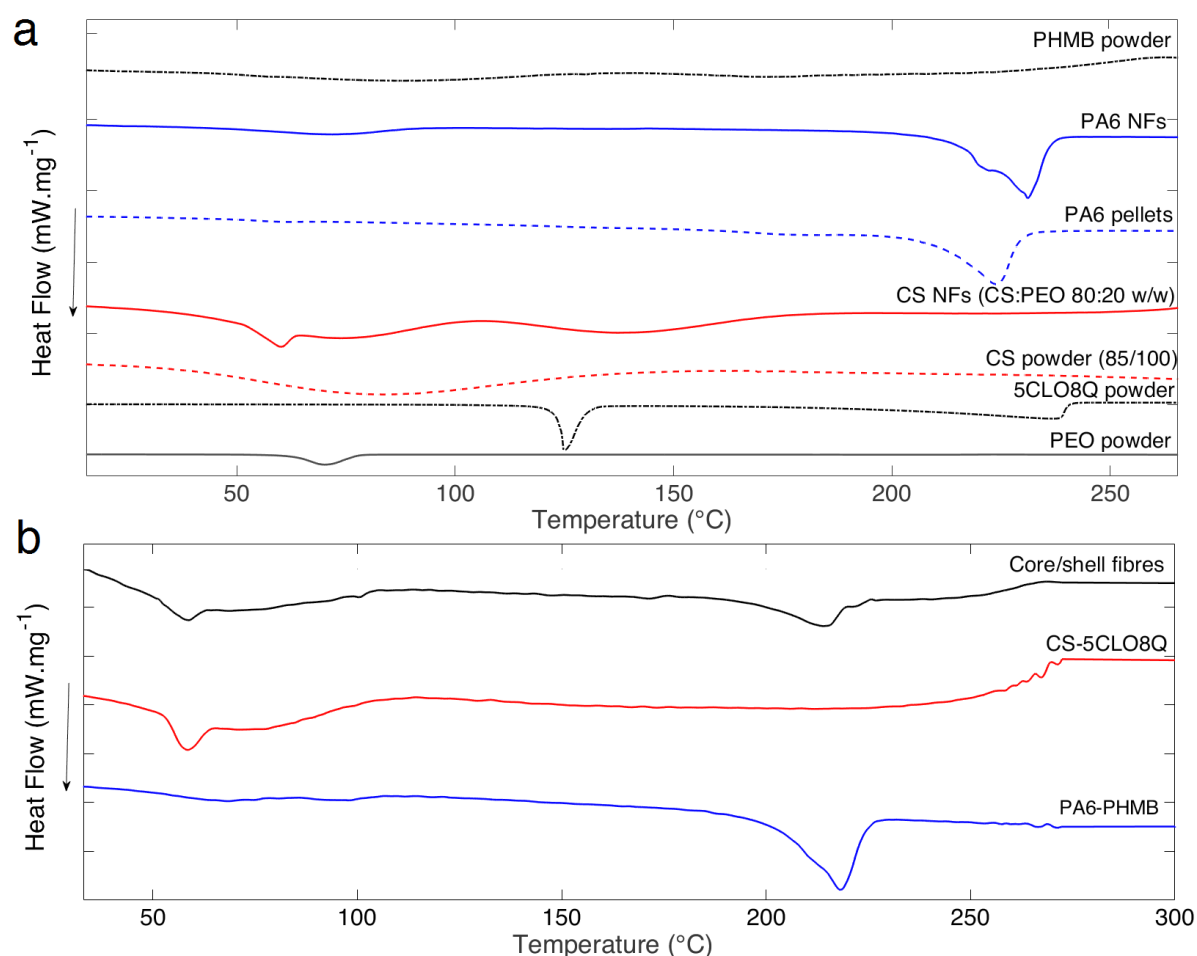


**Figure 6.9.** DSC analysis of **(a)** the pristine CS powder, PA6 pellets, PEO powder, 5CLO8Q powder, PHMB powder, and the drug-free nanofibre mats composed of 3% (w/v) CS [CS:PEO at 80:20 (w/w)] (CS NFs) and 21% (w/v) PA6 (PA6 NFs); **(b)** the drug-containing core/shell, CS-5CLO8Q and PA6-PHMB NFs.

Changes in the crystallinity of the electrospun NFs were investigated by DSC. The glass transition ( $T_g$ ) of pure CS has been described very vaguely in the literature, with values ranging from -23 to 220 °C, due to its semi-crystalline nature and variations in the ratios of intra and intermolecular hydrogen bonds that occur in the polysaccharide as the polymer decomposes [29, 30]. In this study, the  $T_g$  of pure CS (85/100) powder was determined, displaying an endothermic peak at 203 °C, which agrees with previously published work performed using 96% deacetylated chitosan of a similar MW [31]. Similarly, CS-5CLO8Q NFs showed no apparent changes in their  $T_g$  values, compared to the CS-only NFs.

The pristine PA6 pellets presented a  $T_g$  at 60 °C, coming into agreement with the manufacturer's report (Sigma-Aldrich). The  $T_g$  values of the PA6-only and PA6-PHMB NFs were determined to be 50 and 47 °C, respectively, indicating a slight decrease. This could be

attributed to the nanofibrous configuration increasing the chain mobility in the amorphous phase, and due to the integration of PHMB affecting the reorganization of the PA6 chains [32].

The composite PA6-PHMB/CS-5CLO8Q core/shell NFs presented an evident change in  $T_g$  (equal to an approximate 11 °C increase), with an exothermic peak at 214 °C. This significant increase in the  $T_g$  value for the composite core/shell structure can be attributed to possible intermolecular interactions and folding rearrangements that occur among the CS polymer chains, along the PA6 core [33, 34]. Furthermore, dissimilarities in the nucleation and growth of crystallisation between the core and shell material may have also influenced the  $T_g$  transition [24].

Based on the enthalpy change ( $\Delta H_m$ ), assuming that the values for PA6 and the core/shell PA6-PHMB/CS-5CLO8Q NFs correspond to the polyamide melting enthalpy, it was feasible to estimate the amount of PA6 present in the core of the core/shell NFs, using the following formula:

$$\text{PA6 (\%)} = \frac{\Delta H_m(\text{core/shell fibres})}{\Delta H_m(\text{PA6})} \times 100 \quad (6.1)$$

where  $\Delta H_{m(\text{core/shell})}$  and  $\Delta H_{m(\text{PA6})}$  represent the heat of fusion values for the core/shell and PA6-PHMB electrospun mats, respectively. The proportion of PA6 within the cores of the fibres was determined to be 48.5%.

**Table 6.4.** Thermal properties of the electrospun nanofibrous scaffolds. All chitosan solutions were made as 80:20 (w/w) CS:PEO. The values in parenthesis ( ) refer to transitions of the composite fibres, corresponding to the PEO present within the CS blends.

Sample	$T_m$ (°C)	$\Delta H_m$ (J/g)	$T_g$ (°C)	$T_{\text{onset}}$ (°C)
CS-5CLO8Q (NFs)	(58.4)	(83)	203	240
PA6-PHMB (NFs)	218	188.4	47	340
Core/shell* (NFs)	(58.8), 226	(54.5), 91.4	214	285
CS-only (NFs)	(60)	(101)	203	260
CS 85/100 (powder)	---	---	200	290
PA6-only (NFs)	231	180.5	50	340
PA6 (pellets)	224	305	60	365
PEO 900K Da (powder)	70	168	-65	340

Abbreviations:  $T_m$ , melting temperature.  $\Delta H_m$ , heat of fusion.  $T_g$ , glass transition temperature.  $T_{\text{onset}}$ , decomposition onset temperature. \*Core/shell is PA6-PHMB/CS-5CLO8Q



### 6.3.5 Mechanical characteristics of the produced core/shell NFs

The mechanical properties of the CS-5CLO8Q, PA6-PHMB, and core/shell NFs are shown in Figures 6.10 and Table 6.5. As demonstrated by the representative stress/strain curves shown in Figure 6.10a, the addition of PA6 within the core of the core/shell NFs successfully improved the overall mechanical stability of the construct.

The CS-5CLO8Q and PA6-PHMB nonwoven electrospun mats presented an ultimate tensile strength (UTS) of  $7.3 \pm 1.4$  MPa and  $11.6 \pm 0.7$  MPa, respectively. The UTS of the drug-free electrospun mats were similar to those for the drug-containing NFs, whereas the UTS of the thicker-in-diameter core/shell NFs outperformed the single polymer fibres, at  $20.7 \pm 2.5$  MPa. The PA6-PHMB NFs presented the highest fracture strain at  $36.3\% \pm 7.5\%$ , whereas the PA6-only NFs appeared to be stiffer, with an elongation-at-break at  $20.3\% \pm 2.8\%$ , likely due fibre-to-fibre interaction variations associated with differences in the fibre diameters among the two groups. The core/shell NFs appeared to be influenced by the presence of CS, and were stiffer than the PA6-PHMB group, with an elongation-at-break at  $14.1\% \pm 2.1\%$ , which represented an improvement over the value of  $10.4\% \pm 1.4\%$  recorded for the CS-5CLO8Q electrospun mats. The Young's modulus of the composite core/shell fibres demonstrated a four-fold increase, to  $217.5 \pm 12.6$  MPa, compared with  $50.3 \pm 5.4$  MPa and  $41.0 \pm 8.8$  MPa, for CS-5CLO8Q and PA6-PHMB, respectively.

The mechanical properties identified for the electrospun PA6-containing NFs agree with those reported in previously published studies [35]. However, PA6 nanofibrous mats produced via electrospinning appear to be inferior to those produced by microfibre fabrication techniques, such as melt spinning, which may be due to the lower degree of chain orientation that occurs during the formation of asymmetrically electrospun (as-spun) NFs [36, 37]. Further investigations of single fibres and fibre-to-fibre friction properties could provide additional insights. The relatively low mechanical properties of the as-spun CS-containing nonwoven mats also concur with previous stress/strain studies that examined NFs produced from CS blends that incorporated PEO [37, 38]. Interestingly, the tensile properties of the core/shell NFs exceeded those for both CS and PA6.

Composite NFs present higher tensile strengths than their single-component counterparts, potentially due to improved molecular orientations and conformations, increased crystallinity, and increased intermolecular interactions [37]. The produced bicomponent NFs displayed increased fibre diameters relative to the single-polymer fibres, a morphological trait that plays a critical role in improving the mechanical stability of composite fibrous structures [35, 36]. Additionally, energy dissipation, caused by the phase-separated "beads-in-fibre" morphology,

may also positively influence the toughness of the composite fibres [16]. These interactions may facilitate a better distribution of the energy crossing through the PA6-containing core, stabilising the CS-containing sheath, thus retarding its fracture.

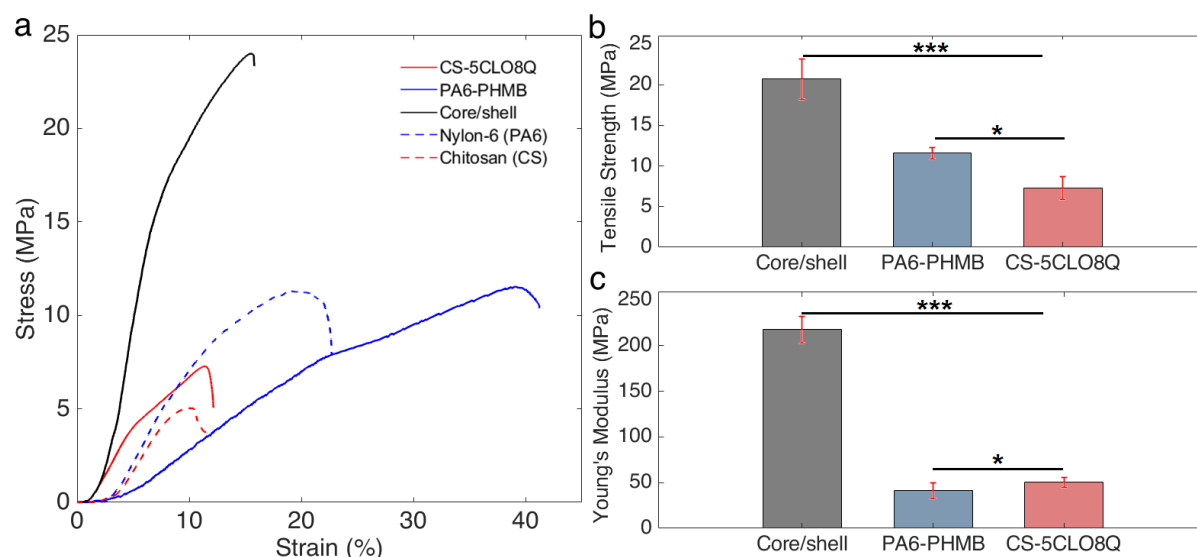


**Figure 6.10.** Mechanical properties **(a)** Representative tensile stress-strain curves of the drug-containing, drug-free, and core/shell electrospun mats. **(b)** Ultimate tensile strength and **(c)** Young's modulus of the drug-containing and core/shell NFs. Error bars show the standard deviations. \*\*\*  $p < 0.001$  and \*  $p < 0.05$ . Core/shell represents PA6-PHMB/CS-5CLO8Q.

**Table 6.5.** Overview of the mechanical properties of the electrospun scaffolds.

Nanofibrous scaffold	Ultimate Tensile Strength (MPa)	Elongation at Break (%)	Young's Modulus (MPa)
Chitosan (CS)	$6.6 \pm 0.8$	$12.5 \pm 4.1$	$50.5 \pm 8.3$
Nylon-6 (PA6)	$10.7 \pm 0.6$	$20.3 \pm 2.8$	$64.9 \pm 7.8$
CS-5CLO8Q	$7.3 \pm 1.4$	$10.4 \pm 1.4$	$50.3 \pm 5.4$
PA6-PHMB	$11.6 \pm 0.7$	$36.3 \pm 7.5$	$41.0 \pm 8.8$
Core/shell*	$20.7 \pm 2.5$	$14.1 \pm 2.1$	$217.5 \pm 12.6$

\*Core/shell is PA6-PHMB/CS-5CLO8Q

### 6.3.6 Drug release mechanism of the antimicrobial NFs

Generally, electrospun NFs that are produced through the blending of a polymer with a drug typically display a rapid burst of the drug, released into the medium through small diffusion pathways, which can be influenced by the drug to polymer affinity and the solubility of the drug in the release medium [39]. In contrast, co-axially electrospun, drug-loaded systems allow for the encapsulation of antimicrobial agents within the fibre cores, increasing the diffusion pathway and, thus, retarding part of the initial burst and sustaining a more modulated release. The release kinetics were examined at pH 7.2 and 6.2 to resemble a physiological and a slightly more acidic environment that could exist in an intra-abdominal diseased bacterial infected tissue [40], respectively.

#### 6.3.6.1 The release kinetics of the single-drug containing NFs

For the CS NFs containing 5CLO8Q, initial bursts of  $7.1\% \pm 0.68\%$ , at pH 6.2, and  $6.3\% \pm 0.27\%$ , at pH 7.2, were observed within the first 6 h of incubation, followed by the slow release of 15% of the total 5CLO8Q loaded within 14 days (Figures 6.11a). Quinolines are poorly water-soluble; and thus, strongly affected by the release media present in their surroundings. The release of 5CLO8Q from CS appeared to follow a non-Fickian release ( $n = 0.81$ , at pH 7.2, and  $0.85$ , at pH 6.2) pattern, based on the Korsmeyer-Peppas model (described in detail in *Section 3.4.10*), which indicated that CS erosion, swelling, and dissolution are critical for the release of 5CLO8Q. Furthermore, the entrapment of the 5CLO8Q molecule near the core of the CS fibres would also explain this phenomenon, as the XPS results did not identify the chlorine molecule, which can be found in the benzene ring of the 5CLO8Q molecule, near the NF surface, which is supported by the hydrogen bonding interactions observed between CS and 5CLO8Q, based on the FTIR analysis. The same pattern, as expected, was observed for the 5CLO8Q present in the core/shell NFs, as the antimicrobial agent was present within the CS-sheath. The 60-nm difference in fibre diameter between the CS-5CLO8Q and core/shell NFs did not appear to affect the release profile of the 5CLO8Q.

In the PA6 NFs that contained PHMB, the release of the antimicrobial substance appeared to be strongly affected by the pH of the medium (Figure 6.11b). At pH 7.2, a burst release, corresponding to  $56.7\% \pm 3.20\%$ , was observed during the first 6 h, and 100% of the PHMB contained by the fibres was released within 4 days. However, at pH 6.2, an initial release of  $30.6\% \pm 2.70\%$  occurred during the first 6 h, with  $63.5\% \pm 1.20\%$  of the contained drug being

released within 14 days. The release of PHMB from PA6 fibres followed a Fickian diffusion pattern ( $n = 0.26$ , at pH 7.2, and 0.40, at pH 6.2). The cationic nature of the very basic biguanide molecules results in PHMB gradually becoming positively charged as the pH decreases. In an aqueous environment, the PHMB conformation alternates with the hydrophobic methylenic region facing inwards and the biguanide groups facing outwards [41]. Polyamides have been shown to be significantly affected by pH, and the isoelectric point identified at pH 7.2 shifts as the pH acidifies, due to pH-dependent protonation, which ultimately causes swelling when the pH exceeds the  $pK_a$  of the polymer [42, 43]. The increase in the net charge of biguanides could ultimately shift the isoelectric equilibrium present at pH 7.2, increasing the susceptibility of chemical interactions between the two molecules, retarding the release of PHMB at pH 6.2.

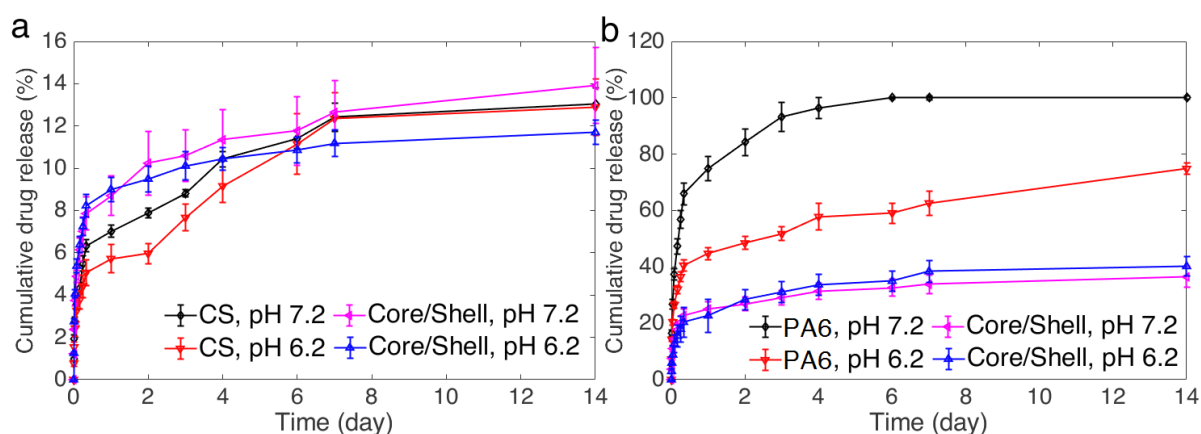


**Figure 6.11.** Comparative cumulative release of (a) 5CLO8Q and (b) PHMB, from the antimicrobial CS and core/shell NFs, at pH 7.2 and 6.2. Error bars represent standard deviations.  $n = 6$ , derived from two independent drug release studies, conducted using fibre mats from different electrospinning batches. \*Core/shell is PA6-PHMB/CS-5CLO8Q

### 6.3.6.2 The effect of the core/shell structure in the release of PHMB

The core/shell NFs follow a release pattern for the PHMB loaded in the core, which does not appear to be influenced by pH (Figure 6.11b). First, a small burst release occurs within the first 6 h, representing approximately  $20.3\% \pm 2.2\%$ , at pH 7.2, and  $17.9\% \pm 4.6\%$  at pH 6.2, of the encapsulated PHMB, which may be due to some proportion of the electrospun drug appearing near or at the surface of the core/shell fibres [44], as well as due to the presence of inconsistencies that may occur at the beginning of the electrospinning process. Afterwards, a

steady release was evident, at similar rates for both pH 6.2 and 7.2, over a period of 14 days, with a maximal release of  $36.45\% \pm 3.5\%$  at pH 7.2 and  $40.2\% \pm 3.4\%$  at pH 6.2. The core/shell NFs appeared to follow a non-Fickian release mechanism ( $n = 0.85$ , for both pH 7.2 and pH 6.2), which confirmed that the CS present in the sheath governed the release of PHMB from the core/shell structure. The positively charged CS permits the absorption of water molecules and the simultaneous diffusion of PHMB into the release medium. Under this model and these conditions, assuming that CS undergoes a consistent level of degradation, we can estimate the complete, theoretical release of PHMB into the media within a period of  $45 \pm 5$  days, at pH 7.2, and within  $36 \pm 4$  days, at pH 6.2. This modified-release delivery system consisting of the reduction of the initial burst release of the two antimicrobial agents, followed by the subsequent sustain release over the aforementioned periods, can provide the appropriate antimicrobial protection required by the system in the long-term, as well as at the onset, where a higher bacterial-load is apparent directly after the implementation of a mesh [3].

### 6.3.7 Antimicrobial activity of the single and core/shell NFs

The antimicrobial effects of the electrospun NFs were investigated against *S. aureus* and *P. aeruginosa*, the two most frequently encountered pathogens associated with mesh-specific SSIs. The growth inhibition zones, shown in Figure 6.12a, indicated no zone of inhibition for the PA6-only nanofibrous mats, whereas a zone of clearing, due to the accumulation of dead bacteria, was observed for the CS-only electrospun mats. Because the inhibitory potency was only apparent surrounding the borders of the CS-only discs, it was denoted that no chitosan derivatives were secreted into the surrounding area.

The CS-5CLO8Q NFs showed the larger inhibitions zones against *S. aureus*, whereas the PA6-PHMB fibres presented the strongest inhibition against *P. aeruginosa*. The core/shell NFs appeared to be effective at inhibiting the growth of both bacterial strains. The polymer matrix material in which the biocide agent is incorporated largely impacts the degradation rate of the electrospun mat [45]. Therefore, the zones of inhibition for the composite core/shell NFs cannot be directly compared against those for the single polymer-drug systems examined, as the degradation rates differ, according to the polymer system composition and corresponding fibre properties.

Only a small fraction of studies that have investigated the effects of electrospun antimicrobial fibres have used *P. aeruginosa*, as it is much less susceptible to antibiotics and antimicrobial agents than *E. coli*, which is a Gram-negative, representative model organism

that has commonly been used in similar studies [46]. Different responses between these two strains are anticipated because they differ greatly in terms of structural morphology, shape, and metabolic responses. The inhibition zones indicated that the core/shell antimicrobial scaffold showed a less robust response against *P. aeruginosa* compared to *S. aureus*, but effectively presented clear zones of inhibition, even if less intense.

To further evaluate and quantify the bactericidal responses of the electrospun mats, 12-h real-time monitoring growth kinetic experiments (Figure 6.12b; *S. aureus*, Figure 6.12c; *P. aeruginosa*) were performed for each bacterial species assessed after being exposed on the electrospun membranes. *S. aureus* appears to be partially susceptible to the CS-5CLO8Q NFs, with a retarded growth time and lower optical density in comparison with the PA6-only and CS-only electrospun mats. Interestingly, the PA6-PHMB and core/shell NFs effectively suppressed the growth of the bacteria upon exposure to the antimicrobial NFs. The more resilient *P. aeruginosa* strain was not affected by the presence of the CS-only NFs, whereas the CS-5CLO8Q NFs resulted in reduced optical density compared with both the CS-only and PA6-only electrospun mats. The PHMB containing core/shell and PA6-PHMB NFs both successfully eliminated the growth of this Gram-negative bacteria, upon exposure.

The bacterial kinetic experiments contradicted the inhibition zone observations, in which CS-5CLO8Q appeared to be the most effective for inhibiting the growth of the examined bacteria. This discrepancy may be due to CS-5CLO8Q electrospun mats being capable of secreting the antimicrobial substance onto solid-agar plates, thus repelling bacterial growth in the surrounding areas; however, the same fibres may be less effective in preventing bacterial growth when the bacteria are inoculated directly on the nanofibrous matrix surface. These results indicated the strong bactericidal activity presented by PHMB, even at low concentration [0.3% (w/v)]. The composite core/shell NFs appeared to completely halt the growth of the two pathogens, effectively displaying an anti-bacterial surface, due to the synergic antimicrobial activity of PHMB and 5CLO8Q.

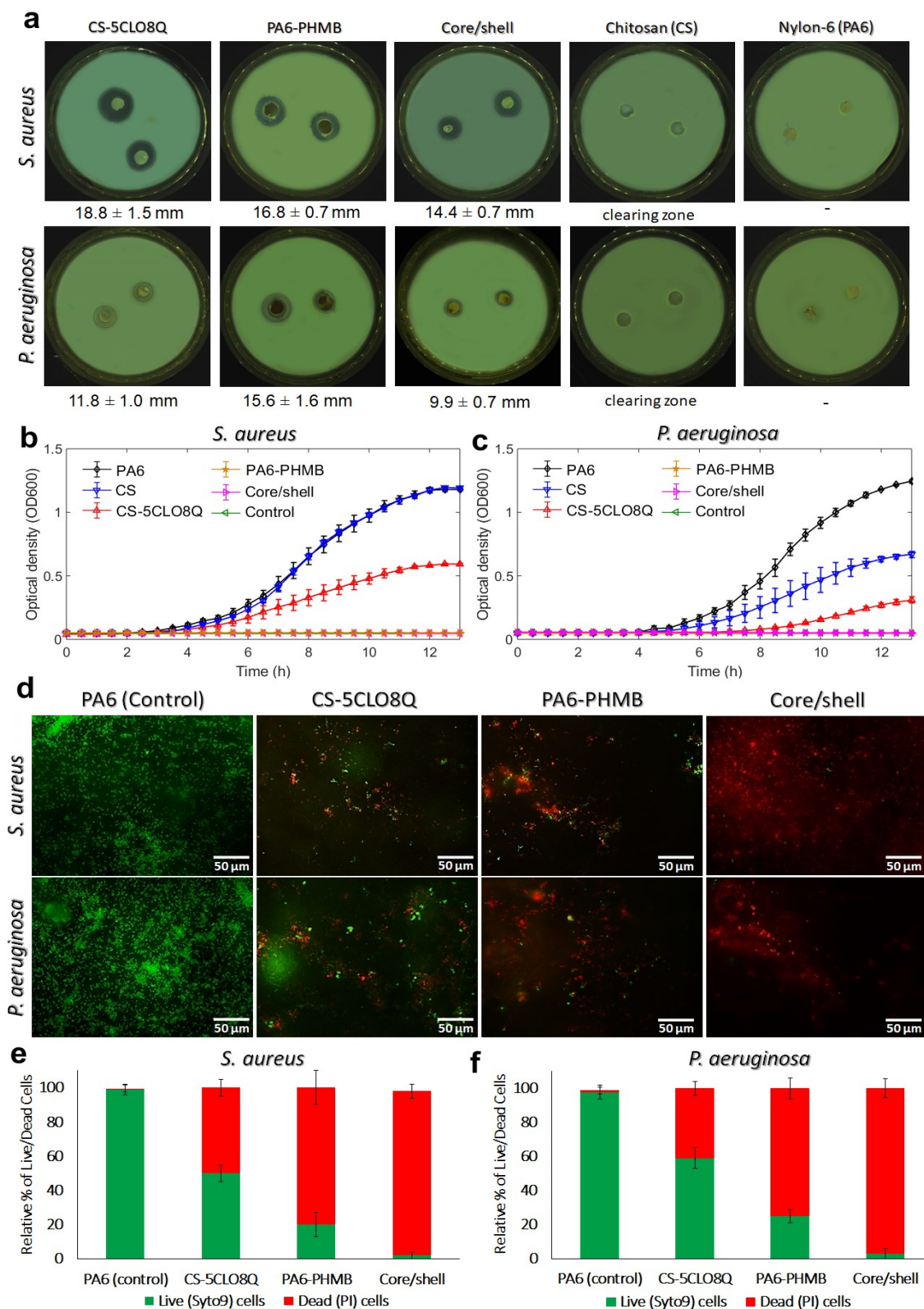


**Figure 6.12.** Antimicrobial properties of the electrospun mats. **(a)** Macrographs of the disc diffusion test, with the corresponding radius values for the zone of inhibition below each image (presented as the mean ± SD). **(b)** *S. aureus* and **(c)** *P. aeruginosa* growth, reflected as optical density (OD<sub>600nm</sub>) over time, in the presence of the electrospun CS, CS-5CLO8Q, PA6, PA6-PHMB,

and core/shell NFs and negative control (no bacteria containing media). **(d)** Fluorescence microscopy assessments, via live/dead BacLight Syto9®/Propidium iodide (PI) bacterial viability assays. **(e–f)** The relative percentages of living (green) and dead (red) cells following exposure to the various groups of electrospun fibres, quantified according to the fluorescent intensity of microscopic images. All data are shown as the mean  $\pm$  SD from two independent experiments ( $n = 6$ ). \*core/shell is PA6-PHMB/CS-5CLO8Q.

The susceptibility of *S. aureus* and *P. aeruginosa* to the core/shell NFs were further evaluated through live/dead staining fluorescence microscopy, followed by the investigation of bacterial morphological characteristics, via SEM microscopy. Syto9 (green) penetrates bacterial membranes and binds to nucleic acid in both living and dead bacteria, whereas PI is impermeable to intact membranes and can only penetrate damaged bacteria to bind nucleic acid manner. As observed in Figure 6.12d, upon exposure to the antimicrobial NFs, the core/shell mats elicited the most potent bactericidal effect, with the majority of the dye binding to cytoplasmic nucleic acids exposed by damaged membranes. Figure 6.12(e-f) indicate the relative percentage of live/dead bacteria following 4-h exposure to the various electrospun mats, as quantified by fluorescent images, which indicated that exposure to the core/shell structure was the most effective for decimating the growth of the two bacterial species examined ( $\geq 98\%$  bactericidal activity).

The robust antimicrobial activity of the core/shell NFs was then compared against a bacteria-contaminated biologic mesh (Strattice®, porcine collagen-based), synthetic mesh (Parietex®, polyester-based), and CS and PLLA fibres, ranging between 1-10  $\mu\text{m}$  and 450-800 nm, in diameter, respectively. The Gram-negative, rod-shaped, *E. coli* (strain DSMZ 30083) was used to compare the bacteria-contaminated materials via growth kinetics and Syto9-stained confocal microscopy. However, because the antimicrobial efficacy had already been assessed against the pathogenic bacterial strains, these assays were conducted to demonstrate the superiority of the bicomponent core/shell NFs over commercially available meshes and other textile fabrics. As can be observed in Figure 6.13, during the 12-h growth kinetics experiment, performed following the exposure of the various materials to *E. coli* for 2 h, the core/shell NFs was the only tested material capable of completely preventing bacterial re-growth, followed by the CS 10-50  $\mu\text{m}$  group, which was able to retard the exponential growth of *E. coli* for only 6 h. These findings further stipulate the ineffectiveness of the currently used hernia meshes to provide a form of antimicrobial protection. This note, based merely on the *in vitro* assessment performed in this study, does not take into account the innate immune system (that would have played a crucial role in attempting to prevent an infection from



settling), but rather solely highlights the lack of an active role towards the prevention of surface colonization and biofilm formation by prostheses today.

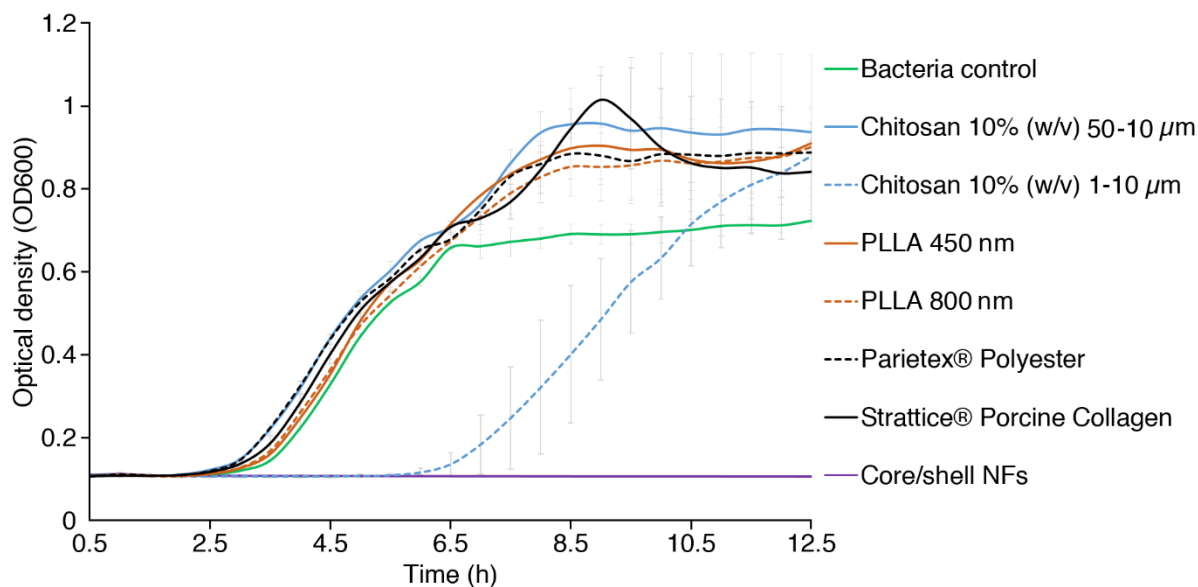


**Figure 6.13.** *Escherichia coli* growth kinetics assessment on different textiles. Comparison of the core/shell NFs with variant forms of microfibres, a polyester-based hernia mesh, and a biologic hernia mesh. The bacteria growth on hernia meshes and other textile forms were assessed using *E. coli*. PLLA: poly (L-lactic acid). All data are shown as the mean  $\pm$  SD from two independent experiments ( $n = 6$ ).

Finally, the SEM micrographs presented in Figures 6.14, which compare the PA6-only fibres with the core/shell antimicrobial NFs in the presence of *S. aureus* and *P. aeruginosa*, and the confocal Syto9® images of the variant materials exposed to *E. coli*, in Figure 6.15, indicate the distinct morphological differences that can be observed between healthy and dead bacteria upon exposure to electrospun mats and the inefficiency of the other tested materials to provide antimicrobial protection. The normal cocci and rod morphologies observed for *S. aureus* and *P. aeruginosa*, respectively, can be observed for these species on the PA6 NF surface. In contrast, characteristic cytoplasmic inclusions, indicating dead bacterial matter, were observed for bacteria exposed to the antimicrobial core/shell electrospun mats.

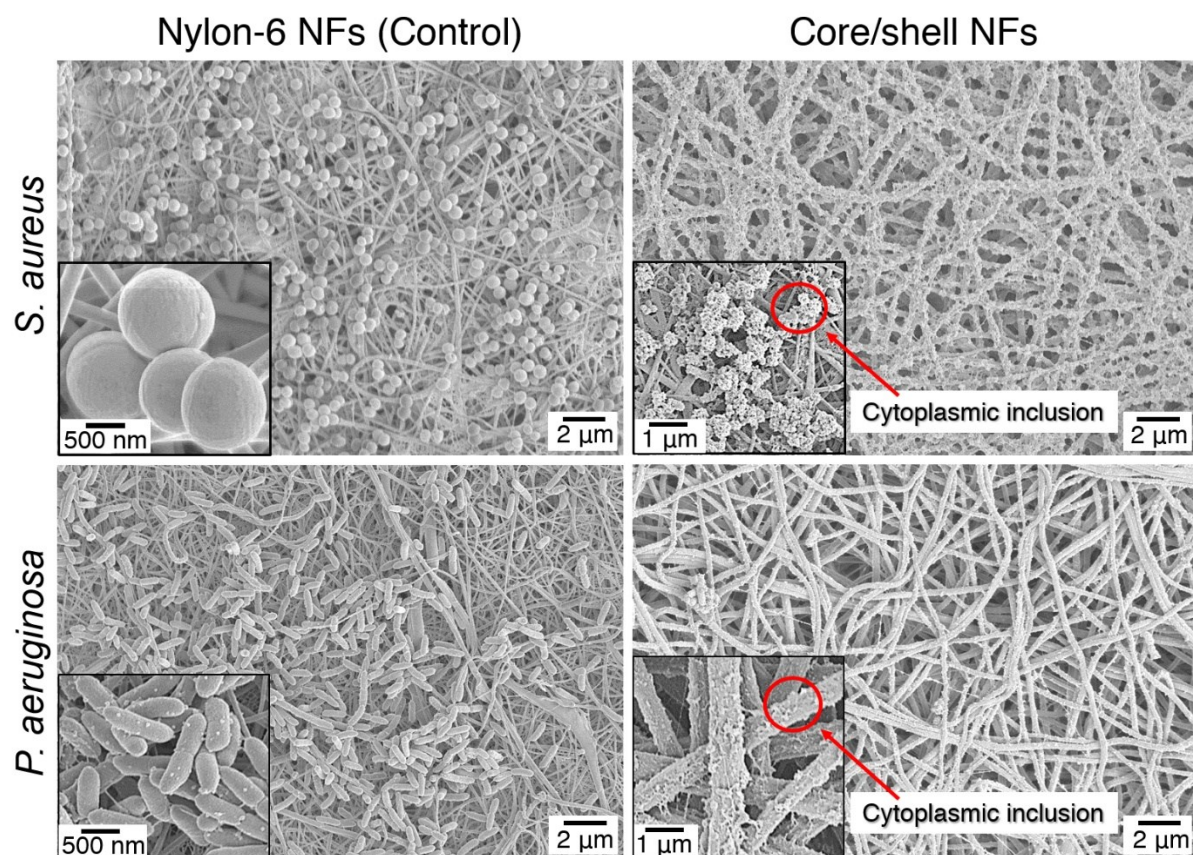


**Figure 6.14.** SEM micrographs of *S. aureus* and *P. aeruginosa* morphological properties upon exposure for 6 h to the electrospun core/shell and PA6 (control) nanofibrous mats. Red arrows indicate cytoplasmic inclusions, indicative of dead or membrane-damaged cells

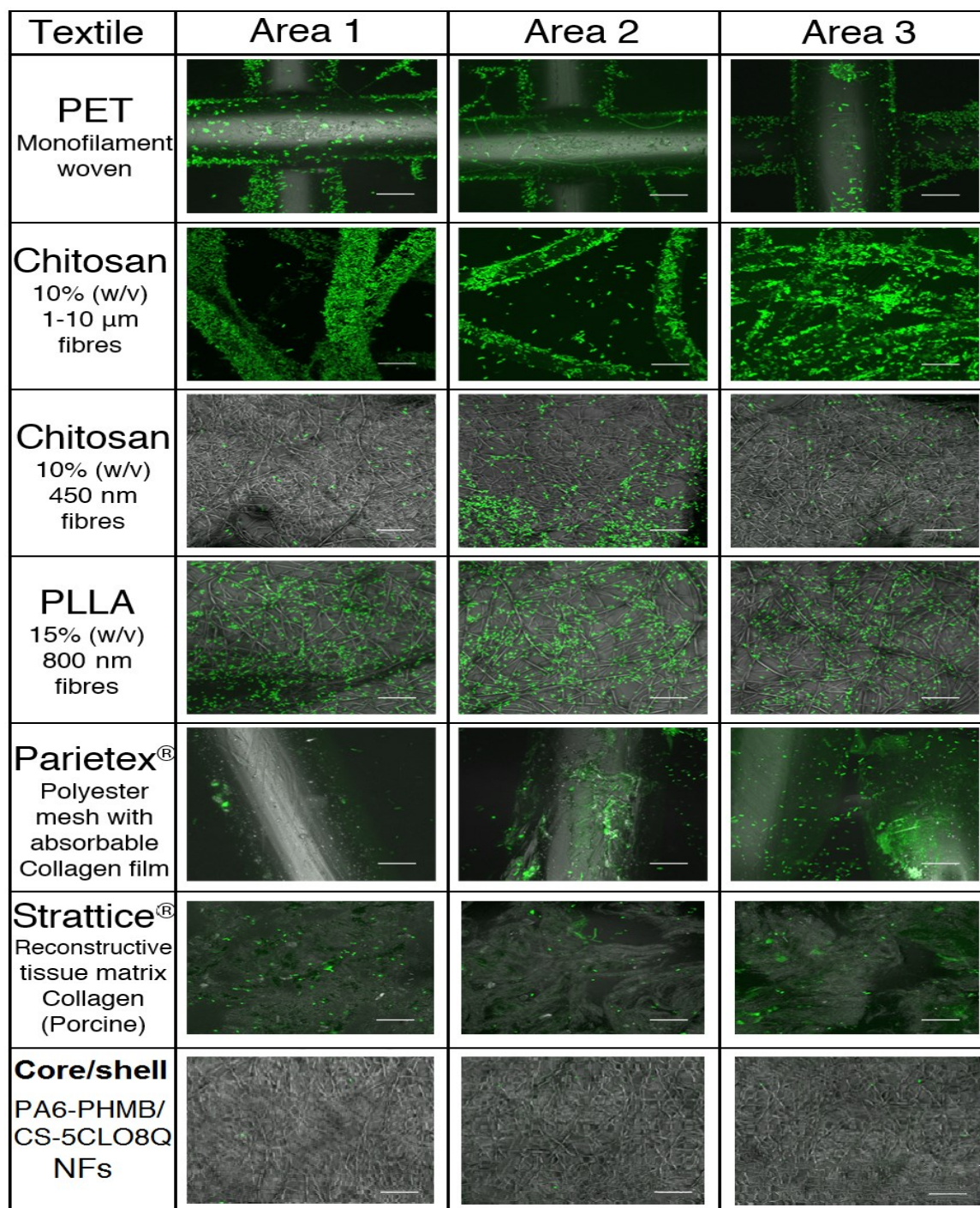


**Figure 6.15.** Confocal laser scanning microscopy (CLSM) images of variant textiles, hernia meshes and the developed core/shell antimicrobial NFs after being incubated for 2-h with *E. coli*. The cells were stained with 5  $\mu\text{M}$  SYTO9 live stain, and the images assessing bacteria attachment and infiltration on variant material surfaces were obtained with the 63x stack. The figure depicts images from three areas of one specimen per group. Scale bar, 20  $\mu\text{m}$ . PET, Poly(ethylene terephthalate); PLLA, poly (L-lactic acid).

## 6.4 Conclusions

In summary, a novel nanofibre-based antimicrobial system was successfully developed, by carefully selecting each constituent, tailoring the material properties, electrospinning parameters and fibre structure, resulting in the development of the core/shell PA6-PHMB/CS-5CLO8Q NFs.

The core/shell electrospun mats presented a homogeneous randomly oriented morphology, with a smooth fibre surface. For the first time in literature, in a single-step fabrication process, a consistent "beads-in-fibre" architecture was observed along the core of the bicomponent NFs, as determined by TEM imaging. The core/shell structure was further validated by assessing the surface chemistry and thermal properties of the composite NFs. This unique architecture gave the PA6 present in the core the right molecular configuration, and to the CS present in the shell the appropriate fibre morphology, to provide enhanced mechanical strength and elasticity to the composite structure, an essential feature for the development of a hernia mesh implant.

The *in vitro* evaluation of antimicrobial activity via agar disc-diffusion testing, dynamic growth kinetics, live/dead staining, and SEM microscopy, illustrated that the composite nanofibrous system developed elicited strong bactericidal activity against *S. aureus*, *P. aeruginosa* and *E. coli*, which was in all cases superior to that presented by the other nanostructured groups developed, as well as micro-structured fibre-based textiles, including a synthetic and a biologic mesh currently used for hernia repair.

The binary antimicrobial system presented spatiotemporal controlled release of the antimicrobial agents, which followed a non-Fickian release model, directed by the CS present in the shell of the structure. This study underlines strong antimicrobial properties of 5CLO8Q and PHMB, and their respective possibilities for the encapsulation, which can lead to tailor drug release kinetics. In addition, these findings advocate the great potential uses of the co-axial electrospinning fabrication technique for the development of advanced NF-based drug-delivery systems. Further, this study depicted the ineffectiveness of synthetic and biologic meshes in actively preventing bacterial contamination, through the assessment of two commonly used mesh material; a 100 USD polyester-based multifilament synthetic mesh, and a 35,000 USD collagen-derived reconstructive tissue matrix (biologic mesh).

The ultralight-weight bicomponent drug-eluting nanostructured antimicrobial hernia mesh designed in this study may ultimately be applicable for the prevention of bacterial infections related to prostheses while merging a new microarchitecture that falls between synthetic and biologic meshes. Further work will have to focus on assessing the compatibility of the system upon implantation in an animal model, *in vivo*.

## 6.5 References

1. Schumpelick, V., & Fitzgibbons, R. J. (2007). *Recurrent hernia: Prevention and treatment*. In Volker Schumpelick & R. J. Fitzgibbons (Eds.), *Recurrent Hernia: Prevention and Treatment* (1st ed., pp. 3–25). Berlin, Germany: Springer. <https://doi.org/10.1007/978-3-540-68988-1>
2. Kelly, S. (2017). Mesh abdominal wall hernia surgery is safe and effective — the harm New Zealand media has done. *New Zealand Medical Journal*, *130*(2), 54–57. <https://doi.org/pubmed.ncbi.nlm.nih.gov/28981495/>
3. Falagas, M. E., & Makris, G. C. (2010). Mesh-related infections after hernia repair. *Hernia Repair*, *11*(1), 97–102. [https://doi.org/10.1007/978-3-642-11541-7\\_13](https://doi.org/10.1007/978-3-642-11541-7_13)
4. De Jonge, S. W., Gans, S. L., Atema, J. J., Solomkin, J. S., Dellinger, P. E., & Boermeester, M. A. (2017). Timing of preoperative antibiotic prophylaxis in 54,552 patients and the risk of surgical site infection. *Medicine Meta-Analysis of Observational Studies in Epidemiology*, *96*(29), 1–12. <https://doi.org/10.1097/MD.0000000000006903>
5. Su, Z., Ding, J., & Wei, G. (2014). Electrospinning: A facile technique for fabricating polymeric nanofibers doped with carbon nanotubes and metallic nanoparticles for sensor applications. *RSC Advances*, *4*(94), 52598–52610. <https://doi.org/10.1039/c4ra07848a>
6. Han, D., & Steckl, A. J. (2019). Coaxial electrospinning formation of complex polymer fibers and their applications. *ChemPlusChem*, *84*(1), 1453–1497. <https://doi.org/10.1002/cplu.201900281>
7. Khalf, A., & Madihally, S. V. (2017). Recent advances in multiaxial electrospinning for drug delivery. *European Journal of Pharmaceutics and Biopharmaceutics*, *112*(1), 1–17. <https://doi.org/10.1016/j.ejpb.2016.11.010>
8. Zhang, M., Zhao, X., Zhang, G., Wei, G., & Su, Z. (2017). Electrospinning design of functional nanostructures for biosensor applications. *Journal of Materials Chemistry B*, *5*(9), 1699–1711. <https://doi.org/10.1039/c6tb03121h>
9. Bösiger, P., Tegl, G., Richard, I. M. T., Le Gat, L., Huber, L., Stagl, V., Mensah, A., Guebitz, G. M., Rossi, R. M., & Fortunato, G. (2018). Enzyme functionalized electrospun chitosan mats for antimicrobial treatment. *Carbohydrate Polymers*, *181*(1), 551–559. <https://doi.org/10.1016/j.carbpol.2017.12.002>
10. Dormidontova, E. E. (2002). Role of competitive PEO-water and water-water hydrogen bonding in aqueous solution PEO behavior. *Macromolecules*, *35*(3), 987–1001. <https://doi.org/10.1021/ma010804e>
11. Pakravan, M., Heuzey, M. C., & Aji, A. (2011). A fundamental study of chitosan/PEO electrospinning. *Polymer*, *52*(21), 4813–4824. <https://doi.org/10.1016/j.polymer.2011.08.034>
12. Yu, J., Lee, A. R., Lin, W. H., Lin, C. W., Wu, Y. K., & Tsai, W. B. (2014). Electrospun PLGA fibers incorporated with functionalized biomolecules for cardiac tissue engineering. *Tissue Engineering - Part A*, *20*(13–14), 1896–1907. <https://doi.org/10.1089/ten.tea.2013.0008>
13. Kamboj, S., & Rana, V. (2014). Physicochemical, rheological and antioxidant potential of corn fiber gum. *Food Hydrocolloids*, *39*(1), 1–9. <https://doi.org/10.1016/j.foodhyd.2013.12.015>
14. Huang, W., Wang, M. J., Liu, C. L., You, J., Chen, S. C., Wang, Y. Z., & Liu, Y. (2014). Phase separation in electrospun nanofibers controlled by crystallization induced self-assembly. *Journal of Materials Chemistry A*, *2*(22), 8416–8424. <https://doi.org/10.1039/c4ta00417e>
15. Chen, G., Fang, D., Wang, K., Nie, J., & Ma, G. (2015). Core-shell structure PEO/CS nanofibers based on electric field induced phase separation via electrospinning and its application. *Journal of Polymer Science, Part A: Polymer Chemistry*, *53*(19), 2298–2311. <https://doi.org/10.1002/pola.27702>
16. Wang, C., & Hsiue, T. T. (2017). Core-shell fibers electrospun from phase-separated blend solutions: Fiber formation mechanism and unique energy dissipation for synergistic fiber

- toughness. *Biomacromolecules*, *18*(9), 2906–2917.  
<https://doi.org/10.1021/acs.biomac.7b00863>
17. Kim, C. H., Khil, M. S., Kim, H. Y., Lee, H. U., & Jahng, K. Y. (2006). An improved hydrophilicity via electrospinning for enhanced cell attachment and proliferation. *Journal of Biomedical Materials Research - Part B Applied Biomaterials*, *78B*(2), 1–18.  
<https://doi.org/10.1002/jbm.b.30484>
  18. Liu, W., Zhan, J., Su, Y., Wu, T., Wu, C., Ramakrishna, S., Mo, X., Al-Deyab, S. S., & El-Newehy, M. (2014). Effects of plasma treatment to nanofibers on initial cell adhesion and cell morphology. *Colloids and Surfaces B: Biointerfaces*, *113*(1), 101–106.  
<https://doi.org/10.1016/j.colsurfb.2013.08.031>
  19. Tuson, H. H., & Weibel, D. B. (2013). Bacteria-surface interactions. *Soft matter*, *9*(18), 4368–4380. <https://doi.org/10.1039/C3SM27705D>
  20. Yuan, Y., Hays, M. P., Hardwidge, P. R., & Kim, J. (2017). Surface characteristics influencing bacterial adhesion to polymeric substrates. *RSC Advances*, *7*(23), 14254–14261.  
<https://doi.org/10.1039/C7RA01571B>
  21. Kasaai, M. R. (2010). The use of various types of NMR and IR spectroscopy for structural characterization of chitin and chitosan. In Se-Kwon Kim (Ed.), *Chitin, Chitosan, Oligosaccharides and Their Derivatives: Biological Activities and Applications* (1st ed., pp. 70–98). Boca Raton, USA: CRC Press. <https://doi.org/10.1201/EBK1439816035>
  22. Amaral, I. F., Granja, P. L., & Barbosa, M. A. (2005). Chemical modification of chitosan by phosphorylation: An XPS, FT-IR and SEM study. *Journal of Biomaterials Science, Polymer Edition*, *16*(12), 1575–1593. <https://doi.org/10.1163/156856205774576736>
  23. Behler, K., Havel, M., & Gogotsi, Y. (2007). New solvent for polyamides and its application to the electrospinning of polyamides 11 and 12. *Polymer*, *48*(22), 6617–6621.  
<https://doi.org/10.1016/j.polymer.2007.08.058>
  24. Nirmala, R., Navamathavan, R., Kang, H. S., El-Newehy, M. H., & Kim, H. Y. (2011). Preparation of polyamide-6/chitosan composite nanofibers by a single solvent system via electrospinning for biomedical applications. *Colloids and Surfaces B: Biointerfaces*, *83*(1), 173–178. <https://doi.org/10.1016/j.colsurfb.2010.11.026>
  25. Odian, G. (2004). Principles of Polymerization. In George Odian (Ed.), *Step polymerization* (3rd ed., pp. 198–349). New York, USA: John Wiley & Sons.  
<https://doi.org/10.1002/047147875x>
  26. González, V., Guerrero, C., & Ortiz, U. (2000). Chemical structure and compatibility of polyamide–chitin and chitosan blends. *Journal of Applied Polymer Science*, *78*(4), 850–857.  
[https://doi.org/10.1002/1097-4628\(20001024\)78:4<850::AID-APP190>3.0.CO;2-N](https://doi.org/10.1002/1097-4628(20001024)78:4<850::AID-APP190>3.0.CO;2-N)
  27. Al-Sagheer, F., & Muslim, S. (2010). Thermal and mechanical properties of chitosan/SiO<sub>2</sub> hybrid composites. *Journal of Nanomaterials*, *2*(3), 1–7. <https://doi.org/10.1155/2010/490679>
  28. Regulation (EU) No 528/2012 concerning the making available on the market and use of biocidal products. (2015). *The European Parliament And Of The Council*, *13*(1), 181–303. Retrieved from [http://dissemination.echa.europa.eu/Biocides/ActiveSubstances/1347-02/1347-02\\_Assessment\\_Report.pdf](http://dissemination.echa.europa.eu/Biocides/ActiveSubstances/1347-02/1347-02_Assessment_Report.pdf)
  29. El-Hefian, E. A., Nasef, M. M., Yahaya, A. H., & Khan, R. A. (2010). Preparation and characterization of chitosan/agar blends: rheological and thermal studies. *Journal of the Chilean Chemical Society*, *55*(1), 130–136. <https://doi.org/10.4067/S0717-97072010000100031>
  30. Dong, Y., Ruan, Y., Wang, H., Zhao, Y., & Bi, D. (2004). Studies on glass transition temperature of chitosan with four techniques. *Journal of Applied Polymer Science*, *93*(4), 1553–1558. <https://doi.org/10.1002/app.20630>
  31. Sakurai, K., Maegawa, T., & Takahashi, T. (2000). Glass transition temperature of chitosan and miscibility of chitosan/poly(N-vinyl pyrrolidone) blends. *Polymer*, *41*(19), 7051–7056.

- [https://doi.org/10.1016/S0032-3861\(00\)00067-7](https://doi.org/10.1016/S0032-3861(00)00067-7)
32. El-Ola, S. M. A. (2008). Recent developments in finishing of synthetic fibers for medical applications. *Designed Monomers and Polymers*, 11(6), 483–533. <https://doi.org/10.1163/156855508X363816>
  33. El-Hefian, E. A., Nasef, M. M., & Yahaya, A. H. (2014). Chitosan-based polymer blends: current status and applications. *Journal of Chem Society of Pakistan*, 36(1), 1–11. <https://doi.org/10.1155/2020/8586136>
  34. Elhendawi, H., Felfel, R. M., Abd El-Hady, B. M., & Reicha, F. M. (2014). Effect of synthesis temperature on the crystallization and growth of in situ prepared nanohydroxyapatite in chitosan matrix. *ISRN Biomaterials*, 1, 1–8. <https://doi.org/10.1155/2014/897468>
  35. Bazbouz, M. B., & Stylios, G. K. (2010). The tensile properties of electrospun nylon 6 single nanofibers. *Journal of Polymer Science, Part B: Polymer Physics*, 48(15), 1719–1731. <https://doi.org/10.1002/polb.21993>
  36. Yao, J., Bastiaansen, C., & Peijs, T. (2014). High strength and high modulus electrospun nanofibers. *Fibers*, 2(2), 158–186. <https://doi.org/10.3390/fib2020158>
  37. Qasim, S. B., Najeeb, S., Delaine-Smith, R. M., Rawlinson, A., & Ur Rehman, I. (2017). Potential of electrospun chitosan fibers as a surface layer in functionally graded GTR membrane for periodontal regeneration. *Dental Materials*, 33(1), 71–83. <https://doi.org/10.1016/j.dental.2016.10.003>
  38. Yuan, T. T., DiGeorge Foushee, A. M., Johnson, M. C., Jockheck-Clark, A. R., & Stahl, J. M. (2018). Development of electrospun chitosan-polyethylene oxide/fibrinogen biocomposite for potential wound healing applications. *Nanoscale Research Letters*, 13(1), 1–12. <https://doi.org/10.1186/s11671-018-2491-8>
  39. Cleeton, C., Keirouz, A., Chen, X., & Radacsi, N. (2019). Electrospun nanofibers for drug delivery and biosensing. *ACS Biomaterials Science & Engineering*, 5(9), 4183–4205. <https://doi.org/10.1021/acsbmaterials.9b00853>
  40. Simmen, H. P., & Blaser, J. (1993). Analysis of pH and pO<sub>2</sub> in abscesses, peritoneal fluid, and drainage fluid in the presence or absence of bacterial infection during and after abdominal surgery. *The American Journal of Surgery*, 166(1), 24–27. [https://doi.org/10.1016/S0002-9610\(05\)80576-8](https://doi.org/10.1016/S0002-9610(05)80576-8)
  41. de Paula, G. F., Netto, G. I., & Mattoso, L. H. C. (2011). Physical and chemical characterization of poly(hexamethylene biguanide) hydrochloride. *Polymers*, 3(2), 928–941. <https://doi.org/10.3390/polym3020928>
  42. Kirby, B. J., & Hasselbrink, E. F. (2004). Zeta potential of microfluidic substrates: 2. Data for polymers. *Electrophoresis*, 25(2), 203–213. <https://doi.org/10.1002/elps.200305755>
  43. Kong, M., Chen, X. G., Xing, K., & Park, H. J. (2010). Antimicrobial properties of chitosan and mode of action: A state of the art review. *International Journal of Food Microbiology*, 144(1), 51–63. <https://doi.org/10.1016/j.ijfoodmicro.2010.09.012>
  44. Sohrabi, A., Shaibani, P. M., Etayash, H., Kaur, K., & Thundat, T. (2013). Sustained drug release and antibacterial activity of ampicillin incorporated poly(methyl methacrylate)-nylon 6 core/shell nanofibers. *Polymer*, 54(11), 2699–2705. <https://doi.org/10.1016/j.polymer.2013.03.046>
  45. Kurtz, I. S., & Schiffman, J. D. (2018). Current and emerging approaches to engineer antibacterial and antifouling electrospun nanofibers. *Materials*, 11(7), 1–16. <https://doi.org/10.3390/ma11071059>
  46. Rieger, K. A., & Schiffman, J. D. (2014). Electrospinning an essential oil: Cinnamaldehyde enhances the antimicrobial efficacy of chitosan/poly(ethylene oxide) nanofibers. *Carbohydrate Polymers*, 113(2), 561–568. <https://doi.org/10.1016/j.carbpol.2014.06.075>





---

# Chapter 7

## Conclusions & Recommendations

---

### 7.1 Concluding remarks

The central focus of this doctoral thesis was to explore material-oriented strategies to address existing challenges associated with (1) wound healing and (2) mesh-associated surgical site infections following hernia surgery. The project aimed to develop advanced, fibre-based biomaterials, at micro/nano-dimensions, with tuneable compositions, morphological, physical, mechanical, and biological properties.

The specific objectives of this thesis were:

1. The manufacturing of electrospun fibre-based composite biomaterials, by integrating natural and synthetic polymer blends, with adjustable properties.
2. The evaluation of the impact of the electrospun scaffolds architecture regarding physiochemical and mechanical stability, biocompatibility (in the case of skin-like substitutes), and drug release profile and antimicrobial efficiency (in the case of hernia meshes).
3. The design and build a nozzle-free electrospinning device intended to augment the meagre fibre production associated with lab-based electrospinning equipment.
4. Assess the effect of the PGS proportion and degree of polymerisation towards the mechanics and wetting properties of the composite scaffolds.
5. Describe the photocrosslinking of the PVP/PGS fibres in the presence of riboflavin.
6. Develop an alternative, straightforward, and rapid protocol for the extraction of silk fibroin from *Bombyx mori* silkworm cocoons.
7. Compare the antimicrobial properties of the developed drug-eluting nanostructured hernia mesh to those of commercially available prosthesis and other forms of textiles.

The fabrication process used for biomaterial design was the electrospinning technique, which is a fibre production method capable of formulating scaffolds with a microarchitecture that resembles the fibrillar configuration of the ECM of human tissues.

The research on which this thesis is based, investigated the microstructural, physicochemical, and mechanical properties of novel composite ECM-like scaffolds for use as skin substitutes and the influence of the fibroblast behaviours of these composites on cell adhesion, proliferation and morphology (*Chapters 4 and 5*). Subsequently, a nanofibrous, bicomponent, antimicrobial, hernia mesh, capable of facilitating the two-compartment release of antimicrobial substances, was designed and evaluated for its ability to attain the appropriate mechanics of a hernia mesh and to inhibit pathogenic bacteria from instigating infection (*Chapter 6*).

The body of work conducted in this thesis successfully expands upon the field of biomedical engineering and fulfils the aforementioned aims and objectives, by expanding the applications of the electrospinning process for the development of advanced composite fibre-based biomaterials.

For clarity, the discussion and concluding remarks below separately address (1) the high-throughput production of electrospun scaffolds designed to act as skin substitutes and (2) the co-axially electrospun, antimicrobial hernia mesh NFs designed to prevent bacterial adherence, colonisation and subsequent mesh-associated SSI.

### **7.1.1 Conclusions regarding the skin-substitute, biomaterials**

Clinical constraints continue to hinder the development of efficient skin substitute products for the management of cutaneous wounds. Skin tissue engineering is a well-established and rapidly evolving field that presents multifaceted challenges. Several scaffolds have been developed during the past decades that offer therapeutic benefits or facilitate the regeneration capacities of injured skin. However, the development of a truly clinically viable, biomimetic biomaterial remains a necessary goal, as the scaffolds currently in use today present simplistic, non-biomimetic architectures that do not fulfil all the requirements or originate from human or animal xenografts/allografts or tissue-derived sources, a complicated and expensive process that carries its own limitations. Thus, advanced biomimetic scaffolds that can be produced efficiently and cost-effectively remain necessary to generate an environment that is conducive to tissue regeneration.

This portion of the project focused on the production of polymer scaffolds that closely resembled decellularised skin, while simultaneously providing mechanical and structural integrity that facilitates cell attachment and proliferation. The wide array of physical and

biochemical attributes that must be met for a skin substitute to be effective has allowed for the exploration of many different avenues, combining various characteristics, in the search for the optimal technology. The nonwoven ECM-like scaffolds that were developed for this project, fabricated using the high-throughput, nozzle-free, electrospinning technology, demonstrated the feasibility and potential uses of electrospun biomaterials to address the challenges associated with skin grafting and tissue-derived skin substitution products, under many circumstances, by employing an alternative production route.

This is the first time reported that free surface electrospinning was successfully adapted to produce continuous microfibres deriving from ternary polymer blends, rather than single-polymer solutions such as PCL, PVP and PVA. This key contribution is of significance as it demonstrates that it is feasible to high-throughput generate composite fibres out of more complex polymer systems, using a nozzle-free electrospinning device, something that has only been reported with conventional nozzle-based setups.

The selected polymers used in these studies have been well-established in tissue engineering research due to their good mechanics, biocompatibility and biodegradability, ease of manufacturing, and low costs. However, many of the designed material systems subsequently posed difficulties associated with the complexity of material fabrication and characterisation. The positive effects of composite electrospun fibres compared with single-synthetic-polymer material systems were illustrated for both of the material systems developed in these studies: PVP/PGS and PCL-backbone SF/(p)PGS.

The benefits of the fibrous structure of the biomaterial systems were initially illustrated by the ability of the PVP/PGS fibres to better imitate a cellular microenvironment, which supported HDF growth and scaffold expansion. HDFs were found to adhere four times more efficiently on PVP/PGS electrospun mats than on PGS gels that lacked the ECM-like fibril complexity of the electrospun materials and the corresponding superiority in terms of physical and structural integrity.

These properties were demonstrated microscopically when assessing the morphologies of HDFs grown on PCL-only fibres, which resembled spheroid, fibroblast-like cells, compared with cells grown on the ternary PCL-backbone SF/(p)PGS substrate, which presented a healthy, polygonal, spindle-shaped, elongated morphology. SF-containing scaffolds supported cell proliferation and viability, *in vitro*, to a significantly better degree than PCL-only fibres.

In *Chapter 4*, elongation-at-break and Young's modulus of the PVP/PGS fibres exhibited proportional relationships with the molecular weight of PVP and with the proportion of PGS

within the blends, such that PVP/PGS at 50:50 demonstrated a 20-fold increase in elasticity compared with the 80:20 group. As described in Table 2.1 (*Chapter 2*), which represents the skin's tensile properties, this adjustable elasticity may be beneficial for future research in an animal model, to assess the effects of the various composite groups developed for use in wound closure applications for injuries induced at mechanically dissimilar anatomical sites. For instance, the more supple skin present in the arm could be assessed using the PVP/PGS 60:40 group, whereas the stiffer anatomical regions, such as the forehead and the back, could be evaluated using the PVP/PGS 80:20 and 70:30 groups. Electrospun fibres present a very high aspect ratio making them much more malleable than other forms of biomaterials that are used for wound healing [6]. The ability to tune the mechanics of these scaffolds by simply adjusting the proportions of the two polymers while retaining their fibrous morphology is advantageous for skin TE applications and the replacement of dermal tissue, allowing the regulation of correct fate decisions among the cell populations during the wound healing process [1].

The successful photocrosslinking of the PVP/PGS fibres facilitated the assessment of their biocompatibility with HDFs by retarding the otherwise rapid degradation of PVP by cellular media and represented a novel process, described for the first time in this thesis. Maintaining the integrity of the PVP/PGS fibres revealed that PVP/PGS 70:30 presented the most efficient adherence and proliferation properties.

Cell attachment and proliferation were not found to depend on the fibre diameter or the proportion of PGS within the composite fibres, up to the point at which the scaffold's fibrous morphology was lost. The PVP/PGS scaffolds that retained the fibrous morphology significantly improved cell-material interactions, cell adhesion on the material's surface, proliferation and spreading. This comes into agreement with previously published works that compared solid PCL films with PCL fibres through cell culture and animal model experiments. Metwally et al. [2], attributed this incident to the better surface potential due to the fibrous topography —  $574.4 \pm 11.2 \text{ mV}$  for PCL fibres, as opposed to  $220.6 \pm 6.7 \text{ mV}$  PCL films) — and the increased roughness associated with the films. The PCL membranes adhesiveness was significantly improved for PCL fibres with cells present filopodia cells, as opposed to the films that presented spheroid cells with poor filopodia formation and weak adhesion. Denchai et al. [3] compared randomly-oriented PCL fibres with PCL cast films on the subcutaneous tissue of rats. The authors reported a significantly greater proportion of proinflammatory macrophages (M1) due to improved protein absorption, and subsequent exponential increase of pro-healing M2 macrophages that directed MSCs migration and differentiation, between days four and

seven. In the case of the PCL films, a large population of M1 cells was retained throughout the duration of the study.

For both systems, variations in the fibre diameter ( $\pm 20\%$ ) within the same composite groups did not appear to have significant effects on the HDF attachment properties or cellular viability. However, viability appeared to correlate with the proportions of the subsequent polymers used within the composite structure.

In *Chapter 5*, an SF-based biomaterial system, SF:PCL:(p)PGS, which integrated the regenerated SF with PCL to increase the structural integrity of the scaffold and contained two different polymerised forms of PGS, permitted the development of a composite structure with wettability properties that could be modulated and that presented good *in vitro* stability. The ability to adjust the hydrophobicity of biomaterials is crucially important for obtaining the appropriate conditions necessary for cellular adhesion, proliferation, and the reduction of inflammation [4, 5]. The fibrous topography of electrospun membranes has been found to significantly increase the material's surface hydrophilicity compared to other topographies such as films [6].

The electrospun construct presented adjustable wettability properties due to the incorporation of PGS, which can be beneficial for the retention of a moist area and the uptake of wound exudates. Further, the sizes of the pores and porosity could contribute to a surface capable of reducing bacterial contamination from the external environment and, thus, diminishing the risks of infection. Furthermore, the addition of PCL generated more easily handled and stable construct, whereas the incorporation of silk fibroin increased the *in vitro* biocompatibility of HDFs.

Biocompatibility was assessed by measuring metabolic activity, using Alamar blue®. Studies have shown that Alamar blue and MTT assays are equally suitable as high-throughput screening assays for the determination of cytotoxicity [7–9]. In this study, the Resazurin-based assay was found to be useful for determining cell viability and cell growth on electrospun membranes and provided consistency during the experiments. Cell viability was further assessed by examining cellular morphology and expansion, and consistency between imaging and assay-based techniques provided increasing confidence in the assessment.

In this study, the skin fibroblast cell-line (BJ5ta; ATCC® CRL4001™) donated for this work, was chosen as it was of human origin and economically viable because it required fewer media supplements. Unfortunately, no literature was identified using this cell-line for similar studies. Because the BJ5ta cells represent an hTERT-immortalised cell line, variations may exist in

the physiological attributes between those observed in primary cells and those presented by this continuous cell-line. Although these immortalised cells can retain critical morphological features, they tend to be more adherent, more readily viable, and, in some instances, express a broader range of chemokines and other markers [10]. However, for the scope of the work conducted and as a proof-of-concept study, this immortalised cell-line provided consistent and reproducible results for a genetically identical and homogeneous population of fibroblasts, which was deemed to be sufficient.

### **7.1.2 Conclusions regarding the nanostructured drug-eluting antimicrobial hernia mesh**

This thesis also focused on the development of a nanofibre-inspired hernia mesh, designed to prevent infections caused due to mesh contamination. Here, for the first time in the literature, a bicomponent, nanofibrous system, comprised of chitosan and nylon-6, was used to demonstrate how the selected antimicrobial agents, 5CLO8Q and PHMB, can work synergistically to prevent bacterial colonisation on surfaces.

This study was guided by a surgical team at the Innospatial University Hospital, in Berne, Switzerland, which offered valuable insights regarding the significant challenges faced during and after hernia repair, and what is needed to overcome these challenges, from a surgical perspective. Currently, hernia meshes are made of natural (e.g., collagen) or synthetic materials (such as PP or PE) [11, 12]. As described in detail in the literature, biologic meshes can be costly, limited to the animal source, carry ethical challenges and complicated to obtain, whereas synthetic meshes are associated with a wide array of limitations, from material, biological, and mechanical standpoints. Today, there is no synthetic mesh that has been developed that is morphologically similar to biologic meshes, and able to provide antimicrobial protection, while retaining the appropriate mechanical requirements.

The ultralight-weight bicomponent, nanofibrous, hernia mesh assessed in this study was developed through the co-axial electrospinning technique. The core/shell NFs produced, with an average fibre diameter of  $270 \pm 68$  nm, incorporated a dual antimicrobial system with a nylon-6-core and biocompatible chitosan in the shell (on the fibre surface). A unique structure, consisting of a “beads-in-fibres” morphology, first time reported through a single-step fabrication process, was described and verified by TEM and XPS and by evaluating the enthalpy transition of nylon-6 between the core/shell and single nylon-6 NFs.

The drug release profile of the bicomponent nanofibrous mesh was obtained under the two most relevant pH conditions, while the drug release profile was described, in-depth. By finely selecting the polymer-drug combos, so that a hydrophilic polymer is paired with a hydrophobic drug and vice versa, the increased drug affinity allowed for the sustained release of the antimicrobial agents from two-compartments; the surface and the core of the NFs.

The large surface area of nanofibrous membranes, and by increasing the diffusion pathways through the core/shell morphology, co-axial fibres have been proven to elicit controllable drug release profiles and improved bactericidal properties than loaded films [13, 14]

Finally, the effectiveness of the nanostructured composite system against *S. aureus*, *P. aeruginosa* and *E. coli* was thoroughly determined, through the assessment of inhibition zones, growth kinetics, live/dead staining, and microscopic evaluations, comparing the antimicrobial fibres against synthetic fibres, biologic and synthetic hernia meshes. The developed antimicrobial mesh presented a robust bactericidal activity across all the examined pathogens. The developed construct reported antimicrobial responses similar to porcine dermal graft (bioprosthesis) containing rifampin and minocycline (Xenmatrix™ AB) and PP meshes coated with rifampicin and ofloxacin [15]. Nevertheless, the use of antimicrobial agents and antiseptics rather than antibiotics that steadily increase the emerge of new resistant subtypes of MRSA is a valid approach that can provide long-term protection against infection [16].

The use of chlorhexidine and allicin through the soaking of PP meshes [17] and triclosan-chitosan combo in the form of PP-embedded gels [18] have reported partial bacteria clearance and three-log reduction of bacterial contamination, respectively, in the earlier works. However, the integration of the antimicrobial substances with the ECM-like nanotopography and improved drug release profile, given by the electrospun matrices, allows for the fabrication of synthetic-based meshes that accommodate antimicrobial protection, while retaining a biosynthetic-like morphology, which subsequent studies could prove to be overall beneficial towards the healing process of the fascia at the affected area.

By comparing the nanostructured construct with different forms of commercially available prosthesis, the findings came into agreement with previously published appraisals [15, 19] that denote the inability of the available material system to provide active antimicrobial protection; a novel path expanding towards research surrounding implantable devices.

The minimum inhibitory concentrations of the tested antimicrobial agents have previously



been assessed in the literature, reported at  $0.2 \text{ gm}\cdot\text{L}^{-1}$  for PHMB [20, 21] and  $0.4 \text{ gm}\cdot\text{L}^{-1}$  for 5CLO8Q [22]. The antimicrobial activity of the composite antimicrobial NFs was robust – able to suppress the growth of the two pathogenic bacterial species (*S. aureus* and *P. aeruginosa*) that account for more than 90% of all infections reported on contaminated surgical meshes. The drug concentrations used in this study were based on regulations established by the FDA and the European Commission [22–24].

### 7.1.3 Research and experimental limitations

This thesis has potential limitations that should be noted. Due to the nature of the research questions that were formed, and as the work was conducted at the Institute for Materials and Processes of the Engineering School, the material development and characterisation areas of the research prevail the *in vitro* assessment of the developed biomaterials. In addition, limited space at the Institute for Bioengineering facilities due to refurbishments and subsequent closure and reopening with limited capacity due to the COVID-19 pandemic, render the continuation of the *in vitro* assessment of the biomaterials using more advanced models.

The use of a continuous cell-line rather than primary cells further limited the extent of the *in vitro* assessment. This was due to budget constraints. The initial research question behind the work conducted in Chapter 4, was built on observations made by Martino and Forte [25], Nasrollahi et al. [26], and the Dennis Discher's group (Engler et al. [27]) surrounding cell lineage specification and differentiation, cellular mechanical memory and the ability of dermal cells to adapt and reconstruct the ECM at an injured site based on the mechanics of the skin.

Initially, the electrospun membranes would have been seeded with primary fibroblasts, followed by identifying the various subpopulations through phenotypic characterisation, which would have allowed for the determination of the proportion and capability of the matrices to control fibroblast-to-myofibroblasts differentiation [28]. This can be done molecularly by quantifying the expression levels of  $\alpha$ -smooth muscle actin ( $\alpha$ -SMA), and, more recently, through the surface enzyme amine oxidase, copper containing 3 (AOC3) [29], as well as via fluorescence microscopy by staining the nuclei with DAPI, rhodamine-conjugated phalloidin for F-actin, and FITC-labelled anti-SMA [30]. Keratinocytes could have also been used to assess mobility and migration on the electrospun matrices. Through the cell culturing of macrophages, functional polarisation (M1/M2) could further be evaluated, which would be a great indicator of the ability of the biomaterial to regulate inflammation and avoid excessive collagen deposition, especially in chronic wounds [31, 32]

The degradation studies were conducted by submerging the electrospun mats in PBS at pH 7.2. This was done predominately as the pH was the same as the culture media. Nevertheless, this approach did not take into account scaffold degradation that could have been mediated by the 10% w/v FBS present within the culture media. In addition, intact skin presents a slightly acidic pH ranging from 4.0 to 6.0, while the pH fluctuates after a wound occurs, due to the skin's acidic milieu, making it for a brief period — at the early stages of the wound healing process — neutral. On the other hand, the environment of a chronic wound is alkaline ranging between pH 7.2 to 8.9, with yet more alkaline environment being introduced after an infection has settled [33, 34]. Moreover, the degradation studies were assessed in room temperature; the human skin temperature varies and is generally a few centigrade below the body's temperature at approximately 33 °C [35]. Considering these, further assessment of the polymer degradation and stability of the material systems should take into account enzyme-mediated degradation, alkaline and acidic pH values, as well as conditioning the media to skin-relevant temperature.

As described in more detail in the future work section below, an animal study can affirm whether the reasoning behind the development of mechanically tuneable elasticities and variations in the hydrophilicity can positively impact the wound healing responses of the tissue and the contraction time, *in vivo*.

In regard to the nanostructured hernia mesh developed, the most significant limitation of this study was the absence of an *in vitro* cell culture evaluation. This would have been of great importance towards the biomaterial's biocompatibility, even in the form of simplistic toxicological evaluation. Unfortunately, while working in the S2 laboratory at Empa, access to the mammalian cell culture facilities was not granted concurrently due to anti-contamination regulations. However, the polymers used to produce the bicomponent core/shell NFs are considered to be biocompatible in the literature, and the tested concentrations of PHMB and 5CLO8Q were based on existing guidelines and represent doses that do not elicit toxic responses. That said, it does not exclude that adverse responses may be observed due to the combination of the two antimicrobial agents within the composite structure.

The nanostructured construct was mechanically assessed via tensile testing. The specimens were conditioned in standard atmospheric conditions, under were tested under dry conditions. Along with assessing the ability of the material to retain sutures and the burst pressure, it would be of interest to examine the material under wet conditions at 37 °C, as well as, at different time points upon submersion in a solution. The nanostructured construct presented tensile properties relevant to those of commercially available hernia meshes, but a low elongation-at-break, similar to heavy-weight meshes that present a high young modulus

but are less elastic. A 10-20% increase at the elastic break of the material by adjusting the composition of the core/shell structure would be required.

Moreover, from bench to bedside (clinic), to transform this material system onto a preclinical product will require for further assessment of the construct in an animal model. This can provide further insights towards the induced inflammatory responses, collagen deposition and myofascial elasticity, as well as the integration and bioabsorbability of the implant.

## 7.2 Thesis contributions

The primary contributions of this thesis are the three unprecedented material systems developed: PVP/PGS, SF:PCL:(p)PGS, and PA6-PHMB/CS-5CLO8Q. This thesis was able to address, to a substantial degree, the aims outlined in *Section 1.2 Thesis Aims and Objectives*. Along the journey of this research work, several processes were instigated to resolve side issues that arose, leading to some additional novel methods, observations, and findings. The main outcomes are enumerated below. Based on the studies conducted during the course of this thesis research, the following conclusions can be drawn:

### Development of nozzle-free electrospinning device

1. A step-by-step guide was provided describing the design and development of a free-surface, roller-based, electrospinning device that expands on the conventional electrospinning technique by permitting the high-throughput production of polymer micro/nanofibrous materials, at an 11-fold higher rate than conventional electrospinning and in a cost-effective manner. This is the first time that a free surface electrospinning device is reported to have successfully produced continuous composite fibres deriving from binary and ternary polymer blends.

### PVP/PGS electrospun mats

2. The PVP/PGS fibrous scaffolds developed in *Chapter 4*, describe the UV-facilitated crosslinking of the composite fibres in the presence of a photoinitiator, riboflavin, where the crosslinking process is described in detail. This was evident by FTIR analysis and by determining the effect that the duration of UV treatment has on the water contact angle of the scaffold, which prevented the rapid degradation of PVP and allowed the assessment of the biomaterial *in vitro*.
3. The PVP/PGS fibres presented tuneable mechanical properties, which were modulated by adjusting the [PVP:PGS] ratio and the molecular weight of the PVP – increasing the concentration of PGS within the blends, correlated to an increase in the elongation-at-break point of the electrospun mats and subsequent reduction of the tensile strength. The fibres produced using the highest proportion of PVP within the blends presented a ten-fold increase in the Young's modulus (on average) compared with the fibres that presented the highest proportion of PGS, where the elongation-at-break followed an inverse correlation among the proportionality of the two polymers.

4. The PVP/PGS fibrous scaffolds adhered to the HDFs and allowed them to expand four times more efficiently than PVP/PGS gels that did not retain the ECM-like morphology.

### **SF:PCL:(p)PGS electrospun mats**

5. Ternary, biocompatible, silk fibroin-based electrospun fibres, with an ECM-like morphology, were successfully produced, and the presence of the counterpart polymers within the final composite was validated by FTIR and XPS.
6. In *Chapter 5*, a fast, straightforward protocol for the extraction of silk fibroin from *Bombyx mori* cocoons was described, utilising  $\text{Na}_2\text{CO}_3$  to degum the cocoons, LiBr to dissolve the fibroin and ethanol to precipitate the protein from LiBr. The protocol was capable of extracting higher quantities of the protein in one-third of the time required by the molecular cassette cut-off method, representing a more economically viable method than those currently in a laboratory setting.
7. The integration of either pPGS or PGS within the composite fibres was found to influence the wetting properties of the fibrous membranes. Increasing the concentration of PGS within the ternary blends gradually lowered the water contact angle of the scaffolds, with the phenomenon occurring at an earlier time point (upon settlement of a water droplet) in electrospun mats produced with PGS rather than pPGS. The improved wetting behaviour of the PGS in comparison to pPGS could be explained by the greater number of ester linkages.
8. The integration of the biocompatible, regenerated silk fibroin protein into the ternary blends was demonstrated microscopically to facilitate the expansion of HDFs at a significantly increased rate compared with PCL-only fibres.
9. SEM observations of the silk fibroin-containing composite electrospun mats presented a healthy, polygonal HDF morphology with multiple long spindles expanding, compared with the spheroid-shaped fibroblasts grown on the PCL-only fibre substrate.

### **Antimicrobial nanofibrous mesh: PA6-PHMB/CS-5CLO8Q**

10. Co-axially electrospun NFs, which integrated a dual antimicrobial system facilitated by the nanoencapsulation of PHMB and 5CLO8Q within a PA6 core and a CS shell, respectively, were successfully fabricated. The concentrations of the antimicrobial substances within the fibres were based on the FDA and EEA maximum toxicity level guidelines.

11. TEM observations illustrated the consistent fabrication of a “beads-in-fibres” morphology, derived from the merger of a continuous shell and a discontinuous core, a fibre configuration that was described for the first time through a single-step fabrication process.
12. The “beads-in-fibres” core/shell structure of specimens electrospun at various flow rates was confirmed by TEM imaging and by XPS analysis, by evaluating the theoretical atomic value of each material within the system. Furthermore, due to the amorphous nature of CS, in contrast to PA6, which is thermoset, the amount of PA6 within the core of the fibres was evaluated, based on the enthalpies of the PA6-only and the core/shell NFs (~ 48.5%).
13. The composite fibres presented increased thermal stability compared to the bulk materials and the single-polymer fibres. The nanofibrous construct weighed between 5–10 g.m<sup>-2</sup> appertain to ultralight-weight ( $\leq 35$  g.m<sup>-2</sup>) hernia meshes.
14. The core/shell structure successfully improved the tensile properties and mechanical stability of the CS fibres, presenting a two-fold increase in tensile strength, at  $20.7 \pm 2.5$  MPa, and a four-fold increase in Young’s modulus, at  $217.5 \pm 12.6$  MPa, compared with the nylon-6-only NFs, but by sacrificing the elongation-at-break ( $14.1\% \pm 2.1\%$ ) which remained in similar value with the CS-only NFs. These values fell within the mechanical requirements for a hernia mesh, which were described in detail in *Section 2.5.1 Hernia Mesh Architecture: Morphological, Physiochemical and Mechanical Properties*.
15. The bicomponent nanofibrous system was found to provide a two-step sequential release model of the two antimicrobial substances, which combined a small burst release (accounting for approximately 20% of the total drug-loaded) followed by the sustained release of the drug over the span of one month. This approach can provide antimicrobial protection directly after mesh implementation, where a higher bacterial-load is present, as well as in the long-term; taking into account spore-forming bacteria that may initially lie dormant. Further exploration of the drug release mechanism indicated that the co-axial fibres followed a non-Fickian model, indicating that, in contrast to the PA6-PHMB drug-containing NFs, the drug-release mechanism of the core/shell NFs was influenced by the swelling behaviour of the CS present in the shell.
16. Initially, the antimicrobial efficiency of the system was assessed using the disc diffusion technique against two pathogenic species: *S. aureus* and *P. aeruginosa*. These

findings indicated that although the disc diffusion test can be used to determine whether a specific pathogen is susceptible to an antimicrobial substance or an antibiotic, it cannot be used for the direct comparison of the effects elicited by distinct substances contained within dissimilar polymers/substrates. These findings represent a useful observation for the evaluation of antimicrobial electrospun fibres, which has been neglected in the presentation of antimicrobial efficacy in the literature.

17. The superiority of the bicomponent composite construct towards its ability to eliminate and prevent the growth of Gram-positive and Gram-negative bacterial strains was confirmed by a 12-h growth kinetics experiments. The results showed no subsequent growth, and live/dead fluorescence testing indicated 98% cell death, whereas SEM imaging of the fixed bacteria showed the formation of cytoplasmic inclusions upon contact with the antimicrobial fibres.
18. Finally, the antimicrobial efficacy of the developed construct was evaluated against micro and nanofibres composed of synthetic polymers, and biologic and synthetic hernia meshes that are currently used on the market for hernia repair. The growth kinetics results and Syto9<sup>®</sup> confocal images agreed with the pictures depicted in Figure 2.6 of *Chapter 2 Literature Review*, demonstrating the failure of the available hernia prostheses to prevent an infection from occurring, while simultaneously affirming the superiority of the developed bicomponent NFs. The developed nanofibrous system could be an economically viable new approach that brings together structural and morphological traits of synthetic and biologic meshes, along with antimicrobial protection in a single construct.

Overall, this thesis was deemed to be successful by contributing valuable knowledge to the research areas of biomaterials, skin tissue engineering, nanoencapsulation, drug release, antimicrobial surfaces, and through the description of an alternative strategy for the development of antimicrobial biomimetic surgical prostheses. The studies described here can provide future researchers with constructive insights into the development of advanced fibre-based biomaterials through electrospinning.

### 7.3 Recommendations and future directions

The work presented in this thesis forms the basis for the development of novel electrospun composite biomaterials for wound management and antimicrobial prosthesis, and subsequent work can be directed by these developments. Encouraged by the research outcomes presented in this thesis, the following are areas that could be further investigated.

#### Skin tissue engineering

1. Further validation of viability was intended, through the quantitation of dsDNA using NanoDrop® spectrophotometric quantification. Additionally, the ability of the scaffolds to support differentiation could be analysed by quantifying the relative mRNA expression of wound-healing genes (Collagen I,  $\alpha$ -SMA, VEGF, HIF-2 $\alpha$ , TGF-B1, GAPDH, SCF, SDF-1 $\alpha$  and HSP-90 $\alpha$ ) via RT-PCR, using the appropriate primers [36]. Understanding changes in gene expression could reveal the elicited responses of fibroblasts in the presence of the composite fibres and the degree to which the scaffolds influence cellular responses. Unfortunately, this work could not be completed due to the extended time spent refurbishing the Institute for Bioengineering facilities at the University of Edinburgh and the subsequent closure due to the COVID-19 outbreak following my return from a year-long placement at Empa, St. Gallen, Switzerland.
2. A wound-healing assay, such as a simple, *in vitro* scratch test, could also provide some preliminary understanding of collective cell migration and cell-matrix interactions that occur in the presence of electrospun mats [37].
3. The *in vitro* evidence presented in this thesis allows for an initial appraisal of the feasibility of using these novel fibrous membranes, prior to performing the animal sacrifices that would be required to test the *in vivo* performance of these biomaterials. The *in vitro* platform used to assess the biocompatibility of the developed electrospun mats represents the first step towards preclinical and future clinical translation. The use of an animal model would allow the assessment of wound contraction (in wound area over days), histological neo-epithelium, granulation, and scar tissue analyses, using haematoxylin and eosin and picosirius red staining, and immunohistochemistry analyses to examine M1/M2 macrophages, blood vessel formation, and immune cell infiltrates.
4. Although the inherently porous structure of electrospun scaffolds provides fenestrations that are inadequate for the passage of most cell types, they are sufficient



for nutrient and cytokine transport. Whilst cellular expansion in the form of a monolayer is not problematic for the development of wound dressings and skin substitutes, as the construct is merely meant to facilitate cell migration and proliferation at the surface of the skin, three-dimensional (3D) structures can further enhance fluid retention and exudate absorption. However, macroporous scaffolds may be less beneficial because they would likely increase the risk of infection from a contaminated outer surface. The developed composite blends could be further assessed in the form of 3D electrospun structures, by combining 3D printing and electrospinning [38], freeze-drying electrospun fibres into moulds to form 3D structures [39], or gas-foaming to expand the scaffold's 2D structure [40]. These 3D constructs could be used to further assess the interplay between keratinocytes and fibroblasts, in bilayer or multilayer constructs that could further provide insights regarding the abilities of the developed biomaterials to reduce fibrosis.

5. In addition to the regenerative capacities of the developed material system, which is the primary focus of treatment for skin loss or damage, these biomaterials could also be used as the basis for developing artificial skin constructs that can act as soft sensors and for tactile sensing. Although such an approach surrounds biosensing and electrical engineering rather than influencing and attempting to control cellular responses, skin sensors, could allow for applications such as wireless health monitoring and the integration of wearable sensors that can monitor and measure pertinent skin parameters (such as temperature, oxygen, pH, lactate, glucose and cytokines, including IL-6) [16].
6. Through the integration of metal nanoparticles (NPs), such a material system could be used to assess pH variations, in the form of electrochemical or colourimetric biosensing. Determining the pH of a wound is a good indicator of infection that could be used to monitor chronic wounds. In preliminary studies, Tungsten oxide ( $\text{WO}_3$ ) NPs were integrated within the polymer blends developed in this thesis to generate an electrochemical pH-skin sensor. During the initial stage,  $\text{WO}_3$ -NPs were incorporated within the polymer blends and electrospun. Then, one-side of the electrospun mat was sputter-coated with a 1- $\mu\text{m}$ -thick Au layer. An Ag paste was used to introduce a copper wire or conductive fabric into the  $\text{WO}_3$ -containing side of the construct. After, a pseudo-reference electrode was glued in the Au-side, incorporating a platinum-based counter electrode as reference. The use of  $\text{WO}_3$ -NPs can further provide a form of antimicrobial protection [17]. This construct is still in the design stage and has not been yet evaluated.

## Hernia mesh engineering

1. The mechanics of the nanofibrous mesh could be further assessed for burst strength, which could be a good indicator of determining the intraabdominal wall pressure limitations of the material [18]. Furthermore, the nanofibrous construct should be assessed for its ability to retain sutures, staples, and tacks for mesh fixation. Due to the high dissimilarity with commercial hernia meshes, such as differences in knitting, fibre diameter, the polymer chemistry, and porosity, evaluating the mechanics under similar conditions can be difficult and may not provide decisive conclusions, when compared with the nanofibrous hernia mesh developed.
2. To avoid cells treating the bicomponent antimicrobial mesh as a flat sheet and to enhance cell infiltration, several techniques can be employed to widen the pores of the nanofibrous structure. For a successful hernia closure and limiting the chances reherniation, the integration of the mesh material by the host tissue is crucial for determining the time required for the partial or full absorption of the material. To strengthen a patient's attenuated fascia, appropriate tissue ingrowth is required, and determining an optimal balance between inflammation, cellular and vascular infiltration, and matrix remodelling is crucial for determining the time required for construct resorption and preventing excessive collagen deposition. The following approaches could be used to change the configuration of the pores, allowing the in-depth penetration of cells into the scaffold and overcoming the small pore size constraints associated with the electrospinning process.
  - a. Cryogenic electrospinning is a technique that uses a sub-zero (in °C) temperature collector to facilitate the simultaneous formation of nanofibres and ice crystals. The scaffold's porosity can be adjusted from 10–500 µm, depending on various controllable factors, such as size and the amount of ice crystals. The ice crystals are then removed by freeze-drying the fibrous scaffolds, leaving large void spaces, which permit cell infiltration [19].
  - b. Gas foaming has been widely used to formulate porous scaffolds. This method introduces gas (most commonly CO<sub>2</sub>) into a polymer matrix. The rapid release of CO<sub>2</sub> creates gas bubbles that allow the formation of large pores, averaging 300 µm in diameter [20].
3. Among general surgeons, there is an ongoing debate about whether a permanent hernia mesh is more appropriate than a bioabsorbable material that degrades at a similar rate at which the fascia is regenerated. One potential approach would be the

direct coating of electrospun fibres onto the surface of a synthetic mesh, subsequently offering antimicrobial protection against bacteria contamination, while retaining the mechanical stability of the synthetic mesh (Figure 7.1).

4. Finally, based on the robust activity of the bicomponent antimicrobial mesh that was developed in this study, another potential approach would be to chemically graft the antimicrobial agent onto the surface of the NFs. This could ultimately generate an antimicrobial surface capable of preventing infection through contact killing, leaching or a repelling surface, without the potential cytotoxic effects associated with the release of the antimicrobials. A considerable amount of work has already been conducted in this direction, which can be found in Appendix C (*Grafting PHMB on O-carboxymethylated chitosan*), describing, for the first time, the grafting of PHMB onto the backbone of chitosan, employing a carbodiimide crosslinker (EDC/NHS coupling chemistry).

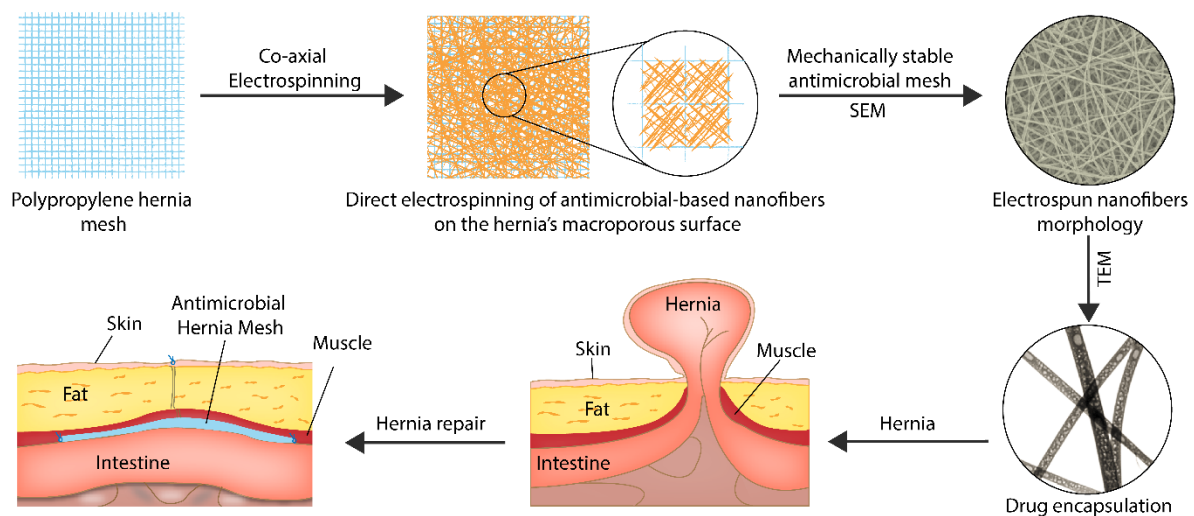


**Figure 7.1** Schematic representation depicting the direct electrospinning of antimicrobial nanofibres to coat the surface of a synthetic macroporous polypropylene hernia mesh.

## 7.4 References

1. Hodgkinson, T., & Bayat, A. (2011). Dermal substitute-assisted healing: Enhancing stem cell therapy with novel biomaterial design. *Archives of Dermatological Research*, 303(5), 301–315. <https://doi.org/10.1007/s00403-011-1131-2>
2. Metwally, S., Ferraris, S., Spriano, S., Krysiak, Z. J., Kaniuk, Ł., Marzec, M. M., Kim, S. K., Szewczyk, P. K., Gruszczyński, A., Wytrwal-Sarna, M., Karbowniczek, Joanna E., Bernasik, A., Kar-Narayan, S., Stachewicz, U., & Stachewicz, U. (2020). Surface potential and roughness controlled cell adhesion and collagen formation in electrospun PCL fibers for bone regeneration. *Materials and Design*, 194, 1–11. <https://doi.org/10.1016/j.matdes.2020.108915>
3. Denchai, A., Tartarini, D., & Mele, E. (2018). Cellular response to surface morphology: Electrospinning and computational modeling. *Frontiers in Bioengineering and Biotechnology*, 6(10), 1–11. <https://doi.org/10.3389/fbioe.2018.00155>
4. Liu, Y., Tian, K., Hao, J., Yang, T., Geng, X., & Zhang, W. (2019). Biomimetic poly(glycerol sebacate)/polycaprolactone blend scaffolds for cartilage tissue engineering. *Journal of Materials Science: Materials in Medicine*, 30(5), 1–11. <https://doi.org/10.1007/s10856-019-6257-3>
5. Liang, S. L., Yang, X. Y., Fang, X. Y., Cook, W. D., Thouas, G. A., & Chen, Q. Z. (2011). In vitro enzymatic degradation of poly(glycerol sebacate)-based materials. *Biomaterials*, 32(33), 8486–8496. <https://doi.org/10.1016/j.biomaterials.2011.07.080>
6. Deng, L., Kang, X., Liu, Y., Feng, F., & Zhang, H. (2018). Characterization of gelatin/zein films fabricated by electrospinning vs solvent casting. *Food Hydrocolloids*, 74, 324–332. <https://doi.org/10.1016/j.foodhyd.2017.08.023>
7. Hamid, R., Rotshteyn, Y., Rabadi, L., Parikh, R., & Bullock, P. (2004). Comparison of alamar blue and MTT assays for high through-put screening. *Toxicology in Vitro*, 18(5), 703–710. <https://doi.org/10.1016/j.tiv.2004.03.012>
8. Rampersad, S. N. (2012). Multiple applications of alamar blue as an indicator of metabolic function and cellular health in cell viability bioassays. *Sensors (Switzerland)*, 12(9), 12347–12360. <https://doi.org/10.3390/s120912347>
9. Bonnier, F., Keating, M. E., Wróbel, T. P., Majzner, K., Baranska, M., Garcia-Munoz, A., Blanco, A., & Byrne, H. J. (2015). Cell viability assessment using the Alamar blue assay: A comparison of 2D and 3D cell culture models. *Toxicology in Vitro*, 29(1), 124–131. <https://doi.org/10.1016/j.tiv.2014.09.014>
10. Montano, M. (2014). Model systems. In Monty Montano (Ed.), *Translational Biology in Medicine* (1st ed., Vol. 1, pp. 9–33). Boston, USA: Woodhead Publishing. <https://doi.org/10.1533/9781908818652.9>
11. Baylón, K., Rodríguez-Camarillo, P., Elías-Zúñiga, A., Díaz-Elizondo, J. A., Gilkerson, R., & Lozano, K. (2017). Past, present and future of surgical meshes: A review. *Membranes*, 7(3), 1–23. <https://doi.org/10.3390/membranes7030047>
12. Elango, S., Perumalsamy, S., Ramachandran, K., Tech, B., & Vadodaria, K. (2017). Mesh materials and hernia repair. *Biomedicine*, 7(3), 14–23. <https://doi.org/10.1051/bmdcn/2017070316>
13. Wang, N., Zhao, Y., & Jiang, L. (2008). Low-cost, thermoresponsive wettability of surfaces: Poly(*N*-isopropylacrylamide)/polystyrene composite films prepared by electrospinning. *Macromolecular Rapid Communications*, 29(6), 485–489. <https://doi.org/10.1002/marc.200700785>
14. Cleeton, C., Keirouz, A., Chen, X., & Radacsi, N. (2019). Electrospun nanofibers for drug delivery and biosensing. *ACS Biomaterials Science & Engineering*, 5(9), 4183–4205. <https://doi.org/10.1021/acsbomaterials.9b00853>

15. Guillaume, O., Pérez-Tanoira, R., Fortelny, R., Redl, H., Moriarty, T. F., Richards, R. G., Eglin, D., & Petter-Puchner, A. (2018). Infections associated with mesh repairs of abdominal wall hernias: Are antimicrobial biomaterials the longed-for solution? *Biomaterials*, *167*(1), 15–31. <https://doi.org/10.1016/j.biomaterials.2018.03.017>
16. Lakhundi, S., & Zhang, K. (2018). Methicillin-resistant *Staphylococcus aureus*: Molecular characterization, evolution, and epidemiology. *Clinical Microbiology Reviews*, *31*(4), 1–103. <https://doi.org/10.1128/CMR.00020-18>
17. Pérez-Köhler, B., García-Moreno, F., Brune, T., Pascual, G., & Bellón, J. M. (2015). Preclinical bioassay of a polypropylene mesh for hernia repair pretreated with antibacterial solutions of chlorhexidine and allicin: An in vivo study. *PLoS ONE*, *10*(11), 1–8. <https://doi.org/10.1371/journal.pone.0142768>
18. Çakmak, A., Çirpanli, Y., Bilensoy, E., Yorganci, K., Çaliş, S., Saribaş, Z., & Kaynaroğlu, V. (2009). Antibacterial activity of triclosan chitosan coated graft on hernia graft infection model. *International Journal of Pharmaceutics*, *381*(2), 214–219. <https://doi.org/10.1016/j.ijpharm.2009.05.059>
19. Wolf, M. T., Carruthers, C. A., Dearth, C. L., Crapo, P. M., Huber, A., Burnsed, O. A., Londono, R., Johnson, S. A., Daly, K. A., Stahl, E. C., Freund, J. M., Medberry, C. J., Carey, L. E., Nieponice, A., Amoroso, N. J., & Badylak, S. F. (2014). Polypropylene surgical mesh coated with extracellular matrix mitigates the host foreign body response. *Journal of Biomedical Materials Research Part A*, *102*(1), 234–246. <https://doi.org/10.1002/jbm.a.34671>
20. Chindera, K., Mahato, M., Kumar Sharma, A., Horsley, H., Kloc-Muniak, K., Kamaruzzaman, N. F., Kumar, S., McFarlane, A., Stach, J., Bentin, T. & Good, L. (2016). The antimicrobial polymer PHMB enters cells and selectively condenses bacterial chromosomes. *Scientific Reports*, *6*(1), 1–13. <https://doi.org/10.1038/srep23121>
21. Rita, C., Nikhil, V., & Surapaneni, S. K. (2017). Determination of minimum inhibitory concentration (MIC) of a polyhexamethylene biguanide (PHMB) solution: A potential root canal irrigant. *Annual Research and Review in Biology*, *15*(2), 1–7. <https://doi.org/10.9734/ARRB/2017/34141>
22. Lawung, R., Cherdtrakulkiat, R., Nabu, S., Prachayasittikul, S., Isarankura-Na-Ayudhya, C., & Prachayasittikul, V. (2018). Repositioning of 8-hydroxyquinoline derivatives as a new promising candidate for combating multidrug resistant *Neisseria gonorrhoeae*. *Excli Journal*, *17*(3), 840–846. <https://doi.org/10.17179/excli2018-1602>
23. Committee on Consumer Safety, E. C. (2017). Final opinion on polyaminopropyl biguanide (PHMB) - Submission III. *European Scientific Committee on Consumer Safety (SCCS)*, *1581*(16), 1–90. <https://doi.org/10.2875/144004>
24. Regulation (EU) No 528/2012 concerning the making available on the market and use of biocidal products. (2015). *The European Parliament And Of The Council*, *13*(1), 181–303. Retrieved from [http://dissemination.echa.europa.eu/Biocides/ActiveSubstances/1347-02/1347-02\\_Assessment\\_Report.pdf](http://dissemination.echa.europa.eu/Biocides/ActiveSubstances/1347-02/1347-02_Assessment_Report.pdf)
25. Martino, F., Perestrelo, A. R., Vinarský, V., Pagliari, S., & Forte, G. (2018). Cellular mechanotransduction: From tension to function. *Frontiers in Physiology*, *9*(1), 1–21. <https://doi.org/10.3389/fphys.2018.00824>
26. Nasrollahi, S., Walter, C., Loza, A. J., Schimizzi, G. V., Longmore, G. D., & Pathak, A. (2017). Past matrix stiffness primes epithelial cells and regulates their future collective migration through a mechanical memory. *Biomaterials*, *146*(1), 146–155. <https://doi.org/10.1016/j.biomaterials.2017.09.012>
27. Engler, A. J., Sen, S., Sweeney, H. L., & Discher, D. E. (2006). Matrix elasticity directs stem cell lineage specification. *Cell*, *126*(4), 677–689. <https://doi.org/10.1016/j.cell.2006.06.044>
28. Chen, H., Lui, Y. S., Tan, Z. W., Lee, J. Y. H., Tan, N. S., & Tan, L. P. (2019). Migration and phenotype control of human dermal fibroblasts by electrospun fibrous substrates. *Advanced Healthcare Materials*, *8*(9), 1–10. <https://doi.org/10.1002/adhm.201801378>

29. Hsia, L. T., Ashley, N., Ouaret, D., Wang, L. M., Wilding, J., & Bodmer, W. F. (2016). Myofibroblasts are distinguished from activated skin fibroblasts by the expression of AOC3 and other associated markers. *Proceedings of the National Academy of Sciences of the United States of America*, 113(15), E2162–E2171. <https://doi.org/10.1073/pnas.1603534113>
30. Pot, S. A., Liliensiek, S. J., Myrna, K. E., Bentley, E., Jester, J. V., Nealey, P. F., & Murphy, C. J. (2010). Nanoscale topography-induced modulation of fundamental cell behaviors of rabbit corneal keratocytes, fibroblasts, and myofibroblasts. *Investigative Ophthalmology and Visual Science*, 51(3), 1373–1381. <https://doi.org/10.1167/iovs.09-4074>
31. Garg, K., Pullen, N. A., Oskeritzian, C. A., Ryan, J. J., & Bowlin, G. L. (2013). Macrophage functional polarization (M1/M2) in response to varying fiber and pore dimensions of electrospun scaffolds. *Biomaterials*, 34(18), 4439–4451. <https://doi.org/10.1016/j.biomaterials.2013.02.065>
32. Wang, Y., Yao, D., Li, L., Li, L., Qian, Z., He, W., Ding, R., Liu, H., & Fan, Y. (2020). Effect of electrospun silk fibroin-silk sericin films on macrophage polarization and vascularization. *ACS Biomaterials Science and Engineering*, 6(6), 3502–3512. <https://doi.org/10.1021/acsbomaterials.0c00175>
33. Jones, E. M., Cochrane, C. A., & Percival, S. L. (2015). The effect of pH on the extracellular matrix and biofilms. *Advances in Wound Care*, 4(7), 431–439. <https://doi.org/10.1089/wound.2014.0538>
34. Ono, S., Imai, R., Ida, Y., Shibata, D., Komiya, T., & Matsumura, H. (2015). Increased wound pH as an indicator of local wound infection in second degree burns. *Burns*, 41(4), 820–824. <https://doi.org/10.1016/j.burns.2014.10.023>
35. Te Lindert, B. H. W., & Van Someren, E. J. W. (2018). Skin temperature, sleep, and vigilance. In Michael J. Aminoff, François Boller, & Dick F. Swaab (Eds.), *Handbook of Clinical Neurology* (Vol. 156, pp. 353–365). California, USA: Elsevier. <https://doi.org/10.1016/B978-0-444-63912-7.00021-7>
36. Gao, W., Sun, L., Fu, X., Lin, Z., Xie, W., Zhang, W., Zhao, F., & Chen, X. (2018). Enhanced diabetic wound healing by electrospun core-sheath fibers loaded with dimethylxalylglycine. *Journal of Materials Chemistry B*, 6(2), 277–288. <https://doi.org/10.1039/c7tb02342a>
37. Grada, A., Otero-Vinas, M., Prieto-Castrillo, F., Obagi, Z., & Falanga, V. (2017). Research techniques made simple: analysis of collective cell migration using the wound healing assay. *Journal of Investigative Dermatology*, 137(2), e11–e16. <https://doi.org/10.1016/j.jid.2016.11.020>
38. Vong, M., Speirs, E., Klomkliang, C., Akinwumi, I., Nuansing, W., & Radacsi, N. (2018). Controlled three-dimensional polystyrene micro- and nano-structures fabricated by three-dimensional electrospinning. *RSC Advances*, 8(28), 15501–15512. <https://doi.org/10.1039/c7ra13278f>
39. Duan, G., Jiang, S., Jérôme, V., Wendorff, J. H., Fathi, A., Uhm, J., Altstädt, V., Herling, M., Breu, J., Freitag, R., Agarwal, S., & Greiner, A. (2015). Ultralight, soft polymer sponges by self-assembly of short electrospun fibers in colloidal dispersions. *Advanced Functional Materials*, 25(19), 2850–2856. <https://doi.org/10.1002/adfm.201500001>
40. Joshi, M. K., Pant, H. R., Tiwari, A. P., Kim, H. J., Park, C. H., & Kim, C. S. (2015). Multi-layered macroporous three-dimensional nanofibrous scaffold via a novel gas foaming technique. *Chemical Engineering Journal*, 275(1), 79–88. <https://doi.org/10.1016/j.cej.2015.03.121>
41. Jun, I., Han, H.S., Edwards, J., & Jeon, H. (2018). Electrospun fibrous scaffolds for tissue engineering: Viewpoints on architecture and fabrication. *International Journal of Molecular Sciences*, 19(3), 1–14. <https://doi.org/10.3390/ijms19030745>
42. Wu, J., & Hong, Y. (2016). Enhancing cell infiltration of electrospun fibrous scaffolds in tissue regeneration. *Bioactive Materials*, 1(1), 56–64. <https://doi.org/10.1016/j.bioactmat.2016.07.001>



---

# Appendix A

## Supplement

---

### Appendix A: Chapter 3

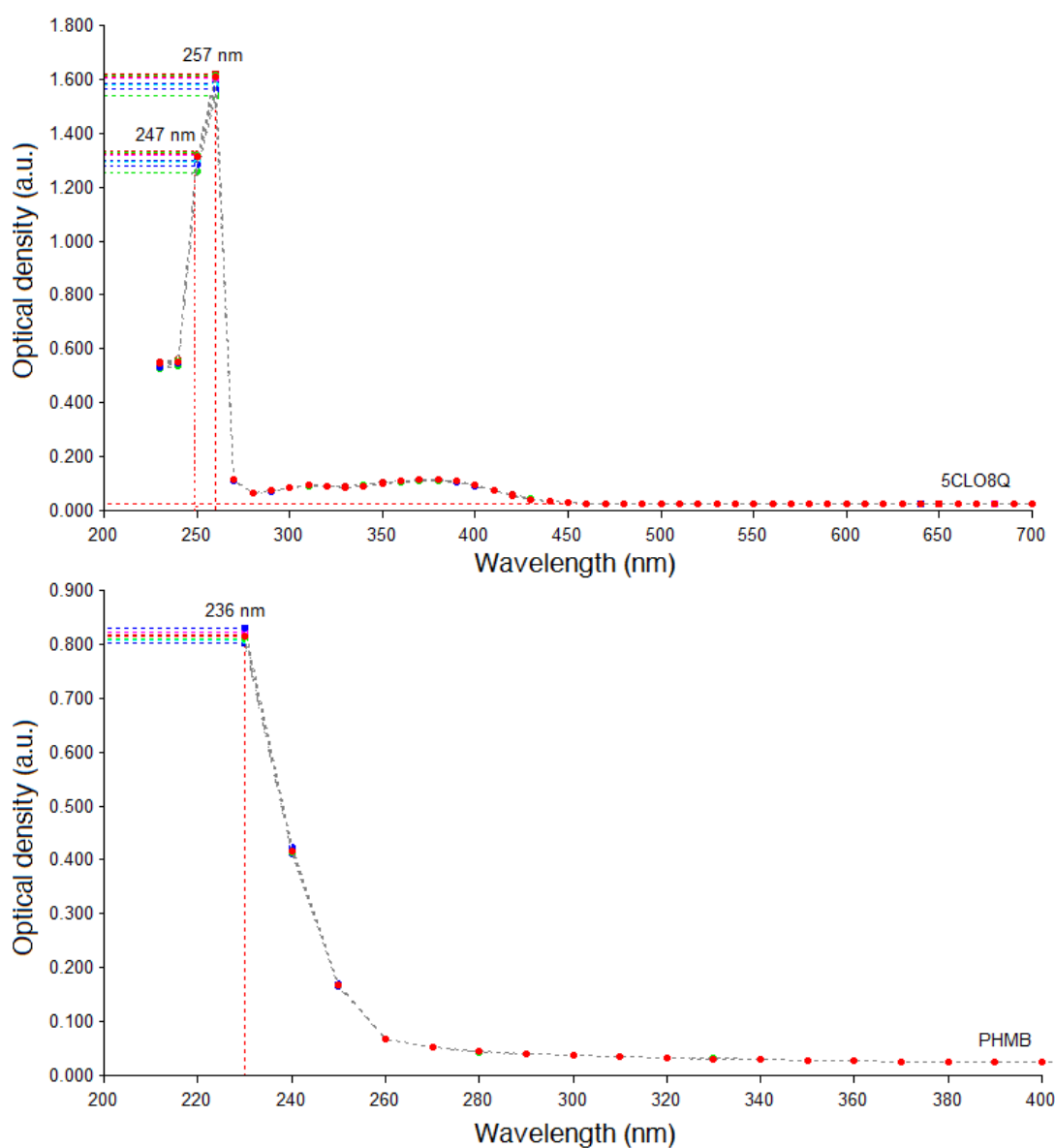


**Figure A-1** Absorbance spectra of 5-chloro-8-quinolinol (5CLO8Q) (top) and poly(hexanide) (PHMB) (bottom).



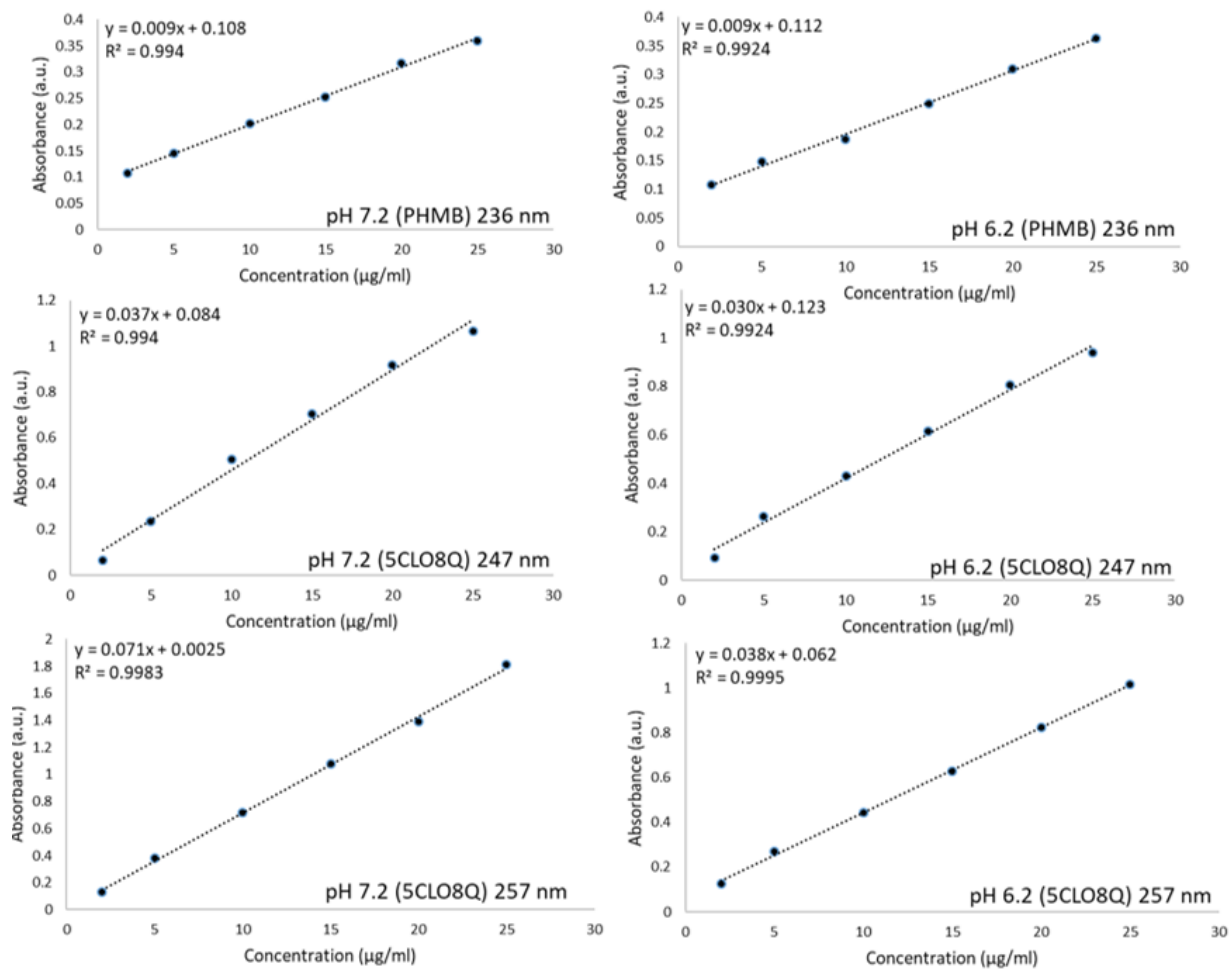


**Figure A-2** Standard curves of PHMB (236 nm) and 5CLO8Q (247 and 257 nm) at pH 7.2 and 6.2.

## Appendix A: Chapter 4

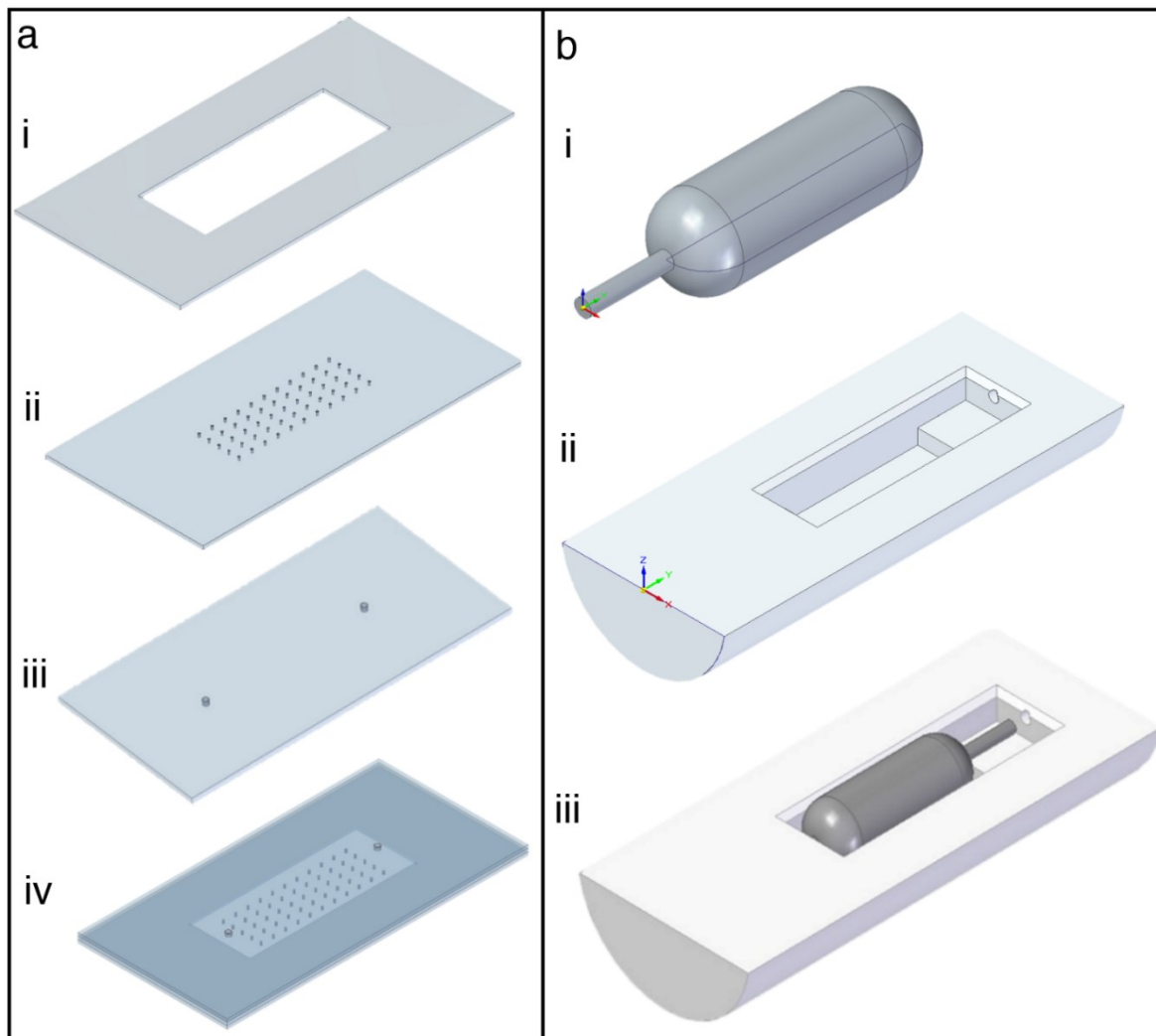


**Figure A-3 CAD designs of the nozzle-free electrospinning device. (a)** Multi-channel gas lid; **(i)** mid glass plane, **(ii)** top glass plane with two 8 mm holes **(iii)** bottom glass plane with 55 holes of 3 mm diameter and **(iv)** complete lid assembly. **(b)** Spinneret assembly; **(i)** stainless steel roller electrode, **(ii)** Teflon® bath and **(iii)** complete spinneret assembly.

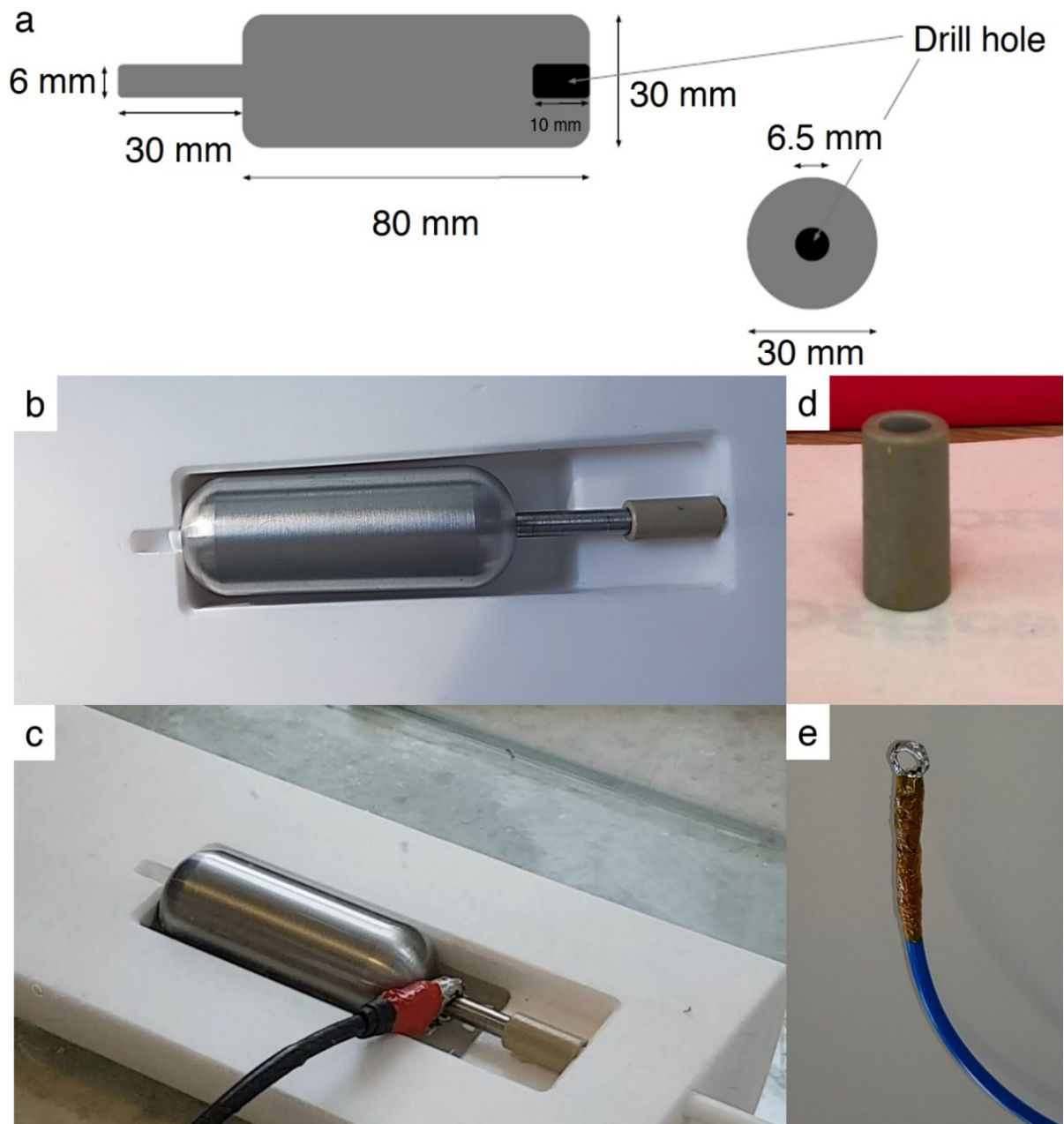


**Figure A-4** The nozzle-free electrospinning setup spinneret assembly. (a) 2D design of the stainless-steel cylinder. Photographs of (b) the cylinder within the Teflon® bath; (c) after inserting the high-voltage electrode; (d) PEEK connector; and (e) the high-voltage cable soldered to form a ring.

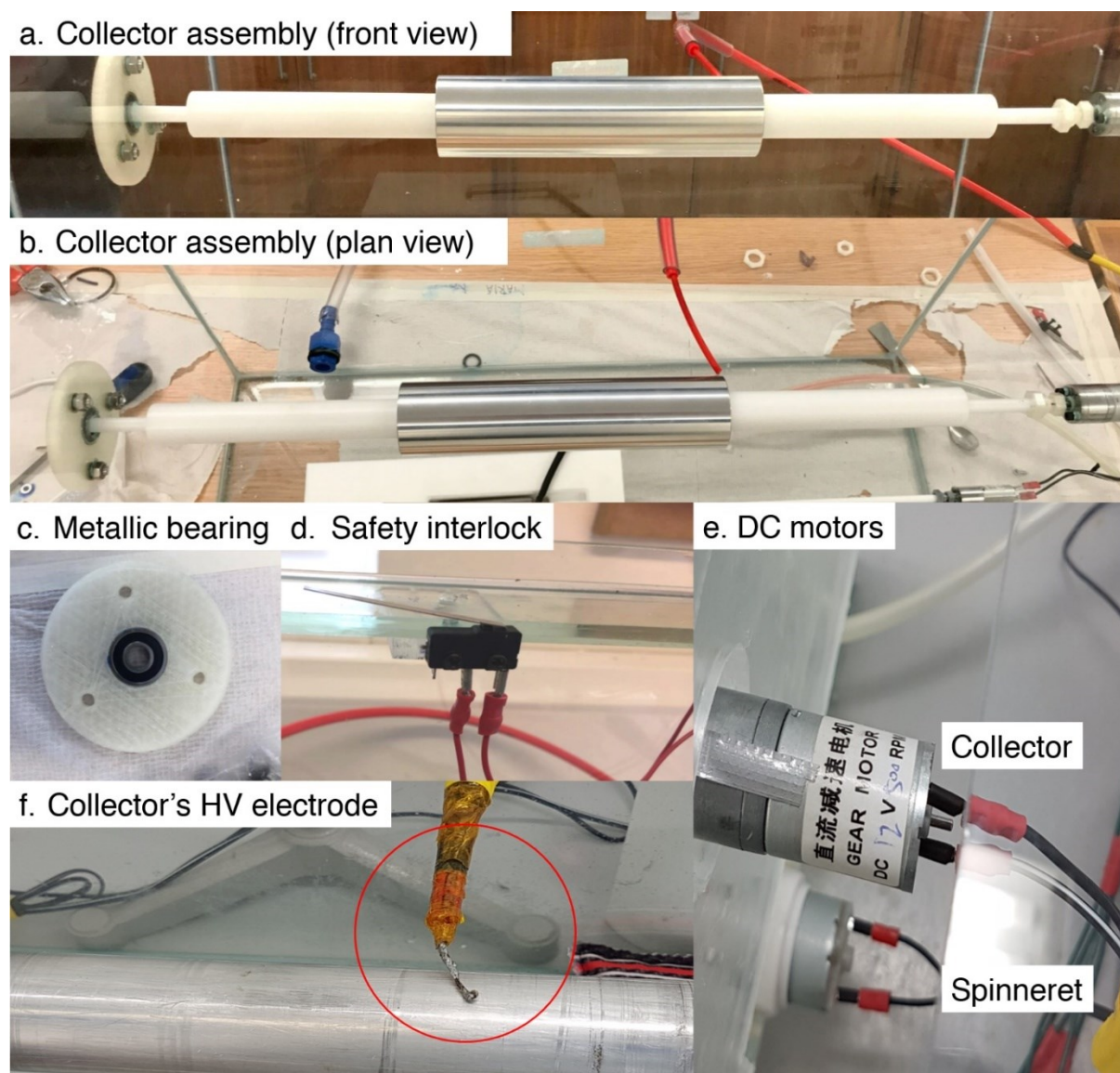


**Figure A-5 The nozzle-free electrospinning setup collector assembly.** Photographs of the collector assembly **(a)** front view and **(b)** plan view. Photographs of the **(c)** 3D printed metallic bearing; **(d)** device's safety interlock (RS Components, UK); **(e)** 12 V DC motor fitted to the collector (15 N·cm<sup>-1</sup>, 6 rpm, RS Components, UK) powered by an adjustable power supply (DPPS-16-30, Voltcraft, Germany), and a 12 V DC motor fitted to the spinneret (6 N·cm<sup>-1</sup>, 4500 rpm, Bosch, Germany) rotating at a constant speed of 10 rpm; and **(f)** high-voltage collector's electrode.

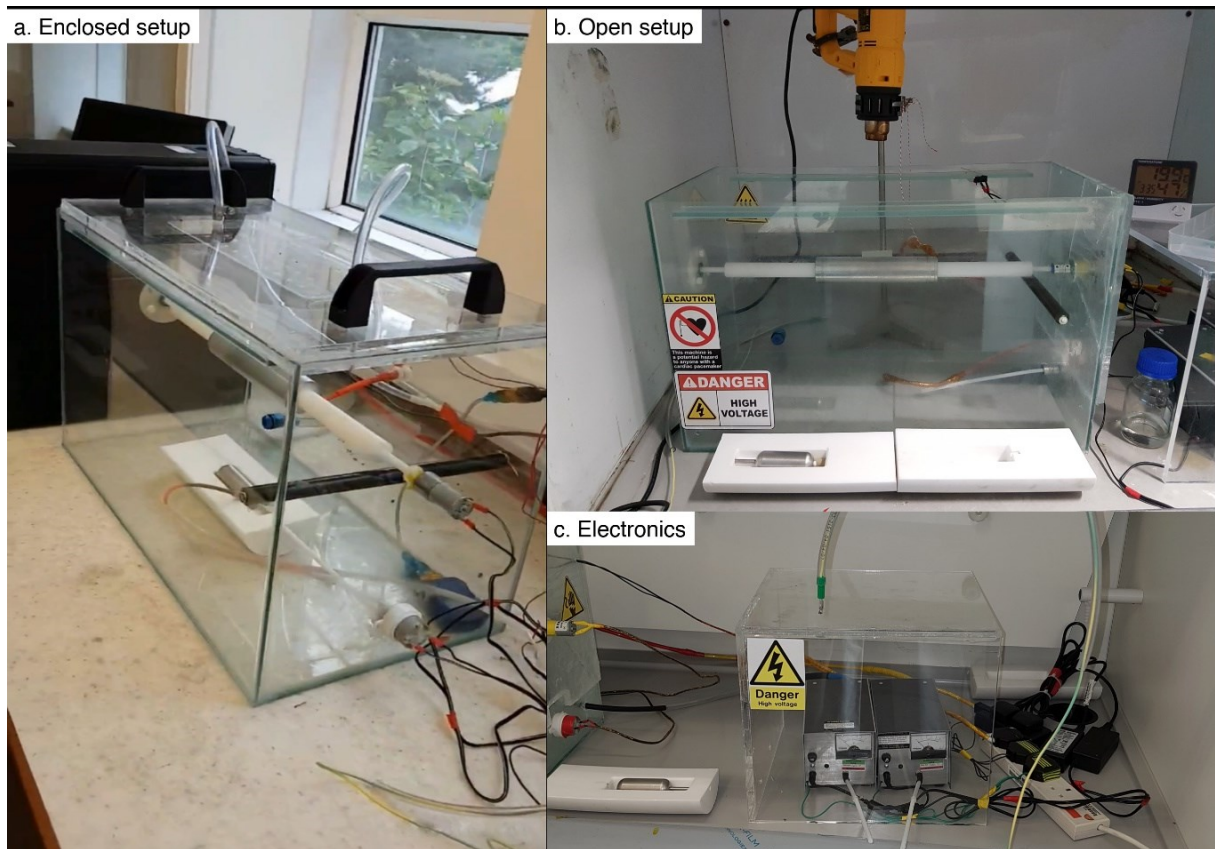


**Figure A-6** Photographs of the nozzle-free electrospinning device. **(a)** Gas flow is provided via the lid assembly at the enclosed setup, whereas **(b)** hot airflow is provided via a heat gun at the open setup. **(c)** The high voltage DC power supplies (HV350REG(-) and HV350REG(+), Information Unlimited, Amherst, USA) used to charge the spinneret and collector.

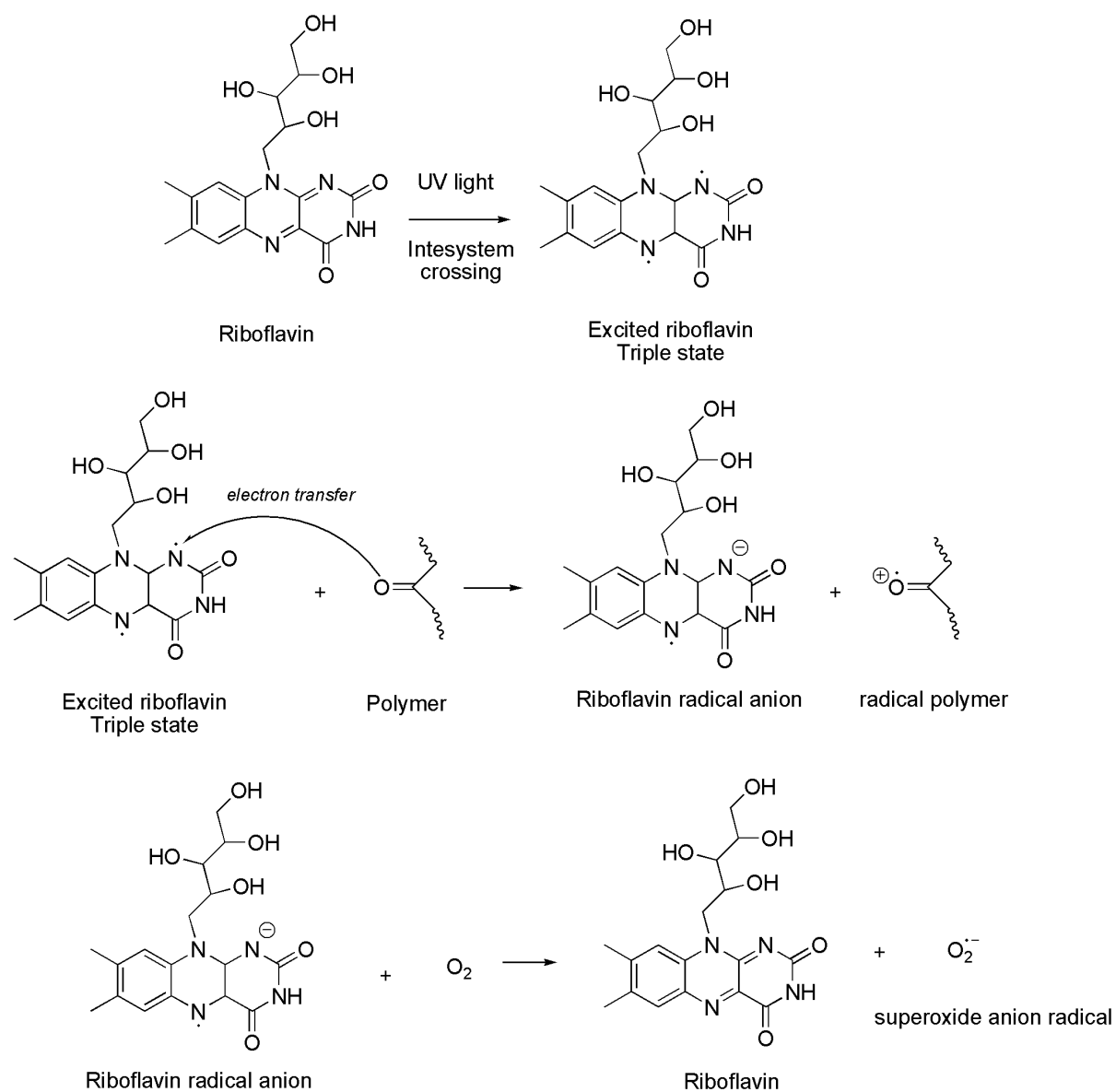


**Figure A-7** Type I reactions induced by excited riboflavin. UV crosslinking of PVP/PGS mediated by riboflavin.

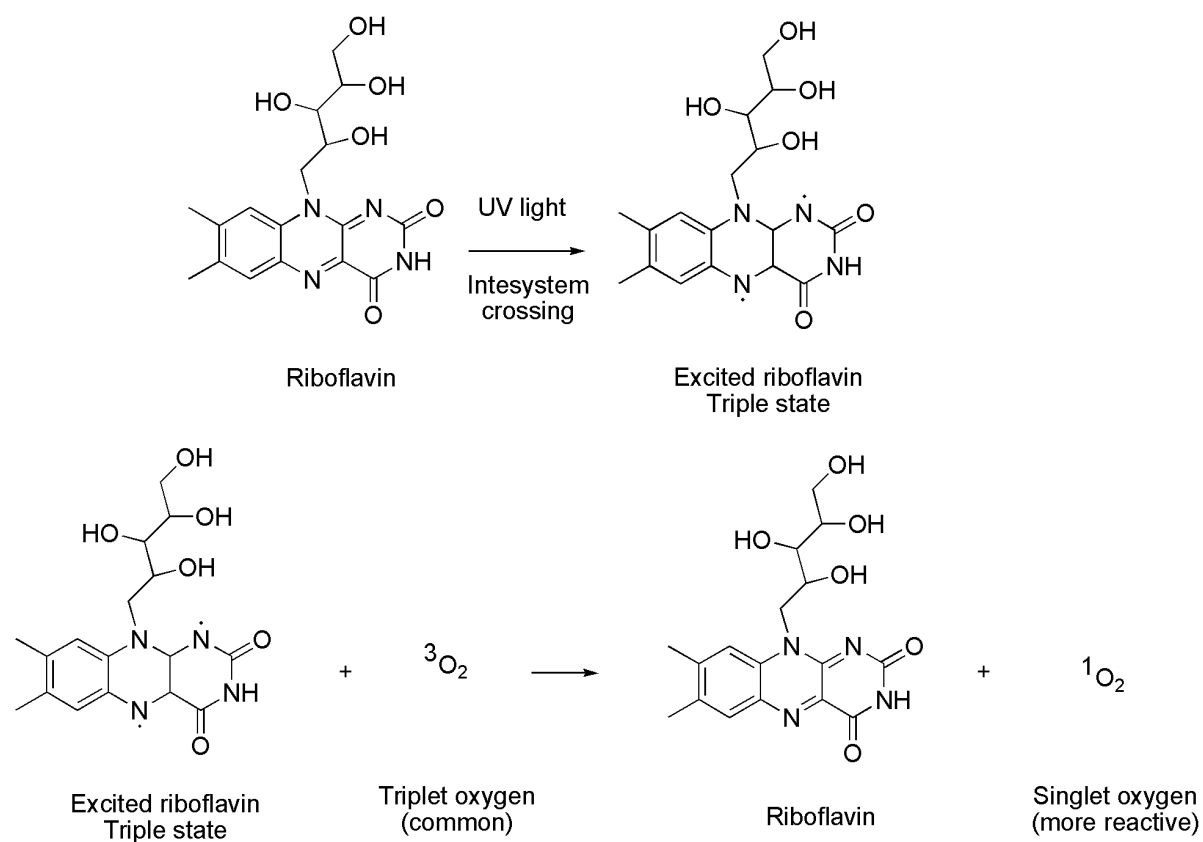


**Figure A-8** Type II reactions induced by excited riboflavin. UV crosslinking of PVP/PGS mediated by riboflavin.

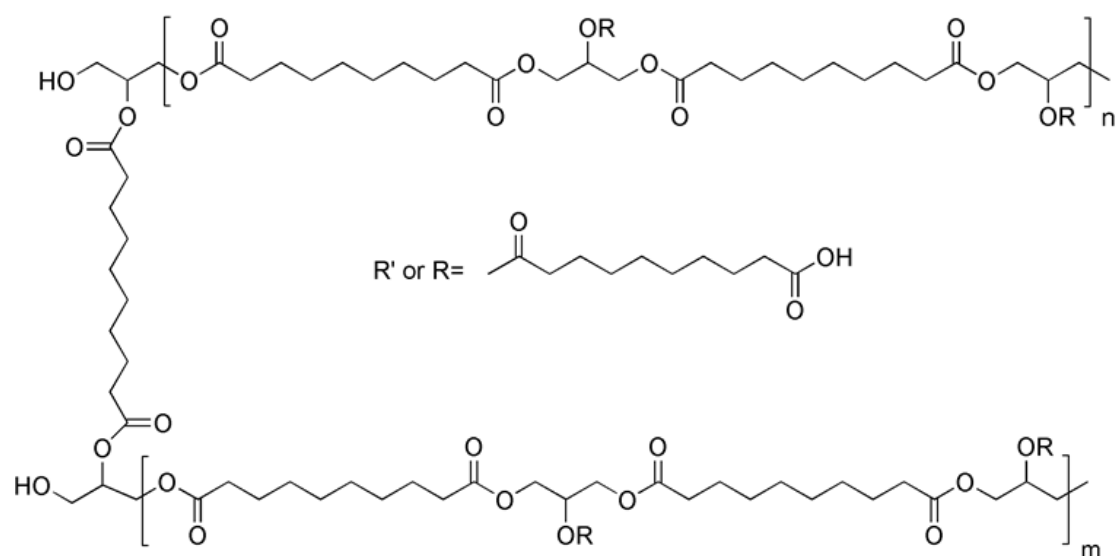


**Figure A-9** Riboflavin-induced photocrosslinking of poly(glycerol sebacate)(PGS).

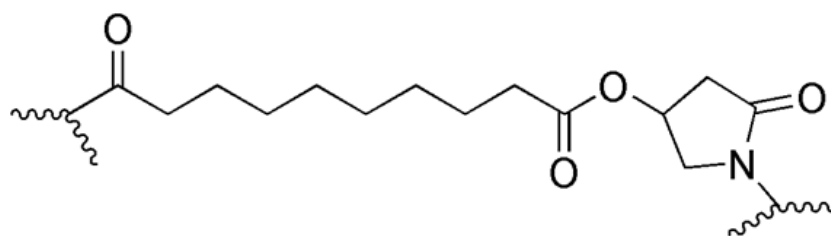


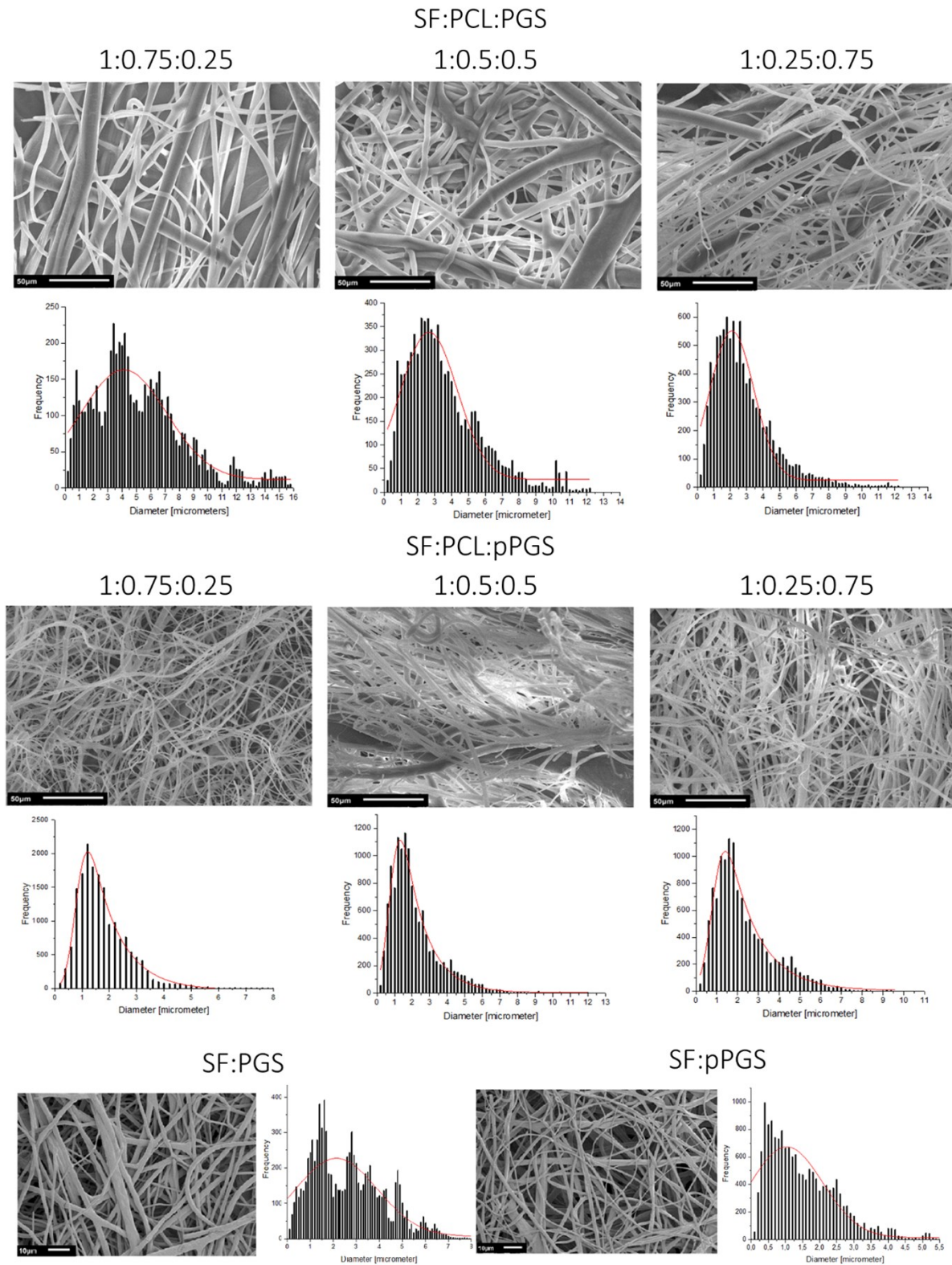
**Figure A-10** Riboflavin-induced photocrosslinking of polyvinylpyrrolidone (PVP).



## Appendix A: Chapter 5



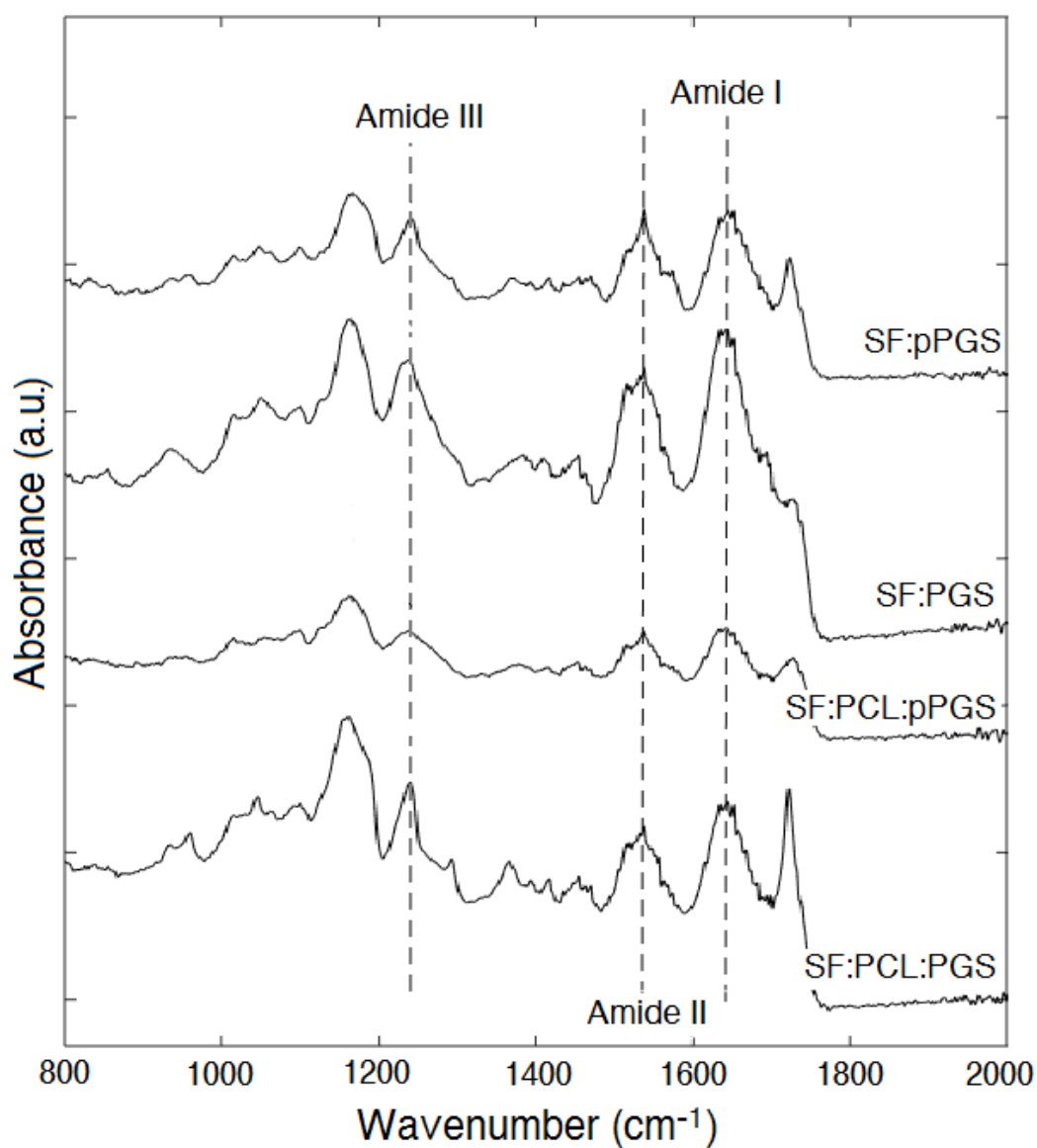
**Figure A-11 Silk fibroin extraction with photographs.** (a) *Bombyx mori* silkworm cocoons after dissecting the worm, (b) cut into small pieces, (c) weighed and (d) 0 min of degumming the cocoons in 0.01 M  $\text{Na}_2\text{CO}_3$ , at 100 °C for 30 min, (e) after 30 min, (f) rinsing the degummed silk in deionised water, 3 times for 20 min each, (g) left to dry at room temperature, overnight. (h) Then, 9.3 M LiBr solution is added to the dried silk fibre mesh, at a ratio of 1:4 SF:LiBr solution (w/v), to dissolve the fibroin, and placed in an oven, for 4 h at 50 °C. (i) SF is precipitated by gradually adding the SF-LiBr solution, dropwise, to pure ethanol in a ratio of 1:30 SF-LiBr:EtOH (v/v), under agitation conditions for 1 h. (j-k) LiBr residues were removed by filtration and washed with ultrapure water. (l) The purified SF is oven-dried, at 50 °C. (m-n) The dried SF is then milled into a powder, using a mortar, and (o) dissolved in formic acid/ $\text{CaCl}_2$ , to obtain a final SF concentration of 12% (w/v).



**Figure A-12** SEM images and fibre diameters distribution graphs of the trinary; SF:PCL:PGS and SF:PCL:pPGS, and binary; SF:PGS and SF:pPGS, electrospun mats.

**Table A-1** Electrospinning and solution parameters.

Process parameters	Measurements
Solution conductivity ( $\text{mS}\cdot\text{cm}^{-1}$ )	0.2 - 0.4
pH	$6.2 \pm 1.5$
Relative Humidity (%)	30-60
Temperature ( $^{\circ}\text{C}$ )	18-28
Distance between electrodes (cm)	15
Atmosphere	$\text{N}_2$
Potential difference (kV)	60

**Figure A-13** ATR-FTIR spectra of the silk fibroin specific region of the binary and ternary electrospun mats.

**Table A-2** Degradation analysis of the PCL-backbone SF:PGS and pPGS ternary scaffolds of the various blend ratios over time.

Time	SF:PCL:PGS			SF:PCL:pPGS		
	Weight Loss (%)			Weight Loss (%)		
	1:0.75:0.25	1:0.5:0.5	1:0.25:0.75	1:0.75:0.25	1:0.5:0.5	1:0.25:0.75
30 m	3.0	19.8	26.1	19.5	24.4	34.3
1 h	7.0	22.8	28.9	16.0	26.2	33.6
4 h	7.8	25.0	29.2	16.3	24.3	32.1
24 h	9.9	22.0	31.9	17.1	25.2	34.3
3 d	9.5	24.4	33.4	14.1	19.6	26.1
7 d	15.0	22.9	33.6	12.1	25.6	30.8
21 d	26.9	18.0	33.1	11.2	16.9	28.7
30 d	25.2	6.2	42.6	3.0	19.2	18.5



**Figure A-14** Photograph of the degradation study of the PCL-backbone SF:PGS and pPGS ternary scaffolds of various blend ratios over time.

## Appendix A: Chapter 6

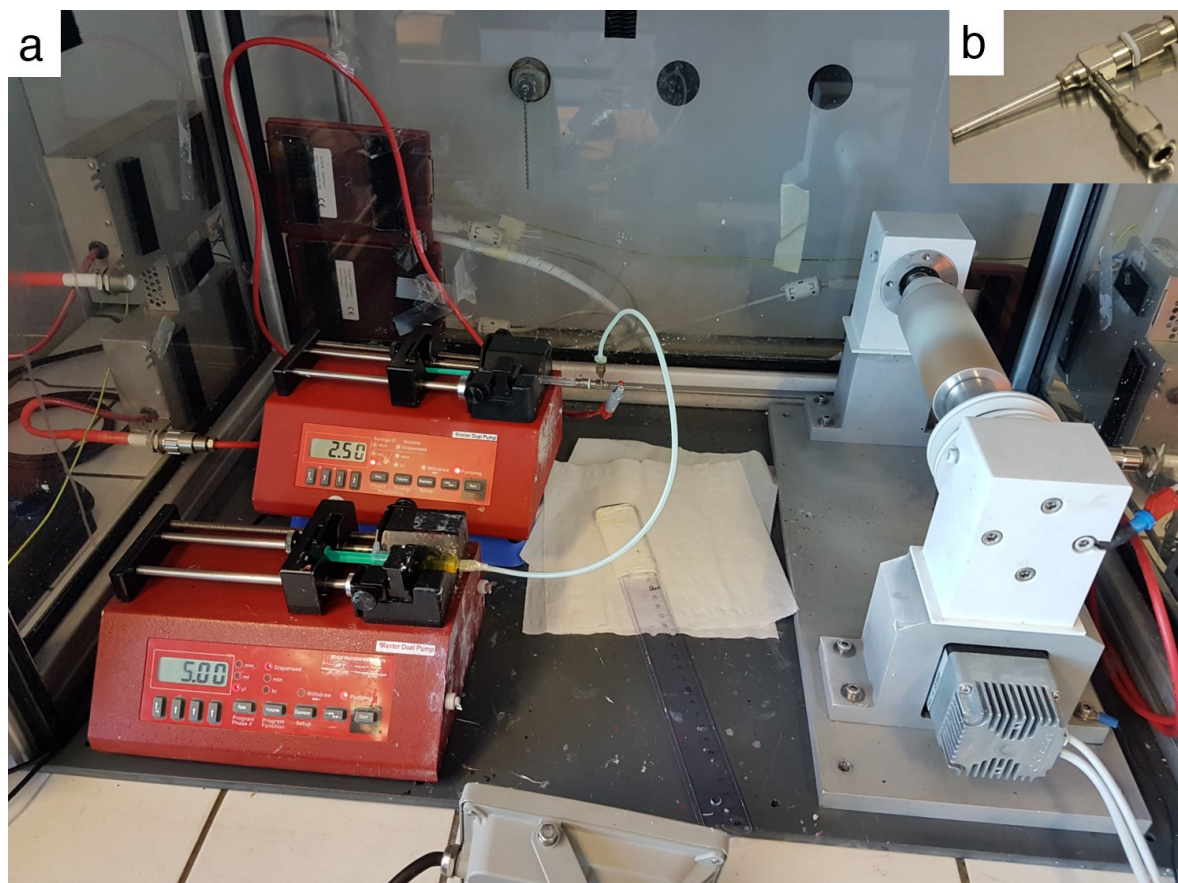


**Figure A-15 Co-axial electrospinning.** Photographs of **(a)** the co-axial electrospinning setup used to produce core/shell PA6-PHMB/CS-5CLO8Q nanofibrous membranes; and **(b)** the co-axial spinneret consisting of a 0.9-mm diameter nozzle (outer) for the shell solution and 0.57-mm diameter nozzle (inner) for the core solution. The core to shell feed rate was 2.5 to 5.0  $\mu\text{L}\cdot\text{min}^{-1}$ , with the potential difference set to 22 kV (+18 kV to charge the spinneret and -4 kV to charge the collector).

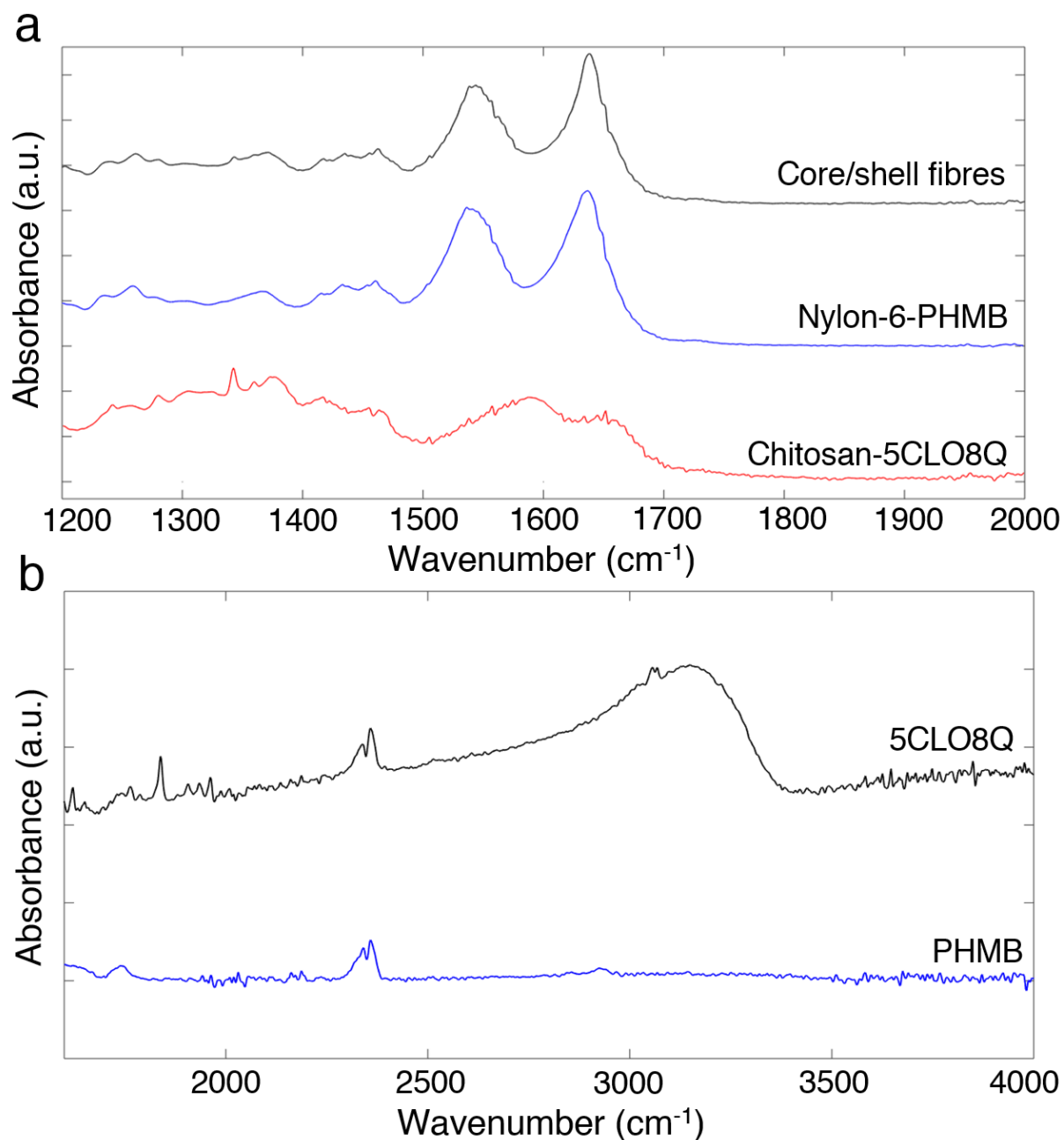


**Figure A-16** FTIR-ATR analysis of **(a)** region-specific spectra (1200-2000 cm<sup>-1</sup>) of the drug-containing CS-5CLO8Q, PA6-PHMB, and core/shell NFs, and **(b)** the pristine antimicrobial substances; 5CLO8Q and PHMB powders.

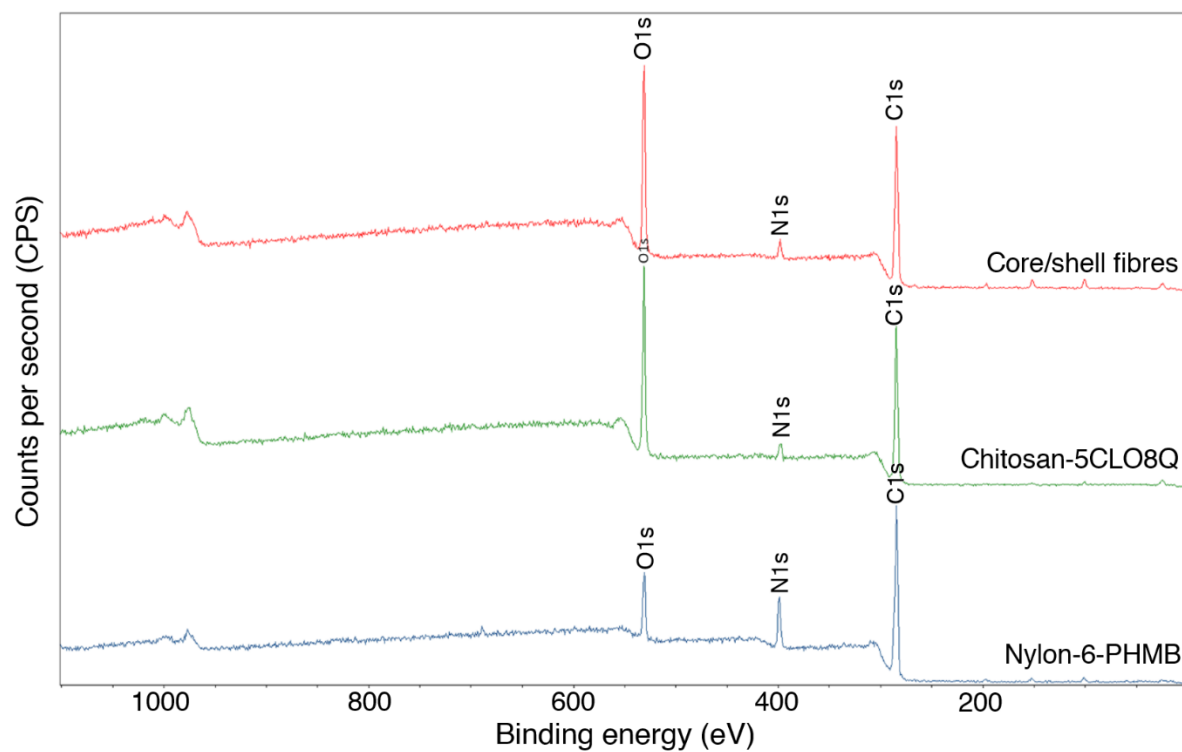


**Figure A-17** XPS survey of the PA6-PHMB, CS-5CLO8Q and core/shell PA6-PHMB/CS-5CLO8Q nanofibrous mats.

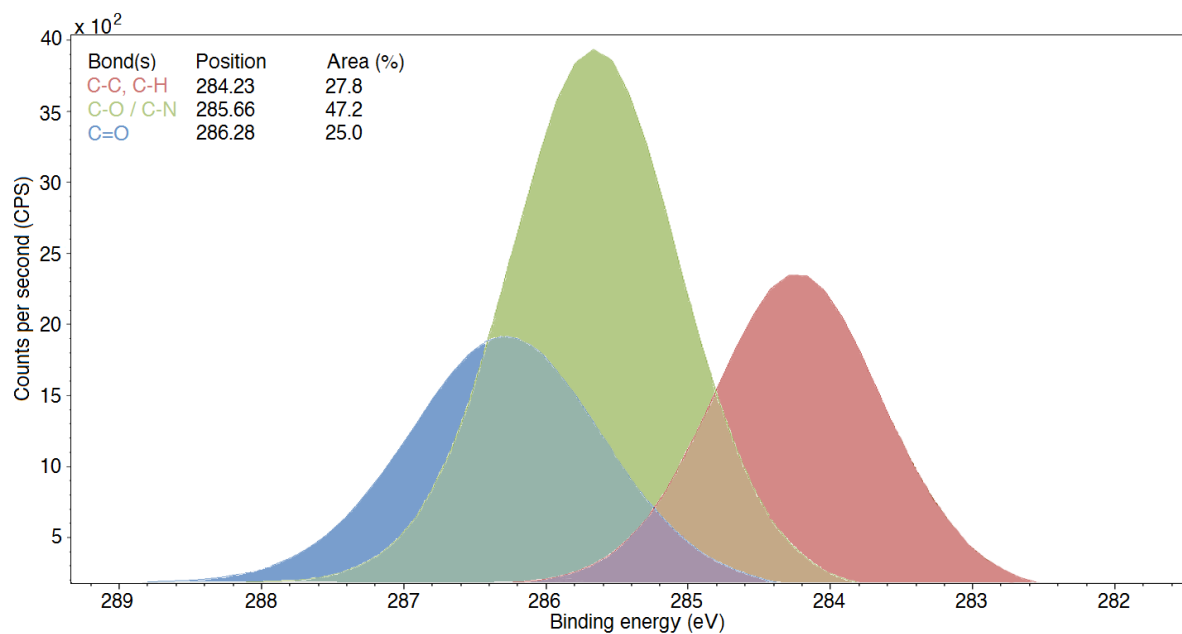


**Figure A-18** C1s XPS spectrum of the core/shell PA6-PHMB/CS-5CLO8Q nanofibrous mats.

---

# Appendix B

## Copyright Permissions, Publications and Conferences

---

### Copyright Permission for Reuse in a Thesis

**Publisher: Elsevier**

**For the research articles used on Chapters 4 and 5**

- The statement below was obtained from:  
<https://www.elsevier.com/solutions/sciencedirect/support/rights-and-permissions>
- The permission was obtained from:  
<https://www.copyright.com/publishers/rightslink-permissions>

#### ***Can I use material from my Elsevier journal article within my thesis/dissertation?***

*"Yes. Authors can include their articles in full or in part in a thesis or dissertation for non-commercial purposes."*

*As an Elsevier journal author, you have the right to include the article in a thesis or dissertation (provided that this is not to be published commercially) whether in full or in part, subject to proper acknowledgement; see the Copyright page for more information. No written permission from Elsevier is necessary.*

*This right extends to the posting of your thesis to your university's repository provided that if you include the published journal article, it is embedded in your thesis and not separately downloadable."*



## Copyright Permission for Reuse in a Thesis

**Publisher: Elsevier**

**For the research articles used in Chapters 4 and 5**



RightsLink®

[Home](#) | 
 [?](#) Help | 
 [Email Support](#) | 
 [Sign in](#) | 
 [Create Account](#)



### Nozzle-free electrospinning of Polyvinylpyrrolidone/Poly(glycerol sebacate) fibrous scaffolds for skin tissue engineering applications

Author: Antonios Keirouz, Giuseppe Fortunato, Mei Zhang, Anthony Callanan, Norbert Radacs

Publication: Medical Engineering & Physics

Publisher: Elsevier

Date: September 2019

© 2019 IPEM. Published by Elsevier Ltd. All rights reserved.

Please note that, as the author of this Elsevier article, you retain the right to include it in a thesis or dissertation, provided it is not published commercially. Permission is not required, but please ensure that you reference the journal as the original source. For more information on this and on your other retained rights, please visit: <https://www.elsevier.com/about/our-business/policies/copyright#Author-rights>

[BACK](#)

[CLOSE WINDOW](#)



RightsLink®

[Home](#) | 
 [?](#) Help | 
 [Email Support](#) | 
 [Sign in](#) | 
 [Create Account](#)



### High-throughput production of silk fibroin-based electrospun fibers as biomaterial for skin tissue engineering applications

Author: Antonios Keirouz, Mariia Zakharova, Jaehoon Kwon, Colin Robert, Vasileios Koutsos, Anthony Callanan, Xianfeng Chen, Giuseppe Fortunato, Norbert Radacs

Publication: Materials Science and Engineering: C

Publisher: Springer Nature

Date: July 2020

Copyright © 2020, Springer Nature

Please note that, as the author of this Elsevier article, you retain the right to include it in a thesis or dissertation, provided it is not published commercially. Permission is not required, but please ensure that you reference the journal as the original source. For more information on this and on your other retained rights, please visit: <https://www.elsevier.com/about/our-business/policies/copyright#Author-rights>

[BACK](#)

[CLOSE WINDOW](#)

## Copyright Permission for Reuse in a Thesis

Publisher: Springer-Nature

For the research article used in Chapter 6

- The statement below was obtained from:

<https://www.springer.com/gp/rights-permissions/obtaining-permissions/882>

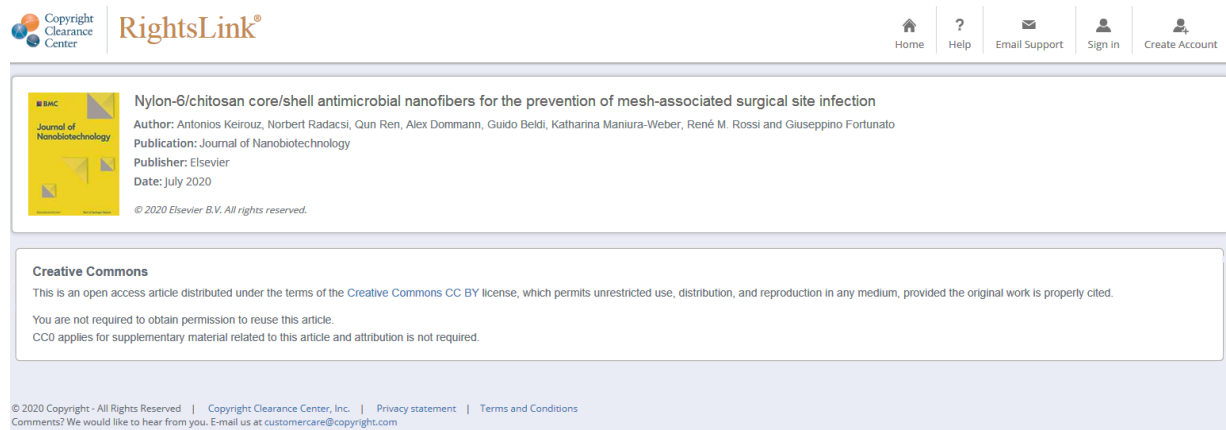
- The permission was obtained from:

<https://www.copyright.com/publishers/rightslink-permissions>

### ***Author Reuse Policy***

*"Authors have the right to reuse their article's version of record, in whole or in part, in their own thesis. Additionally, they may reproduce and make available their thesis, including Springer Nature content, as required by their awarding academic institution.*

*Authors must properly cite the published article in their thesis according to current citation standards."*



The screenshot shows the RightsLink interface. At the top left is the Copyright Clearance Center logo and the RightsLink® logo. On the top right are navigation links: Home, Help, Email Support, Sign In, and Create Account. The main content area displays the following information:

- Journal of Nanobiotechnology** (with BMC logo)
- Title:** Nylon-6/chitosan core/shell antimicrobial nanofibers for the prevention of mesh-associated surgical site infection
- Author:** Antonios Keirouz, Norbert Radacs, Qun Ren, Alex Dommann, Guido Beldi, Katharina Maniura-Weber, René M. Rossi and Giuseppe Fortunato
- Publication:** Journal of Nanobiotechnology
- Publisher:** Elsevier
- Date:** July 2020
- Copyright:** © 2020 Elsevier B.V. All rights reserved.

Below this information is a **Creative Commons** section stating: "This is an open access article distributed under the terms of the Creative Commons CC BY license, which permits unrestricted use, distribution, and reproduction in any medium, provided the original work is properly cited. You are not required to obtain permission to reuse this article. CC0 applies for supplementary material related to this article and attribution is not required."

At the bottom of the page, there is a footer with the following text: "© 2020 Copyright - All Rights Reserved | Copyright Clearance Center, Inc. | Privacy statement | Terms and Conditions. Comments? We would like to hear from you. E-mail us at [customer-care@copyright.com](mailto:customer-care@copyright.com)"

## Copyright Permission for Reuse in a Thesis

**Publisher: John Wiley and Sons**

**For parts of the skin literature review used in Chapter 2**

- The statement below was obtained from:

<https://olabout.wiley.com/WileyCDA/Section/id-826716.html>

- The permission was obtained from:

<https://www.copyright.com/publishers/rightslink-permissions>

### Article Sharing Policy

*"You may also share any version of your article with individual colleagues and students if you are asked for a copy, as part of teaching and training at your institution (excluding open online sharing), and as part of a grant application, submission of thesis, or doctorate."*



2D and 3D electrospinning technologies for the fabrication of nanofibrous scaffolds for skin tissue engineering: A review

Publication: Wiley Interdisciplinary Reviews - Nanomedicine and Nanobiotechnology

Publisher: John Wiley and Sons

Date: Mar 12, 2020

© 2020 Wiley Periodicals, Inc.

Order Completed

Thank you for your order.

This Agreement between Mr. Antonios Keirouz ("You") and John Wiley and Sons ("John Wiley and Sons") consists of your license details and the terms and conditions provided by John Wiley and Sons and Copyright Clearance Center.

Your confirmation email will contain your order number for future reference.

License Number 4926530109038

License date Oct 12, 2020

#### 📄 Licensed Content

Licensed Content Publisher	John Wiley and Sons
Licensed Content Publication	Wiley Interdisciplinary Reviews - Nanomedicine and Nanobiotechnology
Licensed Content Title	2D and 3D electrospinning technologies for the fabrication of nanofibrous scaffolds for skin tissue engineering: A review
Licensed Content Author	Antonios Keirouz, et al
Licensed Content Date	Mar 12, 2020
Licensed Content Volume	12
Licensed Content Issue	4
Licensed Content Pages	32

#### 📄 About Your Work

Title	Electrospinning for skin tissue engineering and drug-eluting antimicrobial biomaterials
Institution name	The University of Edinburgh
Expected presentation date	Dec 2020

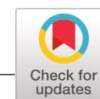
#### 📄 Order Details

Type of use	Dissertation/Thesis
Requestor type	Author of this Wiley article
Format	Print and electronic
Portion	Text extract
Number of Pages	5
Will you be translating?	No

#### 📍 Requestor Location

Requestor Location	Mr. Antonios Keirouz School of Engineering The University of Edinburgh Edinburgh, EH9 3JL United Kingdom Attn: Mr. Antonios Keirouz
--------------------	--

Received: 10 December 2019 | Revised: 13 February 2020 | Accepted: 14 February 2020  
DOI: 10.1002/wnan.1626



ADVANCED REVIEW



WILEY

## 2D and 3D electrospinning technologies for the fabrication of nanofibrous scaffolds for skin tissue engineering: A review

Antonios Keirouz<sup>1,2</sup> | Michael Chung<sup>1,2</sup> | Jaehoon Kwon<sup>1</sup> |  
Giuseppino Fortunato<sup>2</sup> | Norbert Radacsi<sup>1</sup>

<sup>1</sup>School of Engineering, Institute for Materials and Processes, The University of Edinburgh, Edinburgh, UK

<sup>2</sup>Empa, Swiss Federal Laboratories for Materials Science and Technology, Laboratory for Biomimetic Membranes and Textiles, St. Gallen, Switzerland

### Correspondence

Norbert Radacsi, School of Engineering, Institute for Materials and Processes, The University of Edinburgh, Robert Stevenson Road, Edinburgh, EH9 3FB, UK.  
Email: n.radacsi@ed.ac.uk

### Abstract

This review provides insights into the current advancements in the field of electrospinning, focusing on its applications for skin tissue engineering. Furthermore, it reports the evolution and present challenges of advanced skin substitute product development and explores the recent contributions in 2D and 3D scaffolding, focusing on natural, synthetic, and composite nanomaterials. In the past decades, nanotechnology has arisen as a fascinating discipline that has influenced every aspect of science, engineering, and medicine. Electrospinning is a versatile fabrication method that allows researchers to elicit and explore many of the current challenges faced by tissue engineering and regenerative medicine. In skin tissue engineering, electrospun nanofibers are particularly attractive due to their refined morphology, processing flexibility—that allows for the formation of unique materials and structures, and its extracellular matrix-like biomimetic architecture. These allow for electrospun nanofibers to promote improved re-epithelization and neo-tissue formation of wounds. Advancements in the use of portable electrospinning equipment and the employment of electrospinning for transdermal drug delivery and melanoma treatment are additionally explored. Present trends and issues are critically discussed based on recently published patents, clinical trials, and in vivo studies.

This article is categorized under:

Implantable Materials and Surgical Technologies > Nanotechnology in Tissue Repair and Replacement

Therapeutic Approaches and Drug Discovery > Emerging Technologies

Implantable Materials and Surgical Technologies > Nanomaterials and Implants

### KEYWORDS

electrospinning, portable electrospinning, three-dimensional, tissue engineering, wound healing

## 1 | INTRODUCTION

At present, nanostructured materials have attracted considerable attention due to the unique properties that arise from their size-dependent structural behavior, making them of interest in the fields of tissue engineering (TE), drug delivery



# WIREs

NANOMEDICINE AND NANOBIO TECHNOLOGY

Volume 12, Number 4, July/August



[wires.wiley.com/nanomed](http://wires.wiley.com/nanomed)



WILEY

DOI: 10.1002/wnan.1655



Contents lists available at ScienceDirect

## Medical Engineering and Physics

journal homepage: [www.elsevier.com/locate/medengphy](http://www.elsevier.com/locate/medengphy)

# Nozzle-free electrospinning of Poly(vinylpyrrolidone)/Poly(glycerol sebacate) fibrous scaffolds for skin tissue engineering applications<sup>☆</sup>



Antonios Keirouz<sup>a,b</sup>, Giuseppino Fortunato<sup>b</sup>, Mei Zhang<sup>a,c</sup>, Anthony Callanan<sup>c</sup>, Norbert Radacsi<sup>a,\*</sup>

<sup>a</sup>The School of Engineering, Institute for Materials and Processes, The University of Edinburgh, King's Buildings, Edinburgh EH9 3FB, United Kingdom

<sup>b</sup>Empa, Swiss Federal Laboratories for Materials Science and Technology, Laboratory for Protection and Physiology, St. Gallen CH-9014, Switzerland

<sup>c</sup>The School of Engineering, Institute for Bioengineering, The University of Edinburgh, The King's Buildings, Edinburgh EH9 3JL, United Kingdom

### ARTICLE INFO

#### Article history:

Received 3 January 2019

Revised 15 May 2019

Accepted 9 June 2019

#### Keywords:

PGS

PVP

UV

Nozzle-free electrospinning

Elastic

Polymer

### ABSTRACT

A novel composite for skin tissue engineering applications by use of blends of Poly(vinylpyrrolidone) (PVP) and Poly(glycerol sebacate) (PGS) was fabricated via the scalable nozzle-free electrospinning technique. The formed PVP:PGS blends were morphologically, thermochemically and mechanically characterized. The morphology of the developed fibers correlated to the blend ratio. The tensile modulus appeared to be affected by the concentration of PGS within the blends, with an apparent decrease in the elastic modulus of the electrospun mats and an exponential increase of the elongation at break. Ultraviolet (UV) crosslinking of the composite fibers significantly decreased the construct's wettability and stabilized the formed fiber mats, which was indicated by contact angle measurements. *In vitro* examination showed good viability and proliferation of human dermal fibroblast cells. The present findings provide valuable insights for tuning the elastic properties of electrospun material by incorporating this unique elastomer as a promising future candidate for skin substitute constructs.

© 2019 IPPEM. Published by Elsevier Ltd. All rights reserved.

### 1. Introduction

Skin tissue engineering (TE) requires the development of biomimetic scaffolds that provide all the necessary biochemical mechanisms and topographical cues for efficient skin regeneration [1,2].

Nanostructured materials are favorable towards the fabrication of porous fibrous meshes as they permit the development of structures that closely resemble the native extracellular matrix (ECM) where cells can adhere, proliferate, freely migrate and induce neo-vascularization [3,4]. Presently, the majority of the skin substitute models are non-resorbable scaffolds based on allographs [3,5]. Nonetheless, much focus is being directed to the development of bioresorbable scaffolds that convey all the requirements to act as short-term matrices, capable of being slowly resorbed by the newly formed tissue [6].

Among the spectrum of biomaterials available, utilizing natural and synthetic polymers remain at the center of attention [7]. Poly(glycerol sebacate) (PGS) is a recently discovered *Federal Drug Administration* (FDA) approved semi-crystalline thermoset, with promising applications for soft tissue engineering [8,9]. PGS is synthesized via the polycondensation of glycerol and sebacic acid to form a pre-polymer, which can be further covalently crosslinked [10,11]. Poly(polyol sebacate)-derived polymers such as PGS refer to a family of ester-bonded elastomers formed via the polycondensation of polyol alcohols, containing multiple hydroxyl groups (e.g., glycerol, isomalt, xylitol) and the dicarboxylic acid present in sebacic acid [12,13].

PGS is a very attractive biomaterial as it exhibits tailored mechanical properties and bioresorbability pertinent to varying the polycondensation parameters and stoichiometry, which correlate to the surface degradability of its ester linkages [14,15]. As a result, PGS has been exponentially investigated *in vitro* and *in vivo* on studies focusing on cardiac [16–18], vascular [19,20], cartilage [9,21], nerve guidance [22,23], retina [24–26], adipose [27], skin [28,29], as well as a potential drug carrier [30,31].

Among the available fabrication techniques such as freeze-drying, solvent casting, and particulate leaching, reactive injection molding, phase separation, and self-assembly – electrospinning has been contemplated as an ideal candidate for fabricating,

<sup>☆</sup> **In brief:** A nozzle-free electrospinning device was designed for the fabrication of biocompatible PVP:PGS nonwoven fibrous mats, which presented compelling mechanical properties adjustable apropos to the blend ratio and the PVP's molecular weight.

\* Corresponding author.

E-mail address: [n.radacsi@ed.ac.uk](mailto:n.radacsi@ed.ac.uk) (N. Radacsi).

<https://doi.org/10.1016/j.medengphy.2019.06.009>

1350-4533/© 2019 IPPEM. Published by Elsevier Ltd. All rights reserved.

DOI: 10.1016/j.medengphy.2019.06.009



Contents lists available at ScienceDirect

## Materials Science &amp; Engineering C

journal homepage: [www.elsevier.com/locate/msec](http://www.elsevier.com/locate/msec)

## High-throughput production of silk fibroin-based electrospun fibers as biomaterial for skin tissue engineering applications

Antonios Keirouz<sup>a,c</sup>, Mariia Zakharova<sup>a</sup>, Jaehoon Kwon<sup>a</sup>, Colin Robert<sup>a</sup>, Vasileios Koutsos<sup>a</sup>, Anthony Callanan<sup>b</sup>, Xianfeng Chen<sup>b</sup>, Giuseppino Fortunato<sup>c</sup>, Norbert Radacsi<sup>a,\*</sup>

<sup>a</sup> School of Engineering, Institute for Materials and Processes, The University of Edinburgh, King's Buildings, Edinburgh EH9 3FB, United Kingdom

<sup>b</sup> School of Engineering, Institute for Bioengineering, The University of Edinburgh, King's Buildings, Edinburgh EH9 3JL, United Kingdom

<sup>c</sup> Laboratory for Biomimetic Membranes and Textiles, Empa, Swiss Federal Laboratories for Materials Science and Technology, Lerchenfeldstrasse 5, CH-9014, St. Gallen, Switzerland



## ARTICLE INFO

## Keywords:

Poly(glycerol sebacate)  
Poly(caprolactone)  
Silk fibroin  
Nozzle-free electrospinning  
wound healing

## ABSTRACT

In this work, a nozzle-free electrospinning device was **built** to obtain high-throughput production of silk fibroin-based biocompatible composite fibers with tunable wettability. Synthetic biomaterials tend to present sub-optimal cell growth and proliferation, with many studies linking this phenomenon to the hydrophobicity of such surfaces. In this study, electrospun mats consisting of Poly(caprolactone) blended with variant forms of Poly(glycerol sebacate) (PGS) and regenerated silk fibroin were fabricated. The main aim of this work was the development of fiber mats with tunable hydrophobicity/hydrophilicity properties depending on the esterification degree and concentration of PGS. A variation of the conventional protocol used for the extraction of silk fibroin from *Bombyx mori* cocoons was employed, achieving significantly increased yields of the protein, in a third of the time required via the conventional extraction protocol. By altering the surface properties of the electrospun membranes, the trinary composite biomaterial presented good *in vitro* fibroblast attachment behavior and optimal growth, indicating the potential of such constructs towards the development of an artificial skin-like platform that can aid wound healing and skin regeneration.

## 1. Introduction

Tissue-engineered skin substitutes and advanced wound dressing biomaterials require for several criteria to be met. First, they need to be biocompatible to overcome immune rejection and inflammation [1]. In addition, an appropriately hydrophilic interface between the tissue and the biomaterial is required, which effectively facilitates cell adhesion and proliferation. Furthermore, the construct needs to be lightweight to minimize foreign body sensation, biodegradable, and facilitate an architecture that allows for the appropriate water retention, nutrient transport, breathability, and structural stability that offers an optimal regenerative niche [2,3,4]. To facilitate these requirements, a range of biocompatible materials have been extensively studied, focusing on wound management and skin tissue repair [5]. Among them, electrospun biomaterials are favorable toward the reconstruction of fibrous skin tissue-like scaffolds as they allow the development of structures that closely resemble the native extracellular matrix (ECM), where cells can adhere, proliferate, freely migrate, and induce neovascularization [6,7]. Electrospinning is an excellent and well-established technique

that can fabricate constructs in the form of non-woven networks of fibers [8]. The electrospun fiber morphology, granted by the micro- and nano-dimensions, can facilitate the absorption of exudates and allow for efficient gas exchange at the wound bed, while being capable of modulating how the dermal cells adapt and proliferate [9,10]. These features can ultimately provide and improve the care, recovery time, and healing process of injured skin tissue.

One of the main challenges in the development of electrospun-based biomaterials surrounds the meager production rates of conventional electrospinning and the principal use of synthetic hydrophobic polymeric material. One can apprehend that a polymer system integrating the unique properties of different materials can provide distinct features to the final composite structure. Considering this, a unique composite structure, based on electrospun fibers and consisting of synthetic and naturally-derived material, was developed. Nonetheless, finding the appropriate solvent system, obtaining the desired critical entanglement concentration of each polymer and the required viscosity (below the overlap concentration of the polymer-system) to achieve a stable Taylor cone and a consistent jet during electrospinning can be challenging.

\* Corresponding author.

E-mail address: [n.radacsi@ed.ac.uk](mailto:n.radacsi@ed.ac.uk) (N. Radacsi).

<https://doi.org/10.1016/j.msec.2020.110939>

Received 9 September 2019; Received in revised form 23 January 2020; Accepted 6 April 2020

Available online 08 April 2020

0928-4931/ © 2020 Elsevier B.V. All rights reserved.

DOI: 10.1016/j.msec.2020.110939

## RESEARCH

## Open Access



# Nylon-6/chitosan core/shell antimicrobial nanofibers for the prevention of mesh-associated surgical site infection

Antonios Keirouz<sup>1,2</sup>, Norbert Radacsi<sup>2</sup>, Qun Ren<sup>3</sup>, Alex Dommann<sup>4</sup>, Guido Beldi<sup>5</sup>, Katharina Maniura-Weber<sup>3</sup>, René M. Rossi<sup>1</sup> and Giuseppino Fortunato<sup>1\*</sup>

## Abstract

The state-of-the-art hernia meshes, used in hospitals for hernia repair, are predominantly polymeric textile-based constructs that present high mechanical strength, but lack antimicrobial properties. Consequently, preventing bacterial colonization of implanted prosthetic meshes is of major clinical relevance for patients undergoing hernia repair. In this study, the co-axial electrospinning technique was investigated for the development of a novel mechanically stable structure incorporating dual drug release antimicrobial action. Core/shell structured nanofibers were developed, consisting of Nylon-6 in the core, to provide the appropriate mechanical stability, and Chitosan/Polyethylene oxide in the shell to provide bacteriostatic action. The core/shell structure consisted of a binary antimicrobial system incorporating 5-chloro-8-quinolinol in the chitosan shell, with the sustained release of Poly(hexanide) from the Nylon-6 core of the fibers. Homogeneous nanofibers with a "beads-in-fiber" architecture were observed by TEM, and validated by FTIR and XPS. The composite nanofibrous meshes significantly advance the stress-strain responses in comparison to the counterpart single-polymer electrospun meshes. The antimicrobial effectiveness was evaluated in vitro against two of the most commonly occurring pathogenic bacteria; *S. aureus* and *P. aeruginosa*, in surgical site infections. This study illustrates how the tailoring of core/shell nanofibers can be of interest for the development of active antimicrobial surfaces.

**Keywords:** Chitosan, Nylon-6, Co-axial electrospinning, Hernia meshes, Antimicrobial fibers, Drug release

## Introduction

Hernia repair is one of the most commonly performed elective operations with approximately 100,000 hernia repair surgeries being carried out in the UK, over 700,000 in the US, and 1,100,000 inguinal and abdominal wall hernia surgeries in China every year [1, 2]. Inguinal hernia surgery is the most frequent accounting for over 75%, followed by epigastric and incisional at 15% and other forms 10% [3]. The majority of inguinal hernias occur in men

(98%), with 30% of patients developing a second hernia on the opposite side of the groin [4]. Suture closures are recognized for having high recurrence rates, while synthetic and bioprosthetic meshes carry their own downsides, such as being heavyweight, which induces foreign body sensation, leading to fibrosis and tissue adhesion, post-surgical infection, etc. [5]. The use of hernia meshes reduces recurrence by 30–50% compared to suture repair [6, 7]. In general, intravenous and oral administration of prophylactic antibiotics does not ensure sufficient protection against surgical site infection [8].

Nanofibrous scaffolds, developed via the electrospinning process can be valuable towards the development of a biodegradable antimicrobial layer as the fibers formed are lightweight, can attain a large surface area per unit

\*Correspondence: giuseppino.fortunato@empa.ch

<sup>1</sup> Laboratory for Biomimetic Membranes and Textiles, Empa, Swiss Federal Laboratories for Materials Science and Technology, Lerchenfeldstrasse 5, CH-9014 St. Gallen, Switzerland

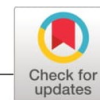
Full list of author information is available at the end of the article



© The Author(s) 2020. This article is licensed under a Creative Commons Attribution 4.0 International License, which permits use, sharing, adaptation, distribution and reproduction in any medium or format, as long as you give appropriate credit to the original author(s) and the source, provide a link to the Creative Commons licence, and indicate if changes were made. The images or other third party material in this article are included in the article's Creative Commons licence, unless indicated otherwise in a credit line to the material. If material is not included in the article's Creative Commons licence and your intended use is not permitted by statutory regulation or exceeds the permitted use, you will need to obtain permission directly from the copyright holder. To view a copy of this licence, visit <http://creativecommons.org/licenses/by/4.0/>. The Creative Commons Public Domain Dedication waiver (<http://creativecommons.org/publicdomain/zero/1.0/>) applies to the data made available in this article, unless otherwise stated in a credit line to the data.



Received: 10 December 2019 | Revised: 6 March 2020 | Accepted: 3 April 2020  
DOI: 10.1002/app.49341



## ARTICLE

Applied Polymer  
SCIENCE WILEY

# High-throughput fabrication of carbonized electrospun polyacrylonitrile/poly(acrylic acid) nanofibers with additives for enhanced electrochemical sensing

Huey Ling Tan<sup>1</sup> | Maria Kana Sanira Putri<sup>2</sup> | Siti Shawalliah Idris<sup>1</sup> |  
Niklas Hartikainen<sup>2</sup> | Noor Fitrah Abu Bakar<sup>1</sup> | Antonios Keirouz<sup>2</sup> |  
Norbert Radacsi<sup>2</sup>

<sup>1</sup>Faculty of Chemical Engineering,  
Universiti Teknologi MARA, Shah Alam,  
Selangor, Malaysia

<sup>2</sup>School of Engineering, Institute for  
Materials and Processes, The University of  
Edinburgh, King's Buildings,  
Edinburgh, UK

**Correspondence**

Huey Ling Tan, Faculty of Chemical  
Engineering, Universiti Teknologi MARA,  
40450 Shah Alam, Selangor, Malaysia.  
Email: hueyling@uitm.edu.my

Norbert Radacsi, School of Engineering,  
Institute for Materials and Processes, The  
University of Edinburgh, King's Buildings,  
Edinburgh, EH9 3FB, UK.  
Email: n.radacsi@ed.ac.uk

**Funding information**

The University of Edinburgh, Grant/  
Award Number: 100-IRMI/INT 16/6/2  
(010/2017); Universiti Teknologi MARA;  
University of Edinburgh

**Abstract**

Lightweight, polyacrylonitrile-derived electrodes with different additives were fabricated using high-throughput nozzle-free electrospinning. The electrospun precursor nanofibers (PNFs) containing iron oxide, gold nanoparticles, or reduced graphene oxide (rGO) were subjected to oxidative stabilization and carbonization to obtain a carbon-rich conductive nanofiber structure. Scanning electron microscopy showed that the carbon nanofibers contracted between 11 and 55% while the Fourier-transform infrared spectroscopy confirmed that the carbon nanofibers were thermally stable. Thermogravimetric and differential scanning calorimetry results revealed that the cross-linking of the chain molecules and cyclization were completed. Next, cyclic voltammetry results indicated that the electroactivity of the modified screen-printed carbon electrodes was decreased by 85% due to the presence of carbon glue. The modified device presented significant enhanced electrochemical responses with the inclusions of nanoparticles, with rGO showing a 2.13 times higher electroactive surface area, followed by iron oxide (two times) and gold nanoparticles (1.37 times) than the equivalent PNFs.

**KEYWORDS**

cyclic voltammetry, degradation, electroactive surface area, nanoparticles, nozzle-free electrospinning

**Abbreviations:** AuNPs, gold nanoparticles; CNFs, carbon nanofibers; CV, cyclic voltammetry; GO, graphene oxide; IO, iron (III) oxide; NFs, nanofibers; PAA, Polyacrylic acid; PAN, polyacrylonitrile; PNFs, precursor nanofibers; rGO, reduced graphene oxide; SPCE, screen-printed carbon electrode.

This is an open access article under the terms of the Creative Commons Attribution-NonCommercial License, which permits use, distribution and reproduction in any medium, provided the original work is properly cited and is not used for commercial purposes.

© 2020 The Authors. *Journal of Applied Polymer Science* published by Wiley Periodicals, Inc.

*J Appl Polym Sci.* 2020;e49341.  
<https://doi.org/10.1002/app.49341>

[wileyonlinelibrary.com/journal/app](http://wileyonlinelibrary.com/journal/app)

1 of 15

## 1 | INTRODUCTION

The development of analytical methods and platforms that are sensitive, affordable and easy to use, is of utmost importance for the effective sensing of analytes. Nanofibers (NFs) have attracted great attention due to

DOI: 10.1002/app.49341

## Electrospun Nanofibers for Drug Delivery and Biosensing

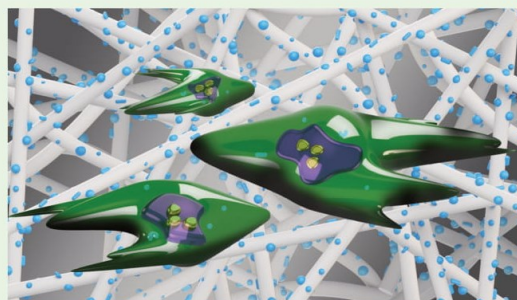
Conor Cleeton,<sup>†</sup> Antonios Keirouz,<sup>†</sup> Xianfeng Chen,<sup>‡</sup> and Norbert Radacsi<sup>\*,†</sup>

<sup>†</sup>School of Engineering, Institute for Materials and Processes, The University of Edinburgh, Robert Stevenson Road, Edinburgh EH9 3FB, United Kingdom

<sup>‡</sup>School of Engineering, Institute for Bioengineering, The University of Edinburgh, King's Buildings, Mayfield Road, Edinburgh EH9 3JL, United Kingdom

**ABSTRACT:** Early diagnosis and efficient treatment are of paramount importance to fighting cancers. Monitoring the foreign body response of a patient to treatment therapies also plays an important role in improving the care that cancer patients receive by their medical practitioners. As such, there is extensive research being conducted into ultrasensitive point-of-care detection systems and “smart” personalized anticancer drug delivery systems. Electrospun nanofibers have emerged as promising materials for the construction of nanoscale biosensors and therapeutic platforms because of their large surface areas, controllable surface conformation, good surface modification, complex pore structure, and high biocompatibility. Electrospun nanofibers are produced by electrospinning, which is a very powerful and economically viable method of synthesizing versatile and scalable assemblies from a wide array of raw materials. This review describes the theory of electrospinning, achievements, and problems currently faced in producing effective biosensors/drug delivery systems, in particular, for cancer diagnosis and treatment. Finally, insights into future prospects are discussed.

**KEYWORDS:** electrospinning, nanofibers, drug delivery, biosensing, cancer



### 1. INTRODUCTION

Mortality statistics by geographical location reflect a concerning consistency in cancer. The disease accounts for a large proportion of recorded deaths in many areas of the world, with 9 million deaths by cancer being approximated worldwide in 2016,<sup>1</sup> accounting for 15.8% of the overall 57 million reported deaths. Some technological advancements in the past decades have provided the necessary framework to address some of the medical issues associated with specialized therapy procedures. In almost all cancers, the average 5-year survival rate has improved by up to 2.3% in 2016 alone.<sup>2</sup> Nevertheless, mortality rates for neoplastic related deaths have declined in a comparatively stagnant fashion relative to circulatory diseases over the past three decades (Figure 1). Currently, employed methods of treatment include a combination of surgery, chemotherapy, radiation therapy, immunotherapy, and target-specific therapies.<sup>3</sup> A fundamental shortcoming of these treatments is that they are often implemented as part of a mitigating methodology when cancer diagnostics have identified malignant tumors.

The need to pursue more effective means of cancer treatment becomes clear when currently employed methods are considered. Synergistic radiotherapy/surgical resection and systemic chemotherapy—the commonly applied therapeutic strategy<sup>4</sup>—are limited in their application because of adverse health effects that accompany their administration. In the absence of selectivity for neoplastic cells, common health side

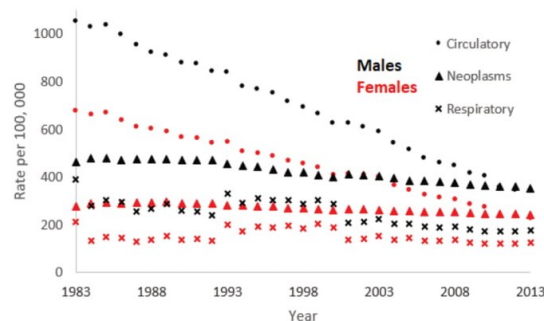


**Figure 1.** Age-standardized mortality rates by cause of death from 1982 to 2013. Produced by the authors using published U.K. government statistics.<sup>2</sup>

effects that are observed might include kidney malfunction, nerve injury, nausea and vomiting,<sup>5</sup> normal cell toxicity, and death due to extreme dosages.<sup>6</sup> This is a direct result of the traditional drug delivery process, i.e., repeated administration of treatment via the oral or parenteral route.<sup>7</sup> Naturally, with

Received: June 14, 2019

Accepted: August 12, 2019

Published: August 12, 2019

**Design and development of a nozzle-free electrospinning device for the high-throughput production of biomaterial nanofibers**

Muhammad Waqas\*, Antonios Keirouz\*, Maria Kana Sanira Putri, Faraz Fazal, Francisco Javier Diaz Sanchez, Dipa Ray, Norbert Radacsi†, and Vasileios Koutsos

School of Engineering, Institute for Materials and Processes, The University of Edinburgh, Robert Stevenson Road, Edinburgh, EH9 3FB, United Kingdom.

\*These authors contributed equally to the article

†Corresponding author. Tel.: +44 (0) 131 651 7112. E-mail address: n.radacsi@ed.ac.uk

**Abstract**

The design and fabrication of a temperature-controlled nozzle-free electrospinning device for the mass production of electrospun biomaterial nanofibers are provided in detail. The setup described is capable of producing fibers in an upward motion using a rotating mandrel partially immersed within a polymer solution bath, producing multiple Taylor cones. Free-surface electrospinning can overcome limitations linked with single and multi-nozzle-based setups, such as meager production rates and clogging. One key feature of the device is the use of cryo-collector mandrel capable of collecting fibers in sub-zero temperatures, allowing the production of ultra-porous nanostructures for tissue engineering. A multi-channel gas chamber allows the conditioning of the atmosphere, temperature, and airflow, while the design of the chamber ensures that there is no exposure of the user to the high-voltage components. All the CAD files, as well as step-by-step assembly instructions along with a list of the materials used, are provided.

**1 Introduction**

The unique properties presented by fibrous materials in the nano/microscale has directed the advancement of several fiber-processing techniques today. As a highly versatile method, electrospinning can process solutions, suspensions, or melts into fibers of varying diameters with low a standard deviation (low polydispersity), and is the only process, at present, capable of mass-producing continuous nanofibers (NFs).(1)

### 3D Electrospinning: A Technology for the Facile and Precise Fabrication of 3D Macrostructures with Microfibrous Features

Michel Vong<sup>a,\*</sup>, Francisco Javier Diaz Sanchez<sup>a</sup>, Antonios Keirouz<sup>a</sup>, Wiwat Nuansing<sup>b,c</sup>, Norbert Radacsi<sup>a,\*</sup>

<sup>a</sup>School of Engineering, Institute for Materials and Processes, The University of Edinburgh, Sanderson Building, King's Buildings, Edinburgh, EH9 3FB, United Kingdom

<sup>b</sup>School of Physics, Institute of Science, Suranaree University of Technology, Thailand

<sup>c</sup>SUT CoE on Advanced Functional Materials (SUT-AFM), Suranaree University of Technology, Thailand

\*Corresponding authors: [michel.vong@ed.ac.uk](mailto:michel.vong@ed.ac.uk) and [n.radacsi@ed.ac.uk](mailto:n.radacsi@ed.ac.uk)

#### Abstract

Fabrication of macroscopic three-dimensional (3D) structures made of nanofibers of widely used polymers is reported. 3D structures have several benefits over conventional flat two-dimensional (2D) structures by the added dimension. The structures have been fabricated by the 3D electrospinning technology that can build 3D structures rapidly due to certain additives in the solution and appropriate process conditions. The process parameters of 3D electrospinning have been identified and investigated to better understand the formation mechanism of the 3D build-up for polystyrene (PS), polyacrylonitrile (PAN), and polyvinylpyrrolidone (PVP). Different types of electrodes were inserted in the electrospinning chamber to alter the electric field and have better control over the shape of the 3D structure. The upscalability of this technology was investigated by using a standard electrospinner and a nozzle-free electrospinning setup. It was possible to manufacture 3D structures with these devices, highlighting the versatility of this technology. 3D electrospinning opens the pathway for the facile fabrication of macroscopic 3D structure with microfibrous features on a commercial scale.

**Keywords:** 3D electrospinning, formation mechanism, upscalability, polystyrene, polyacrylonitrile, polyvinylpyrrolidone

Electrospinning is a versatile and simple technology that uses high voltage to draw micro- and nano-fibers from polymer solutions. By tuning the electrospinning parameters as well as the polymer solution properties, it is possible to have wide control over the shape and morphology of the fibers. The fibers' diameter, length, surface roughness, porosity, pore interconnectivity, degree of fibers alignment, beads-in-fibers are all controllable properties that can shape the desired fiber configuration.<sup>1-7</sup> Different types of fibers, such as hollow, core-shell, multichannel, branched, peapod or wire-in-tube are also obtainable structures.<sup>8-13</sup> Coupled with the ability to add functional nanoparticles or manufacture metallic or ceramic fibers<sup>14,15</sup>, electrospinning can be purposed for a wide range of applications.

Recently, the electrospinning of unorganized three-dimensional (3D) structures has sparked interest as 3D structures offer some benefits over conventional two-dimensional non-woven electrospun structures. The 3D nature of the electrospun structure can allow it to be more moldable and to be easily fitted into particular locations; for instance, it can be used as a sealant to block leakage in tubing systems.<sup>16</sup> In energy storage and conversion, the use of a 3D carbon nanofibrous structure showed higher elasticity, higher durability and better performance than standard two-dimensional (2D) configurations.<sup>17</sup> This is due to the strong

## **Effects of Strong Electric Fields in Living Organisms: A Review**

Shathes Sivanesvaran<sup>1</sup>, Antonios Keirouz<sup>1</sup>, Ulrich Loening<sup>2</sup>, Norbert Radacsi<sup>1\*</sup>

<sup>1</sup>School of Engineering, Institute for Materials and Processes, The University of Edinburgh, Robert Stevenson Road, Edinburgh EH9 3FB, United Kingdom

<sup>2</sup>School of Engineering, Institute for Bioengineering, The University of Edinburgh, King's Buildings, Mayfield Road, Edinburgh EH9 3JL, United Kingdom

\*Corresponding author. Tel.: +44 (0) 131 651 7112. E-mail address: [n.radacsi@ed.ac.uk](mailto:n.radacsi@ed.ac.uk)

### **Abstract**

This review investigates the biological and morphological effects witnessed in organisms subsequent to exposure to strong electrostatic fields (ESFs). Twelve studies (1960 – 2016) that met selection criteria were evaluated to compare growth and developmental outcome of the various biological kingdoms when subjected to strong static electric fields (SEFs). With the weight of evidence put forth, it is hard to neglect the biologic effects observed upon exposure to electric fields to the epigenetics of different species. Although the exact mechanisms that bring about these effects are yet to be entirely unidentified, with limitations among the experimental design, analytical choices, and the variations among the subsequent findings being observed, it remains a promising field of study of great potential. Fully understanding the biologic mechanisms that facilitate the relationship elicited by an electromagnetic field to a specific organism can benefit areas of the industry surrounding agriculture, farming, climate, and energy.

### Table of Contents

<b>1</b>	<b><i>Introduction</i></b> .....	<b>2</b>
<b>2</b>	<b><i>Static electric fields and electric field sources</i></b> .....	<b>3</b>
<b>3</b>	<b><i>A timeline of the early electro-culture experiments</i></b> .....	<b>4</b>
<b>4</b>	<b><i>The effect of strong electric fields in eukaryotic and prokaryotic organisms</i></b> .....	<b>10</b>
<b>5</b>	<b><i>Key findings</i></b> .....	<b>24</b>
5.1	Effect of polarity .....	24
5.2	Effect of varying species .....	25
5.3	Effect of field intensity.....	25
5.4	Effect of developmental stage .....	26
5.5	Additional mechanisms .....	27
<b>6</b>	<b><i>Mechanisms capable of inducing SEF-induced effects on organisms</i></b> .....	<b>27</b>
<b>7</b>	<b><i>Limitations</i></b> .....	<b>29</b>
<b>8</b>	<b><i>Future Application</i></b> .....	<b>31</b>
<b>9</b>	<b><i>Conclusions</i></b> .....	<b>32</b>
<b>10</b>	<b><i>References</i></b> .....	<b>33</b>

**ELECTROSPIN2018, INTERNATIONAL CONFERENCE**

16th to 18th January 2018 | Wallenberg Research Centre at Stias | Stellebosch, South Africa

**24. NEEDLELESS ELECTROSPINNING OF PGS/PVP BLENDS FOR SKIN TISSUE SCAFFOLD FABRICATION****Antonios Keirouz<sup>1\*</sup>, Anthony Callanan<sup>2</sup>, Giuseppino Fortunato<sup>3</sup>, Norbert Radacs<sup>1</sup>**<sup>1</sup> *The School of Engineering, Institute for Materials and Processes, The University of Edinburgh, Robert Stevenson Road, Edinburgh, EH9 3FB, U.K.*<sup>2</sup> *The School of Engineering, Institute for Bioengineering, The University of Edinburgh, The King's Buildings, Edinburgh, EH9 3JL, U.K.*<sup>3</sup> *Empa, Swiss Federal Laboratories for Materials Science and Technology, Laboratory for Protection and Physiology, St. Gallen, CH-9014, Switzerland**\*Corresponding author. Tel.: +44 (0) 131 651 7112. E-mail address: a.keirouz@ed.ac.uk*

Biomimetic electrospun scaffolds, as skin substitutes, permit for the development of structures that closely resemble the physical characteristics present by the native extracellular matrix, where cells can adhere, proliferate, freely migrate and, ultimately induce neo-tissue formation at the injured site.

The human skin is a non-linear, anisotropic and viscoelastic organ, where distinct areas differ greatly in regard to mechanical behaviour [1]. Hence, the mechanical properties of specific sites, based on the anatomical attributes of the human body, must be taken under consideration during fabrication, in order to advance the currently available products in the market.

Poly(glycerol sebacate) (PGS)/Polyvinylpyrrolidone (PVP) blends have yet to be exploited for such applications. In the present study, the effect of PGS/PVP blending in the development of electrospun scaffolds with tunable properties was examined.

PGS is an FDA approved thermoelastic polymer and an ideal candidate for soft tissue engineering, as it is vastly biocompatible and gradually biodegradable [2]. PGS was synthesized via polycondensation, by mixing equimolar of glycerol and sebacic acid at 120°C under inert nitrogen atmosphere, as initially reported by Wang et al. [3]. The synthesized PGS was characterized and the degree of esterification was measured using FT IR spectroscopy.

A home-made apparatus, comprised of a rotating cylinder electrode inside a Teflon pool, where the polymer solution was placed, and a biased rotating collector electrode under constant hot air flow, was used for this study. Potential difference of 70kV was applied between the two rotating electrodes (+35/-35 kV), resulting in the formation of multiple Taylor cones on the rotating electrode surface immersing in the solution bath, from which jets stretched to form fibres in an upwards motion.

Electrospinning thermosetting polymers, such as PGS, can be an arduous process due to its insolubility in organic solvents and its low glass-transition temperature [2]. To overcome this burden, PGS was dissolved in HFIP and blended with PVP (1.3M g.mol<sup>-1</sup>) in a 1:1:0.25 ratio of DMF/Ethanol/Water, to provide the needed mechanical support for fibre formation. As the PGS to PVP ratio increased, so did the elasticity of the corresponding scaffolds. Due to this, the mechanical properties of the fibre mats improved significantly, while forming highly porous nets - however, fibre uniformity was not preserved at greater proportions of PGS. The fibers' diameter ranged from 500 nm to 2 µm.

The present findings provide important insights for tuning the elastic properties of electrospun scaffolds by incorporating this unique elastomer. Fibroblast and keratinocyte biocompatibility are currently under investigation.

[1] A. Ni Annaidh, K. Bruyère, M. Destrade, M. D. Gilchrist, and M. Otténio, "Characterization of the anisotropic mechanical properties of excised human skin," *J. Mech. Behav. Biomed. Mater.*, vol. 5, no. 1, pp. 139-148, 2012.

[2] E. M. Jeffries, R. A. Allen, J. Gao, M. Pesce, and Y. Wang, "Highly elastic and suturable electrospun poly(glycerol sebacate) fibrous scaffolds," *Acta Biomater.*, vol. 18, pp. 30-39, 2015.

[3] Y. Wang, G. A. Ameer, B. J. Sheppard, and R. Langer, "A tough biodegradable elastomer," *Nat. Biotechnol.*, vol. 20, no. 6, pp. 602-606, 2002.



# Needleless Electrospinning for Elastic PGS/PVP scaffolds as skin substitutes

Antonios Keirouz<sup>1</sup>, Anthony Callanan<sup>1</sup>, Giuseppino Fortunato<sup>2</sup>, Norbert Radacsi<sup>1</sup>

<sup>1</sup>The School of Engineering, The University of Edinburgh, Robert Stevenson Road, Edinburgh, EH9 3FB, U.K.

<sup>2</sup>Empa, Swiss Federal Laboratories for Materials Science and Technology, St. Gallen, CH-9014, Switzerland



## Introduction

**Skin tissue engineering (TE)** for regenerative medicine requires the development of biomimetic electrospun scaffolds, as skin substitutes, which closely resemble the physical and biochemical properties of the native extracellular matrix (ECM).

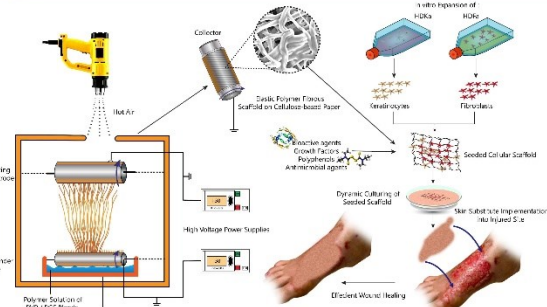
**Resorbable scaffolds** that mimic the dermis and epidermis layers of the skin, convey all the necessary mechanisms to act as a short-term matrix capable of inducing cell adhesion, proliferation, migration and ultimately neo-tissue formation at the injured site.

**Artificial skin** finds applications in a wide range of sectors encompassing:

- Wound healing & tissue repair.
- Prevention from infectious agents, dehydration & nutrient deficiency.
- Flexible & stretchable robotics.
- Sensor systems capable of exceeding the propensity of the human skin.

**Novel nanofibrous Poly(glycerol sebacate) (PGS) / Poly(vinylpyrrolidone) (PVP)** composite scaffolds were produced by the needleless electrospinning process and were characterized regarding their imminent applications to tissue regeneration.

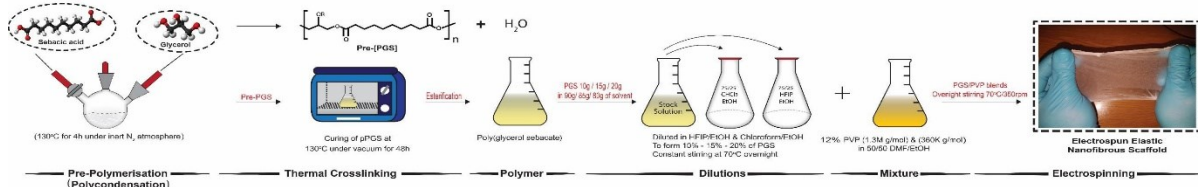
**Elastomers**, such as PGS, carry the ability to develop scaffolds and implants that highly resemble the mechanical properties of the tissue at a native state.



**Needleless electrospinning.** Nanofibrous scaffolds for skin tissue engineering applications.

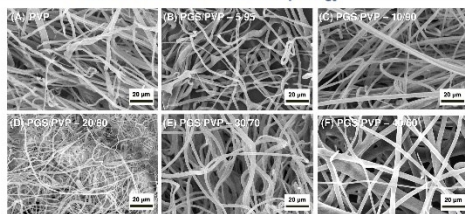
## Experimental Procedure & Methodology

**Poly(glycerol sebacate) (PGS)** is a synthetic biocompatible elastomer with tuneable biodegradable properties, first synthesized by Wang et al. 2002, specifically for soft tissue engineering.

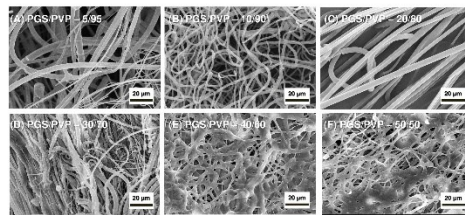


## Results

### PGS/PVP Scaffolds – Surface Morphology

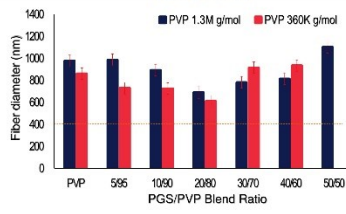


**PVP 360K g/mol.** SEM images (20 keV accelerating voltage) of 12% PVP in DMF/EtOH (A) and 10% PGS in HPI/CF blends at different ratios (B-F).



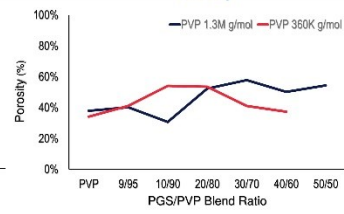
**PVP 1.3M g/mol.** SEM images (20 keV accelerating voltage) of 12% PVP in DMF/EtOH and 10% PGS in HPI/CF blends at different ratios (A-F).

### Fiber Diameter

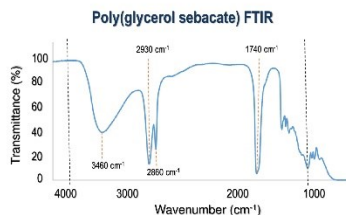


**Average fiber size.** Comparison of PVP 1.3M and 360K g/mol PGS/PVP blends. Error bars=SE, n>3 (1,000).

### Porosity

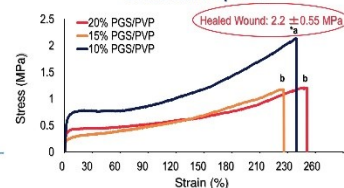


**Nanofibrous membrane porosity.** Comparison of PVP 1.3M and 360K g/mol PGS/PVP blends. n>3 (1,000).



**Fourier-transform infrared spectrum** of equimolar Sebacic acid and Glycerol (1:1) confirming PGS synthesis.

### Mechanical Properties



**Stress-strain curve** of diverse PGS concentrations blended with 12% PVP 1.3M g/mol. n=3, \*p<0.05.

## Conclusion & Future Work

PGS/PVP scaffolds were successfully fabricated using the needleless electrospinning setup. The morphological characteristics and the mechanical properties were examined. The present findings provide important insights for tuning the elastic properties of electrospun scaffolds by incorporating this unique elastomer.

**Future directions** will emphasize on the integration of Polycaprolactone (PCL) and Gelatine, in order to improve the biodegradability of the developed scaffolds, followed by fibroblast and keratinocyte biocompatibility investigations, and ultimately the incorporation of biomolecules and sensor systems to exceed the potential of the artificial constructs.

## References

Wang, Y., Ameer, G. A., Sheppard, B. J., & Langer, R. (2002). **A tough biodegradable elastomer.** *Nature Biotechnology*, 20(6), 602–606.



Corresponding author:  
a.keirouz@ed.ac.uk

**Tony Keirouz**

**ELECTROSPIN2018**  
5TH INTERNATIONAL CONFERENCE  
ON ELECTROSPINNING  
STELLENBOSCH - sti<sup>o</sup>s



**Empa**

Materials Science and Technology

## Electrospun Nylon-6-Poly(hexanide)/Chitosan-5-Chloro-8-quinolinol core/shell antimicrobial nanofibers for the prevention of surgical site infection on hernia meshes

Antonios Keirouz<sup>1,2</sup>, Norbert Radacsi<sup>2</sup>, Ren Zulian Qun<sup>1</sup>, René Rossi<sup>1</sup>, Giuseppino Fortunato<sup>1</sup>

<sup>1</sup>*Empa, Swiss Federal Laboratories for Materials Science and Technology, St. Gallen, CH-9014, Switzerland. E-mail: antonios.keirouz@empa.ch*

<sup>2</sup>*The School of Engineering, Institute for Materials and Processes, The University of Edinburgh, Robert Stevenson Road, Edinburgh, EH9 3FB, U.K. E-mail: a.keirouz@ed.ac.uk*

**Background:** Hernia repair infection is a prevalent problem, with an increased number of cases developing post-operation *surgical site infection* (SSI). Traditionally, a mesh infection is managed by surgical removal of the mesh and administering antibiotics, which vastly increases the chances of hernia recurrence. Nowadays, the use of hernia meshes for hernia repair are textile based constructs that present high mechanical strength, but lack any antibacterial properties. Accordingly, the *aim* of this study was the development of an adequately mechanically stable construct.

**Experimental:** Nanofibrous scaffolds, developed via co-axial electrospinning can be advantageous towards the assembly of an antimicrobial hernia mesh, as the composed fibers are lightweight and bear a high surface-to-volume ratio, which can accommodate features of diverse materials in a bilayer format. Chitosan (CS) was chosen as the shell polymer, due to its polycationic properties and increased biocompatibility, whereas nylon-6 (PA6) was placed in the core of the fibers to promote an enhanced mechanical integrity. The effect of 5-Chloro-8-quinolinol (5CLO8Q) and Poly(hexanide) (PHMB) was examined. The used drug concentrations were based on the guidance of the *Scientific Committee on Consumer Safety* of the European Union [1] and previously published work [2]. To achieve a high drug loading efficiency and a sustained release, 5CLO8Q was paired with CS in the shell, and PHMB was paired with PA6 in the core. The antimicrobial composite fibers were thoroughly characterized and their antimicrobial efficiency was demonstrated against two of most commonly associated with SSI bacterial strains; *Staphylococcus aureus* and *Pseudomonas aeruginosa*.

**Results:** The developed core/shell fibers presented a homogenous morphology with average fiber diameters of  $270 \pm 68$  nm, as opposed to  $181 \pm 22$  nm for drug encapsulated PA6-PHMB and  $210 \pm 31$  nm for CS-5CLO8Q. The composite fibers expressed an increased hydrophilicity, XPS related the surface chemistry to that of the CS present on the shell and revealed a bead-in-shell morphology. Based on the enthalpies obtained by the DSC, we were able to estimate the amount of PA6 within the core of the core/shell nanofibers (NFs) at 48.5 wt.%. The tensile testing indicated an ample improvement of the young modulus and tensile strength of the composite core/shell fibers, which quadrupled at  $217.5 \pm 12.6$  MPa and doubled at  $20.7 \pm 2.5$  MPa, compared to the PA6 and CS-only fibers. A complementary antimicrobial system, where non-Fickian sustained release of PHMB from the core of the fibers was observed, with 5CLO8Q improving the polycationic-based bactericidal activity of CS in the shell. The addition of 5CLO8Q augment to elicit the bactericidal activity of the CS-only fibers, whereas the core/shell PA6-PHMB/CS-5CLO8Q nanofibrous constructs, completely suppressed the growth of the two pathogenic Gram (+) and (-) bacterial strains examined.

**Conclusion:** The antimicrobial core/shell system presented an improved synergetic bactericidal activity, eradicating the growth of the bacterial pathogens. The core/shell structure united the unique properties of CS and PA6 to develop a thermochemically, physiologically and mechanically superior composite product. This meticulous study exemplifies how co-axial electrospinning can convince the development of advanced drug-delivery systems based on electrospun NFs, which could be engaged on hernia meshes for the prevention of post-surgical infections.

**Key Words:** co-axial electrospinning, hernia, antimicrobial mesh

### References

- [1] Scientific Committee on Consumer Safety. Opinion on Polyaminopropyl Biguanide (PHMB) Submission III [J]. *Edetorial Publications Office of the European Union*, 2018, **10**(1): 1-90.
- [2] Stoyanova N, Paneva D, Mincheva R, *et al.* Poly(l-lactide) and poly(butylene succinate) immiscible blends: From electrospinning to biologically active materials [J]. *Materials Science and Engineering C*, 2014, **41**(1): 119–126.



## Nozzle-free electrospinning of PCL-backbone Silk fibroin/Poly(glycerol sebacate) fibrous skin substitute mats

Antonios Keirouz<sup>1,2</sup>, Mariia Zakharova<sup>1</sup>, Jae Hoon Kwon<sup>1</sup>, Anthony Callanan<sup>1</sup>, Vasileios Koutsos<sup>1</sup>,  
Giuseppino Fortunato<sup>2</sup>, Norbert Radacsi<sup>1</sup>

<sup>1</sup>The University of Edinburgh, School of Engineering, Robert Stevenson Road, Edinburgh, EH9 3FB, U.K. E-mail: a.keirouz@ed.ac.uk

<sup>2</sup>Empa, Swiss Federal Laboratories for Materials Science and Technology, Laboratory for Protection and Physiology, St. Gallen, CH-9014, Switzerland. E-mail: antonios.keirouz@empa.ch

Biomimetic electrospun material for wound healing and skin regeneration emphasize on the development of biologically responsive constructs that incorporate an Extracellular matrix (ECM)-like architecture, which mitigates the necessary support for guiding cellular response and activities, ultimately allowing for mediated reepithelialization and neo-tissue formation.

Natural polymeric-based materials, such as *silk fibroin* (SF), encompass great biocompatibility. *Poly(glycerol sebacate)* (PGS) is an attractive biomaterial that exhibits tailored mechanical properties and bioresorbability pertinent to varying its polycondensation parameters [1]. *Poly(caprolactone)* (PCL) is a well-studied semi-crystalline synthetic bio-polymer, where its prevalent use lays on its good elastic properties. Main *aim* of this study was the fabrication of PCL-backbone SF/PGS electrospun mats that appose the diverse properties of these materials in a final construct. **In this work:**

1. A nozzle-free electrospinning apparatus was developed, comprised of a rotating cylinder electrode submerged within a Teflon pool, and a biased rotating collector electrode under constant supply of nitrogen gas (Figure 1). A high potential difference of 60 kV was applied between the two rotating electrodes (+30/-30 kV), resulting in the formation of multiple Taylor cones on the rotating electrode surface immersed in the solution bath, from which jets stretched to form fibers in an upwards motion.

2. A variation of the conventional protocol for the extraction of silk fibroin from *Bombyx mori* cocoons (molecular cut-off technique), based on ethanol precipitation, was exploited [2,3].

3. The effect of the pre-polymerized (pPGS) and cured forms of PGS on the composite's chemical behavior, mechanical stability, wettability and viability, was assessed. **We found:**

1. The fiber morphology and mechanical behavior are dependent on the polymerization time of the PGS.

2. FTIR, XPS, DSC and TGA asserted the presence of all three polymers in the composite structure.

3. The degradation rate of PGS within the scaffolds was retarded by the presence of SF and PCL.

4. The wettability was manipulated based on the proportion of PGS and pPGS within the scaffold.

5. *In vitro* studies with fibroblasts presented good viability, attachment and proliferation properties.

Our findings suggest that the ternary model developed can be a promising candidate as substitute constructs for skin regeneration.

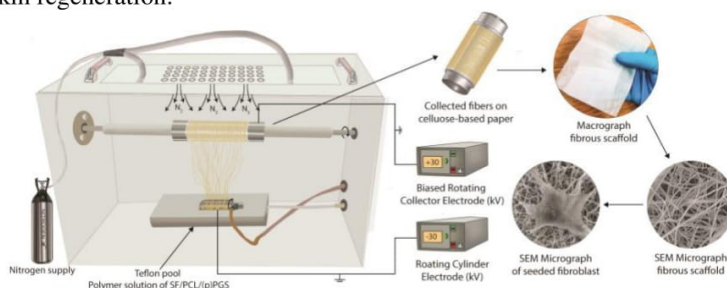


**Figure 1.** Schematic representation of the nozzle-free electrospinning setup. A macrograph of the fibrous scaffold and SEM micrographs of the fibers with and without seeded fibroblasts.

**Key Words:** nozzle-free electrospinning, Poly(glycerol sebacate), Poly(caprolactone), silk fibroin

### References

- [1] Wang Y, Ameer G A, Sheppard J P, Langer R. A tough biodegradable elastomer [J]. *Nature Biotechnology*, 2002, **20**(1): 602–606.
- [2] Huang Y, Bailey K, Wang S, Feng X. Silk fibroin films for potential applications in controlled release [J]. *Reactive and Functional Polymers*, 2017, **116**(5): 57–68.
- [3] Rockwood D N, Preda, R C, Yücel T, *et al.* Materials fabrication from *Bombyx mori* silk fibroin [J]. *Nature Protocols*, 2011, **6**(11): 1612–1631.



# Nozzle-free Electrospinning of Silk fibroin-based Nanofibers for Skin Regeneration

Antonios Keirouz<sup>1,2</sup>, Mariia Zakharova<sup>1</sup>, Jaehoon Kwon<sup>1</sup>, Colin Robert<sup>1</sup>, Vasileios Koutsos<sup>1</sup>,

Anthony Callanan<sup>1</sup>, Xianfeng Chen<sup>1</sup>, Giuseppino Fortunato<sup>2</sup>, Norbert Radacs<sup>1</sup>

<sup>1</sup> The School of Engineering, The University of Edinburgh, Robert Stevenson Road, Edinburgh, EH9 3FB, United Kingdom

<sup>2</sup> Empa, Swiss Federal Laboratories for Materials Science and Technology, Lerchenfeldstrasse 5, St. Gallen, CH-9014, Switzerland



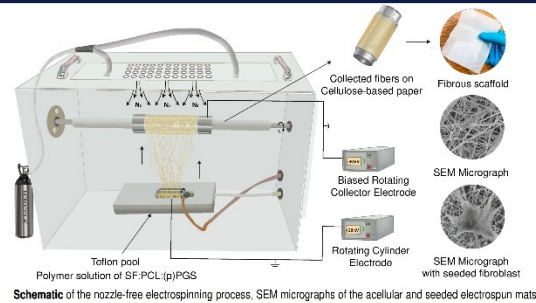
Institute for  
Materials &  
Processes

## Introduction

**Biomimetic electrospun materials** for wound healing and skin regeneration emphasizes on the development of biologically compatible constructs that incorporate an extracellular matrix (ECM)-like architecture, which provides the necessary support to guide cellular activities for re-epithelialization.

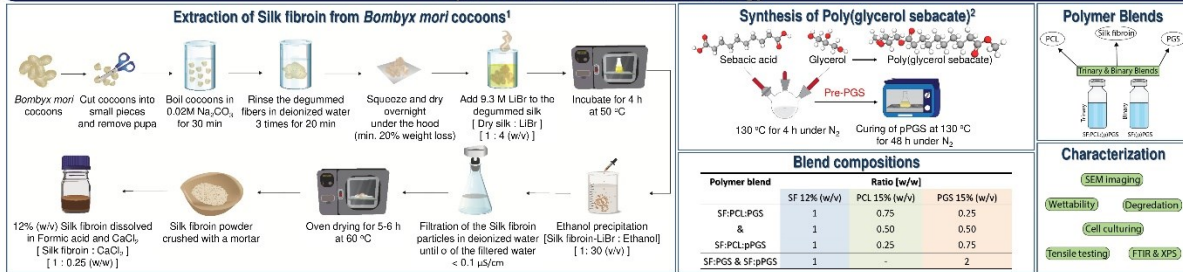
- **Nozzle-free electrospinning** is a cost-effective fabrication technique that allows for the high-throughput production of non-woven nano and microfibrillar mats.
- **Poly(glycerol sebacate) (PGS)** is a biocompatible and biodegradable thermoset elastomer that has emerged as a promising material for soft tissue engineering applications.
- **Silk fibroin (SF)** is a valuable material for the development of wound healing dressings due to its excellent biocompatibility, good oxygen and vapor permeability, and minimum inflammatory responses.

**In this study**, non-acrylate PGS was synthesized and blended with a *Bombyx mori* fibroin-acidic system, where **Polycaprolactone (PCL)** was incorporated as a backbone-polymer carrier to stabilize and improve the spinnability of the composite polymer blends.

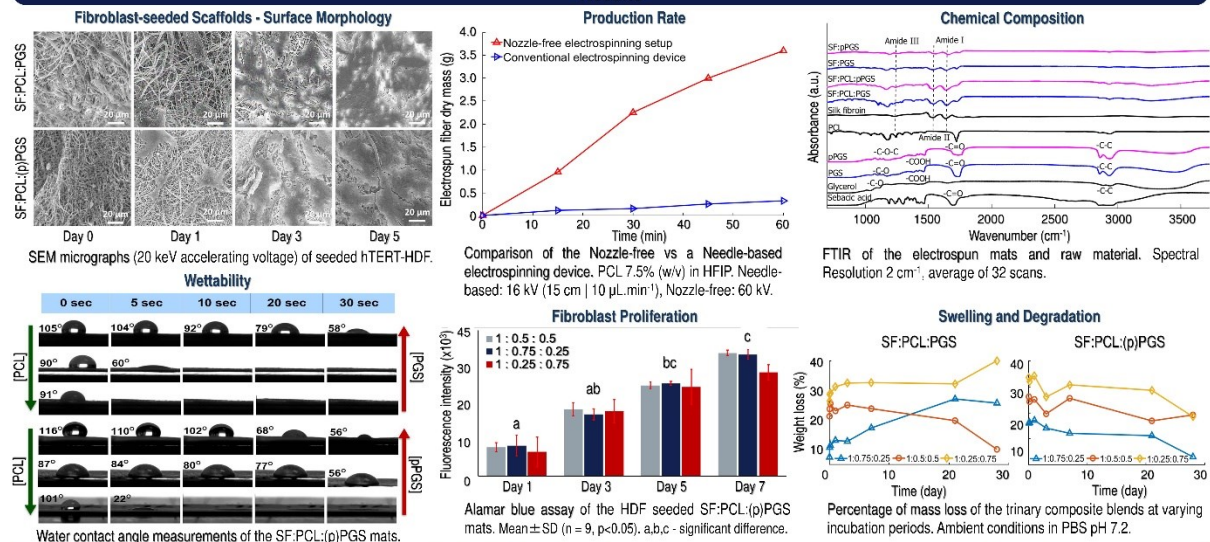


Schematic of the nozzle-free electrospinning process. SEM micrographs of the acellular and seeded electrospun mats

## Experimental Procedure & Methodology



## Results



## Conclusion & Future Work

This work proposes the fabrication of a **PCL-backbone : Silk fibroin : (p)PGS system** that provides superior collective properties.

- A **variation** of the conventional protocol for the **extraction of Silk fibroin** from *B. mori* cocoons was exploited.
- The composite blends, presented good fibroblast proliferation, adjustable fiber morphology, and wettability properties found on the curing time and ratio of PGS.

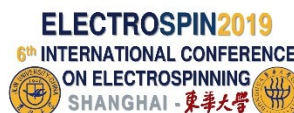
## References

1. Rockwood, D. N. et al. *Materials fabrication from Bombyx mori silk fibroin*. Nature Protocols 6, 1612–1631 (2011).
2. Wang, Y. et al. *A tough biodegradable elastomer*. Nature Biotechnology 20, 602–606 (2002).



Corresponding author:  
a.keirouz@ed.ac.uk

Tony Keirouz



Empa

Materials Science and Technology



# Co-axially Electrospun Hernia Meshes with spatially controlled release of antimicrobials

Antonios Keirouz<sup>1,2</sup>, Norbert Radacsi<sup>1</sup>, Giuseppino Fortunato<sup>2</sup>

<sup>1</sup>The School of Engineering, The University of Edinburgh, Robert Stevenson Road, Edinburgh, EH9 3FB, U.K.  
<sup>2</sup>Empa, Swiss Federal Laboratories for Materials Science and Technology, St. Gallen, CH-9014, Switzerland



Institute for Materials & Processes

## Introduction

**Hernia repair infection** is a prevalent problem, with an increased number of cases developing postoperative **surgical site infection (SSI)**. Traditionally, the infection is managed by surgical removal of the mesh and administration of antibiotics, which vastly increases the chances of surgical complications and hernia recurrence.

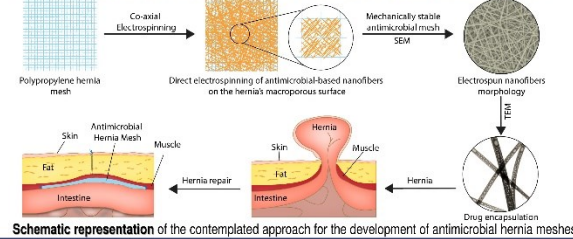
**Nowadays**, the use of hernia meshes for hernia repair are **textile-based constructs** that present high mechanical strength, but **lack any antimicrobial properties**.

### A hernia mesh needs to be:

- Lightweight (35-80 g.m<sup>-2</sup>) and adequately flexible (to reduce pain and foreign body sensation)
- Maintain sufficient tensile properties (Tensile strength: 16 N/cm, Suture retention: 20 N/cm)<sup>1</sup>
- Chemically inert, non-carcinogenic and non-immunogenic
- Capable of restoring the natural respiratory movement of the abdominal wall
- **Resistant to infection**

The aim of this study was the development of a mechanically stable construct that integrates a strong antimicrobial activity, which could be integrated within a hernia format.

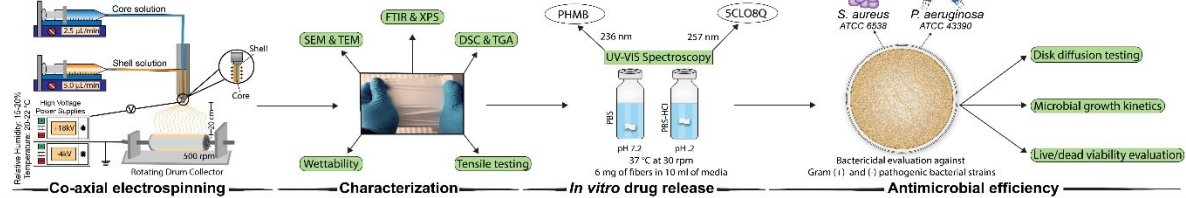
The **co-axial electrospinning technique** employed can be used to obtain nanofibrous constructs that bear high surface-to-volume ratio, which can accommodate features of diverse materials, formulating structures that can elicit sustained drug release and enhanced mechanical strength.



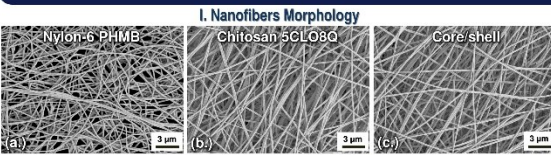
## Experimental Procedure & Methodology

**Core solution:** 21% w/v Nylon-6 (pellets) + 0.3% w/v Poly(hexamide) (PHMB) in Formic acid.

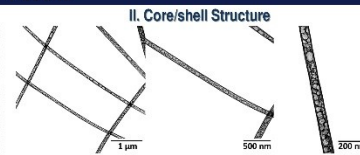
**Shell solution:** 3% w/v of 80:20 w/w Chitosan (85/100) : PEO (900,000 g/mol) + 15% w/w 5-chloro-8-quinoline (5CLO8Q) in 50% aqueous Acetic acid.



## Results



SEM micrographs (2 kV accelerating voltage, 8 nm Gold) of the electrospun nanofibers. (a.) Nylon-6 PHMB, (b.) Chitosan 5CLO8Q and (c.) Core/shell Nylon-6 PHMB / Chitosan 5CLO8Q.

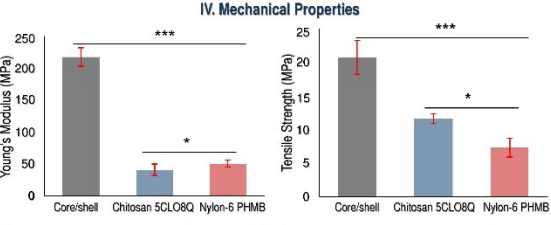


TEM micrographs (80 kV accelerating voltage) of the Nylon-6 PHMB / Chitosan 5CLO8Q electrospun antimicrobial nanofibers.

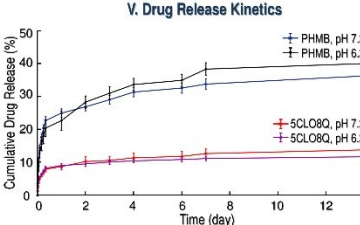
### III. Surface Chemistry

Atom %	C1s	N1s	O1s
Nylon-6	76	12	12
Chitosan	65	3	32
Core/shell	66	4	30

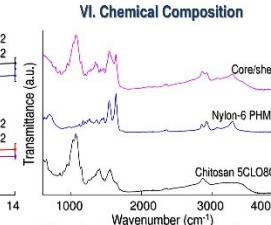
XPS analysis of the electrospun mats, C1s (284 eV), N1s (398 eV) and O1s (531 eV).



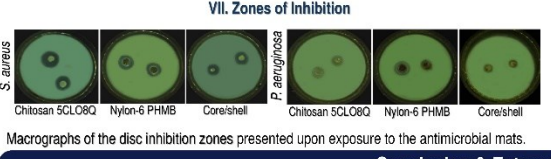
Stress/strain tensile testing of Chitosan 5CLO8Q (red), Nylon-6 PHMB (blue) and Core/shell (grey) nanofibrous electrospun mats. Error bars = standard deviations, \*\*\* p<0.001 and \*p<0.05.



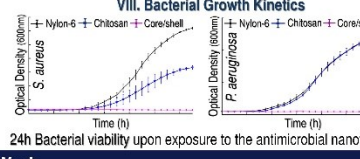
Binary non-Fickian drug release mechanism. Core (Nylon-6 PHMB) / shell (Chitosan 5CLO8Q) at pH 7.2 and 6.2.



FTIR of the electrospun mats. Spectral Resolution 2 cm<sup>-1</sup>, average of 32 scans.



Macrophgraphs of the disc inhibition zones presented upon exposure to the antimicrobial mats.



24h Bacterial viability upon exposure to the antimicrobial nanofibers.

### IX. Core/shell Nanofibers Overview

Fiber diameter:	270 ± 68 nm
Porosity:	80 ± 4.4 %
Water contact angle:	49.8 ± 7.6°
Melting temperature:	214 °C
Glass transition:	226 °C
Decomposition onset:	285 °C

Key properties of the composite fibers.

## Conclusion & Future Work

The **binary antimicrobial system** presented sustained drug release and strong bactericidal activity, **eradicating** the growth of the two model microbial pathogens. **This study adverts** the potential of the co-axial electrospinning technique for the development of a core/shell structure that unites the unique properties of chitosan and nylon-6 for the development of a mechanically, thermochemically and physiologically superior composite construct. **Future directions** will emphasize on the integration of this novel dynamically functioning core/shell Nylon-6 PHMB/Chitosan 5CLO8Q system with Polypropylene hernia meshes (the most commonly used mesh on the market), by directly electrospinning a layer of antimicrobial fibers on the hernia mesh's macroporous surface.

## References

1. Dzekan, C. R. et al. Mechanical properties of the abdominal wall and biomaterials utilized for hernia repair. J. Mechanical Behavior of Biomedical Materials (2017).
2. Scientific Committee on Consumer Safety, Opinion on Polyaminopropyl Biguanide (PHMB). Submission N° [J]. Editorial Publications Office of the European Union (2015).
3. Soyunova N. et al. Poly(L-lactide) and poly(D,L-lactide) immiscible blends to biologically active materials [J]. Materials Science and Engineering C (2014).



Corresponding author:  
a.keirouz@ed.ac.uk

Tony Keirouz



THE UNIVERSITY of EDINBURGH  
 School of Engineering  
 Research Conference 2019  
 John McIntyre Conference Centre



Empa

Materials Science and Technology

# BioMedEng19

## Nylon-6/Chitosan core/shell nanofibers with spatially controlled release of antimicrobials for the prevention of surgical site infection on hernia meshes

A. Keirouz<sup>1,2</sup>, N. Radacsi<sup>1</sup>, R.Z. Qun<sup>2</sup>, R. René<sup>2</sup>, G. Fortunato<sup>2</sup>

<sup>1</sup>The School of Engineering, Institute for Materials and Processes, The University of Edinburgh, Robert Stevenson Road, Edinburgh, EH9 3FB, U.K.

<sup>2</sup>Empa, Swiss Federal Laboratories for Materials Science and Technology, Laboratory for Biomimetic Membranes and Textiles, St. Gallen, CH-9014, Switzerland

### Introduction

Hernia repair infection is a prevalent problem, with an increased number of cases developing postoperative surgical site infection (SSI). Traditionally, the infection is managed by surgical removal of the mesh and administration of antibiotics, which vastly increases the chances of surgical complications and hernia recurrence. Nowadays, the use of hernia meshes for hernia repair are textile-based constructs that present high mechanical strength, but lack any antimicrobial properties. **The aim** of this study was the development of a mechanically stable construct that integrates a strong antimicrobial activity, which could be integrated within a hernia mesh in a bilayer format.

### Methods

Electrospinning is a cost-effective fabrication technique for the development of non-woven nanofibrous mats. Via the co-axial electrospinning method employed in this study, it is feasible to obtain constructs that bear high surface-to-volume ratio, which can accommodate features of diverse materials, formulating structures that can elicit sustained drug release and enhanced mechanical strength (Figure 1). Chitosan (CS) was chosen as the shell polymer, due to its polycationic properties and increased biocompatibility, whereas nylon-6 (PA6) was placed in the core of the fibers to promote an enhanced mechanical integrity. The effect of a binary antimicrobial system consisting of 5-Chloro-8-quinolinol (5CLO8Q) and Poly(hexanide) (PHMB) on two model pathogenic bacteria (*S. aureus* and *P. aeruginosa*) was examined. The produced scaffolds were thoroughly characterized via SEM, TEM, FTIR, XPS, DSC, TGA, water contact angle measurements, mechanical testing, drug release studies, fluorescence microscopy, bacteria inhibition and kinetic studies.

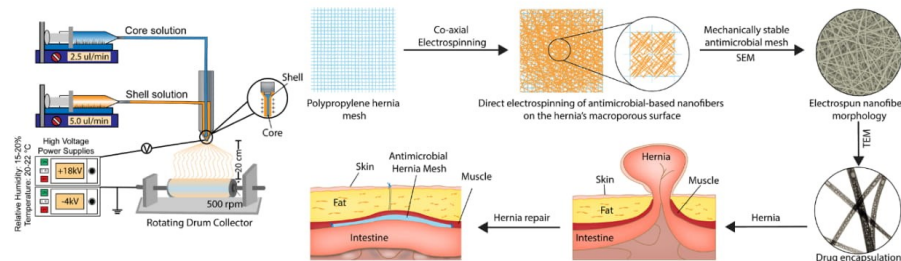


**Figure 1.** Schematic representation of the contemplated approach for the development of antimicrobial hernia meshes via co-axial electrospinning of Nylon-6 PHMB / Chitosan- 5CLO8Q.

### Results & Discussion

The developed core/shell fibers presented a homogenous morphology with average fiber diameters of  $270 \pm 68$  nm, and an increased hydrophilic surface as oppose to the counterpart fibers produced. TEM analysis omdcated a discontinuous phase of Nylon-6 in the core of the fibers. FTIR and XPS, displayed the presence of both polymers in the final construct and confirmed the existence of chitosan in the shell of the structure. The composite fibers presented a quadrupled Young modulus at  $217.5 \pm 12.6$  MPa and a doubled tensile strength at  $20.7 \pm 2.5$  MPa, as oppose to the single polymer containing fibers. A complementary antimicrobial system, which followed a non-Fickian drug release mechanism, relating to the properties of the chitosan present in the shell of the fibers was observed. The polycationic effect of the two bactericidal agents was confirmed through the establishment of a coherent antimicrobial activity against both Gram (+) and (-) bacterial strains.

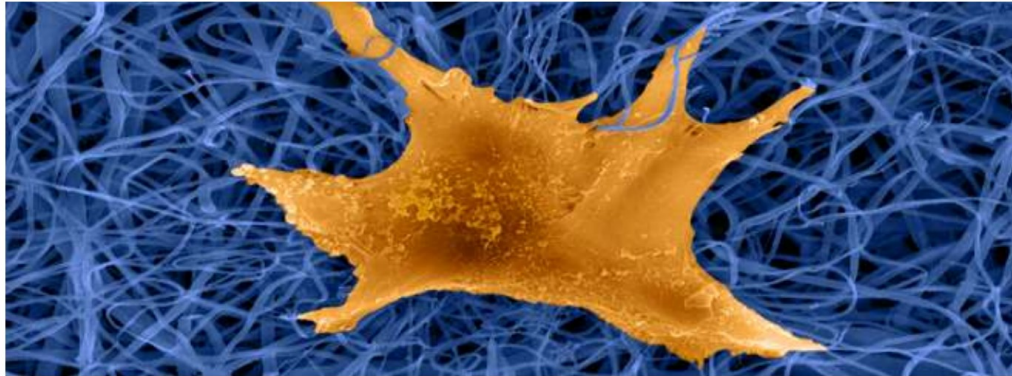
### Conclusion

The binary antimicrobial system presented sustained drug release and strong bactericidal activity, eradicating the growth of the two model microbial pathogens. This study adverts the potential of the co-axial electrospinning technique for the development of a core/shell structure that unites the unique properties of chitosan and nylon-6 for the development of a mechanically, thermochemically and physiologically superior composite construct. Future directions will emphasize on the integration of this novel dynamically functioning core/shell Nylon-6 PHMB/Chitosan 5CLO8Q system with Polypropylene hernia meshes (the most commonly used mesh on the market), by directly electrospinning a layer of antimicrobial fibers on the hernia mesh's macroporous surface.

## ADVANCED SCIENCE NEWS

### How can bioinspired nanofibers regenerate skin and aid wound healing?

*Electrospinning is an emerging fabrication technology that holds great promise in advancing skin tissue engineering and in developing an array of novel therapies.*



Electrospinning is an emerging fabrication technology that has attracted a lot of attention in recent years in fields ranging from medicine and tissue engineering to energy and environmental science due to the ease of producing well-defined, fibrous woven or non-woven materials. The process begins when a polymer solution or melt is exposed to a high electric field that causes it to deform and spin, and manipulates it to very fine meshes of micro/nanostructured fibers.

The constant advancement and unfolding of such material, along with the beneficial features of nanoscale structures, have made them eligible candidates of interest for the progress and development of an array of therapies.

Researchers from the University of Edinburgh and the Swiss Federal Laboratories for Materials Science and Technology (Empa) explore the possibilities that electrospinning holds for skin tissue engineering in a recent review published in WIREs Nanomedicine and Nanotechnology.

When a wound occurs, a dynamic series of highly coordinated physiochemical events promote repair and reinstate its functionalities. If the injury or burn is excessive or the patient suffers from a chronic (non-healing, persistent) wound due to e.g., underlying type II diabetes, managing and controlling the outcome of the damaged area remains a challenge for clinicians today. Electrospun nanostructured filaments can inspire the development of a healthy extracellular matrix, where manipulation of their properties can aid the wound healing process and trigger a more prompt recovery.

Researchers around the globe are working tirelessly to bring forward discoveries derived from this fabrication technology. Not only can electrospinning help burn patients, but it can also facilitate drug delivery and skin cancer related on-site treatment. The current and forthcoming developments centering around manipulating the unique properties of these nanoscaled filaments will facilitate an optimized performance, and will offer answers to important issues faced by clinicians in wound management.

Antonios Keirouz, lead author of this study, indicated that: "The constant evolvement and rapid advancements of this field will propel the already present innovative ideas towards fast-track clinical translation, giving rise to nanostructured products that can directly have a positive impact to the patients' outcomes."

Michael Chung, who investigated the progress of the electrospinning technology in the development of three-dimensional polymeric scaffolds, added: "Novel techniques are continuously emerging and advancing to establish greater geometrical control over 3D nanofibrous scaffold assembly. 3D materials made by electrospinning are not only constantly improving in their skin-mimicking capabilities but also fabrication is becoming more cost- and time-effective."

In an ongoing clinical trial running on spray painting fibers directly onto the wound, using a hand-held device — which can reduce pain and peel off after the area is healed — to advanced drug delivery bandages that can modulate and adapt the release of substances on-site, the advancements of recent fabrication approaches of three-dimensional nanofiber-based materials will lead the future of modeling skin-material interactions.

Dr. Norbert Radacsi, Assistant Professor and manager of the NanoMaterials Laboratory of the School of Engineering at the University of Edinburgh, said: "Portable, hand-held electrospinning devices and the combination of electrospinning with 3D printing are important milestones for skin tissue engineering as these new techniques enable the clinical applications of electrospinning technology for patient care."

His collaborator, Dr. Giuseppino Fortunato project leader and senior scientist at the Laboratory for Biomimetic Membranes and Textiles at Empa, who has spent a vast part of his research career investigating and improving the applications of electrospun nanofibrous materials, added, "There is still space for technological improvements of the electrospinning procedures with respect to skin tissue engineering, e.g., to allow for improved cell adhesion, to improve the rate of neovascularization or for scaffold materials to resist wound contraction and fibrosis."

This rapid and constant progress of the electrospinning field, making the production of such nanomaterials all the more pragmatic while considering the affordability of this process, will have a real positive effect and play critical roles in the future of wound management.

Reference: A. Keirouz, et al. '2D and 3D electrospinning technologies for the fabrication of nanofibrous scaffolds for skin tissue engineering: A review', WIREs Nanomedicine & Nanobiotechnology (2020). DOI: 10.1002/wnan.162

Source: <https://www.advancedsciencenews.com/how-can-bioinspired-nanofibers-regenerate-skin-and-aid-wound-healing/>

---

# Appendix C

## Grafting PHMB on O-Carboxymethylated Chitosan

---

### Carboxymethylation of chitosan

Chitosan (degree of de-acetylation 85/100) was first O-carboxymethylated (O-CMCS), the procedure of which, is outlined here. First, chitosan (10 g) was dissolved with sodium hydroxide (27 g) in water (200 mL). The solution was left for 24 h at -20 °C to swell and alkalis. Then, monochloroacetic acid (30 g) in isopropanol (40 mL) was added dropwise for 30 min and reacted at 50 °C for 7 h. After stopping the reaction by the addition of absolute ethanol (20 mL), the resultant product was separated by filtration in ethanol 70% (v/v) and dehydrated in absolute ethanol. The primary product of the CMCS sodium salt (CSMS-OCH<sub>2</sub>COONa) was converted into its acid form by protonation in 32% (v/v) HCl(ac). The resultant suspension was collected by filtration (Cola-Palmer filtration centrifugal tubes) and centrifuged for 20 min at 5000 rpm. The process was based on two previously published protocols [1, 2]. The reaction scheme is shown in Figure C-1. Experiments carried out in later stages were conducted using O-CMCS purchased from Santa Cruz Biotechnology (CAS 83512-85-0).

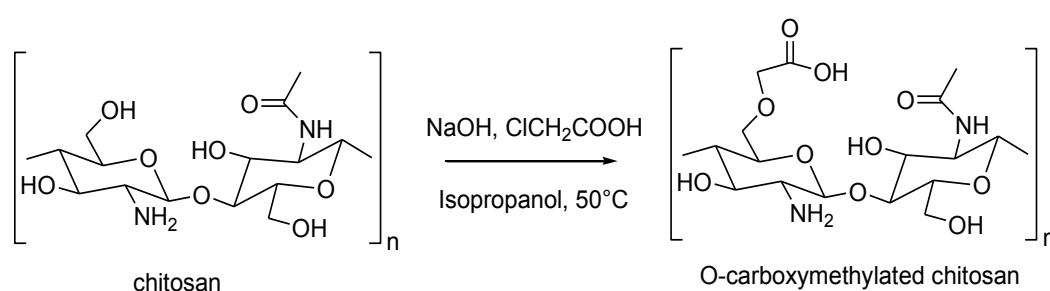


**Figure C-1** Reaction scheme of O-carboxymethylation of chitosan at C-2.

## CS-g-PHMB grafting using EDC/sulfo-NHS amide coupling

Firstly, 10 mg·mL<sup>-1</sup> O-CMCS were dissolved in 0.1 M MES [2-(N-morpholino)ethane sulfonic acid] buffer (pH 4.7-6.0) to achieve complete solubilisation of the polymer. The solution was mixed thoroughly at room temperature, and EDC [1-(3-dimethylaminopropyl)-N'-ethylcarbodiimide hydrochloride] was added to the resultant solution. EDC's final concentration was at a ten-fold molar excess in relation to the O-CMCS. This allowed for the formation of an unstable ester intermediate between the carboxylic acid at C-2 of the O-CMCS molecule and the EDC crosslinker. Then, sulfo-NHS (sulfo-N-hydroxysuccinimide) was added to the reaction medium until a final concentration of 5 mM was reached. The proportion of [EDC : sulfo-NHS] was maintained at 1:1 M. sulfo-NHS was chosen over NHS to increase the solubility of the carboxylate molecule and to retard its rapid hydrolysis.

Then, PHMB was dissolved in the same buffer employed for the dissolution of the O-CMCS. The final concentration of PHMB was determined based on the degree of substitution as described in the *Additional methodology information* section below. The subsequent reaction was left for 24 h at room temperature under magnetic stirring. The MES buffer was adjusted with PBS to increase the pH to 7-8. The reasoning behind the reaction been uninterrupted for an extended period is because successful conjugation is dependent on the PHMB's nucleophilicity, which is relatively "low" due to nitrogen electron pair conjugation. This allowed for a stable amide conjugate to form, referred to as PHMB-g-CMCS, between the amine-reactive Sulfo-NHS ester and the PHMB amine. The resultant product was purified dropwise in ethanol, subsequently centrifugated and filtered. The reaction scheme is summarised in Figure C-2 below.

The final product was assessed with FTIR and Nuclear magnetic resonance (NMR). The results from the NMR of the grafted polymer were deemed inconclusive due to the poor solubility of the product in DMF, and the NMR spectrum presenting traits of non-reacted O-CMCS.

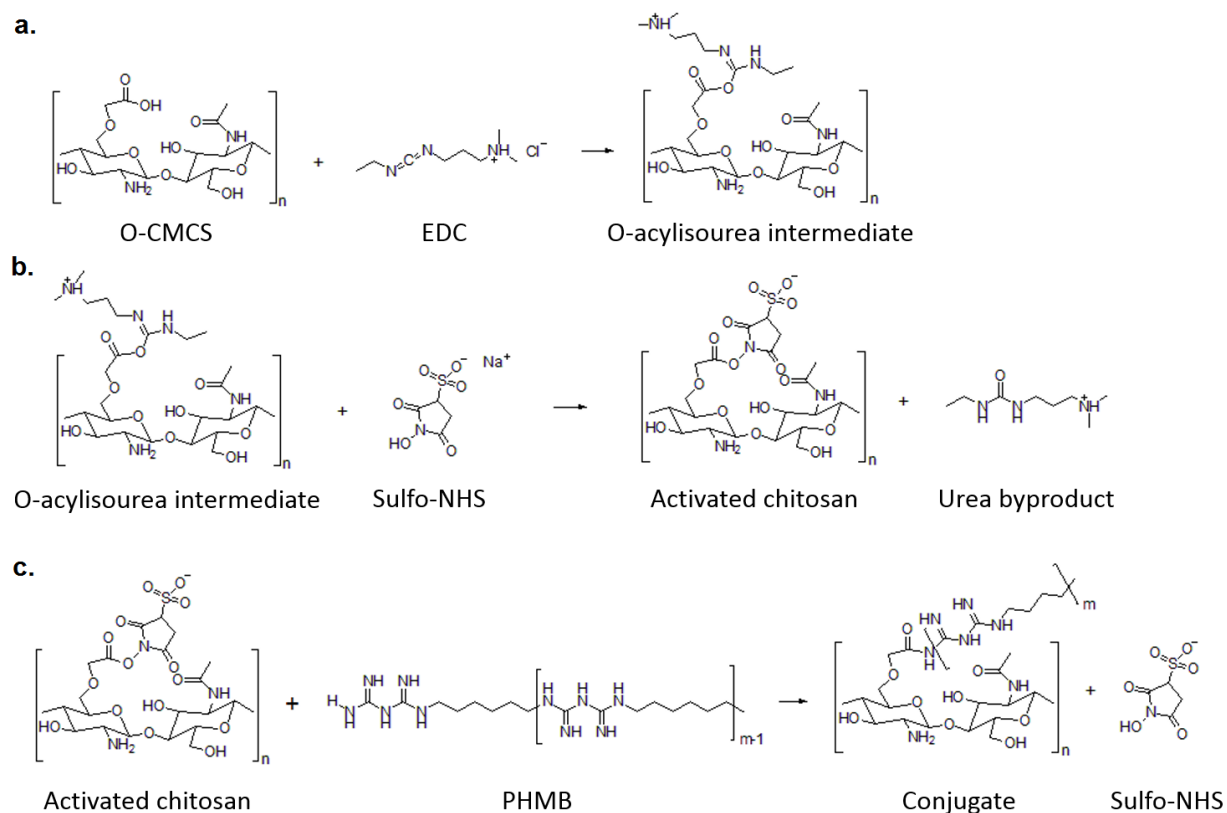


**Figure C-2** The reaction scheme summarises the grafting PHMB on O-Carboxymethylated chitosan (O-CMCS) using EDC/sulfo-NHS chemistry. **(a)** A nitrogen atom from the EDC's carbodiimide group subtracts the hydrogen from the carboxyl present in the O-CMCS polymer. The resultant carboxylate attacks the nitrogen atom (which bears a partial positive charge) from the carbodiimide group, resulting in the O-acylisourea intermediate observed in the first step of the reaction scheme. **(b)** The intermediate product then reacts with the NHS to form an active ester through the nucleophilic attack of the hydroxyl present in the NHS's carbonyl group. **(c)** This results in the activated amine sulfo-NHS-chitosan ester complex, which is capable to efficiently react with the amine of the PHMB forming a stable amide at the conjugate structure.



## Additional methodology information

Information about the suppliers and materials used can be found in Table 3.2, in *Section 3.3.4 Stock chemicals, reagents, cells and equipment*.

$$MW_{(O-CMCS)} = 100,000 - 300,000 \text{ g}\cdot\text{mol}^{-1}, MW_{(O-CMCS)_n} = 249.12 \text{ g}\cdot\text{mol}^{-1} (\text{C}_{10}\text{H}_{19}\text{NO}_6)_n$$

$$MW_{(PHMB)} = 213.33 \text{ g}\cdot\text{mol}^{-1} (\text{C}_8\text{H}_{17}\text{N}_5)_n, MW_{(\text{Sulfo-NHS})} = 217.13 \text{ g}\cdot\text{mol}^{-1}, MW_{(\text{EDC})} = 115.09 \text{ g}\cdot\text{mol}^{-1}$$

To dissolve 0.125 g of O-CMCS in 10 mL of PBS or MES 0.1 M:

$$m_{(O-CMCS)} = \frac{0.125 \text{ g}}{249.12 \text{ mol}^{-1}} = 0.0005 \text{ mole}$$

$$m(\text{PHMB}) = 0.002 \times 213.33 = 0.4266 \text{ g}$$

To make a 1:1 M ratio: [O-CMCS: sulfo-NHS]  $\rightarrow 1 < n \rightarrow m_{\text{sulfo-NHS}} = m_{(O-CMCS)} \times MW_{(\text{Sulfo-NHS})}$ , which can then be precipitated in polar protic solvents.

To prepare 0.1 M phosphate-buffered saline (pH 7.4): Dissolve 21.324 g  $\text{KH}_2\text{PO}_4$  and 90.690 g  $\text{Na}_2\text{HPO}_4$  into distilled water and bring to 2 L. From this solution, 250 mL will be taken and brought to 1 L to prepare 0.1 M PBS.

To prepare 0.1 M MES buffer (pH 5.0): Dissolve 21.3 g of MES monohydrate in 900 mL of water. Add 1 M NaOH solution until pH 5 is brought to 1 L.

## Solution preparation and electrospinning

The conjugated CS-g-PHMB polymer (240 mg) was dissolved with 40 mg of PEO  $900,000 \text{ g}\cdot\text{mol}^{-1}$  in 5 mL of acetic acid 10% (v/v) in distilled water under magnetic stirring in room temperature. The polymer solution was then electrospun in a controlled temperature/humidity chamber. The relative humidity was kept at 20% and the temperature at 20 °C. A parametric study was conducted to determine the most stable electrospinning conditions and the corresponding morphology of the produced fibres. The parametric study is summarised in Table C-1. SEM micrographs of the NFs produced under the optimised electrospinning conditions are shown in Figure C-3.

**Table C-1** Parametric study assessing the stability of the Taylor cone during electrospinning and the fibre morphology of the final product electrospun using the CS-g-PHMB/PEO in 10% (v/v) AcOH solution. The potential difference values represent (+) kV for the nozzle-tip and (-) kV for the flat collector's surface. Working distance refers to the distance of the electrospinning path; from the nozzle-tip to the surface of the collector. Needle inner diameter: 21G is 0.71 mm, 22G is 0.64 mm, 23G is 0.58 mm, 27G is 0.361 mm and 30G is 0.25 mm.

Potential difference (kV)	Working distance (cm)	Flow rate ( $\mu\text{L}\cdot\text{min}^{-1}$ )	Needle Gauge (G)	Fibre diameter (nm)	Observations during electrospinning and general remarks
+8/-3	15	10	22	No	Unstable Taylor cone
+12/-3	15	10	22	no	Unstable Taylor cone
+12/-3	15	5	22	150 $\pm$ 36	Solidifies at the tip on extrusion and merged fibre morphology
+8/-2	15	5	22	156 $\pm$ 21	Solidifies at the tip on extrusion and merged fibre morphology
+10/-5	15	5	22	173 $\pm$ 25	Unstable Taylor cone
+10/-5	20	5	22	191 $\pm$ 30	Unstable Taylor cone
+15/-5	20	5	21	161 $\pm$ 24	Stable Taylor cone, homogeneous fibre morphology
+15/-5	20	10	23	215 $\pm$ 31	Stable Taylor cone, homogeneous fibre morphology
+15/-5	20	20	23	172 $\pm$ 23	Unstable Taylor cone, beaded fibre morphology
+15/-5	20	10	27	159 $\pm$ 29	Stable Taylor cone, secondary fibre morphologies
+15/-5	20	20	27	180 $\pm$ 32	Stable Taylor cone, but not homogenous "wet" fibres
+15/-5	20	20	30	178 $\pm$ 17	Stable Taylor cone, very homogenous fibers
+15/-5	20	15	27	177 $\pm$ 20	Stable Taylor cone, homogeneous fibres with no secondary morphologies (and a smooth fibre surface structure)

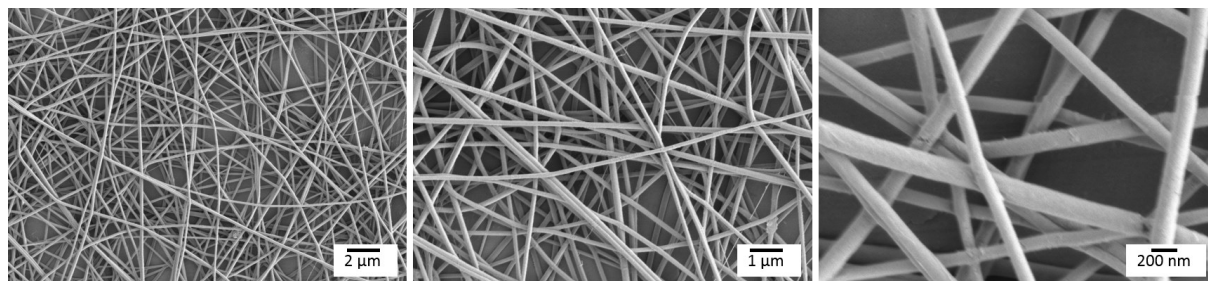


**Figure C-3** SEM micrographs of CS-g-PHMB/PEO electrospun NFs produced using a conventional electrospinning device at +15/-5 kV, 20 cm working distance,  $15 \mu\text{l}\cdot\text{min}^{-1}$ , using a 27G needle. Average fibre diameter of  $177 \pm 20 \text{ nm}$ .

### FTIR analysis of the synthesised CS-g-PHMB

The Figure C-4 below shows the FTIR spectra obtained for the O-CMCS, the PHMB, and the synthesised CS-g-PHMB. The peaks at  $1484 \text{ cm}^{-1}$  and  $1589 \text{ cm}^{-1}$  of the O-CMCS spectrum can be attributed to the  $\text{COO}^-$  group symmetric and asymmetric stretching vibrations, respectively. The strong peak at  $1589 \text{ cm}^{-1}$  could also overlap with the deforming  $\text{NH}_2$  vibration. At  $1052 \text{ cm}^{-1}$  the absorption peak of the secondary -OH can be observed. Where the cluster band forming at approximately  $1150 \text{ cm}^{-1}$  represents the various C-O-C stretching vibrations of the sugar ring. The successful synthesis of O-CMCS at C-2, comes into agreement with previously published research [3, 4].

In the PHMB spectrum, the biguanide structure can be identified with the characteristic C-H and C-C vibrations at  $2320 \text{ cm}^{-1}$  and  $2355 \text{ cm}^{-1}$ , respectively. Additionally, the intense peak at  $1537 \text{ cm}^{-1}$  and  $1650 \text{ cm}^{-1}$  can be attributed to the -OH stretching and -NH bend vibrations, respectively. Whereas the peaks at  $1435 \text{ cm}^{-1}$  and  $1463 \text{ cm}^{-1}$  are associated with the -CN stretching of the primary amine/methylene combination (-NH/-CH) and the secondary amine, respectively. Finally, the strong peak at  $2847 \text{ cm}^{-1}$  and the peak at  $3290 \text{ cm}^{-1}$  could be attributed to -NH stretching vibrations, where the defined peak at  $3129 \text{ cm}^{-1}$  is attributed to the -CH stretching of the methylene tail. This FTIR spectrum is in agreement with previously published work [5].

The ester on the activated chitosan and the primary amine of the PHMB have reacted to form an amide observed with a strong peak at  $1690 \text{ cm}^{-1}$ , corresponding to the C=O stretching of the primary amide. The broad peaks at approximately  $3300 \text{ cm}^{-1}$  – which is not present in the PHMB and CS molecules – could be attributed to -NH stretching in the conjugated structure. The remainder of the peaks of both CS and PHMB, appear to be present in the conjugated structure but with more intense peaks, possibly due to hydrogen bonding and a

variation at the size of the conjugated polymer. Finally, the CS-g-PHMB spectrum appears to be slightly shifted towards higher frequencies for the lower wavenumber regions (1000 – 1800  $\text{cm}^{-1}$ ) compared to the PHMB and O-CMCS spectra.

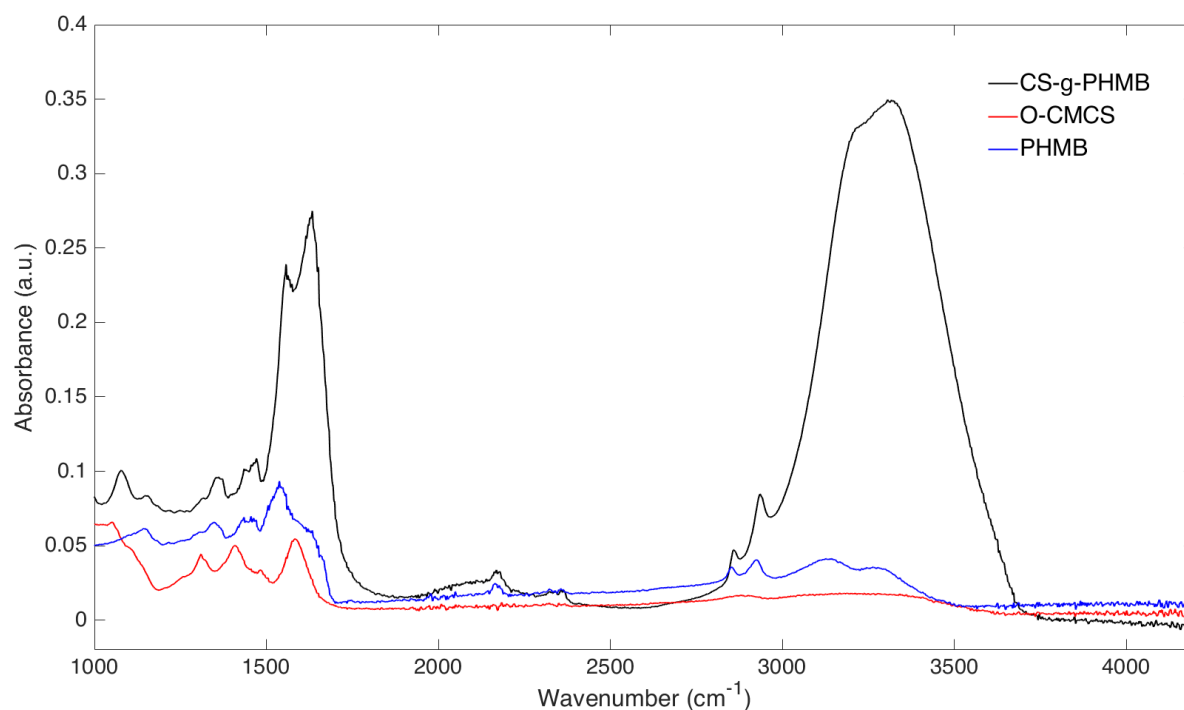


**Figure C-4** FTIR spectra of the PHMB and O-CMCS pristine powders, and the CS-g-PHMB conjugated polymer. FTIR was performed on oven-dried samples using an FTIR spectrophotometer (Varian 640-IR, Varian Medical Systems, USA). The measurements were carried out using the ATR-crystal mode in the mid-infrared scanning range of 4200–800  $\text{cm}^{-1}$  with a spectral resolution of 2  $\text{cm}^{-1}$ . The spectra above represent the average of 126 scans to enhance the signal-to-noise ratio.

## Conclusion

The preliminary work presented in this Appendix flourishes from the research conducted in Chapter 6 of this thesis. As previously observed in this thesis, the robust effect of the PA6-PHMB/CS-5CLO8Q core/shell NFs relied on the release of the antimicrobial substances from the bicomponent NFs. The importance of this relies on the concept that by placing the biguanide groups of the PHMB in the surface of the CS fibres, we can attain a surface structure that can kill bacteria on contact. This would be a non-antibiotic-based approach that could ultimately prevent bacteria from adhering to surfaces and prevent colonisation and subsequent infection.

Nevertheless, it is important to note that these data are preliminary and further work needs to be conducted to better determine the reproducibility of the process and the reliability of the grafting protocol under different conditions before being able to draw any definite conclusions. If the protocol deems to be highly consistent, additional work needs to be performed to establish the mechanical stability and physical properties of the subsequent electrospun fibres, and determine whether the antimicrobial effect is still present, and to what extent, post-grafting. This would be an interesting alternative approach, as oppose to drug-eluting nanofibres, which could elicit permanent antimicrobial protection that can prevent mesh-related surgical site infections while minimising potential toxicity due to the release of the antimicrobial substance in the surrounding tissue, over an extended period. However, upon implementation, surface proteins could entrap and coat the structure of the material and thus reduce its bactericidal properties. Additionally, an examination of the by-products and the degradation rate of the grafted compound will need to be further evaluated if developing a bioabsorbable hernia mesh. The proof of principle work conducted here, describing the grafting of the polycationic molecule, PHMB, in the surface of chitosan is described for the first time in literature.

## References

1. Zheng, M., Han, B., Yang, Y., & Liu, W. (2011). Synthesis, characterization and biological safety of O-carboxymethyl chitosan used to treat Sarcoma 180 tumor. *Carbohydrate Polymers*, *86*(1), 231–238. <https://doi.org/10.1016/j.carbpol.2011.04.038>
2. Liu, X. F., Guan, Y. L., Yang, D. Z., Li, Z., & Yao, K. De. (2001). Antibacterial action of chitosan and carboxymethylated chitosan. *Journal of Applied Polymer Science*, *79*(7), 1324–1335. [https://doi.org/10.1002/1097-4628\(20010214\)79:7<1324::AID-APP210>3.0.CO;2-L](https://doi.org/10.1002/1097-4628(20010214)79:7<1324::AID-APP210>3.0.CO;2-L)
3. Zhong, Q. K., Wu, Z. Y., Qin, Y. Q., Hu, Z., Li, S. D., Yang, Z. M., & Li, P. W. (2019). Preparation and properties of carboxymethyl chitosan/alginate/tranexamic acid composite films. *Membranes*, *9*(1), 1–7. <https://doi.org/10.3390/membranes9010011>
4. Farag, R. K., & Mohamed, R. R. (2013). Synthesis and characterization of carboxymethyl chitosan nanogels for swelling studies and antimicrobial activity. *Molecules*, *18*(1), 190–203. <https://doi.org/10.3390/molecules18010190>
5. De Paula, G. F., Netto, G. I., & Mattoso, L. H. C. (2011). Physical and chemical characterization of poly(hexamethylene biguanide) hydrochloride. *Polymers*, *3*(2), 928–941. <https://doi.org/10.3390/polym3020928>